

**APPLIED
COMPUTATIONAL
ELECTROMAGNETICS
SOCIETY
JOURNAL**

June 2021
Vol. 36 No. 6
ISSN 1054-4887

The ACES Journal is abstracted in INSPEC, in Engineering Index, DTIC, Science Citation Index Expanded, the Research Alert, and to Current Contents/Engineering, Computing & Technology.

The illustrations on the front cover have been obtained from the research groups at the Department of Electrical Engineering, The University of Mississippi.

THE APPLIED COMPUTATIONAL ELECTROMAGNETICS SOCIETY

<http://aces-society.org>

EDITORS-IN-CHIEF

Atef Elsherbeni

Colorado School of Mines, EE Dept.
Golden, CO 80401, USA

Sami Barmada

University of Pisa, ESE Dept.
56122 Pisa, Italy

ASSOCIATE EDITORS

Mohammed Hadi

Kuwait University, EE Dept.
Safat, Kuwait

Alistair Duffy

De Montfort University
Leicester, UK

Wenxing Li

Harbin Engineering University
Harbin 150001, China

Maokun Li

Tsinghua University
Beijing 100084, China

Mauro Parise

University Campus Bio-Medico of Rome
00128 Rome, Italy

Yingsong Li

Harbin Engineering University
Harbin 150001, China

Riyadh Mansoor

Al-Muthanna University
Samawa, Al-Muthanna, Iraq

Lijun Jiang

University of Hong Kong, EEE Dept.
Hong, Kong

Shinichiro Ohnuki

Nihon University
Tokyo, Japan

Kubilay Sertel

The Ohio State University
Columbus, OH 43210, USA

Antonio Musolino

University of Pisa
56126 Pisa, Italy

Abdul A. Arkadan

Colorado School of Mines, EE Dept.
Golden, CO 80401, USA

Salvatore Campione

Sandia National Laboratories
Albuquerque, NM 87185, USA

Wei-Chung Weng

National Chi Nan University, EE Dept.
Puli, Nantou 54561, Taiwan

Alessandro Formisano

Seconda Università di Napoli
81031 CE, Italy

Piotr Gas

AGH University of Science and Technology
30-059 Krakow, Poland

Long Li

Xidian University
Shaanxa, 710071, China

Steve J. Weiss

US Army Research Laboratory
Adelphi Laboratory Center (RDRL-SER-M)
Adelphi, MD 20783, USA

Jiming Song

Iowa State University, ECE Dept.
Ames, IA 50011, USA

Maokun Li

Tsinghua University, EE Dept.
Beijing 100084, China

Atif Shamim

King Abdullah University of Science and Technology (KAUST)
Thuwal 23955, Saudi Arabia

Marco Arjona López

La Laguna Institute of Technology
Torreon, Coahuila 27266, Mexico

Paolo Mezzanotte

University of Perugia
I-06125 Perugia, Italy

Luca Di Rienzo

Politecnico di Milano
20133 Milano, Italy

Lei Zhao

Jiangsu Normal University
Jiangsu 221116, China

Sima Noghianian

Wafer LLC
Beverly, MA 01915, USA

Qiang Ren

Beihang University
Beijing 100191, China

Nunzia Fontana

University of Pisa
56122 Pisa, Italy

Stefano Selleri

DINFO – University of Florence
50139 Florence, Italy

Amedeo Capozzoli

Univerita di Napoli Federico II, DIETI
I-80125 Napoli, Italy

Yu Mao Wu

Fudan University
Shanghai 200433, China

EDITORIAL ASSISTANTS

Matthew J. Inman

University of Mississippi, EE Dept.
University, MS 38677, USA

Shanell Lopez

Colorado School of Mines, EE Dept.
Golden, CO 80401, USA

EMERITUS EDITORS-IN-CHIEF

Duncan C. Baker

EE Dept. U. of Pretoria
0002 Pretoria, South Africa

Allen Glisson

University of Mississippi, EE Dept.
University, MS 38677, USA

Ahmed Kishk

Concordia University, ECS Dept.
Montreal, QC H3G 1M8, Canada

Robert M. Bevensee

Box 812
Alamo, CA 94507-0516, USA

Ozlem Kilic

Catholic University of America
Washington, DC 20064, USA

David E. Stein

USAF Scientific Advisory Board
Washington, DC 20330, USA

EMERITUS ASSOCIATE EDITORS

Yasushi Kanai

Niigata Inst. of Technology
Kashiwazaki, Japan

Alexander Yakovlev

University of Mississippi, EE Dept.
University, MS 38677, USA

Levent Gurel

Bilkent University
Ankara, Turkey

Mohamed Abouzahra

MIT Lincoln Laboratory
Lexington, MA, USA

Ozlem Kilic

Catholic University of America
Washington, DC 20064, USA

Erdem Topsakal

Mississippi State University, EE Dept.
Mississippi State, MS 39762, USA

Sami Barmada

University of Pisa, ESE Dept.
56122 Pisa, Italy

Fan Yang

Tsinghua University, EE Dept.
Beijing 100084, China

Rocco Rizzo

University of Pisa
56123 Pisa, Italy

William O'Keefe Coburn

US Army Research Laboratory
Adelphi, MD 20783, USA

EMERITUS EDITORIAL ASSISTANTS

Khaled ElMaghoub

Trimble Navigation/MIT
Boston, MA 02125, USA

Kyle Patel

Colorado School of Mines, EE Dept.
Golden, CO 80401, USA

Christina Bonnington

University of Mississippi, EE Dept.
University, MS 38677, USA

Anne Graham

University of Mississippi, EE Dept.
University, MS 38677, USA

Madison Le

Colorado School of Mines, EE Dept.
Golden, CO 80401, USA

Allison Tanner

Colorado School of Mines, EE Dept.
Golden, CO 80401, USA

Mohamed Al Sharkawy

Arab Academy for Science and Technology, ECE Dept.
Alexandria, Egypt

JUNE 2021 REVIEWERS

**Ali Al-Azza
Stamatios Amanatiadis
AmirNader Askarpour
Sami Barmada
Zhe Chen
Burak Dokmetas
Nebojsa Doncov
Ozgur Ergul
Piotr Gas
Christian Hearn
Niamat Hussain
Tianqi Jiao
Fatih Kaburcuk
Ankush Kapoor
Yue Li
Yingsong Li
Nanda M.
Farzad Moradiannejad
Subhashini Neelamegam
Yoginder Negi
Lan Nguyen
Kingsford Obeng Kwakye
Elangovan P.
Panagiotis Papakanellos
Marcelo Perotoni
Lionel Pichon
Dudla Prabhakar**

**Zbynek Raida
Saman Rajebi
N. RajeshKumar
Rengasamy Rajkumar
Luis Ramirez
Lingyun Ren
Qiao Ren
Nitin Saluja
Luca Sani
NVSN Sarma
Stefano Selleri
Meriah Sidi Mohammed
Manuel Sierra Castañer
Ashish Singh
Kwok Kan So
Wanchun Tang
Alireza Tavousi
Dattaprasad Torse
Christopher Trueman
Lu Wang
Steven Weiss
Wei-Chung Weng
Qi Wu
Qingfeng Zhang
Fan Zhang
Lei Zhao
Yong Jin Zhou**

TABLE OF CONTENTS

Computational Performance of GTD-RT Applied for Evaluation of Electromagnetic Scattering on Rough Surfaces
Asmaa E. Farahat and Khalid F. A. Hussein.....610

Interpretation Method of GATEM Data based on PID Controller Iteration Downward Continuation Method
Shanshan Guan, Bingxuan Du, Dongsheng Li, Yuan Wang, Yu Zhu, Qiong Wu, and Yanju Ji.....622

The Behavior of Electromagnetic Wave Propagation in Photonic Crystals with or without a Defect
Ayse N. Basmaci632

A Modified Hybrid Integral Equation to Electromagnetic Scattering from Composite PEC-Dielectric Objects Containing Closed-Open PEC Junctions
Jinbo Liu, Hongyang Chen, Hui Zhang, Jin Yuan, and Zengrui Li642

Gain Enhancement Planar Lens Antenna based on Wideband Focusing Gradient Meta-surface
Qiming Yu, Shaobin Liu, Zhengyu Huang, Xiangkun Kong, Yuehong Hu, and Yongdiao Wen650

Design of Microstrip Parallel-Coupled Lines with High Directivity using Symmetric-Centered Inductors
Somchat Sonasang and Niwat Angkawisittpan.....657

Compact Dual-Passband Three-Dimensional FSS with Good Angular Stability and Both-Side Fast Roll-Off Characteristics
Zhengyong Yu, Baozhu Li, Shenggao Ding, and Wanchun Tang664

Development and Verification of Indirect Lightning-Induced Transient Protection Circuit for Avionics System
Sung-Yeon Kim, Jeong-Su Park, and Wang-Sang Lee.....670

Tunable Terahertz Plasmon-Induced Transparency in Resonator-Coupled Dirac Semimetal Waveguides
Daobin Wang, Jiahuan Yang, Wei Wang, Lihua Yuan, and Xiaoxiao Li.....676

| | |
|--|-----|
| On Electric Field Distribution and Temperature Rise Effect of High Power VLF Antenna Xianqiang Li, Kedan Mao, Ao Wang, Ji Tian, and Wenchuang Zhou | 684 |
| Design and Analysis of a Triple-band Non-zonal Polarization Electromagnetic Metamaterial Absorber Han Wu, Shijun Ji, Ji Zhao, Zhiyou Luo, and Handa Dai..... | 697 |
| Radiation Pattern Synthesis and Mutual Coupling Compensation in Spherical Conformal Array Antennas Taimur Ahmed Khan, Muhammad Irfan Khattak, and Adnan Tariq | 707 |
| Reduced Cross-Polarization Patch Antenna with Optimized Impedance Matching Using a Complimentary Split Ring Resonator and Slots as Defected Ground Structure Narayanasamy RajeshKumar, Palani D. Sathya, Sharul K. A. Rahim, and Akaa A. Eteng..... | 718 |
| Parameter Design of Conformal PML Based on 2D Monostatic RCS Optimization Yongjie Zhang and Xiaofeng Deng..... | 726 |
| Analysis and Development of an Efficient Cross-Slot Loaded Compact Electromagnetic Band Gap Antenna El Amjed Hajlaoui and Ziyad M. Almohaimeed | 734 |
| A Low-Profile Broadband Circularly Polarised Wide-Slot Antenna with an Artificial Magnetic Conductor Reflector Fangfang Fan, Xiao Fan, Xiaoyu Wang, and Zehong Yan | 740 |
| Broadband CPW-Fed Circularly Polarized Square Slot Antenna for Universal UHF RFID Handheld Reader Rui Ma and Quanyuan Feng..... | 747 |
| Ultra-wideband Flexible Implantable Antenna for Wireless Capsule Endoscopy System with Performance Improvement Yang Feng, Pan Chen, Shaopeng Pan, and Gaosheng Li..... | 755 |
| Compact 2x2 and 4x4 MIMO Antenna Systems for 5G Automotive Applications Mohamed O. Khalifa, Ahmad M. Yacoub, and Daniel N. Aloï..... | 762 |
| Complementary SRR-Based Reflector to Enhance Microstrip Antenna Performance Mustafa H. B. Ucar..... | 779 |
| Reconfigurable 2×1 CPW-Fed Rectangular Slot Antenna Array (RSAA) Based on Graphene for Wireless Communications Dalia M. Elsheakh and Osama M. Dardeer..... | 788 |

| | |
|---|-----|
| Improved Thevenin Equivalent Model of MMC Considering Pre-charge Conditions and DC Side Fault Conditions | |
| Enshu Jin, Zhenyu Song, Xiaofan Yang, and Xin Yu..... | 796 |
| Characteristic Analysis and Control of a Rotary Electromagnetic Eddy Current Brake | |
| Qiao Ren, Jimin Zhang, and Jinnan Luo | 806 |
| Modeling the Microwave Transmissivity of Row Crops | |
| Jeil Park, Praveen Gurralla, Brian K. Hornbuckle, and Jiming Song | 816 |

Computational Performance of GTD-RT Applied for Evaluation of Electromagnetic Scattering on Rough Surfaces

Asmaa E. Farahat and Khalid F. A. Hussein

Microwave Engineering Department
Electronics Research Institute, Cairo, 11843, Egypt
asmaa@eri.sci.eg, khalid_elgabaly@yahoo.com

Abstract — In this paper, a new robust computational method that applies the geometrical theory of diffraction (GTD) in conjunction with the ray tracing (RT) technique is developed to evaluate the electromagnetic scattering pattern due to a plane wave represented as beam of parallel rays incident on a rough surface of quite arbitrary statistical parameters. The development of the proposed technique is explained in detail taking into consideration the generation of the geometrical model of the rough surface. The Fresnel reflection model is applied under the assumption of arbitrary electrical and optical properties of the rough surface material. Also the polarization of the plane wave primarily incident on the rough surface is taken into consideration. The algorithm developed in the present work accounts for multiple bounces of an incident ray and, hence, it can be considered arbitrary higher-order GTD-RT technique. The accuracy of the obtained results is verified through the comparison with the experimental measurements of the scattering pattern of a light beam incident on rough sheets with specific statistical properties. The numerical results of the present work are concerned with investigating the dependence of the scattering pattern on the surface roughness, refractive index, angle of incidence, and the resolution of the geometric model of the rough surface. Also, it is shown that, for limited resolution of the rough surface model, the accuracy of the calculated scattered field depends on the angle of incidence of the primary beam and the surface roughness.

Index Terms — GTD-RT technique, polarization, random rough surfaces, scattering measurement.

I. INTRODUCTION

Studying electromagnetic (EM) scattering from random rough surfaces, especially in the visible and infrared spectral range, is of great importance for many applications and scientific research purposes. The characterization of rough surfaces through the investigation of the EM and light scattering finds wide fields of scientific research [1-8]. One of the most

important applications is the optical tomography, in which the scattering patterns for a beam incident on an objective material provide extensive information such as the surface roughness and optical properties. The characterization of the materials and devices used in VLSI manufacturing is usually accomplished by studying the light scattered from the surfaces of such constituents. Both theoretical and experimental investigation of EM scattering from rough surfaces has great importance in many scientific, commercial, and military applications such as the earth remote sensing for studying the ocean surface and the terrain at long length scales [9-11].

Some analytic and semi-analytic techniques have been proposed for evaluating the EM scattering from rough surfaces [12-26]. These include (i) the small-amplitude perturbation theory, in which the scattered field is expanded in powers of the surface profile function through linear terms, (ii) the Kirchhoff approximation, in which the scattering is treated as reflection from the plane tangent to the surface at each point, (iii) the extinction theorem in which the scattering equations, based on this theorem are solved numerically and, finally, (iv) the techniques based on the Rayleigh scattering equation. In [21], the relationship between the pattern of the scattered light and the statistical properties of the scattering surface given by Beckmann–Kirchhoff theory is utilized to measure the surface roughness through an iterative procedure proposed by inverting this relationship, to retrieve the height autocorrelation function. In [22], different ways in which light scatter can be used to measure surface roughness are described. It provides reviews of the most common types of light scattering used for this purpose. These are the angle resolved scatter and the total integrated scatter. In the first type, the light scattered in the different directions is measured and studied, but in the second type, the light scattered in all the directions except for the specular direction is measured and analyzed. In [23], the scattering of electromagnetic waves from a rough surface interface between the free space and a dielectric medium is evaluated using mathematical and numerical treatment. The boundary values of the field and its

normal derivative on the interface are obtained using the extinction theorem. Then, the angular distribution of the ensemble average of reflected and transmitted field intensities are calculated. In this method, one-dimensional profiles for the rough surface are generated through a Monte Carlo method to solve the scattering equations numerically. In [24], a numerical solution of the reduced Rayleigh equation for the scattering of light from two-dimensional penetrable rough surfaces is achieved. The pattern of the light scattered from the surface is calculated by considering a horizontally or vertically polarized light wave incident on two-dimensional Gaussian or cylindrical rough surfaces of either isotropic or anisotropic statistical properties. The work of [15] provides physical optics solution for the scattering of a partially-coherent wave from a rough surface of dielectric material. A summary of other techniques used for the assessment of electromagnetic scattering from rough surfaces is provided in [16]. The methods reviewed in [16] include the Meecham–Lysanov method, phase-perturbation method, small-slope approximation, operator expansion method, tilt-invariant approximation, local weight approximation, weighted curvature approximation, Wiener–Hermite approach, unified perturbation expansion, full-wave approach, improved Green’s function methods, volumetric method and integral equation method.

The present paper applies the Geometrical Theory of Diffraction (GTD) in conjunction with the Ray Tracing (RT) to account for scattering of optical waves and other electromagnetic waves from rough surfaces. Such GTD-RT technique accounts for higher order scattering by considering multiple bounces of the ray incident on a rough surface. Moreover, the Fresnel reflection and transmission coefficients are calculated to take into consideration the effect of the material of the rough surface. This method is applicable for random rough surfaces of both metallic and dielectric materials with quite arbitrary statistical parameters. The proposed GTD-RT technique is fully numerical and avoids the approximations encountered in the analytical or semi-analytical techniques that result in significant inaccuracies (except for the high frequency formulation which is the spirit of the ray theory).

The numerical results for the scattering pattern evaluated using the GTD-RT method is investigated through experimental verification. The polarization of the plane wave incident on the rough surface is taken into consideration. The present work investigates the dependence of the accuracy of the resulting scattering pattern on the resolution of the geometric model of the rough surface. Also, it studies the dependence of the accuracy of the calculated scattered field on the angle of incidence of the primary beam and the surface roughness.

II. GENERATION OF RANDOM ROUGH SURFACE MODEL

In this section we describe a simple spatial-domain method to generate a random rough surface with predetermined statistical properties. The most important statistical properties of such a random surface are the mean value of the surface height, h_{mean} , the root-mean-squared-height h_{rms} , and the correlation length between the heights of the neighboring points on the surface, L_c .

Let the dimensions of the surface be $L_x \times L_y$ which is discretized to $Q_x \times Q_y$ points (vertices) along x and y directions, respectively. The correlation lengths are L_{cx} and L_{cy} along x and y directions, respectively. The coordinates of each point in surface are (x, y, z) , where z is the random height whereas x and y represent a uniform horizontal grid. The horizontal distances between two adjacent points are Δx and Δy along x and y directions, respectively. The roughness degree of such a surface depends on the ratio between h_{rms} and the correlation length. For a square isotropic surface, $L_{cx} = L_{cy} = L_c$, $L_x = L_y = L$, $Q_x = Q_y = Q$, and $\Delta x = \Delta y = \Delta$. For such a surface let N_{Lc} be the number of the surface points taken along the correlation length and, hence, L_c can be calculated as follows:

$$L_c = (N_{Lc} - 1) \Delta. \quad (1)$$

In this case the degree of roughness R_D or, simply, the roughness can be defined as:

$$R_D = \frac{2h_{\text{rms}}}{L_c}. \quad (2)$$

To generate a rough surface numerically, a two-dimensional array of discrete Gaussian random numbers with zero-mean, $\mu = 0$, and a standard deviation $\sigma = h_{\text{rms}}$ are generated. These random numbers represent the heights of the discrete points on the random surface. In this manner the heights are uncorrelated. To get a rough surface model with a specific correlation length, a Savitzky-Golay filter with a correlation window size of N_{Lc} is applied to smooth the rows and then the columns of the generated array of random numbers [27]. The mean value of the resulting (smoothed) array is subtracted from the values of the array elements which are then scaled to get their standard deviation equal to the required root-mean-squared height of the surface.

III. EVALUATION OF OPTICAL WAVE SCATTERING ON RANDOM ROUGH SURFACES

This section is concerned with the evaluation of the optical scattering from random rough surfaces with arbitrary statistical parameters using the GTD in conjunction with the RT technique. The geometrical model of the rough surface is created as described in Section 2 such that the plane of incidence is parallel to

x-z plane. The plane wave polarization is considered vertically polarized (V-polarized) if the electric field lies completely in the plane of incidence and is considered horizontally polarized (H-polarized) if the electric field lies completely in the plane parallel to the x-y plane.

A. Applicability of the GTD-RT technique for optical scattering on rough surfaces

For an optically rough surface model, the following conditions are practically satisfied. To get accurate numerical assessment of the optical wave scattering on such a surface using the GTD-RT technique, the following condition should be satisfied [25]:

$$\lambda \ll L_c \sqrt{1 + R_D^2}, \quad \lambda \gg \Delta. \quad (3)$$

If the conditions given by (3) are satisfied, the GTD-RT technique can be applied to evaluate the scattering of an optical ray (or beam of rays) incident on such rough surface model.

B. Application of GTD-RT for assessment of scattering of parallel rays on rough surfaces

This section provide a detailed description of the proposed GTD-RT technique when applied to evaluate the optical and EM scattering due to a plane wave illuminating a rough surface as shown in Fig. 1. The incident plane wave is represented by a number of rays; each ray is associated with an amount of power that is to be calculated so as to satisfy uniform power distribution over the transverse plane of the incident wave. The phase associated with each of the scattered rays is obtained by calculating the total distance travelled during ray tracing. The rough surface absorption or reflectance is evaluated by calculating the Fresnel coefficients at the point of incidence. Finally, a method is proposed to calculate the scattering pattern over the upper half space. Both first order and higher order ray tracing are described through systematic algorithm facilitated to be applied as a simulation tool for optical and EM scattering on rough surface.

The random rough surface is discretized to a grid of vertices arranged uniformly in the x and y directions and separated by steps Δx and Δy , respectively. The number of vertices along x and y directions are P and Q, respectively. Each vertex of this uniform grid has a random height $z_{p,q}$, where the indices p and q refer to the vertex row and column of the grid in the x and y directions, respectively. Thus, the position vector of a vertex on the rough surface can be expressed as:

$$V_{p,q} = x_{p,q} \hat{a}_x + y_{p,q} \hat{a}_y + z_{p,q} \hat{a}_z, \quad (4)$$

where,

$$x_{p,q} = p\Delta x, \quad y_{p,q} = q\Delta y. \quad (5)$$

Each vertex of the grid representing the rough surface is connected with the adjacent vertices using triangular

meshing. The normal vector at each vertex of the surface is the average of the normal vectors of the adjacent triangular patches sharing this vertex. The procedure to apply the proposed GTD-RT method is detailed in the following subsections.

B.1 Ray representation of the incident plane wave

The vector propagation constant of the incident plane wave can be expressed as:

$$k_i = k_0 \hat{a}_{k_i} = k_0 (\hat{a}_x k_{ix} + \hat{a}_z k_{iz}), \quad (6)$$

where, k_0 is the free space wavenumber, \hat{a}_{k_i} is the unit vector in the direction of propagation, and,

$$k_{ix} = \sin \theta_i, \quad k_{iz} = \cos \theta_i. \quad (7)$$

The incident plane wave is represented by a number of parallel rays by setting a ray incident on each vertex $V_{p,q}$ of the rough surface. Each ray is associated with an amount of power $\rho_{i,p,q}$ which is determined so as to satisfy uniform power density distribution over the transverse plane. Without any loss in generality, it is assumed that the propagation unit vector of the plane wave \hat{a}_{k_i} , is always in the x-z plane (the squint angle is zero). Consider the transverse plane (normal to \hat{a}_{k_i}) that passes through the point $O_q = (0, y_{p,q}, 0)$. The transverse plane intercepts the plane $y = y_{p,q}$ in the line $L_{i,q}$ that passes through the point O_q .

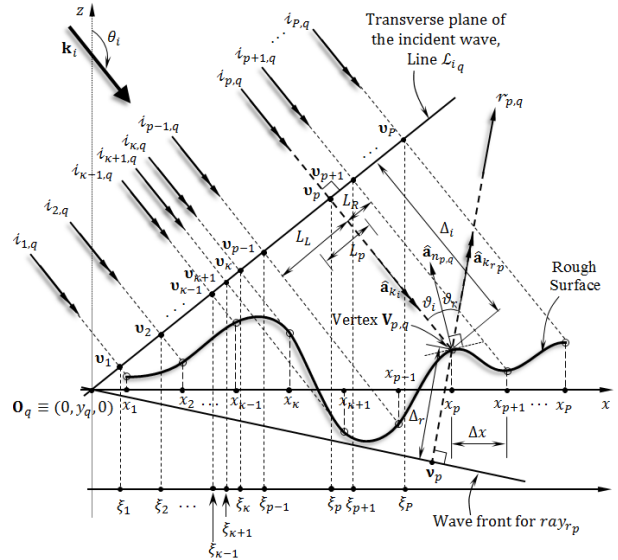


Fig. 1. The plane of incidence $y = (q - 1)\Delta y$. Application of the ray tracing technique to calculate the scattering of plane waves on rough surfaces.

B.2 Calculating the power associating each of the incident rays

Starting from the 1st row of vertices of the mesh representing the rough surface and moving sequentially

to the Q^{th} row, the following procedure is applied to scan the vertices on the q^{th} row, $V_{p,q}$, sequentially from $p = 1$ to $p = P$:

- 1- From each vertex, $V_{p,q}$, draw a line perpendicular to the transverse plane of the incident wave, as shown in Fig. 1, and find the intersection point v_p whose position vector relative to the point O_q is $v_p = (\xi_{p,q}, 0, \zeta_{p,q})$. This can be achieved as follows:

$$v_p \cdot \hat{a}_{k_i} = 0 = \xi_{p,q} k_{ix} + \zeta_{p,q} k_{iz}. \quad (8)$$

Let Δ_i be the distance from the intersection point v_p to the vertex $V_{p,q}$; consequently, one has:

$$V_{p,q} = v_p + \Delta_{i,p,q} \hat{a}_{k_i}. \quad (9)$$

This relation can be split into the following scalar equations:

$$\xi_{p,q} = x_{p,q} - k_{ix} \Delta_{i,p,q}, \quad (10a)$$

$$\zeta_{p,q} = z_{p,q} - k_{iz} \Delta_{i,p,q}. \quad (10b)$$

Equations (8), (10a) and (10b) can be solved together to get $\Delta_{i,p,q}$, $\xi_{p,q}$ and $\zeta_{p,q}$ as follows. Substitute from (10a,b) into (8), one gets:

$$\Delta_i = x_{p,q} \sin \theta_i + z_{p,q} \cos \theta_i. \quad (11)$$

- 2- Define ξ_{max} as the maximum value of x -component of v_p evaluated during the progress of scanning the vertices on the q^{th} row sequentially from $p = 1$ to $p = P$. Initially set $\xi_{\text{max}} = 0$, and define a flag variable $Y_{p,q}$ for the incident ray at this vertex.
- 3- With scanning the vertices on the q^{th} row moving from left to right, the index p increases by one for each vertex where the intersection point v_p is calculated as described above and the value of ξ_{max} is updated; that is, if $\xi_{p,q} > \xi_{\text{max}}$, then this ray is considered active ($Y_{p,q} = 1$) and the ξ_{max} is updated as $\xi_{\text{max}} = \xi_{p,q}$. If $\xi_{p,q} \leq \xi_{\text{max}}$, then the ray incident on this vertex is considered inactive ($Y_{p,q} = 0$), which means that the vertex (p,q) is shadowed from the incident wave by some part of the surface. Consequently, the ray $i_{p,q}$ does not contribute to the scattered field, which implies that the power associating this ray should be set to zero. Thus, as shown in Fig. 1, the area illuminated by each incident ray on the transverse plane are not equal and can be expressed as,

$$\Lambda_{p,q} = \frac{1}{2} (L_R + L_L) \Delta y, \quad (12)$$

where L_R is the distance between the point v_p and the nearest right-hand point, v_{p_R} , on the line $\mathcal{L}_{i,q}$ corresponding to an active ray, and L_L is the distance between the point v_p and the nearest left-hand point, v_{p_L} , corresponding to an active ray. Thus, one has:

$$L_R = |v_{p_R} - v_p|, \quad (13)$$

$$L_L = |v_{p_L} - v_p|. \quad (14)$$

Consequently, to get uniform power density on the transverse plane, the power associating each ray $i_{p,q}$, should be proportional to $\Lambda_{p,q}$ and, hence, can be expressed as,

$$P_{i_{p,q}} = \Lambda_{p,q} P_d, \quad (15)$$

where, P_d is the power density of the incident plane wave.

B.3 Calculating the directions of the reflected rays

The ray $i_{p,q}$ incident on the rough surface at the vertex $V_{p,q}$, makes an angle ϑ_i with $\hat{a}_{n_{p,q}}$, which is the unit vector normal to surface at this vertex. The reflected ray at the same vertex is $r_{p,q}$; it lies in the same plane of \hat{a}_{k_i} and $\hat{a}_{n_{p,q}}$ and makes an angle $\vartheta_r = \vartheta_i$ with $\hat{a}_{n_{p,q}}$. Hence, the unit vector of the propagation constant $\hat{a}_{k_{r_p}}$ of the reflected ray $r_{p,q}$ can be determined as follows:

$$\hat{a}_{k_{r_p}} = \frac{1}{|\hat{a}_{k_i} - z(\hat{a}_{k_i} \cdot \hat{a}_{n_{p,q}}) \hat{a}_{n_{p,q}}|} \left[\hat{a}_{k_i} - 2(\hat{a}_{k_i} \cdot \hat{a}_{n_{p,q}}) \hat{a}_{n_{p,q}} \right]. \quad (16)$$

The unit vector $\hat{a}_{k_{r_p}}$ can be written in terms of its components as follows:

$$\hat{a}_{k_{r_p}} = k_{rxp} \hat{a}_x + k_{ryp} \hat{a}_y + k_{rzp} \hat{a}_z. \quad (17)$$

B.4 Calculating the phases of the reflected rays in the far zone

To calculate the phase associated with each scattered ray, the distance travelled by the ray should be evaluated. $\Delta_{r,p,q}$ From each vertex, $V_{p,q}$, draw the normal to the wave front of the reflected ray as shown in Fig. 1. Find the intersection point v_p whose position vector relative to the point O_q is $v_p = (\alpha_p, \beta_p, \gamma_p)$. This can be achieved as follows:

$$v_p \cdot \hat{a}_{k_{r_p}} = 0 = \alpha_p k_{rxp} + \beta_p k_{ryp} + \gamma_p k_{rzp}. \quad (18)$$

Let $\Delta_{r,p,q}$ be the distance from the vertex $V_{p,q}$ to the intersection point v_p . Thus,

$$v_p = V_{p,q} - \Delta_{r,p,q} \hat{a}_{k_{r_p}}. \quad (19)$$

This can be written in scalar equations as follows,

$$\alpha_p = x_{p,q} - k_{rx} \Delta_{r,p,q}, \quad (20a)$$

$$\beta_p = y_{p,q} - k_{ry} \Delta_{r,p,q}, \quad (20b)$$

$$\gamma_p = z_{p,q} - k_{rz} \Delta_{r,p,q}. \quad (20c)$$

Solve equations (18), (20a), (20b) and (20c) together to get Δ_r , as follows:

$$\Delta_{r_{p,q}} = x_{p,q} k_{r_x} + x_{p,q} k_{r_y} + z_{p,q} k_{r_z}. \quad (21)$$

Thus, the phase associated with the $r_{p,q}$ can be expressed as,

$$\Delta\Phi_{p,q} = \frac{2\pi}{\lambda} (\Delta_{i_{p,q}} - \Delta_{r_{p,q}}). \quad (22)$$

B.5 Higher order scattering

An incident ray having its first collision with a vertex of the rough surface model may suffer higher order collisions at other vertices. A ray incident on a vertex $V_{p,q}$ may be subjected to higher order reflection if the reflected ray collides with the rough surface at another vertex. Figure 2 shows the geometry required to discuss the condition that such a reflected ray should satisfy to collide with the rough surface. The angle between the ray reflected at the vertex $V_{p,q}$ and the horizontal line, τ_r , can be expressed as:

$$\tau_r = \frac{\pi}{2} - \cos^{-1} k_{r_z}. \quad (23)$$

According to the geometry presented in Fig. 2, this ray will escape from other possible collisions with the rough surface if $\tau_r > \tau_D$, where τ_D is defined as,

$$\tau_D = \tan^{-1} \left(R_D - \frac{2z_{p,q}}{L_C} \right). \quad (24)$$

Thus, only the reflected ray that satisfies the following condition can probably collide with another point on the rough surface before going to the far zone causing second-order scattering:

$$\tau_r < \tau_D. \quad (25)$$

For optimization of the computational complexity the reflected rays not satisfying the condition (25) will not be checked for higher order reflections on the rough surface.

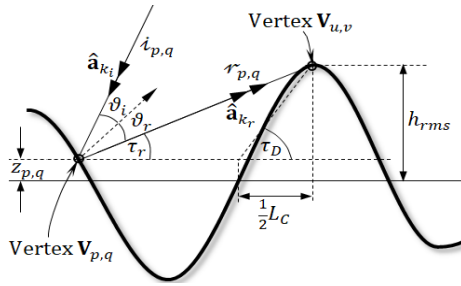


Fig. 2. Condition required to consider higher order reflection of an incident ray.

It is clear from (25) that a higher surface roughness causes larger number of rays to be subjected to higher order reflections. Only for those reflected rays that satisfy (25) the following procedure is applied.

The ray that has the t^{th} bounce at the vertex $V_{p,q}$ collides with the rough surface at the vertex $V_{u,v}$ if the

following condition is satisfied:

$$\hat{a}_{k_r}^{(t)} \cdot \hat{a}_{p,q}^{u,v} = 1, \quad (26)$$

where $\hat{a}_{k_r}^{(t)}$ is the unit vector in the direction of the reflected ray due to the t^{th} bounce, and $\hat{a}_{p,q}^{u,v}$ is the unit vector in the direction from $V_{p,q}$ to $V_{u,v}$:

$$\hat{a}_{p,q}^{u,v} = \frac{V_{u,v} - V_{p,q}}{|V_{u,v} - V_{p,q}|}. \quad (27)$$

If the condition (25) is satisfied then this ray will have its $(t+1)^{\text{th}}$ bounce at the vertex $V_{u,v}$ as shown in Fig. 2. It should be noted that for each bounce of a ray, the direction of the reflected ray is calculated as described in Section III.B.3. The phase associating a ray arriving at the far zone can be calculated as follows:

$$\Delta\Phi_{p,q} = \frac{2\pi}{\lambda} (\Delta_{i_{p,q}} - \Delta_{r_{u,v}}) + \sum_{v=2}^{N_{O_{p,q}}} \frac{2\pi}{\lambda} D^{(v-1)}, \quad (28)$$

where $D^{(v-1)}$ is the distance travelled by the reflected ray between the $(v-1)^{\text{th}}$ and the v^{th} bounce points on the rough surface at the $(v-1)^{\text{th}}$ bounce point, where $v \geq 2$, $N_{O_{p,q}}$ is the maximum number of considered bounces, which is equal to the order of GTD-RT technique.

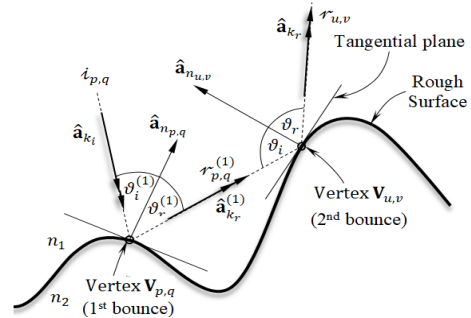


Fig. 3. Double bounce of a ray at the vertices $V_{p,q}$ and $V_{u,v}$ on the rough surface.

IV. NUMERICAL RESULTS AND EXPERIMENTAL MEASUREMENTS

In this section, the accuracy of the results obtained by the GTD-RT method proposed for the assessment of optical scattering on rough surfaces is examined by comparison with the results obtained by experimental measurements. The improvement of the accuracy of the results obtained from higher-order GTD-RT is investigated by comparing the scattering patterns evaluated using a second-order to those obtained using the first-order GTD-RT. Also, the dependence of the optical scattering on the surface roughness and its dependence on the refractive index of the medium under

the rough surface are studied. The effect of the resolution of the rough surface model on the accuracy of the evaluated scattering pattern is investigated.

A. Experimental assessment of the accuracy of the GTD-RT method proposed for evaluating scattering from rough surfaces

The GTD-RT method proposed in the present work for the evaluation of the far field pattern due to plane wave scattering on rough surfaces of arbitrary statistical parameters is assessed by comparison with some experimental measurements. The source of the incident plane wave is a light source of $\lambda = 635\text{nm}$. The pattern of radiation from this source is presented in Fig. 4 as measured by the optical power meter model Thorlabs® PM100 with the optical sensor S120B. The experimental setup for measuring the scattering pattern is presented in Fig. 5. The rough sheet subjected to the incident beam is placed on a vertical wall. The light source is oriented so that the incident beam makes an angle of 45° with the normal to the sheet. The optical sensor connected to the power meter rotates from -90° to 90° with the normal to the sheet to read the intensity of the light scattered from the flat sheet under test. Two white sheets of different roughness degrees are used for assessment of the proposed numerical technique: a glossy white sheet of roughness, $R_D = 0.09$, and a matte white sheet of roughness, $R_D = 0.225$.

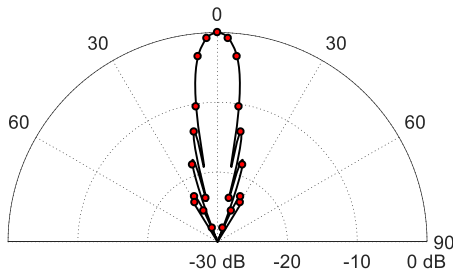


Fig. 4. Radiation pattern of the light beam used for experimental measurements, $\lambda = 635\text{ nm}$.

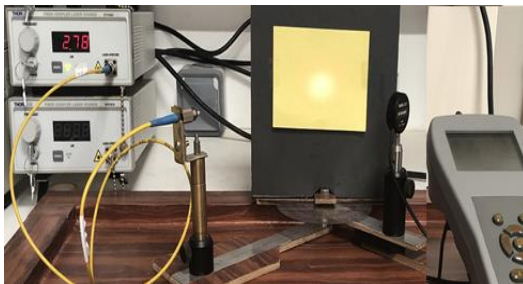
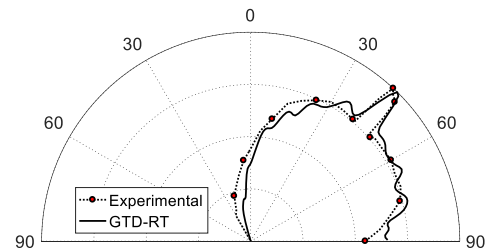
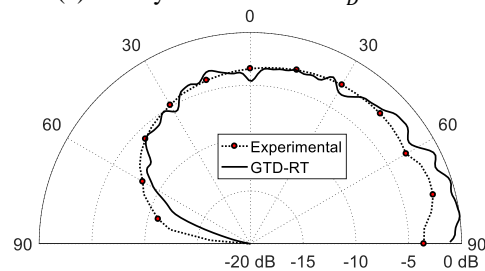


Fig. 5. Experimental setup for measuring the scattering pattern due to a light beam incident on a sheet of rough surface using 635 nm laser source and Thorlabs® optical power meter model PM100 with optical detector model S120B.

A flat sheet of surface roughness, $R_D = 0.09$ is illuminated using the light beam shown in Fig. 5. The optical scattering pattern is measured using the optical power meter through the experimental setup as described above. The measured scattering pattern is compared with that obtained using the second-order GTD-RT method proposed in the present work as shown in Fig. 6 (a). Due to the low degree of roughness of the reflecting surface the scattering pattern shows both specular and diffuse reflection properties. The agreement of the measured pattern with that numerically assessed shows the accuracy of the proposed GTD-RT method for evaluation of scattering of plane waves on rough surfaces. The same experiment is repeated for a flat sheet of surface roughness $R_D = 0.225$. The measured scattering pattern is compared with that obtained using the second-order GTD-RT method proposed in the present work as shown in Fig. 6 (b). For the application of the GTD-RT, the correlation length of the rough surface model is assumed to be $L_C = 7.16\ \mu\text{m}$. Both the calculated and measured scattering pattern show diffuse reflection property of the reflecting surface due to the high degree of roughness. The measured scattering pattern agrees with that numerically assessed showing good accuracy of the proposed GTD-RT method.



(a) Glossy white sheet of $R_D = 0.09$



(b) Matte white sheet of $R_D = 0.225$

Fig. 6. Comparison between the scattering patterns obtained through experimental measurements and GTD-RT method for V-polarized optical plane wave of $\lambda = 635\text{ nm}$ incident on flat white sheets of different values of the roughness, $L_C = 7.16\ \mu\text{m}$, $\theta_i^{(n)} = 45^\circ$.

B. Dependence of the scattering pattern on the surface roughness

As experimentally demonstrated, in Section 4.1 the electromagnetic scattering from a surface of medium

roughness exhibits both specular and diffuse properties whereas a highly rough surface causes only diffuse scattering. The scattering pattern for a rough surface is strongly dependent on the surface roughness as shown in Fig. 7 for different values of the angle of incidence. It is clear that the beam width of the scattered optical power increases with increasing the roughness degree. For low roughness ($R_D = 0.01$), the scattering pattern has a high narrow peak in the specular direction determined by Snell's law and insignificant diffuse scattering over the upper space. With increasing the surface roughness ($R_D = 0.05, 0.1$) the diffuse scattering increases whereas the specular scattering decreases and, hence, the scattered beam is broadened and the peak in the specular direction is weakened. For high degrees of roughness, ($R_D = 0.15$), the rough surface produces nearly complete diffuse scattering where the peak due to specular scattering is almost diminished. Also, it is clear that the angle of incidence affects the shape and width of the scattering pattern, where the specular component of the scattered beam seems to be greater with increasing the angle of incidence for a given value of the surface roughness. In the meantime, the backscatter decreases with increasing the angle of incidence for a given value of the surface roughness. Generally, with increasing the surface roughness, irrespective of the angle of incidence $\theta_i^{(n)}$, the backscattered field is clearly increased.

C. Dependence of the accuracy of the calculated scattering pattern on the resolution of the rough surface model

To get accurate results for the scattering coefficients in the far zone using GTD-RT due to a plane wave incident on a rough surface, the number of the incident rays should be large enough to get accurate ray representation of the scattered power distribution over the half-space. The larger the number of incident rays the more accurate the obtained scattering coefficients. As the number of the incident rays is equal to the number of vertices on the rough surface, high resolution of the rough surface is required to get accurate results for the scattering coefficients in the different directions. The case of a surface of roughness $R_D = 0.1$ combines the properties of both diffuse and specular reflections. For this reason, such a roughness is considered to examine the effect of the rough surface resolution on the accuracy of the results obtained for the scattering pattern.

Figure 8 shows the scattering patterns obtained due to a vertically polarized plane incident on a rough surface model with different resolutions (number of vertices constructing its geometric model). For low resolution model (250×250), the scattering pattern seems to have large errors especially in the direction normal to the rough surface and in the specular direction. With increasing the resolution, the accuracy is improved asymptotically (especially in the specular direction) to

get very accurate results for a rough surface model of resolution (3000×3000).

D. Dependence of the scattering on the polarization of incident field

The scattering of either H-polarized or V-polarized plane wave incident on a rough surface which is an interface between the free space and a dielectric medium is investigated for different values of the surface roughness and refractive indices. As shown in Fig. 9 (a), for high value of the refractive index ($n = 10$), the scattering patterns for the H-polarized and the V-polarized waves are very close to each other. As shown in Fig. 9 (b), Fig. 10 (a) and Fig. 10 (b) for lower values of the refractive index ($n = 3.16, n = 1.5$), respectively, the scattering patterns for the two polarizations are different from each other. It is clear that decreasing the refractive index has the effect of increasing the backscattering of the V-polarized wave and increasing the scattering of the H-polarized wave in the forward direction parallel to the surface.

Increasing the roughness of the surface has the effect of decreasing the specular scattering on behalf of the diffuse scattering for both types of polarization, which is clear by comparison between the scattering pattern presented in Fig. 10 (a) and Fig. 10 (b).

V. COMPUTATIONAL PERFORMANCE OF THE HIGHER-ORDER GTD-RT IN COMPARISON TO THE FIRST-ORDER GTD-RT

The aim of the present section is to investigate the computational complexity and the accuracy of the results obtained by the first and higher-order GTD-RT proposed in the present work.

A. Accuracy of the results

The computational cost of applying second-order GTD-RT is considerably large when compared to that of the first-order GTD-RD. The purpose of the present section is to compare the improvement of the solution obtained using the second-order GTD-RT over that obtained using the first-order method. For this purpose, three ensembles of rough surface models with different statistical parameters are generated. The ensemble has 20 different samples of rough surfaces generated with the same statistical parameters. The rough surface models of the first, second and third ensembles have roughness degrees $R_D = 0.06, 0.10$, and 0.15 , respectively where the correlation length is $L_C = 7.16 \mu\text{m}$. For these three ensembles, Figs. 11 (a), (b) and (c), show the scattering patterns resulting due to a plane wave incident at angle 45° with the normal to the surface. It is clear that, in all the cases, the improvement due to the application of the second-order GTD-RT can be negligible even for high degrees of roughness.

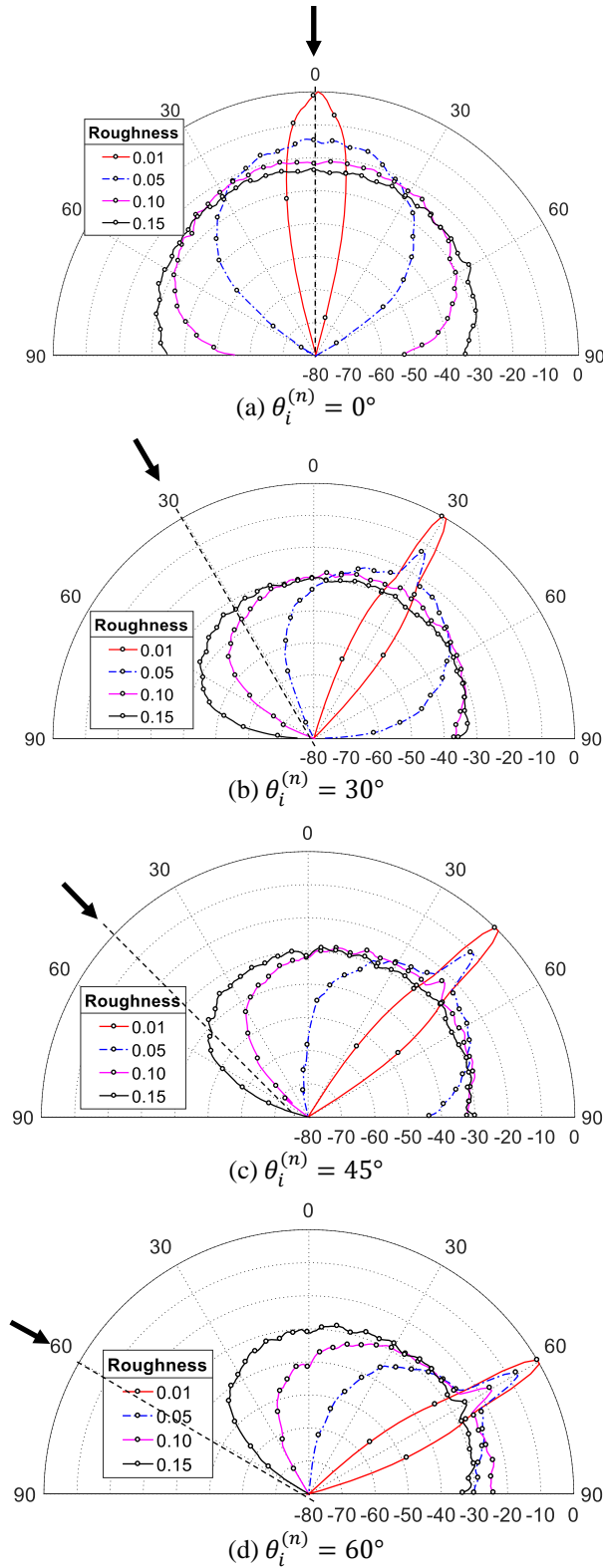


Fig. 7. The scattering patterns due to V-polarized plane wave incident on a rough surface model of resolution 1000×1000 , $L_C = 7.16 \mu\text{m}$ with different values of the degree of roughness and the angle of incidence.

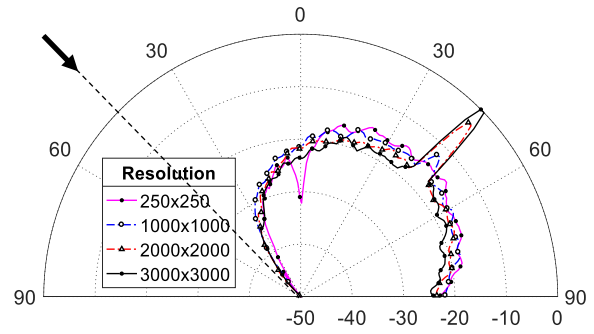


Fig. 8. The scattering patterns due to V-polarized plane wave incident in the direction $\theta_i^{(n)} = 45^\circ$ on a $63.5 \times 63.5 \mu\text{m}$ rough surface model of different resolutions; $R_D = 0.1$; $\lambda = 635 \text{ nm}$, $L_C = 7.16 \mu\text{m}$.

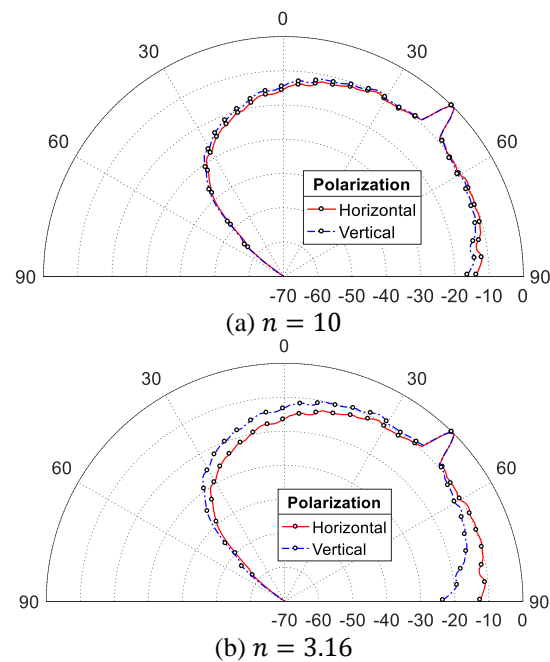


Fig. 9. The scattering patterns due to H-polarized and V-polarized plane waves incident in the direction $\theta_i^{(n)} = 45^\circ$ on a $63.5 \times 63.5 \mu\text{m}$ rough surface of resolution 1500×1500 vertices and $R_D = 0.10$; $\lambda = 635 \text{ nm}$, $L_C = 7.16 \mu\text{m}$.

Considering that the results obtained by the second-order method are more accurate than those obtained by the first-order method, Fig. 12 shows the percentage difference between the scattered fields obtained using the two methods averaged over all the directions of the half space for different values of the surface roughness. It is clear that the error due to the application of the first-order RT instead of the second-order RT increases with increasing the surface roughness. However, even for highly rough surfaces ($RD = 0.3$), the percentage error does not exceed 2.5%. As the application of the second

or higher-order GTD-RT is computationally complex, the negligible improvement of the accuracy over the first-order GTD-RT makes the latter be more efficient for evaluating optical scattering from rough surfaces.

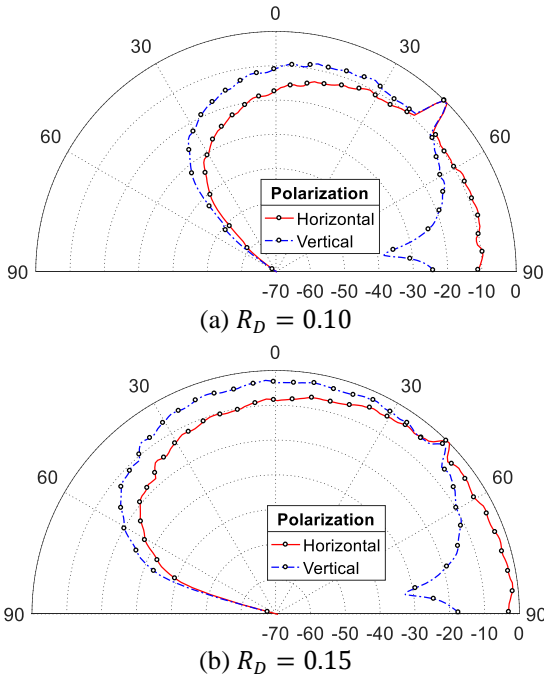


Fig. 10. The scattering patterns due to H-polarized and V-polarized plane waves incident in the direction $\theta_i^{(n)} = 45^\circ$ on a $63.5 \times 63.5 \mu\text{m}$ rough surface of resolution 1500×1500 vertices; $\lambda = 635 \text{ nm}$, $L_C = 7.16 \mu\text{m}$, $n = 1.5$.

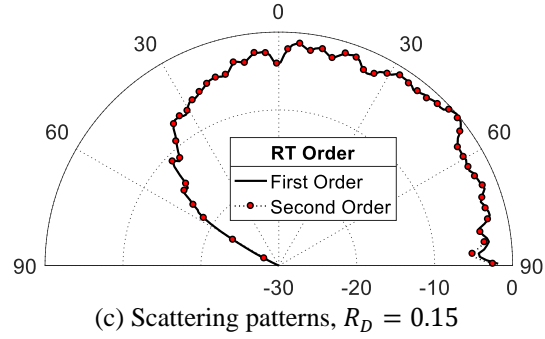
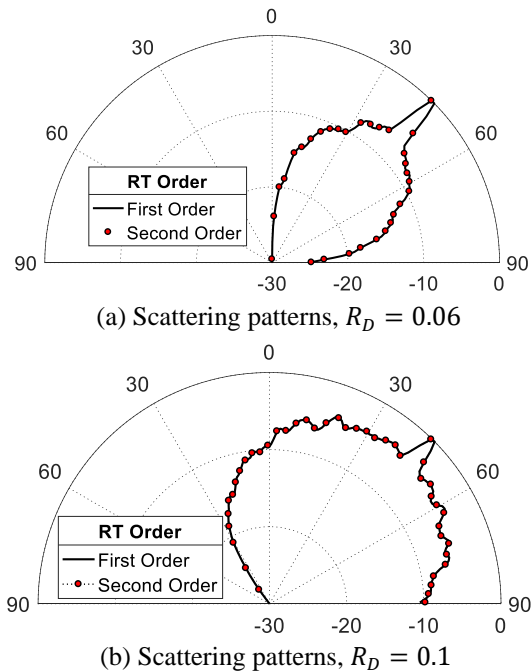


Fig. 11. The scattering of V-polarized optical plane wave of $\lambda = 635 \text{ nm}$ incident on rough surfaces of $L_C = 7.16 \mu\text{m}$, $\theta_i^{(n)} = 45^\circ$, evaluated by the application of first-order and second-order GTD-RT.

Fig. 12. Average error resulting from the application of the application of the first-order RT relative to the solution obtained by the second-order RT against the degree of roughness. For Simulation, the rough surface has the dimensions $63.5 \times 63.5 \mu\text{m}$ and the resolution of segmentation is 1000×1000 vertices; $L_C = 7.16 \mu\text{m}$, $n = 1.5$, $\lambda = 635 \text{ nm}$.

B. Computational time

The dependencies of the computational time and the corresponding percentage error in the magnitude of the backscattered field on the surface roughness are presented in Fig. 13 when applying the first, second and third-order GTD-RT.

It is shown that for the first-order RT, the computational time is slightly decreased with increasing the roughness degree. With increasing the surface roughness, more rays of the incident wave are blocked by the rough surface and, hence, the total number of rays to be traced is further reduced leading to a slight reduction of the computational time. On the contrary, for second-order RT, the possibility of a ray to suffer multiple bounces on the rough surface increases with increasing the surface roughness leading to considerable increase of the computational time. On the other hand, irrespective of the RT order, the percentage error of the

backscatter field magnitude increases with increasing the degree of roughness. With increasing the surface roughness a higher-order order RT is required to keep the solution accurate.

It can be seen from Figs. 13 (a), (b) that for roughness degree of about 0.225, the computational time taken by the second-order RT is about 100 s, which is twice that taken by the first-order RT (50 s). However, the computational error is improved from 3.6% to 2.9% due to the application of the second-order RT instead of the first-order RT.

Thus, the computational time is doubled whereas the error is improved by only 0.7% due to the application of the second-order RT instead of the first-order RT.

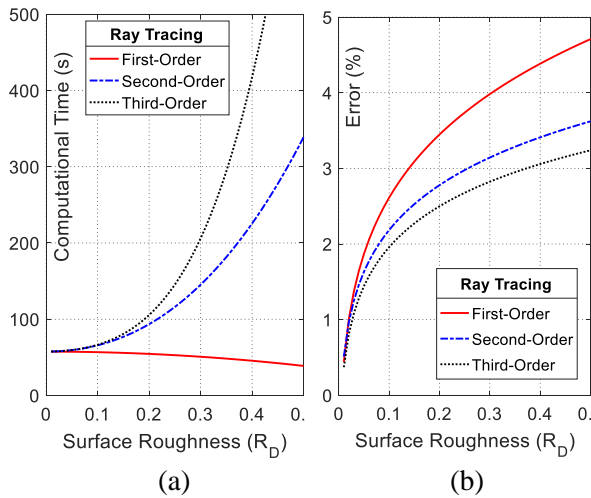


Fig. 13. Dependence of (a) the computational time, and (b) the corresponding percentage error in the magnitude of the backscattered field on the surface roughness.

C. Rate of convergence of ensemble-averaged backscattering with the ensemble size

One of the metrics that is commonly used to assess the computational performance of a numerical method that depends on set of random samples (an ensemble) is the minimum number of samples required to get accurate results after making ensemble averaging. In our case, the ensemble is a set of rough surface models with the same statistical properties. Each of these rough surface samples is subjected to a plane wave to evaluate the scattered field using the GTD-RT proposed in the present work. Then an ensemble averaging is carried out to get the average scattered field. This is known as a Monte-Carlo averaging process. Figure 14 shows the dependence of the ensemble average of the backscattered coefficients for a vertically polarized wave incident on a rough surface with the indicated parameters for different values of the surface roughness. For a rough surface with $R_D = 0.09$, the ensemble-averaged backscattering coefficient is settled down at -20 dB whereas, for a rough surface

with $R_D = 0.09$, the ensemble-averaged backscattering coefficient is settled down at -5 dB. In both cases the ensemble average of the backscattered field has fast convergence with the ensemble size. This reflects the efficiency of the proposed GTD-RT and the perfectness of the rough surface models of the ensemble.

Direction of incidence of the optical wave is $\theta_i^{(n)} = 45^\circ$. For Simulation, the rough surface has the dimensions $63.5 \times 63.5 \mu\text{m}$ and the resolution of segmentation is 1000×1000 vertices; $L_C = 7.16 \mu\text{m}$, $n = 1.5$, $\lambda = 635 \text{ nm}$. The reference solution to which the errors are referred to is obtained by experimental measurements

Also, it is shown that the rate of convergence of the ensemble average depends on the surface roughness. For surface roughness $R_D = 0.09$, an ensemble size of 10 samples can be enough to get accurate results, whereas, for $R_D = 0.225$, an ensemble size of 15 samples is required to get accurate results. Thus, the rate of convergence of the ensemble average increases with decreasing the surface roughness.

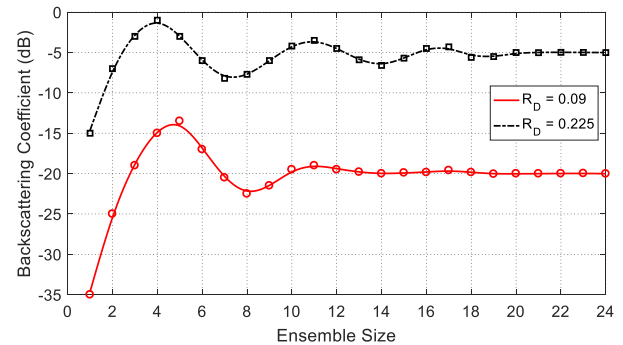


Fig. 14. Convergence of the ensemble-averaged backscattering coefficient with increasing the ensemble size for different values of the surface roughness. Direction of incidence of the optical wave is $\theta_i^{(n)} = 45^\circ$. For Simulation, the rough surface has the dimensions $63.5 \times 63.5 \mu\text{m}$ and the resolution of segmentation is 1000×1000 vertices; $L_C = 7.16 \mu\text{m}$, $n = 1.5$, $\lambda = 635 \text{ nm}$.

D. Novelty of the proposed GTD-RT technique

The novelty of the propose GTD-RT technique for the assessment of scattering of plane waves on rough surfaces can be highlighted as follows:

- The method of illuminating the rough surface by the incident power is novel and computationally efficient. This method uses a number of incident rays equal to the number of vertices on the rough surface model. Thus, no intersection points are required to be calculated which saves considerable time.
- Novel and computationally efficient method of calculating shadowing effects of the rough surface. The blocked rays are not considered in the subsequent ray

tracing, which leads to significant improvement of the computational time.

- Novel and computationally efficient algorithm for considering the rays subjected to multiple bounces on the rough surface as described in detail in Section III.B.5.

The samples of the rough surface are perfectly generated using the method described in [27] which leads to fast convergence of the ensemble averaging process. It is found that a number of 10-15 (small-size ensemble) can be enough to get accurate results.

VI. CONCLUSION

The GTD-RT technique is proposed to evaluate the electromagnetic scattering from a rough surface of quite arbitrary statistical parameters. The method of generating the geometrical model of the rough surface is explained. The Fresnel reflection model is applied for arbitrary electrical and optical properties of the rough surface material taking into account the polarization of the incident plane wave. The algorithm developed in the present work can be considered a higher order GTD-RT that accounts for multiple bounces of an incident ray. The accuracy of the obtained results is verified through the comparison with the experimental measurements of the scattering pattern of a light beam incident on samples of rough sheets with specific statistical properties. The presented numerical results are concerned with studying the dependence of the resulting scattering pattern on the surface roughness, refractive index, angle of incidence, and the resolution of the geometric model of the rough surface. Also, it is shown that, for limited resolution of the rough surface model, the accuracy of the calculated scattered field depends on the angle of incidence of the primary beam and the surface roughness.

REFERENCES

- [1] A. Manallah and M. Bouafia, "Application of the technique of total integrated scattering of light for micro-roughness evaluation of polished surfaces," *Physics Procedia*, vol. 21, pp. 174-179, 2011.
- [2] T. A. Germer, "Polarized light diffusely scattered under smooth and rough interfaces," *Polarization Science and Remote Sensing, International Society for Optics and Photonics*, vol. 5158, pp. 193-205, Dec. 2003.
- [3] N. Pinel, C. Bourlier, and J. Saillard, "Degree of roughness of rough layers: Extensions of the Rayleigh roughness criterion and some applications," *Progress in Electromagnetics Research*, vol. 19, pp. 41-63, 2010.
- [4] V. A. Ruiz-Cortés and J. C. Dainty, "Experimental light-scattering measurements from large-scale composite randomly rough surfaces," *JOSA A*, vol. 19, no. 10, pp. 2043-2052, 2002.
- [5] A. Manallah and M. Bouafia, "Application of the technique of total integrated scattering of light for micro-roughness evaluation of polished surfaces," *Physics Procedia*, vol. 21, pp. 174-179, 2011.
- [6] M. F. Spencer and M. W. Hyde IV, "Rough surface scattering for active-illumination systems," *SPIE Newsroom*, pp. 1-2, 2013.
- [7] G. R. Jafari, S. M. Mahdavi, A. Iraj Zad, and P. Kaghazchi, "Characterization of etched glass surfaces by wave scattering," *Surface and Interface Analysis: An International Journal Devoted to the Development and Application of Techniques for the Analysis of Surfaces, Interfaces and Thin Films*, vol. 37, no. 7, pp. 641-645, 2005.
- [8] M. Zamani, F. Shafiei, S. M. Fazeli, M. C. Downer, and G. R. Jafari, "Analytic height correlation function of rough surfaces derived from light scattering," *Physical Review E*, vol. 94, no. 4, p. 042809, 2016.
- [9] M. Sanamzadeh, L. Tsang, J. T. Johnson, R. J. Burkholder, and S. Tan, "Scattering of electromagnetic waves from 3D multilayer random rough surfaces based on the second-order small perturbation method: Energy conservation, reflectivity, and emissivity," *JOSA A*, vol. 34, no. 3, pp. 395-409, 2017.
- [10] Z. S. Wu, J. J. Zhang, and L. Zhao, "Composite electromagnetic scattering from the plate target above a one-dimensional sea surface: Taking the diffraction into account," *Progress in Electromagnetics Research*, vol. 92, pp. 317-331, 2009.
- [11] L. Guo, and Z. Wu, "Application of the extended boundary condition method to electromagnetic scattering from rough dielectric fractal sea surface," *Journal of Electromagnetic Waves and Applications*, vol. 18, no. 9, pp. 1219-1234, 2004.
- [12] H. H. Qamar, K. F. A. Hussein, and M. B. El-Mashade, "Assessment of signal strength in indoor optical wireless communications using diffuse infrared radiation," *2019 36th National Radio Science Conference (NRSC). IEEE*, 2019.
- [13] J. E. Harvey, J. J. Goshy, and R. N. Pfisterer, "Modeling stray light from rough surfaces and subsurface scatter," *Reflection, Scattering, and Diffraction from Surfaces IV. International Society for Optics and Photonics*, vol. 9205, p. 92050I, Sep. 2014.
- [14] P. Beckmann, "Scattering by composite rough surfaces," *Proceedings of the IEEE*, vol. 53, no. 8, pp. 1012-1015, 1965.
- [15] M. W. Hyde, S. Basu, M. F. Spencer, S. J. Cusumano, and S. T. Fiorino, "Physical optics solution for the scattering of a partially-coherent wave from a statistically rough material surface," *Optics Express*, vol. 21, no. 6, pp. 6807-6825, 2013.
- [16] T. M. Elfouhaily and C. A. Guérin, "A critical

- survey of approximate scattering wave theories from random rough surfaces,” *Waves in Random Media*, vol. 14, no. 4, R1-R40, 2004.
- [18] S. O. Rice, “Reflection of electromagnetic waves from slightly rough surfaces,” *Communications on Pure and Applied Mathematics*, vol. 4, no. 2-3, pp. 351-378, 1951.
- [19] J. Tian, J. Tong, J. Shi, and L. Gui, “A new approximate fast method of computing the scattering from multilayer rough surfaces based on the Kirchhoff approximation,” *Radio Science*, vol. 52, no. 2, pp. 186-193, 2017.
- [20] E. I. Thorsos, “The validity of the Kirchhoff approximation for rough surface scattering using a Gaussian roughness spectrum,” *The Journal of the Acoustical Society of America*, vol. 83no. 1, pp. 78-92, 1988.
- [21] M. A. Demir and J. T. Johnson, “Fourth-and higher-order small-perturbation solution for scattering from dielectric rough surfaces,” *JOSA A*, vol. 20, no. 12, pp. 2330-2337, 2003.
- [22] R. L. Voti, G. L. Leahu, S. Gaetani, C. Sibilina, V. Violante, E. Castagna, and M. Bertolotti, “Light scattering from a rough metal surface: Theory and experiment,” *JOSA B*, vol. 26, no. 8, pp. 1585-1593, 2009.
- [23] T. V. Vorburger, R. Silver, R. Brodmann, B. Brodmann, and J. Seewig, “Light scattering methods,” in: R. Leach (Ed.), *Optical Measurements of Surface Topography*, Springer, Berlin, pp. 287-311, 2011.
- [24] J. A. Sanchez-Gil and M. Nieto-Vesperinas, “Light scattering from random rough dielectric surfaces,” *JOSA A*, vol. 8, no. 8, pp. 1270-1286, 1991.
- [25] T. Nordam, P. A. Letnes, and I. Simonsen, “Numerical simulations of scattering of light from two-dimensional rough surfaces using the reduced Rayleigh equation,” *Frontiers in Physics*, vol. 1, no. 8, 2013.
- [26] H. H. Qamar, A. E. Farahat, K. F. A. Hussein, and M. B. El Mashade, “Assessment of scattering of plane waves on optically illuminated area of rough surface,” *Progress in Electromagnetics Research*, vol. 86, pp. 77-102, 2020.
- [27] H. H. Qamar, M. B. El-Mashade, A. E. Farahat, and K. F. A Hussein, “Convergence of ensemble averaging for optical scattering on rough surfaces using GTD-RT,” in *6th International Conference on Advanced Control Circuits and Systems (ACCS) & 2019 5th International Conference on New Paradigms in Electronics & information Technology (PEIT)*, IEEE, pp. 167-175, 2019.
- [28] S. A. M. Soliman, A. E. Farahat, K. F. A. Hussein, and A. A. Ammar, “Spatial domain generation of random surface using Savitzky-Golay filter for simulation of electromagnetic polarimetric systems,” *Applied Computational Electromagnetics Society Journal*, vol. 34, no. 1, 2019.

Interpretation Method of GATEM Data based on PID Controller Iteration Downward Continuation Method

Shanshan Guan¹, Bingxuan Du¹, Dongsheng Li¹, Yuan Wang¹, Yu Zhu¹, Qiong Wu^{1*},
and Yanju Ji^{1,2}

¹Department of Instrumentation and Electrical Engineering
Jilin University, Changchun 130026, China

²Key Laboratory of Earth Information Detection Instrumentation of Ministry of Education,
Jilin University, Changchun 130026, China
guanshanshan@jlu.edu.cn, dubx20@mails.jlu.edu.cn, lidongsheng86@sina.cn, wangyuan_ciee@jlu.edu.cn,
zhuyu@jlu.edu.cn, wuqiong_515@sina.cn*, jiyj@jlu.edu.cn

Abstract — The Ground-source Airborne Time-domain Electromagnetic (GATEM) system has advantages for high efficiency and complex areas such as mountainous zone. Because of ignoring the impact of flight height, the section interpretation method seriously affects the interpretation and imaging accuracy of shallow anomalies. The PID controller iteration downward continuation method is proposed. Based on the original iteration continuation method, the differential coefficient and integral coefficient are added. The result shows that the new method remarkably decreases the iteration number, and the accuracy are verified by comparison with the numerical integration solution. The PID controller iteration downward continuation method is applied to the interpretation of GATEM data. For synthetic data, the interpretation results of continued electromagnetic response are closer to the true model than the $z = 30$ m interpretation results. The method is also applied to GATEM field data in Yangquan City, Shanxi Province, China. The interpretation results perform reliability using PID controller iteration downward continuation method in a GATEM field.

Index Terms —GATEM system, interpretation, PID controller iteration downward continuation method.

I. INTRODUCTION

The Ground-source Airborne Time-domain Electromagnetic (GATEM) system contains a long grounded electric source as the transmitter unit, and the portable receiving device, which is mounted on the platform of aircraft. The GATEM system can realize efficient and fast geological survey tasks in complex areas, such as beach, volcanic geological structure, and seawater intrusion structure [1-4]. It has the advantages of large exploration depth, low flight cost, and high

security comparing with those of the airborne time-domain electromagnetic system. In recent years, it has gradually become a research hotspot of the time-domain electromagnetic system.

To recognize electrical resistivity anomaly, data procession is necessary for the GATEM field data. Scholars have carried out many studies on it. Sasaki et al. [5] realize a three-dimensional inversion for grounded electrical source airborne transient electromagnetic (GREATEM) based on the least square method. This method is verified by a theoretical model; however, it is not used in field data interpretation. Allah et al. [6] apply a three-dimensional numerical simulation method to fit field data by changing related parameters of the model. Although the results are almost the same with geological data, it takes a lot of time. Liang et al. [7] realize an inversion algorithm for GREATEM using the deformed Born iteration method. This method is verified by the theoretical model and applied to the field data. The results are basically consistent with the geological data. Wu et al. [8] realize GATEM modeling and interpretation methods for a rough medium. The interpretation method based on artificial neural networks is applied to the field data, and the results are consistent with the geological data. A section interpretation method (the long wire source is solved by splitting into a large number of electric dipoles [9-10]) is widely used because of its simplicity and high efficiency [1,4,11-12]. However, this method is limited to the high-precision interpretation of ground electromagnetic data. The effect of the flight height on interpretation is ignored during data processing, so the interpreted electrical resistivity is bound to differ from the true electrical resistivity. To avoid the impact of the flight height on interpretation, this paper proposes an interpretation method based on PID controller iteration downward continuation method.

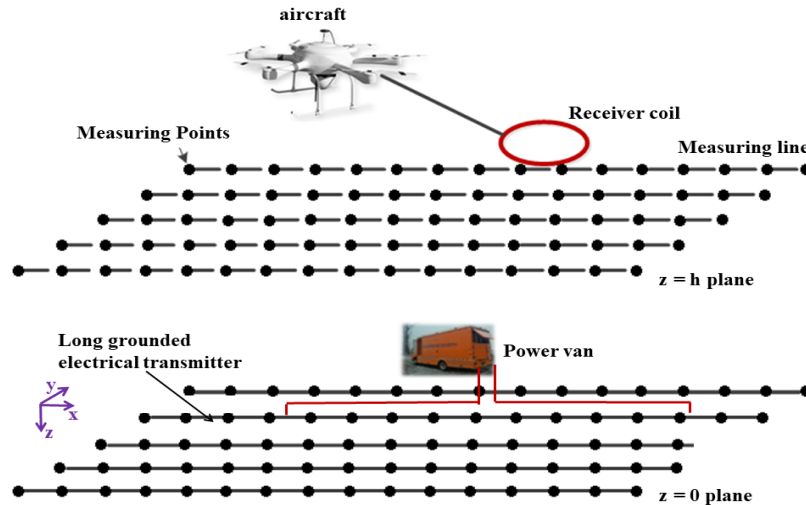


Fig. 1. Configuration of the GAFEM system and schematic diagram of measuring points in a two-dimensional (2D) plane field.

The FFT downward continuation method has an amplification effect on high-frequency noise. To solve the problem, scholars have conducted relevant research in recent years. A stable downward continuation algorithm is presented [13], which is based on the stable vertical derivatives computation obtained by the ISVD method and Taylor series expansion of the potential field. Xu et al. put forward the iteration downward continuation method, which is much better than the FFT [14-15]. At the same time, it does not require solving algebraic equations. Ali et al. [16] present a discrete equivalent source method to perform a stable downward continuation of gravity anomaly. Through automatically selecting an effective amount of the discrete sources, the coefficient matrix size is reduced. The common methods have disadvantages in obtaining optimal results because of divergence and instability. The mean-value theorem for potential field is derived [17]. Compared with the FFT and Taylor series method, the integrated second vertical derivative Taylor series method has very little boundary effect and is still stable in noise. The downward continuation method is also used to the aeromagnetic data [18]. By continuing the field to a level which is a fraction of the distance to the source, it ensures stability by preventing continuation down to or past the source, but its application is restricted to the tilt angle of vertically dipping magnetized contacts. In order to solve the problems, it continues the data to a distance that is a fraction of the current depth, rather than by a fixed distance [19]. The new method is considerably more general in application.

When using the section interpretation method to interpret GATEM data, the accuracy of the shallow anomaly is affected because of ignoring the flight height. In this paper, a PID controller iteration downward

continuation method is proposed to improve the interpretation accuracy of the GATEM data. In order to improve the calculation speed, the integral and differential terms are added to the original iteration continuation method, and the PID coefficients k_p , k_d and k_i are studied. Finally, the PID controller iteration downward continuation method is used in simulated data interpretation, and it is also applied in GATEM field data of Yangquan, Shanxi Province, China.

II. METHODS

A. The GATEM response

The GATEM system mainly contains a several-km-long grounded electrical transmitter and an aircraft equipped with an induction coil and a receiver (Fig. 1). The grounded electrical transmitter comprises of high-powered transmitter and a long grounded wire. The transmitter injects a bipolar square wave current $+$, 0 , $-$, 0 into the ground. The aircraft's operating height might range from 10 m to 500 m and flight speed might be 4 - 20 m/s. The vertical component of the induced electromotive force (V_z) due to a step function current in a horizontal layered earth model is expressed as follows [20]:

$$V_z = -i\omega\mu_0 \frac{IS}{4\pi} \int_{-L}^L \frac{y}{R} \int_0^\infty (1 + r_{TE}) e^{u_0 z} \frac{\lambda^2}{u_0} J_1(\lambda R) d\lambda dx', \quad (1)$$

where I is the transmitter current, S is the area of induction coil, $2L$ is the length of the ground wire, r_{TE} is the reflection coefficient, λ is the Hankel transform integral variable, $u_0 = \lambda$ in the quasistatic electromagnetic field, R is the source-receiver distance

$R = [(x-x')^2 + y^2]^{1/2}$, x' is the integral variable, x is the horizontal longitudinal offset, y is the horizontal

transverse offset, $\omega=2\pi f$ and f is frequency (Hz), μ_0 is the magnetic permeability, and J_1 is the first-order Bessel function. In this case, z is the vertical offset, positive down.

Equation 1 can be calculated by the Hankel transformation algorithm [21], which can be converted from a frequency domain to a time domain by using the Guptasarma digital filtering method [22], then a theoretical induced electromotive force at the $z = 0$ plane is obtained. To verify the correctness of equation 1 calculation, the result is compared with the analytical solution [23]:

$$V_z = -\mu_0 S \frac{\partial H_z}{\partial t} = \frac{2I}{\pi\mu_0\sigma y^3} \left\{ \left(1 + \theta^2 y^2\right) e^{-\theta^2 y^2} \operatorname{erf}(\theta L) - \frac{L}{R} \left(1 + \frac{y^2}{2R^2}\right) \operatorname{erf}(\theta R) + \frac{\theta L y^2}{\sqrt{\pi} R^2} e^{-\theta^2 R^2} \right\}, \quad (2)$$

where $R = [y^2 + L^2]^{1/2}$, $\theta = \sqrt{\frac{\mu_0\sigma}{4t}}$, σ is the electrical conductivity, erf is the error function $\operatorname{erf}(x) = \frac{2}{\sqrt{\pi}} \int_0^x e^{-\eta^2} d\eta$.

An example of a homogeneous half-space with $100 \Omega \cdot \text{m}$ is calculated. The calculation parameters are as follows: the length of the long grounded electric source is 1 m, the transmitter current $I = 10 \text{ A}$, the receiver coil equivalent area $S = 1 \text{ m}^2$, and the receiver location coordinates $x = 0 \text{ m}$, $y = 400 \text{ m}$, $z = 0 \text{ m}$. The calculated response is compared with the analytical solution (Equation 2), which is shown in Fig. 2. They coincide with each other.

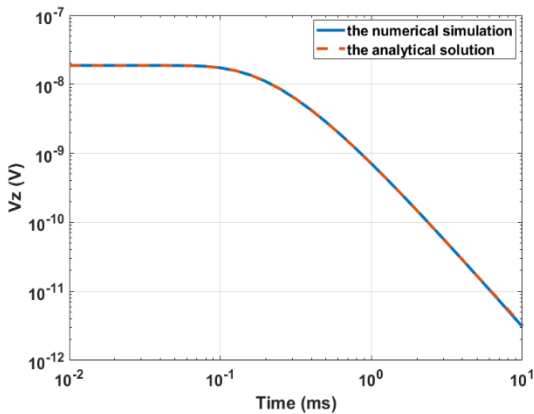


Fig. 2. Comparison of the numerical simulation and analytical solution of the GATEM response in a homogeneous half-space.

A schematic diagram of measuring points in a 2D

plane field is shown in Figure 1. The electromagnetic responses at different measuring points are calculated by using the above method of 1D numerical solution method. Then, the theoretical electromagnetic responses of the observation surface $z = h$ and the reference surface $z = 0$ are constructed.

B. The PID controller iteration downward continuation method

1) Downward continuation theory

The GATEM responses usually are interpreted by section interpretation method which is limited to the high-precision interpretation of ground data. Downward continuation of GATEM response is important in the interpretation to improve data interpretation accuracy, because the receiving height of GATEM detection is usually tens of meters above the ground and the section interpretation method might be affected by receiving height. Xu [14] derives the potential field iteration method formula and proposes a downward continuation theory based on the iteration method. Its basic theory is that it transforms unstable downward continuation to stable upward continuation. First, the magnetic fields of $z = 0$ plane assign $z = h$ plane as its initial values. Then, the magnetic fields at the reference surface are upward continued. Finally, the difference between the upward continuation result and the magnetic field at $z = 0$ plane is calculated, which is used to revise the magnetic fields at $z = h$ plane. We repeat the process until precision is satisfied. The original iteration equation is as follows [14]:

$$u^{n+1}(x, y, z = 0) = u^n(x, y, z = 0) + k_p \cdot e_r^n, \quad (3)$$

where $u^{n+1}(x, y, z = 0)$ is the electromagnetic response after downward-continuation at $z = 0$ plane, k_p is the proportionality factor, n is the number of iterations, $e_r^n = u^n(x, y, z = h) - f(x, y, z = h)$ is an error term, $u^n(x, y, z = h)$ is the upward continuation electromagnetic response of $u^n(x, y, z = 0)$ at $z = h$ plane, h is the flight height, and $f(x, y, z = h)$ is the measured electromagnetic response at $z = h$ plane.

A large number of data need lot of continuation time, so the iterative process could not be proceeded successfully. In this paper, based on an original downward continuation iteration method, the downward continuation that combines the PID controller theory is proposed. A proportional-integral-differential controller is added. So, original iteration equation 3 can be revised [24]:

$$u^{n+1}(x, y, z = 0) = u^n(x, y, z = 0) + k_p \cdot e_r^n + k_i \cdot \sum_{i=1}^n e_r^i + k_d \cdot (e_r^n - e_r^{n-1}), \quad (4)$$

where k_i is the integral coefficient, k_d is the differential coefficient, $\sum_{i=1}^n e_r^i$ is the integral term and $e_r^n - e_r^{n-1}$ is

the differentiation term. By adjusting the proportionality factor, differential coefficient, and integral coefficient together, the convergence speed is accelerated.

2) Optimal parameters for the PID controller iteration downward continuation

The proportionality factor, differential coefficient, and integral coefficient can be determined by experience or artificial fish swarms algorithm (AFSA). AFSA can better obtain optimal parameter values. The objective function is defined as:

$$\eta = \max \left\{ \frac{u^n(x, y, z = h) - f(x, y, z = h)}{u^n(x, y, z = h)} \times 100 \right\}. \quad (5)$$

The process of AFSA is as follows: (1) Artificial fish is initialized. It includes the number of artificial fish, the position of an artificial fish swarm, the maximum try number for foraging behavior, and an accuracy value. The individual position of artificial fish swarm is initialized by chaotic transformation. (2) The food concentration function, quality of individual artificial fish and distance between two artificial fish are calculated. (3) The artificial fish updates itself by foraging, swarming and following. (4) When the value of relative

error objective function η is less than preset accuracy, the proportionality factor k_p , differential coefficient k_d , and integral coefficient k_i are obtained.

Figures 3 (a)-(c) show transient process curves that correspond to different PID parameters when $t = 0.01$ ms. The numbers of iterations are 50000 when parameters of the PID controller iteration are $k_p = 2$, $k_d = 0.2$ and $k_i = 0.1$, 42710 when $k_p = 3$, $k_d = 0.5$ and $k_i = 0.1$, and 31390 when $k_p = 4$, $k_d = 0.9$ and $k_i = 0.3$. Figures 3 (d)-(f) show transient process curves that correspond to different PID parameters when $t = 0.25$ ms. The numbers of iterations are 4123 when $k_p = 2$, $k_d = 0.2$ and $k_i = 0.1$, 3415 when $k_p = 3$, $k_d = 0.5$ and $k_i = 0.1$, and 2094 when $k_p = 4$, $k_d = 0.9$ and $k_i = 0.3$. Figures 3 (g)-(i) show transient process curves that correspond to different PID parameters when $t = 3.16$ ms. The number of iterations is 11040 when $k_p = 2$, $k_d = 0.2$ and $k_i = 0.1$, 8872 when $k_p = 3$, $k_d = 0.5$ and $k_i = 0.1$, and 5724 when $k_p = 3$, $k_d = 0.5$ and $k_i = 0.1$. Figure 3 shows that the number of iterations is changing with time. The reason is that absolute errors of electromagnetic responses are varied on the ground and in the air at different times. The number of iterations gets minimal when $k_p = 4$, $k_d = 0.9$ and $k_i = 0.3$.

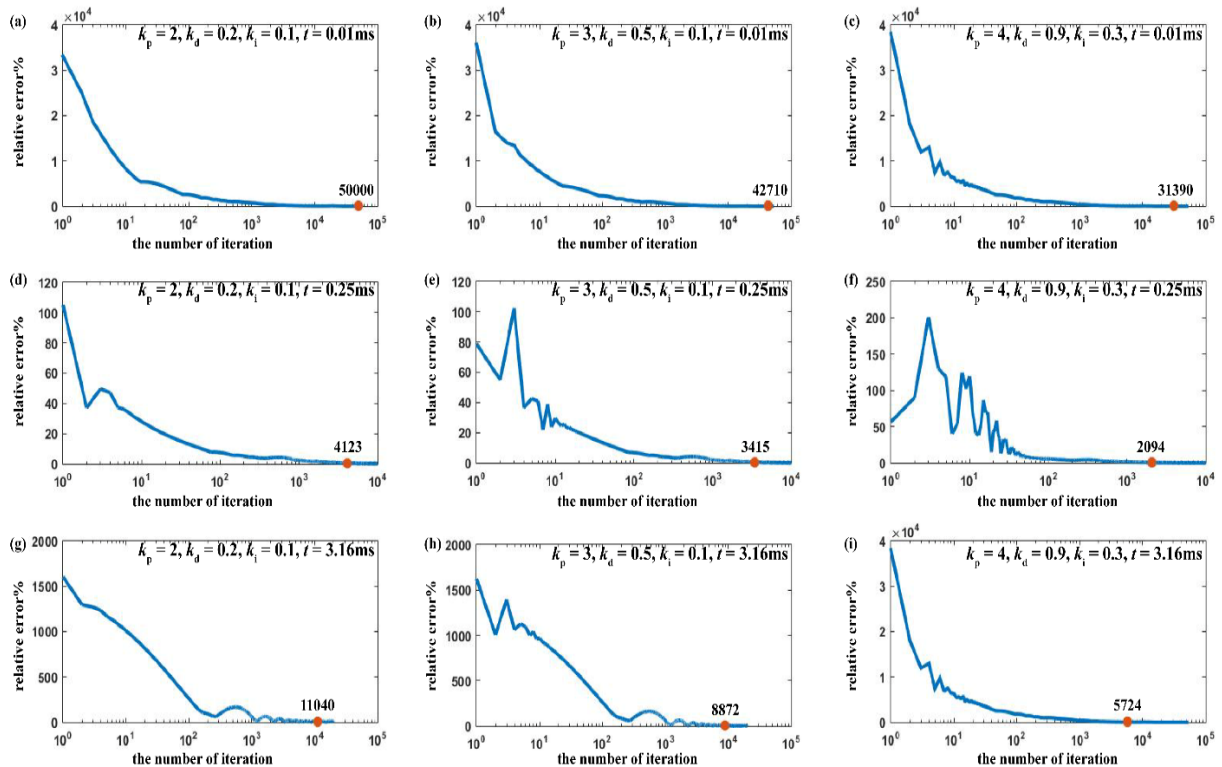


Fig. 3. PID transient process curves. (a)-(c) Transient process curves that correspond to different PID parameters when $t = 0.01$ ms. The numbers of iterations are 50000, 42710, and 31390 at the orange point. (d)-(f) Transient process curves that correspond to different PID parameters when $t = 0.25$ ms. The numbers of iterations are 4123, 3415, and 2094 at the orange point. (g)-(i) Transient process curves that correspond to different PID parameters when $t = 3.16$ ms. The numbers of iterations are 11040, 8872, 5724 at the orange point.

Figure 4 shows the transient process curves based on the original iteration and PID controller iteration when $t = 0.05$ ms. The optimal proportionality factor of the original iteration is $k_p = 2$. The parameters of the PID controller iteration are $k_p = 4$, $k_d = 0.9$ and $k_i = 0.3$. The iteration number of an original iteration method is 16210, which is above 5 times PID controller iteration number 3155. In other words, with same accuracy, the PID controller iteration method has less time-consuming. These results indicate that the PID controller iteration downward continuation method is effective and efficient.

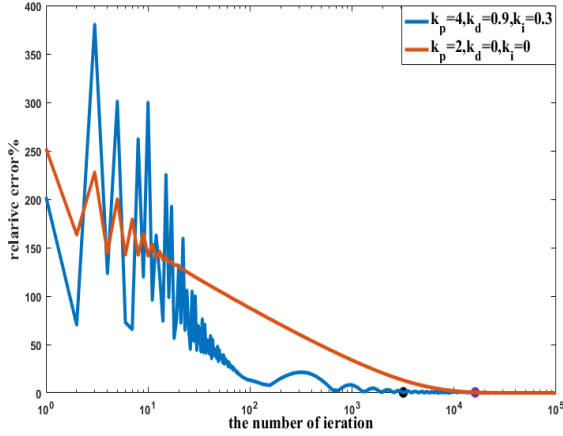


Fig. 4. Transient process curves based on the original downward continuation iteration method and PID controller iteration downward continuation method when $t = 0.05$ ms.

C. Interpretation methods

The GATEM responses can be interpreted by section interpretation method. The long grounded electric source is solved by splitting into numbers of electric dipoles. The electromagnetic response can be [10]:

$$V_z = \sum_{i=1}^N \frac{IS\mu_0 y ds}{8\pi t \theta^2 r_i^5} \left[3\text{erf}(\theta r_i) - \frac{2}{\sqrt{\pi}} \theta r_i (3 + 2\theta^2 r_i^2) e^{-\theta^2 r_i^2} \right]. \quad (6)$$

where ds is the length of electric dipole, t is the sampling time, $r_i = \sqrt{(x-x_i)^2 + y^2}$. After the value of θ is obtained, the apparent electrical resistivity will be $\rho = \frac{\mu}{4t\theta^2}$. The diffusion depth can be estimated by

$$\text{Spies [25]: } d = \sqrt{\frac{2t\rho}{\mu}}.$$

III. RESULTS

A. Precision validation

To validate the effectiveness of the PID controller iteration downward continuation method, electromagnetic responses on the ground and in the air are calculated based on a uniform half-space model when the

conductivity is equal to 0.01 S/m. The distance between the survey points is 10 m. The survey points are selected randomly, which are at $x = 0$ m, $y = 150$ m; $x = 0$ m, $y = 200$ m; $x = 150$ m, $y = 200$ m; and $x = 200$ m, $y = 200$ m. The PID controller iteration parameters are $k_p = 4$, $k_d = 0.9$ and $k_i = 0.3$. The downward continuation results are shown in Fig. 5. The black line is the electromagnetic response for $h = 30$ m. The red dotted line is analytical solution on the ground. The blue line is electromagnetic response after downward continuation. The Fig. 5 shows that downward continuation results are coincide with analytical solution. The average relative error of all the survey points is only 0.08%.

B. Interpretation results

1) Theoretical model

To verify the interpretation results of the downward continuation data, an example of a quasi-two-dimensional three-layer geology model was designed and is shown in Fig. 6 (a) and Fig. 7 (a). The calculation parameters are as follows: the start point of the grounded electrical transmitter is $x = -500$ m, $y = 0$ m, and the end point is $x = 500$ m, $y = 0$ m on the ground. The transmitter current is $I = 10$ A, the induction coil equivalent area is $S = 10000$ m², and the receiver locations are $x = 20$ m - 100 m, $y = 500$ m and $z = 30$ m. The model parameters of Fig. 6 (a) are as follows: the bedrock has 200 $\Omega \cdot \text{m}$ electrical resistivity, and the low-resistivity layer is recorded at 20 $\Omega \cdot \text{m}$, whose depth varies from -60 m to -80 m. The model parameters of Fig. 7 (a) are as follows: The depth of the low-resistivity layer varies from -160 m to -180 m. The other model parameters are the same as Fig. 6 (a). The $z = 30$ m electromagnetic responses are calculated, and then the responses are downward continuation to the ground. The continued electromagnetic response and $z = 30$ m electromagnetic response are interpreted by section interpretation method. The interpretation results are shown in Figs. 6 (b), (c) and Figs. 7 (b), (c).

Figures 6 (b) and 7 (b) are the interpretation results of the $z = 30$ m electromagnetic response, and Figs. 6 (c) and 7 (c) are the interpretation results of continued electromagnetic responses. For the shallow abnormality case, the results of the $z = 30$ m electromagnetic responses, as shown in Fig. 6 (b), indicate that the thickness is much greater than that of the results for continued electromagnetic responses, as shown in Fig. 6 (c). For the deep abnormality case, the results of the low resistivity abnormality are similar. But the shallow part of continued electromagnetic responses, as shown in Fig. 7 (c), is more similar to the true model than the results of the $z = 30$ m electromagnetic response, as shown in Fig. 7 (b). The results show that continued electromagnetic responses are nearly equivalent to the true model. The accuracy of data interpretations could be improved by the PID controller iteration downward continuation method.

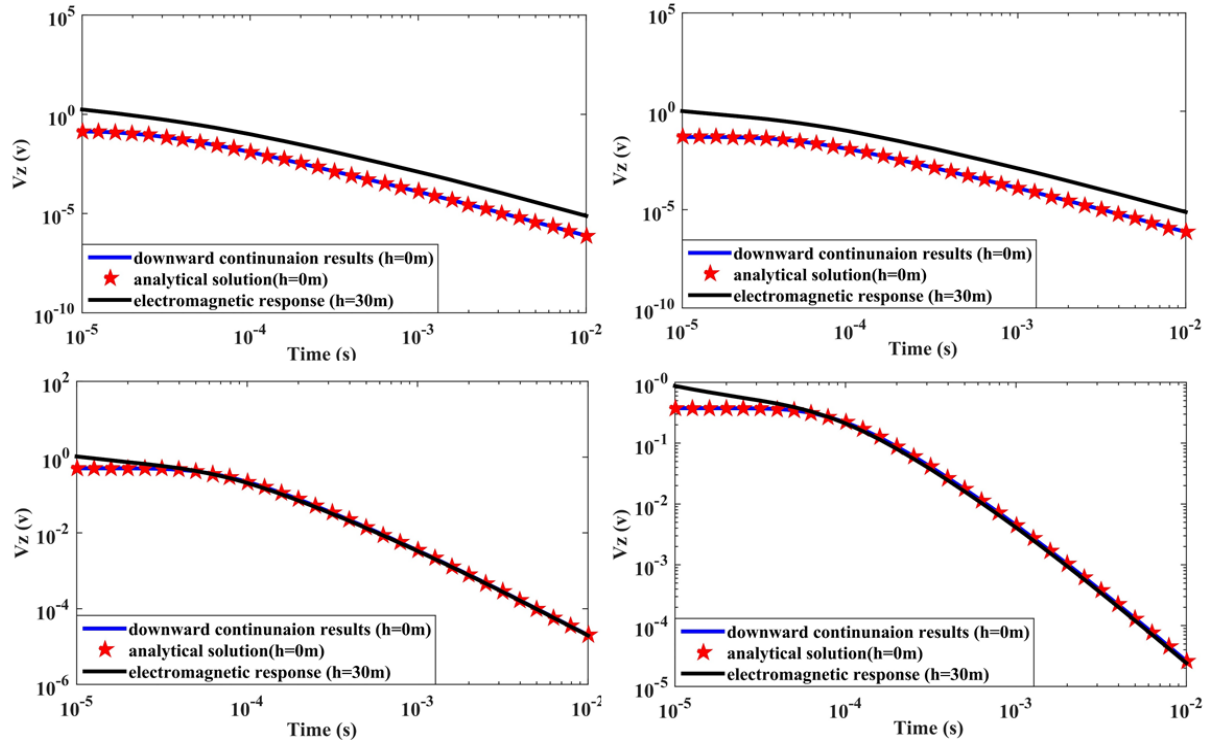


Fig. 5. Downward continuation results at different survey points: (a) $x=0$ m, $y=150$ m; (b) $x=0$ m, $y=200$ m; (c) $x=150$ m, $y=200$ m; (d) $x=200$ m, $y=200$ m.

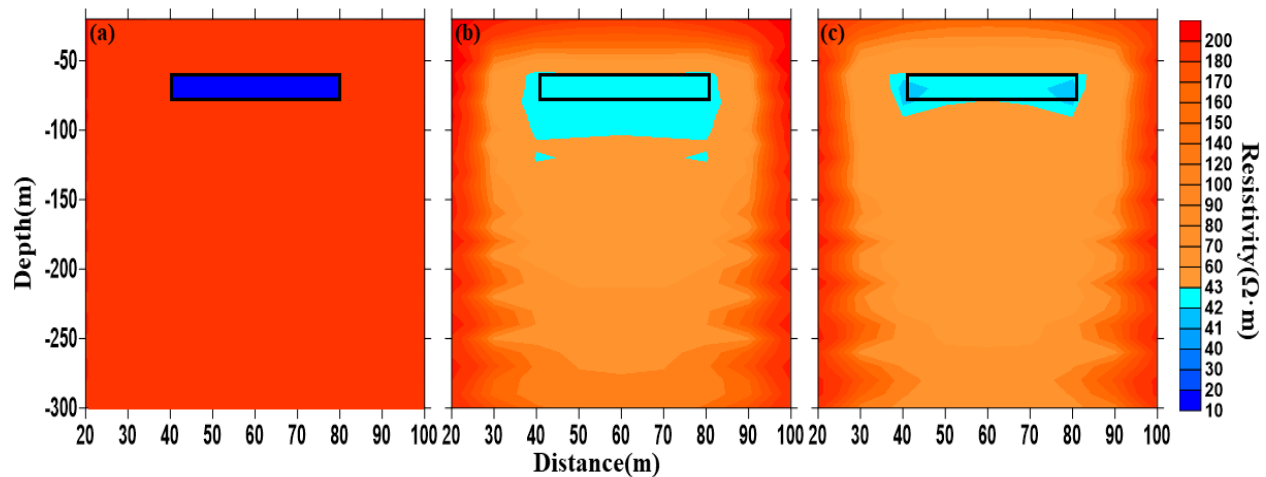


Fig. 6. Comparison between depth section images of the shallow abnormality: (a) theoretical model, (b) interpretation results derived from the $z = 30$ m electromagnetic response, and (c) interpretation results derived from continued electromagnetic responses. The black outlines serve as a reference to the theoretical model.

2) Field data results

To verify an effectiveness of the PID controller iteration downward continuation method, it is applied to field data. We conducted an exploration experiment at Shouyang, Jinzhong City, Shanxi Province, China, in 2016 December by using a GATEM system. The field site is chosen because there is a borehole in the survey

area. According to the Shanxi Geological Survey, the order of the geological structures from the top to the bottom is Quaternary strata, Permian system, Carboniferous system and Ordovician system. The Quaternary strata mainly consists of loess and clay, and the electrical resistivity is relatively low. The Permian system is composed of mudstone, sandstone, fine-

grained sandstone and coal seams, and the electrical resistivity is relatively high. It is the main coal-bearing stratum that can be exploited. The main constituents of the Carboniferous system are siltstone, mudstone, bauxite, limestone and coal seam. The Ordovician system is the basement of the coal seam, and the main lithology is dark gray layered limestone with high electrical resistivity. The survey area covers the known mined-out area. The electrical resistivity of this area is very low, and the surface depth is approximately 100 m. The mined-out area thickness is 20 m. The mined-out area and Permian system contain water; therefore, the electrical resistivity may be lower than itself, and the low-resistivity layer may be thicker than the mined-out area thickness.

The survey area and flight path are shown in Fig. 8. The electrical transmitting system used a grounded wire source with a length of 2 km. The transmitter current was 40 A, the frequency was 12.5 Hz, and the transmitter waveform was a bipolar square wave which was +40 A, 0 A, -40 A, 0 A. The induction coil area was 2,160 m², the sampling rate of receiver was 30 kHz, the receiver locations were $x = 60 \text{ m} - 1980 \text{ m}$, $y = 300 \text{ m}$ and the flight altitude was $z = 30 \text{ m}$. The flight path was parallel to the grounded wire source.

Baseline correction is performed on field data by a method based on wavelet transform [26]. Decay curves are stacked 8 times to suppress random noise. To remove

the electromagnetic signal noise, an exponential fitting-adaptive Kalman filter (EF-AKF) is used [12]. The denoised field data is continuation downward to the ground. The continued electromagnetic data, the results of raw data and the denoised $z = 30 \text{ m}$ field data are interpreted [10]. The depth section images are shown in Fig. 9.

Figure 9 (a) presents the interpretation results of raw data, Fig. 9 (b) presents the results of denoised $z = 30 \text{ m}$ field data, and Fig. 9 (c) presents the results of the continued electromagnetic data. The low resistivity layer under 200 m, in Fig. 9 (a), is the mined-out area with accumulated water, which is deeper than the true depth. The thickness of low resistivity layer is more than 100 m which is much thicker than its true thickness. The low resistivity layer at 100 m, in Figs. 9 (b) and (c), which are consistent with the survey area. In Fig. 9 (b), the results of denoised $z = 30 \text{ m}$ field data, the thickness of low resistivity layer is around 50 m. In Fig. 9 (c), the results for the continued electromagnetic data, the thickness of the low resistivity layer is average 36 m which is smaller than the results of denoised $z = 30 \text{ m}$ field data and closer to true thickness. The results show that the PID controller iteration downward continuation method can be effectively applied to the denoised field data and it can approve the interpretation accuracy of GATEM data.

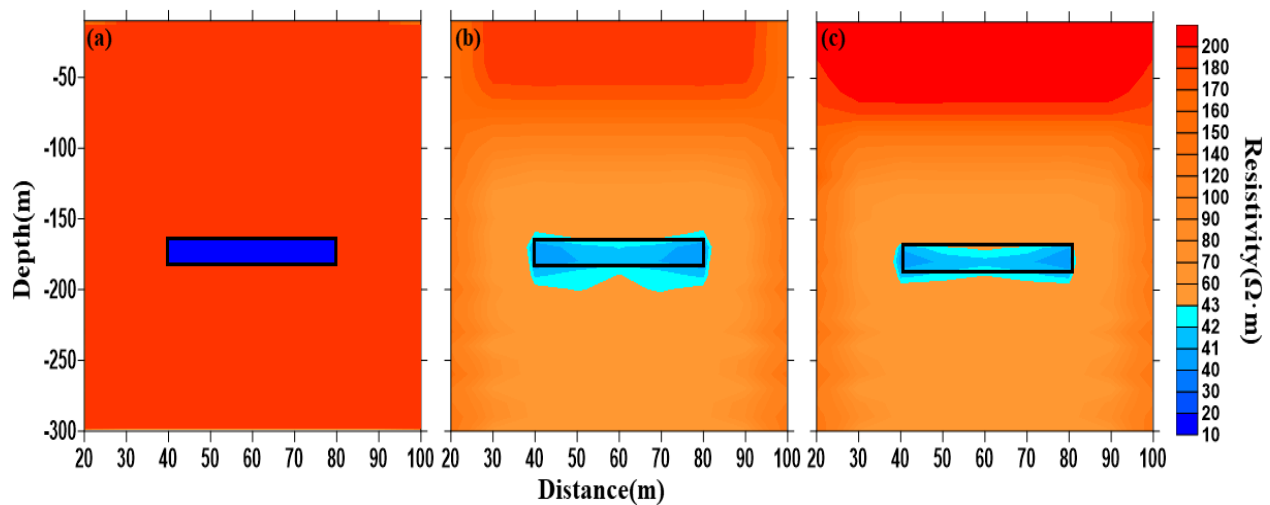


Fig. 7. Comparison between depth section images of the deep abnormality: (a) theoretical model, (b) interpretation results derived from the $z = 30 \text{ m}$ electromagnetic response, and (c) interpretation results derived from continued electromagnetic responses. The black outlines serve as a reference to the theoretical model.

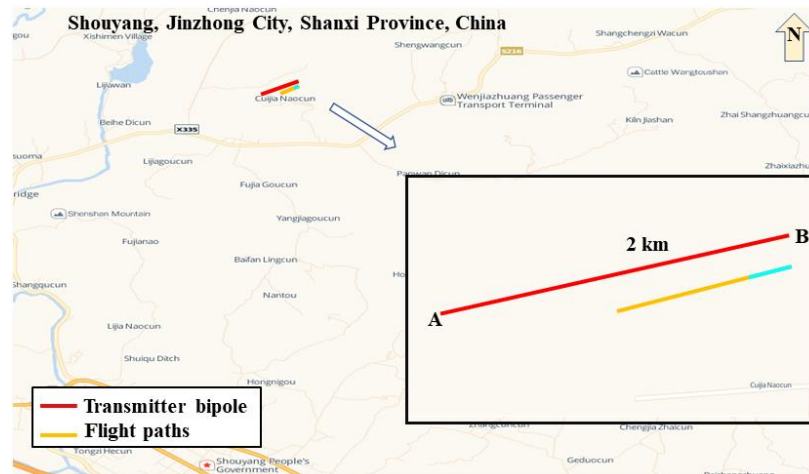


Fig. 8. Survey area for Shouyang, Jinzhong City, Shanxi Province in China. The red line is the transmitter line with 2 km length, and the electrical dipole A is 0. The yellow line is the flight path which is parallel to the red line. The blue line is the chosen section for verifying the application of the downward continuation.

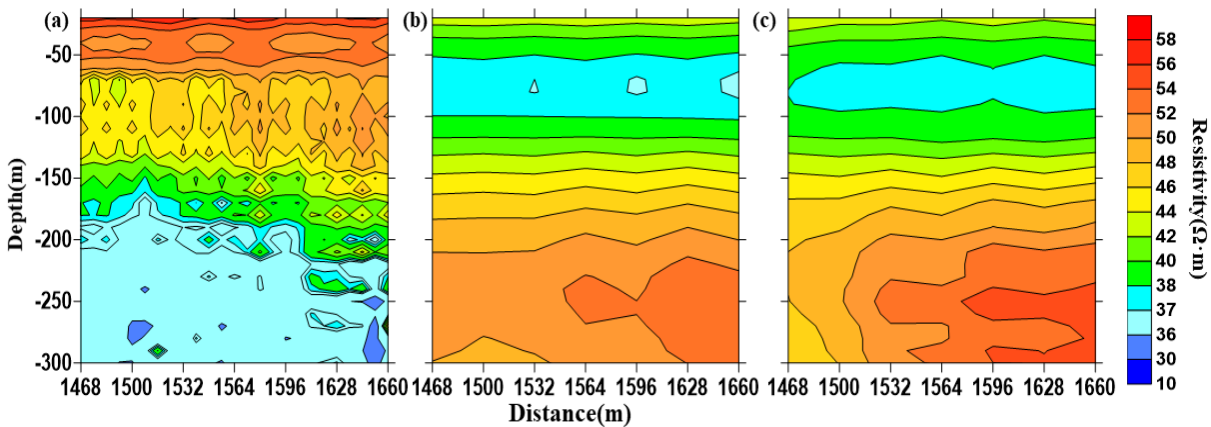


Fig. 9. Depth section images from the field data: (a) the results of raw data, (b) the results of the $z = 30$ m field data, and (c) the interpretation results of the continued electromagnetic continuation.

IV. CONCLUSION

The GATEM system is an effective method for the exploration of low resistivity anomalies in complex areas. In this paper, a PID controller iteration downward continuation method is proposed to improve the interpretation and imaging accuracy of GATEM data. The integral and differential term are added into the traditional iterative method. Compared with the analytical solution, the continuation downward accuracy of the iterative method is verified, and the iteration time is effectively reduced. This method is validated using synthetic data interpretation and is compared with the interpretation results of the $z = 30$ m electromagnetic response. The results show that interpretation of continued electromagnetic response is more consistent with the true model, especially for the shallow anomalous body. To further verify the effectiveness, this method is applied to

field data of Shouyang, Yangquan City, Shanxi Province, China, which improves the quality of the GATEM field data results. This method has significant implications for the GATEM exploration.

ACKNOWLEDGMENT

This study was carried out within the framework of the project '3D Numerical Simulation of ATEM Based on Conformal Mesh Technique (JJKH20190127KJ)' supported by the Planning Project of Science and Technology and Humanities and Social Science Research of the Education Department of Jilin Province and the project 'Research on Sub-diffusion Multi-parameter extraction method of Ground-source Airborne Electromagnetic data based on fully connected neural network (42004059)' and 'Research on Key Technologies of Electromagnetic Detection of Induction-Polarization

Symbiosis Effects of Dual Phase Conductive Medium Based on SQUID technique (42030104)' supported by the National Natural Science Foundation of China.

REFERENCES

- [1] T. Mogi, K. Kusunoki, H. Kaieda, H. Ito, A. Jomori, N. Jomori, and Y. Yuuki, "Grounded electrical-source airborne transient electromagnetic (GREATEM) survey of Mount Bandai," *North-Eastern Japan, Exploration Geophysics*, vol. 40, no. 1, pp. 1-7, Feb. 2009.
- [2] H. Ito, H. Kaieda, T. Mogi, A. Jomori, and Y. Yuuki, "Grounded electrical-source airborne transient electromagnetic (GREATEM) survey of Aso volcano," *Japan. Explor. Geophys.*, vol. 45, pp. 43-48, Mar. 2014.
- [3] M. J. Yi, J. H. Kim, N. H. Sung, M. H. Han, K. Motschka, R. Supper, A. Ahl, and A. Jomori, "Test airborne EM surveys at a black-shale type uranium deposit in Korea," *Near Surface Geoscience 2016 - 22nd European Meeting of Environmental and Engineering Geophysics*, Sep. 2016.
- [4] D. Li, Z. Tian, Y. Ma, J. Gu, Y. Ji, and S. Li, "Application of grounded electrical source airborne transient electromagnetic (GREATEM) system in goaf water detection," *Journal of Environmental & Engineering Geophysics*, vol. 24, no. 3, pp. 387-397, Sep. 2019.
- [5] Y. Sasaki, M. J. Yi, J. Choi, and J. S. Son, "Frequency and time domain three-dimensional inversion of electromagnetic data for a grounded-wire source," *Journal of Applied Geophysics*, vol. 112, pp. 106-114, Jan. 2015.
- [6] S. A. Allah and T. Mogi, "Three-dimensional resistivity modeling of GREATEM survey data from ontake volcano," *Northwest Japan [JJ]. Earth Planets & Space*, vol. 68, no. 1, pp. 76, Dec. 2016.
- [7] B. Liang, C. Qiu, F. Han, C. Zhu, N. Liu, H. Liu, F. Liu, G. Fang, and Q. H. Liu, "A new inversion method based on distorted born iterative method for grounded electrical source airborne transient electromagnetic," *IEEE Transactions on Geoscience and Remote Sensing*, vol. 56, no. 2, pp. 877-887, Mar. 2018.
- [8] Q. Wu, D. S. Li, C. D. Jiang, Y. J. Ji, Y. L. Wen, and H. Luan, "Ground-source airborne time-domain electromagnetic (GATEM) modelling and interpretation method for a rough medium based on fractional diffusion," *Geophysical Journal International*, vol. 217, no. 3, pp. 1915-1928, June 2019.
- [9] T. Mogi, Y. Tanaka, K. Kusunoki, T. Morikawa, and N. Jomori, "Development of grounded electrical source airborne transient EM (GREATEM)," *Exploration Geophysics*, vol. 29, pp. 61-64, June 1998.
- [10] Y. Ji, G. Yang, and S. Guan, "Interpretation research on electrical source of time domain ground - Airborne electromagnetic data," *2011 International Conference on Green Environmental Sustainable Development*, Jan. 2011.
- [11] D. Li, Y. Wang, J. Lin, S. Yu, and Y. Ji, "Electromagnetic noise reduction in grounded electrical-source airborne transient electromagnetic signal using a stationary wavelet-based denoising algorithm," *Near Surface Geophysics*, vol. 15, no. 2, pp. 163-173, Apr. 2017.
- [12] Y. Ji, Q. Wu, Y. Wang, J. Lin, D. Li, S. Du, S. Yu, and S. Guan, "Noise reduction of grounded electrical source airborne transient electromagnetic data using an exponential fitting-adaptive Kalman filter," *Exploration Geophysics*, vol. 49, no. 3, pp. 243-252, Mar. 2017.
- [13] M. Fedi and G. Florio, "A stable downward continuation by using the ISVD method," *Geophysics Journal International*, vol. 151, pp. 146-156, Apr. 2002.
- [14] S. Xu, "A comparison of effects between the iteration method and FFT for downward continuation of potential fields," *Chinese Journal of Geophysics*, vol. 50, no. 1, pp. 285-289, Jan. 2007.
- [15] S. Xu and H. Yu, "The interpolation-iteration method for potential field continuation from undulating surface to plane," *Acta Geophysica Sinica*, vol. 50, no. 6, pp. 1811-1815, Nov. 2007.
- [16] A. E. Ali, Z. Liu, Y. Bai, A. G. Farwa, A. S. Ahmed, and G. Peng, "A stable gravity downward continuation for structural delineation in Sulu Sea region," *Journal of Applied Geophysics*, vol. 155, pp. 26-35, Aug. 2018.
- [17] C. Zhang, Q. Lv, J. Yan, and G. Qi, "Numerical solutions of the mean-value theorem: New methods for downward continuation of potential fields," *Geophysical Research Letters*, pp. 3461-3470, Apr. 2018.
- [18] G. R. J. Cooper, "The downward continuation of the tilt-angle," *Near Surface Geophysics*, vol. 14, no. 5, pp. 385-390, Oct. 2016.
- [19] G. R. J. Cooper, "The downward continuation of aeromagnetic data from magnetic source ensembles," *Near Surface Geophysics*, vol. 17, pp. 101-107, Apr. 2019.
- [20] M. Nabighian, "Electromagnetic methods in applied geophysics," *Society of Exploration Geophysicists*, vol. 1, pp. 528, Jan. 1988.
- [21] D. Guptasarma and B. Singh, "New digital linear filters for Hankel J0 and J1 transforms," *Geophysical Prospecting*, vol. 45, pp. 745-762, Oct. 1997.
- [22] D. Guptasarma, "Optimization of short digital linear filters for increased accuracy," *Geophysical*

Prospecting, vol. 30, pp. 501-514, Aug. 1982.

- [23] M. Nabighian, "Foreword and introduction," *Geophysics*, vol. 49, pp. 849-853, July 1984.
- [24] A. B. Rad and W. L. LO, "Predictive PI controller," *International Journal of Control*, vol. 60, no. 5, pp. 953-975, Nov. 1994.
- [25] B. R. Spies, "Depth of investigation in electromagnetic sounding methods," *Geophysics*, vol. 54, no. 7, pp. 872-888, July 1989.
- [26] Y. Wang, Y. Ji, S. Li, J. Lin, F. Zhou, and G. Yang, "A wavelet-based baseline drift correction method for grounded electrical source airborne transient electromagnetic signals," *Explor. Geophys.*, vol. 44, pp. 229-237, Dec. 2013.



Shanshan Guan received the Ph.D. degree in Measuring and Testing Technology and Instrument from Jilin University, Changchun, China, in 2012. In 2019, she was a Visiting Scholar with the Southern University of Science and Technology, China.

Since 2012, she has been with the College of Instrumentation and Electrical Engineering, Jilin University, where she is currently an Associate Professor. Her research interests include the development of transient electromagnetic instruments and data forward, and inverse algorithms.



Qiong Wu received the B.S. degree in Electrical Engineering and Automation from Jilin University, Changchun, China, in 2013 and the Ph.D. degree in Detection Technology and Automatic Equipment from Jilin University, Changchun, China, in 2019. From 2016 to 2017, she was an exchange student in Sustainable Resources Engineering, Faculty of Engineering, Hokkaido University, Sapporo, Japan. Her research interest includes modelling and interpretation method for grounded electrical source airborne electromagnetics.

The Behavior of Electromagnetic Wave Propagation in Photonic Crystals with or without a Defect

Ayşe N. Basmacı

Vocational School of Technical Sciences
Tekirdag Namik Kemal University, Tekirdag, 59030, Turkey
anbasmaci@nku.edu.tr

Abstract — In this study, the electromagnetic wave propagation behavior of two-dimensional photonic crystal plates with a defect is investigated. For this purpose, the partial differential equation for the electromagnetic wave propagation in various photonic crystal plates containing a defect or not is obtained by using Maxwell's equations. The defect is also defined in the electromagnetic wave propagation equation appropriately. In order to solve the electromagnetic wave propagation equation, the finite differences method is used. The material property parameters of the photonic crystal plates are determined with respect to the defects. Accordingly, the effects of material property parameters on electromagnetic wave propagation frequencies, phase velocities, and group velocities are examined. The effects of the size and position of the defects on the electromagnetic wave propagation frequencies are also discussed. The highest electromagnetic wave propagation fundamental frequency value obtained from the analyses performed is 1.198 Hz. This fundamental frequency value is obtained for the electromagnetic wave propagation in the t-shaped photonic crystal plate. Electromagnetic field distribution maps for the fundamental frequencies of the photonic crystal plates whose electromagnetic wave propagation behaviors are examined are obtained with the ANSYS package program based on the finite differences time-domain (FDTD) method.

Index Terms — Central finite differences method, electromagnetic wave propagation, Maxwell's equations, photonic crystals.

I. INTRODUCTION

According to the developments in optics and optoelectronics, the use of different types of materials in metamaterials, photonic crystals, and waveguides has gradually increased [1-6]. These structures are designed by combining different types of materials along a specified axis in certain ways. Phononic structures that are open to acoustic effects, in other words, affected by

acoustic wave propagation, are also functionally similar to photonic structures [7-11].

Whether it is a photonic or a phononic structure, both structures consist of layers, and each layer has different material property parameters. The material property parameters include the permittivity (ϵ) and permeability (μ) of the structure. While analyzing the behavior of electromagnetic wave propagation in photonic structures, each layer's electromagnetic wave propagation behavior in the periodic layer group forming the structures should be considered separately. Photonic structures with a defect in some layers have also been investigated [12-14].

In the literature, there are studies that theoretically examine the electromagnetic wave propagation behavior occurring in each layer of one-dimensional and two-dimensional photonic structures [15-19], as well as experimental studies in which these structures are manufactured using various production methods [20,21]. For instance, [22-24] are among the studies investigating the electromagnetic wave propagation behavior in two-dimensional and three-dimensional plate structures.

In order to examine the electromagnetic wave propagation behavior in optical structures, many studies are guiding the formation of the partial differential equation for electromagnetic wave propagation using Maxwell's equations [25-32]. The ideal numerical method for solving the obtained partial differential equation for electromagnetic wave propagation is determined. The finite differences method is preferred in solving complex problems for which an exact solution cannot be achieved [29-33]. In [34-37], the central finite differences method is used for analyzing the electromagnetic wave propagation behavior of optical structures with microcavities, ellipses, and circular holes. The main reason for using the central finite differences method in these studies is that some nodes of the two-dimensional (2-D) structures whose electromagnetic wave propagation behaviors are investigated have different material property parameters (ϵ , μ) from each other.

In this study, the behaviors of electromagnetic wave propagation occurring in the two-dimensional plates with or without a defect are investigated. The effects of the location and size of the defect in the plates on the electromagnetic wave propagation frequencies are also examined. For this purpose, the material property parameters (ε , μ) of the defects are determined as zero. Accordingly, the frequencies of electromagnetic wave propagation in the plate with the defect are obtained using the central finite differences method. In addition, phase velocities and group velocities of the electromagnetic wave propagation are examined. The electromagnetic field distribution maps for the fundamental frequencies of the photonic crystal plates are visualized by using the ANSYS Lumerical package program. The novelty of this study is that it describes the effects of the defect locations and defect sizes of the 2-D photonic crystal plates formed in different shapes on frequencies of the electromagnetic wave propagation in the photonic crystal plates.

II. THEORETICAL ANALYSIS

The partial differential equation for the electromagnetic wave (EMW) propagation occurring in the two-dimensional plate is obtained using Maxwell's equations. The finite difference method is preferred in the solution of the electromagnetic wave propagation equation to examine the behavior of electromagnetic wave propagation in two-dimensional plates which have a defect or which have not. A two-dimensional plate positioned in the Cartesian coordinate system can be seen in Fig. 1.

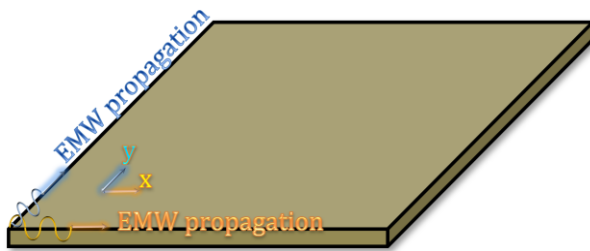


Fig. 1. A view of a 2-D plate.

In a source free, linear, isotropic and homogenous region, The first-order Maxwell's curl equations are as follows [38]:

$$\nabla \cdot \vec{E} = \frac{\rho}{\varepsilon}, \quad (1a)$$

$$\nabla \cdot \vec{H} = 0, \quad (1b)$$

$$\nabla \times \vec{E} = -i\omega\mu\vec{H}, \quad (1c)$$

$$\nabla \times \vec{H} = -i\omega\varepsilon\vec{E}, \quad (1d)$$

where $i: \sqrt{-1}$, ρ is the charge density, μ is the permeability, ε is the permittivity, E is the electrical field, and H is the magnetic field.

Using Eqs. (1c) and (1d), Eq. (2) is obtained as in the following form:

$$\nabla \times (\nabla \times \vec{H}) = \nabla(\nabla \cdot \vec{H}) - \nabla^2 \vec{H} = \nabla \times \left(-\mu \frac{\partial \vec{H}}{\partial t} \right), \quad (2)$$

where $H(x,y,t)$ represents the electromagnetic wave propagation field of the 2-D plate. Partial differential equation with respect to time and position related to electromagnetic wave propagation obtained by solution of Eq. (2) is as follows:

$$\frac{\partial^2 H(x,y,t)}{\partial x^2} + \frac{\partial^2 H(x,y,t)}{\partial y^2} - \mu\varepsilon \frac{\partial^2 H(x,y,t)}{\partial t^2} = 0. \quad (3)$$

D_x represents the material property parameters of (μ_x , ε_x) on the x-axis, and D_y represents the material property parameters of (μ_y , ε_y) on the y-axis. Accordingly, Eq. (3) is rearranged as follows:

$$D_x \frac{\partial^2 H(x,y,t)}{\partial x^2} + D_y \frac{\partial^2 H(x,y,t)}{\partial y^2} - \frac{\partial^2 H(x,y,t)}{\partial t^2} = 0. \quad (4)$$

Solving Eq. (4) for $D_x=D_y=1$ and $H(x,y,t) = h e^{-i(-\beta_m x - \beta_n y + \omega t)}$ for the linear isotropic case, Eq. (5) is obtained as follows:

$$\beta_m^2 + \beta_n^2 - \omega_{mn}^2 = 0, \quad (5a)$$

$$\beta_m: \frac{m\pi}{a}, \beta_n: \frac{n\pi}{b} \text{ and } m: 0,1,2 \dots, n: 0,1,2 \dots, \quad (5b)$$

$$\omega_{mn} = \sqrt{\left(\frac{m\pi}{a}\right)^2 + \left(\frac{n\pi}{b}\right)^2}, \quad (5c)$$

where h , β_m , β_n , ω_{mn} , represents travelling wave, wave number for the x-axis, wave number for the y-axis and electromagnetic wave propagation frequency, respectively. In this study, the permittivity (ε) and permeability (μ) values of the plate are assumed as 1 for the defect-free parts of the plate. In keeping with this assumption, there are some studies on silicon-based photonic metamaterials in the literature [40,41]. The b/a ratio of the 2-D plate is considered in units, where a represents the plate's width and b represents the plate's length, and its value is considered as 1/1. The exact solution of Eq. (4) given in Eqs. (5a-5c) is obtained when the material property parameters D_x and D_y are equal to 1. In the fundamental mode, where the value of the (m , n) mode pair is equal to (1,1), the value of ω_{11} from the exact solution of Eq. (4) is obtained as 4.442 Hz. Especially in the analysis of the electromagnetic wave propagation behavior occurring in the plate with a defect, the central finite differences method should be used to solve Eq. (4). Accordingly, to apply the finite differences method, the 2-D plate is expressed with nodes, as shown in Fig. 2. Besides, the representation of any node is represented by (k,l), while Δ represents the neighborhoods with respect to the specified (k,l) node.

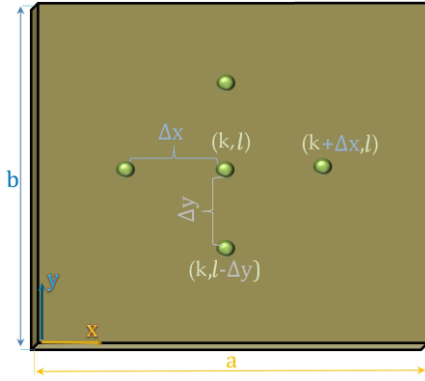


Fig. 2. Central finite differences notation of the plate.

According to the derivative values obtained using the Taylor series expansion and given in Table 1, the central finite differences method is applied to Eq. (4).

Table 1: The central finite differences notation [39]

| Derivative | The Central Finite Differences Notation $O(h^2)$ |
|---|---|
| $h(x, y)$ | $\approx q_{k,l}$ |
| $\frac{\partial^2 h(x, y)}{\partial x^2}$ | $\approx \frac{q_{k-1,l} - 2q_{k,l} + q_{k+1,l}}{\Delta x^2}$ |
| $\frac{\partial^2 h(x, y)}{\partial y^2}$ | $\approx \frac{q_{k,l-1} - 2q_{k,l} + q_{k,l+1}}{\Delta y^2}$ |

By defining the neighbours of the (k, l) node with the Taylor Series expansion, the expression obtained is as follows:

$$q_{k\pm 1,l} = q_{k,l} \pm \frac{\Delta x}{1!} \frac{\partial q}{\partial x} + \frac{\Delta x^2}{2!} \frac{\partial^2 q}{\partial x^2} \pm R, \quad (6a)$$

$$q_{k,l\pm 1} = q_{k,l} \pm \frac{\Delta y}{1!} \frac{\partial q}{\partial y} + \frac{\Delta y^2}{2!} \frac{\partial^2 q}{\partial y^2} \pm R, \quad (6b)$$

where R represents truncation. The order of the truncation here is $O(h^2)$ since it comes after the second-order derivative.

Applying $H(x, y, t) = h(x, y)e^{-i\omega t}$ transformation to Eq. (4), Eq. (7a) is obtained. Equation (7a) is rearranged according to the values given in Table 1 by the method of central finite differences and thus Eq. (7b) is obtained. Relevant equations are as the following forms:

$$D_x \left[\frac{\partial^2 h(x, y)}{\partial x^2} \right] + D_y \left[\frac{\partial^2 h(x, y)}{\partial y^2} \right] + \omega^2 h(x, y) = 0, \quad (7a)$$

$$D_x \left[\frac{q_{k-1,l} - 2q_{k,l} + q_{k+1,l}}{\Delta x^2} \right] + D_y \left[\frac{q_{k,l-1} - 2q_{k,l} + q_{k,l+1}}{\Delta y^2} \right] + \omega^2 q_{k,l} = 0. \quad (7b)$$

Boundary conditions need to be determined to solve Eq. (7b). There is no electromagnetic interaction in the frame parts of the 2-D plate, which is seen in Fig. 4 and consists of 4 nodes. The nodes of this plate that interact with each other are (1,1), (2,1), (1,2), and (k, l) , respectively. Using these nodes, an eigenvector $M(\omega)$ is

obtained to determine the frequency values by solving Eq. (7b). For the plate with four nodes starting from the node (1,1) to (2,2), the eigenvector $M(\omega)$ obtained by arranging Eq. (7b) according to the values $k:2$ and $l:2$ is as follows:

$$M(\omega) = \begin{bmatrix} p(\omega) & s & z & 0 \\ s & p(\omega) & z & 0 \\ z & 0 & p(\omega) & s \\ 0 & z & s & p(\omega) \end{bmatrix}_{k \times l} = 0. \quad (8)$$

The terms in Eq. 8 are defined as follows:

$$p(\omega) = -2 \left(\frac{D_x}{\Delta x^2} + \frac{D_y}{\Delta y^2} + \omega^2 \right), \quad (9a)$$

$$s = \frac{D_x}{\Delta x^2}, \quad (9b)$$

$$z = \frac{D_y}{\Delta y^2}. \quad (9c)$$

For the plate with four nodes, the distance for each adjacent node is defined as $\Delta x = \Delta y = \frac{1}{3}$.

The steps of the theoretical analysis are summarized in the flowchart, as also seen from Fig. 3.

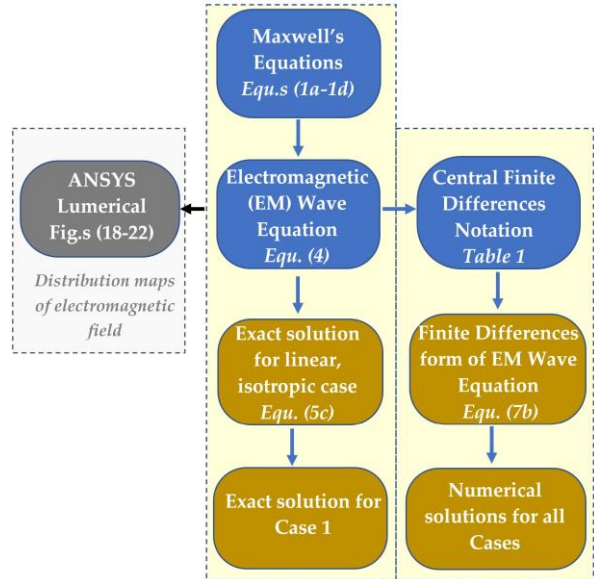


Fig. 3. The flowchart summarizing the theoretical analysis.

Electromagnetic wave propagation frequencies, in other words, ω_{mn} eigenvalues, are obtained by equating the determinant of the eigenvector $M(\omega)$ to zero.

Besides, the phase velocities, v_{phase} and group velocities, v_{group} regarding the electromagnetic wave propagation occurring in the plate are calculated with the following formulas:

$$v_{phase} = \frac{\omega_{mn}}{\beta_n}, \quad (10a)$$

$$v_{group} = \frac{\partial \omega_{mn}}{\partial \beta_n} \tag{10b}$$

The behaviour of electromagnetic wave propagation occurring in a two-dimensional plate can be defined using Eqs. (7b) and (8). Accordingly, electromagnetic wave propagation frequencies are obtained for six different cases where the plate has a defect from various parts, whether it has not. Figure 4 shows the first case (Case 1) where the plate has not any defect.

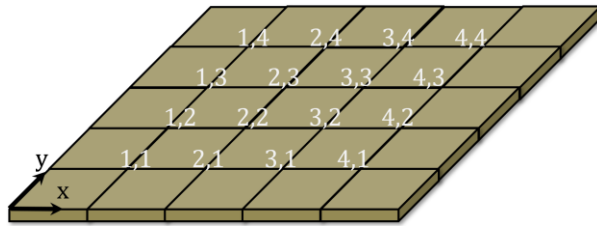


Fig. 4. A plate which has not any defect – Case 1.

In all other cases except the first case, plates have a defect in their various parts. Figure 5 shows the second case (Case 2), where the plate has an unsymmetrical O-shaped defect. In this case, there are two nodes with a defect. Nodes with the defect are (3,2) and (3,3) nodes, respectively.

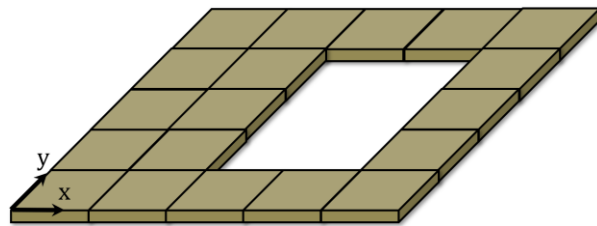


Fig. 5. A plate with an unsymmetrical O-shaped defect – Case 2.

Figure 6 shows the third case (Case 3), where the plate has a symmetrical O-shaped defect. In this case, there are four nodes with a defect. Nodes with the defect are (2,2), (2,3), (3,2) and (3,3) nodes, respectively.

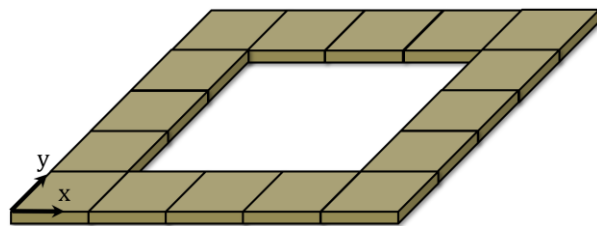


Fig. 6. A plate with a symmetrical O-shaped defect – Case 3.

Figure 7 shows the fourth case (Case 4), where the plate has an unsymmetrical C-shaped defect. In this case, there are four nodes with a defect. Nodes with the defect are (3,2), (3,3), (4,2) and (4,3) nodes, respectively.

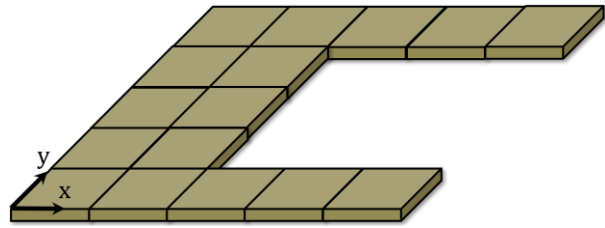


Fig. 7. A plate with a C-shaped defect – Case 4.

Figure 8 shows the fifth case (Case 5), where the plate has a L-shaped defect. In this case, there are four nodes with a defect. Nodes with the defect are (3,3), (4,3), (3,4) and (4,4) nodes, respectively.

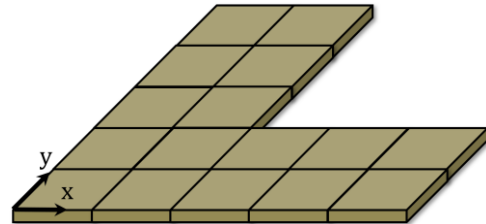


Fig. 8. A plate with a L-shaped defect – Case 5.

Figure 9 shows the sixth case (Case 6), where the plate has a symmetrical t-shape and corner defects. In this case, there are four nodes with a defect. Nodes with the defect are (1,1), (1,4), (4,1) and (4,4) nodes, respectively.

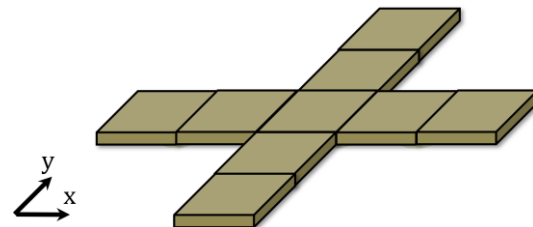


Fig. 9. A t-shaped plate with corner defects – Case 6.

The frequencies of the electromagnetic wave propagation occurring in the 2-D plate, which has the defect in its various regions, are analyzed using the method of central finite differences for multiple cases, defined according to the nodes where the defect has been placed in the plate. In this analysis made with the method of central finite differences, the material property parameters (ϵ, μ) of the nodes with the defect are defined as zero.

III. RESULTS AND DISCUSSIONS

The frequencies related to the electromagnetic wave propagation occurring in the defect-free plate defined as Case 1 are examined for various (m, n) modes. This analysis is carried out using both the exact solution and the finite differences method. As shown in Fig. 10 and Fig. 11, the electromagnetic wave propagation frequencies obtained from the exact solution are relatively close to the values of the frequencies obtained by the finite difference method. Additionally, Fig. 10 shows that the frequencies of electromagnetic wave propagation increase linearly as the wavenumber increases.

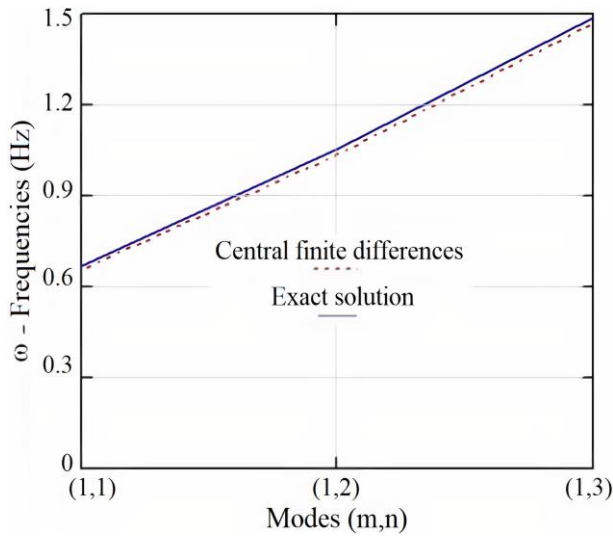


Fig. 10. Dispersion relation ($\beta-\omega$) of the electromagnetic wave for Case 1.

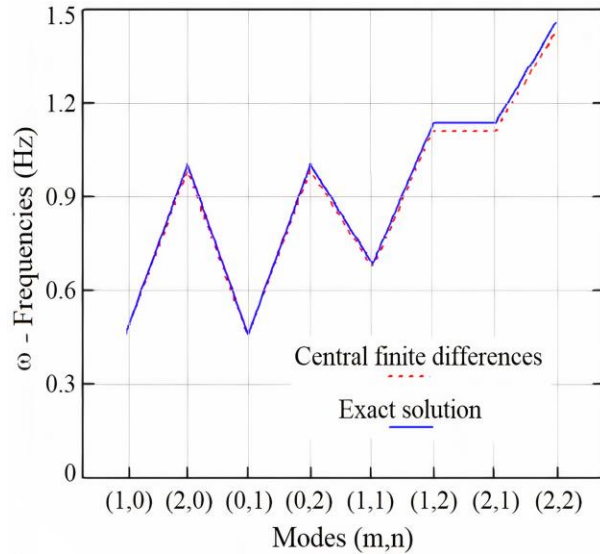


Fig. 11. Comparison of the frequencies obtained by the exact solution and finite differences method for Case 1.

Table 2: The frequency investigation of five different cases (Cases 2-6) of the plate

| | Case No | Mode – (m,n) | Frequency (Hz) |
|--|---------|--|----------------|
| D E F E C T - F R E E | 1 | (1,0) | 0.492 |
| | | (2,0) | 0.984 |
| | | (0,1) | 0.492 |
| | | (0,2) | 0.984 |
| | | (1,1) - Fundamental Mode for 2-D Plate | 0.696 |
| | | (1,2) | 1.100 |
| | | (2,1) | 1.100 |
| | | (2,2) | 1.391 |
| I N T E R N A L D E F E C T E D | 2 | (1,0) | 0.492 |
| | | (2,0) | 0.984 |
| | | (0,1) | 0.492 |
| | | (0,2) | 0.984 |
| | | (1,1) | 0.911 |
| | | (1,2) | 1.260 |
| | | (2,1) | 1.428 |
| | (2,2) | 1.821 | |
| | 3 | (1,0) | 0.492 |
| | | (2,0) | 0.984 |
| | | (0,1) | 0.492 |
| | | (0,2) | 0.984 |
| | | (1,1) | 1.125 |
| | | (1,2) | 1.485 |
| (2,1) | | 1.485 | |
| (2,2) | 2.251 | | |
| 4 | (1,0) | 0.492 | |
| | (2,0) | 0.984 | |
| | (0,1) | 0.492 | |
| | (0,2) | 0.984 | |
| | (1,1) | 0.912 | |
| | (1,2) | 1.260 | |
| | (2,1) | 1.432 | |
| | (2,2) | 1.824 | |
| C O R N E R D E F E C T E D | 5 | (1,0) | 0.492 |
| | | (2,0) | 0.984 |
| | | (0,1) | 0.492 |
| | | (0,2) | 0.984 |
| | | (1,1) | 0.846 |
| | | (1,2) | 1.245 |
| | | (2,1) | 1.245 |
| | (2,2) | 1.695 | |
| | 6 | (1,0) | 0.492 |
| | | (2,0) | 0.984 |
| | | (0,1) | 0.492 |
| | | (0,2) | 0.984 |
| | | (1,1) | 1.198 |
| | | (1,2) | 2.009 |
| (2,1) | | 2.009 | |
| (2,2) | 2.397 | | |

In this study, plates can be grouped into three different classes in terms of the shape of the defects they have. These classes include plates without defects, plates with internal defects, and plates with corner defects, respectively. Case 1 represents the class of plates without defects. Case 2, Case 3, and Case 4 represent the class of plates with internal defects. Case 5 and Case 6 represent the class of plates with corner defects. As can be seen from Table 2, the frequency values of electromagnetic wave propagation occurring in the plates for all these cases are calculated in the lower modes with the finite differences method.

Figure 12 depicts the dispersion relation of the electromagnetic wave for all cases. Among these six cases, the lowest electromagnetic wave propagation frequencies are obtained for Case 1, while the highest wave propagation frequencies are obtained for Case 6. In addition, the second highest electromagnetic wave propagation frequencies are obtained for Case 3.

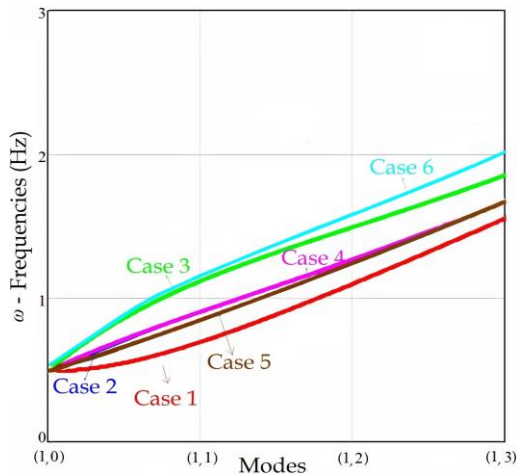


Fig. 12. Dispersion relation of the electromagnetic wave in the lower modes for all cases.

Figure 13 shows the dispersion relation of the electromagnetic wave in the higher modes. In Fig. 12, curves related to the dispersion relation of the electromagnetic wave obtained for Case 2 and Case 4 in the lower modes are almost coincident, whereas, in Fig. 13, the difference between these curves can be clearly seen in the higher modes. The frequencies of electromagnetic wave propagation obtained for Case 2, Case 3, and Case 4 reach a peak value and then their values decrease to zero. It should also be noted that the frequency values of the electromagnetic wave propagation obtained for Case 2, Case 3, and Case 4 decrease towards zero in (1.27), (1.23), and (1.28) modes, respectively. The electromagnetic wave propagation frequency values obtained for Case 1 increase linearly with the increase in the mode values, whereas the electromagnetic wave propagation frequency

values obtained for Case 5 and Case 6 increase exponentially.

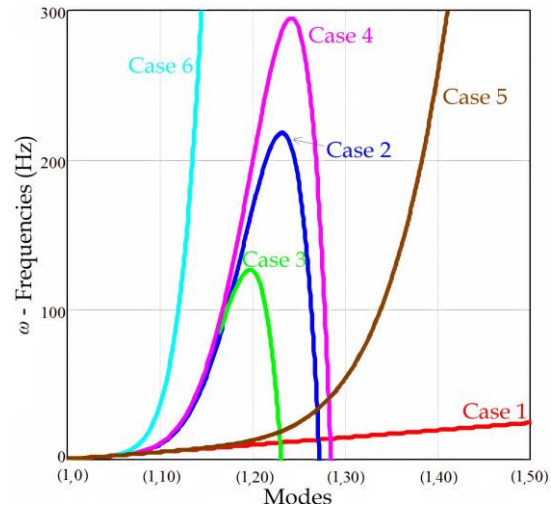


Fig. 13. Dispersion relation of the electromagnetic wave in the higher modes for all cases.

The phase and group velocity values in Figs. 14-17 are obtained by means of Eqs. (10a) and (10b). Figure 14 shows the phase velocity values obtained in the lower modes. All phase velocity values obtained in the lower modes decrease with the increase of the mode values. It should be noted that the highest phase velocity value is obtained for Case 6, whereas the lowest phase velocity value is obtained for Case 1.

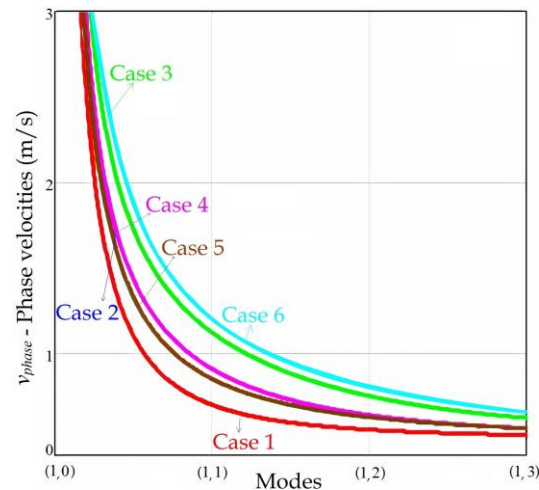


Fig. 14. Phase velocities in the lower modes for all cases.

As can be seen from Fig. 15, values of the phase velocities obtained for Case 2, Case 3, and Case 4 in the higher modes decrease towards zero after reaching a certain peak. The peak values of the phase velocities obtained for Case 2, Case 3, and Case 4 are 9.6 m/s,

6.5 m/s, and 12.4 m/s, respectively.

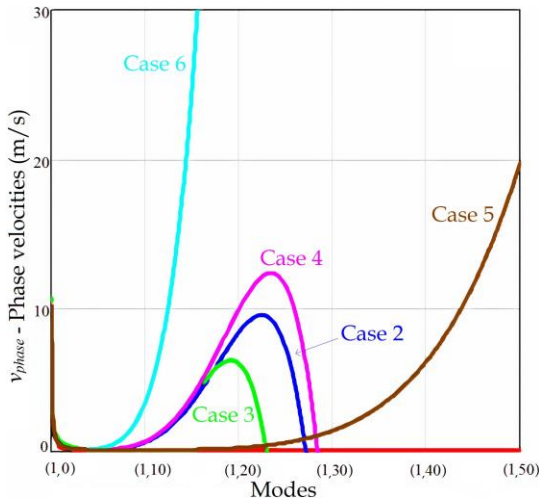


Fig. 15. Phase velocities in the higher modes for all cases.

Figure 16 depicts the group velocities in the lower modes for all cases. In the lowest modes, while the mode value increases from (1,0) to (1,1), the group velocities obtained for Case 3 and Case 6 decrease negatively exponentially, the group velocities obtained for Case 2 and Case 4 decrease linearly, the group velocities obtained for Case 5 increase linearly at the low slope, and the group velocities obtained for Case 1 increase logarithmically. In addition, in all other modes greater than (1.1), the group velocities increase with the increase of the modes for all cases.

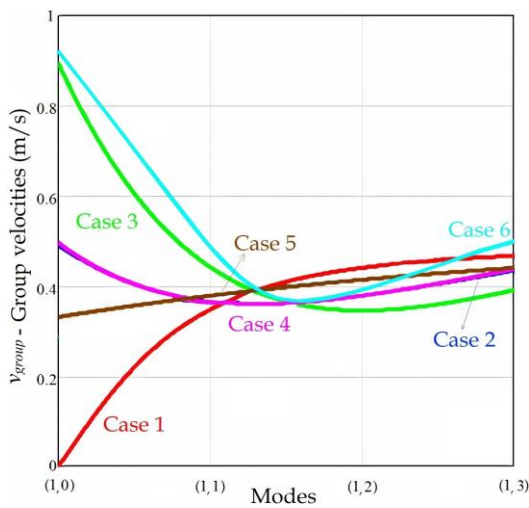


Fig. 16. Group velocities in the lower modes for all cases.

As shown in Fig. 17, the values of the group velocities obtained for Case 2, Case 3, and Case 4 in the higher modes decrease towards zero after reaching a certain peak. Peak values of the group velocities obtained for Case 2, Case 3, and Case 4 are 33.1 m/s, 17.9 m/s, and 25.6 m/s, respectively.

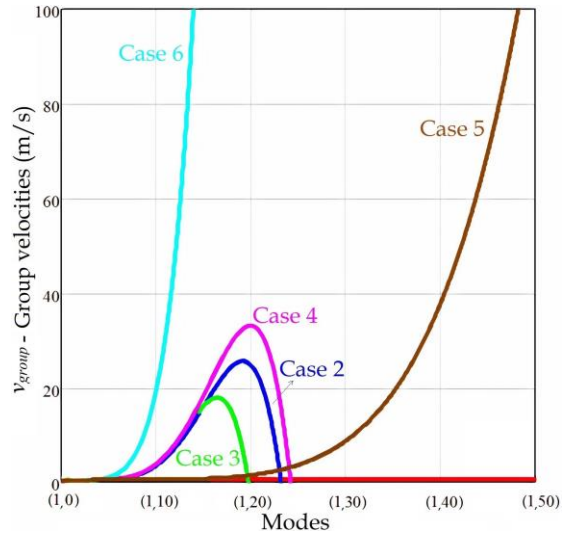


Fig. 17. Group velocities in the higher modes for all cases.

In Figs. 18-22, electromagnetic field distribution and material property parameters (ϵ, μ) distribution maps of five different cases (Cases 2-6) of the plate with the defect are depicted. The electromagnetic field and material property parameters (ϵ, μ) distribution maps in the (1,1) mode, the fundamental frequency mode for 2-D plates, are obtained using the ANSYS package program based on finite differences time-domain method. It should be noted that the data obtained from electromagnetic field distribution maps show a very good agreement with the data obtained from material property parameters (ϵ, μ) distribution maps.

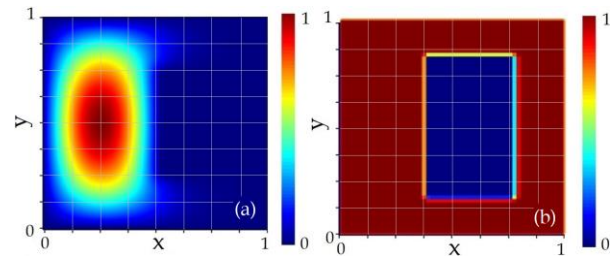


Fig. 18. Distribution maps of (a) electromagnetic field, and (b) material property parameters (ϵ, μ) for Case 2.

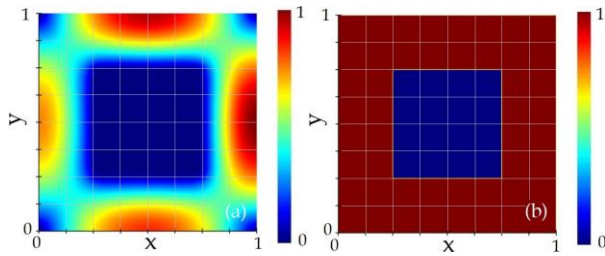


Fig. 19. Distribution maps of (a) electromagnetic field, and (b) material property parameters (ϵ, μ) for Case 3.

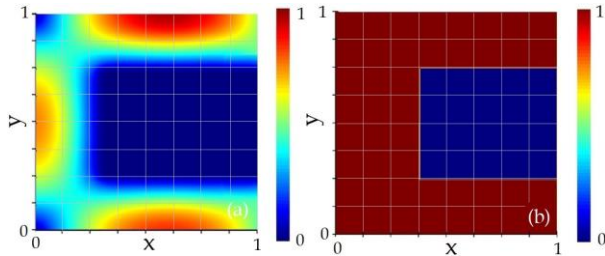


Fig. 20. Distribution maps of (a) electromagnetic field, and (b) material property parameters (ϵ, μ) for Case 4.

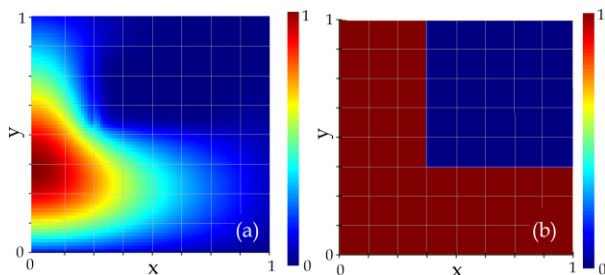


Fig. 21. Distribution maps of (a) electromagnetic field, and (b) material property parameters (ϵ, μ) for Case 5.

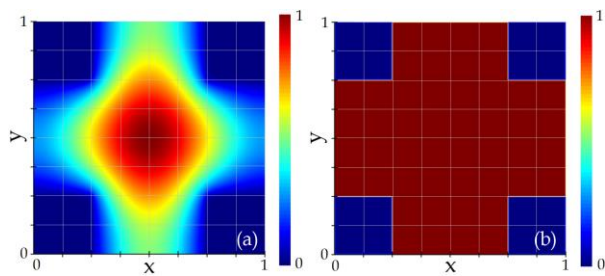


Fig. 22. Distribution maps of (a) electromagnetic field, and (b) material property parameters (ϵ, μ) for Case 6.

VI. CONCLUSION

In this study, the behaviors of electromagnetic wave propagation occurring in the two-dimensional plates having defects in their different parts are investigated. The behavior of electromagnetic wave propagation in the two-dimensional plate which has not any defect is also

examined. For this purpose, the electromagnetic wave propagation frequencies are obtained in the fundamental mode for a total of six different cases, including the five different cases of defects in different parts of the plate and the condition of being defect-free. For the five cases where the plate has a defect, the effects of the defect's region and its size on the fundamental frequencies of electromagnetic wave propagation are discussed. The electromagnetic wave propagation frequencies obtained for six different cases are compared. As the material property parameters (ϵ, μ) of some nodes on the plate take zero value, in other words, with the increase in the size of the defected part of the plate, the obtained electromagnetic wave propagation frequency values also increase. The highest electromagnetic wave propagation frequency values are obtained for the corner-defected, t-shaped plate, while the electromagnetic wave propagation frequency values obtained for the O-shaped plate are second in the ranking. When the frequencies of the electromagnetic wave propagation are examined in the higher modes, it also allows making comments about the characteristics of the phase and group velocities. In the higher modes, the frequency values of the electromagnetic wave propagation occurring in the internal-defected plates become zero after a certain mode value. In addition, the increase in the frequencies of the electromagnetic wave propagation that occur in the corner-defected plates in the higher modes is exponential and continuous with the increase in the mode values. The lowest electromagnetic wave propagation frequency values are obtained when the plate does not have a defect. The electromagnetic wave propagation frequencies obtained in this case increase linearly with the increase in the mode values.

In this study, the preferred numerical solution method is the central finite differences method. Choosing the central finite differences method as the solution method enables adjusting the material properties parameters of any point of the structure whose electromagnetic wave propagation frequencies are examined. Thus, the electromagnetic wave propagation behavior for any complex structure can be easily determined.

In future studies, it is also possible to apply the analysis to three-dimensional structures and determine the acoustic wave propagation behavior in complex phononic structures by taking advantage of the central finite differences method.

REFERENCES

- [1] K. H. Chung, T. Kato, S. Mito, H. Takagi, and M. Inoue, "Fabrication and characteristics of one-dimensional magnetophotonic crystals for magneto-optic spatial light phase modulators," *Journal of Applied Physics*, vol. 107, pp. 09A930, Apr. 2010.
- [2] E. A. Kadomina, E. A. Bezus, and L. L. Doskolovich, "Generation of interference patterns of evanescent electromagnetic waves at Fabry-

- Perot resonances of 1D photonic crystal modes,” in *3rd. International Conference “Information Technology and Nanotechnology,” (ITNT-2017)*, Samara, pp. 42-47, 2017.
- [3] A. M. Singer, A. M. Heikal, H. El-Mikati, S. S. A. Obayya, and M. F. O. Hameed, “Ultra-low loss and flat dispersion circular porous core photonic crystal fiber for terahertz waveguiding,” *Applied Computational Electromagnetics Society Journal*, vol. 35, no. 6, pp. 709-717, June 2020.
- [4] Y. Zhang, Z. Cao, G. Lu, D. Zeng, M. Li, and R. Wang, “Reconfigurable array designed for directional EM propagation using energy band theory of photonic crystals,” *Applied Computational Electromagnetics Society Journal*, vol. 33, no. 11, pp. 1209-1216, Nov. 2018.
- [5] S. Jahani and Z. Jacob, “All-dielectric metamaterials,” *Nature Nanotechnology*, vol. 11, pp. 23-36, Jan. 2016.
- [6] S.-Y. Sung, A. Sharma, A. Block, K. Keuhn, and B. J. H. Stadler, “Magneto-optical garnet waveguides on semiconductor platforms: Magnetics, mechanics, and photonics,” *Journal of Applied Physics*, vol. 109, pp. 07B738, Mar. 2011.
- [7] H. Sun, S. Huang, Q. Wang, S. Wang, and W. Zhao, “Improvement of unidirectional focusing periodic permanent magnet shear-horizontal wave electromagnetic acoustic transducer by oblique bias magnetic field,” *Sensors and Actuators A: Physical*, vol. 290, pp. 36-47, May 2019.
- [8] A. Ayman, S. Prasad, and V. Singh, “Tuning the band structures and electromagnetic density of modes in fused Silica slab by acoustic waves,” *Optik – International Journal for Light and Electron Optics*, vol. 204, 164105, Feb. 2020.
- [9] A. Rostami, H. Kaatuzian, and B. Rostami-Dogolsara, “Acoustic 1 x 2 demultiplexer based on fluid-fluid phononic crystal ring resonators,” *Journal of Molecular Liquids*, vol. 308, 113144, Apr. 2020.
- [10] A. Rostami, H. Kaatuzian, and B. Rostami-Dogolsara, “Design and analysis of tunable acoustic channel drop filter based on fluid-fluid phononic crystal ring resonators,” *Wave Motion*, vol. 101, 102700, Mar. 2021.
- [11] A. Trzaskowska, P. Hakonen, M. Wiesner, and S. Mielcarek, “Generation of a mode in phononic crystal based on 1D/2D structures,” *Ultrasonics*, vol. 106, 106146, Aug. 2020.
- [12] A. Madani and S. R. Entezar, “Tunable enhanced Goos-Hanchen shift in one-dimensional photonic crystals containing graphene monolayers,” *Superlattices and Microstructures*, vol. 86, pp. 105-110, Oct. 2015.
- [13] A. Aghajamali, T. Alamfard, and C. Nayak, “Investigation of reflectance properties in a symmetric defective annular semiconductor-superconductor photonic crystal with a radial defect layer,” *Physica B: Physics of Condensed Matter*, 412770, Mar. 2021.
- [14] T. Jalali, A. Gharaati, and M. Rastegar, “Enhanced of Faraday rotation in defect modes of one-dimensional magnetophotonic crystals,” *Materials Science-Poland*, vol. 37, no. 3, pp. 446-453, Oct. 2019.
- [15] O. V. Shramkova and Y. A. Olkhovskiy, “Electromagnetic wave transmission and reflection by a quasi-periodic layered semiconductor structure,” *Physica B: Physics of Condensed Matter*, vol. 406, no. 8, pp. 1415-1419, Apr. 2011.
- [16] A. N. Basmaci, “Characteristics of electromagnetic wave propagation in a segmented photonic waveguide,” *Journal of Optoelectronics and Advanced Materials*, vol. 22, no. 9-10, pp. 452-460, Sep.-Oct. 2020.
- [17] H. Wang, Y. Chen, and C. Huang, “The electromagnetic waves propagation characteristics of inhomogeneous dusty plasma,” *Optik – International Journal for Light and Electron Optics*, vol. 196, 163148, Nov. 2019.
- [18] F. Meng, L. Du, A. Yang, and X. Yuan, “Low loss surface electromagnetic waves on a metal-dielectric waveguide working at short wavelength and aqueous environment,” *Optics Communications*, vol. 433, pp. 10-13, Feb. 2019.
- [19] A. B. Khanikaev, S. H. Mousavi, C. Wu, N. Dabidian, K. B. Alici, and G. Shvets, “Electromagnetically induced polarization conversion,” *Optics Communications*, vol. 285, pp. 3423-3427, July 2012.
- [20] M. Askari, D. Hutchins, P. J. Thomas, L. Astolfi, R. L. Watson, M. Abdi, M. Ricci, S. Laureti, L. Nie, S. Freear, R. Wildman, C. Tuck, M. Clarke, E. Woods, and A. T. Clare, “Additive manufacturing of metamaterials: A review,” *Additive Manufacturing*, vol. 36, 101562, Dec. 2020.
- [21] K. Bi, Q. Wang, J. Xu, L. Chen, C. Lan, and M. Lei, “All-dielectric metamaterial fabrication techniques,” *Advanced Optical Materials*, vol. 9, 2001474, Nov. 2021.
- [22] T. Gao, H. Sun, Y. Hong, and X. Qing, “Hidden corrosion detection using laser ultrasonic guided waves with multi-frequency local wavenumber estimation,” *Ultrasonics*, vol. 108, 106182, Dec. 2020.
- [23] T. F. Khalkhali and A. Bananej, “Effect of shape of scatterers and plasma frequency on the complete photonic band gap properties of two-dimensional dielectric-plasma photonic crystals,” *Physics Letters A*, vol. 380, pp. 4092-4099, Dec. 2016.
- [24] B. Zamir, R. Ali, and M. Bashir, “Electromagnetic wave propagation in a superconducting parallel-

- plate waveguide filled with an indefinite medium,” *Results in Physics*, vol. 13, 102312, June 2019.
- [25] K. S. Kunz and R. J. Luebbers, *The Finite Difference Time Domain Method for Electromagnetics*. CRC Press, London, 1993.
- [26] S. Caorsi and G. Cevini, “Assessment of the performances of first- and second-order time-domain ABC’s for the truncation of finite element grids,” *Microwave Optical Technology Letters*, vol. 38, no. 1, pp. 11-16, May 2003.
- [27] J. Li and Z. Zhang, “Unified analysis of time domain mixed finite element methods for Maxwell’s equations in dispersive media,” *Journal of Computational Mathematics*, vol. 28, no. 5, pp. 693-710, Sep. 2010.
- [28] L. Li, B. Wei, Q. Yang, and D. Ge, “Piecewise linear recursive convolution finite element time domain method for electromagnetic analysis of dispersive media,” *Optik – International Journal for Light and Electron Optics*, vol. 198, 163196, Dec. 2019.
- [29] S. Elshahat, I. Abood, Z. Liang, J. Pei, and Z. Ouyang, “Dispersive engineering of W2 steeple-house-defect waveguide photonic crystals,” *Results in Physics*, vol. 19, 103547, Dec. 2020.
- [30] J.-Y. Lee, J.-H. Lee, and H.-K. Jung, “Linear lumped loads in the FDTD method using piecewise linear recursive convolution method,” *IEEE Microwave and Wireless Components Letters*, vol. 16, no. 4, Apr. 2006.
- [31] S. S. Neoh and F. Ismail, “Time-explicit numerical methods for Maxwell’s equation in second-order form,” *Applied Mathematics and Computation*, vol. 392, 125669, Mar. 2021.
- [32] X. Jia, Q. Meng, X. Wang, and Z. Zhou, “Numerical study of a quasi-zero-index photonic metamaterials,” *Optics Communications*, vol. 364, pp. 158-164, Apr. 2016.
- [33] F. Kaburcuk and A. Z. Elsherbeni, “A speeding up technique for lossy anisotropic algorithm in FDTD method,” *Applied Computational Electromagnetics Society Journal*, vol. 31, no. 12, pp. 1377-1381, Dec. 2016.
- [34] B. Meng, L. Wang, W. Huang, X. Li, X. Zhai, and H. Zhang, “Wideband and low dispersion slow-light waveguide based on a photonic crystal with crescent-shaped air holes,” *Applied Optics*, vol. 51, no. 23, pp. 5735-5742, Aug. 2012.
- [35] C. Shi, J. Yuan, X. Luo, S. Shi, S. Lu, P. Yuan, W. Xu, Z. Chen, and H. Yu, “Transmission characteristics of multi-structure bandgap for lithium niobate integrated photonic crystal and waveguide,” *Optics Communications*, vol. 461, 125222, Apr. 2020.
- [36] C. Shi, J. Yuan, X. Luo, S. Shi, S. Lu, P. Yuan, W. Xu, Z. Chen, and H. Yu, “Multi-channel slow light coupled-resonant waveguides based on photonic crystal with rectangular microcavities,” *Optics Communications*, vol. 341, pp. 257-262, Apr. 2015.
- [37] V. Varmazyari, H. Habibiyan, and H. Ghafoorifard, “Slow light in ellipse-hole photonic crystal line-defect waveguide with high normalized delay bandwidth product,” *Journal of the Optical Society of America B*, vol. 31, pp. 771-779, Mar. 2014.
- [38] D. M. Pozar, *Microwave Engineering*. 4th Edition, John Wiley & Sons, Inc., Amherst, Massachusetts, 2012.
- [39] J. H. Mathews and K. D. Fink, *Numerical Methods using Matlab*. Prince Hall, New Jersey, 1999.
- [40] M. Moitra, B. A. Slovick, Z. G. Yu, S. Krishnamurthy, and J. Valentine, “Experimental demonstration of a broadband all-dielectric metamaterial perfect reflector,” *Applied Physics Letters*, vol. 104, 171102, Apr. 2014.
- [41] J. C. Ginn and I. Brener, “Realizing optical magnetism from dielectric metamaterials,” *Physical Review Letters*, vol. 108, 097402, Feb. 2012.



Ayşe Nihan Basmacı received her B.Sc., M.Sc. and Ph.D. degrees in Electrical Electronics Engineering from Pamukkale University in 2008, 2011 and 2017, respectively. Between 2008 and 2012, she worked as an Engineer at Turk Telekom Company. She also has been an Assistant Professor at Tekirdag Namik Kemal University, Vocational School of Technical Sciences, in the last 2 years. Her research interests include electromagnetic wave propagation, photonics, advanced materials, computational electromagnetics, electromagnetic fields, electromagnetic waves, and microwave filter design.

A Modified Hybrid Integral Equation to Electromagnetic Scattering from Composite PEC-Dielectric Objects Containing Closed-Open PEC Junctions

Jinbo Liu, Hongyang Chen, Hui Zhang, Jin Yuan, and Zengrui Li

State Key Laboratory of Media Convergence and School of Information and Communication Engineering
Communication University of China, Beijing, 100024, China
zrli@cuc.edu.cn

Abstract — To efficiently analyze the electromagnetic scattering from composite perfect electric conductor (PEC)-dielectric objects with coexisting closed-open PEC junctions, a modified hybrid integral equation (HIE) is established as the surface integral equation (SIE) part of the volume surface integral equation (VSIE), which employs the combined field integral equation (CFIE) and the electric field integral equation (EFIE) on the closed and open PEC surfaces, respectively. Different from the traditional HIE modeled for the objects whose closed and open PEC surfaces are strictly separate, the modified HIE can be applied to the objects containing closed-open junctions. A matrix equation is obtained by using the Galerkin's method of moments (MoM), which is augmented with the spherical harmonics expansion-based multilevel fast multipole algorithm (SE-MLFMA), improved by the mixed-potential representation and the triangle/tetrahedron-based grouping scheme. Because in the improved SE-MLFMA, the memory usage for storing the radiation patterns of basis functions is independent of the SIE type in the VSIE, it is highly appropriate for the fast solution of the VSIE that contains the HIE. Various numerical experiments demonstrate that during the calculation of composite objects containing closed-open PEC junctions, the application of the modified HIE in the VSIE can give reliable results with fast convergence speed.

Index Terms — Fast solver, integral equation, method of moments, multilevel fast multipole algorithm.

I. INTRODUCTION

In the electromagnetic analysis of composite perfect electric conductor (PEC)-dielectric objects, using the method of moments (MoM) to solve the volume surface integral equation (VSIE) is one of the most competitive approaches [1-9]. During the numerical modeling of composite objects, the electric field integral equation (EFIE) is usually formulated on all the PEC surfaces because it is independent of the surface type [2, 3], and then the EFIE is combined with the volume integral equation (VIE) established in the dielectric region to

form the EFIE-VIE, a general VSIE form [2]. Whereas, when closed PEC surfaces are contained by the calculated objects, using the EFIE alone may encounter the internal-resonance problems [2, 9]. Moreover, it is typically difficult to iteratively solve the matrix equation derived from the EFIE, which is a first-kind Fredholm integral equation. To deal with the internal-resonance problems as well as to accelerate the iterative solution, some articles put forward the concept of hybrid integral equation (HIE) [4-7]. That is, establishing the combined field integral equation (CFIE) on the closed PEC surfaces of the objects [8, 9], which is the second-kind and derived from the linear combination of the EFIE and the magnetic field integral equation (MFIE), while the open surfaces keep the EFIE. Nevertheless, only the situation that the closed and open surfaces are strictly separate was discussed [4-7], while for the objects containing closed-open junctions, the traditional HIE is out of action. To overcome this drawback, the authors modified the traditional HIE to make it suitable for the PEC objects containing closed-open junctions [10]. In this paper, the modified HIE acts as the surface integral equation (SIE) part of the VSIE, combined with the VIE to form the modified HIE-VIE, a new VSIE type, to compute the composite PEC-dielectric objects that contain closed-open PEC junctions.

Using the MoM, the VSIE is converted into a matrix equation, the iterative solution process of which is usually accelerated by fast solvers such as the multilevel fast multipole algorithm (MLFMA) [2, 11-16]. Due to the addition theorem of Green's function and the diagonalization of the translation operator, the MLFMA drastically reduces the overall computational complexity from the order of $O(N^2)$ to $O(N \log N)$ through three steps: aggregation, translation, and disaggregation. To enhance the computing efficiency, the radiation patterns (RPs) of the basis functions should be computed and stored in advance. In order to minimize the sampling redundancy introduced by numerical quadrature rules, the RPs can be expanded by spherical harmonics, yielding the spherical harmonic expansion-based MLFMA (SE-MLFMA) [13-16], which is extended to the fast solution of HIE-VIE in

this paper. On the other hand, in the conventional SE-MLFMA that is dyadic form [13, 14], the memory usage of RPs is relevant to the SIE type in the VSIE. To be more specific, the memory usage costed by storing the RPs for the CFIE is double times of that for the EFIE. Therefore, if the conventional SE-MLFMA is used to accelerate the solution of HIE-VIE where the HIE is composed by the CFIE and EFIE, the RPs about the HIE are needed to be prior classified according to whether they belong to the CFIE or the EFIE part, which is quite inconvenient. To avoid this problem, this paper will adopt the improved SE-MLFMA formulated by using the mixed-potential representation [15, 16], and the RPs memory usage is then independent of the SIE type. Furthermore, the improved SE-MLFMA is grouped by a triangle/tetrahedron-based scheme, making the memory usage of RPs depend on the total number of triangles and tetrahedrons instead of the number of basis functions in the conventional SE-MLFMA. Since the total number of triangles and tetrahedrons is usually much less than that of basis functions, a considerable memory usage is saved.

The rest of this paper is organized as follows. In Section II, the modified HIE-VIE is established to be suitable for the numerical modeling of composite objects containing closed-open PEC junctions, followed by the discretization using the Galerkin's MoM. The SE-MLFMA improved by the mixed-potential representation and the triangle/tetrahedron-based grouping scheme is adopted to fast solve the HIE-VIE, which will be elaborated in Section III. Various numerical experiments are shown in Section IV to demonstrate the validity and efficiency of the proposed method. Finally, some conclusions about the application of the modified HIE-VIE are summarized.

II. DERIVATION OF THE HIE-VIE AND THE MOM SOLUTION

Suppose that in the free space, there is an electromagnetic wave (\vec{E}^i, \vec{H}^i) illuminating a composite PEC-dielectric object that contains both closed and open PEC surfaces S_c and S_o as well as the dielectric region V with the permittivity ϵ . The scattered field (\vec{E}^s, \vec{H}^s) is the superposition of fields produced by the equivalent surface and volume currents as:

$$\begin{cases} \vec{E}^s = - \left[\begin{aligned} & j\omega\mu_0 \int_S \vec{J}_s(\vec{r}') G dS' + \frac{j}{\omega\epsilon_0} \nabla \int_S \nabla' \cdot \vec{J}_s(\vec{r}') G dS' \\ & + j\omega\mu_0 \int_V \vec{J}_v(\vec{r}') G dV' + \frac{j}{\omega\epsilon_0} \nabla \int_V \nabla' \cdot \vec{J}_v(\vec{r}') G dV' \end{aligned} \right], \\ \vec{H}^s = \nabla \times \int_S \vec{J}_s(\vec{r}') G dS' + \nabla \times \int_V \vec{J}_v(\vec{r}') G dV' \end{cases} \quad (1)$$

where ϵ_0 and μ_0 are the permittivity and permeability of the free space, and \vec{J}_s and \vec{J}_v are the equivalent surface and volume currents at the source point \vec{r}' , respectively. With the wavenumber k and the time-harmonic factor

$e^{j\omega t}$, the Green's function of the free space is:

$$G = G(\vec{r}, \vec{r}') = \frac{e^{-jk|\vec{r}-\vec{r}'|}}{4\pi|\vec{r}-\vec{r}'|} \quad (2)$$

In the region V , the VIE is established by making the total field equal to the sum of the incident and the scattered fields as [2]:

$$\frac{\vec{D}(\vec{r})}{\epsilon(\vec{r})} = \vec{E}^i(\vec{r}) + \vec{E}^s(\vec{r}) \quad \vec{r} \in V, \quad (3)$$

where \vec{D} is the electric flux density. By vanishing the tangential component of the total electric field on both the open and closed PEC surfaces, the EFIE based on the mixed-potential form is deduced as [2, 3]:

$$\hat{t}(\vec{r}) \cdot [\vec{E}^s(\vec{r}) + \vec{E}^i(\vec{r})] = 0 \quad \vec{r} \in S_c + S_o, \quad (4)$$

where \hat{t} is any tangential vector to the surface at the observation point \vec{r} . The EFIE is combined with the VIE to form the generally used EFIE-VIE, which is ill-conditioned at the resonant frequencies.

Imposing the boundary condition of the magnetic field over the closed PEC surface S_c , the MFIE can be established as [2, 9]:

$$\hat{n}(\vec{r}) \times [\vec{H}^i(\vec{r}) + \vec{H}^s(\vec{r})] = \vec{J}(\vec{r}) \quad \vec{r} \in S_c, \quad (5)$$

where \hat{n} is the outwardly directed normal. Further, similar to form the CFIE [2, 9], we can linearly combine the MFIE with the EFIE to form the so-called HIE as [4-7]:

$$\text{HIE} = \alpha(\vec{r}) \text{EFIE} + \beta(\vec{r}) \eta_0 \text{MFIE} \quad \vec{r} \in S_c + S_o, \quad (6)$$

where α and β are both \vec{r} -dependent real combined coefficients, and η_0 is the free-space intrinsic impedance. Combining the VIE and the HIE together can build the HIE-VIE, a new VSIE type. Compared with the EFIE-VIE implementation, the HIE-VIE may have a good convergence behavior when the composite objects contain closed PEC surfaces, which will be investigated during the numerical experiment. To determine the values of α and β in (6), for the traditional HIE, it is stated in [5] that $\beta(\vec{r}) = 1 - \alpha(\vec{r})$ with $0 < \alpha(\vec{r}) < 1$ for $\vec{r} \in S_c$, while $\beta(\vec{r}) = 0$ and $\alpha(\vec{r}) = 1$ for $\vec{r} \in S_o$. If the closed and open PEC surfaces of the calculated object are strictly separate, we can straightforwardly set α and β as stated above. In contrast, if the object contains closed-open junctions where the closed and open PEC surfaces have conjunct boundary, it is necessary to further discuss how to set the values of α and β .

In the initial process of the MoM, the equivalent current is expanded with basis functions. Because of the convenience of discretizing arbitrarily shaped objects and the quality of naturally avoiding pseudo line or surface charges, the divergence-conforming RWG [3] and SWG [17] basis functions based on triangular patches and tetrahedral volumes are being widely used. Using the Galerkin's MoM [1], the HIE-VIE is transformed into a generalized impedance matrix equation as:

$$\begin{bmatrix} Z^{SS} & Z^{SV} \\ Z^{VS} & Z^{VV} \end{bmatrix} \begin{Bmatrix} I^S \\ I^V \end{Bmatrix} = \begin{Bmatrix} b^S \\ b^V \end{Bmatrix}, \quad (7)$$

where $\{I^S\}$ and $\{I^V\}$ are the subvectors of unknown expansion coefficients, $\{b^S\}$ and $\{b^V\}$ are the excitation subvectors, respectively. $[Z^{PQ}]$ (P, Q is S or V) denotes the impedance submatrix representing the interactions between various types of test and basis functions. Besides, the calculation of submatrices $[Z^{VS}]$ and $[Z^{VV}]$ are independent of the SIE type, which can be found in [16]. The submatrix $[Z^{SS}]$ is the same as that generated by the pure HIE, according to whose calculation the article [10] reported how to choose the values of α and β in detail. In this paper, we will discuss the same question from the calculation of $[Z^{SV}]$. The submatrix entry Z_{mn}^{SV} , denoting the interaction between the n th SWG basis function \vec{f}_n^V with domain V_n and the m th RWG test function \vec{f}_m^S with domain S_m , is calculated as:

$$\begin{aligned} Z_{mn}^{SV} &= j\omega\mu_0 \int_{S_m} \alpha(\vec{r}) \vec{f}_m^S(\vec{r}) \cdot \int_{V_n} \chi(\vec{r}') \vec{f}_n^V(\vec{r}') GdV' dS \\ &+ \frac{j}{\omega\epsilon_0} \int_{S_m} \alpha(\vec{r}) \vec{f}_m^S(\vec{r}) \cdot \nabla_s \int_{V_n} \nabla' \cdot [\chi(\vec{r}') \vec{f}_n^V(\vec{r}')] GdV' dS \quad (8) \\ &+ \eta_0 \int_{S_m} \beta(\vec{r}) \vec{f}_m^S(\vec{r}) \cdot \left\{ \hat{n}(\vec{r}) \times \int_{V_n} [\chi(\vec{r}') \vec{f}_n^V(\vec{r}')] \times \nabla GdV' \right\} dS \end{aligned}$$

with

$$\chi(\vec{r}') = 1 - \frac{\epsilon_0}{\epsilon(\vec{r}')}, \quad (9)$$

where ∇_s denotes the surface gradient operation. It is noticed that for the second term of the right hand side in (8), the gradient operator is placed on the observation point \vec{r} , leading to a two-order singularity when \vec{r} approaches \vec{r}' . To reduce the order of singularity, taking the surface Gauss theorem, the second term in the right-hand side of (8) is usually transformed as:

$$\begin{aligned} &\int_{S_m} \alpha(\vec{r}) \vec{f}_m^S(\vec{r}) \cdot \nabla_s \int_{V_n} \nabla' \cdot [\chi(\vec{r}') \vec{f}_n^V(\vec{r}')] GdV' dS \\ &= \int_{S_m} \nabla_s \cdot \left[\alpha(\vec{r}) \vec{f}_m^S(\vec{r}) \int_{V_n} \nabla' \cdot [\chi(\vec{r}') \vec{f}_n^V(\vec{r}')] GdV' \right] dS \\ &- \int_{S_m} \nabla_s \cdot \left[\alpha(\vec{r}) \vec{f}_m^S(\vec{r}) \right] \int_{V_n} \nabla' \cdot [\chi(\vec{r}') \vec{f}_n^V(\vec{r}')] GdV' dS \quad (10) \\ &= \int_{\partial S_m} \alpha(\vec{r}) \left[\hat{n}_{\partial S_m} \cdot \vec{f}_m^S(\vec{r}) \right] \int_{V_n} \nabla' \cdot [\chi(\vec{r}') \vec{f}_n^V(\vec{r}')] GdV' dl \\ &- \int_{S_m} \nabla_s \cdot \left[\alpha(\vec{r}) \vec{f}_m^S(\vec{r}) \right] \int_{V_n} \nabla' \cdot [\chi(\vec{r}') \vec{f}_n^V(\vec{r}')] GdV' dS \end{aligned}$$

where ∂S_m denotes the boundary of S_m , and $\hat{n}_{\partial S_m}$ is the outer-normal direction of ∂S_m . In (10), the singularity order is degraded to one. On the other hand, it is observed that the surface divergence operator is forced on the product $\alpha(\vec{r}) \vec{f}_m^S(\vec{r})$, which is then requested to be divergence conforming. Under this restriction, if the domain S_m of \vec{f}_m^S just belongs to a junctional region containing both the closed surface S_c and open surface S_o , the value of $\alpha(\vec{r})$ for $\vec{r} \in S_c$ and for $\vec{r} \in S_o$ must be the same. In other words, $\alpha(\vec{r})$ should be constant

everywhere. This conclusion is the same as that drew in [10]. Therefore, we set:

$$\begin{aligned} \alpha(\vec{r}) &= \alpha_0 \quad \forall \vec{r} \in S_c + S_o \\ \beta(\vec{r}) &= \begin{cases} 1 - \alpha_0 & \forall \vec{r} \in S_c \\ 0 & \forall \vec{r} \in S_o \end{cases}, \quad (11) \end{aligned}$$

where α_0 is constant and $0 < \alpha_0 < 1$. Moreover, with a constant α , the first term in the right-hand side of (10) will be cancelled out as [3]. Please note that mathematically, the values of α and β in (8) are dependent on the position of the observation point, but not the row of the matrix as [4-7]. If the closed and open PEC surfaces are separate, depending on the observation point position and the matrix row are equivalent. Nevertheless, this equivalence is invalid when the closed and open PEC surfaces are conjoint.

Substituting (11) into (6) yields the modified HIE as:

$$\text{HIE} = \begin{cases} \alpha_0 \text{EFIE} & \forall \vec{r} \in S_o \\ \text{CFIE} = \alpha_0 \text{EFIE} + (1 - \alpha_0) \eta_0 \text{MFIE} & \forall \vec{r} \in S_c \end{cases}. \quad (12)$$

It states that the modified HIE consists of two parts: the CFIE on the closed surface S_c , and the EFIE scaled down by multiplying a coefficient α_0 on the open surface S_o . The modified HIE can be combined with the VIE to form the modified HIE-VIE for the calculation of composite objects containing closed-open PEC junctions.

III. SE-MLFMA IMPLEMENTATION

In the SE-MLFMA, the impedance matrix generated by the MoM is decomposed into two parts as $[Z_N] + [Z_F]$, where $[Z_N]$ and $[Z_F]$ denote the matrices representing the interactions between the basis and test functions in the near and far groups, respectively. In our implementation, the grouping scheme is based on triangles and tetrahedrons [15, 16], rather than the most commonly used edge-based grouping scheme [2, 11-14]. That is to say, the index of the leaf box which a given triangle or tetrahedron belongs to is determined by comparing the box center coordinate with the triangle or tetrahedron barycenter. It was reported in [16] that how to use the SE-MLFMA to accelerate the VSIE solution of EFIE-VIE type. In this section, we focus on the SE-MLFMA application on the HIE part of the HIE-VIE matrix, which is $[Z^{SS}]$.

The n th RWG basis function is defined over a common edge of length l_n shared by two adjacent triangles T_n^\pm of areas A_n^\pm as:

$$\vec{f}_n^S(\vec{r}') = \pm \frac{l_n}{2A_n^\pm} (\vec{r}' - \vec{r}_n^\pm), \quad (13)$$

where the sign “ \pm ” means the current flowing direction is outward or inward to T_n^\pm , and \vec{r}_n^\pm is the free vertex of T_n^\pm to the common edge. Since the RWG basis function is defined on two adjacent triangles, the submatrix entry Z_{mn}^{SS} consists of four double surface integrals,

$$\begin{aligned}
Z_{Fmm}^{SS++} &= \frac{l_m l_n}{4A_m^+ A_n^+ \pi^2} \left\{ j\omega\mu_0 \int_{T_m^+} \alpha_0 (\vec{r} - \vec{r}_m^+) \cdot \int_{T_n^+} (\vec{r}' - \vec{r}_n^+) G dS' dS - \frac{j}{\omega\epsilon_0} \int_{T_m^+} \nabla_s \cdot [\alpha_0 (\vec{r} - \vec{r}_m^+)] \int_{T_n^+} \nabla'_s \cdot (\vec{r}' - \vec{r}_n^+) G dS' dS \right. \\
&\quad \left. + \eta_0 \int_{T_m^+} \beta_m^+ (\vec{r} - \vec{r}_m^+) \cdot \hat{n}(\vec{r}) \times \int_{T_n^+} (\vec{r}' - \vec{r}_n^+) \times \nabla G dS' dS \right\} \\
&= \frac{l_m l_n k}{64A_m^+ A_n^+ \pi^2} \left\{ -\alpha_0 \frac{2}{\omega\epsilon_0} \oint \left[\int_{T_m^+} e^{-jk(\vec{r}-\vec{r}_m^+)} dS \right] T_L(\vec{k}, \vec{r}_{m'n'}) \cdot \left[\int_{T_n^+} e^{-jk(\vec{r}'-\vec{r}_n^+)} dS' \right] d^2 \hat{k} \right. \\
&\quad \left. - \beta_m^+ \eta_0 \oint \left\{ \int_{T_m^+} [\hat{n}(\vec{r}) \times (\vec{r} - \vec{r}_m^+) \times \vec{k}] e^{-jk(\vec{r}-\vec{r}_m^+)} dS \right\} T_L(\vec{k}, \vec{r}_{m'n'}) \cdot \left[\int_{T_n^+} (\vec{r}' - \vec{r}_n^+) e^{-jk(\vec{r}'-\vec{r}_n^+)} dS' \right] d^2 \hat{k} \right. \\
&\quad \left. - \alpha_0 \omega\mu_0 \oint \left[\tilde{V}_m^*(\vec{k}) - \vec{r}_m^+ \tilde{S}_m^*(\vec{k}) \right] T_L(\vec{k}, \vec{r}_{m'n'}) \cdot \left[\tilde{V}_n(\vec{k}) - \vec{r}_n^+ \tilde{S}_n(\vec{k}) \right] d^2 \hat{k} \right. \\
&\quad \left. - \alpha_0 \frac{2}{\omega\epsilon_0} \oint \tilde{S}_m^*(\vec{k}) T_L(\vec{k}, \vec{r}_{m'n'}) \tilde{S}_n(\vec{k}) d^2 \hat{k} \right. \\
&\quad \left. - \beta_m^+ \eta_0 \oint \hat{n}(\vec{r}) \times \left[\tilde{V}_m^*(\vec{k}) - \vec{r}_m^+ \tilde{S}_m^*(\vec{k}) \right] \times \vec{k} T_L(\vec{k}, \vec{r}_{m'n'}) \cdot \left[\tilde{V}_n(\vec{k}) - \vec{r}_n^+ \tilde{S}_n(\vec{k}) \right] d^2 \hat{k} \right\} \quad (16)
\end{aligned}$$

representing the mutual interactions between the four triangles involved in the basis and test functions. In the following, for the purpose of easy reading, only the integral involving two ‘‘positive’’ triangles is considered, and other three ones can be obtained by simply changing the signs. If two positive triangles T_m^+ and T_n^+ are grouped into the m 'th and n 'th leaf boxes of the centers coordinates $\vec{r}_{m'}$ and $\vec{r}_{n'}$, respectively, then via the addition theorem of Green's function, (2) is rewritten as:

$$G(\vec{r}, \vec{r}') = \frac{-jk}{(4\pi)^2} \oint e^{-jk(\vec{r}-\vec{r}_m^+)} T_L(\vec{k}, \vec{r}_{m'n'}) e^{-jk(\vec{r}'-\vec{r}_n^+)} d^2 \hat{k}, \quad (14)$$

with the translation operator [2],

$$T_L(\vec{k}, \vec{r}_{m'n'}) = \sum_{l=0}^L (-j)^l (2l+1) h_l^{(2)}(k|\vec{r}_{m'n'}|) P_l(\hat{k} \cdot \hat{r}_{m'n'}), \quad (15)$$

where $\vec{r}_{m'n'} = \vec{r}_{m'} - \vec{r}_{n'}$, L is the order of multipole expansion, $h_l^{(2)}$ is the second-kind spherical Hankel function of order l , and P_l denotes the Legendre Polynomial of degree l . In the far-group interaction, Substituting (14) and (15) into the expression of Z_{mm}^{SS} results in (16), where β_m^+ is $1 - \alpha_0$ when the triangle T_m^+ belongs to the closed surface S_c , or 0 for $T_m^+ \in S_o$, and the asterisk denotes the complex conjugate. It is seen that the scalar \tilde{S}_β and vector \tilde{V}_β with:

$$\begin{cases} \tilde{S}_\beta(\vec{k}) = \int_{T_\beta^+} e^{-jk(\vec{r}_\beta - \vec{r}')} dS' \\ \tilde{V}_\beta(\vec{k}) = \int_{T_\beta^+} \vec{r}' e^{-jk(\vec{r}_\beta - \vec{r}')} dS' \end{cases} \quad \beta = m, n, \quad (17)$$

contain all information needed by the aggregation and disaggregation processes in the leaf boxes in the MLFMA, which means that they can be regarded as the RPs defined on triangles. Using the symmetry of RPs, the memory usage in bytes by storing the RPs is:

$$\text{Mem}_{\text{RP}} = 4cN_t(L+1)^2 \quad c = \begin{cases} 8 & \text{single precision} \\ 16 & \text{double precision} \end{cases}, \quad (18)$$

where N_t is the number of triangles.

Further, in the improved SE-MLFMA [15, 16], the RPs of triangles can be expressed as a series of the spherical harmonics as:

$$\begin{cases} \tilde{S}_\beta(\vec{k}) = \sum_{p=0}^P \sum_{q=-p}^p S_{pq}^\beta Y_{pq}(\hat{k}) \\ \tilde{V}_\beta(\vec{k}) = \sum_{p=0}^P \sum_{q=-p}^p \tilde{V}_{pq}^\beta Y_{pq}(\hat{k}) \end{cases}, \quad (19)$$

where Y_{pq} is the orthonormalized spherical harmonics [18]. The expansion coefficients are computed by:

$$\begin{cases} S_{pq}^\beta = \int \tilde{S}_\beta(\vec{k}) Y_{pq}^*(\hat{k}) d^2 \hat{k} \\ \tilde{V}_{pq}^\beta = \int \tilde{V}_\beta(\vec{k}) Y_{pq}^*(\hat{k}) d^2 \hat{k} \end{cases}. \quad (20)$$

Instead of the RPs, the expansion coefficients S_{pq}^β and \tilde{V}_{pq}^β can be computed and stored in the setup of the improved SE-MLFMA, while the memory usage in bytes is:

$$\text{Mem}_{\text{SE}} = 2cN_t(P+1)(P+2), \quad (21)$$

where P is the degree of spherical harmonics. Usually, $P = L/2 - 1$ is recommended with a sufficient accuracy. Thus, compared (21) with (18), a large amount of memory usage is saved.

The above content discussed how to apply the SE-MLFMA on the $[Z^{SS}]$ part of (7), while the similar application about other three parts $[Z^{SV}]$, $[Z^{VS}]$ and $[Z^{VV}]$ is shown in [16]. The remaining steps, such as the computation of expansion coefficients as well as aggregation and disaggregation steps at the finest level using the spherical harmonics series, are done in the same way as [14-16]. The analysis on advantages of the

improved SE-MLFMA have been given in [15, 16], which are beyond the scope of this paper. But we still summarize them as follows:

- 1) The memory requirement does not depend on the SIE type, which means that the application of HIE-VIE will not cause any memory increasing compared with the EFIE-VIE implementation. Because of the adoption of mix-potential representation, the complex conjugate of (17) can be reused as the receiving patterns for any SIE type in the disaggregation step, which is impossible for the dyadic-form MLFMA when the MFIE is involved.
- 2) The memory requirement of RPs is only proportional to the total number of triangles and tetrahedrons rather than that of the basis functions, leading to a considerable reduction of core memory requirement. This is due to the grouping scheme based on the triangles and tetrahedrons [15, 16], rather than the commonly edge-based grouping scheme [2, 11-14].
- 3) Compared with the conventional SE-MLFMA, the improved one has a faster execution. Since in the improved SE-MLFMA, the Cartesian components of RPs are permanently used during the whole procedures, the repeated transforms between Cartesian and spherical coordinates, which is inevitable for the conventional SE-MLFMA to eliminate the Gibbs phenomenon [13, 14], are totally eliminated.

IV. NUMERICAL EXPERIMENTS

In the following, the bistatic radar cross section (RCS) results of several objects at $0 \leq \theta \leq 180^\circ$ and $\varphi = 0$ are calculated, all of which are illuminated by an x -polarized plane wave from $+z$ -axis. The generalized minimal residual algorithm (GMRES) with a restart number 100 is adopted as the iterative solver to reach 0.001 relative residual error [19]. The constant α_0 in (11) is 0.5. Unless otherwise stated, the leaf box size of the MLFMA is fixed to 0.25λ , in which situation the degree of spherical harmonics $P = 2$ with the order of multipole expansion $L = 5$. During the HIE-VIE modeling for the composite objects containing closed-open PEC junctions, the CFIE is established on the closed PEC surface, and the EFIE is on the remaining open surface. All the calculations serially execute on a computer with 3.2 GHz CPU and 16 GB RAM in single precision.

The first case is a composite object, which is a closed hemisphere of radius 5λ coated with 0.05λ thickness material from the top surface, midmost clung to an open square plate of variable side length l , as shown inside Fig. 1 (a). The relative permittivity of the coating material is $\varepsilon_r = 2.2 - j0.00198$. A moderate mesh size is chosen to discretize the object, while the numbers of triangles and unknowns with respect to different values of l are given in Table 1. Besides, the numbers of tetrahedrons and the triangles belonging to the closed hemisphere are fixed to 118,401 and 59,960, respectively.

The numerical results from the EFIE-VIE and the modified HIE-VIE with $l = 10\lambda$ and $l = 30\lambda$ are shown in Figs. 1 (a) and (b). The traditional HIE-VIE result, i.e., $\alpha(\vec{r})$ is 0.5 for $\vec{r} \in S_c$ and 1 for $\vec{r} \in S_o$, is also given. It is observed that the results from EFIE-VIE and modified HIE-VIE are in agreement everywhere, while the result from traditional HIE-VIE shows a totally unacceptable difference. This phenomenon states the necessity of modifying the traditional HIE. In order to investigate how the proportion of the closed PEC surface occupying the whole PEC structure of the composite object influences the performance of the modified HIE-VIE or the EFIE-VIE, Fig. 2 shows the number of iterations with respect to various l . It is observed that when $l = 10\lambda$, the coverage speed of the HIE-VIE is about 2.6 times faster than the EFIE-VIE (iterations 231 vs. 601). Along with the increase of l , the number of iterations from the HIE-VIE will sharply increase, while that from the EFIE-VIE is relatively stable. This phenomenon illuminates that the HIE-VIE can be more efficient for the calculation in which the closed surface occupies a main proportion of the whole PEC structure. On the other hand, the iteration number from the HIE-VIE is always less than the EFIE-VIE. Therefore, we may draw the conclusion that no matter what the proportion of the closed PEC surface in the whole object is, the HIE-VIE can always be adopted safely and reliably.

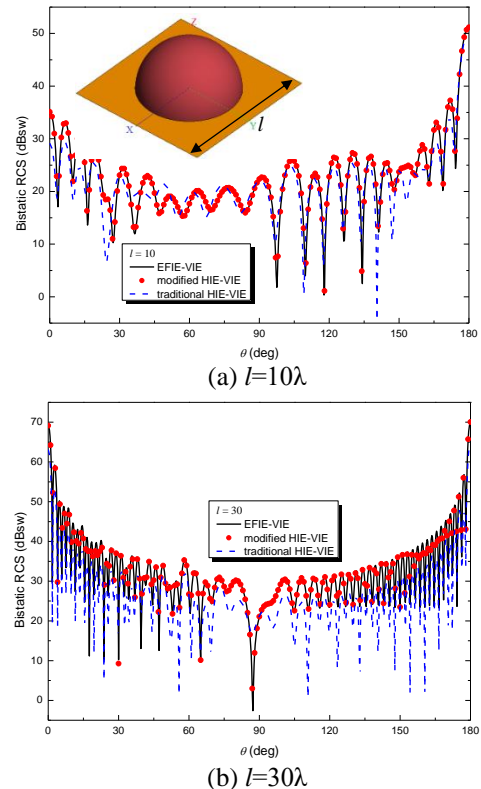


Fig. 1. Bistatic RCS results from a coated hemisphere of radius 5λ clung to a square plate of side length l .

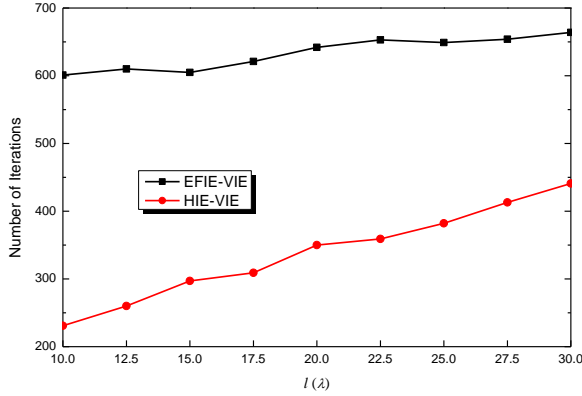


Fig. 2. Numbers of iterations with respect to various l in the calculation of the composite object shown inside Fig. 1 (a), while the GMRES with 100 restart number is the iterative solver to reach 0.001 relative residual error.

Table 1: Numbers of triangles and unknowns with respect to different values of l

| l (λ) | Number of Triangles | Number of Unknowns |
|-------------------|---------------------|--------------------|
| 10 | 64,298 | 373,270 |
| 12.5 | 76,736 | 391,008 |
| 15 | 91,612 | 413,713 |
| 17.5 | 109,991 | 441,320 |
| 20 | 131,317 | 473,253 |
| 22.5 | 156,119 | 510,397 |
| 25 | 183,805 | 551,875 |
| 27.5 | 214,801 | 597,272 |
| 30 | 247,065 | 646,698 |

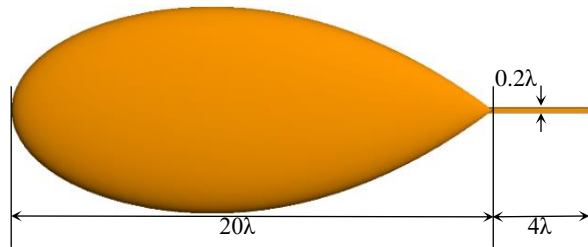


Fig. 3. An almond of length 20λ , penetrated by a narrow strip from the tip, whose width is 0.2λ , and the length from the tip of the almond is 4λ .

Table 2: Memory usage of RPs and CPU time per MVP versus different L and P

| Box Size | Method | Parameter | RP Mem (MB) | MVP Time (s) | |
|----------------|--------|-----------|-------------|--------------|-------|
| | | | | EFIE | HIE |
| 0.25 λ | Trad | $L=5$ | 67.40 | 0.592 | 0.662 |
| | | $P=2$ | 11.23 | 0.506 | 0.532 |
| | Imp | $P=3$ | 18.72 | 0.539 | 0.561 |
| 0.3 λ | Trad | $L=6$ | 91.73 | 0.721 | 0.895 |
| | | $P=2$ | 11.23 | 0.538 | 0.575 |
| | Imp | $P=3$ | 18.72 | 0.575 | 0.619 |

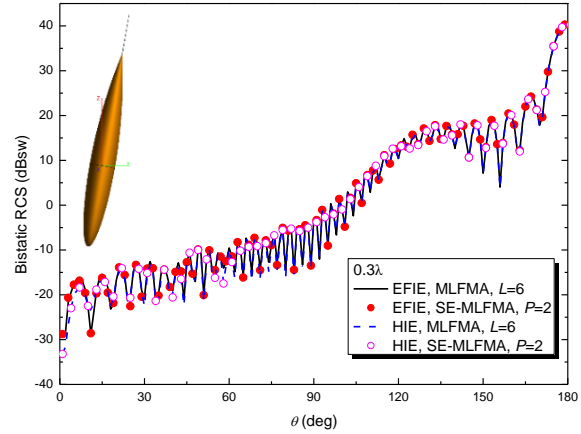


Fig. 4. Bistatic RCS results from the object shown in Fig. 3, with an intersection angle of 10° between the axis of the almond and $+z$ -axis.

The second object is a pure-PEC almond of length 20λ [20], penetrated by a narrow strip from the tip, as shown in Fig. 3. The width of the strip is 0.2λ , while the length from the tip of the almond is 4λ . In order to make the incident plane wave illuminate the closed-open PEC junction structure adequately, in which situation whether the junction structure is properly modeled or not will have a strong influence on the RCS results, there is an intersection angle of 10° between the axis of the almond and $+z$ -axis as shown inside Fig. 4. This object is discretized into 92,126 unknowns, while the numbers of triangles belonging to the closed almond and the open strip are 61,200 and 145, respectively. In this case, the pure SIE methods, EFIE and HIE, are used to model the object. To illustrate the effectiveness of the improved SE-MLFMA, both the traditional MLFMA and the improved SE-MLFMA are used, while two kinds of leaf box sizes (0.25λ with $L=5$ and 0.3λ with $L=6$) in the MLFMA are adopted during the calculation, respectively. Please note in our implementation, the traditional MLFMA is also expressed by the mixed-potential representation and grouped based on the triangles, thus, the memory usage of RPs is independent of the SIE type and in proportion to the number triangles. Table 2 gives the detail information on the memory usage of RPs (*RP Mem*) and the CPU time per matrix-vector product (MVP time) during the iterative solution with different SIE type (EFIE or HIE). It is observed that compared with the traditional MLFMA (*trad*), the improved SE-MLFMA (*imp*) saves a considerable core memory usage, matching with (18) or (21). Besides, the improved SE-MLFMA is even faster than the traditional MLFMA in the MVP implementation. This is because the aggregation of the outgoing waves and the disaggregation of the incoming waves at the finest level can be computed in an efficient way by summation of the spherical harmonics instead of the integrations. When the leaf box size is 0.3λ , the EFIE

and HIE are used to calculate the bistatic RCS results accelerated by the MLFMA with $L=6$ and SE-MLFMA with $P=2$, respectively, which are displayed in Fig. 4. Excellent agreements are observed, indicating that although the sharp tips and edges are contained, the results from the HIE are also dependable, while the formula $P = L/2 - 1$ can still provide an acceptable accuracy for the HIE accelerated by the SE-MLFMA. During the calculation, the numbers of iteration from the HIE and EFIE are 76 and 712, respectively. Since in this example, the closed almond part occupies an absolutely large proportion of the whole object, the advantage of HIE to the EFIE on the convergence speed is quite clear.

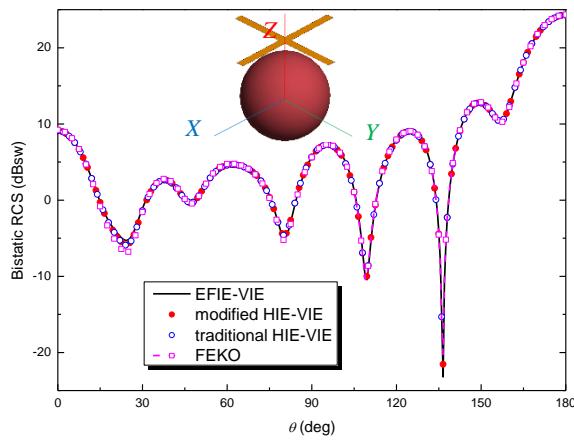


Fig. 5. Bistatic RCS results from composite object. The radius of PEC sphere is 1λ , the thickness of the coating material is 0.05λ with $\epsilon_r = 3.35$, and the distance between the PEC cross and the center of sphere is 1.5λ .

The third case is a composite object. A PEC cross, each branch size of which is $3\lambda \times 0.2\lambda$, is placed over a coated sphere, as shown inside Fig. 5. The radius of PEC sphere is 1λ , the thickness of the coating material is 0.05λ with $\epsilon_r = 3.35$, and the distance between the PEC cross and the center of sphere is 1.5λ . With a 0.07λ average mesh size, this object is discretized into 55,135 unknowns with 6,160 closed triangles, 322 open triangles and 19,570 tetrahedrons. In this case, since the closed and open PEC surfaces are totally separate, both the traditional HIE-VIE and the modified one can be adopted safely. The bistatic RCS results from the EFIE-VIE, the traditional HIE-VIE and the modified HIE-VIE implementations are shown in Fig. 5, while for comparison, the result from the electromagnetic simulation commercial software Altair FEKO using the SIE-based method is also shown [21]. Good agreement is observed among them. The iteration number from the modified HIE-VIE is 103, almost equal to 106 that is from the traditional one, and about 2.7 times faster than that from the EFIE-VIE which is 280. This case states that for the composite objects whose closed and open

PEC surfaces are separate, the modified HIE-VIE can also give reliable result and has a similar convergence behavior compared with the traditional one. In other words, the modified HIE implementation is always effective on reducing the iteration number for any kind of composite objects without losing the numerical accuracy.

V. CONCLUSIONS

The modified HIE is combined with the VIE to form the HIE-VIE, a new VSIE type, to exactly model the composite PEC-dielectric objects that contain closed-open PEC junctions. For the SIE part of the VSIE, different from the traditional HIE establishing for objects whose closed and open PEC surfaces are strictly separate, in the modified HIE, the combined coefficient α multiplied the EFIE in (6) must be constant everywhere. Compared with the EFIE-VIE implementation, the use of modified HIE-VIE can always improve the efficiency of the iterative solution to some extent with a high accuracy. The validity and efficiency are verified by various numerical experiments, while during the calculation, the improved SE-MLFMA, whose memory usage for storing the RPs is independent of the SIE type, is used to accelerate the iterative solution.

ACKNOWLEDGMENT

This work was supported by the National Natural Science Foundation of China (Grant Numbers 62071436 and 61971384), and the Fundamental Research Fund for the Central Universities (Grant Numbers CUC210B013 and CUC19ZD001).

REFERENCES

- [1] R. F. Harrington, *Field Computation by Moment Methods*. MacMillan, New York, 1968.
- [2] W. C. Chew, J. M. Jin, E. Michielssen, and J. M. Song, *Fast and Efficient Algorithms in Computational Electromagnetics*. Boston, MA, USA: Artech House, 2001.
- [3] S. M. Rao, D. R. Wilton, and A. W. Glisson, "Electromagnetic scattering by surfaces of arbitrary shape," *IEEE Trans. Antennas Propag.*, vol. 30, no. 3, pp. 409-418, May 1982.
- [4] L. Gürel and Ö. Ergül, "Extending the applicability of the combined-field integral equation to geometries containing open surfaces," *IEEE Antennas Wireless Propag. Lett.*, vol. 5, pp. 515-516, 2006.
- [5] Ö. Ergül and L. Gürel, "Iterative solutions of hybrid integral equations for coexisting open and closed surfaces," *IEEE Trans. Antennas Propag.*, vol. 57, no. 6, pp. 1751-1758, June 2009.
- [6] Z. H. Fan, D. Z. Ding, and R. S. Chen, "The efficient analysis of electromagnetic scattering from composite structures using hybrid CFIE-

- IEFIE,” *Progress in Electromagnetics Research B*, vol. 10, pp. 131-143, 2008.
- [7] B. Karaosmanoğlu, C. Önel, and Ö. Ergül, “Optimizations of EFIE and MFIE combinations in hybrid formulations of conducting bodies,” in *2015 International Conference on Electromagnetics in Advanced Applications (ICEAA)*, Turin, Italy, Oct. pp. 1276-1279, 2015.
- [8] J. R. Mautz and R. F. Harrington, “H-field, E-field and combined-field solutions for conducting bodies of revolution,” *Arch. Elektron. Übertragungstechn. (Electron. Commun.)*, vol. 32, pp. 157-164, 1978.
- [9] P. Ylä-Oijala and M. Taskinen, “Calculation of CFIE impedance matrix elements with RWG and $n \times$ RWG functions,” *IEEE Trans. Antennas Propag.*, vol. 51, no. 8, pp. 1837-1846, Aug. 2003.
- [10] J. Liu, J. Yuan, W. Luo, Z. Li, and J. Song, “On the use of hybrid CFIE-EFIE for objects containing closed-open surface junctions,” *IEEE Antennas Wireless Propag. Lett.*, vol. 20, no. 7, pp. 1249-1253, July 2021.
- [11] S. Velamparambil, W. C. Chew, and J. M. Song, “10 million unknowns: is it that big?” *IEEE Antennas Propag. Mag.*, vol. 45, no. 2, pp. 43-58, Apr. 2003.
- [12] Ö. Ergül and L. Gürel, “Rigorous solutions of electromagnetics problems involving hundreds of millions of unknowns,” *IEEE Antennas Propag. Mag.*, vol. 53, no. 1, pp. 18-26, Feb. 2011.
- [13] Ismatullah and T. F. Eibert, “Surface integral equation solutions by hierarchical vector basis functions and spherical harmonics based multilevel fast multipole method,” *IEEE Trans. Antennas Propag.*, vol. 57, no. 7, pp. 2084-2093, July 2009.
- [14] T. F. Eibert, “A diagonalized multilevel fast multipole method with spherical harmonics expansion of the k-space integrals,” *IEEE Trans. Antennas Propag.*, vol. 53, no. 2, pp. 814-817, Feb. 2005.
- [15] M. He, J. Liu, and K. Zhang, “Improving the spherical harmonics expansion based multilevel fast multipole algorithm (SE-MLFMA),” *IEEE Antennas Wireless Propag. Lett.*, vol. 12, pp. 551-554, 2013.
- [16] J. Liu, M. He, Z. Li, and J. Su, “The application of improved spherical harmonics expansion-based multilevel fast multipole algorithm in the solution of volume-surface integral equation,” *Int. J. Antenn. Propag.*, vol. 2018, 7 pages, Apr. 2018.
- [17] D. H. Schaubert, D. R. Wilton, and A. W. Glisson, “A tetrahedral modeling method for electromagnetic scattering by arbitrarily shaped inhomogeneous dielectric bodies,” *IEEE Trans. Antennas Propag.*, vol. 32, no. 1, pp. 77-85, Jan. 1984.
- [18] R. F. Harrington, *Time Harmonic Electromagnetic Fields*. New York: McGraw-Hill, 1961.
- [19] Y. Saad and M. H. Schultz, “GMRES: A generalized minimal residual algorithm for solving nonsymmetric linear systems,” *SIAM J. Sci. and Stat. Comput.*, vol. 7, no. 3, pp. 856-869, 1986.
- [20] A. C. Woo, H. T. G. Wang, M. J. Schuh, and M. L. Sanders, “EM programmer's notebook-benchmark radar targets for the validation of computational electromagnetics programs,” *IEEE Antennas Propag. Mag.*, vol. 35, no. 1, pp. 84-89, Feb. 1993.
- [21] Altair. (2014). FEKO, Suite 7.0 [Online]. Available: <http://www.feko.info>

Gain Enhancement Planar Lens Antenna based on Wideband Focusing Gradient Meta-surface

Qiming Yu, Shaobin Liu, Zhengyu Huang, Xiangkun Kong, Yuehong Hu, and Yongdiao Wen

College of Electronic and Information Engineering
Nanjing University of Aeronautics and Astronautics, Nanjing, 211106, China
yqm1604504@nuaa.edu.cn, lsb@nuaa.edu.cn, huangzynj@nuaa.edu.cn, xkkong@nuaa.edu.cn,
1961540605@qq.com, flymew@126.com

Abstract — A three-layered transmitting focusing gradient meta-surface (FGMS) has been proposed, which can achieve broadband gain enhancement from 8.2 GHz to 10 GHz. The element of broadband transmitting FGMS has high transmitting efficiencies that over 0.7 and achieve $[0, 2\pi]$ phase range with a flat and linear trend in the operating band. The FGMS can transform the spherical waves into plane waves. Three patch antennas working at 8.2 GHz, 9.1 GHz, and 10 GHz respectively are placed the focus of broadband FGMS as the spherical-wave source to build a broadband planar lens antenna system. It achieves a simulation gain of 15.44 dBi which is 7.51dB higher than that of the bare patch antenna at 10 GHz with satisfying SLLs and beamwidths. However, it enhanced the gain of the bare patch antenna in a wide operating band. Finally, the FGMS and the patch antenna are fabricated and measured. The measured results are in good agreement with the simulations.

Index Terms — Broadband gain enhancement, focusing gradient meta-surface, lens antenna, transmissive.

I. INTRODUCTION

Nowadays, meta-surfaces as a class of metamaterials that have been widely studied [1-4]. As a two-dimensional material in metamaterials, it has many advantages, such as low profile, easy manufacturing, miniaturization, ease to conformal, etc. The gradient meta-surface is the most research-worthy category, which can manipulate the phase and polarization of the wave to control the phase and amplitude. So far, gradient meta-surface has been greatly developed and applied in the microwave field, which can achieve the functions of polarization split [5], radar cross-section reduction [6], anomalous refraction/reflection [7], transformation [8], and focusing [9].

The phase gradient meta-surface (PGMS) is a subclass of MS which has been proposed by Yu [10]. The focusing GMS (FGMS) can transform spherical wave to plane wave, but the point source should be

placed at the focal point of the PGMS. Due to the reciprocity of electromagnetic waves, vice versa. This performance can be used in the design of a high gain planar lens antenna by placing the feed antenna at the focus of the FGMS [11-13].

Lens antennas have a wide range of applications in remote wireless communication systems, which effectively combines the advantages of parabolic antennas and phased array antennas to produce extremely high gains. Lens antennas employing meta-surfaces such as zero/low index metamaterial [14] or gradient-refractive-index metamaterial [15] have been heavily researched. Reflect-array [16] and transmit-array [17] antennas have received extensive attention because of their simple structure and thinness. A high-gain transmitting lens antenna by employing layered phase-gradient meta-surface (MS) has been proposed [18]. The meta-surface is engineered to focus the propagating plane wave to a point with high efficiency. A single-layer focusing gradient meta-surface built by one element-group has been proposed [19]. The lens antenna achieves a pencil-shaped radiation pattern with a simulation maximum gain of 16.7dB at 10GHz. But today's lens antennas are mostly narrowband, can't meet the needs of remote wireless communication systems. Therefore, it is necessary to develop a broadband high gain lens based on FGMS.

In this work, a three-layered transmitting FGMS has been proposed, which can achieve broadband gain enhancement from 8.2 to 10GHz. The broadband transmitting FGMS element requires stable phase compensation, high transmit efficiency, and the phase of the phase-shifting element changes flatly and linearly in the wide frequency band. Then elements with different types and compensation phases are located on the surface according to the hyperbolic phase distribution to build broadband focusing FGMS. The FGMS can transform the spherical waves into plane waves, which can be used to build a planar lens antenna. Three patch antennas working at 8.2 GHz, 9.1 GHz, and 10 GHz respectively are placed the focus of broadband FGMS as the

spherical-wave source to build a broadband planar lens antenna system, that enhanced the gain of the bare patch antenna in a wide operating band.

II. MULTILAYER TRANSMITTING FOCUSING GMS DESIGN

A. Design principle of GMS

The phase gradient meta-surface can be simply divided into two types: transmissive and reflective. Compared with the reflecting FGMS, the design of the transmitting FGMS is more difficult, which requires not only stable phase compensation but also high transmit efficiency. Figure 1 shows the working mechanism of transmitting focusing FGMS. Transmitting focusing FGMS can convert incident plane waves into spherical waves emitted by the source located at its focus and vice versa. This performance can be used in the design of a high gain planar lens antenna by placing the feed antenna at the focus of the FGMS.

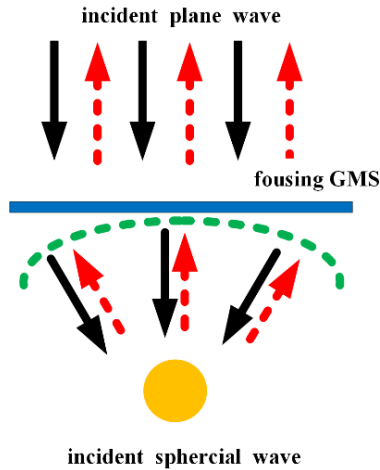


Fig. 1. The schematics of focusing FGMS. The green dashed line shows the hyperbolic phase distribution of the meta-surface given by Eq. (1).

Usually the phase distribution of the focused FGMS unit obeys the hyperbolic formula:

$$\Phi(x, y) = \frac{2\pi}{\lambda_0} \left(\sqrt{x^2 + y^2 + L^2} - L \right) + \Phi_0, \quad (1)$$

where L is the focal length of the lens, λ_0 is the free space wavelength, x and y are the position coordinate of the lens unit on the lens. When the plane incident waves perpendicular to the transmitting focusing FGMS, the transmitted electromagnetic wave is deflected toward the phase delay direction. The anomalous refraction can be explained by the generalized law of refraction, which is defined by the following formula:

$$n_t \sin(\theta_t) - n_i \sin(\theta_i) = \frac{\lambda}{2\pi} \frac{d\phi}{dx}, \quad (2)$$

where ϕ is the phase distribution of the focused FGMS unit, n_t and n_i are the refractive index of the refracted medium and incident medium, θ_t and θ_i are the refracted and incident angle of electromagnetic wave, λ is the wavelength of electromagnetic waves:

$$d\phi / dx = 2\pi / np, \quad (3)$$

where n is the number of phase shifting elements for constructing the supercell of FGMS. In this design, the entire transmitting FGMS is placed in an air box, so $n_t = n_i = 1$,

$$\theta_t = \sin^{-1} \left(\frac{\lambda}{2\pi} \times \frac{2\pi}{np} \right). \quad (4)$$

When the element has achieved $[0, 2\pi]$ phase range, a transmitting focusing FGMS that regulates the transmission direction of the electromagnetic wave can be obtained by designing a reasonable phase gradient and arranging the elements into an array.

B. Element design

Designing broadband transmitting focusing FGMS, in addition to satisfying the two above conditions, it is also required that the transmission phase of the phase-shifting element changes in a flat and linear manner in the operating frequency band. As shown in Fig. 2, the element of meta-surface structure is composed of four metallic layers and three intermediate dielectric layers, each metallic layer contains a square ring outside and a square patch inside. the dielectric substrate is F4b, which has a permittivity of 2.65, a thickness of 2.5 mm, and a loss tangent of 0.001. To efficiently control the phase gradient, the side length of the inside square patch is chosen to vary while fix $a=8\text{mm}$, $l=7.9\text{mm}$, $w=0.1\text{mm}$, $d=2.5\text{mm}$. So, the total thickness of the FGMS is 7.5 mm.

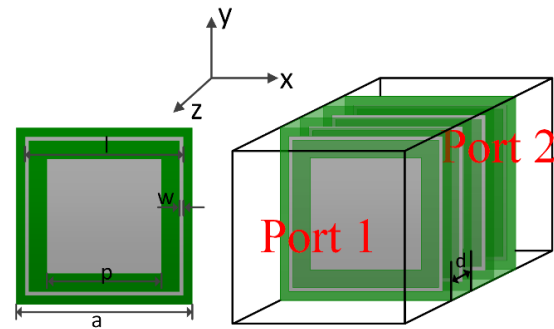


Fig. 2. Structure of the FGMS element and the simulated setup. (a) Top view; (b) perspective view.

Figure 3 shows the transmission coefficients of a phase-shifting element with different p . In the 8.2~10GHz frequency band, the amplitude of the transmission coefficient curve ranges from 0.7 to 1 as the change of square patch length. It indicates that the designed element of FGMS has a relatively large transmissivity. Figure 4

shows the phase of S_{21} for which indicates that the phase range. The three layers element has achieved $[0, 2\pi]$ phase range with a flat and linear trend in the operating band. It satisfies the requirement for transmitting FGMS design.

A supercell that provides a linear phase gradient has been designed, which can manipulate the EM waves effectively. The supercell is composed of seven elements. The inside square metal patch side (p) of each element has a length of 7.2mm, 7mm, 6.6mm, 6.2mm, 5.7mm, 4.8mm, 4mm from large to small, meanwhile the other parameters of the elements remain unchanged. Each phase-shifting element can compensate for the phase of 51.43° .

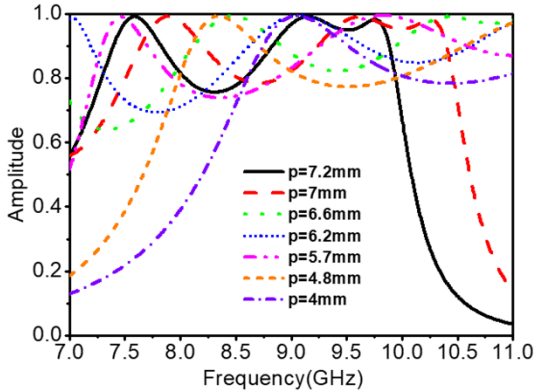


Fig. 3. Transmission coefficients of phase shifting element with different value of p .

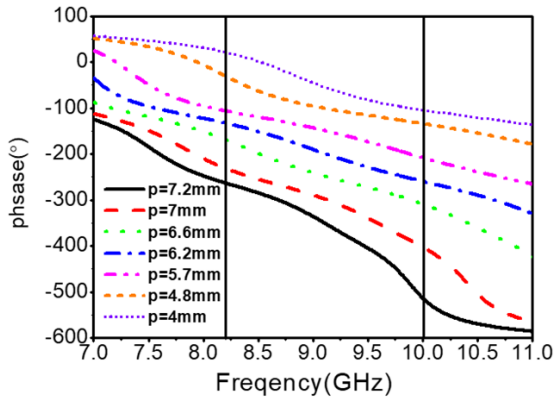


Fig. 4. Transmission phases of the seven elements with different value of p .

C. Focusing GMS design

In the previous part, a supercell, that can cover enough phase range with high transmitting efficiencies, has been designed. The supercell, that composed of seven different phase compensation elements, is used for building a (two- dimensional) 2D focusing FGMS. To determine the phase that needs to be compensated for

each element position on the plane of the FGMS, equation (1) can be written as follows:

$$\Delta \varphi(m,n) = \frac{2\pi}{\lambda_0} \left(\sqrt{(mp)^2 + (np)^2 + L^2} - L \right) + 2k\pi, \quad (5)$$

where $k=0,1,2,\dots$, m (n) is the number of the element in x (y)-direction, $\Delta \varphi(m, n)$ is the phase difference between the element placed at the location of (mp, np) and the element placed at the origin ($m=0, n=0$).

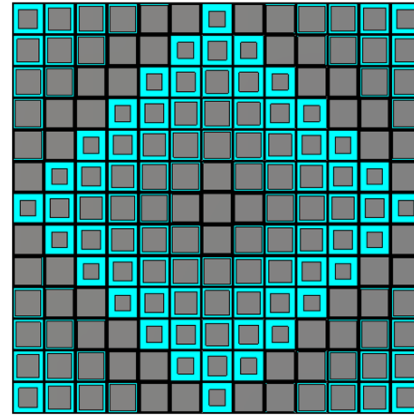
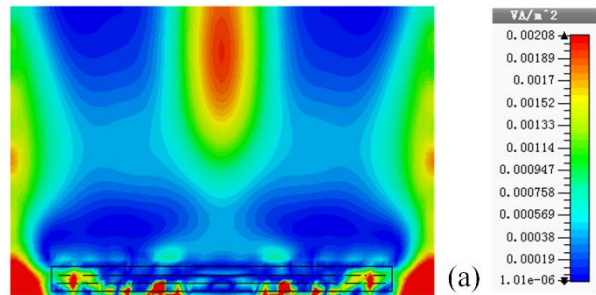


Fig. 5. The prototype of designed planar transmission type focusing FGMS.

We use 7 elements to cover about 2π phase shift which was mentioned above. Figure 5 shows the prototype of the designed planar transmission type focusing FGMS, which with elements of 13×13 and a size of $104\text{mm} \times 104\text{mm}$. Due to the central symmetry of the distribution of FGMS phase-shifting element and the symmetry of element, so the designed wideband FGMS is polarization insensitive. To yield the focusing phenomenon, a plane wave is located 20mm over the MS to illuminate it. Figure 6 shows the focusing effect of the proposed design FGMS. The simulated electric field (E_x) amplitude distributions on xoz -plane at 8.2GHz, 9.1GHz, and 10GHz have been shown. The power densities on the xoz -plane have been focused on a spot. Due to the polarization insensitivity of the FGMS structure, the same behavior exists in the yoz -plane.



(a)

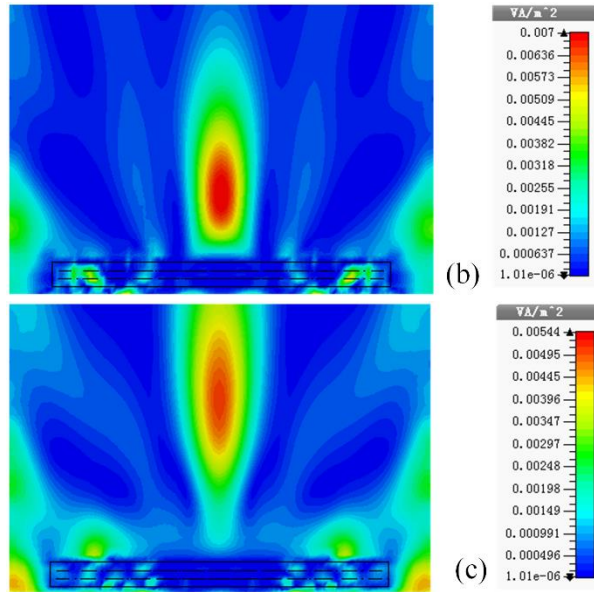


Fig. 6. Focusing effect of the proposed design FGMS. Simulated electric field (E_x) amplitude distributions on xoz -plane. (a) 8.2 GHz; (b) 9.1 GHz; (c) 10 GHz.

III. HIGH-GAIN LENS ANTENNA APPLICATION

We can design a wideband, gain enhancement planar lens antenna operating at X-band based on the designed FGMS. The proposed FGMS can transform the spherical wave emitted by the patch antenna to a near-plane wave, which enables gain enhancement. The schematic of the lens antenna is shown in Fig. 7. A patch antenna has been located 30mm away from the FGMS to feed the FGMS. The antenna placement position needs to be close to the focus of FGMS. Three patch antennas are designed to verify the gain effect of wideband lenses based on FGMS. An antenna structure as shown in Fig. 7, radiant surface is a round metal patch and coaxial feed has been used. The substrate is F4b, which has a permittivity of 2.65 and a loss tangent of 0.001.

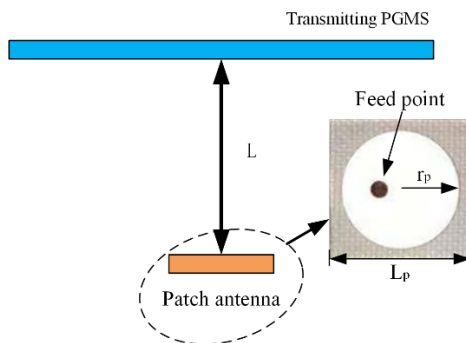


Fig. 7. The schematic of the lens antenna.

Three patch antennas working at 8.2 GHz, 9.1 GHz, and 10 GHz respectively are designed and the measured reflection coefficients with and without the FGMS are shown in Fig. 8. It can be seen from Fig. 8 that the resonant frequency band of the antenna is deviated after loading the lens, mainly due to the existence of parasitic coupling between the radiation source antenna and the FGMS. The measured results are in good agreement with the simulation results.

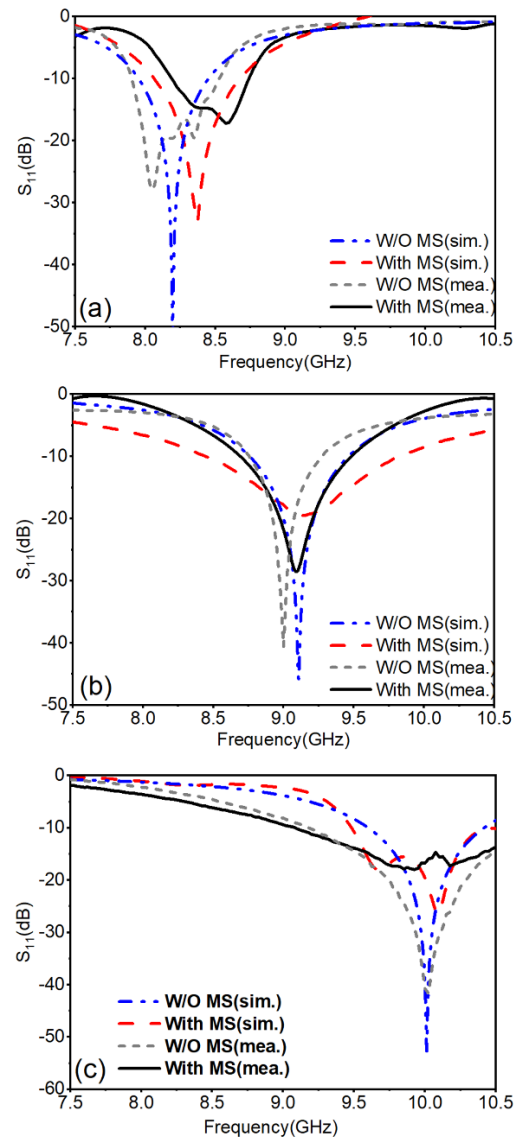


Fig. 8. S_{11} of three patch antennas with and without loading the FGMS. (a) 8.2GHz; (b) 9.1GHz; (c) 10 GHz.

Figures 9 (a) and (b) show the sample of lens antenna with FGMS. Hard foam of the thickness of 30mm has been loaded between patch antenna and

FGMS to fix patch antenna and FGMS. Figure 9 (c) shows the test scenario of an anechoic chamber.

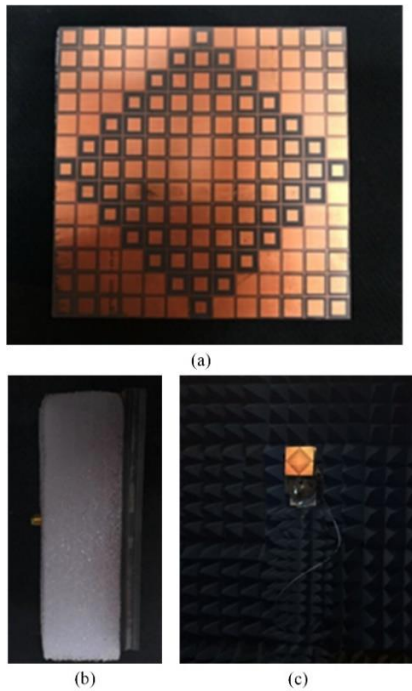


Fig. 9. The sample of lens antenna with FGMS. (a) Front view; (b) side view; (c) the test scenario of anechoic chamber.

To demonstrate the performances of the system more clearly, we display the far-field radiation patterns of the patch antenna with and without the FGMS at 8.2GHz, 9.1GHz, and 10GHz of two orthogonal planes in Fig.10.

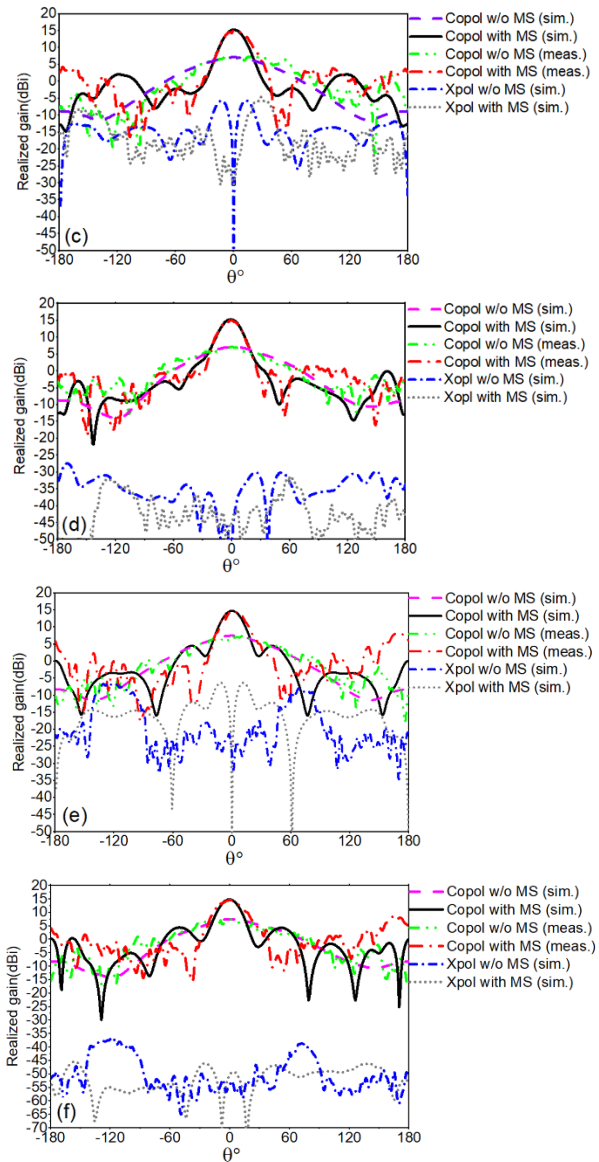
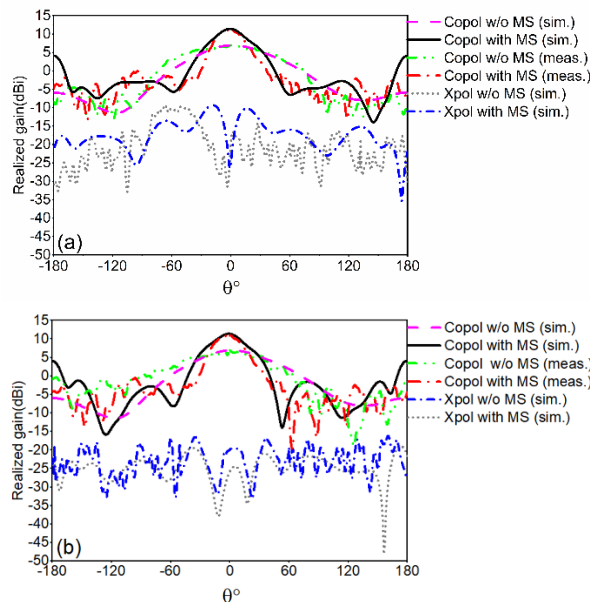


Fig. 10. Simulated and measured far-field radiation patterns of the patch antenna with and without the FGMS. (a) 8.2 GHz, xoz -plane; (b) 8.2 GHz, yo z -plane; (c) 9.1 GHz, xoz -plane; (d) 9.1 GHz, yo z -plane; (e) 10 GHz, xoz -plane; (f) 10 GHz, yo z -plane.

As is shown in Figs. 10 (a) and (b), the lens antenna has a simulation gain of 11.92 dBi which is 5.15dB higher than that of the bare patch antenna at 8.2 GHz. The measured peak gain is 11.04 dBi which is 4.66 dB higher than that of the bare patch antenna at 8.2 GHz. As is shown in Figs. 10 (c) and (d), the lens antenna has a simulation gain of 15.60 dBi which is 8.44 dB higher than that of the bare patch antenna at 9.1 GHz. The measured maximum gain is 14.9 dBi which is 7.54 dB higher than that of the bare patch antenna at 9.1 GHz. As shown in Figs. 10 (e) and (f), the lens antenna has a

simulation gain of 15.44 dBi which is 7.51dB higher than that of the bare patch antenna at 10 GHz. The measured peak gain is 14.26 dBi which is 6.66 dB higher than that of the bare patch antenna at 10 GHz. Compared with the measured results, the simulation results are about 1dB higher, which is acceptable by considering the possible machining errors and test errors.

In the case of the pure patch antenna without adding the lens, the antenna efficiency of 89.5% is obtained at 9.1GHz. Note that the aperture efficiency is evaluated with respect to the utmost directivity which can be calculated through the equation:

$$\eta = G / D_{\max} = G / (4\pi PQ / \lambda_0^2) \times 100\%, \quad (6)$$

with $P = 104$ mm and $Q = 30$ mm is the length and width of the focusing meta-surface, respectively. In the case of the patch antenna with adding the lens, the antenna efficiency of 41% is obtained at 9.1GHz.

The lens antenna based on FGMS designed in this paper has been proven to achieve gain enhancement over a wide range of frequencies from 8.2 to 10GHz. In addition, small overall size with less number of elements inevitably brings a decrease in the peak gain.

Table 1: Comparison of the performances between previous literature and this work

| Ref. | WF f/GHz | Aperture Efficiency | F/D Ratio | Unit Cell Number |
|--------------|--------------|------------------------|--------------|---------------------|
| [18] | 10 | 31.4% | 0.19 | 196 |
| [19] | 9.9- 10.2 | N.A. | 0.29 | 144 |
| [20] | 15-18 | 6.17% | 0.43 | 576 |
| [21] | 9.275 | 56.3% | 0.8 | 121 |
| This work | 9.1-10 | 41% | 0.28 | 144 |

WF=Working Frequency.

The comparisons between the results of this work with earlier transmit-arrays are shown in the following Table 1. From the Table 1, we can see that the designed lens antenna has good performance in terms of antenna working bandwidth and aperture efficiency. The proposed lens antenna has a smaller F/D ratio, which will facilitate the requirements of low-profile antennas. In addition, fewer units cell number of transmit-arrays mean easier processing and lower costs.

IV. CONCLUSION

In conclusion, a gain enhancement broadband planar lens antenna operating from 8.2GHz to 10GHz based on wideband focusing gradient meta-surface is simulated, fabricated, and measured. The prototype of the designed planar transmission type focusing FGMS has elements of 13×13 and a size of $104 \text{ mm} \times 104 \text{ mm} \times 7.5 \text{ mm}$. High transmitting efficiencies of the elements, the phase of the phase-shifting element

changes with a flat and linear manner in a wide frequency band, and a good focusing effect of the FGMS guarantee the good performances of the broadband transmitting lens antenna. It achieves a simulation gain of 15.44 dBi which is 7.51dB higher than that of the bare patch antenna at 10 GHz with satisfying SLLs and beamwidths. Moreover, the gain is improved from 8.2GHz to 10 GHz, which implements broadband FGMS.

ACKNOWLEDGMENT

This work was supported by National Natural Science Foundation of China (Grant No. 62071221, 62071442), Postgraduate Research & Practice Innovation Program of Jiangsu Province (Grant No. KYCX19_0189), China Scholarship Council (Grant No. 201906830067).

REFERENCES

- [1] J. Zhao, B. Li, Z. N. Chen, and C. W. Qiu, "Redirection of sound waves using acoustic metasurface," *Appl. Phys. Lett.*, vol. 103, no. 15, p. 151604, 2013.
- [2] Y. Li, J. Zhang, S. Qu, J. Wang, H. Chen, Z. Xu, and A. Zhang, "Wideband radar cross section reduction using two-dimensional phase gradient metasurfaces," *Appl. Phys. Lett.*, vol. 104, no. 22, p. 221110, 2014.
- [3] X. Wan, W. X. Jiang, H. F. Ma, and T. J. Cui, "A broadband transformation-optics metasurface lens," *Appl. Phys. Lett.*, vol. 104, no. 15, p. 151601, 2014.
- [4] C. Saeidi and D. Weide, "Wideband plasmonic focusing metasurfaces," *Appl. Phys. Lett.*, vol. 105, no. 5, p. 053107, 2014.
- [5] T. Cai, G. M. Wang, X. F. Zhang, J. G. Liang, Y. Q. Zhuang, D. Liu, and H. X. Xu, "Ultra-thin polarization beam splitter using 2-D transmissive phase gradient metasurface," *IEEE Trans. Antennas Propagat.*, vol. 63, no. 12, pp. 5629-5636, 2015.
- [6] Y. Li, J. Zhang, S. Qu, J. Wang, H. Chen, Z. Xu, and A. Zhang, "Wideband radar cross section reduction using two-dimensional phase gradient metasurfaces," *Appl. Phys. Lett.*, vol. 104, no. 22, p. 221110, 2014.
- [7] Z. Wei, Y. Cao, X. Su, Z. Gong, Y. Long, and H. Li, "Highly efficient beam steering with a transparent metasurface," *Opt. Express*, vol. 21, no. 9, pp. 10739-10745, 2013.
- [8] C. Pfeiffer and A. Grbic, "Bianisotropic metasurfaces for optimal polarization control: Analysis and synthesis," *Phys. Rev. A*, vol. 2, no. 4, p. 044011, 2014.
- [9] F. Monticone, N. M. Estakhri, and A. Alù, "Full control of nanoscale optical transmission with a composite metascreen," *Phys. Rev. Lett.*, vol. 110, no. 20, p. 203903, 2013.
- [10] N. Yu, P. Genevet, M. A. Kats, F. Aieta, J. P. Tetienne, F. Capasso, and Z. Gaburro, "Light

propagation with phase discontinuities: Generalized laws of reflection and refraction,” *Science*, pp. 333-337, 2011.

- [11] A. Belen, P. Mahouti, F. Güneş, and Ö Tari, “Gain enhancement of a traditional horn antenna using 3D printed square-shaped multi-layer dielectric lens for X-band applications,” *Appl. Comput. Electromagn. Soc. J.*, vol. 36, no. 2, pp. 132-138, 2021.
- [12] A. Belen and E. Tetik, “Realization of modified elliptical shaped dielectric lens antenna for X band applications with 3D printing technology,” *Appl. Comput. Electromagn. Soc. J.*, vol. 35, no. 8, pp. 916-921, 2020.
- [13] S. Loredó, G. León, O. F. Robledo, and E. G. Plaza, “Phase-only synthesis algorithm for transmitarrays and dielectric lenses,” *Appl. Comput. Electromagn. Soc. J.*, vol. 33, no. 3, pp. 259-264, 2018.
- [14] H. X. Xu, G. M. Wang, and T. Cai, “Miniaturization of 3-D anisotropic zero-refractive-index metamaterials with application to directive emissions,” *IEEE Trans. Antennas Propag.*, vol. 62, no. 6, pp. 3141-3149, 2014.
- [15] H. X. Xu, G. M. Wang, Z. Tao, and T. Cai, “An octave-bandwidth half Maxwell fish-eye lens antenna using three-dimensional gradient-index fractal metamaterials,” *IEEE Trans. Antennas Propag.*, vol. 62, no. 9, pp. 4823-4828, 2014.
- [16] R. S. Malfajani and Z. Atlasbaf, “Design and implementation of a dual-band single layer reflectarray in X and K bands,” *IEEE Trans. Antennas Propag.*, vol. 62, no. 8, pp. 4425-4431, 2014.
- [17] A. H. Abdelrahman, A. Z. Elsherbeni, and F. Yang, “Transmitarray antenna design using cross-slot elements with no dielectric substrate,” *IEEE Antennas Wireless Propag. Lett.*, vol. 13, pp. 177-180, 2014.
- [18] H. Li, G. Wang, H. X. Xu, T. Cai, and J. Liang, “X-band phase-gradient metasurface for high-gain lens antenna application,” *IEEE Trans. Antennas Propag.*, vol. 63, no. 11, pp. 5144-5149, 2015.
- [19] H. Li, G. Wang, J. Liang, X. Gao, H. Hou, and X. Jia, “Single-layer focusing gradient metasurface for ultrathin planar lens antenna application,” *IEEE Trans. Antennas Propag.*, vol. 65, no. 3, pp. 1452-1457, 2017.
- [20] H. Hai-Sheng, W. Guang-Ming, L. Hai-Peng, C. Tong, and G. Wen-Long, “Ultra-thin broadband flat metasurface to focus electromagnetic waves and its application in high-gain antenna,” *Acta Physica Sinica*, vol. 65, no. 2, 2016.
- [21] X. Zhao, C. Yuan, L. Liu, S. Peng, Q. Zhang, and H. Zhou, “All-metal transmit-array for circular polarization design using rotated cross-slot elements for high-power microwave applications,” *IEEE*

Trans. Antennas Propag., vol. 65, no. 6, pp. 3253-3256, 2017.



Qiming Yu was born in Zhejiang Province, China, in 1992. He received the B.S. degree and M.S. degree from Nanchang University, Nanchang, China, in 2014 and 2016, respectively. He is currently pursuing the Ph.D. degree in Nanjing University of Aeronautics and Astronautics, Nanjing, China. His current research interests include frequency selective surface, rasorber and lens antenna.



Shaobin Liu received the Ph.D. degree in Electronics Science and Technology from the National University of Defense Technology in 2004. However, in 2003, he was already promoted as Professor. He is currently a Professor of Electromagnetic and Microwave Technology at the Nanjing University of Aeronautics and Astronautics. His research focuses on plasma stealthy antennas, frequency selective surface and absorber, rasorber, radio frequency, electromagnetic compatibility.

Design of Microstrip Parallel-Coupled Lines with High Directivity using Symmetric-Centered Inductors

Somchat Sonasang¹ and Niwat Angkawisittpan^{2*}

¹Department of Electrical Engineering, Faculty of Engineering, Mahasarakham University
Maha Sarakham 44150, Thailand
somchat.sonasang@gmail.com

²Research Unit for Computational Electromagnetics and Optical Systems, Faculty of Engineering
Mahasarakham University, Maha Sarakham 44150, Thailand
*niwat.a@msu.ac.th

Abstract — A technique for directivity improvement of the microstrip parallel-coupled lines using symmetric-centered inductors is presented in this paper. The design procedure of the symmetric-centered inductors using the closed-form equations is given. The proposed technique was performed with a design at the operating frequency of 0.9 GHz on an FR4 substrate. Validity of the proposed technique is verified by simulations and measurements in comparisons with conventional parallel-coupled lines. The measured results exhibit the isolation of -30.10 dB and directivity of 19.28 dB at the operating frequency of 0.9 GHz. The directivity from the measured results is improved by more than 4 dB at 0.9 GHz and more than 6 dB at 1.05 GHz compared with the conventional parallel-coupled lines. In addition, the proposed technique for the microstrip parallel-coupled line can achieve a high directivity with the compact size (21.0 mm x 4.70 mm). The novelty of this paper is by introducing the proposed and closed-form design equations for the compact symmetric-centered inductors with high directivity.

Index Terms — Microstrip, parallel-coupled lines, directivity, symmetric-centered inductors.

I. INTRODUCTION

Microstrip parallel-coupled lines are often used as a passive element in microwave applications such as Wilkinson power dividers, Baluns [1], mixers, phase shifters, wideband bandpass filters [2], and feeding networks for antennas [3]. However, microstrip parallel-coupled lines also possess unwanted effects from inhomogeneous dielectric substrate due to inequity in the phase velocity of the even and odd modes. Various compensation techniques have been reported for improving the isolation and enhancement of directivity for microstrip parallel-coupled lines. The principal techniques can be classified into two main categories

including distributed [4-9] and lumped [10-19] compensation approaches. Lumped compensation approaches can further be classified into two well-known techniques including capacitive techniques [11-14], which are used for enhancement of directivity and inductive compensation techniques [15-19] presented are compensated by inductance for enhancement of high directivity microstrip parallel-coupled lines. However, the capacitive techniques require placement in a narrow spacing of the microstrip parallel-coupled lines. Nonetheless, there are drawbacks of parasitic effects in the ground connected and difficulty in layout. In addition, the compound techniques do not decrease the electrical length in the microstrip parallel-coupled lines. compensation technique [20] uses inductance and capacitance for directivity enhancement. Also, the technique requires the large physical size. However, the aforementioned.

The disadvantage of some approaches is the lack of closed-form design equations for additional impedances and electrical length. Also, it turns out that the design process heavily relies on the electromagnetic simulation step. This step consumes much computing time. In addition, some techniques are often not suitable for some standard fabrication tasks or require much space for the design devices, thus more cost demand is certainly required. Distinct advantage of the lumped compensation approach is its easy design process because the design equations can be derived [15].

In this paper, a simple, yet effective lumped compensation technique with symmetric-centered inductors is proposed. This technique can achieve enhancement of directivity, isolation improvement, and compact circuit size for microstrip parallel-coupled lines using symmetric-centered inductors. The closed-form equations for the design of symmetric-centered inductors and the equations for electrical length are proposed for improving the directivity and the isolation of the

microstrip parallel-coupled lines in this paper. In addition, the high directivity and isolation improvement can be obtained in the wider frequency range. In this paper, section II presents the theory for microstrip parallel-coupled lines with the proposed technique. The design equations for the proposed circuit are also given. Section III proposes the concept for the design of the symmetric-centered inductors and the simulated results for the microstrip parallel-coupled lines. Section IV shows the experimental results of the proposed technique. Finally, the conclusions are presented in Section V.

II. THE PROPOSED TECHNIQUE WITH SYMMETRIC-CENTERED INDUCTORS

The schematic of the proposed microstrip parallel-coupled lines is shown in Fig. 1 (a), in which the component has an input port (port 1), a coupled port (port 2), an isolated port (port 3) and a through port (port 4). The symmetric-centered inductors shown in Fig. 1 (b) are face to face configuration, consisting of microstrip parallel-coupled lines and symmetric-centered inductors (L_{sd}).

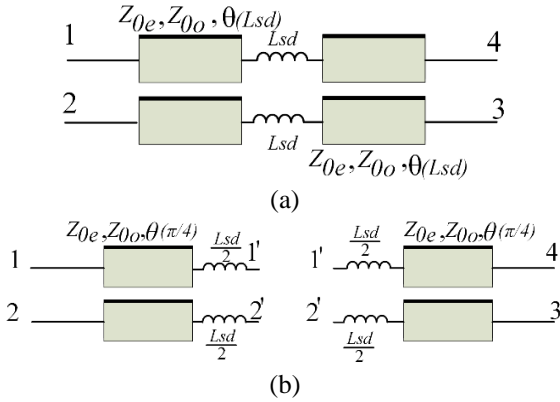


Fig. 1. Schematics of the proposed microstrip parallel-coupled lines with (a) the proposed technique and (b) face to face configuration.

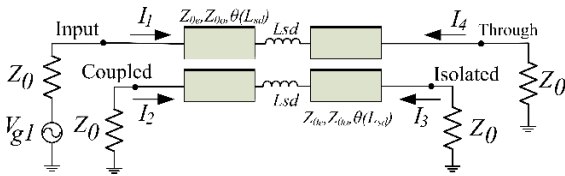


Fig. 2. Electrical schematic of the symmetric-centered inductors for microstrip parallel-coupled lines.

Figure 2 shows the electrical schematic of the symmetric-centered inductors for the microstrip parallel-coupled lines. This schematic was used for analysis of the various coefficients with the network theory.

Generally, the symmetric-centered inductors can be represented in terms of their corresponding two-port network. The equations are expressed by [15,16]:

$$V_1 = I_1 Z'_{11} + I_2 Z'_{12} + I_3 Z'_{13} + I_4 Z'_{14}, \quad (1)$$

$$V_2 = I_1 Z'_{21} + I_2 Z'_{22} + I_3 Z'_{23} + I_4 Z'_{24}, \quad (2)$$

$$V_3 = I_1 Z'_{31} + I_2 Z'_{32} + I_3 Z'_{33} + I_4 Z'_{34}, \quad (3)$$

$$V_4 = I_1 Z'_{41} + I_2 Z'_{42} + I_3 Z'_{43} + I_4 Z'_{44}, \quad (4)$$

where the $Z'_{11} = Z_{11} + Z_{Lsd}$ and $Z'_{22} = Z_{22} + Z_{Lsd}$ in these equations (1-4) have impedance parameters as follows [21]:

$$Z_{11} = -\frac{j}{2}(Z_{0e} \coth \theta_e + Z_{0o} \coth \theta_o), \quad (5)$$

$$Z_{12} = -\frac{j}{2}(Z_{0e} \coth \theta_e - Z_{0o} \coth \theta_o), \quad (6)$$

$$Z_{13} = -\frac{j}{2}(Z_{0e} \operatorname{csch} \theta_e - Z_{0o} \operatorname{csch} \theta_o), \quad (7)$$

$$Z_{14} = -\frac{j}{2}(Z_{0e} \operatorname{csch} \theta_e + Z_{0o} \operatorname{csch} \theta_o), \quad (8)$$

and the Z_{0e}, Z_{0o} are the even and odd mode characteristic impedances and θ_e, θ_o are even and odd mode electrical lengths, respectively. The even and odd mode electrical lengths are:

$$\theta_e = j \frac{\pi}{4}, \quad (9)$$

$$\theta_o = j \frac{\pi}{4} \sqrt{\frac{\epsilon_{effo}}{\epsilon_{effe}}}, \quad (10)$$

where $\epsilon_{effe}, \epsilon_{effo}$ are the even and odd mode effective relative dielectric constants. The phase velocities of the even and odd modes are different in microstrip parallel-coupled lines. Let the symmetric-centered inductors for the microstrip parallel-coupled lines become equal. The impedance parameters (Z) are in the equations (11-14) [21]:

$$Z_{11} = Z_{22} = Z_{33} = Z_{44}, \quad (11)$$

$$Z_{12} = Z_{21} = Z_{34} = Z_{43}, \quad (12)$$

$$Z_{13} = Z_{24} = Z_{31} = Z_{42}, \quad (13)$$

$$Z_{14} = Z_{23} = Z_{32} = Z_{41}. \quad (14)$$

Let the isolation coefficient (S_{31}) reach zero ($S_{31} \rightarrow 0$) for perfect isolation performance. The coupling coefficient (S_{21}), isolation coefficient (S_{31}) and the directivity can be derived and shown in the equations (15-17):

$$S_{21} = 20 \log \left(\frac{V_2}{V_1} \right), \quad (15)$$

$$S_{31} = 20 \log \left(\frac{V_3}{V_1} \right), \quad (16)$$

$$Directivity = 20 \log \left(\frac{V_2}{V_3} \right) = S_{21} - S_{31}. \quad (17)$$

The symmetric-centered inductors are connected at the center of the microstrip parallel-coupled lines. The equations (1-17) are used to determine the isolation coefficients in terms of coupler electrical parameters, which can be derived as the mentioned symmetric-centered inductors. Furthermore, the directivity can be improved at the operating frequency (f_o) as soon as the isolation coefficient is null. The impedance of symmetric-centered inductors is obtained in the function of Z-impedance in equation (18) as:

$$Z_{Lsd} = - \frac{\left(Z_{11}^2 Z_{13} + 2Z_{11}Z_{13}Z_0 - 2Z_{11}Z_{12}Z_{14} + Z_{13}^2 Z_0 - Z_{13}^3 + Z_{13}Z_{14}^2 - 2Z_{12}Z_{14}Z_0 \right)}{Z_{11}Z_{13} + Z_{13}Z_0 - Z_{12}Z_{14}}, \quad (18)$$

then the symmetric-centered inductors are as the equation (19):

$$L_{sd} = \frac{1}{2\pi f_o} \operatorname{Im} \left(\frac{Z_{0o}Z_{0e}^2 - Z_{0e}Z_{0o}^2 + Z_0^2 \sinh \theta_o + Z_0^2 \sinh \theta_e - 2Z_0^3 \varphi}{Z_o Z_{0e} \sinh \theta_o + Z_{0o} \sinh \theta_e - Z_o^2 \varphi} \right), \quad (19)$$

where $\varphi = \cosh \theta_e - \cosh \theta_o$ and Z_0 is the characteristic impedance of the coupled lines, $\theta_e = \pi/4$ is the even mode electrical length, and $\theta_o = (\pi/4)k$ is the odd mode electrical length of the coupled lines when $k = \sqrt{\varepsilon_{effo}/\varepsilon_{effe}}$. The equation (19) proposes a closed-form expression to design the symmetric-centered inductors for high directivity at the desired frequency. For

the microstrip parallel-coupled lines with symmetric-centered inductors, the isolation coefficient can reach zero if the new electrical length $\theta(L_{sd})$ is as follows:

$$\theta(L_{sd}) = \frac{\cot^{-1} \left(\frac{4\pi f_o L_{sd} + Z_{0e} \cot \theta_e + Z_{0o} \cot \theta_o}{2Z_{0e}} \right)}{\pi}. \quad (20)$$

III. DESIGN AND SIMULATED RESULTS OF THE SYMMETRIC-CENTERED INDUCTORS

To validate the performance of the proposed technique, a 10-dB conventional parallel-coupled line and the proposed parallel-coupled line operating at the operating frequency of 0.9 GHz are designed and simulated. An FR4 substrate ($h=1.6$ mm, $\varepsilon_r = 4.55$, and $\tan \delta = 0.02$) is used for both parallel-coupled lines. The symmetric-centered inductors are designed and determined from the equations (18-19). The calculation of the symmetric-centered inductors from equation

(19) and the electrical length $\theta(L_{sd})$ from equation (20) are 3.3 nH and 0.22π rad, respectively. These physical parameters of the symmetric-centered inductors and the conventional parallel-coupled lines are shown in Table 1. The topologies of the conventional parallel-coupled lines and the proposed parallel-coupled lines are shown in Figs. 3 (a) and 3 (b), respectively.

Table 1: Parameters of the conventional parallel-coupled lines and the proposed parallel-coupled lines

| Technique | Components | $\theta(rad)$ | W,S,L (mm) |
|------------------------------|--|---------------|-----------------|
| Conventional coupled lines | - | 0.25π | 2.25, 0.2, 23.4 |
| Symmetric-centered inductors | $L_{sd} = 3.3$ nH Transmission line (W,L) = 0.4, 1.3 mm | 0.22π | 2.25, 0.2, 21 |

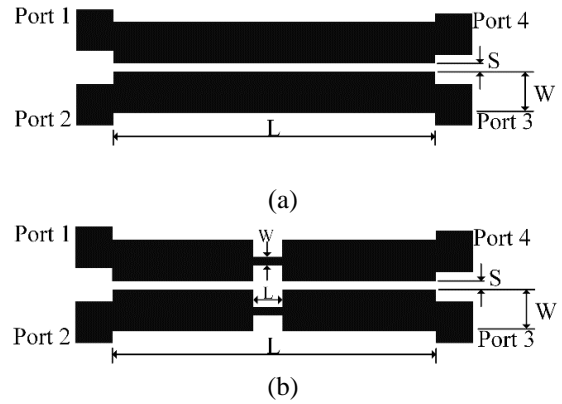


Fig. 3. Schematics of the parallel-coupled lines: (a) conventional parallel-coupled lines, and (b) the proposed parallel-coupled lines.

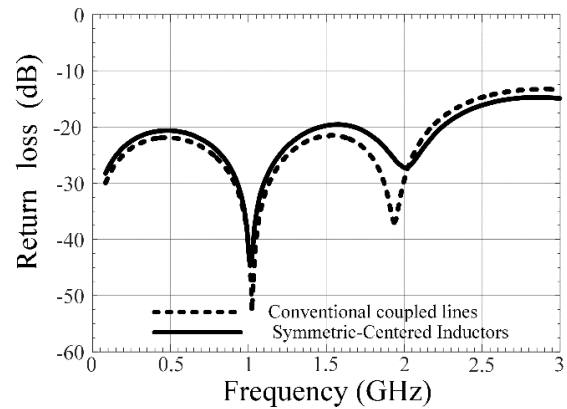


Fig. 4. Simulated results of return loss for the conventional coupled lines and the proposed parallel-coupled lines.

In Figs. 4, 5, 6, and 7, the EM simulated results [22] of the conventional microstrip parallel-coupled lines, and the proposed parallel-coupled lines are shown, including return loss, coupling factor, isolation, and directivity. The simulated results of the return loss are less than -20 dB at the operating frequency of 0.9 GHz and the second harmonic frequency of 1.8 GHz, as seen in Fig. 4. In addition, the coupling factor is 10 dB at the operating frequency of 0.9 GHz for both coupled lines, as shown in Fig. 5. The isolation performance at the operating frequency of 0.9 GHz is less than -23.9 dB for both parallel-coupled lines, as shown in Fig. 6. In Fig. 7, the directivity of the proposed parallel-coupled lines at the operating frequency of 0.9 GHz is 14.8 dB. The proposed design achieves an improvement of 1.4 dB compared with the conventional parallel-coupled lines.

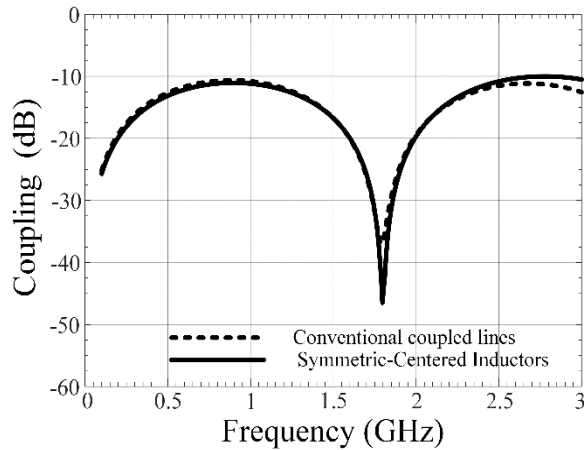


Fig. 5. Simulated results of coupling factor for the conventional coupled lines and the proposed parallel-coupled lines.

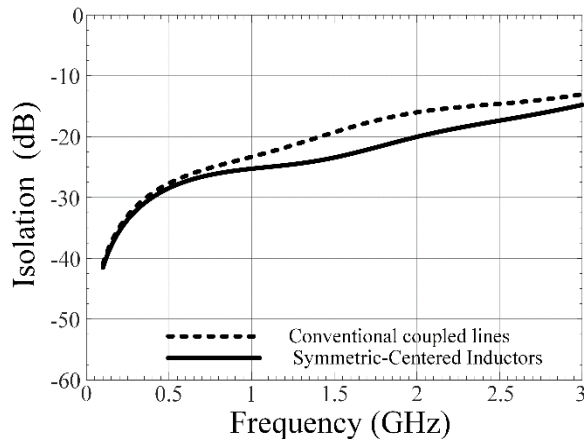


Fig. 6. Simulated results of isolation for the conventional coupled lines and the proposed parallel-coupled lines.

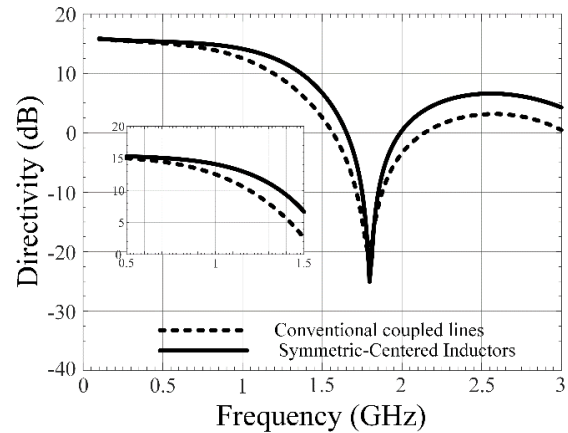


Fig. 7. Simulated results of directivity for the conventional coupled lines and the proposed parallel-coupled lines.

IV. EXPERIMENTAL RESULTS

Measurements are performed to validate the directivity of the proposed parallel-coupled lines. The results are compared with the results of conventional parallel-coupled lines. The prototypes are designed and fabricated on the FR4 substrate. PCB photographs of the conventional and proposed circuits are shown in Fig. 8. In addition, the electrical length (θ) is reduced from 0.25π to 0.22π as in Table 1.

Measurements are performed using the E5071C network analyzer calibrated from 0.1 to 3.0 GHz. Figure 9 shows measured return loss of the proposed parallel-coupled lines compared with the conventional parallel-coupled lines in the frequency range of 0.1 to 3.0 GHz. At the operating frequency of 0.9 GHz, the return losses of both parallel-coupled lines are lower than -20 dB. It is confirmed that the reflected power is low at the operating frequency. The coupling coefficients are about -10 dB at the operating frequency for both parallel-coupled lines as design. The measured results are shown in Fig. 10. The measured isolation performance obtained from the proposed parallel-coupled lines is -30.10 dB. It is about 2.17 dB, which is better than that of the conventional parallel-coupled lines from 0.1 to 3.0 GHz as shown in Fig. 11. In Fig. 12, the measured directivity at the operating frequency of the proposed and conventional parallel-coupled lines are 19.28 dB and 15.00 dB, respectively. It shows that the proposed technique provides directivity performance about 4.28 dB, which is better than that of the conventional technique. However, the highest directivity performance obtained from the proposed technique is 19.8 dB at the frequency of 1.05 GHz. At the frequency of 1.05 GHz, the proposed technique obtained a 6.05 dB improvement in directivity performance. Tables 2, 3 and 4 summarize the performances of the previous and proposed techniques. It is observed that the

electrical length equation and closed-form equation for the symmetric-centered inductors can be achieved. The proposed structure is easily fabricated. The frequency range of the proposed technique with higher directivity compared to the conventional techniques is wider than those of previous techniques. In addition, the proposed technique requires compact circuit size compared to the sizes of the previous techniques.

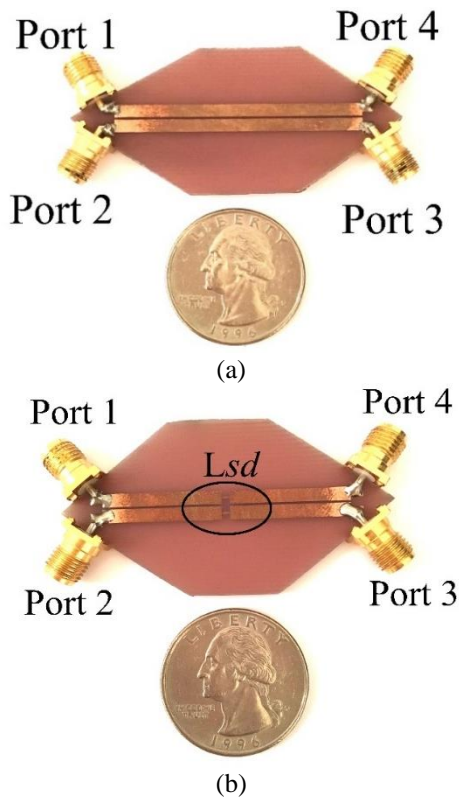


Fig. 8. Photographs of fabricated circuits: (a) conventional coupled lines and (b) proposed coupled lines.

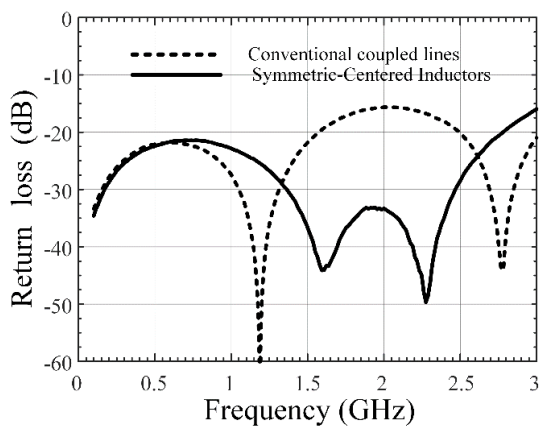


Fig. 9. Measured results for return loss of both parallel-coupled lines.

Table 2: Fabrication and electrical length equation comparison of inductive compensation for parallel-coupled lines

| Ref. | Operating Frequency (GHz) | Electrical Length Equation | Fabrication |
|-----------|---------------------------|----------------------------|-------------|
| [17] | 0.9 | No | Complicated |
| [18] | 2.4 | No | Complicated |
| [20] | 1.6 | No | Complicated |
| This work | 0.9 | Yes | Easy |

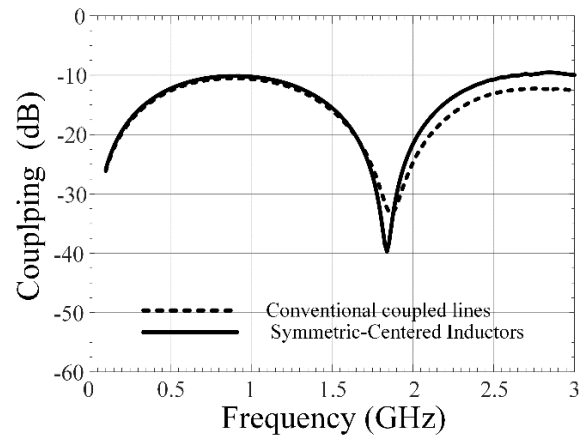


Fig. 10. Measured results for the coupling factors of both parallel-coupled lines.

Table 3: Frequency range with higher directivity comparison of inductive compensation for parallel-coupled lines

| Ref. | Operating Frequency (GHz) | Frequency Ranges with Higher Directivity (Compared to Conventional Technique) (GHz) |
|-----------|---------------------------|---|
| [17] | 0.9 | 0.1-2.0 |
| [18] | 2.4 | 2.0-2.8 |
| [20] | 1.6 | 1.2-2.0 |
| This work | 0.9 | 0.1-3.0 (wider) |

Table 4: Size comparison of inductive compensation for parallel-coupled lines

| Ref. | Operating Frequency (GHz) | Size (mm x mm) |
|-----------|---------------------------|----------------|
| [17] | 0.9 | 53.40 x 23.13 |
| [18] | 2.4 | 18.39 x 18.31 |
| [20] | 1.6 | 19.90 x 18.60 |
| This work | 0.9 | 21.00 x 4.70 |

V. CONCLUSIONS

A technique using the symmetric-centered inductors has been proposed to enhance the directivity performance of microstrip parallel-coupled lines in this paper. The

design of the symmetric-centered inductors is simplified using the closed-form equations. The electrical length is also given. The simulated and measured results are used to validate the proposed technique. Since there are many microwave communication circuits whose circuits consist of microstrip parallel-coupled lines, it is believed that the proposed technique can be easily modified for use in modern wireless communications such as microwave resonators, couplers, and filters with compact size requirements.

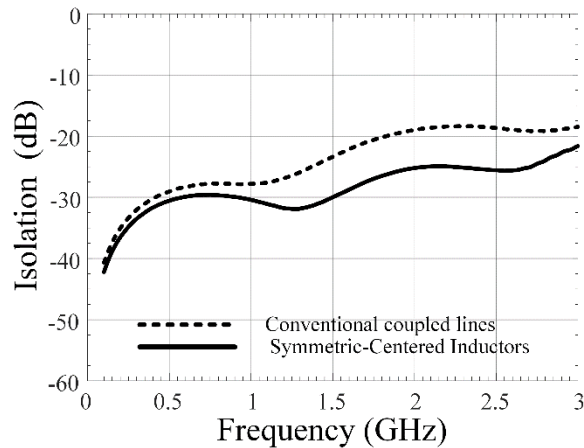


Fig. 11. Measured results for isolation performance of both parallel-coupled lines.

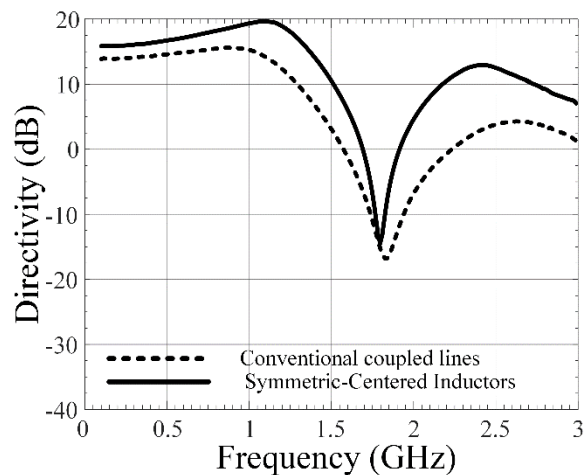


Fig. 12. Measured results for directivity performance of both parallel-coupled lines.

ACKNOWLEDGMENTS

This work was financially supported by Mahasarakham University, Maha Sarakham University, Thailand with the budget year of 2015. Gratitude is extended to Computational Electromagnetics and Optical Systems (CEMOS), Faculty of Engineering,

Mahasarakham University, Maha Sarakham, Thailand for the experiments. The authors are grateful to acknowledge Asst. Prof. Ravee Phromlounsri, Udon Thani Rajabhat University, Thailand for his usefulness suggestions.

REFERENCES

- [1] H. Ma, J. Lu, Y. Li, L. Liu, and J. Wang, "Design of a compact wideband balun bandpass filter with high selectivity," *Appl. Comput. Electromagn. Soc. J.*, vol. 31, no. 4, pp. 396-400, Apr. 2016.
- [2] C. Shao, Y. Li, L. Wang, and C. Jin, "Compact wideband parallel-coupled microstrip line bandpass filter with in-line structure," *Appl. Comput. Electromagn. Soc. J.*, vol. 32, no. 2, pp. 153-157, Feb. 2017.
- [3] S. Kim and J. Kim, "Design of reconfigurable antenna feeding network using coupled-line switch for 5G millimeter-wave communication system," *Appl. Comput. Electromagn. Soc. J.*, vol. 33, no. 8, pp. 861-867, Aug. 2018.
- [4] A. Podell, "A high directivity microstrip coupler technique," *IEEE G-MTT 1970 Int. Microwave Symp.*, Newport Beach, CA, pp. 33-36, May 1970.
- [5] D. D. Paolino, "MIC overlay coupler design using spectral domain technique," *IEEE Trans. Microw. Theory Tech.*, vol. 26, no. 9, pp. 646-649, Sep. 1978.
- [6] B. Sheleg and B. E. Spielman, "Broad-band directional couplers using microstrip with dielectric overlays," *IEEE Trans. Microw. Theory Tech.*, vol. 22, no. 12, pp. 1216-1220, Dec. 1974.
- [7] L. Su, T. Itoh, and J. Rivera, "Design of an overlay directional coupler by a full-wave analysis," *IEEE Trans. Microw. Theory Tech.*, vol. 31, no. 12 pp. 1017-1022, Dec. 1983.
- [8] S. Uysal and H. Aghvami, "Synthesis, design, and construction of ultra-wide-band nonuniform quadrature directional couplers in inhomogeneous media," *IEEE Trans. Microw. Theory Tech.*, vol. 37, no. 6, pp. 969-976, June 1989.
- [9] J. L. Klein and K. Chang, "Optimum dielectric overlay thickness for equal even- and odd-mode phase velocities in coupled microstrip circuits," *Electron. Lett.*, vol. 26, no. 5, pp. 274-276, Mar. 1990.
- [10] S. L. March, "Phase velocity compensation in parallel-coupled microstrip," *1982 IEEE MTT-S Int. Microwave Symp. Dig.*, Dallas, TX, pp. 410-412, June 1982.
- [11] G. Schaller, "Optimization of microstrip directional couplers with lumped capacitors," *AEU-Int. J. Electron. C.*, vol. 31, pp. 301-307, July-Aug. 1977.
- [12] M. Dydyk, "Accurate design of microstrip directional couplers with capacitive compensation," *IEEE Int. Dig. on Microwave Symp.*, Dallas, TX,

- pp. 581-584, May 1990.
- [13] D. Kajfez, "Raise coupler directivity with lumped compensation," *Microwaves*, vol. 27, pp. 64-70, Mar. 1978.
- [14] I. J. Bahl, "Capacitively compensated high performance parallel coupled microstrip filters," *IEEE MTT-S Int. Microwave Symp. Dig.*, Long Beach, CA, pp. 679-682, June 1989.
- [15] R. Phromloungsri, M. Chongcheawchamnan, and I. D. Robertson, "Inductively compensated parallel-coupled microstrip lines and their applications," *IEEE Trans. Microw. Theory Tech.*, vol. 54, no. 9, pp. 3571-3582, Sep. 2006.
- [16] R. Phromloungsri, V. Chamnanphrai, and M. Chongcheawchamnan, "Design high-directivity parallel-coupled lines using quadrupled inductive-compensated technique," *2006 Asia-Pacific Microwave Conference*, Yokohama, Japan, pp. 1380-1383, Dec. 2006.
- [17] S. Lee and Y. Lee, "An inductor-loaded microstrip directional coupler for directivity enhancement," *IEEE Microw. Wirel. Compon. Lett.*, vol. 19, no. 6, pp. 362-364, June 2009.
- [18] S. Lee and Y. Lee, "A design method for microstrip directional couplers loaded with shunt inductors for directivity enhancement," *IEEE Trans. Microw. Theory Tech.*, vol. 58, no. 4, pp. 994-1002, Apr. 2010.
- [19] J. Ha, W. Shin, and Y. Lee, "An inductive-loading method for directivity enhancement of microstrip coupled-line couplers," *IEEE Microw. Wirel. Compon. Lett.*, vol. 27, no. 4, pp. 356-358, Apr. 2017.
- [20] H. M. Liu, S. J. Fang, Z. B. Wang, and Y. Zhou, "Miniaturization of trans-directional coupled line couplers using series inductors," *Prog. Electromagn. Res. C.*, vol. 46, pp. 171-177, Jan. 2014.
- [21] D. M. Pozar, *Microwave Engineering*, 4th Edition, Wiley, New York, Nov. 2011.
- [22] Sonnet Lite, ver. 13.51, Sonnet Software, Syracuse, NY, 2019.



Somchat Sonasang was born in Nong Bua Lam Phu Province, Thailand on October, 27, 1982. He received a B.Eng. from Rajamangala University of Technology Isan (RMUTI), Nakhon Ratchasima, Thailand in 2006, and an M.Eng. from Khon Kaen University (KKU), Khon Kaen, Thailand in 2013. He is currently working towards a Ph.D. at Mahasarakham University (MSU), Maha Sarakham, Thailand. His current research interests include microwave circuits and non-destructive tests.



Niwat Angkawisitpan was born in Khon Kaen, Thailand. He received his B.Eng. in Electrical Engineering with honors from Khon Kaen University, Thailand in 1997. He received his M.Sc. in Electrical & Computer Engineering from Purdue University, Indiana, USA in 2003. He received his Ph.D. in Electrical Engineering from University of Massachusetts Lowell, Massachusetts, USA in 2009. Since 2009, he has been with the Research Unit for Computational Electromagnetics and Optical Systems (CEMOS), Faculty of Engineering, Mahasarakham University, Maha Sarakham, Thailand as a Lecturer. He has authored or co-authored several papers in scientific journals and conference proceedings. His research interests include compact microstrip devices, meta-material applications for RF and microwave circuits, and electromagnetic material characterization.

Compact Dual-Passband Three-Dimensional FSS with Good Angular Stability and Both-Side Fast Roll-Off Characteristics

Zhengyong Yu^{1*}, Baozhu Li², Shenggao Ding¹, and Wanchun Tang³

¹ School of Computer and Communication
Jiangsu Vocational College of Electronics and Information, Huai'an, 223003, China
yonglly@sina.com

² Beijing National Research Center for Information Science and Technology (BNRist)
Tsinghua University
libaozhu@tsinghua.edu.cn

³ School of Electrical and Automation Engineering
Nanjing Normal University, Nanjing, 210023, China
ewwctang@nju.edu.cn

Abstract — A compact dual-passband three-dimensional (3D) frequency selective surface (FSS) is proposed based on multiple square coaxial waveguides (SCWs), which exhibits good angular stability and both-side fast roll-off characteristics. The unit cell of the proposed 3D FSS is composed of one parallel plate waveguide (PPW) propagation path and two SCW propagation paths. By etching a centered annular slot, each SCW path forms two identical short SCWs. Each short SCW inherently generates one square slot resonance. In each SCW path, on the account of electromagnetic coupling between two square slot resonators provided by two short SCWs, the square slot resonant mode will split into even-/odd-resonant modes. Accordingly, each SCW path can provide a flat second-order passband with two transmission poles. Due to the reflection and out of phase of electromagnetic waves, four transmission zeros located at both sides of the passbands are introduced for high frequency selectivity, realizing both-side fast roll-off performances. In order to explain the operating principle, the electric-field distributions at transmission-zero/pole frequencies are investigated. Finally, an FSS prototype is fabricated and measured, and the results exhibit good angular stability for both TE and TM polarizations under incident angles from 0° to 60°. In addition, the proposed 3D FSS has a compact unit cell.

Index Terms — Both-side fast roll-off, dual-passband, dual polarizations, Frequency Selective Surface (FSS), three-dimensional (3D).

I. INTRODUCTION

During the past decade, frequency selective surfaces (FSSs) have been widely investigated due to their superior

spatial filtering characteristics for some practical applications [1-4]. To meet the demands of satellite communications, dual-passband FSSs are attracting more and more attention. Dual-passband FSSs are usually realized by using complementary structure [5], convoluted structure [6], and composite structure [7]. However, these first-order dual-band FSSs in [5-7] have limitations of flatness of the passbands due to the lacking of more transmission poles. Two dual-band FSSs with one second-order passband are proposed based on shunted SIW cavity technology in [8] and multilayered cascaded technology in [9], respectively. To further promote the flatness, a dual-band FSS with second-order bandpass responses is achieved by the multi-layered array of sub-wavelength inductive wire grids and capacitive patches [10]. By using circular aperture-coupled patches, another second-order dual-passband FSS is realized in [11]. As an alternative approach, a dual-band bandpass FSS with arbitrary band ratios is designed by using three-dimensional (3D) composite topology composed of an array of three-layer parallel strip lines with inserted metallic rods, as well as two identical single-layer patch arrays [12]. Moreover, a profile, dual-band FSS with two third-order passbands is designed in [13]. Nevertheless, these FSSs in [10-13] without any transmission zeros (TZs) suffer from slow roll-off out of the passbands, resulting in poor frequency selectivity. To overcome such a limitation, a dual-band FSS with three transmission zeros is presented by utilizing a hybrid structure of double square loop slots and substrate integrated waveguide cavities, which exhibits higher frequency selectivity and passband insensitivity to the incident angles and polarizations [14]. In [15], a dual-band FSS with close band spacing is proposed by cascading a two-

layer periodic array, two transmission zeros at upper side of each passband are introduced for high frequency selectivity. With the aid of the couplings between the back-to-back annular ring resonators, a dual-band FSS with quasi-elliptic bandpass responses is realized in [16]. Unfortunately, these FSSs in [14-16] have large electrical size, leading to poor angular stability. In [17], we present a dual-passband 3D FSS with high selectivity and small band ratio based on the combination of an air-filled square waveguide and a cuboid dielectric block with double square loops, achieving good angular stability and small electrical size. However, there are no transmission zeros at the left side of the lower passbands in [14-17]. Furthermore, a via-based dual-passband 2.5D FSS is realized in virtue of electromagnetic coupling in [18], three transmission zeros are located at both sides of two passbands, exhibiting both-side fast roll-off performances, but it only operates under single polarization. Consequently, there is still a challenge for the dual-passband FSS design to achieve flat passbands, both-side fast roll-off characteristics, good angular stability, dual polarizations, and compact electrical size simultaneously.

In this paper, a compact dual-passband 3D FSS with good angular stability and both-side fast roll-off characteristics is proposed based on multiple square coaxial waveguides (SCWs). The electric-field distributions at transmission-zero/pole frequencies are analyzed for better explaining the operating principle. Finally, an FSS prototype is fabricated and measured, and its experimental results are well coincided with simulated ones.

II. UNIT CELL DESIGN AND SIMULATION

Figure 1 (a) gives the perspective view of the proposed 3D FSS, whose unit cell consists of two SCW propagation paths and one parallel plate waveguide (PPW) propagation path. These two SCW paths, namely, path 1 and path 2, are filled with dielectric 1. By etching two centered annular slots on the inner and middle tubes, each SCW path forms two identical short SCWs. The PPW path (i.e., path 3) is supported by two adjacent outer tubes combined with dielectric 2. The relative dielectric constants of the dielectric 1 and dielectric 2 are expressed as ϵ_{r1} and ϵ_{r2} , respectively. The detailed geometry is shown in Figs. 1 (b) and (c). The period and thickness of the unit cell are denoted by p and t , respectively. The parameters a , b and c represent side lengths of three tubes. The parameters s_1 and s_2 are the widths of two centered annular slots.

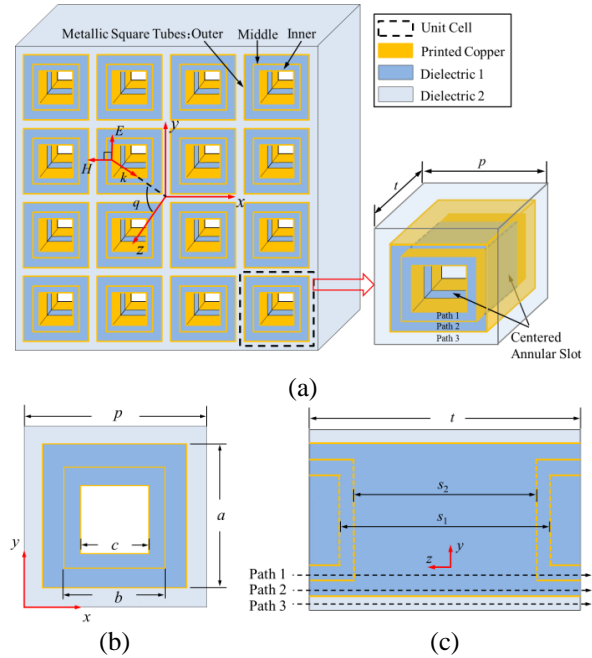


Fig. 1. Unit cell of the proposed 3D FSS: (a) perspective view, (b) top view, and (c) side view.

Figure 2 provides the simulated transmission and reflection coefficients of the presented 3D FSS by full-wave simulator HFSS. The design parameters of the proposed 3D FSS are listed in Table 1. It is observed that two flat second-order passbands are obtained around f_1 (3.55 GHz) and f_2 (5.145 GHz). In the lower band, two transmission poles are realized at f_{p1} (3.53 GHz) and f_{p2} (3.6 GHz). In the higher band, the other two transmission poles are produced at f_{p3} (5.08 GHz) and f_{p4} (5.19 GHz). Moreover, four transmission zeros at f_{z1} (3.11 GHz), f_{z2} (3.82 GHz), f_{z3} (4.65 GHz) and f_{z4} (5.82 GHz), are located at both sides of the passbands, resulting in both-side fast roll-off characteristics. As expected, its frequency selectivity is greatly improved. The 3dB bandwidths of the lower and higher bands are 0.24 GHz (3.43–3.67 GHz) and 0.41 GHz (4.94–5.35 GHz), and corresponding fractional bandwidths are 6.76% and 7.97%, respectively.

Table 1: Design parameters of the proposed 3D FSS

| p | a | b | c |
|-------|-------|--------|--------------------------------|
| 12 mm | 11 mm | 8 mm | 6 mm |
| t | s_1 | s_2 | $\epsilon_{r1}, \epsilon_{r2}$ |
| 11 mm | 8 mm | 7.4 mm | 7.5, 2.2 |

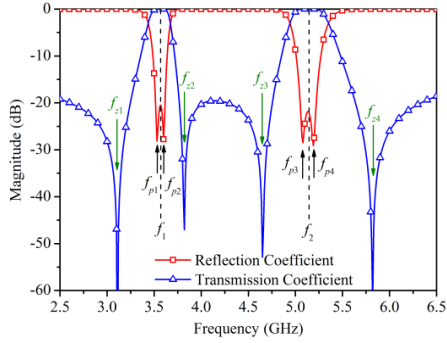


Fig. 2. Simulated transmission and reflection coefficients of the proposed 3D FSS.

III. OPERATING PRINCIPLE

Figure 3 gives the electric-field distributions at four transmission-pole frequencies. As shown in Fig. 3 (a), when the electromagnetic waves strike upon the proposed 3D FSS, the path 2 is mainly excited. From the top view, the electric-field vectors at f_{p1} are basically concentrated upon the square slots on external end-faces of the two short SCWs in path 2. From the side view, as it can be observed that the electric-field vectors reach largest value in two short SCWs in path 2, whereas the other areas become very weak, and the direction of the electric-field vectors keeps unchanged along the z -axis. As a result, f_{p1} is provided by even-resonant mode between two square slot resonators in two short SCWs, and the center location of the path 2 is equivalent to an ideal magnetic wall. At f_{p2} , the path 2 is also excited, as illustrated in Fig. 3 (b). The electric-field vectors with the same magnitude and opposite direction are distributed in two short SCWs in path 2, which reveals f_{p2} is produced by odd-resonant mode between two square slot resonators in two short SCWs, and the center location of the path 2 can be considered as an ideal electric wall. Similarly, it can be seen from Figs. 3 (c) and (d) that f_{p3} and f_{p4} are generated by even- and odd-resonant modes in path 1, respectively.

Figure 4 shows the electric-field distributions at four transmission-zero frequencies. In Fig. 4 (a), it is worth noticing that the path 2 under even-resonant mode and path 3 are excited simultaneously. The electromagnetic waves are reflected at the end of the short SCW in path 2 because of the open-end discontinuity. Additionally, the electric-field vectors in path 2 and path 3 have opposite directions at the output ports, where the electric-field vectors are combined out of phase, leading to generate one transmission zero at f_{z1} . Figure 4 (b) shows that the path 1 and path 2 under odd-resonant modes are excited at the same time. The electromagnetic waves are also reflected in path 2, and the electric-field vectors in path 1 and path 2 are combined out of phase, which provides

the other transmission zero at f_{z2} . Figures 4 (c) and (d) show the generation mechanism of the transmission zeros f_{z3} and f_{z4} respectively. The electromagnetic waves are reflected at the end of the short SCW in path 1, and the directions of electric-field vectors in path 1 and path 3 are opposite at the output ports, which contributes to the transmission zeros f_{z3} and f_{z4} .

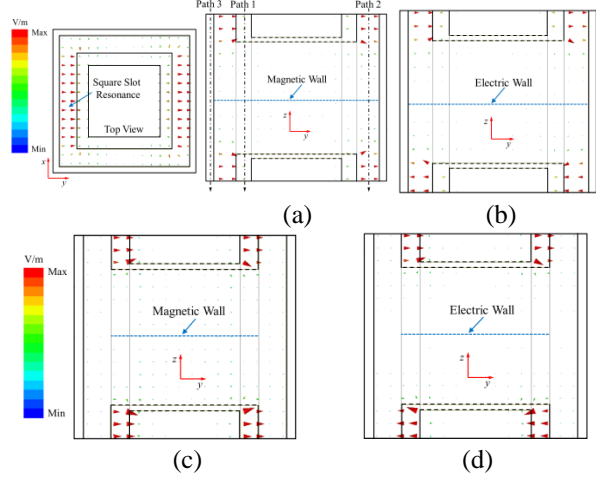


Fig. 3. Electric-field distributions at four transmission-pole frequencies: (a) f_{p1} , (b) f_{p2} , (c) f_{p3} , and (d) f_{p4} .

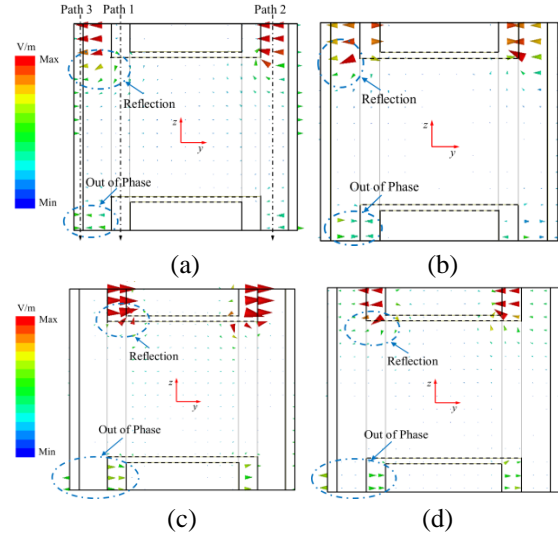


Fig. 4. Electric-field distributions at four transmission-zero frequencies: (a) f_{z1} , (b) f_{z2} , (c) f_{z3} , and (d) f_{z4} .

IV. FABRICATION AND MEASUREMENT

The fabricated FSS prototype is composed of five kinds of the building parts, as shown in Fig. 5 (a). The building part A is one piece of double sided board made of F4B material with relative permittivity of 2.2, loss tangent of 0.001 and thickness of 1.0 mm, in which 17 opening slots cut half way along the board are periodically

created. The building parts B_1 and B_2 are two types of single sided boards, which are made of TP-2 composite material ($\epsilon_r=7.5$, $\tan\delta=0.003$) with a thickness of 1.5 mm. Similarly, the building parts C_1 and C_2 are also single sided boards made of TP-2 composite material ($\epsilon_r=7.5$, $\tan\delta=0.003$) with a thickness of 1.0 mm. Each building part is manufactured by using printed circuit board technology. In Fig. 5 (b), for assembly, firstly, the pieces (part A) are cross-joined together through the opening slots to construct a frame, which achieves path 3. Subsequently, the pieces (parts B_1 and B_2) are inserted into the frame, one by one, for forming path 2. The same operation is carried out for parts C_1 and C_2 to construct path 1. Additionally, the junctions of the printed coppers are covered by conductive silver pulp for good electrical contact. Finally, the size of the fabricated 3D FSS is 213 mm \times 213 mm with 16 \times 16 (256) unit cells, as displayed in Fig. 5 (c). The electrical size of the unit cell ($p \times p \times t$) is as compact as $0.14\lambda_0 \times 0.14\lambda_0 \times 0.13\lambda_0$, where λ_0 denotes the free-space wavelength at f_1 . The free-space method is applied to obtain the frequency response of the proposed 3D FSS, and its measurement setup contains two horn antennas (from 1 to 18 GHz), one FSS prototype, one vector network analyzer, as well as one rotatable screen covered by absorbers. The FSS prototype is placed within the rectangular through-hole window in the center of the rotatable screen for the measurement of incident stability. Two horn antennas connected by the vector network analyzer are located about 1.2 m apart from each side of the centered rotatable screen. In addition, the measurement setup is surrounded by using the absorbing screens. TE or TM polarization wave is obtained when the long side of the two horn antennas is parallel or perpendicular to the ground in our measurement setup. For the transmission coefficients measurement, the propagation loss is firstly eliminated by the normalization of the measured results without the FSS, and the environment noise is eliminated by the measured results of an identically sized metallic plate. Furthermore, for considering the multipath effects, the time-domain gating function of the vector network analyzer is applied to calibrate the measured results.

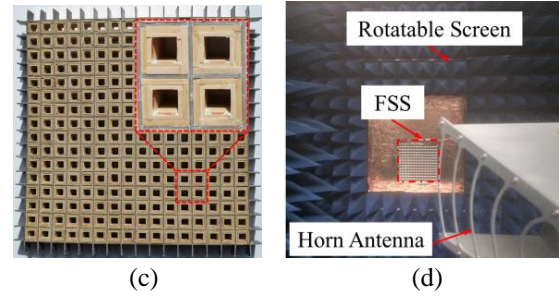
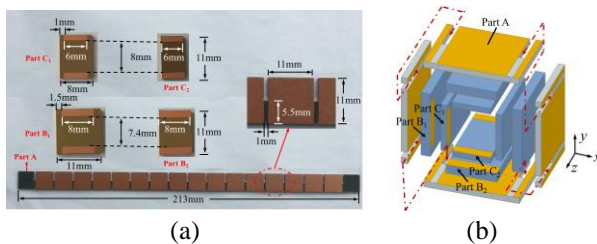
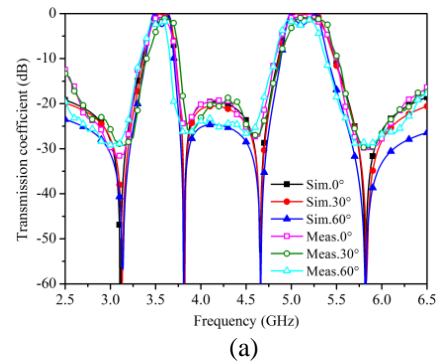


Fig. 5. Fabrication and measurement of the proposed 3D FSS. (a) Building parts and dimensions, (b) assembly process, (c) FSS prototype, and (d) measurement setup.

The measured results under different incident angles and polarizations are depicted in Fig. 6 compared with the simulated ones. It is clear that the transmission coefficients keep very stable versus variable incident angles up to 60° for transverse electric (TE) and transverse magnetic (TM) polarizations. The measured insertion losses within passbands gradually become larger as the incident angle increases, because of the variations of wave impedances for the incident waves. The measured insertion losses at the center frequency of the lower and higher bands are 0.8 and 1.0 dB under the normal incidence, respectively, which are larger than the simulated ones. It results from the conductor losses unconsidered in the simulated model. The other discrepancies between the measurement and simulation result from fabrication tolerance, assembly tolerance and measurement error. However, the measured results have demonstrated the desired performances of the proposed 3D FSS. Table 2 shows the comparison between the presented FSS and recently published researches with similar performances. Obviously, the proposed 3D FSS has an overwhelming advantage in flat passbands, both-side fast roll-off characteristics, good angular stability, dual polarizations, and compact unit cell.



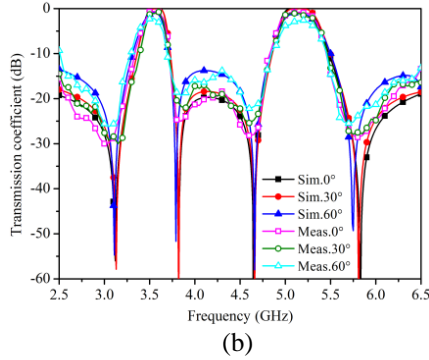


Fig. 6. Measured and simulated results of the proposed 3D FSS. (a) TE polarization. (b) TM polarization.

Table 2: Comparison of the FSS designs with similar responses

| Ref. | Unit Cell Size and Thickness | TZs Num. | Polarization | Angular Stability (TE/TM) |
|------------------|---|----------|--------------|---------------------------------------|
| [10] | $0.094\lambda_0 \times 0.094\lambda_0 \times 0.23\lambda_0$ | 0 | Dual | $45^\circ/45^\circ$ |
| [11] | $0.495\lambda_0 \times 0.495\lambda_0 \times 0.05\lambda_0$ | 0 | Dual | $30^\circ/30^\circ$ (only sim.) |
| [12] | $0.07\lambda_0 \times 0.055\lambda_0 \times 0.09\lambda_0$ | 0 | Single | 40° |
| [14] | $0.49\lambda_0 \times 0.49\lambda_0 \times 0.032\lambda_0$ | 3 | Dual | $30^\circ/30^\circ$ |
| [15] | $0.37\lambda_0 \times 0.37\lambda_0 \times 0.22\lambda_0$ | 4 | Dual | $45^\circ/45^\circ$ |
| [16] | $0.38\lambda_0 \times 0.38\lambda_0 \times 0.135\lambda_0$ | 4 | Dual | $30^\circ/30^\circ$ |
| [17] | $0.188\lambda_0 \times 0.188\lambda_0 \times 0.094\lambda_0$ | 4 | Dual | $60^\circ/60^\circ$ |
| [18] | $0.27\lambda_0 \times 0.096\lambda_0 \times 0.03\lambda_0$ | 3 | Single | 60° (only sim.) |
| This work | $0.14\lambda_0 \times 0.14\lambda_0 \times 0.13\lambda_0$ | 4 | Dual | $60^\circ/60^\circ$ |

V. CONCLUSION

A compact, dual-polarized, dual-passband 3D FSS, exhibiting good angular stability and both-side fast roll-off characteristics, has been presented based on multiple SCWs. Thanks to the electromagnetic coupling between two square slot resonators provided by two short SCWs in the SCW path, each SCW path can provide a flat second-order passband. Four transmission zeros are introduced for realizing both-side fast roll-off performances with the aid of the reflection and out of phase of electromagnetic waves. For explaining the operating principle of the proposed 3D FSS, the electric-field distributions at the frequencies of the transmission zeros/poles are investigated. Finally, an FSS prototype is fabricated and measured. The consistency between measurement and simulation validates our design.

ACKNOWLEDGMENT

This work was supported by Doctor Studio Project, Qing Lan Project, RF Integrated Circuits and Systems Innovation Team (No. JSEIYC2020002), Natural Science Foundation of the Jiangsu Higher Education Institutions of China (No. 19KJB510002), “333 Project” Research Funding Project of Jiangsu Province (No. BRA2018315), National Natural Science Foundation of China (No. 61571232) and Huai’an Innovation Service Capacity Construction Project (HAP201904).

REFERENCES

- [1] B. A. Munk, *Frequency Selective Surfaces: Theory and Design*. New York, NY, USA: Wiley, 2000.
- [2] M. Y. Wang, L. Zhao, J. Wang, X. H. Liang, S. J. Zhang, Y. S. Li, and W. H. Yu, “A low-profile miniaturized frequency selective surface with insensitive polarization,” *Applied Computational Electromagnetics Society Journal*, vol. 33, no. 9, pp. 1003-1008, 2018.
- [3] M. Idrees, S. Buzdar, S. Khalid, and M. A. Khalid, “A miniaturized polarization independent frequency selective surface with stepped profile for shielding applications,” *Applied Computational Electromagnetics Society Journal*, vol. 31, no. 5, pp. 531-536, 2016.
- [4] W. X. Li, C. M. Wang, Y. Zhang, and Y. S. Li, “A miniaturized frequency selective surface based on square loop aperture element,” *International journal of antennas and propagation*, vol. 2014, article ID 701279, 2014.
- [5] X. Hu, X. Zhou, L. Wu, L. Zhou, and W. Yin, “A miniaturized dual-band frequency selective surface (FSS) with closed loop and its complementary pattern,” *IEEE Antennas Wireless Propag. Lett.*, vol. 8, pp. 1374-1377, 2009.
- [6] P. Zhao, Z. Zong, W. Wu, and D. Fang, “A convoluted structure for miniaturized frequency selective surface and its equivalent circuit for optimization design,” *IEEE Trans. Antennas Propag.*, vol. 64, no. 7, pp. 2963-2970, 2016.
- [7] S. Yadav, C. P. Jain, and M. M. Sharma, “Polarization independent dual-bandpass frequency selective surface for Wi-Max applications,” *Int. J. RF Microw. Comput. Aided Eng.*, vol. 28, no. 6, pp. e21278, 2018.
- [8] V. Krushna Kanth and S. Raghavan, “Dual-band frequency selective surface based on shunted SIW cavity technology,” *IEEE Microwave and Wireless Components Letters*, vol. 30, no. 3, pp. 245-248, 2020.
- [9] A. Chatterjee and S. K. Parui, “A triple-layer dual-bandpass frequency selective surface of third order response with equivalent circuit analysis,” *Int. J. RF Microw. Comput. Aided Eng.*, vol. 30, no. 2, pp. e22047, 2020.
- [10] M. Gao, S. M. A. M. H. Abadi, and N. Behdad,

“A dual-band, inductively coupled miniaturized-element frequency selective surface with higher order bandpass response,” *IEEE Trans. Antennas Propag.*, vol. 64, no. 8, pp. 3729-3734, 2016.

- [11] H. Zhou, S. B. Qu, B. Q. Lin, J. Q. Zhang, C. Gu, H. Ma, Z. Xu, P. Bai, and W. D. peng, “Dual band frequency selective surface based on circular aperture-coupled patches,” *Microw. Opt. Technol. Lett.*, vol. 53, no. 8, pp. 1784-1786, 2011.
- [12] B. Li and Z. Shen, “Dual-band bandpass frequency-selective structures with arbitrary band ratios,” *IEEE Trans. Antennas Propag.*, vol. 62, no. 11, pp. 5504-5512, 2014.
- [13] G. Xu, G. V. Eleftheriades, and S. V. Hum, “Generalized synthesis technique for high-order low-profile dual-band frequency selective surfaces,” *IEEE Trans. Antennas Propag.*, vol. 66, no. 11, pp. 6033-6042, 2018.
- [14] G. Q. Luo, W. Hong, H. J. Tang, J. X. Chen, and K. Wu, “Dualband frequency-selective surfaces using substrate-integrated waveguide technology,” *IET Microw. Antennas Propag.*, vol. 1, no. 2, pp. 408-413, 2007.
- [15] M. B. Yan, J. F. Wang, S. B. Qu, M. D. Feng, Z. Q. Li, H. Y. Chen, J. Q. Zhang, and L. Zheng, “Highly-selective, closely-spaced, dual-band FSS with second-order characteristic,” *IET Microw. Antennas Propag.*, vol. 10, no. 10, pp. 1087-1091, 2016.
- [16] B. Zhang, C. Jin, X. Ye, and R. Mittra, “Dual-band dual-polarized quasi-elliptic frequency selective surfaces,” *IEEE Antennas Wireless Propag. Lett.*, vol. 18, no. 2, pp. 298-302, 2019.
- [17] Z. Yu, X. Yang, J. Zhu, C. Wang, Y. Shi, and W. Tang, “Dual-band three-dimensional FSS with high selectivity and small band ratio,” *Electron. Lett.*, vol. 55, no. 14, pp. 798-799, 2019.
- [18] S. Yang, Q. Chen, J. Bai, and Y. Fu, “Design of ultra-thin closely spaced dual-band bandpass frequency selective surface,” *Electron. Lett.*, vol. 53, no. 24, pp. 1583-1585, 2017.



Zhengyong Yu was born in Huaian, China, in 1982. He received the B.S. degree from the Huaiyin Institute of Technology, Huaian, China, in 2006, the M.S. degree from the Nanjing University of Science and Technology, Nanjing, China, in 2008, and the Ph.D. degree from Nanjing

Normal University, in 2020.

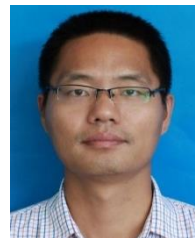
He is currently an Associate Professor and Senior Engineer in Jiangsu Vocational College of Electronics and Information. He is Jiangsu Province 333 project personnel training object, and Jiangsu Province Qing Lan Project Academic Leader. His current research

interests include fundamental electromagnetic theory, frequency selective surfaces and near-field antennas.



Baozhu Li was born in Henan Province, China, in 1990. She received the B.S. degree in Electrical Engineering from Nanjing Normal University Zhongbei College, Nanjing, in 2013, and the Ph.D. degree in Physical Electronics from School of Physics and Technology, Nanjing Normal University, in 2020. She was a Visiting Ph.D. Student funded by Scholarship Council in ELEDIA Research Center at University of Trento, Italy, from Sep. 2018 to Jan. 2020.

She is currently a Postdoctoral Researcher in Beijing National Research Center for Information Science and Technology at Tsinghua University and an Associate Faculty Member of the ELEDIA Research Center. Her research interests include electromagnetic environment and inverse propagation problems.



Shenggao Ding was born in Huaian, China, in 1980. He received the B.S. degree from the North China Electric Power University, Baoding, China, in 2002, the M.S. degree from the Nanjing University of Posts and Telecommunications, Nanjing, China, in 2006. He was a Visiting

Scholar with the University of South Carolina, Columbia, USA, from 2019 to 2020.

He is currently a Lecturer in Jiangsu Vocational College of Electronics and Information. His current research interests include RF and Microwave Components/Circuits for Wireless Communications, 5G Mobile Antennas and Internet of Things.



Wanchun Tang was born in China in 1967. He received the B.S. degree from Tsinghua University, Beijing, China, in 1990, the M.S. degree from the Nanjing University of Science and Technology, Nanjing, China, in 1995, and the Ph.D. degree from the City University of Hong Kong, Hong Kong, in 2003, all in Electrical Engineering.

He was a Full Professor with the Department of Communication Engineering, NJUST, and is currently a Specially Invited Full Professor with the Jiangsu Key Laboratory on Optoelectronic Technology, School of Physics and Technology, Nanjing Normal University, Nanjing. He has authored or coauthored over 100 journal and conference papers. His current research interests include modeling and optimization of RFIC, antennas, signal integrity, and power integrity design in package.

Development and Verification of Indirect Lightning-Induced Transient Protection Circuit for Avionics System

Sung-Yeon Kim, Jeong-Su Park, and Wang-Sang Lee*

Department of Electronic Engineering, Gyeongsang National University (GNU)
501, Jinju-daero, Jinju, Gyeongnam, 52828, Republic of Korea

*wsang@gnu.ac.kr

Abstract — In this paper, an indirect lightning-induced transient protection circuit for avionics system is proposed, and its effectiveness is verified. The proposed circuit consists of a metal oxide varistor (MOV), a transient voltage suppression (TVS) diode, and a resistor. Compared with the conventional circuits (MOV or TVS diode), the improved noise suppression of the proposed circuit against indirect lightning strikes are experimentally verified in accordance with radio technical commission for aeronautics (RTCA) DO-160G Sec. 22. The highest attenuation levels of indirect lightning strike WF5A reference voltage and current signals are approximately 91.0% and approximately 98.4% for the input lightning signals, respectively.

Index Terms — Indirect lightning, lightning induced transient, lightning protection, pin injection test, RTCA DO-160G Sec. 22

I. INTRODUCTION

Surge voltages derived from direct lightning strikes cause malfunction or damage to the electronic equipment in aircrafts; this phenomenon is referred to as the indirect effects of direct lightning strikes. The lightning indirect effects are caused by the currents induced by lightning strikes on avionics as well as damage to the aircraft due to direct lightning strikes. There is an increase in the use of miniaturized, solid-state components in aircraft electronics and electric power systems [1],[2]. Moreover, modern aircrafts are increasingly constructed from composite materials, in particular, carbon-fiber composites in place of metal skins, a practice that reduces the electromagnetic shielding previously furnished by the conductive skin as a by-product [3-7]. The application of protection design for indirect lightning strikes on avionics is becoming more important. To establish aircraft airworthiness from lightning-induced effects, the standards and guidelines such as RTCA DO-160G & SAE ARP 5415A and EUROCAE ED-14G are widely used [8]. RTCA DO-160G airworthiness certification standard for civil aviation aircraft defines the need for flight and safety essential

equipment, emphasizing the need for induced lightning protection of aviation electronic equipment. According to this standard, flight essential equipment must verify that the system meets the requirements for lightning protection and electromagnetic environment requirements including it.

This study was conducted based on RTCA DO-160G Sec. 22. The standard is used by the Federal Aviation Administration (FAA) and defines lightning-induced transient susceptibility aircraft test specifications. Lightning-induced transient sets the test standard considering the installation location of the electronic device and the interlocking concept. RTCA DO-160G Sec. 22 consists of pin injection tests and cable bundle tests. The simplified test setup of RTCA DO-160G Sec. 22 pin injection test is shown in Fig. 1.

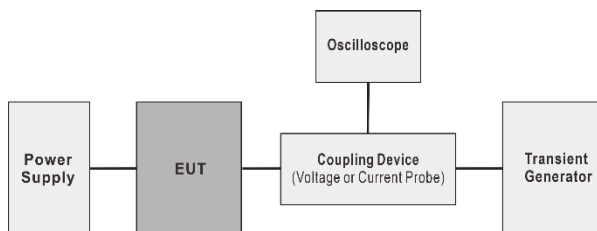


Fig. 1. Simplified test setup of RTCA DO-160G Sec. 22 pin injection test [8].

Table 1. Pin injection test level [9]

| Peak Level | Test Waveform No. | |
|---------------------|-------------------|-------------------|
| | WF3 | WF5A |
| V_{oc} / I_{sc}^* | V_{oc} / I_{sc} | V_{oc} / I_{sc} |
| 1 | 100/4 | 50/50 |
| 2 | 250/10 | 125/125 |
| 3 | 600/24 | 300/300 |
| 4 | 1500/60 | 750/750 |
| 5 | 3200/128 | 1600/1600 |

* V_{oc} : Peak open circuit voltage (Unit: V), I_{sc} : Peak short circuit current (Unit: A).

Table 1 shows the pin injection test level. Pin injection tests level criteria are divided into levels 1 to 5 depending on the installation environment of the equipment. Level 3 applies to equipment and interconnect wiring mounted in environments such as electromagnetically open areas (control rooms) of aircraft, which are made primarily of metal [9]. This study considers the installation and configuration of aviation electronics and applies pin injection tests, Category B (WF3 and WF5A). The WF3 and WF5A voltage/current of RTCA DO-160G Sec. 22 are shown in Fig. 2. Level 3 is the most in demand in aviation electronics development companies.

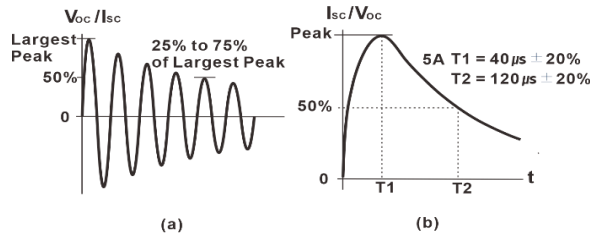


Fig. 2. Voltage/Current waveform of RTCA DO-160G Sec.22: (a)WF3 and (b) WF5A.

II. INDIRECT LIGHTNING PROTECTION CIRCUIT DESIGN

Indirect lightning transient protection and clamping on avionics include series resistors, metal oxide varistors (MOV), gas discharge tubes (GDT), transient voltage suppression (TVS) diodes, and a trace width. The MOV, GDT, and TVS diodes which can be easy to apply to aviation electronics are highly effective for transient suppression without major design changes [10].

Table 2. Comparison of typical MOV, TVS diode, and the proposed circuit

| Item | MOV | TVS Diode | Proposed Circuit |
|--------------------------|----------------------------|-----------------------------------|---------------------------------|
| Energy capability | High (Hundreds of joules) | Low (Number of joules) | Very high (Hundreds of joules) |
| Surge current capability | High (Hundreds of amperes) | Low to moderate (Tens of amperes) | Very high (Hundreds of amperes) |
| Response time | Slow (ns level) | Fast (ps level) | Fast (ps level) |
| Clamping voltage | High (Hundreds of volts) | Low (Tens of volts) | Low (Tens of volts) |
| Lifespan | Long (Thousands of times) | Intermediate (Hundreds of times) | Very long (Thousands of times) |

Table 2 shows the characteristics of MOV, TVS diode, and proposed circuit. The TVS diode can suppress and protect external instantaneous stress input through external pins by the protection circuit of the input terminal. It can be applied in both directions. The characteristic of the TVS diode can be clamped at lower voltages, low capacitance, low leakage current, and fast response time. However, it is required to use the clamping voltage precisely and is suitable for sensitive circuit parts due to the high price. The peak clamping voltage of the MOV is higher than the TVS diodes. It has greater tolerance for high energy temperatures, long-term life, competitive price (on average, 10 times cheaper than TVS diode), higher capacitance, and bidirectional components. In addition, it can control high currents. Voltage and current characteristics are symmetrical (DC and AC circuits can be applied). However, it is not suitable for sensitive circuits as a high priority. The proposed indirect lightning protection circuit (ILPC) uses the characteristics of the MOV, TVS diode, and series resistor electronic components to create synergy effects. The ILPC is shown in Fig. 3 aiming to maximize benefits and overcome the disadvantages of the individual part. The proposed protection circuit has the structure of first clamping through MOV that withstands a few large surges. A series resistor (R) reduces a residual noise, a shorter-pulse noise, and control current. The value of R was set to 2Ω and tested due to the impedances (25Ω or 1Ω) of the waveforms (WF3 or WF5A). Third clamping is performed through a TVS diode and controls small surges. By using the proposed ILPC, the incoming current noise can be distributed and the lightning long-term stable protection becomes possible [11].

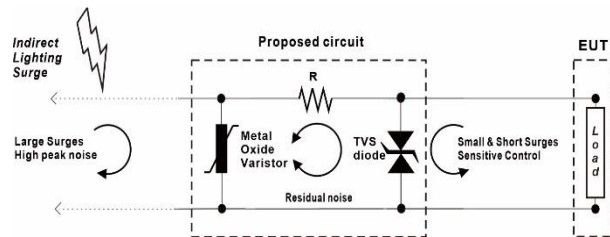


Fig. 3. Proposed indirect lightning protection circuit.

Based on the 28 V power of avionics, the TVS diode applied indirect lightning protection measures applied in positive and negative polarities. Considering the voltage conditions of MIL-STD-704F, a TVS diode with a maximum clamping voltage of ± 50 V and higher was selected. The device chosen was 30KPA43CA made by Littelfuse [12],[13] and a maximum clamping voltage (V_C) of 73 V was selected [12]. The allowable peak pulse current (I_{PP} @ WF3 or WF5A) at WF3 or WF5A is calculated using:

$$I_{PP@WF3 \text{ or } WF5A} = \frac{V_{OC} - V_C}{Z_S}, \quad (1)$$

where Z_S is an impedance that can obtain the ratio of V_{OC} and I_{SC} , V_{OC} is a peak open circuit voltage, and V_C is a maximum clamping voltage. The maximum peak pulse currents ($I_{PP@WF3 \text{ or } WF5A}$) at WF3 and WF5A are approximately 21.1 A and 227 A, respectively. The peak pulse current ($I_{PP@TVS}$) at TVS diode is calculated using:

$$I_{PP@TVS} = \frac{P_{PP@T_P}}{P_{PP@10/1000\mu s}} \times I_{PP}, \quad (2)$$

where P_{PP} is a peak pulse power at TVS diode and I_{PP} is a maximum peak pulse current at a datasheet. The allowable current of TVS diode at WF3 and WF5A can obtain approximately 5120 A and 1107 A, respectively. Therefore, the used TVS diode has an enough margin for WF3 and WF5A. It was confirmed that the indirect lightning input current applied to the signal line during the indirect lightning test can be applied within the maximum current of the TVS diode. In case of the MOV circuit application, the MOV can handle the peak pulse current. The peak pulse current is the maximum current at which the MOV voltage does not change by more than 10% [14][15]. The MOV operating DC voltage $V_{M(AC)}$ should be selected to be higher than the maximum allowable DC voltage operating circuit voltage. The ILPC design clamping MOV should be higher than 30.8 V (28 V power of avionics + 10%) and a maximum clamping voltage of over 50 V. The clamping voltage is over 50 V but higher than the TVS diode clamping voltage. This is because MOV is more resistant to indirect lightning strikes than the TVS diode. The maximum current (I_{Surge}) flowing in the MOV during the surge is lower than the indirect lightning surge current (I_{ILS}) [14]. I_{Surge} is calculated using:

$$I_{Surge} = \frac{V_{OC} + V_O(1+10\%) - V_C}{R}, \quad (3)$$

where R is a value of resistor (2 Ω). The maximum current ($I_{Surge@WF3 \text{ or } WF5A}$) at WF3 and WF5A are approximately 268.9 A and 118.9 A, respectively. Using V20E30AUTO ($V_C = 93V$, $V_{DC} = 34V$, $I_{ILS} = 3000A$) as MOV made by Littelfuse [15], it was confirmed that the indirect lightning input current can be applied within the maximum current of MOV. Before the experimental verification, the simulation was performed using the PSPICE program. The waveforms (WF3 and WF5A) of RTCA DO-160G Sec. 22 were applied to each element (MOV and TVS) and the proposed circuit, and the performance was confirmed and compared in Figs. 4 and 5.

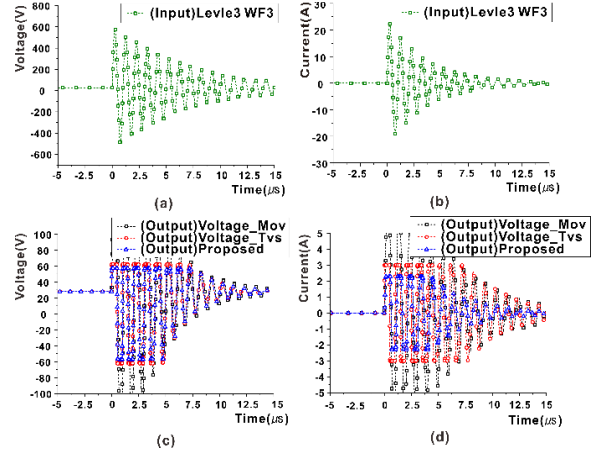


Fig. 4. Simulated comparisons of MOV, TVS diode, and proposed circuits for WF3: (a) and (b) voltage and current WF3, (c) and (d) voltage and current comparisons for WF3, respectively.

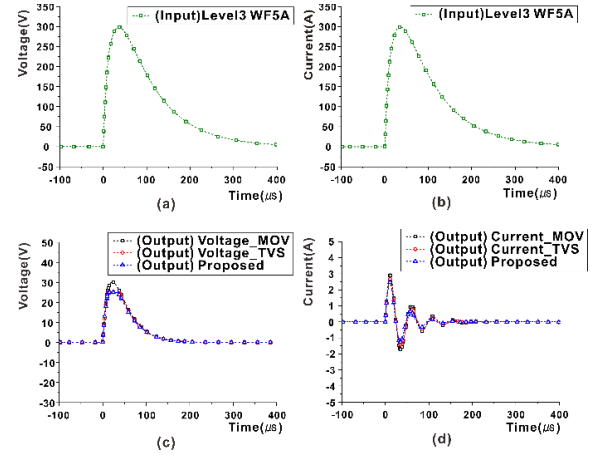


Fig. 5. Simulated comparisons of MOV, TVS diode, and proposed circuits for WF5A: (a) and (b) voltage and current for WF5A, (c) and (d) voltage and current comparisons for WF5A, respectively.

III. RESULTS AND DISCUSSIONS

To experimentally verify the ILPC the proposed circuit, the pin injection test based on RTCA DO-160G Sec. 22 lightning-induced transient susceptibility has been conducted. Pin injection tests are primarily for damage assessment and involve the injection of transients directly into EUT interface circuits [8]. Figure 6 shows the test setup of RTCA DO-160G Sec. 22. The pin injection generators (MIG OS-M and MIG 0600MS by EMC Partner), the injection probe (CN-MIG-BT3 by

EMC partner), the oscilloscope (MSO-X 4154A by Keysight Technologies), the high voltage differential probe (TT-SI9091 by TESTEC), the current clamp probe (Pearson Electronics 3525), and the electric load (PLZ164WA by Kikusui Electric Co.) were used to the test. Waveforms applied to the pin injection test were tested on WF3 and WF5A of level 3. In order to determine the effect of indirect lightning for each of the devices applied by an accredited testing laboratory, a comparative test was conducted by dividing into MOV, TVS diode, and ILPC.

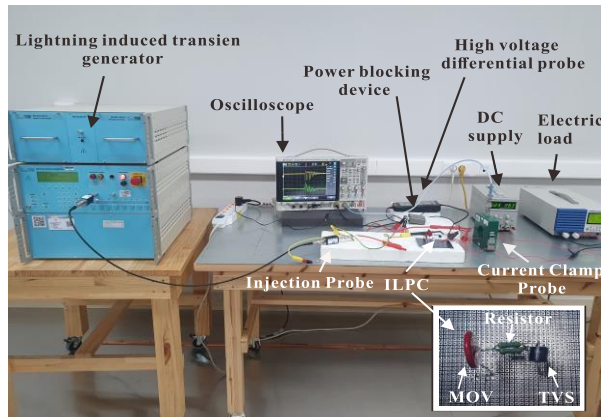


Fig. 6. Proposed indirect lightning protection circuit.

The measured results for WF3 and WF5A are shown in Figs. 7 and 8, respectively. In the WF3 and WF5A tests, it was confirmed that ILPC has the best characteristics of voltage and current reduction. During the test, visual inspection and tolerance items were checked, and no specifics were found. In particular, the characteristics of the indirect lightning filter were confirmed using WF5A, in which a large induced lightning was induced. Table 3 shows the results of pin injection test with regard to WF3 and WF5A by comparison between the MOV, TVS, and the proposed circuits. The calculated measurement uncertainties with 95% confidence level for the pin injection test (voltage and current) in Fig. 6 are 10V and 0.63A, respectively. Compared to the input signals (600 V for WF3 and 300 V for WF5A), the peak voltage of the proposed circuit to which the MOV is applied has attenuation of approximately 74.7% and 87%, and the attenuation of approximately 80.2% and 87.7% when the TVS diode is applied, respectively. The peak current of the circuit to which the MOV is applied has attenuation of approximately 69.2% and 98.2% compared to the input signal (24A for WF3, 300A for WF5A), and approximately

75.4% and 98.2% of attenuation when the TVS diode is applied, respectively. On the other hand, the highest attenuation levels of the proposed circuit in the indirect lightning strike WF5A reference voltage and current signals are approximately 91.0% and approximately 98.4% for the input lightning signals, respectively. As a result, it means that the propose circuit is possible to improve the noise suppression and protect avionics from noised caused by indirect lightning.

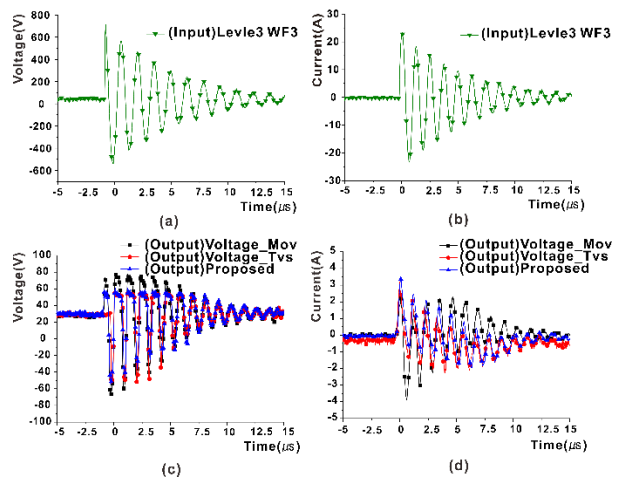


Fig. 7. Measured comparisons of MOV, TVS diode, and proposed circuits for WF3: (a) and (b) voltage and current WF3, (c) and (d) voltage and current comparisons for WF3, respectively.

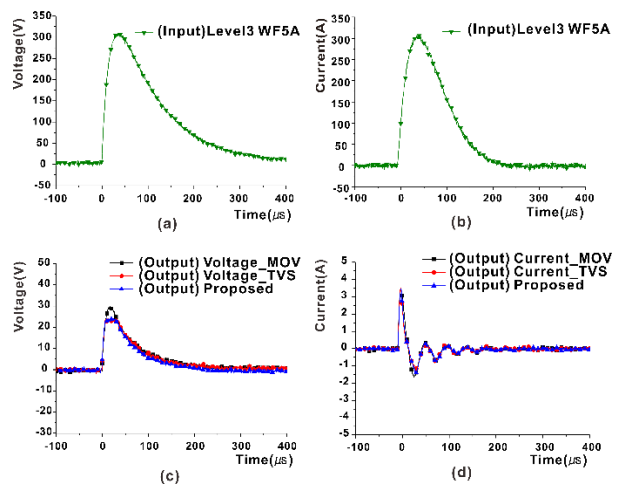


Fig. 8. Measured comparisons of MOV, TVS diode, and proposed circuits for WF5A: (a) and (b) voltage and current for WF5A, (c) and (d) voltage and current comparisons for WF5A, respectively.

Table 3. The results of pin injection test with regard to WF3 and WF5A

| Waveforms | V_{Peak} (U = 10 V, 95% Confidence Level) | | | | I_{Peak} (U = 0.63 A, 95% Confidence Level) | | | |
|-----------|---|-----------|-----------|---------------|---|-----------|-----------|---------------|
| | Input | Reference | | Prop. Circuit | Input | Reference | | Prop. Circuit |
| | | MOV | TVS Diode | | | MOV | TVS Diode | |
| WF3 | 600 V | 152 V | 119 V | 117 V | 24 A | 7.4 A | 5.9 A | 5.4 A |
| | 100% | -74.67% | -80.17% | -80.5% | 100% | -69.17% | -75.42% | -77.50% |
| WF5A | 300 V | 39 V | 37 V | 27 V | 300 A | 5.5 A | 5.3 A | 4.8 A |
| | 100% | -87.00% | -87.67% | -91.00% | 100% | -98.17% | -98.23% | -98.40% |

IV. CONCLUSION

In this paper, we proposed an ILPC for indirect avionics filters. Previously, a large protective device had to be attached to the outside of avionics, but the proposed indirect lightning filter can be modified and changed simply by reducing the size and weight. The RTCA DO-160G Sec. 22 test was conducted according to the verified procedure. As a result of the test, ILPC complies with WF3 and WF5A providing lower clamping voltage and current. Owing to its high resistance to noise from indirect lightning strikes, it can be expected to act as a filter for a very long-term protection circuit. The proposed ILPC can be applied to avionics devices that that the aircraft is powered itself, and it can be applied immediately as a power line indirect lightning protection filter for aviation-mounted electronic devices such as aircraft transceivers, communications, navigation, flight recorder, monitoring, control system, the display and management systems etc. This ILPC is an effective way to prevent indirect lightning strikes of avionics systems.

REFERENCES

- [1] F. A. Fisher and J. A. Plumer, *Lightning Protection of Aircraft*. Washington D.C., USA: NASA, Oct. 1977.
- [2] M. O. Goni, E. Kaneko, and A. Ametani, "Simulation of lightning return stroke currents and its effect to nearby overhead conductor," *Applied Computational Electromagnetics Society Journal*, vol. 24, no. 5, pp. 469-477, Oct. 2009.
- [3] D. Morgan, C. J. Hardwick, S. J. Haigh, and A. J. Meakins, "The interaction of lightning with aircraft and the challenges of lightning testing," *AerospaceLab*, vol. 5, no. 11, pp. 1-10, Dec. 2012.
- [4] C. C. Goodloe, *Lightning protection guidelines for aerospace vehicles, NASA/TM-1999-209734*, Springfield, VA, USA: NASA, pp. 1-48, May 1999.
- [5] M. D'Amore and M. Sabrina Sarto, "Time-domain analysis of lightning interaction to aeronautical structures composite materials," *2017 IEEE EMC Int'l Symp.*, Austin, TX, USA, pp. 397-402, Aug. 1997.
- [6] L. Chemartin, P. Lalande, B. Peyrou, A. Chazottes, and P. Q. Elias, "Direct effects of lightning on aircraft structure: analysis of the thermal, electrical and mechanical constraints," *AerospaceLab*, vol. 5, no. 9, pp. 1-15, Dec. 2012.
- [7] J. P. Parmantier, F. Issac, and V. Gobin, "Indirect effects of lightning on aircraft and rotorcraft," *AerospaceLab*, vol. 5, no. 11, pp. 1-27, Dec. 2012.
- [8] Radio Technical Commission for Aeronautics Inc., *RTCA/DO-160G*, "Environmental conditions and test procedures for airborne equipment, Sec. 22 Lightning induced transient susceptibility", pp. 22-1-22-42, Dec. 2010.
- [9] H. P. Rimal and A. Faba, "Lightning indirect effect protection in avionic environment," *2017 IEEE 3rd Int'l Forum on Research and Technologies for Society and Industry (RTSI)*, Modena, Italy, pp. 1-5, Sep. 2017.
- [10] C. A. McCreary and B. A. Lail, "Lightning transient suppression circuit design for avionics equipment," *2012 IEEE Int'l Symp. on Electromagnetic Compatibility*, Pittsburgh, PA, USA, pp. 93-98, Aug. 2012.
- [11] Y. G. Sim, T. S. Ahn, J. H. Park, J. P. Yang, and S. H. Han, "Development and verification of lightning induced transient protection device for avionics computer," *Journal of Advanced Navigation Technology (JANT)*, vol. 19, no. 5, pp. 395-402, Oct. 2015.
- [12] M. Clark, "Lightning protection for aircraft per RTCA/DO-160D and ARINC 429 protocol," *MicroNote 126*, Microsemi Corporation, Scottsdale, AZ, USA, pp. 1-5, July 2004.
- [13] TVS Diode Axial Leaded – 30000W > 30KPA series datasheet, TVS Diode (30KPA43CA), Littelfuse, Inc., Aug. 2020, Littelfuse [Online]. Available: https://www.littelfuse.com/~media/electronics/datasheets/tvs_diodes/littelfuse_tvs_diode_30kpa_datasheet.pdf
- [14] N. Tsukamoto, and M. Ishii, "Repetitive impulse withstand performance of metal-oxide varistors," *IEEE Trans. on Power Delivery*, vol. 32, no. 4, pp. 1674-1681, Aug. 2017.
- [15] Metal-Oxide Varistors (MOVs) Radial Leaded Varistors > AUMOV Varistor Series, MOV (V20E30AUTO), Littelfuse, Oct. 2019. Available: https://www.littelfuse.com/~media/electronics/datasheets/varistors/littelfuse_aumov_datasheet.pdf



Sung-Yeon Kim received the B.S. degree in Electronic Engineering from Pukyong National University (PKNU), Busan, South Korea, in 2008, received the M.S. degree in Electronic Engineering from Gyeongsang National University (GNU), Jinju, South Korea, 2017, where he is currently pursuing the Ph.D. degree.

His current research interests include electromagnetic interference (EMI)/EMC analysis, Modeling, Measurement, Shielding, RF/Microwave Antenna & Circuit. From 2008 to 2014, he was with the Digital Media Communication Division, Samsung Electronics Co., Ltd (SEC), Suwon-si, South Korea. From 2014, he was with the Electromagnetic Compatibility Avionics Center, Digital Industry Division, Korea Testing Laboratory (KTL), Jinju-si, South Korea.



Jeong-Su Park received the B.S. degree in Electronic Engineering from Gyeongsang National University (GNU), Jinju, South Korea, in 2019, where he is currently pursuing the M.S. degree.

His current research interests include wireless communication systems for UAVs, RF-based energy harvesting, RF/Microwave circuit and system, and RFID/IoT sensors.



Wang-Sang Lee received the B.S. degree from Soongsil University, Seoul, South Korea, in 2004, and the M.S. and Ph.D. degrees in Electrical Engineering from the Korea Advanced Institute of Science and Technology (KAIST), Daejeon, South Korea, in 2006 and 2013, respectively.

From 2006 to 2010, he was with the Electromagnetic Compatibility Technology Center, Digital Industry Division, Korea Testing Laboratory (KTL), Ansan-si, South Korea, where he was involved in the international standardization for radio frequency identification (RFID) and photovoltaic systems as well as electromagnetic interference (EMI)/EMC analysis, modeling, and measurements for information technology devices. In 2013, he joined the Korea Railroad Research Institute (KRRRI), Uiwang-si, South Korea, as a Senior Researcher, where he was involved in the position detection for high-speed railroad systems and microwave heating for low-vibration rapid tunnel excavation system. Since 2014, he has been an Associate Professor with the Department of Electronic Engineering, Gyeongsang Nat'l University (GNU), Jinju, South Korea. From 2018 to 2019, he was a Visiting Scholar with the ATHENA Group, Georgia Institute of Technology, Atlanta, GA, USA. His current research interests include near- and far-field wireless power and data communications systems, RF/microwave antenna, circuit, and system design, RFID/Internet of Things (IoT) sensors, and EMI/EMC.

Lee is a member of IEC/ISO JTC1/SC31, KIEES, IEIE, and KSR. He was a recipient of the Best Paper Award at IEEE RFID in 2013, the Kim Choong-Ki Award—Electrical Engineering Top Research Achievement Award at the Department of Electrical Engineering, KAIST, in 2013, the Best Ph.D. Dissertation Award at the Department of Electrical Engineering, KAIST, in 2014, the Young Researcher Award at KIEES in 2017, and the Best Paper Awards at IEIE in 2018 and KICS in 2019.

Tunable Terahertz Plasmon-Induced Transparency in Resonator-Coupled Dirac Semimetal Waveguides

Daobin Wang, Jiahuan Yang, Wei Wang, Lihua Yuan, and Xiaoxiao Li

Department of Applied Physics
Lanzhou University of Technology, Lanzhou, 730050, China
photonics_wang@yahoo.com

Abstract — The bulk Dirac semimetal (BDS) is an interesting material, similar to graphene, which can dynamically adjust its optical properties via a variation in its Fermi energy or electrical voltage. In this work, a BDS-based plasmonic device, which enables tunable terahertz plasmon-induced transparency, was proposed and designed. By using the finite element method, the surface plasmon polariton and plasmon-induced transparency of this device were systematically investigated. The results demonstrate that the plasmon-induced transparency of such device can be dynamically tuned by varying its Fermi energy. When the Fermi energy changes from 55 meV to 95 meV, the maximum group delay time of the device increases from 13.2 ps to 21 ps. In the case of a cascading device, the maximum group delay time can be further pushed up to 44.57 ps. The influence of the ambient refractive index on the optical properties of the proposed device was also considered and investigated.

Index Terms — Bulk Dirac semimetal, plasmon-induced transparency, surface plasmon polariton, slow light.

I. INTRODUCTION

Plasmon-induced transparency (PIT) is a novel physical phenomenon, which occurs at the interface between a metal and a dielectric material [1]. This phenomenon was first discovered in several atomic media, and it is known as electromagnetically induced transparency (EIT) [2, 3]. Later, it was found that a similar phenomenon can also be observed in photonic crystals [4], metamaterials [5], acoustic devices [6], coupled dielectric resonators [7], and nanodevices based on the surface plasmon polariton (SPP) [8]. The EIT effect that occurs at the interface between a metal and a dielectric material is known as PIT. The mechanism behind the PIT phenomenon and its application in various fields have triggered a strong interest in the scientific community around the world [9, 10].

Precious metals, such as gold, silver, and copper, are usually employed to generate the SPP. However, their refractive index and permittivity cannot be arbitrarily

adjusted. For this reason, the PIT cannot be regulated and cannot meet the needs of dynamic adjustment necessary in several applications. To overcome this issue, researchers gradually turned their attentions to a 2D material, graphene, which is an allotrope of graphite with a thickness of only one atomic layer. Its refractive index and permittivity can be dynamically adjusted by modifying its Fermi energy or voltage [11, 12]. Based on this feature, researchers have proposed and investigated several graphene-based tunable PIT schemes [13-15]. Recently, a material similar to graphene has attracted a large interest in the scientific community. This material is the bulk Dirac semimetal (BDS), also known as the 3D Dirac semimetal. As a three-dimensional analog of graphene, the optical properties of the BDS can also be adjusted via its Fermi energy. However, this material does exhibit a high electron mobility. For example, at the temperature of 5 K, its mobility can reach 9×10^6 cm²/V/s [16], whereas the mobility of graphene measures 2×10^5 cm²/V/s [11]. Several BDS-based SPP and PIT implementation schemes have been proposed and compared with the graphene-based ones [17-22]. Chen et al. designed a metamaterial based on BDS with each unit cell containing an H-shaped structure [17]. The two side strips of the H-shaped structure serve as the dark SPP modes, whereas the central one serves as the bright SPP mode. The interplay between the bright and dark modes is at the basis of the PIT phenomenon. Chen et al. extended this scheme to include two H-shaped structures per unit cell [18]. Differently from Ref. [17], the authors of Ref. [19] used the interplay between two bright modes to achieve the PIT in BDS. The unit cell of such structure consists of two BDS blocks with different sizes. Each block acts as a bright SPP mode. The weak hybridization between them generates the tunable PIT effect in the BDS material. A simpler BDS-based PIT system was proposed and investigated in Ref. [20]. Zhao et al. [21] introduced a BDS-based metamaterial able to achieve a tunable multiple PIT effect. Such metamaterial used a slightly more complex unit cell with four different BDS rods on a dielectric substrate. According to the electric field distributions provided in Ref. [21], the generation

of the multiple PIT effect was originated from the introduction of the bonding mode between the different rods in addition to the bright-bright mode coupling. Wang et al. described a terahertz metamaterial structure [22] with a fourfold symmetry unit cell. They found that the PIT effect being not sensitive to polarization can be achieved by using BDS. Unfortunately, the aforementioned solutions are all based on three-dimensional structures, which are not suitable to develop 2D planar BDS waveguide devices. Recently, Zhai and her collaborators proposed and verified an interesting 2D SPP device based on the BDS material [23]. The basic components of this waveguide device are a side-coupled T-shaped cavity. They found that PIT effect on terahertz band can be achieved in such plasmonic system by introducing a position offset. However, the maximum group delay time that this device can provide is only 11.001 ps.

Due to their different refractive index, many methods developed to achieve PIT in silver or graphene cannot be directly applied to BDS. In this paper, the optical properties of the BDS were investigated and a tunable terahertz plasmonic device generating the PIT effect is proposed. The finite element method (FEM) was carried out in COMSOL Multiphysics to explore the SPP characteristics of the proposed device and reveal the origin of the PIT effect. The basic components of such solution are a BDS waveguide, a rectangular resonator, and a mushroom-shaped resonator. The two resonators are directly coupled to the BDS waveguide, and, for this reason, each resonator can be treated as a bright mode. The interplay between two bright modes lead to the PIT effect in the proposed device. The electrical tunability of the PIT effect was investigated and demonstrated, and the influence of the structural parameters was also considered. The group time delay was calculated to check and measure the subluminal light propagation, i.e., the “slow light” [24]. Furthermore, in order to enhance the PIT effect, multiple cascading devices were designed and their SPP characteristics were investigated. Finally, a refractive index sensor based on the BDS waveguide was developed and its sensing performance was calculated. The results of this work provide a useful reference for the development of novel BDS-based plasmonic devices.

II. STRUCTURE AND MATERIALS

Two main generation mechanisms are known to be at the basis of the PIT effect in metal-insulator-metal (MIM) waveguides. The first one is the bright-dark mode coupling, and the other is the bright-bright mode coupling. In this work, the latter mechanism was chosen to induce the PIT effect in the BDS waveguide. For this purpose, a mushroom-shaped resonator (MSR) and a rectangular resonator (RR) were carefully designed to

provide the bright modes. Their arrangement in the vicinity of the BDS waveguide is shown in Fig. 1. The connection between the BDS waveguide and the resonators is a direct coupling, and both the MSR and the RR serve as the bright modes. The radius and height of the MSR are here labelled as R and h_m , respectively. The width and height of the RR are denoted as W_r and h_r , respectively. The width of the BDS waveguide is W_g . The white area in Fig. 1 represents the air, whereas the dark gray area represents the Dirac semimetal.

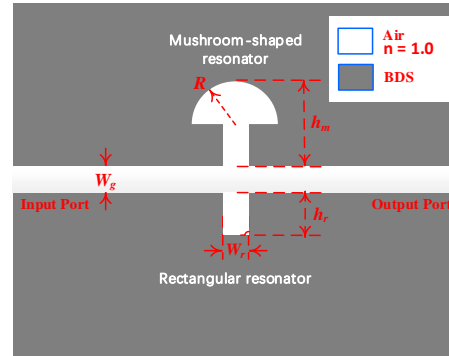


Fig. 1. Schematic diagram of proposed BDS-based plasmonic device.

A three-dimensional Dirac semimetal is an unusual quantum material with massless Dirac fermions. It typically possesses the Fermi - Arc surface states. Common BDS materials include Cd_3As_2 , Na_3Bi , and ZrTe_5 [25]. By only considering the electronic intra-band transition, the permittivity of the 3D Dirac semimetals can be described via a Drude-like formula [16]. This expression is called the one-band model. Alternatively, both the electronic inter-band and intra-band transitions can be taken simultaneously into account. This model is known as the two-band model and it more accurately describes the optical properties of the BDS. Herein, the two-band model was used to derive the expression of the relative permittivity of the BDS material:

$$\varepsilon = \varepsilon_b + j \frac{\sigma}{\omega \varepsilon_0}. \quad (1)$$

Here, σ corresponds to the total dynamic conductivity of the BDS material, ε_0 to the permittivity of vacuum, and ω to angular frequency of the light. Moreover, ε_b is the effective background dielectric constant and its value is set to 1. The tool used to calculate the longitudinal conductivity, σ , was the Kubo-Greenwood formulation in the random-phase approximation (RPA) [26, 27]. From this theory, when the long-wave and low temperature limits are met, the complex conductivity of the sample can be written as follows [28]:

$$\begin{aligned} \text{Re}\sigma(\Omega) &= \frac{e^2}{\hbar} \frac{gk_F}{24\pi} \Omega \theta(\Omega-2) \\ \text{Im}\sigma(\Omega) &= \frac{e^2}{\hbar} \frac{gk_F}{24\pi^2} \left\{ \frac{4}{\Omega} - \Omega \ln \left(\frac{4\varepsilon_c^2}{|\Omega^2-4|} \right) \right\}, \end{aligned} \quad (2)$$

where $g = 40$, e , and \hbar represent the degeneracy factor, the electron charge, and the reduced Planck constant, respectively. The Fermi energy of the BDS material can be written as E_F . In addition, $\varepsilon_c = E_c/E_F$ represents the ratio between the cut-off energy E_c and the Fermi energy E_F . The cut-off energy, E_c , specifies the linear range of the Dirac spectrum. In Eq. (2), the Fermi momentum is defined by $k_F = E_F/\hbar v_F$, where v_F corresponds to the Fermi velocity with a value of 10^6 m/s in this work. In order to take into account the Drude damping, the following expression was used to describe the photon energy $\Omega = \hbar\omega/E_F + j\hbar\tau^{-1}/E_F$. Here, τ represents the carrier relaxation: its expression is $\tau = \mu E_F/ev_F^2$, where the carrier mobility can be defined as $\mu = 3 \times 10^4$ cm²/V/s. Figure 2 displays the real and the imaginary parts of the dynamic conductivity of the BDS material at different Fermi energies.

III. RESULTS AND DISCUSSION

To clarify the physics behind the PIT effect generation, the transmission spectrum and the mode field distributions for the device shown in Fig. 1 were calculated. The finite element method provided by the commercial software COMSOL Multiphysics was used for this purpose. The scattered waves, escaping the computational region, are absorbed by the perfectly matched layer (PML) boundary condition. The transmittance (T) and the reflectivity (R) were calculated according to the following expressions:

$$T = |S_{21}|^2 \quad R = |S_{11}|^2, \quad (3)$$

here, S_{21} and S_{11} are the scattering matrix elements of the device. The optical absorption of the device was determined via the formula $A = 1 - R - T$. The results for an energy $E_F = 75$ meV with optimized structural parameters $W_g = W_r = 50$ μm , $R = 200$ μm , $h_m = 280$ μm , and $h_r = 80$ μm , are shown in Fig. 3. The transmission spectrum is represented by a red solid line in Fig. 3, whereas the reflection spectrum is shown by the blue dashed line. The distributions of the magnetic field, H_z , for the 320.4 μm , 347.2 μm , and 361 μm wavelengths are shown in the insets of Fig. 3. The results show that a transmission peak, also known as the transparency window, with its central wavelength at 347.2 μm appears

in the transmission spectrum. The occurrence of the PIT effect in the device can be attributed to the coupling between the detuned resonators. The MSR and RR can be treated as two detuned resonators, which provide different light paths for the incident waves. When the optical signals from the different optical paths couple back into the output waveguide, the coherent interference between them results in the generation of the PIT effect. In order to investigate the subluminal propagation of the light caused by the PIT the transmitted phase, $\phi(\omega)$, and the group delay time, t_g , were calculated for the proposed device. The value of t_g was defined by using the first-order derivative of the transmitted phase, $\phi(\omega)$, with respect to the circular frequency, ω . The results are shown in Fig. 4: A group delay-time up to 18.64 ps can be measured for the central wavelength of the PIT window. This observation fully demonstrates that the proposed device exhibits an excellent slow light transmission performance when the PIT effect takes place.

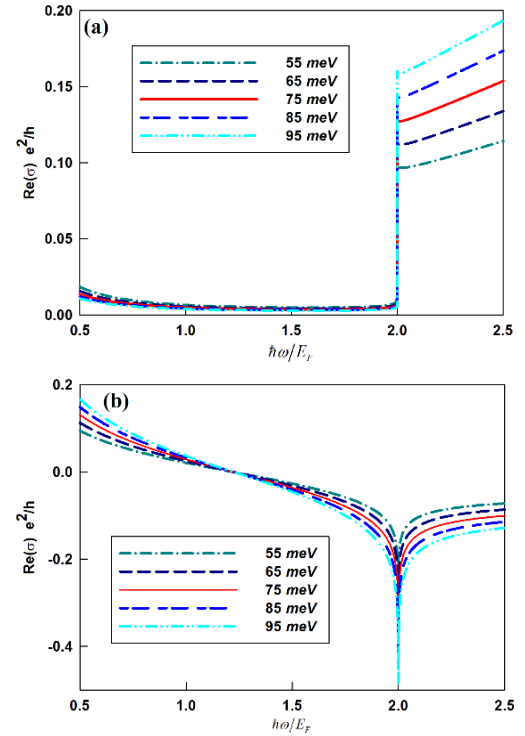


Fig. 2. Real (a) and the imaginary (b) parts of the dynamic conductivity of the BDS material at different Fermi energies. The unit of the vertical axis is e^2/\hbar , while the horizontal axis is the normalized frequency $\hbar\omega/E_F$, $\varepsilon_c = 3$.

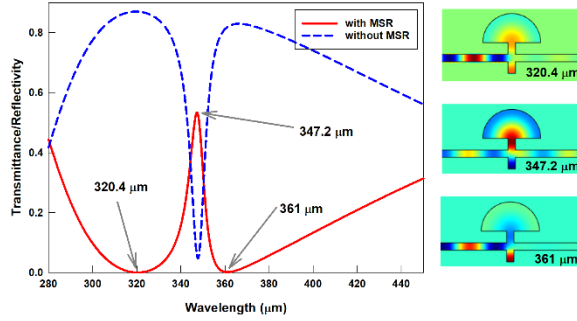


Fig. 3. Transmission and reflection spectra of the proposed device, the insets show the field distribution of H_z at the wavelength of 320.4 μm , 347.2 μm and 361 μm , respectively.

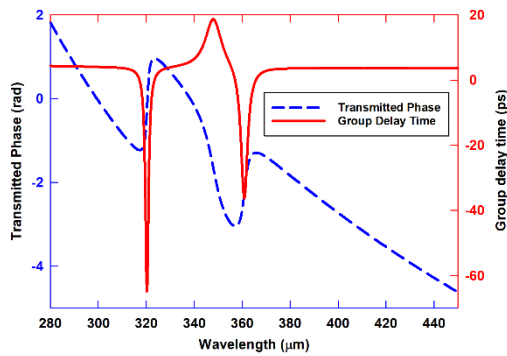


Fig. 4. Variations of the transmitted phase and the group delay time with respect to the wavelength of incident light.

The radius of the semicircular resonant cavity has a large influence on the generation of the PIT effect. To examine its influence, both the transmittance and the group time delay were calculated for the different values of the radius of the MSR. The results are shown in Fig. 5. The variation of the transmission performance of the device with radius R is very remarkable. As R increases, the central wave-length of the PIT window gradually increases, however the maximum transmittance gradually decreases. The variation of the group delay-time as a function of the radius R is shown in Fig. 5 (b). The maximum group delay time at the PIT window also increases upon an increase in the radius R .

Although a variation in the structural parameters can be used to effectively modulate the PIT effect, as shown above, the PIT effect cannot be dynamically adjusted in the range required in many practical applications. However, this can be achieved by adjusting the Fermi energy or the voltage applied to the device. The voltage applied to the device can change the carrier density and Fermi energy of the BDS. Therefore, the PIT effect of the proposed device can also be dynamically controlled

by the voltage. The regulation relationship between Fermi energy E_F and gate voltage V can be explained by a parallel-plate capacitor model [29]. An approximate expression is shown as follows:

$$E_F \approx \hbar v_F \left(\frac{\pi \epsilon_0 \epsilon_d V}{ed} \right)^{1/2}. \quad (4)$$

Here d is the length between the two electrodes, ϵ_d is the relative permittivity of dielectric filled between the two electrodes, and ϵ_0 is the vacuum permittivity. To investigate the effectiveness of this method, the Fermi energy was modified from 55 meV to 95 meV in steps of 10 meV. At each energy step, the transmission spectrum and the group delay time were measured, as shown in Fig. 6. The results in Fig. 6 (a) show that the central wavelength of the PIT window exhibits only a slight redshift as the Fermi energy gradually increases. However, the maximum transmittance at the PIT window, increases upon an increase in the Fermi energy. Increasing the Fermi energy of the BDS increases, in fact, the carrier concentration of the material, and ultimately reduced its losses. Figure 6 (b) shows that by varying the Fermi energy of the BDS the group delay time can be regulated. The maximum group delay time at the PIT window increases with an increase in the Fermi energy, E_F . When $E_F=95$ meV, the maximum group delay time reaches 21 ps.

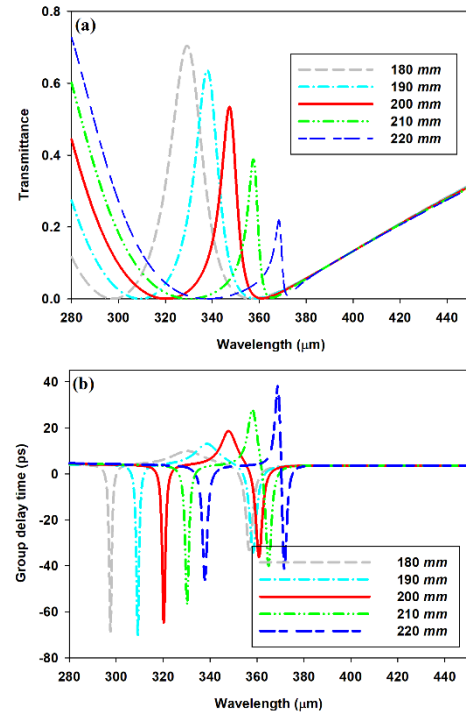


Fig. 5. Transmission spectra (a) and the group delay times (b) of the proposed device for different radius.

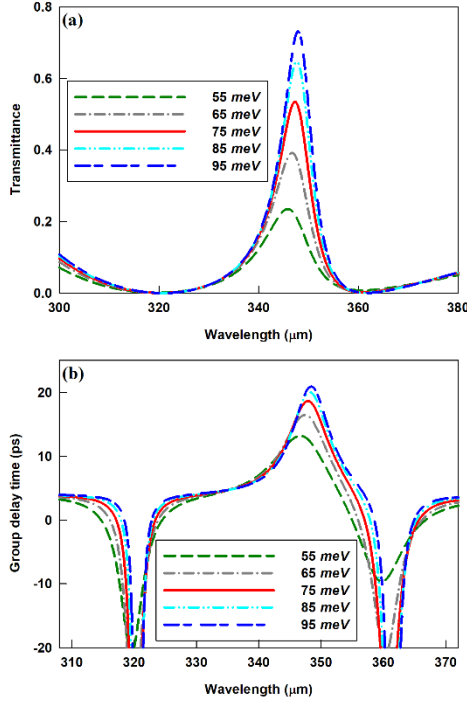


Fig. 6. Transmission spectra (a) and the group delay times (b) of the proposed device for different Fermi energy.

An important application of the PIT effect is the manufacturing of refractive index sensors. The BDS-based plasmonic device proposed in this work can as well be used as a refractive index sensor. In this scenario, the refractive index of the environment varies with the analyte to be monitored, such as a contaminated gas. To investigate the refractive index sensitivity of such device, the ambient refractive index was varied in the 1–1.06 range with a step of 0.01. The transmission spectrum of the device at each ambient refractive index is shown in Fig. 7. As the ambient refractive index increases, the central wavelength of the PIT window increases as well, exhibiting a redshift. The refractive index sensitivity is defined as $S = \Delta f / \Delta n$, where Δf corresponds to the central frequency shift of PIT window, Δn to the variation in the ambient refractive index. According to Fig. 7, the average frequency shift of the center of the PIT window is 0.00821 THz per 0.01 increment in the ambient refractive index value. This measurement provides a refractive index sensitivity of 0.821 THz per RIU.

In order to further enhance the PIT effect, a cascading device with configuration shown in Fig. 8 (a) was designed. This device contains two meta-atoms, each consisting of a mushroom-shaped resonator and a rectangular resonator. The spatial separation between them

is $S = 250 \mu\text{m}$. The values of R , h_r , and h_m were fixed to 200, 80, and 280 μm , respectively. The Fermi energy measured $E_F = 75 \text{ meV}$. The calculated transmittance and the group delay time for this cascading device are shown in Fig. 8 (b): The maximum transmittance of the PIT window appears to be significantly reduced when compared to the non-cascading device. The optical impulse is scattered and then, absorbed when it passes through each meta-atom. Therefore, upon an increase in the meta-atom concentration, a higher energy loss takes place. Nevertheless, the group delay time, t_g , is greatly enhanced in the cascading device. As shown in the inset of Fig. 8 (b), t_g at the central wavelength of the PIT window increases from 18.64 ps to 37.78 ps.

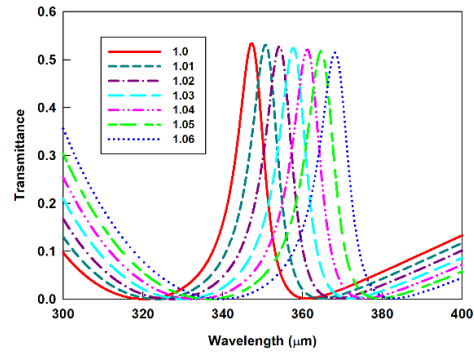


Fig. 7. Transmission spectra of the proposed device for different refractive indices of the analytes.

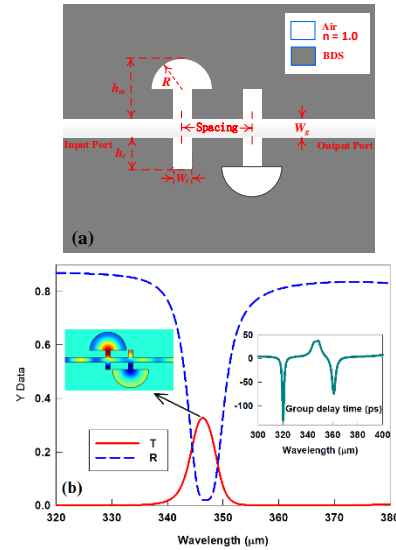


Fig. 8. Schematic diagram (a) and transmission performance (b) of the cascading device, the insets of (b) show the group delay time and the distribution of the magnetic field.

The performance of the electrically tunable PIT of the cascading device is shown in Fig. 9. The transmittance and the group delay time were measured at different Fermi energies and the results are shown in Figs. 9 (a) and (b), respectively. Figure 9 (a) shows that the maximum transmittance at the PIT window increases as a function of E_F . When E_F reaches 95 meV, the maximum transmittance can even approach 0.6. This indicates that increasing the Fermi energy is an effective means to compensate for the transmission losses present in the cascading device. The group delay time can similarly be enhanced by modulating the Fermi energy. Figure 9 (b) shows that as the Fermi energy increases from 55 meV to 95 meV, the maximum group delay time at the PIT window increases to 44.57 ps.

Finally, the impact of the ambient refractive index on the PIT effect of the cascading device was investigated. To perform this series of measurements, the ambient refractive index was increased from 1.0 to 1.06 in steps of 0.01. The transmittance of the cascading device as a function of the ambient refractive index is shown in Fig. 10. As in the case of the non-cascading device, the center frequency of the PIT window of the cascading one exhibits a redshift with an increase in the ambient refractive index. At each 0.01 increment, the average shift of the central frequency of the PIT window measures 0.0082 THz. This indicates that the cascading device has a sensitivity of 0.82 THz per RIU.

As we can see from Figs. 7-10, the more meta-atoms are cascaded, the larger propagation loss conspicuously becomes. The propagation loss is the obstacle that hinders the practical application of the cascade scheme. One possible solution is to replace the passive dielectric part of the cascade device with gain material [30] or nonlinear material [31] to compensate for propagation loss. In Table 1, the slow-light performance of different designs is compared with that of our proposed device. One can see that our proposed device is capable of providing a group delay time of up to 44.57 ps if two meta-atoms are used in cascade. The device in [35] also exhibits very high group delay time. However, the device is a three-dimensional structure and cannot be two-dimensionally integrated in a chip. Our results fully demonstrate the advantages of the BDS-based plasmonic device in terms of slow light performance.

In the end, it is valuable to discuss the experimental implementability of the device proposed in this paper. So far, three preparation methods of BDS films have been proposed, which are melt growth [36], chemical vapor deposition [37] and molecular beam epitaxy [38]. After the BDS film is fabricated, the waveguide and resonant cavity shown in Fig. 1 can be prepared experimentally using photoresist technology and dry etching [39]. Thus, the solution proposed in this paper is fully implementable on experiments.

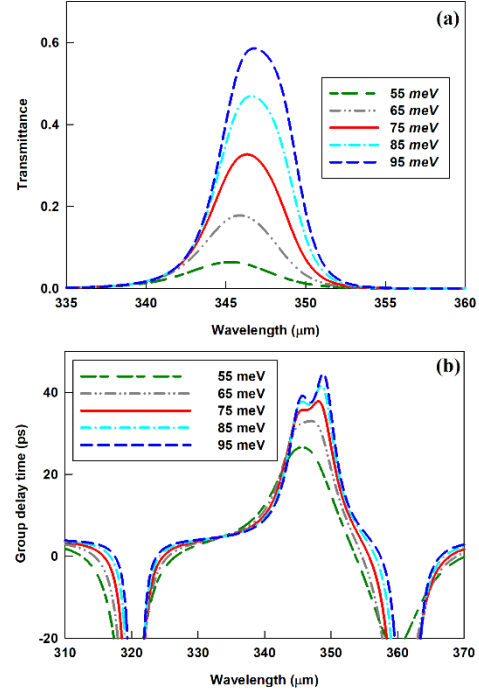


Fig. 9. Transmission spectra (a) and the group delay times (b) of the cascading device for different E_F .

Table 1: Comparison of the proposed device and other published designs

| Reference | Dimension | Material | Group Delay Time (ps) |
|-----------|-----------|----------|-----------------------|
| [32] | 2D | Silver | 1.8 |
| [33] | 2D | Graphene | 1.1 |
| [34] | 3D | Graphene | 13.28 |
| [35] | 3D | Graphene | 43 |
| [17] | 3D | BDS | 6.81 |
| [23] | 2D | BDS | 11.001 |
| This work | 2D | BDS | 44.57 |

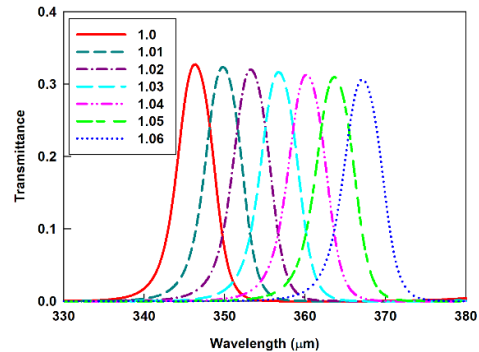


Fig. 10. Transmission spectra of the cascading device for different refractive indices of the analytes.

VI. CONCLUSION

In summary, a solution to generate the PIT effect in BDS materials was proposed and investigated. Initially, the origin of the PIT effect was discussed and explained based on the transmission spectra and the field distributions. Then, the electrical tunability and the influence of the structural parameters were investigated in detail. According to the results, a group delay time up to 44.57 ps can be achieved with the proposed plasmonic device. If the ambient refractive index changes, the central wavelength of the PIT window of the device shifts remarkably. These observations suggest that the solution proposed in this work can provide a useful reference for the production of both high-performance slow-light devices and refractive index sensors.

ACKNOWLEDGMENT

This work was supported in part by the National Natural Science Foundation of China (no. 61367007); the Natural Science Fund of Gansu Province of China (no. 20JR10RA154).

REFERENCES

- [1] X. X. Niu, X. Y. Hu, Q. C. Yan, J. K. Zhu, H. T. Cheng, Y. F. Huang, C. C. Lu, Y. L. Fu, and Q. H. Gong, "Plasmon-induced transparency effect for ultracompact on-chip devices," *Nanophotonics*, vol. 8, no. 7, pp. 1125-1149, July 2019.
- [2] A. M. Akulshin, S. Barreiro, and A. Lezama, "Steep anomalous dispersion in coherently prepared Rb vapor," *Physical Review Letters*, vol. 83, no. 21, pp. 4277-4280, 1999.
- [3] H. Failache, P. Valente, G. Ban, V. Lorent, and A. Lezama, "Inhibition of electromagnetically induced absorption due to excited-state decoherence in Rb vapor," *Physical Review A*, vol. 67, no. 4, p. 043810, 2003.
- [4] M. F. Yanik, W. Suh, Z. Wang, and S. H. Fan, "Stopping light in a waveguide with an all-optical analog of electro-magnetically induced transparency," *Physical Review Letters*, vol. 93, no. 23, p. 233903, 2004.
- [5] N. Papasimakis, V. A. Fedotov, N. I. Zheludev, and S. L. Prosvirnin, "Metamaterial analog of electromagnetically induced transparency," *Physical Review Letters*, vol. 101, no. 25, p. 253903, 2008.
- [6] F. M. Liu, M. Z. Ke, A. Q. Zhang, W. J. Wen, J. Shi, Z. Y. Liu, and P. Sheng, "Acoustic analog of electromagnetically induced transparency in periodic arrays of square rods," *Physical Review E*, vol. 82, no. 2, p. 026601, Aug. 2010.
- [7] Y. Yang, I. I. Kravchenko, D. P. Briggs, and J. Valentine, "All-dielectric metasurface analogue of electromagnetically induced transparency," *Nature Communications*, vol. 5, no. 1, pp. 1-7, Dec. 2014.
- [8] Z. R. Zhang, L. W. Zhang, H. Q. Li, and H. Chen, "Plasmon induced transparency in a surface plasmon polariton waveguide with a comb line slot and rectangle cavity," *Applied Physics Letters*, vol. 104, no. 23, p. 231114, June 2014.
- [9] Z. H. He, H. J. Li, S. P. Zhan, G. T. Cao, and B. X. Li, "Combined theoretical analysis for plasmon-induced transparency in waveguide systems," *Optics Letters*, vol. 39, no. 19, pp. 5543-5546, Oct. 2014.
- [10] J. J. Chen, Z. Li, S. Yue, J. J. Xiao, and Q. H. Gong, "Plasmon-induced transparency in asymmetric T-shape single slit," *Nano Letters*, vol. 12, no. 5, pp. 2494-2498, Apr. 2012.
- [11] G. X. Ni, A. S. McLeod, Z. Sun, L. Wang, L. Xiong, K. W. Post, S. S. Sunku, B. Y. Jiang, J. Hone, C. R. Dean, M. M. Fogler, and D. N. Basov, "Fundamental limits to graphene plasmonics," *Nature*, vol. 557, no. 7706, pp. 530-533, May 2018.
- [12] Y. C. Fan, N. H. Shen, F. L. Zhang, Q. Zhao, H. J. Wu, Q. H. Fu, Z. Y. Wei, H. Q. Li, and C. M. Soukoulis, "Graphene plasmonics: A platform for 2D optics," *Advanced Optical Materials*, vol. 7, no. 3, p. 1800537, Dec. 2018.
- [13] X. L. Zhao, C. Yuan, L. Zhu, and J. Q. Yao, "Graphene-based tunable terahertz plasmon-induced transparency metamaterial," *Nanoscale*, vol. 8, no. 33, pp. 15273-15280, July 2016.
- [14] H. Xu, M. Z. Zhao, M. F. Zheng, C. X. Xiong, B. H. Zhang, Y. Y. Peng, and H. J. Li, "Dual plasmon-induced transparency and slow light effect in monolayer graphene structure with rectangular defects," *Journal of Physics D: Applied Physics*, vol. 52, no. 2, p. 025104, Nov. 2018.
- [15] X. Y. He, F. Liu, F. T. Lin, and W. Z. Shi, "Graphene patterns supported terahertz tunable plasmon induced transparency," *Optics Express*, vol. 26, no. 8, pp. 9931-9944, Apr. 2018.
- [16] O. V. Kotov, and Y. E. Lozovik, "Dielectric response and novel electromagnetic modes in three-dimensional Dirac semimetal films," *Physical Review B*, vol. 93, no. 23, p. 235417, June 2016.
- [17] H. Chen, H. Y. Zhang, X. H. Guo, S. D. Liu, and Y. P. Zhang, "Tunable plasmon-induced transparency in H-shaped Dirac semimetal metamaterial," *Applied Optics*, vol. 57, no. 4, pp. 752-756, Feb. 2018.
- [18] H. Chen, H. Y. Zhang, M. D. Liu, Y. K. Zhao, S. D. Liu, and Y. P. Zhang, "Tunable multiple plasmon-induced transparency in three-dimensional Dirac semimetal metamaterials," *Optics Communications*, vol. 423, pp. 57-62, Sep. 2018.
- [19] S. Yang, R. L. Zhou, D. Liu, Q. W. Lin, and S. Li, "Controlling the plasmon-induced transparency system based on Dirac semimetal at mid-infrared

- band,” *Optics Communications*, vol. 449, pp. 13-18, Oct. 2019.
- [20] H. Chen, H. Y. Zhang, M. D. Liu, Y. K. Zhao, X. H. Guo, and Y. P. Zhang, “Realization of tunable plasmon-induced transparency by bright-bright mode coupling in Dirac semimetals,” *Optical Materials Express*, vol. 7, no. 9, pp. 3397-3407, Sep. 2017.
- [21] J. X. Zhao, J. L. Song, Y. Zhou, R. L. Zhao, and J. H. Zhou, “Tunable multiple plasmon-induced transparency in a simple terahertz Dirac semi-metal based metamaterial,” *Optical Materials Express*, vol. 9, no. 8, pp. 3325-3332, Aug. 2019.
- [22] T. L. Wang, M. Y. Cao, Y. P. Zhang, and H. Y. Zhang, “Tunable polarization-nonsensitive electromagnetically induced transparency in Dirac semimetal metamaterial at terahertz frequencies,” *Optical Materials Express*, vol. 9, no. 4, pp. 1562-1576, Apr. 2019.
- [23] T. Zhou, X. Y. Gou, W. Xu, Y. Li, X. Zhai, H. Li, and L. Wang, “Dynamically tunable plasmon-induced transparency in a T-shaped cavity waveguide based on bulk Dirac semimetals,” *Plasmonics*, vol. 16, no. 2, pp. 323-332, 2021.
- [24] D. Bortman-Arbiv, A. D. Wilson-Gordon, and H. Friedmann, “Phase control of group velocity: From subluminal to superluminal light propagation,” *Physical Review A*, vol. 63, no. 4, p. 043818, 2001.
- [25] T. Liang, Q. Gibson, M. N. Ali, M. H. Liu, R. J. Cava, and N. P. Ong, “Ultrahigh mobility and giant magnetoresistance in the Dirac semimetal Cd_3As_2 ,” *Nature Materials*, vol. 14, no. 3, pp. 280-284, Mar. 2015.
- [26] V. P. Gusynin, S. G. Sharapov, and J. P. Carbotte, “Magneto-optical conductivity in graphene,” *Journal of Physics: Condensed Matter*, vol. 19, no. 2, p. 026222, Dec. 2006.
- [27] G. W. Hanson, “Dyadic Green’s functions and guided surface waves for a surface conductivity model of graphene,” *Journal of Applied Physics*, vol. 103, no. 6, p. 064302, Mar. 2008.
- [28] H. Xiong, Q. Shen, and Q. Ji, “Broadband dynamically tunable terahertz absorber based on a Dirac semimetal,” *Applied Optics*, vol. 59, no. 16, pp. 4970-4976, May 2020.
- [29] J. S. Gómez-Díaz and J. Perruisseau-Carrier, “Graphene-based plasmonic switches at near infrared frequencies,” *Optics Express*, vol. 21, no. 13, pp. 15490-15504, June 2013.
- [30] N. Liu, H. Wei, J. Li, Z. X. Wang, X. R. Tian, A. L. Pan, and H. Xu, “Plasmonic amplification with ultra-high optical gain at room temperature,” *Scientific Reports*, vol. 3, p. 1967, June 2013.
- [31] B. Liu, Y. C. Liao, J. F. Hu, J. Liu, X. D. He, and Z. P. Chen, “Plasmon-induced reflection and its application for all-optical diode based on paralleled double-stub resonators,” *Applied Physics Express*, vol. 12, no. 3, p. 032011, Feb. 2019.
- [32] Y. J. Zhu, T. Wang, X. Han, and B. Y. Wang, “Plasmon-induced transparency effect in a single circular split-ring core ring resonator side-coupled to a metal-isolator-metal waveguide,” *Journal of Applied Physics*, vol. 117, no. 13, p. 133108, Apr. 2015.
- [33] P. Qiu, W. Qiu, Z. Lin, H. B. Chen, J. B. Ren, J. X. Wang, Q. Kan, and J. Q. Pan, “Dynamically tunable plasmon-induced transparency in on-chip graphene-based asymmetrical nanocavity-coupled waveguide system,” *Nanoscale Research Letters*, vol. 12, no. 1, pp. 1-8, May 2017.
- [34] W. Jia, P. Ren, Y. Jia, and C. Fan, “Active control and large group delay in graphene-based terahertz metamaterials,” *Journal of Physical Chemistry C*, vol. 123, no. 30, pp. 18560-18564, July 2019.
- [35] X. Yan, T. Wang, S. Xiao, T. Liu, H. Hou, L. Cheng, and X. Jiang, “Dynamically controllable plasmon induced transparency based on hybrid metal-graphene metamaterials,” *Scientific Reports*, vol. 7, no. 1, pp. 1-10, Oct. 2017.
- [36] M. N. Ali, Q. Gibson, S. Jeon, B. Zhou, A. Yazdani, and R. J. Cava, “The crystal and electronic structures of Cd_3As_2 , the three-dimensional electronic analogue of graphene,” *Inorganic Chemistry*, vol. 53, no. 8, pp. 4062-4067, 2014.
- [37] A. Wang, P. Xiang, X. Ye, W. Zheng, D. Yu, and Z. Liao, “Surface engineering of antisymmetric linear magnetoresistance and spin-polarized surface state transport in Dirac semimetals,” *Nano Letters*, vol. 21, no. 5, pp. 2026-2032, 2021.
- [38] Y. Nakazawa, M. Uchida, S. Nishihaya, S. Sato, A. Nakao, J. Matsuno, and M. Kawasaki, “Molecular beam epitaxy of three-dimensionally thick Dirac semimetal Cd_3As_2 films,” *APL Materials*, vol. 7, no. 7, p. 071109, 2019.
- [39] W. Nickel, M. Oschatz, S. Rico-Francés, S. Klosz, T. Biemelt, G. Mondin, A. Eychmüller, J. Silvestre-Albero, and S. Kaskel, “Synthesis of ordered mesoporous carbon materials by dry etching,” *Chemistry*, vol. 21, no. 42, pp. 14753-14757, 2015.



Daobin Wang was born in 1976. He received the B.S. degree from Xi’an Jiaotong University and the Ph.D. degree from Beijing University of Posts and Telecommunication, Beijing, China. He is currently an Associate Professor at Lanzhou University of Technology, Lanzhou, China. His research interests include optical fiber communication, radio over fiber, and nano-photonics.

On Electric Field Distribution and Temperature Rise Effect of High Power VLF Antenna

Xianqiang Li¹, Kedan Mao², Ao Wang¹, Ji Tian¹, and Wenchuang Zhou¹

¹ School of Automation
Wuhan University of Technology, Wuhan, 430070, China
lxq@whut.edu.cn, WAO@whut.edu.cn

² Nuclear Power Institute of China, Chengdu, 610005, China
15382442567@163.com

Abstract — When a high-power very low frequency (VLF) communication system is in operation, the end of the antenna is in an alternating strong electric field environment. Due to dielectric loss, abnormal temperature rise may occur at the end of the antenna. To solve the problem, analysis on the electric field distribution and temperature rising effect at the end of the antenna is first carried out in this paper. The factors that affect the electric field distribution and temperature rising, including the amplitude and frequency of the excitation voltage, the diameter of the antenna conductor and the material properties of the outer sheath of the antenna, are studied in detail. A novel approach to improve the electric field distribution and to suppress temperature rising is proposed by designing a dielectric loss eliminator, and the effectiveness of the designed device is verified by simulation.

Index Terms — Dielectric loss eliminator, electric field, temperature field, VLF antenna.

I. INTRODUCTION

Very low frequency (VLF) communication systems have several attractive features including stable and reliable propagation, capability to penetrate seawater and soil and intrinsic rejection to ionospheric disturbance interference [1-3]. Therefore, the VLF communication systems have been widely developed for applications such as submarine communication, long-distance communication, mineral exploration, and geophysics [4-9]. Vehicle-mounted VLF communication systems, whose antenna are lifted by balloons, have gained most research interests in recent years due to their flexibility and mobility, high transmission efficiency, and minimum requirement of floor space [10,11].

However, when a high-power VLF communication system is in operation, the end of the antenna will be exposed in the environment with strong and highly-varying electric field, where abnormal temperature rise

might occur due to dielectric loss on the outer sheath material of the antenna. This can lead to disastrous consequences such as antenna breaking and balloon escaping. Hence, it is of primary importance to investigate the electric field distribution and temperature rise effects at the end of antenna to ensure safe and reliable operation of the vehicle-mounted VLF communication systems.

In a vehicle-mounted high-power VLF communication system, if the balloon is utilized to lift the antenna to transmit signals, the electric field intensity near the end region of the antenna can be extremely high. If the local electric field intensity exceeds the air ionization field intensity, the air will be ionized and the corona discharge phenomenon will occur [12]. Corona discharge will cause additional power loss, radio interference, as well as noise interference. More severely, corona discharge can cause unexpected breakdown of the high-power VLF communication system. In addition, since the outer sheath and load-bearing materials at the end of the antenna, which are made of polymer composite materials, are exposed in an environment with high-amplitude alternating electric field, dielectric heating is likely to occur and it can cause the antenna fracture in certain extreme conditions. Especially for the balloon-lifting type high-power VLF communication system, the breaking of the antenna will lead to catastrophic consequences of the balloon disconnection.

At present, there is rare research on electric field distribution and temperature rise at the terminal of VLF antenna. In [13], The selection of insulators in station-type VLF arrays is studied. Since high-power VLF transmit antennas usually operate in high voltage and large current conditions, electrical insulation must be paid attention to. In [14], Liu carried out simulation analysis of the radiation characteristics of the VLF dual-tail antenna and the near-field characteristics of the airborne platform by establishing the electromagnetic theoretical model of the airborne VLF dual-tail antenna system, and the strong corona of single-tail antenna

communication problem was optimized. In [15], Liu used finite element simulation software to establish the model of the aircraft and the VLF launching system, so as to study the electromagnetic environment of the airborne dual towed antenna, the near-field radiation characteristics of the towed antenna, the internal electromagnetic field, as well as the distribution and value of induced current of the aircraft by simulation calculation. In [16], a new method for establishing an airborne VLF single/dual towed antenna system model was proposed. The electromagnetic radiation characteristics and impedance characteristics of single/dual towed antennas were discussed by simulation calculations. It pointed out that the performance of dual towed antennas is better than single tow antenna. The electric field distribution of the insulator at the terminal of the VLF antenna is obtained by simulation modeling. The magnitude and distribution of the voltage and current on the VLF antenna are obtained through integration [17]. Yang [18] theoretically analyzed the mechanism of electric field distortion and high local field intensity at the terminal of VLF communication antenna. At the same time, the affecting factors are discussed. Zhou [19] introduced the generation mechanism of the corona of the VLF transmitting antenna, theoretically derived the calculation method of the corona voltage of the VLF transmitting antenna, and analyzed the influencing factors of corona voltage calculation under different operating conditions. The distribution characteristics of the electric field at the terminal of the VLF antenna are obtained by numerical calculation. The improvement measure is proposed to solve the problem of electric field distortion, and the effectiveness of the improvement measures is verified by simulation calculation. Meanwhile, the factors that affecting the distribution of electric fields are also studied [20]. Shi [21] simulated the VLF antenna array and constructed a minimum protection distance model for electromagnetic radiation hazards. Through numerical calculation, the variation law of the comprehensive field intensity value of the VLF antenna array near area with the transmission power and loading frequency was obtained. Finally, the accuracy of the simulation is verified by experiments. The temperature field at the terminal of the VLF antenna is theoretically analyzed, and the heating principle at the terminal of the VLF antenna is expounded, and the temperature variations at the terminal of the VLF antenna under different operating conditions were discussed through finite element simulation modeling [22].

To summarize the existing works, there are few studies on coupled electro-thermal field at the end of antenna, especially for high-power balloon-lift VLF communication systems. Therefore, it is of great significance to carry out research on the electric field distribution and the temperature rise at the end of the

transmitting antenna of high-power VLF communication system and to take effective measures to improve the electric field distribution and suppress temperature rising.

In this work, the distribution characteristics of the electric field and temperature field at the end of high-power VLF antenna are studied separately. Hence, the factors that affect the electric field and temperature at the end of the VLF antenna are studied through simulation calculations. The measure to solve electric field distortion and temperature rise (Dielectric Loss Eliminator) are proposed and the effectiveness of the measures is verified. It provides a certain reference for the design of the antenna.

II. PRELIMINARIES

In this section, the composition of the VLF antenna structure is introduced. The electric field distribution and the temperature rise caused by the dielectric loss at the end of the VLF antenna are analyzed theoretically.

A. Structure of a VLF antenna

The complete antenna system is shown in Fig. 1. A floating balloon and a ground vehicle are connected at each end of the antenna. The floating balloon is used to lift the antenna for signal transmission. The ground vehicle is used for tethering the floating platform after retrieval and towing the floating platform during release. The 1~3 km VLF antenna connects the two and serves as a connection and signal radiation.

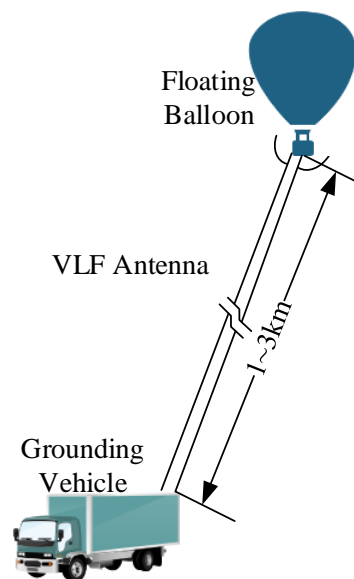


Fig. 1. Schematic diagram of antenna system.

As shown in Fig. 2, a typical VLF antenna is composed of four layers, including outer sheath, antenna conductor, inner sheath, and the aramid. Figure 2 (a) and Fig. 2 (b) present the sectional and vertical view of the

VLF antenna, respectively.

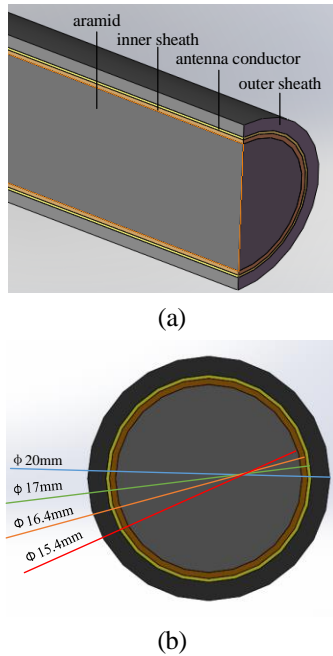


Fig. 2. Structure diagram of VLF antenna: (a) sectional view of the antenna; (b) vertical view of the antenna.

B. Electro-quasi-static equations

According to Faraday law of electromagnetic induction, the coulomb electric field E_q and the induced electric field E_i in the time-varying electric field are induced by electric charge q and varying magnetic field $\partial B / \partial t$ respectively. In the low-frequency electric field, if the induced electric field E_i is much lower than the coulomb field E_q , the $\partial B / \partial t$ term in the Maxwell's equations can be ignored. Hence, the time-varying electric field differential equation of the Maxwell's equations can be simplified to the electro-quasi-static Equations (1) – (4):

$$\nabla \times \mathbf{H} = \mathbf{J} + \frac{\partial \mathbf{D}}{\partial t}, \quad (1)$$

$$\nabla \times \mathbf{E} = 0, \quad (2)$$

$$\nabla \cdot \mathbf{B} = 0, \quad (3)$$

$$\nabla \cdot \mathbf{D} = \rho, \quad (4)$$

where, H is the magnetic field intensity, J is the conduction current density, E is the electric field intensity, B is the magnetic flux density, D is the electric displacement, and ρ is the charge density.

It can be seen from (1) – (4) that both the electrical quasi-static field and the electrostatic field have active and non-rotation in ignoring $\partial B / \partial t$, so the calculation method of the two fields is similar. In addition, the electric field intensity of the electric quasi-static field can

also be expressed as the negative of the potential gradient, i.e.,

$$\mathbf{E} = -\nabla \varphi, \quad (5)$$

where φ is the potential function of the electric quasi-static field.

Therefore, it can be seen that the solutions of the electric quasi-static field and electrostatic field have a similar form. Furthermore, the conditions to be satisfied for inhomogeneous isotropic media are expressed using the constitutive relationships of media in the Maxwell's equations, i.e.,

$$\mathbf{D} = \varepsilon \mathbf{E}, \quad (6)$$

$$\mathbf{B} = \mu \mathbf{H}, \quad (7)$$

$$\mathbf{J} = \sigma \mathbf{E}, \quad (8)$$

where ε , μ , and σ represent the permittivity, permeability, and conductivity of the medium, respectively.

The Poisson equation satisfying potential $\varphi(t)$ can be obtained by substituting (5) and (6) into (4), i.e.,

$$\nabla^2 \varphi = -\frac{\rho(t)}{\varepsilon}. \quad (9)$$

In summary, the electric field of the end of high-power VLF antenna is electric quasi-static field.

C. Theoretical analysis of dielectric loss

The temperature rise of the end of VLF antenna is caused by the existence of alternating electromagnetic fields [23]. Due to the polarization effects and dielectric loss, there are energy consumption and conversion processes in the outer sheath and load-bearing materials of the VLF antenna end. The outer sheath and load-bearing materials have a dielectric loss (mainly polarization loss) in the alternating electric field, which converts electrical energy into thermal energy. It causes a temperature rise at the end of the VLF antenna. According to the principle of dielectric loss, the energy loss per unit time and per volume can be calculated by:

$$W = \frac{\omega}{2} \varepsilon'' E_0^2, \quad (10)$$

$$\varepsilon'' = \varepsilon' \tan \delta, \quad (11)$$

$$\varepsilon' = \varepsilon_r \varepsilon_0, \quad (12)$$

where ε' and $\tan \delta$ can be obtained by consulting the data, ε_r is the relative dielectric constant, and ε_0 is the dielectric constant in vacuum.

Combining (10) – (12) yields the expression of dielectric loss energy W , i.e.,

$$W = \frac{\omega \varepsilon'}{2} (\tan \delta) \int_V |E_0|^2 dv. \quad (13)$$

It can be seen from (13) that, when the parameters of the material are constant, the dielectric loss energy W is proportional to the square of the electric field intensity. Hence, (13) relates the electric field to the dielectric loss

heating, and it fundamentally reveals the relationship between the electric field and the temperature field.

D. Heat transfer equations

Due to the dielectric loss, the antenna can be set as a heat source, and the heat generated in the medium can be obtained according to equation (13). The heat generated within the medium diffuses outward by heat conduction and convection. The heat conduction follows the equations (14),

$$\rho c \frac{\partial T(\vec{r}, t)}{\partial t} - k \Delta T(\vec{r}, t) = F(\vec{r}, t), \quad (14)$$

T is the temperature to be calculated, which is related to both time and space; F is the intensity of the heat source; k , ρ , and c are the thermal conductivity, density, and specific heat capacity, respectively.

Thermal convection follows the following equation,

$$q = h_f (T_s - T_b), \quad (15)$$

h_f is the surface heat transfer coefficient, T_s is the temperature of the surface of the object, T_b is the temperature of the surrounding fluid.

Inside the solid medium, the heat diffuses in the form of heat conduction. Between the antenna and the air, the heat diffuses in the form of thermal convection.

III. DISTRIBUTION CHARACTERISTICS OF ELECTRIC FIELD AND TEMPERATURE FIELD

In this work, the finite element software COMSOL was used to simulate and analyze the distribution characteristics of the electric field and temperature field at the end of VLF antenna.

A. Modelling of a VLF antenna in COMSOL

Although the total length of VLF antenna is 2km, the electric field is only distributed in multi-directional at the end of the antenna, and the electric field only exists along the normal direction in other parts. Therefore, when analyzing the distribution characteristics of electric field and temperature field, only the situation within 1m of the antenna end should be concerned.

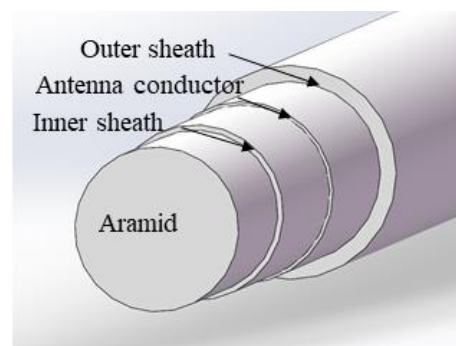
Since the model of VLF antenna and improvement measures are relatively complex and difficult to implement in COMSOL Multiphysics. In this paper, the 3D design software SolidWorks is chosen to build the model and then import it into COMSOL Multiphysics for simulation calculation.

The simulation model of the antenna is shown in Fig. 3. The antenna structure in the simulation is the same as the antenna composition structure described in part A of

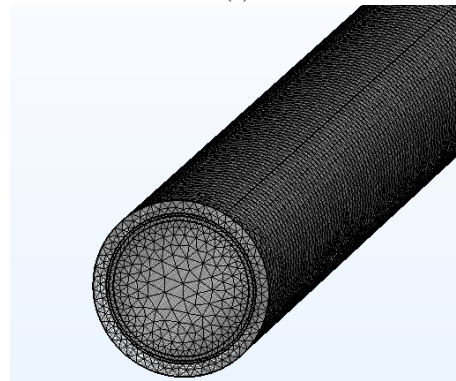
Section II, and the diameters of antenna structure in tensile layer (aramid), inner sheath, antenna conductor (copper layer) and outer sheath layer are 15.4mm, 16.4mm, 17.0mm and 20.0mm respectively. Table 1 gives the relevant parameters of high-power VLF antenna material.

Table 1: Parameters of the material of the VLF antenna

| Material | Relative Permittivity | Conductivity ($S \cdot m^{-1}$) |
|--------------|-----------------------|-----------------------------------|
| Inner sheath | 2.2 | 1.0×10^{-14} |
| Copper | / | 5.8×10^7 |
| Outer sheath | 2.3 | 2.0×10^{-12} |
| Aramid layer | 3.3 | 1.0×10^{-14} |
| Air | 1.0 | 2.0×10^{-12} |



(a)



(b)

Fig. 3. The simulation model of the VLF antenna.

B. Distribution characteristics of electric field

According to the actual operating parameters of a high-power VLF communication system, the magnitude and frequency of the excitation voltage were set to $U=120$ kV and $f=10$ kHz in simulation. The obtained electrical field distribution at the terminal of the high-power VLF antenna is visualized in Fig. 4.

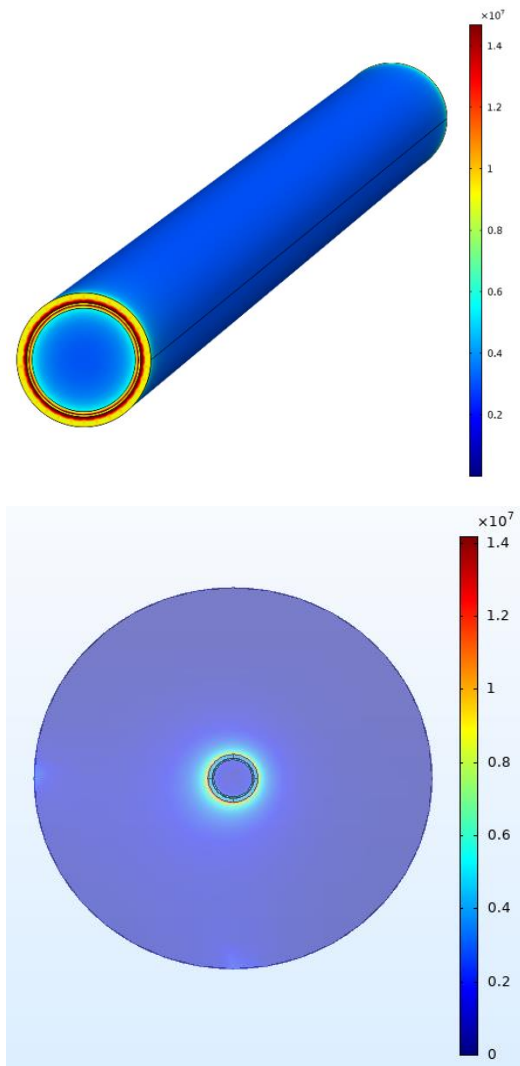


Fig. 4. Distribution of electric field at the end of the VLF antenna.

It can be observed from Fig. 4 that the electric field at the terminal of the antenna is distributed symmetrically about the axis in the radial direction. The electric field intensity of the copper layer is the maximum, and the electric field intensity in the outer sheath shows a decaying trend from the inside to the outside. Furthermore, the electric field intensity of the inner sheath and the aramid layer decreases from the copper layer to the axis, which is lower than the electric field intensity of the outer sheath.

In addition, Fig. 5 shows the radial distribution curve of the electric field at the terminal of the VLF antenna. It can be seen that the electric field intensity of the copper layer at the terminal of the antenna is highest,

up to 1.4×10^7 V/m, and it is much higher than the corona inception field intensity of the air (about 3×10^6 V/m). In this case, air would be ionized, and corona discharge occurs. Meanwhile, the electric field intensity decreased from 1.4×10^7 V/m to 7.0×10^6 V/m within the thickness of the outer sheath. Although the electric field intensity decreases significantly to about half of its original value, it is still higher than the corona inception field intensity in the air.

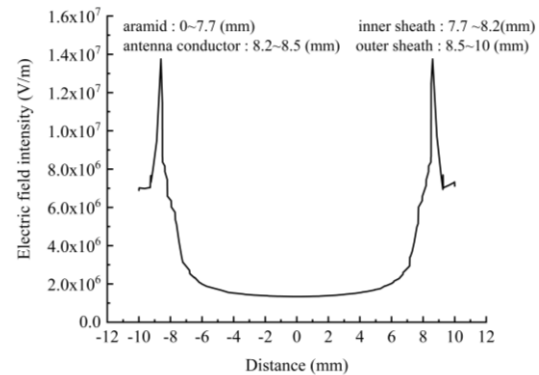


Fig. 5. The radial distribution of the electric field at the terminal of antenna.

C. Distribution characteristics of temperature field

In order to study the distribution characteristics of the temperature field at the terminal of the VLF antenna, in this case, the magnitude and frequency of the excitation voltage were set so $U=120$ kV and $f=30$ kHz, and the initial temperature is $T=40^\circ\text{C}$. The properties of antenna material are given in Table II. In this case, the outer sheath material is Polyethylene. The distribution of the temperature field at the terminal of the VLF antenna was obtained and the result is shown in Fig. 6.

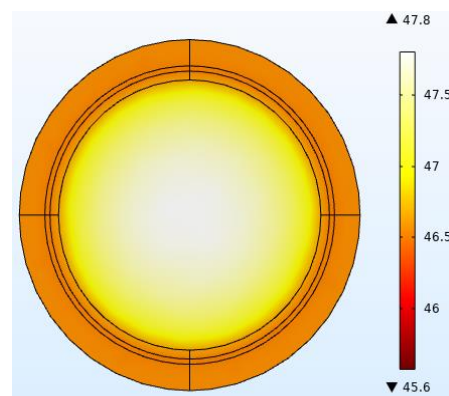


Fig. 6. Temperature distribution at the VLF antenna end.

Table 2: Material properties of antenna

| Material | Relative Permittivity | $\tan \delta$ | Thermal Conductivity W/ (K·m) | Heat Capacity kJ/ (K kg) |
|----------------------------------|-----------------------|----------------------|-------------------------------|--------------------------|
| Inner sheath | 2.2 | 5.0×10^{-4} | 0.48 | 2.2 |
| Aramid | 3.3 | 8.0×10^{-4} | 0.2 | 1.0 |
| Polyethylene (PE) | 2.3 | 2.0×10^{-4} | 0.48 | 2.3 |
| Polyvinyl chloride (PVC) | 2.0 | 1.0×10^{-2} | 0.17 | 1.0 |
| Ethylene propylene rubber (EPDM) | 3.1 | 3.0×10^{-3} | 0.23 | 1.4 |

It can be clearly seen from Fig. 6 that the temperature field at the terminal of the antenna is symmetrically distributed about the axis, and the highest temperature is at the center of the aramid layer, which is 47.8°C, raised by 7.8°C from its initial temperature. Meanwhile, the average temperature rise of the inner sheath is 6.6°C. Furthermore, the temperature rises of the outer sheath layer and the inner sheath layer are close, as can be observed from Fig. 6.

IV. INFLUENCING FACTORS OF ELECTRIC FIELD AND TEMPERATURE

In this section, the effects of excitation source characteristics, diameter of the antenna conductor, and material properties on electric field and temperature field are studied.

A. Influence of excitation source

1) The effect of voltage amplitude

During normal operation, the excitation voltage of the high-power VLF antenna is loaded from the feed window at the bottom of the antenna. According to the actual operating conditions of high-power VLF communication system, the range of excitation voltage is from 20 kV to 120 kV. The maximum electric field intensity value at the end of the VLF antenna are obtained by simulation calculation with $f=10$ kHz. The relationship between the magnitude of the excitation voltage and the electrical field intensity is shown in Fig. 7.

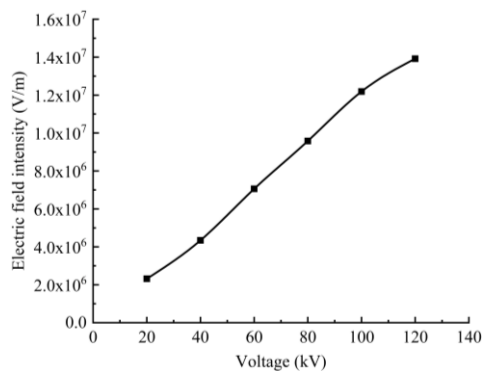
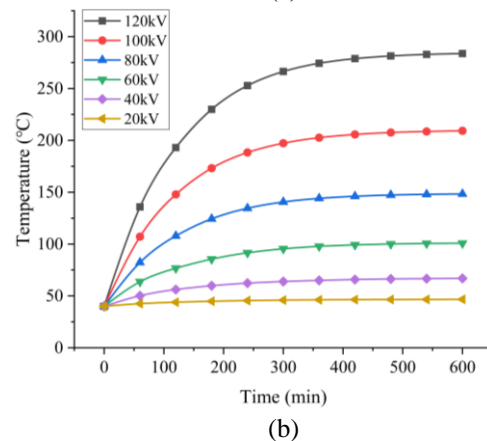
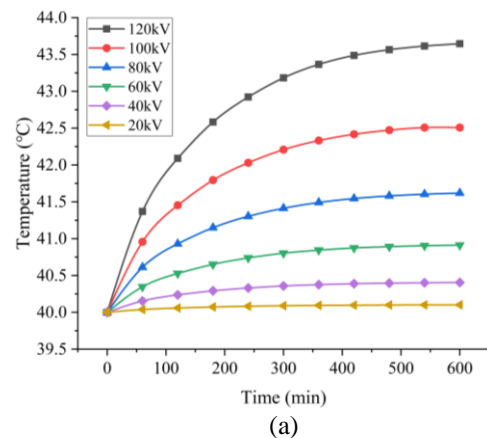


Fig. 7. Relationship between the maximum electric field intensity and the excitation voltage.

It can be seen from Fig. 7 that the electric field intensity at the end of the antenna increases nearly linearly with increased excitation voltage amplitude. The minimal electric field intensity at the end of the antenna is 2.0×10^6 V/m when the excitation voltage amplitude is 20 kV, and the maximum electric field intensity is 1.39×10^7 V/m at 120 kV, which increases by nearly seven times.

In addition, the influence of excitation source voltage amplitude on the temperature field at the end of the antenna with different outer sheath materials is investigated. Figure 8 shows the variation of temperature over time of different outer sheath materials under different magnitudes of the excitation voltage.



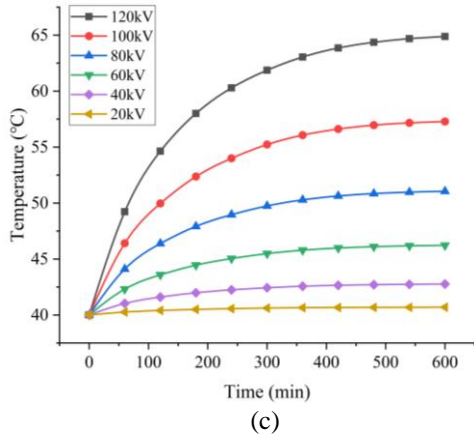


Fig. 8. Temperature rises at the terminal of VLF antenna under different voltage: (a) polyethylene; (b) polyvinyl chloride; (c) ethylene propylene rubber.

Some interesting relationships and characteristics can be observed from Fig. 8. First, the temperature at the end of the VLF antenna increases with increased loading excitation time. When the excitation voltage amplitude is small, the generated heat loss of the medium is not significant, and the thermal equilibrium is reached quickly. As excitation voltage amplitude increases, the heat loss increases gradually.

Second, for the same outer sheath material, the temperature at the end of the VLF antenna increases with increased excitation voltage amplitude. At the same time, the higher the excitation voltage amplitude is, the greater the temperature rise is at the end of the VLF antenna.

Third, under the same excitation voltage amplitude, polyvinyl chloride material has the most significant temperature rise, followed by ethylene propylene rubber, while the temperature rising of the polyethylene materials is the least. When the excitation voltage amplitude is $U=120\text{kV}$, the temperature rises of the three materials are 240°C , 25°C and 3.75°C , respectively. The corresponding temperature growth rates of different materials are 600%, 62.5% and 9.4%, respectively. This is because the tangent of the dielectric loss Angle of polyethylene is much larger than that of the other two kinds of material.

2) *The effect of frequency of the excitation source*

In order to study the influence of the frequency of the excitation source on the electric field distribution at the end of the VLF antenna, in this case simulation was conducted by varying frequency from 3 kHz to 30 kHz, and the amplitude of the excitation voltage is set to 120 kV. The simulation results are shown in Fig. 9.

The Fig. 9 shows that the maximum electric field intensity at the terminal of the VLF antenna maintains

almost a constant of $1.38 \times 10^7 \text{ V/m}$ with varying frequencies. This shows that the frequency of excitation source has little influence on the maximum value of the electric field intensity at the end of the antenna. Therefore, it is reasonable to consider the electromagnetic field in the VLF range as an electric quasi-static field.

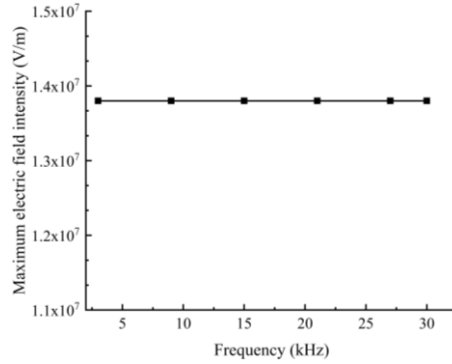
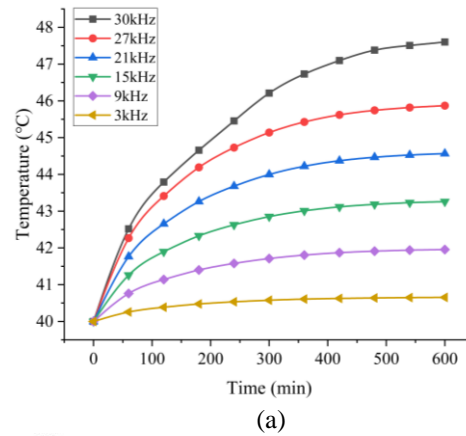
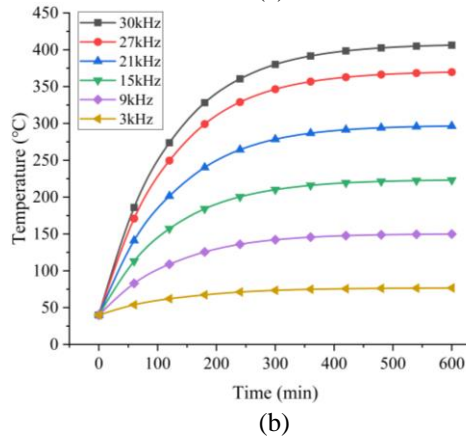


Fig. 9. Maximum electric field intensity with frequency.

Next, to investigate the effect of frequency on the temperature field, the initial temperature is 40°C and other calculation conditions remain unchanged. The results were obtained and shown in Fig. 10.



(a)



(b)

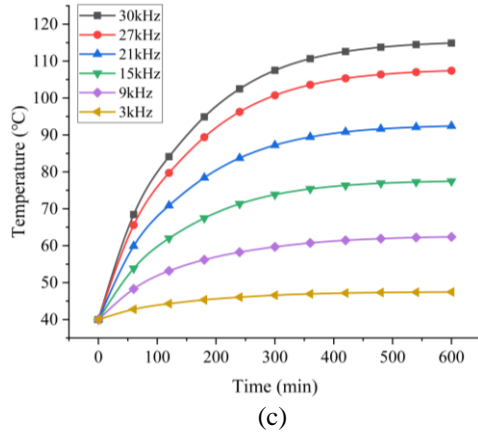


Fig. 10. Temperature rises at the terminal of VLF antenna under different frequency: (a) polyethylene; (b) polyvinyl chloride; (c) ethylene propylene rubber.

According to the simulation results, it can be seen that, first, the temperature at the VLF antenna end increases with increasing of the excitation source loading time. When the frequency of the excitation source is smaller, the heat of the dielectric loss of the material in the alternating electric field is small, and the time to achieve thermal equilibrium is short. With increasing of the frequency of the excitation source, the heat of the dielectric loss is larger.

Second, when the frequency is the same, the temperature rising of polyethylene is smaller, and polyvinyl chloride is the most significant. When the frequency of the excitation source was 30 kHz, the temperature rising of polyvinyl chloride reached 360°C, increasing by 900%; the ethylene-propylene rubber increases by 75°C, an increase of 187%; while the temperature rise of polyethylene is only 8°C, which increases by 20%.

B. Influence of the diameter of the antenna conductor

In this sub-section, the influence of diameter of the antenna conductor on the electric field at the end of the VLF antenna is studied. In simulation, the range of diameter of the antenna conductor is set from 0.05 mm to 1.3 mm, and the step change is 0.25 mm. The electric field intensity under different diameter of the antenna conductor were obtained, and the results are shown in Fig. 9.

It can be seen from Fig. 11 that when the diameter of the antenna conductor increases from 0.05 mm to 1.3 mm, the maximum electric field intensity at the end of the VLF antenna decreases with the increasing of the diameter of the antenna conductor. From 0.05 mm to 0.55 mm, the maximum value of the electric field intensity at the end of the antenna decreases significantly, whereas from 0.55 mm to 1.3 mm, the rate of decrease of the electric field intensity gradually slows down.

When the diameter of the antenna conductor increases from 0.05 mm to 1.3 mm, the maximum electric field intensity at the terminal of antenna decreases from 1.41×10^7 V/m to 5.73×10^6 V/m with a drop of 59.4%.

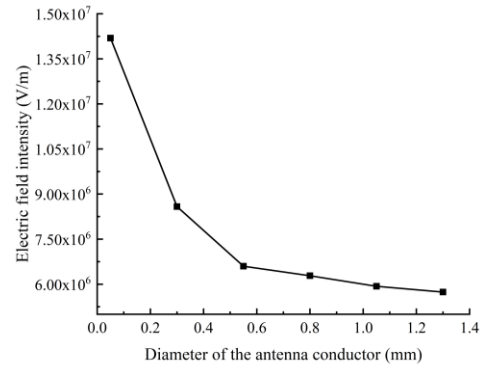


Fig. 11. Electric field intensity with the diameter of the antenna conductor.

It can be also seen from Fig. 11 that the electric field intensity will be affected by changing of the diameter of the antenna conductor. According to the analysis in Section II, the power of the dielectric loss is directly proportional to the square of the electric field intensity. Hence, changing of the diameter of the antenna conductor will affect the distribution of temperature field at the end of the antenna. The corresponding simulation results are shown in Fig. 12 and Fig. 13.

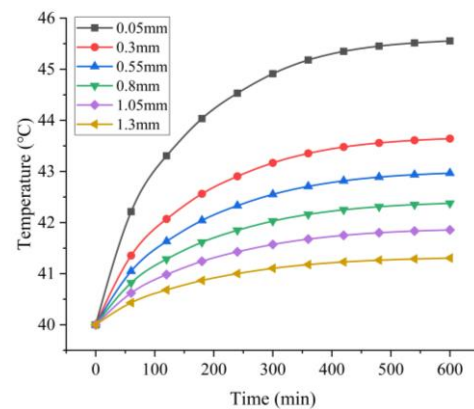


Fig. 12. Temperature rising of polyethylene with different conductor diameter.

As can be seen from Fig. 12 and Fig. 13:

- (1) The temperature rising at the end of the VLF antenna increases with increasing excitation time. At the same time, the thicker the copper layer is, the smaller the temperature rise at the end of the VLF antenna is.
- (2) The temperature rise at the end of the VLF antenna is negatively proportional as the diameter of the antenna conductor increasing in same moment.

(3) When the diameter of the antenna conductor is 1.3mm, the temperature rising to reach thermal equilibrium is only about 1°C. However, when the diameter of the antenna conductor is 0.05mm, the temperature rise is close to 5.5°C, which increases by 450% compared with the diameter of 1.3mm.

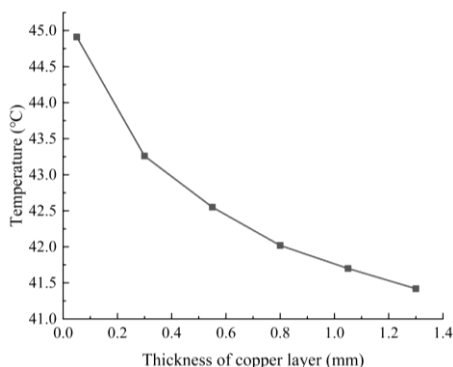


Fig. 13. Temperature rising with thickness of copper layer.

C. Influence of the material properties of outer sheath

It can be seen from Equation (13) that the dielectric loss power is related to the material properties. Therefore, it is necessary to investigate the material properties of the outer sheath of the antenna. The materials in Table 2 are selected for simulation research in this paper.

1) The effect of material conductivity on the electric field

The effect of material conductivity on the electric field is studied in this section. Setting the range of conductivity of the outer sheath material is from $10^{-12} \text{ S} \cdot \text{m}^{-1}$ to $10 \text{ S} \cdot \text{m}^{-1}$. The simulation results are shown in Fig. 14.

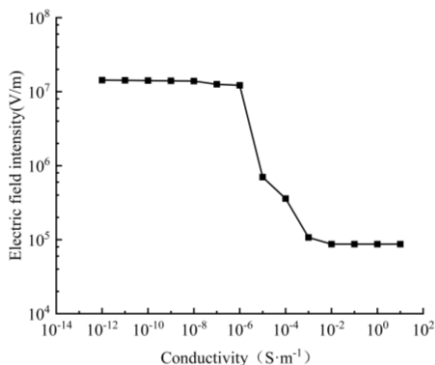


Fig. 14. The curve of electric field intensity with conductivity.

According to Fig. 14:

(1) The electric field intensity at the end of the VLF antenna decreases with the increasing of the conductivity when the conductivity of the outer sheath material changes from $10^{-12} \text{ S} \cdot \text{m}^{-1}$ to $10 \text{ S} \cdot \text{m}^{-1}$. The electric field intensity decreased significantly from $1.43 \times 10^7 \text{ V/m}$ to $8.7 \times 10^4 \text{ V/m}$.

(2) When the conductivity of the outer sheath material is less than $10^{-6} \text{ S} \cdot \text{m}^{-1}$, the amplitude of the electric field intensity at the end of the antenna changes less. whereas the electric field intensity significantly decreased when the outer sheath conductivity increases from $10^{-6} \text{ S} \cdot \text{m}^{-1}$ to $10^{-2} \text{ S} \cdot \text{m}^{-1}$. Continuing to increase the conductivity, the electric field intensity is almost unchanged.

2) The effect of material properties on temperature field

In order to study the influence of different material parameters of outer sheath on the temperature field, setting $U=120 \text{ kV}$, $f=10 \text{ kHz}$, and the initial temperature $T=40^\circ\text{C}$ to obtain the maximum temperature rise of different materials, as shown in Fig. 15.

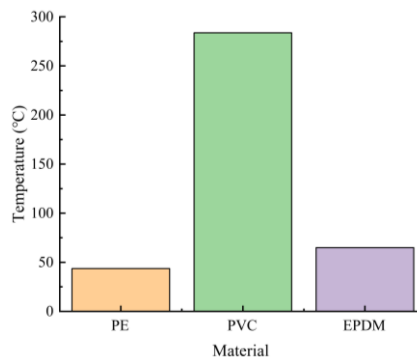


Fig. 15. The curve of temperature rising in different materials.

It can be seen from Fig. 15 that temperature rise exists in all three materials, of which temperature rising of polyvinyl chloride is the most significant, reaching 240°C , followed by ethylene propylene rubber, while the temperature rising of polyethylene is less than 10°C . In addition, the temperature rise of polyvinyl chloride has far exceeded its softening temperature 85°C , so it cannot be used as the outer sheath material, and the other materials meet the requirements.

Similar research has been conducted by Dong of the Wuhan Ship Communication Research Institute [22]. In their simulations on the CST software, the maximum temperature calculations on polyethylene, polyvinyl chloride and ethylene propylene rubber were 41°C , 794°C and 60°C when the voltages were all $100 \text{ kV}/20\text{kHz}$, respectively. The results of this paper are basically consistent with the results of Dong's, but the simulation results on PVC material are more different. The possible

reason is that the $\tan\delta$ setting of PVC is different.

V. ELECTRIC FIELD IMPROVEMENT AND TEMPERATURE RISE SUPPRESSION

Based on the analysis results from the previous section, in order to improve the electric field distribution and suppress the severe temperature rise at the end of the VLF antenna, a dielectric loss eliminator is designed and the effectiveness of the device is verified by simulation.

A. Modelling of a dielectric loss eliminator

In view of the electric field distortion and temperature rise at the end of the VLF antenna, dielectric loss eliminator is designed, which is used to achieve the electric isolation between the antenna and the floating platform, to reduce the electric field intensity, to eliminate the dielectric loss and to suppress the temperature rise [23-25]. Figure 16 shows the schematic diagram of the dielectric loss eliminator. The parameters of the dielectric loss eliminator are shown in Table 3.

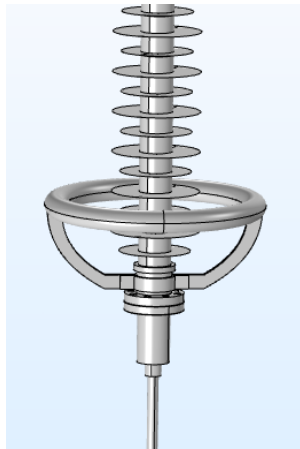


Fig. 16. Schematic diagram of dielectric loss eliminator.

Table 3: Parameters of the dielectric loss eliminator

| Tube Radius/mm | Corona Ring Radius/mm | Corona Ring Height |
|----------------|-----------------------|--------------------|
| 20 | 200 | 172.6 |

The process of solving the equation using the finite element method requires the determination of the definite solution of the equation based on the boundary conditions of the field. The edge value problem at the end of the VLF antenna in this paper is summarized by the constraint equations:

$$\left\{ \begin{array}{l} \nabla^2\varphi = -\frac{\rho}{\varepsilon - i\varepsilon''} \\ \varphi = \varphi(x, y, z) \\ \varphi(r)|_{r \rightarrow \infty} = 0 \\ ((\varepsilon_1' - i_1'')\frac{\partial\varphi}{\partial n}) - ((\varepsilon_2' - i_2'')\frac{\partial\varphi}{\partial n}) = \sigma. \end{array} \right. \quad (16)$$

In order to refine the calculation as much as possible within the range that the computer can bear, the mesh size is set to 1mm.

B. Electric field improvement by dielectric loss eliminator

The improvement effect of the electric field is analyzed after adding the dielectric loss eliminator. Setting the calculation conditions: $U=120$ kV and $f=10$ kHz. The electric field distribution with the dielectric loss eliminator is shown in Fig. 17.

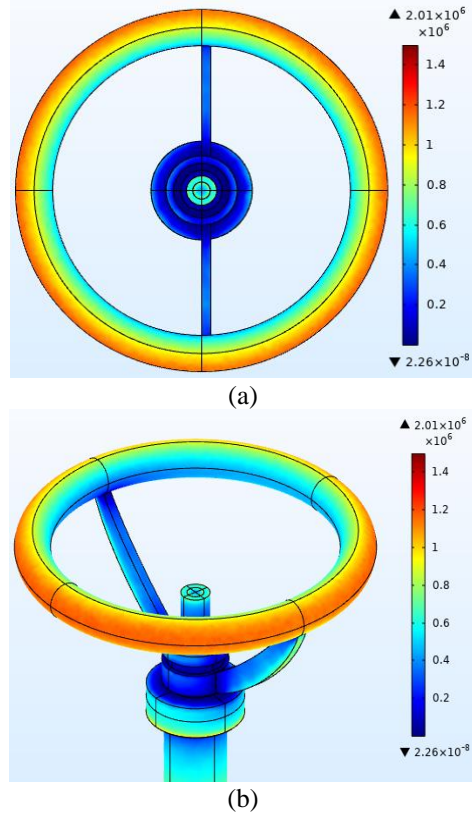


Fig. 17. Distribution of electric field at the terminal of VLF antenna: (a) vertical view; (b) front view.

Compared to Fig. 4, it can be seen from Fig. 17 that the electric field intensity on the outer surface of the dielectric loss eliminator is the highest. After increasing the dielectric loss eliminator, the electric field intensity of the antenna system is significantly reduced, and the maximum electric field intensity is only 2.01×10^6 V/m, which indicates that the dielectric loss eliminator has a significant effect on the improvement of the electric field intensity at the antenna end.

Figure 18 shows the radial distribution of the electric field at the end of the VLF antenna after increasing the dielectric loss eliminator. It can be seen from Fig. 18 that:

(1) The maximum electric field intensity at the end of the VLF antenna is 1.57×10^6 V/m, which is smaller than the corona field intensity of air.

(2) The electric field intensity gradually decreases in the air domain. In the range of radial distance from -9.25 mm to +9.25 mm, the electric field intensity decreases from 1.57×10^6 V/m to 4.4×10^5 V/m, which decreases about 72%, and the electric field intensity at the axis is the lowest.

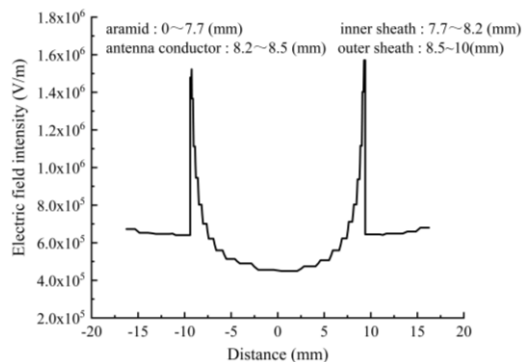


Fig. 18. Radial distribution curve of the electric field at the antenna end.

C. Temperature rise suppression by dielectric loss eliminator

According to the above analysis, the electric field intensity at the terminal of the antenna is improved to a great extent by using the dielectric loss eliminator. Theoretically, the antenna end is in an alternating electric field, and the heating power caused by the dielectric loss is directly proportional to the square of the electric field intensity, so the significant reduction of the electric field intensity will have an obvious inhibitory effect on the temperature rise of the antenna end. The following carries out the simulation calculation of the temperature field at the terminal of the antenna to analyze the temperature rise inhibition effect after adding dielectric loss eliminator. Setting the $U=120$ kV, $f=10$ kHz, and the initial temperature $T=40^\circ\text{C}$. The distribution characteristics of the temperature field at the terminal of the VLF antenna is obtained by simulation calculation, as shown in Fig. 19.

As can be seen from Fig. 19:

(1) The temperature of the metal parts at the end of the antenna barely changes because the current at the terminal of the antenna is zero and there is no Joule heat.

(2) There is a temperature rise phenomenon at the connection between the dielectric loss eliminator and epoxy core rod. The maximum temperature is 40.8°C , and the temperature rise is 0.8°C , which is caused by the dielectric loss of the epoxy core rod in the alternating field. However, when the dielectric loss eliminator is

adopted, the electric field intensity has obviously decreased, so the temperature rise is very small.

(3) The electrical performance parameters of the epoxy core rod are similar to ethylene propylene rubber materials. That is to say, the dielectric constant and tangent of the loss angle of epoxy core rod are similar to ethylene propylene rubber. In Section IV, under $U=120$ kV and $f=10$ kHz, the temperature rise of ethylene propylene rubber exceeds 20°C , while the temperature rise of the epoxy core rod is only 0.8°C . It can be concluded that the temperature rise at the terminal of the VLF antenna can be significantly suppressed by using the dielectric loss eliminator.

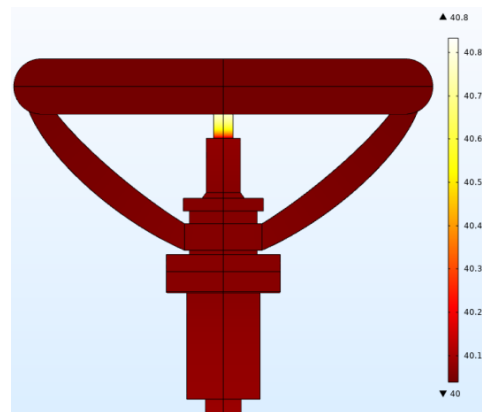


Fig. 19. Cloud diagram of temperature rise.

VI. CONCLUSION

The distribution characteristics and values of the electric field and temperature field at the end of VLF antenna are obtained by the simulation calculation. The effects of the excitation source, the diameter of the antenna conductor, and the material properties of the outer sheath of the antenna on the electric field are studied. It is found that the electric field intensity at the terminal of the VLF antenna increases with increased magnitude of the excitation voltage, whereas the frequency of the excitation has no effect on the electric field. The diameter of the antenna conductor is negatively related to the electric field intensity. In addition, the temperature at the terminal of the VLF antenna is positively correlated with the magnitude and the frequency of the excitation voltage, and the influence of the outer sheath material on the temperature rise is significant.

A dielectric loss eliminator is designed to improve the electric field distribution and suppress the temperature rise, and the effect of the designed device is verified to be very significant by simulation. In practice, the use of the dielectric loss eliminator can effectively avoid VLF antenna breakage accidents due to temperature rise.

REFERENCES

- [1] M. L. Burrows, "ELF communications antennas," *IEEE Electromagn. Wave*, vol. 24, no. 11, pp. 863, May 1978.
- [2] L. B. Pedersen, L. Persson, and M. Bastani, "Airborne VLF measurements and mapping of ground conductivity in Sweden," *J. Appl. Geophys.*, vol. 67, no. 3, pp. 250-258, Nov. 2007.
- [3] T. A. Miš, "The concept of an airborne VLF transmitter with vertical electric dipole antenna," in *Symposium on Antennas and Propagation & USNC/URSI National Radio Science Meeting*, Boston, MA, pp. 1667-1668, 2018.
- [4] L. L. Klessig and V. L. Strite, "The ELF odyssey: National security versus environmental protection," *Environ. Hist. Rev.*, vol. 6, no. 2, pp. 126-128, Oct. 1980.
- [5] Z. W. Jin, "VLF/SLF wave propagation and its application on communication and navigation for submarine," *Equip. Environ. Eng.*, vol. 5, no. 3, pp. 57-61+86, Apr. 2008.
- [6] C. F. Zhan, "Discussion on the technical methods of geological and mineral exploration," *China Standardization*, vol. 5, no. 11, pp. 121-122, Jan. 2019.
- [7] J. J. Doherty, "Submarine communication," *J. Acoust. Soc. Amer.*, vol. 69, no. 1, pp. 335, Nov. 1981.
- [8] R. Barr, D. L. Jones, and C. J. Rodger, "ELF and VLF radio waves," *J. Atmos. Sol.-Terr. Phys.*, vol. 62, no. 17, pp. 1689-1718, June 2000.
- [9] T. S. Zhang, Z. Z. Xu, and M. H. Zheng, "Application of VLF electromagnetic method in ore body spatial location prediction," *Geol. Sci. Technol. Informat.*, vol. 18, no. 4, pp. 85-88, Dec. 1999.
- [10] Y. Wei, "A communication system application based on floating platform," *Communication & Information Technology*, vol. 186, no. 4, pp. 72-74, Dec. 2010.
- [11] H. C. Koons and M. H. Dazey, "High-power VLF transmitter facility utilizing a balloon lofted antenna," *IEEE Transactions on Antennas and Propagation*, vol. 31, no. 2, pp. 243-248, 1983.
- [12] R. Cuggia, J. L. Dubard, and M. Ney, "Numerical characterization of insulators for VLF antennas," *Annual Review of Microbiology*, vol. 6, no. 6, pp. 207-208, 2009.
- [13] T. H. Deng, C. Liu, and J. Zhang, "High voltage insulator for high power VLF transmitting antenna," *Ship Electron. Eng.*, vol. 36, no. 5, pp. 168-171, May 2016.
- [14] Y. Liu, F. S. Deng, H. Q. Sun, W. Zha, J. Liu, and T. Cao, "Electromagnetic characteristics of airborne dual trailing antenna for the submarine communication," in *Proc. 2018 Int. Appl. Comput. Electromagn. Soc. Symp. - China (ACES)*, Beijing, China, pp. 1-2, 29 July-1 Aug. 2018.
- [15] L. Yong, D. Fangshun, S. Hengqing, W. Qisi, and S. Liyuan, "Simulation on the electromagnetic environment in the carrier of airborne VLF wire antennas," in *Proc. 2018 IEEE Int. Conf. Comput. Electromagn. (ICCEM)*, Chengdu, China, pp. 1-3, 26-28 Mar. 2018.
- [16] J. Chen, D. Su, Y. Liu, and N. Wu, "Simulation analysis of airborne VLF Wire Antennas based on FEM," in *Proc. 2011 Int. Conf. Electron., Commun. Control (ICECC)*, Ningbo, China, pp. 2276-2279, 9-11 Sep. 2011.
- [17] R. Cuggia, J. L. Dubard, M. Ney, and C. Pichot, "Numerical characterization of insulators for VLF antennas," in *Proc. 2009 3rd European Conf. Antennas Propag.*, Berlin, Germany, pp. 1570-1572, 2009.
- [18] F. Yang, X. X. Wu, S. M. Chen, and L. Fang, "Characteristics of dielectric loss and electric field homogenization at the terminal opening of high power communication antenna," *Chinese J. Radio Sci.*, vol.33, no. 2, pp. 162-169, May 2018.
- [19] J. G. Zhou, "A calculation method of very low frequency transmitting antennas corona voltage," *Telecom Power Technol.*, vol. 31, no. 4, pp. 49-51, Apr. 2014.
- [20] K. Mao, X. Li, C. Wei, Z. Ma, and X. Wu, "Numerical analysis of electric field distribution at the terminal of VLF antenna," in *Proc. 2019 IEEE 19th Int. Conf. Commun. Technol. (ICCT)*, Xi'an, China, pp. 819-822, 2019.
- [21] X. Y. Shi, Y. B. Wang, B. Huang, and M. Xie, "Research on the safety protection distance of electromagnetic radiation for high power very low frequency antenna array," *Ship Electron. Eng.*, vol. 39, no. 12, pp. 199-203, Dec. 2019.
- [22] J. Dong and J. X. Luo, "Analysis of VLF balloon antenna cable terminal loss and heating-up," *Ship Electron. Eng.*, vol. 35, no. 12, pp. 159-161, Dec. 2015.
- [23] J. Yang. "Research on effectiveness evaluation of long wave VLF communication system," *Information System Engineering*, pp. 24, Sep. 2018.
- [24] L. S. Huang and Y. Z. Jiang. "Matrix quantity method study on the performance of VLF balloon antenna," *Modern Communication Technology*, vol. 001, pp. 17-21, 2005.
- [25] Z. G. Zhang. "Research on VLF horizontal low frame transmitting antenna technology," *China Academy of Naval Research*, MS, 2012.
- [26] B. M. Hamdi, M. Tegar, and A. Mekhaldi. "Optimal design of corona ring on HV composite insulator using PSO approach with dynamic population size," *IEEE Transactions on Dielectrics and Electrical Insulation*, vol. 23, no. 2, pp. 1048-1057, 2016.



Xianqiang Li (M'17) was born in Xiangyang, China in 1973. He received the B.S., M.S. and Ph.D. degrees in High Voltage and Insulation Technology from Wuhan University, Wuhan, China, in 1995, 1998 and 2015, respectively. He is currently a Lecturer of the Electrical Engineering Department of Wuhan University of Technology, Wuhan, China. His research interests include lightning protection and grounding technology, transformer modeling, external insulation of electrical equipment and substation live working.



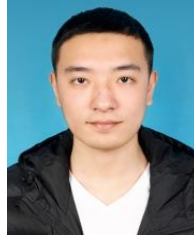
Kedan Mao was born in Leshan, China in 1994. He received the B.E. and M.S. degrees in 2018, and 2020, respectively. He is currently an Assistant Engineer of the Nuclear Power Institute, Chengdu, China. His research interests in external insulation of electrical equipment.



Ao Wang was born in Wuhan, China in 1996. He received the B.Sc. degree in Mechanical Design Manufacture and Automation from Jiangnan University, Wuhan, China. He is pursuing the M.Sc. degree in the School of Automation, Wuhan University of Technology right now. His research interests are electrical theory and new technology.



Ji Tian was born in Hubei, China in 1997. He received the B.Sc. degree in Electrical Engineering from China Three Gorges University, Yichang, China, in 2019. At present, he is pursuing the M.Sc. degree in the School of Automation, Wuhan University of Technology. His research areas are mainly on high voltage technology and electrical insulation.



Wenchuang Zhou was born in Huanggang, China in 1997. He received the B.Sc. degree in Automation from Hubei University of Technology, Wuhan, China, in 2018. At present, he is pursuing the M.Sc. degree in the School of Automation, Wuhan University of Technology. His research interests are high voltage, insulation and laser cleaning insulator contamination.

Design and Analysis of a Triple-band Non-zonal Polarization Electromagnetic Metamaterial Absorber

Han Wu, Shijun Ji*, Ji Zhao, Zhiyou Luo, and Handa Dai

School of Mechanical and Aerospace Engineering, Jilin University, Changchun, 130025, China
 hwu19@mails.jlu.edu.cn, jishijun@126.com*, jzhao@jlu.edu.cn, zyluo19@mails.jlu.edu.cn, dhd@jlu.edu.cn

Abstract — A facile design of a novel triple-band electromagnetic metamaterial absorber (MMA) with polarization insensitive property is proposed in this paper. Each unit of the MMA consists of upper copper resonator and bottom copper plate with middle dielectric FR-4 between them. The MMA performs three absorption peaks at 16.919 GHz, 21.084 GHz and 25.266 GHz with absorption rates 99.90%, 97.76% and 99.18%, respectively. The influence of the main structural parameters on the frequencies and absorption rates is analyzed. The absorption mechanism of the absorber is explained by electric field, magnetic field and surface current distributions, which is supported by the electromagnetic parameters, affected with magnetic resonance. The polarization-insensitivity of TE wave is verified by observing the effects of the polarization angle change from 0-90°. The MMA can be applied in radiation, spectrum imaging detector, electromagnetic wave modulator, and so on.

Index Terms — Electromagnetic metamaterials, polarization-insensitive, resonator, triple-band.

I. INTRODUCTION

Metamaterial is a kind of composite material with subwavelength structure, it has some special physical property which doesn't possess by other nature materials [1, 2]. The composites that own man-made structure can be an important material for the manufacture of electromagnetic wave absorption instruments due to geometrical structure parameters and material properties of the metamaterials can be adjusted. In the 2008, Landy [3] proposed a design concept of electromagnetic wave metamaterial absorber (MMA) for the first time, scholars are beginning to become increasingly interested in using artificial metamaterials to pursue near-perfect absorbers. In recent years, MMA research has gradually spread to the physical, informational and engineering fields. Until now, its potential application has expanded to different industries, such as stealth material [4], super lens [5], sensor [6, 7], thermal imaging instrument [8] and so on [9, 10]. The excellent performance has been shown in

single-band [11-15], dual-band [16-20], multi-band [21-23] and broadband operations [24-27].

In some microwave ranges, multi-band MMA has also appeared frequently in recent studies. The metamaterials have some unique electromagnetic properties, which can be constructed by human design. Jianping Xu et al [28] propose a three-band metamaterial absorber, its absorption peaks are 4.36 GHz, 8.41 GHz and 14.67 GHz, three peaks absorption rates are 99.8%, 97.4% and 99.9% respectively. Nguyen et al. [29] analyzed the causes of polarization insensitivity, with two absorption peaks at 10.15 GHz and 10.50 GHz and the absorption rate of around 96.5%. A bandwidth-enhanced microwave absorber using a resonant metamaterial is presented by Lee et al. [30]. They obtained two absorption peaks at 9.8 GHz and 10.3 GHz, and the absorption rate were 99% and 98%, respectively. Li et al. [21] proposed a new metamaterial absorber with a tetra-arrow resonator (TAR) structure, two absorption peaks operating at 6.16 GHz and 7.9 GHz can be obtained, whose absorptivity came up to 99%. A triple-band metamaterial absorber was presented by Huang et al. [23], the proposed absorber can perform absorption peaks at three resonant frequencies 9.86 GHz, 12.24 GHz and 15.34 GHz with the absorption of 99.4%, 96.7% and 99.1%, respectively. Bian et al. [31] designed and fabricated a novel triple-band polarization-insensitive wide-angle ultra-thin microwave metamaterial absorber, it shows three distinctive perfect absorption peaks at frequencies of 3.07 GHz, 5.65 GHz and 8.11 GHz with absorption rates 99.87%, 99.98% and 99.99%, respectively. A new kind of multi-band metamaterial absorber based on the concentric ring resonators is engineered by Gunduz et al. [32] with the absorption peak of 5.98 GHz and 11.12 GHz, and the absorption rate were 99.16% and 99.95%. Shen et al. [33] designed a microwave triple-band metamaterial absorber with three absorption peaks of 99% at 4.06 GHz, 93% at 6.73 GHz and 95% at 9.22 GHz respectively. However, the absorption peaks of the above absorbers are all below the K-band, and the surface structure is relatively sophisticated, and not all peaks are perfect in terms of

absorption performance.

In this paper, a three-layer structure was used to design the triple-band MMA, which consists of top copper three-fork resonator and bottom copper plate with medium FR-4. Through a large amount of simulation, it can be obtained that this absorber has three absorption peaks of 99.90% at 16.919 GHz, 97.76% at 21.084 GHz and 99.18% at 25.266 GHz, respectively. The MMA has higher absorption rates: the absorption rates of the first and third peaks are over 99.18%, and the absorption rate of the second peak is close to 98%. In addition, the distribution of electromagnetic field and surface current is analyzed in detail, and the polarization insensitivity of the absorber is verified by observing the effect of the polarization angle change on absorption. In order to obtain the outstanding absorption rates, the thickness of dielectric layer and the dimension of unit-cell structure were iteratively optimized by using electromagnetic simulation software, and analyzed how these changes in parameters interfere in the absorption peaks.

II. ABSORPTION MECHANISM

The metamaterials absorbent apparatus has the sub-wavelength characteristic, which is composed of the periodic arrangement of the unit structure, and its resonance characteristics are mainly determined by the geometrical parameters of the unit structure, such as pattern shape, dimension and arrangement, as well as the electromagnetic parameters of each layer, so the reasonable optimization design unit structure in a certain frequency range can realize the effective regulation of the resonant frequency.

In order to achieve perfect absorption, the metamaterial absorber should generally meet two basic requirements: Firstly, the structure of the design unit is optimized so that the equivalent input impedance is matched with the free space impedance [34]. Second, it is required that the metamaterial structure has a sufficiently large imaginary part of the dielectric constant and the magnetic permeability to satisfy the electromagnetic wave can be absorbed as soon as possible after entering the metamaterial structure. To prevent transmission, the bottom layer is covered with a metal film so that $T(\omega) = 0$.

When the electromagnetic wave is normally incident to the surface of the metamaterial structure, retrieved electromagnetic parameters of the metamaterial can be calculated according to the definition of S parameter [34, 35]. The reflection rate and transmission rate were: $R(\omega) = |S_{11}|^2$ and $T(\omega) = |S_{21}|^2$, absorption rate of corresponding metamaterial $A(\omega)$ can be expressed by Equation (1):

$A(\omega) = 1 - R(\omega) - T(\omega) = 1 - |S_{11}|^2 - |S_{21}|^2$. (1)
For S_{21} with a thickness of d , which can be expressed by Equation (2):

$$S_{21}^{-1} = \left[\sin(nkd) - \frac{i}{2} \left(z + \frac{1}{z} \right) \cos(nkd) \right] e^{ikd}. \quad (2)$$

Where, $n = n_1 + in_2$ is the complex refractive index of the metamaterial. $z = z_1 + iz_2$ is complex impedance. $k = \omega/c$ is the number of transmission waves in the metamaterial, c is the speed of light.

The reflectivity $R(\omega)$ and transmittance $T(\omega)$ of the electromagnetic wave in the metamaterial can be written as following Equation (3) and Equation (4):

$$\lim_{Z(\omega)=1} R(\omega) = |S_{11}|^2 = \left[\frac{Z(\omega) - 1}{Z(\omega) + 1} \right]^2 = 0, \quad (3)$$

$$\begin{aligned} \lim_{n_2 \rightarrow \infty} T(\omega) &= |S_{21}|^2 = \lim_{n_2 \rightarrow \infty} (e^{-i(n_1-1)kd} \cdot e^{n_2kd}) \\ &= \lim_{n_2 \rightarrow \infty} e^{-2n_2kd} = 0. \end{aligned} \quad (4)$$

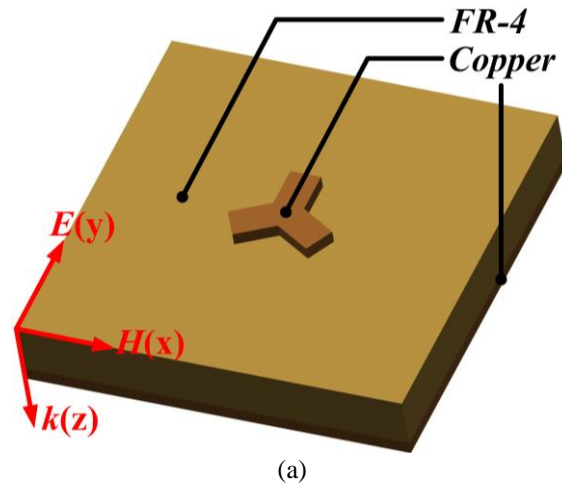
Then the absorption rate of the $A(\omega)$ can be calculated by Equation (5):

$$A(\omega) = 1 - R(\omega) - T(\omega) = 1. \quad (5)$$

According to the above analysis, when the impedance of the metamaterial absorber matches the impedance of the free space [37], that is $Z(\omega) = 1$, only a little proportion of electromagnetic waves are reflected, almost all waves enter the micro-structures of the metamaterial and finally lost.

III. DESIGN AND SIMULATION

The proposed MA structure is composed of the combination of three same size and shape elongated patch resonators as shown in Fig. 1. It consists of the three-layer as described above with copper membranes of the top and bottom layers. The material of the middle layer is FR-4. After geometrical optimization, the optimal structural parameters of the unit cell are obtained as follows: $p=15$ mm, $t_1=0.018$ mm, $a=0.6$ mm, $b=2$ mm, $t_2=1.2$ mm, $t_3=0.018$ mm. $\sigma=5.96 \times 10^7$ S/m is the electric conductivity of copper and $\epsilon_r=4.3$ is the electric permittivity of dielectric spacer, corresponding to the loss tangent $\tan(\delta)=0.025$.



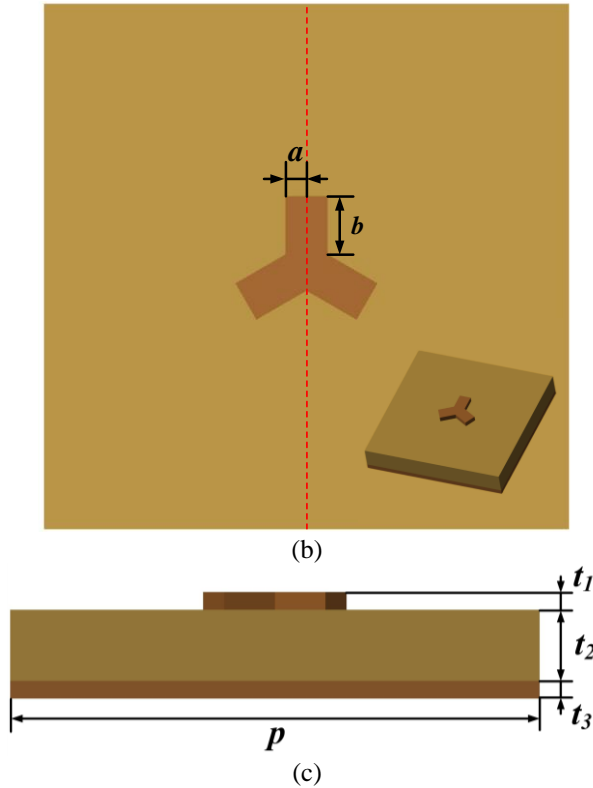


Fig. 1. The structure of the proposed MMA: (a) perspective view of the unit cell, (b) top view, and (c) side view.

The electromagnetic characteristics of the MMA are designed and analyzed by an electromagnetic software CST. The Hexahedron calculation multiplier drives a wired frequency domain analysis solver to solve a frequency range of 10 GHz to 27 GHz. Because the proposed MMA can be seen as an infinitely large periodic plane, so the wave source was set to plane wave with normal incident which was opposite to the z direction, the background was set to normal, boundary condition is set to unit cell both in the x, y direction and open in the z direction. In the simulation, the principle is given as mentioned above, the absorption rate $A(\omega)$ can be derived from Equation (1).

IV. RESULTS AND DISCUSSIONS

Figure 2 shows the calculated absorption spectrum of the triple-band MMA. Obviously, when $T = 0$, $A = 1 - R$, the calculation results are almost consistent with the previous theoretical analysis. The three absorption peaks were 16.919 GHz, 21.084 GHz and 25.266 GHz at 99.90%, 97.76% and 99.18%, respectively. Compared with the multi-band MMA absorption listed in Table 1, the proposed MA this time has higher absorption rates in the K_u and K bands. Two of the peaks are above 99%, another is close to 98%. The polarization insensitivity of

the triple-band MMA is analyzed here. When the TE wave is normal incident on the surface. Electric field vector is parallel to the x -axis, and the incident wave is parallel to the z axis. The polarization angle of TE wave is the deflection angle between the electric field vector and the x -axis. The different absorption effects of MMA can be obtained by changing its angle degrees. Figure 3 shows that when the polarization angle changes, the absorption frequency and absorption rates of the absorber are almost unchanged. The performance of this study shows that the MMA is not sensitive to polarization.

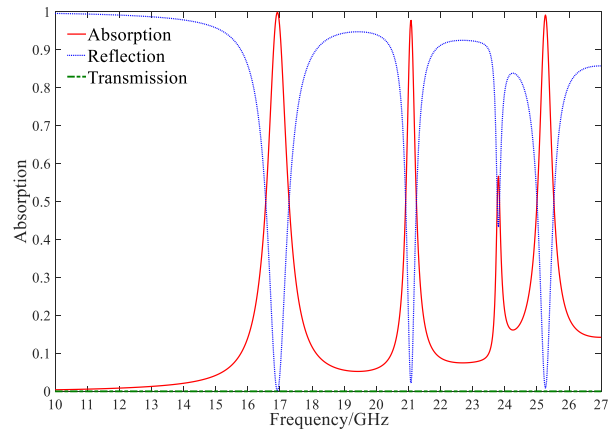


Fig. 2. Triple-band MMA's simulated absorption, reflection and transmission spectra with $p=15$ mm, $a=0.6$ mm, $b=2.0$ mm, $t_1=0.018$ mm, $t_2=1.2$ mm and $t_3=0.018$ mm.

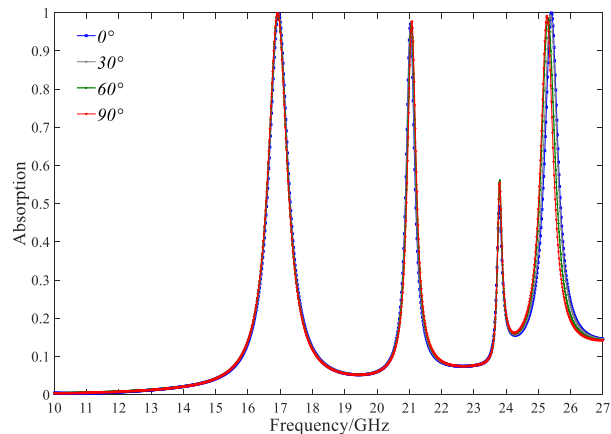


Fig. 3. Absorption spectra at different polarization angles.

The comparison of the CST and HFSS (15 GHz - 27 GHz) results is shown in Fig. 4. Because the algorithm is different, the calculation error is also different. CST is a simulator based on FDTD (Finite Difference Time Domain Method) electromagnetic field solving algorithm, and HFSS is a simulator based on FEM (Finite Element Method) electromagnetic field solving algorithm.

Different mesh partitioning accuracy and different residuals may also lead to deviation of the results, even the difference in the simulation results in the frequency domain will be more obvious. However, the absorption trend of the two groups of simulation spectra is the same, although the resonance frequency is slightly different, the peaks value are highly similar. The relative errors of absorption rate and frequency are shown in Table 1 and Table 2, respectively. The maximum relative error of frequency is only 11.07% and the lowest relative error of absorption rate can be as low as zero.

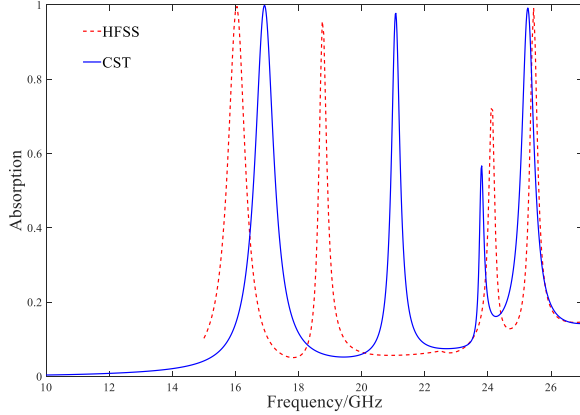


Fig. 4. Comparison of CST and HFSS absorption spectra of the proposed MA.

Table 1: The CST and HFSS simulation data for absorption rate of each resonance peak

| Peaks | HFSS Absorption A_i | CST Absorption \hat{A}_i | Relative Error $= \frac{e_i}{\hat{A}_i} = \frac{A_i - \hat{A}_i}{\hat{A}_i} \times 100\%$ |
|-------|-----------------------|----------------------------|---|
| 1 | 0.996 | 0.999 | -0.3003% |
| 2 | 0.9559 | 0.9776 | -2.22% |
| 3 | 0.9918 | 0.9918 | 0% |

Table 2: The CST and HFSS simulation data for frequency of each resonance peak

| Peaks | HFSS Frequency F_i | CST Frequency \hat{F}_i | Relative Error $= \frac{e_i}{\hat{F}_i} = \frac{F_i - \hat{F}_i}{\hat{F}_i} \times 100\%$ |
|-------|----------------------|---------------------------|---|
| 1 | 16.05 GHz | 16.919 GHz | -0.3035% |
| 2 | 18.75 GHz | 21.084 GHz | -11.07% |
| 3 | 24.45 GHz | 25.266 GHz | -3.2296% |

Here, the electric field, magnetic field and surface current distribution of the absorber is analyzed through the Fig. 5, Fig. 6. and Fig. 7. In the proposed unit, the

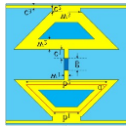

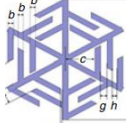
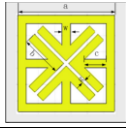
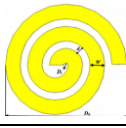
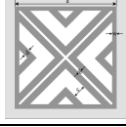

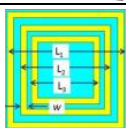
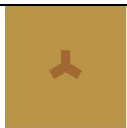
horizontal and vertical direction are electric field direction (E) and magnetic field direction (H), respectively as given by Fig. 1. In the case of a frequency of 16.919 GHz, when the electromagnetic wave incidents into the MMA, electric charges in the top three-fork star structure move in both positive and negative directions on the y -axis, clustered on the sides, and the dipole resonance is formed in this structure, as shown in Fig. 6 (a). Because the top layer is inductive with the charge in the bottom layer, from Fig. 7, that two layers form a reverse current on their respective surfaces. As shown in Fig. 6 (a), in the metamaterial structure designed in this paper, the magnetic dipole resonance is induced due to the existence of reverse current. Thus, most of the magnetic field distribution occupies the intermediate dielectric layer. At the frequency of 16.919 GHz, when the electromagnetic wave incidents into the MMA, most of the energy is consumed due to the combined action of dipole resonance and magnetic dipole resonance. Similarly, at the frequency of 21.084 GHz, due to the action of electromagnetic waves, there is a positive and negative charge aggregation on both sides of the top structure, resulting in a powerful electric field at that position, as illustrated by Fig. 5 (b). It is precisely because the opposite current accumulates on the upper and lower sides respectively that the dipole resonance is formed in the structure. The charges in the upper and lower layers of metal induce each other to generate a reverse current, thus forming a loop, as shown in Fig. 7 (b). As shown in Fig. 6 (b), the magnetic field is mainly distributed in the middle dielectric layer, which clarifies the location of magnetic resonance. Therefore, when the incident frequency of electromagnetic waves is 21.084 GHz, the coupling effect of electric dipole resonance and magnetic dipole resonance completes the loss. At the frequency of 25.266 GHz, the electromagnetic wave is incident, and the top layer and the bottom metal gather more positive and negative charges on the upper and lower sides. Because of the sensing between the charges, the electric field presents a state as shown in Fig. 5 (c), where the top layer of the structure and the bottom metal surface also generate a reverse current, as illustrated by Fig. 7 (c). It can be seen from Fig. 6 (c) that the distribution of the magnetic field concentrated in the intermediate dielectric layer is also due to the presence of magnetic resonance in the structure. Thus, by the same token, the incident electromagnetic wave is consumed at a frequency of 25.266 GHz. The structure can form electrical resonance and magnetic resonance, which can absorb the incident electromagnetic wave with higher absorption rates.

Figure 8 shows the real and imaginary parts of equivalent permittivity and permeability ($Re \epsilon(\omega)$, $Im \epsilon(\omega)$, $Re \mu(\omega)$ and $Im \mu(\omega)$) respectively, which are extracted by retrieved effective parameters. Due to $R(\omega) = |S_{11}|^2 = \left[\frac{Z(\omega)-1}{Z(\omega)+1} \right]^2$ and the impedance $Z(\omega) =$

$\sqrt{\mu/\epsilon}$, relatively perfect impedance matching is achieved at the frequencies of 16.919 GHz, 21.084 GHz and 25.266 GHz. At this point, the absorber responds to the external field, generates the opposite magnetic dipole, resulting in magnetic resonance and forming absorption peaks which were shown in the spectrum [36]. Comparing electric-field distributions at 16.919 GHz, 19.5 GHz, 21.084 GHz, 23 GHz and 25.266 GHz as shown by Fig. 5 and Fig. 9, obviously there are stronger fields at 16.919

GHz, 21.084 GHz and 25.266 GHz, Fig. 8 gives that the real and imaginary parts of the permittivity and the permeability are equal at these frequencies, that to say, the impedance at these frequencies is well matched. While at 16.919 GHz and 21.084 GHz, the real and imaginary parts of the permittivity and the permeability are not equal, which means the impedance don't match, leading to weaker electric fields. There are similar laws for magnetic-field distributions.

Table 3: Absorption rates comparison with other kinds of multi-band MMAs

| Absorber | Absorption Rate | Working Frequency (GHz) | Resonance Frequency (GHz) | Structure of Top Layer | Materials | Unit Cell Size (mm ²) |
|--------------------|----------------------------|-------------------------|----------------------------|--|---------------------------------------|-----------------------------------|
| Reference [28] | 99.80% 97.40% 99.90% | 2-16.5 | 4.60 8.41 14.67 |  | Copper -FR-4- Copper | 10×10 |
| Reference [29] | 95.59% 94.20% | 9.5-11.5 | 10.15 10.50 |  | Copper -FR-4- Copper | 12×12 |
| Reference [30] | 99.00% 98.00% | 8-12 | 9.80 10.30 |  | Conductor -Substrate- Conductor | 15×15 |
| Reference [21] | 99.00% 99.00% | 4-10 | 6.16 7.79 |  | Copper -FR-4- Copper | 14×14 |
| Reference [23] | 99.40% 96.70% 99.10% | 8-17 | 9.86 12.24 15.34 |  | Copper -FR-4- Copper | 18×18 |
| Reference [31] | 99.87% 99.98% 99.99% | 2-10 | 3.07 5.65 8.11 |  | Copper -FR-4- Copper | 21.6×21.6 |
| Reference [32] | 99.16% 99.95% | 4-24 | 5.98 11.12 |  | Copper -FR-4- Copper | 18×18 |
| Reference [33] | 99.00% 93.00% 95.00% | 2-12 | 4.06 6.73 9.22 |  | Copper -FR-4- Copper | 20×20 |
| The presented work | 99.90% 97.76% 99.18% | 10-27 | 16.919 21.084 25.266 |  | Copper -FR-4- Copper | 15×15 |

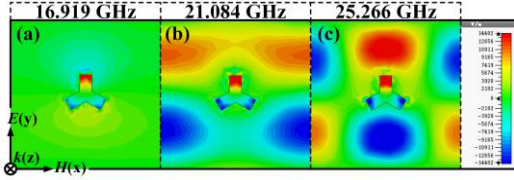


Fig. 5. Electric-field distributions of the MMA: (a) 16.919 GHz, (b) 21.084 GHz, and (c) 25.266 GHz.

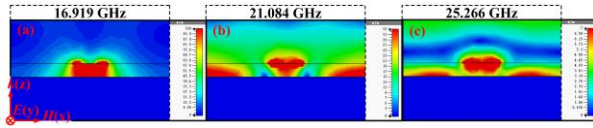


Fig. 6. Magnetic-field distributions: (a) 16.919 GHz, (b) 21.084 GHz, and (c) 25.266 GHz.

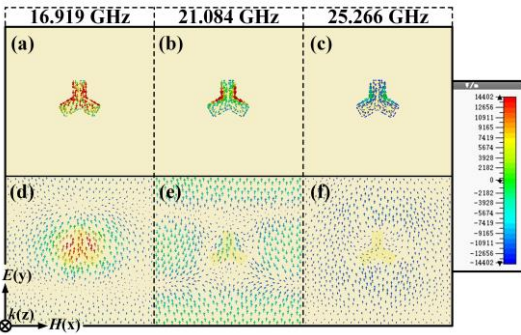


Fig. 7. Surface current distributions: (a) Top layer at 16.919 GHz, (b) top layer at 21.084 GHz, (c) top layer at 25.266 GHz, (d) bottom layer at 16.919 GHz, (e) bottom layer at 21.084 GHz, and (f) bottom layer at 25.266 GHz.

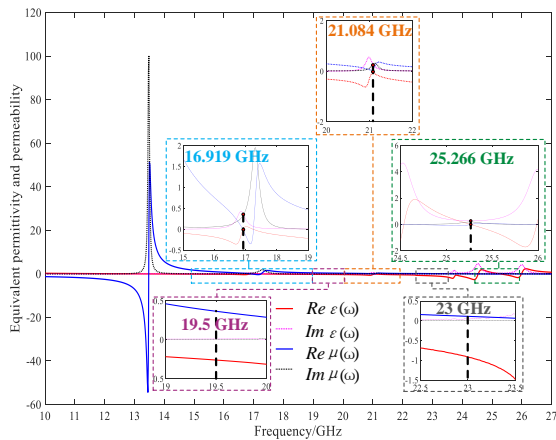


Fig. 8. Extracted electromagnetic parameters: real and imaginary parts of permittivity $Re \epsilon(\omega)$, $Im \epsilon(\omega)$ and permeability $Re \mu(\omega)$, $Im \mu(\omega)$.

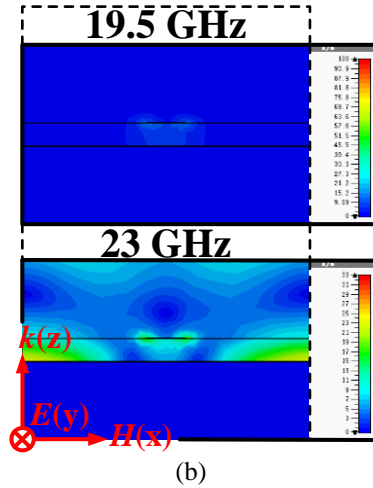
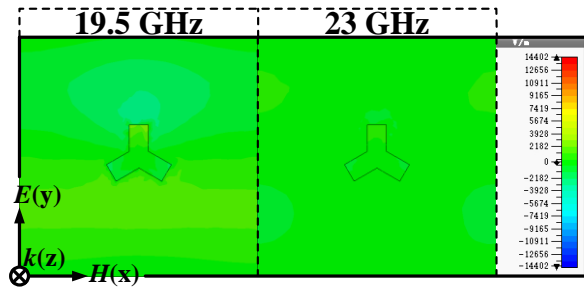


Fig. 9. Electric-field distributions: (a) and magnetic-field distributions: (b) of the MMA for 19.5 GHz and 23 GHz.

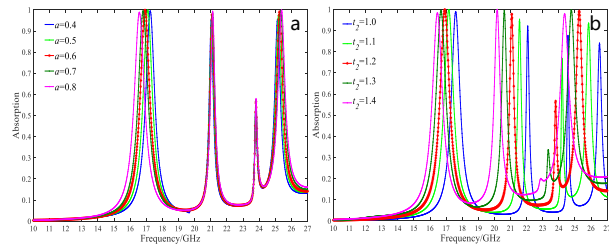


Fig. 10. Relationships of triple-band absorption spectra and geometric parameters. (a) Different line width a . (b) Different thickness t_2 of the dielectric layer.

Optimization of main geometric parameters about the structure is carried out and how key structural parameters affect the MMA absorption rate is analyzed. The effect of the parameter a on absorption rates is shown in Fig. 10 (a) and Table 4. As the parameter a increased from 0.4 mm to 0.8 mm, the three absorption peaks also changed. The absorption of the first crest increased from 0.9954 to 0.9993 and then decreased to 0.9882, and the absorption rate of the second crest gradually increased by 0.0430, while the absorption

rate of the third crest increased by 0.0446. When the absorption rate changes slightly, the central frequency corresponding to the peak is also changed, and the three frequency values are moving 0.663 GHz, 0.085 GHz and 0.255 GHz respectively. Secondly, we analyzed the effect on the absorption rates by changing the thickness of the intermediate dielectric layer t_2 , as shown in Fig. 10 (b) and Table 5. When the thickness t_2 increased from 1.0

mm to 1.4 mm by 0.1 mm step, the 1st and 3rd absorption peaks increased first and then decreased, the second peak increased gradually. The third of these peaks is relatively large, and at the same time as the corresponding frequency is moving 2.159 GHz, the peak absorption rate increases from 0.9795 to 0.9971 and eventually to 0.8409. The frequency variation values corresponding to the first two peaks are 1.139 GHz and 1.904 GHz, respectively.

Table 4: Peaks and frequencies corresponding to different line width values

| a (mm) | Peak 1 | | Peak 2 | | Peak 3 | |
|-------------|--------------------|------------|--------------------|------------|--------------------|------------|
| | Frequency (GHz) | Absorption | Frequency (GHz) | Absorption | Frequency (GHz) | Absorption |
| 0.4 | 17.242 | 0.9953 | 21.033 | 0.9506 | 25.130 | 0.9552 |
| 0.5 | 17.089 | 0.9993 | 21.050 | 0.9671 | 25.198 | 0.9769 |
| 0.6 | 16.919 | 0.9990 | 21.084 | 0.9776 | 25.266 | 0.9918 |
| 0.7 | 16.800 | 0.9949 | 21.101 | 0.9874 | 25.334 | 0.9980 |
| 0.8 | 16.579 | 0.9882 | 21.118 | 0.9935 | 25.385 | 0.9998 |

Table 5: Peaks and frequencies corresponding to thickness values of different dielectric layers

| t_2 (mm) | Peak 1 | | Peak 2 | | Peak 3 | |
|---------------|--------------------|------------|--------------------|------------|--------------------|------------|
| | Frequency (GHz) | Absorption | Frequency (GHz) | Absorption | Frequency (GHz) | Absorption |
| 1.0 | 17.599 | 0.9891 | 20.207 | 0.9214 | 26.524 | 0.8408 |
| 1.1 | 17.174 | 0.9987 | 20.560 | 0.9534 | 25.844 | 0.9353 |
| 1.2 | 16.919 | 0.9990 | 21.084 | 0.9976 | 25.266 | 0.9918 |
| 1.3 | 16.681 | 0.9938 | 20.608 | 0.9937 | 24.773 | 0.9971 |
| 1.4 | 16.460 | 0.9833 | 20.166 | 0.9986 | 24.365 | 0.9795 |

V. CONCLUSION

A novel triple-band MMA has been designed in the microwave range, and its polarization insensitivity is verified. From the calculational results, it can be seen the MMA has three absorption peaks at 16.919 GHz, 21.084 GHz and 25.266 GHz frequencies, with absorption rates of 0.9990, 0.9776 and 0.9918, respectively. Combined with the absorption mechanism, the absorption characteristics are attributed to the electromagnetic coupling that exists between structures. The shape dimensions of the top metal structure and the thickness of the intermediate dielectric layer both have an effect on absorption performance, but the effect of the change of polarization angle is not obvious, so its polarization insensitivity is verified. When the line width a increases from 0.4 mm to 0.8 mm, the change of three peaks is not obvious, the first increases by 0.0111 and then decreases by 0.0039, and the second third increases by 0.0430 and 0.0446 respectively, while the frequency in which it is located has increased to varying degrees. In the process of increasing the thickness of dielectric layer from 1.0 mm to 1.4 mm, the simulation results show that the change has the greatest influence on the third absorption peak, and the value of its frequency forward movement reaches 2.159 GHz. Compared with the previous reports, the proposed MMA presents a greater practical feasibility

in term of low-frequency microwave and polarization-insensitivity, especially all three peak absorption rates are close to 100%, in addition, it has important value in the fields of thermal radiation measuring instrument, spectrum imaging detector and electromagnetic wave modulator.

ACKNOWLEDGMENT

This work is supported by National Natural Science Foundation of China (Grant No 51775237), Key R&D Projects of the Ministry of Science and Technology of China (Grant Nos. 2018YFB1107600 and 2017YFA0701200), Key scientific research project of Jilin Provincial Department of Education (Grant No. JJKH20200972KJ) and Key Projects of Jilin Province Science and Technology Development Plan (Grant No. 20200401121GX) of China.

REFERENCES

- [1] V. G. Veselago, "The electrodynamics of substances with simultaneously negative values of ϵ and μ ," *Soviet Physics Uspekhi*, vol. 10, no. 4, pp. 509-514, 1968.
- [2] R. A. Shelby, D. R. Smith, and S. Schultz, "Experimental verification of a negative index of refraction," *Science*, vol. 292, no. 5514, pp. 77-79,

- Apr. 2001.
- [3] N. I. Landy, S. Sajuyigbe, J. J. Mock, D. R. Smith, and W. J. Padilla, "Perfect metamaterial absorber," *Physical Review Letters*, vol. 100, no. 20, May 2008.
- [4] S. Maci, "A cloaking metamaterial based on an inhomogeneous linear field transformation," *IEEE T. Antenn. Propag.*, vol. 58, no. 4, pp. 1136-1143, Apr. 2010.
- [5] C. P. Scarborough, Z. H. Jiang, D. H. Werner, C. Rivero-Baleine, and C. Drake, "Experimental demonstration of an isotropic metamaterial super lens with negative unity permeability at 8.5 MHz," *Appl. Phys. Lett.*, vol. 101, no. 1, July 2012.
- [6] M. Bakir, M. Karaaslan, E. Unal, O. Akgol, and C. Sabah, "Microwave metamaterial absorber for sensing applications," *Opto.-Electron. Rev.*, vol. 25, no. 4, pp. 318-325, Dec. 2017.
- [7] C. Chen, Y. P. Sheng, and W. Jun, "Computed a multiple band metamaterial absorber and its application based on the figure of merit value," *Opt. Commun.*, vol. 406, pp. 145-150, Jan. 2018.
- [8] N. I. Landy, C. M. Bingham, T. Tyler, N. Jokerst, D. R. Smith, and W. J. Padilla, "Design, theory, and measurement of a polarization-insensitive absorber for terahertz imaging," *Phys. Rev. B*, vol. 79, no. 12, Mar. 2009.
- [9] C. Sabah, M. D. Thomson, F. Z. Meng, S. Tzanova, and H. G. Roskos, "Terahertz propagation properties of free-standing woven-steel-mesh metamaterials: Pass-bands and signatures of abnormal group velocities," *J. Appl. Phys.*, vol. 110, no. 6, Sep. 2011.
- [10] C. Sabah, F. Dincer, M. Karaaslan, E. Unal, O. Akgol, and E. Demirel, "Perfect metamaterial absorber with polarization and incident angle independencies based on ring and cross-wire resonators for shielding and a sensor application," *Opt. Commun.*, vol. 322, no. 322, pp. 137-142, July 2014.
- [11] H. Tao, N. I. Landy, C. M. Bingham, X. Zhang, R. D. Averitt, and W. J. Padilla, "A metamaterial absorber for the terahertz regime: Design, fabrication and characterization," *Optics Express*, vol. 16, no. 10, pp. 7181-7188, May 2008.
- [12] Y. Avitzour, Y. A. Urzhumov, and G. Shvets, "Wide-angle infrared absorber based on a negative-index plasmonic metamaterial," *Phys. Rev. B*, vol. 79, no. 4, Jan. 2009.
- [13] Y. Z. Cheng, H. L. Yang, Z. Z. Chen, and N. Wu, "Perfect metamaterial absorber based on a split-ring-cross resonator," *Appl. Phys. a-Mater.*, vol. 102, no. 1, pp. 99-103, Jan. 2011.
- [14] J. M. Hao, L. Zhou, and M. Qiu, "Nearly total absorption of light and heat generation by plasmonic metamaterials," *Phys. Rev. B*, vol. 83, no. 16, Apr. 2011.
- [15] F. Alves, B. Kearney, D. Grbovic, N. V. Lavrik, and G. Karunasiri, "Strong terahertz absorption using SiO₂/Al based metamaterial structures," *Appl. Phys. Lett.*, vol. 100, no. 11, Mar. 2012.
- [16] Q. Y. Wen, Y. S. Xie, H. W. Zhang, Q. H. Yang, Y. X. Li, and Y. L. Liu, "Transmission line model and fields analysis of metamaterial absorber in the terahertz band," *Optics Express*, vol. 17, no. 22, pp. 20256-20265, Oct. 2009.
- [17] J. P. Zhong, Y. J. Huang, G. J. Wen, H. B. Sun, P. Wang, and O. Gordon, "Single-/dual-band metamaterial absorber based on cross-circular-loop resonator with shorted stubs," *Appl. Phys. a-Mater.*, vol. 108, no. 2, pp. 329-335, Aug. 2012.
- [18] H. M. Lee and J. C. Wu, "A wide-angle dual-band infrared perfect absorber based on metal-dielectric-metal split square-ring and square array," *J. Phys. D. Appl. Phys.*, vol. 45, no. 20, May 2012.
- [19] Y. Ma, Q. Chen, J. Grant, S. C. Saha, A. Khalid, and D. R. S. Cumming, "A terahertz polarization insensitive dual band metamaterial absorber," *Optics Letters*, vol. 36, no. 6, pp. 945-947, Mar. 2011.
- [20] Y. H. Zhao, Q. Z. Hao, Y. Ma, M. Q. Lu, B. X. Zhang, M. Lapsley, I. C. Khoo, and T. J. Huang, "Light-driven tunable dual-band plasmonic absorber using liquid-crystal-coated asymmetric nanodisk array," *Appl. Phys. Lett.*, vol. 100, no. 5, Jan. 2012.
- [21] L. Li, Y. Yang, and C. H. Liang, "A wide-angle polarization-insensitive ultra-thin metamaterial absorber with three resonant modes," *J. Appl. Phys.*, vol. 110, no. 6, Sep. 2011.
- [22] Y. Ozturk and A. E. Yilmaz, "Multiband and perfect absorber with circular fishnet metamaterial and its variations," *Applied Computational Electromagnetics Society Journal*, vol. 31, no. 12, Dec. 2016.
- [23] X. J. Huang, H. L. Yang, S. Q. Yu, J. X. Wang, M. H. Li, and Q. W. Ye, "Triple-band polarization-insensitive wide-angle ultra-thin planar spiral metamaterial absorber," *J. Appl. Phys.*, vol. 113, no. 21, June 2013.
- [24] E. Delihanlar and A. H. Yuzer, "Wearable textile fabric based 3D metamaterials absorber in X-band," *Applied Computational Electromagnetics Society Journal*, vol. 35, no. 2, Feb. 2020.
- [25] J. X. Su, C. Y. Kong, Z. R. Li, X. J. Yuan, and Y. Q. Yang, "Ultra-wideband and polarization-insensitive RCS reduction of microstrip antenna using polarization conversion metasurface," *Applied Computational Electromagnetics Society Journal*, vol. 32, no. 6, pp. 524-530, June 2017.
- [26] J. Q. Wang, C. Z. Fan, P. Ding, J. N. He, Y. G.

- Cheng, W. Q. Hu, G. W. Cai, E. J. Liang, and Q. Z. Xue, "Tunable broad-band perfect absorber by exciting of multiple plasmon resonances at optical frequency," *Optics Express*, vol. 20, no. 14, pp. 14871-14878, July 2012.
- [27] F. Ding, Y. X. Cui, X. C. Ge, Y. Jin, and S. L. He, "Ultra-broadband microwave metamaterial absorber," *Appl. Phys. Lett.*, vol. 100, no. 10, Mar. 2012.
- [28] J. P. Xu, J. Y. Wang, R. C. Yang, J. P. Tian, X. W. Chen, and W. M. Zhang, "Frequency-tunable metamaterial absorber with three bands," *Optik*, vol. 172, no. 172, pp. 1057-1063, Nov. 2018.
- [29] T. T. Nguyen and S. Lim, "Bandwidth-enhanced and wide-angle-of-incidence metamaterial absorber using a hybrid unit cell," *Sci. Rep.-Uk*, vol. 7, no. 1, Nov. 2017.
- [30] J. Lee and S. Lim, "Bandwidth-enhanced and polarisation-insensitive metamaterial absorber using double resonance," *Electron. Lett.*, vol. 47, no. 1, pp. 8-U20, Jan. 2011.
- [31] B. R. Bian, S. B. Liu, S. Y. Wang, X. K. Kong, H. F. Zhang, B. Ma, and H. Yang, "Novel triple-band polarization-insensitive wide-angle ultra-thin microwave metamaterial absorber," *J. Appl. Phys.*, vol. 114, no. 19, Nov. 2013.
- [32] O. T. Gunduz and C. Sabah, "Polarization angle independent perfect multiband metamaterial absorber and energy harvesting application," *J. Comput. Electron.*, vol. 15, no. 1, pp. 228-238, Mar. 2016.
- [33] X. P. Shen, T. J. Cui, J. M. Zhao, H. F. Ma, W. X. Jiang, and H. Li, "Polarization-independent wide-angle triple-band metamaterial absorber," *Optics Express*, vol. 19, no. 10, pp. 9401-9407, May 2011.
- [34] D. R. Smith, S. Schultz, P. Markos, and C. M. Soukoulis, "Determination of effective permittivity and permeability of metamaterials from reflection and transmission coefficients," *Phys. Rev. B*, vol. 65, no. 19, May 2002.
- [35] D. R. Smith, D. C. Vier, T. Koschny, and C. M. Soukoulis, "Electromagnetic parameter retrieval from inhomogeneous metamaterials," *Phys. Rev. E*, vol. 71, no. 3, May 2005.
- [36] P. V. Tuong, J. W. Park, J. Y. Rhee, K. W. Kim, H. Cheong, W. H. Jang, and Y. P. Lee, "Symmetric metamaterials based on flower-shaped structure," *Materials Chemistry and Physics*, vol. 141, no. 1, pp. 535-539, Aug. 2013.



Han Wu was born in Jilin Province, China, in 1993. He received the B.E. degrees in Mechanical Design, Manufacturing and Automation from Changchun University of Science and Technology, Changchun, China, in 2016. Now he is a Ph.D. candidate in Metamaterial Absorber Designing and Electromagnetic Metamaterial studying at Jilin University of China.



Shijun Ji was born in Shaanxi Province, China, in 1978. He received the Ph.D. degree in Mechanical Manufacturing and Automation from Harbin Institute of Technology, Harbin, China, in 2008. He is currently a Professor at Institute of Intelligent Precision Manufacturing of Jilin University, Changchun, China. His current research interests include design and manufacturing of metamaterial absorbers, design and machining of optical components.



Ji Zhao was born in Jilin Province, China, in 1959. He received B.E. degree, M.E. degree and Ph.D. degree from the Department of Mechanical Manufacturing and Automation, Jilin University, in 1982, 1984 and 1994, respectively. He is currently a Professor at Institute of Intelligent Precision Manufacturing of Jilin University, Changchun, China. His main current research interests include design, analysis and manufacturing of complex components such as Metamaterial absorbers, Optical devices and Moulding dies.



Zhiyou Luo was born in Chongqing, China, in 1996. He received B.E. degree from the College of Biological and Agricultural Engineering, Jilin University, in 2019. Now he is a graduate student in the School of Mechanical and Aerospace Engineering, Jilin University. His mainly research interests include design of metamaterial absorbers, analysis of absorption mechanism, and electromagnetic absorption theory.



Handa Dai was born in Jilin Province, China, in 1968. He received B.E. degree, M.E. degree from the School of Mechanical Science and Engineering, Jilin University, in 1993 and 1999, and Ph.D. degree from the College of Materials Science and Engineering, Jilin University, in 2005. Now he is an Assistant Professor at Institute of Intelligent Precision Manufacturing of Jilin University. His mainly research interests include analysis about absorption mechanism of metamaterials and electromagnetic wave absorbing theory.

Radiation Pattern Synthesis and Mutual Coupling Compensation in Spherical Conformal Array Antennas

Taimur Ahmed Khan¹, Muhammad Irfan Khattak¹, and Adnan Tariq²

¹Department of Electrical Engineering
University of Engineering and Technology Peshawar, Pakistan
taimurkhan008@gmail.com, m.i.khattak@uetpeshawar.edu.pk

²Department of Electrical and Computer Engineering
CUI Abbottabad Campus Abbottabad, Pakistan
adnandani521@gmail.com

Abstract — This paper presents a novel technique based on Hybrid Spatial Distance Reduction Algorithm (HSDRA), to compensate the effects of deformity and mutual coupling occurred due to surface change in conformal arrays. This antenna surface deformation shifts the position of null points and loss of the main beam resulting in reduced antenna gain along with substantial undesirable effects on the antenna performance. The proposed algorithm, which cumulatively incorporates the Linearly Constraint Least Square Optimization (LCLSO) and Quadratically Constraint Least Square Optimization (QCLSO) techniques, is formulated to minimize/reduce the absolute distance between the actual (simulated/measured) radiation pattern and the desired radiation pattern while keeping the direction of mainbeam and nulls position under control. In particular, a 4x4 conformal microstrip phased array from planar surface is deformed to prescribe spherical-shape surface with various radii of curvature, is validated. For the enhancement of Gain of the conformal array antenna, Gain Maximization Algorithm is also proposed, the simulated results of which is compared to the traditional Phase compensation technique and unconstrained least squares optimization. The analytical results for both planar and spherical deformed configurations are first evaluated in MATLAB and then validated through Computer Simulation Technology (CST).

Index Terms — Conformal array antenna, least square optimization, mutual coupling compensation, radiation pattern correction.

I. INTRODUCTION

In future 5G networks, antenna integration is intended to be less disturbing, volume saving and less visible to the human eye. Conformal array antennas with improved adaptive beamforming capabilities and robust signal processing are expected to replace the linear array

antennas because of its mechanical design which makes them suitable to be mounted on unique curved surfaces. A conformal array antenna adapts to prescribed curved surface (non-flat surface) forging new shape which are not necessarily limited to the planar or linear array configurations, e.g., circular, cylindrical, parabolic, spherical etc. [1]. Hence it is used in several types of applications such as wearable wireless networks [2], special electronic devices for load-bearing purposes [3], Aerospace designs [4], spacesuit [5] etc.

The conformal array antenna when deformed from the original shape to the prescribe shape it will seriously affect the radiation response of the array. This antenna surface deformation will change the relative position and angle of antenna elements, changing the antenna impedance, steering vector, relative gain, mutual coupling and radiation pattern [6]. The resulting distorted pattern may shift the positions of null points and loss of the main beam which will results in reduced antenna gain along with substantial undesirable effects on the antenna performance. It is therefore; contended that researchers are focusing on decoupling methods in conformal arrays to mitigate the problem associated with mutual coupling, and compensation techniques to control the shape of radiation pattern through precise positioning of the nulls and pointing the broadside beam to any desired direction regardless of the extent of deformation in the conformal surface.

Adaptive beamforming in conformal phased arrays is a powerful technique that adjusts the excitation (gain and phase) of the signals to generate radiation pattern in order to emphasize signal-of-interest (SOI), tuning out the signal-not-of-interest (SNOI) signals [7]. In literature, various compensation methods have been proposed to compensate and correct the field patterns of the conformal phased array antennas. In mechanical calibration methods, the compensation algorithms correct and reconfigure the field patterns by adaptively altering the shape of the

antenna surface and positions of antenna elements using driving mechanisms [8], or mechanical beam steering [9], smart materials employing shaped memory alloys [10], magnetically-actuated antenna tuning [11], and using electro-active polymers in deformable smart antennas [12]. However, these methods require sophisticated control techniques, extra installation space and have limited radiation correction accuracy with the slow response time. Compared to the mechanical calibration methods, the electrical calibration methods have a faster response time to compensate the effect of deformation occurred in conformal array without the requirement of mechanical adjustments. One of the most precise beam steering techniques is the phased array antennas which give the possibility to reconfigure and correct the radiation pattern in both elevation and azimuth planes by adjusting the amplitudes and phases of each element in the array. Several methods including the traditional mathematical methods and optimization algorithms for mutual coupling reduction and radiation pattern correction for conformal phased arrays were proposed in the past. For example: particle swarm optimization (PSO) [13], quasi-analytical method [14], gain maximization algorithm [15], [16], convex optimization technique [17], active element pattern technique [18], Recursive Least Squares method [19], Linear Constrained Minimum Variance (LCMV) algorithm [7], genetic algorithm [20], array interpolation technique [21], Element Pattern Reconstruction [22], Phase compensation [23], and method based on rotating-element electric-field vector (REV) [24].

In [25], a projection method is used to find analytically the amplitude and phase distribution, which provides low sidelobe level for spherical arrays. Similar approach of using projection method has been followed in [26], [27] and [28] to correct the main beam direction for conformal arrays. To study the gain limitation of phase compensated conformal array, the same projection method is used in [29]. To validate the results two prototypes of spherical shapes of radius $r = 20.32\text{cm}$ and $r = 27.94\text{cm}$ are used in which six microstrip element array is used with an inter element spacing of 0.5λ . The results obtained are compared with flat array that reveals that as the radius of the sphere is reduced, the gain also decreases in phase compensated array.

In [30] Chopra et al. investigated the performance on the basis of steering of main beam, interferers nullifying capability and side lobe level suppression, of several beamforming algorithms such as LMS, NLMS, Hybrid LMS, VSS-LMS etc. In [31], Linear Pattern Correction Method (LPCM) has been used in a 6 elements patch array to reduce the effects of mutual coupling. The same technique is also implemented to compensate the pattern of 4 elements linear DRA array antenna and it was shown that pattern correction through LSE is very promising as compare to conventional

OCVM [32]. A new method based upon LSE and electromechanical coupling analysis is presented in [33], in which Network theory model is employed to model the Mutual Coupling effects and constraints are taken on desired points for original pattern recovery. In summary, it is found that different calibration techniques together with various signal processing algorithms can be used to adjust phases and amplitudes of each element in array to precisely control the radiation pattern of conformal array antennas.

In this paper, the 4×4 planar microstrip array antenna is spherically deformed to a conformal surface of radius $r=20\text{cm}$ and $r=30\text{cm}$ and the results are compared for each case to show the performance of the proposed optimization technique. The HSDRA algorithm cumulatively uses the Linearly Constraint Least Square Optimization (LCLSO) and Quadratically Constraint Least Square Optimization (QCLSO) techniques to calculate the correct excitation of the amplitudes and phases to attain the preferred main beam and Side-Lobe Level SLL reduction with particular null placement to achieve the desired radiation pattern for 4×4 spherical conformal microstrip array antenna. Gain maximization algorithm based on maximizing the distance between minimum and maximum points in the pattern while constraining the output power is used to increase the overall gain of the spherical array, which is compared with traditional phase compensation methodology in which phases of excitation were changed so that the all the patterns of element reach at certain reference plane in constructive manner. The results are further compared with unconstrained least squares estimation technique, which is based on reducing the Mean Square Error (MSE) between desired and measured patterns. The results reveal that for the gain enhancement of spherical array structure, the Gain maximization algorithm has better results as compared to unconstrained least square optimization and conventional phase compensation method where as in terms of radiation pattern correction, the Quadratic Constraint Least Square Optimization technique is very efficient and reliable technique to compensate the effects of deformity and mutual coupling occurred due to surface change in conformal arrays.

II. PROBLEM FORMULATION

The physical layout of a ixj microstrip patch conformal array antenna when curved to a spherical surface with a radius r with broadside radiation pattern along $z - axis$ is shown in Fig. 1.

The 4×4 planar array designed for 2.50GHz is spherically deformed at a radius of 30cm and 20cm . The dimension of the microstrip patch in proposed 4×4 array design is depicted in Fig. 2. Each miniaturized microstrip patch has been created on a "Roger RT-6002 (lossy)" substrate having relative dielectric constant $\epsilon_r = 2.94$ with substrate thickness of 1.50mm having length and

width of 51mm and 25mm respectively. The dimensions of a single patch in the ixj array are given below in the Table 1.

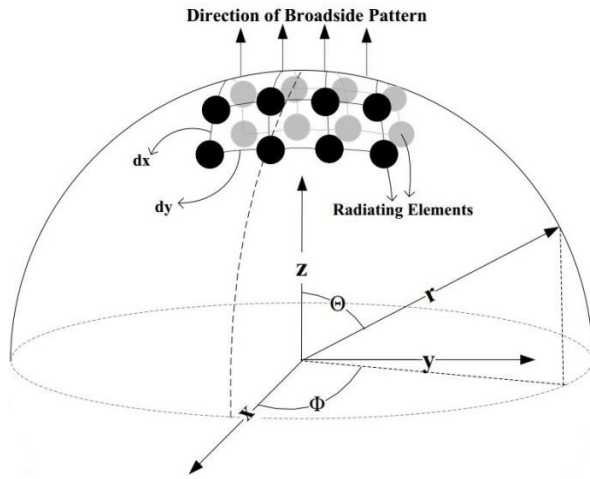


Fig. 1. Illustration of the ixj Array on spherical surface of radius r .

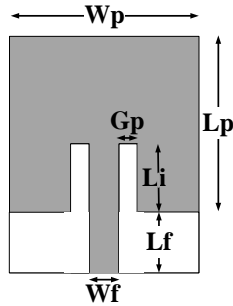


Fig. 2. Single patch antenna.

Table 1: Dimensions of a single patch

| Parameter | Description | Length (mm) |
|-----------|-------------------------------------|-------------|
| Lp | Length of patch | 37 |
| Wp | Width of patch | 25 |
| Lf | Length of feed line | 14 |
| Li | Length of inset feed | 14 |
| Wf | Width of feed line | 4 |
| Gp | Gap between the feed line and patch | 2 |

Two cases are investigated in this research. In the first case the inter element separation dx and dy along x -axis and y -axis between the antenna elements was kept same at 0.5λ respectively, whereas in the second one the inter element separation was changed so that antenna elements are compact to increase gain in

which the spacing in x -axis is kept at $dx = 0.4\lambda$ and spacing in y -axis at $dy = 0.6\lambda$. The positions of each radiating element in the array along x , y and z directions are determined by the following equations respectively:

$$\begin{aligned} x &= r \sin\theta \cos\varphi \\ y &= r \sin\theta \sin\varphi \\ z &= r \cos\theta, \end{aligned} \quad (1)$$

where r represents the radius of the spherical structure and θ and φ are adjusted according to inter element spacing dx and dy along x -axis and y -axis respectively. Based on the position of radiating elements in ixj array, the Array Factor $\mathbf{AF}(\theta_i, \varphi_j)$ is given by:

$$\mathbf{AF}(\theta_i, \varphi_j) = \left\{ \frac{1 \sin\left(I \frac{\psi_x}{2}\right)}{I \sin\left(\frac{\psi_x}{2}\right)} \right\} \left\{ \frac{1 \sin\left(J \frac{\psi_y}{2}\right)}{J \sin\left(\frac{\psi_y}{2}\right)} \right\}, \quad (2)$$

where $\psi_x = kdx \sin\theta \cos\varphi + \beta_x$ and $\psi_y = kdy \sin\theta \sin\varphi + \beta_y$, k is the propagation constant, β_x and β_y are the progressive phase shifts succeeded by each element and can be represented as matrix to invoke in algorithm to control the Array Factor as,

$$\beta_{i,j} = \begin{bmatrix} \beta_{1,1} & \cdots & \beta_{1,j} \\ \vdots & \ddots & \vdots \\ \beta_{i,1} & \cdots & \beta_{i,j} \end{bmatrix}. \quad (3)$$

The variables i and j represents the position of array elements in x -axis and y -axis respectively, λ is the wavelength, θ and φ is the elevation steering angle and azimuth steering angle respectively.

The Array Pattern $\mathbf{F}(\theta, \varphi)$ is evaluated by the Hadamard product of $\mathbf{AF}(\theta_i, \varphi_j)$ and a matrix \mathbf{M} , which is set up by concatenating the individual pattern vectors of radiating patches, $\mathbf{F}(\theta, \varphi) = \mathbf{AF}(\theta_i, \varphi_j) \circ \mathbf{M}$. The Gain Pattern $\mathbf{G}(\theta, \varphi)$ at any arbitrary angle θ and φ can be calculated as:

$$\mathbf{G}(\theta, \varphi) = \mathbf{F}(\theta, \varphi) \cdot \mathbf{w}, \quad (4)$$

where vector $\mathbf{w} = \mathbf{I}_{(i,j)} e^{j\Delta\phi}$ represents the complex weighting function need to guide the ixj^{th} element in 4×4 array. For subsequent analysis, the azimuth angle φ has been taken fixed and the results are presented for the elevation angle θ only.

When 4×4 planar array shape changes to the prescribe spherical shape of radius r , the whole radiation array pattern distorts due to change in $\mathbf{AF}(\theta_i, \varphi_j)$ for each element in the array. The problem is to calculate the correct weights $\mathbf{w}_c(\theta_i, \varphi_j)$ in 4×4 spherical conformal microstrip array to compensate for any radiation pattern errors occurred due to change in the shape.

III. PROPOSED SOLUTION

The approach adopted for mutual coupling reduction and deformity compensation is presented as a flowchart in Fig. 3.

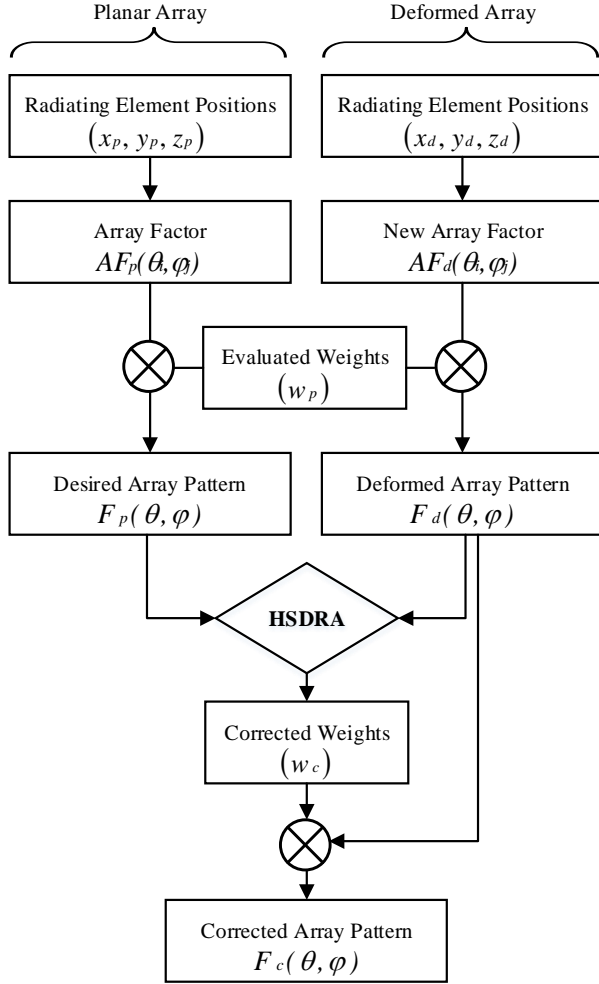


Fig. 3. Compensation technique for spherical deformation.

The 4x4 array antenna is designed and simulated in Computer Simulation Technology (CST) for the center frequency of 2.5GHz. The initial weights w_p assigned to each element of the array are used to obtain the desired radiation pattern by optimizing the field patterns to get the desired mainlobe direction and nulls at the specific positions. In particular, unity weights are assigned to the elements of planar array to show the performance of proposed compensation algorithm. The original positions of array element in planar and spherically deformed structure were found in CST and the Array Factor is calculated on the basis of their position vectors, then the element patterns are concatenated with the Array Factor to form the Array pattern of desired and deformed structure respectively.

The HSDRA algorithm for radiation pattern correction is based on Constraint Least Squares Optimization modified with particular nulls placement. It is given to the deformed array to evaluate the corrected weights which compensate the effects of deformity and

mutual coupling occurred due to surface deformation. Although the compensation technique can be implemented for several geometrical deformations but here only spherical deformation is considered on the planar array. The algorithm is formulated to minimize/reduce the absolute distance between the field pattern of the deformed array and the desired field pattern of planar array while ensuring that the null positions are precisely defined, and are of sufficient depth and the main beam direction is at the desired location. For this, first Linearly Constraint Least Squares Optimization (LCLS0) is used and then Quadratically Constraint Least Squares Optimization (QCLS0) is used on the results obtained from LCLS0 to calculate the correct excitation of the amplitude and phase to synthesize the preferred main beam and nulls direction to achieve the desired radiation pattern for 4x4 spherical conformal microstrip array antenna and the results are shown separately for the comparison.

For the enhancement of Gain of the conformal array antenna, the Gain Maximization Algorithm is proposed, the simulated results of which is compared to the traditional phase compensation technique and basic form of least squares optimization. Gain maximization algorithm is based on maximizing the distance between minimum and maximum points in the pattern while constraining the input and output power to unity to increase the overall gain and performance.

A. Computation for radiation pattern correction

The HSDRA algorithm for radiation pattern correction is based on Constraints Least Squares Optimization which iteratively updates the weights of conformal array while searching for the point of minimum sum of squared errors between the actual field in deformed array E_d and targeted field E_p of planar array. The basic form of Least Square Optimization includes some excitation amplitude distribution weights for maximizing the gain while minimizing the sidelobes to a certain level. It aims to decrease the Mean Square Error (MSE) between the field patterns of deformed spherical array and targeted planar array as shown in equation:

$$\text{minimize } w_d \sum_{\theta, \phi} |F_d w_d - F_p w_p|^2. \quad (5)$$

The individual antenna pattern has been imported from CST for specific radius r whereas the distorted array pattern is compensated by a matrix P obtained as:

$$\begin{aligned} P &= (F_d)^\dagger F_p \\ w_c &= P \cdot w_i \\ E_p &= F_d w_c, \end{aligned} \quad (6)$$

where \dagger indicates the pseudo inverse and is defined as $(F_d)^\dagger = F_d^H (F_d F_d^H)^{-1}$. Here $F_d \in \mathbb{C}^{l \times j}$ is the matrix containing measured/simulated gain pattern of the

vector contain the initial weights $w_i=w_p$ which shape the desired array pattern (in this paper, unity weights are assigned to the elements of planar array to show the performance of proposed algorithm), and w_c contains the recovered corrected weights which correct the radiation pattern errors occurred due to deformity.

The Least Squares Optimization (LSO) method in its basic form generates a solution that is for unknown (guessed) excitation values. This solution contains error distribution either in the main-lobe or sidelobes or both because it does not control the level of individual peaks, rather than it only controls and measures the level of general lobes by reducing the Mean Square Error (MSE) between the resulting field pattern and the desired one. Unfortunately using LSO only without modification for the pattern correction gives guessed values which may not be optimal for the final design. Therefore for recovering precisely some of the points on the pattern the optimization problem need to be constraint. In order to accurately control nulls positions and the direction of main beam, LSO is modified by introducing constraints at those points on the pattern that needs to be recovered and controlled precisely.

The goal in Constraint LSO approach is minimizing the Euclidean distance between simulated/measured and desired pattern while constraining some points (either peak of main lobe, null points or sidelobe points) to find the corrected weights. In Linearly Constraint Least Squares Optimization (LCLSO) method, the Euclidean distance between the measured pattern in deformed array E_d and desired pattern of planar array E_p is minimized while constraining the pattern at some points (either null points or the peak side lobe points) to find the compensated weights w_c . The optimization problem is written as:

$$\text{minimize } w_c \sum_{\theta, \varphi} |F_d w_c - F_p w_p|^2 \quad (7)$$

subject to $F_d w_c = b$,

$$F_c = [F_d(\theta_1, \varphi_1), F_d(\theta_1, \varphi_2) \cdots F_d(\theta_4, \varphi_4)]^T, \quad (8)$$

$$b = [E_p(\theta_1, \varphi_1), E_p(\theta_2, \varphi_2) \cdots E_p(\theta_4, \varphi_4)]^T.$$

Here $F_c \in \mathbb{C}^{q \times (ixj)}$ is a matrix containing the q constraint vectors at ixj positions of 4×4 array at the desired constrained angles in the measured individual element pattern matrix of deformed structure and $b \in \mathbb{C}^{q \times (N)}$ is a vector of q constraint points on the planar array pattern and N represent the ixj^{th} location of radiating elements on the array.

The linear weights reduce the search space so that the solution satisfying the constraint is the only possible solution. Consequently, the compensated pattern performs well at the mainlobe peak and null points (constraint points) but does not care for the rest of the radiation pattern. As a result, higher side-lobe level at the edges,

away from the constraint points can be observed. The error performance of LCLSO, however, improves with increasing the number of constraints chosen at the extremal point evenly spread over the radiation pattern. However, there is an upper limit on the maximum number of constraint points $q < N$.

The problem in LCLSO with controlling the side lobes level is therefore further modified by quadratically constraints, which is given as:

$$\text{minimize } w_c \sum_{\theta, \varphi} |F_d w_c - F_p w_p|^2 \quad (9)$$

Subject to $|F_c w_c - b|^2 \leq \beta$,

where $0 \leq \beta \leq 1$ is a constraining factor, lower the value of β smaller is the search space. This technique provides alternative to the Linearly Constraint LSO because it allows a good compromise, enabling the corrected pattern to follow the desired pattern more closely. The QCLSO compensates the weighting function not only in the main lobe but also on the peaks of the side lobes while at the same time ensuring that the desired null depths are achieved. Since exact solution of QCLSO does not exist, therefore numerical approach using Newton-Raphson method has been used to solve the above optimization problem.

The algorithm is programmed and analyzed for the spherical structure of $r = 20cm$ (maximum deformation) deformed from planar structure. The algorithm uses 12 number/level of iterations for finding the correct excitation of the amplitudes and phases. The average computation time between each iteration is 0.23 seconds and the Total CPU time is approximately 2.74 seconds. A computer of Intel Core i7 (6th Generation) processor with 3.40 GHz CPU speed and 8 GB of RAM was used and the algorithm was programmed and verified in MATLAB 2018a version and CST Studio Suite 2019 version respectively.

B. Computation for gain optimization

To compensate the loss in gain when the array is deformed, an approach using Gain maximization algorithm is introduced which minimizes the Euclidean distance between measured Gain in deformed array $G_d(\theta, \varphi)$ and target Gain in planar array $G_p(\theta, \varphi)$ while minimizing the gain loss to find the compensated weights. The weights are generated for the desired gain pattern which is estimated using the Gain maximization algorithm based on maximizing the distance between minimum and maximum points in the pattern while constraining the input power and output power to unity. So, the problem formulation for this technique is:

$$\text{minimize } \sum_{\theta, \varphi} |F_d w_c - F_p w_p|^2 \quad (10)$$

Subject to: $w_c^H w_c \leq \gamma$,

where γ represents the output power of compensated weights. The input power of weight vectors is kept unity to find all the patterns. In minimizing the gain loss approach the error was minimized while keeping power of weights unity. Hence loss in gain is also minimized. Newton-Raphson method has been used to evaluate the solution of w_c for the above optimization problem.

The concept of Phase compensation technique used in [23] is implemented here to generate a broadside radiation pattern along a tangent reference plane, for gain enhancement. The results obtained with this technique are compared with the proposed method using Least Square Optimization and Gain Maximization Algorithm. A tangent reference plane is considered to the center of the array and the E-fields from each of the radiating elements on the 4x4 spherical array are assured to reach the tangent plane with the matching phase to create constructive interference for gain enhancement. For this, each radiating element on the spherical surface is specified with correct weighting function of amplitudes and phases for the creation of broadside radiation pattern along z-axis. The location of each element on a sphere is determined by the following expressions in terms of angle " θ " measured from z-axis,

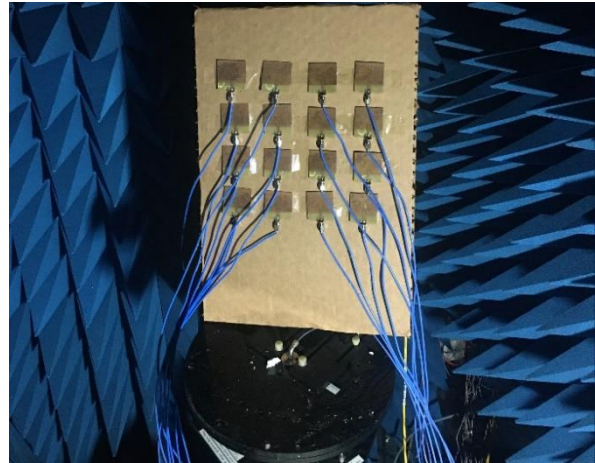
$$\theta_{i,j} = \frac{1}{r} \sqrt{(id_y + d_y/2)^2 + (jd_x + d_x/2)^2}, \quad (11)$$

and the phases of each element required for correction of radiation pattern is computed as $\Delta\phi_e = -jk\Delta z_e$, where $\Delta z_p = r(1 - \sin \theta_{re})$ represents the distance from the radiating element on the spherical surface to the reference plane and θ_{re} is the corresponding angle from the origin along z-axis.

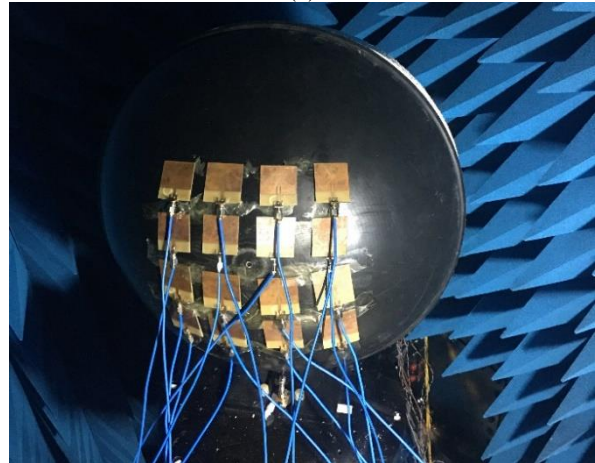
IV. RESULTS AND DISCUSSIONS

Sixteen elements patch antenna in 4x4 spherical configurations have been used for simulation and analysis purposes. Two spherical deformations were investigated where planar array is deformed at 30cm and 20cm radius. Further these two deformations are investigated for equally and unequally inter-element spaced arrays and the results of these deformations are compared with the desired results achieved in planar array configuration. One is equally spaced on both side, that is $dx = dy = 0.5\lambda$, and the other one has $dx < dy$. In unequally spaced case dx is kept at 0.4λ and dy at 0.6λ . 3D electromagnetic simulation and analysis software (CST) is used for the verification of the results. All the radiation patterns, such as desired in planar array, deformed and the corrected one in spherical array, are first evaluated in MATLAB and then validated through CST. To verify the results, the antenna test platform for equally spaced 4x4 array structure is constructed for planar and spherical configurations of $r = 30\text{cm}$ and $r = 20\text{cm}$ as shown in Fig. 4. Similar test platform is

also used for unequal spaced array configuration. The experimental setup includes sixteen numbers of Phase Shifters (DBVCPS02000400A) and variable voltage controlled attenuators (ZX73-2500+), which are connected with two numbers of 1x8 power Splitter/Combiner (ZN8PD1-63W+) feed network connected with high gain power amplifier (PE15A4018) as discussed in Section II of the paper. This test platform is developed to validate the results for QCLSO technique because this method gives most optimum results in term of radiation pattern correction. Phases and Array Factors are calculated using the methodology mentioned in Section III and the position vectors of antenna elements in spherical surface is obtained in CST. A broadside radiation pattern possessing nulls at 30° and -30° has been chosen for analysis. The HSDRA algorithm calculates the weights (amplitudes and phases) for each element of the array, which are provided to attenuators and phase shifter with help of variable power supplies. After receiving the required phase shift and amplitude attenuation/amplification at the individual patch of the conformal array, the corrected radiation pattern measurements were carried out in a fully calibrated Anechoic Chamber.



(a)



(b)

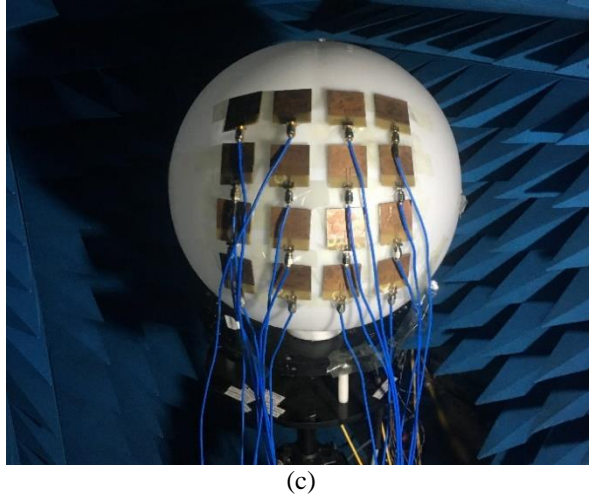


Fig. 4. 4x4 array configuration of: (a) planar array, (b) spherical configuration of 30cm, and (c) spherical configuration of 20cm.

The result of HSDRA algorithm for the radiation pattern correction is shown separately as LCLSO and QCLSO. The results of radiation pattern correction for equally spaced array with geometric spacing of $0.5\lambda \times 0.5\lambda$ and unequally spaced array with geometric spacing of $0.4\lambda \times 0.6\lambda$ are discussed in Fig. 5 and Fig. 6 respectively. The choice of different inter element separation is considered to render the effect of mutual coupling and deformity on the radiation pattern of the spherical array. It is observed that when pattern is compensated with Linearly Constrained Least Squares Optimization (LCLSO), the mainlobe direction is well achieved whereas the sidelobe level increases which is obvious because when the locations are linearly constrained it does not care about the rest of the pattern as it only tries to satisfy the constrained points. Similarly, when the deformation is increased that is that radius of curvature of conformal spherical array is 20cm, the sidelobe level further increases while satisfying the mainlobe direction and losing the nulls points. Whereas the Quadratic Constrained Least Squares Optimization (QCLSO) gives some relaxation in search space of output. This compensation technique gives better fit results at the nulls, at the edges of the mainlobe and has low side lobe level almost approaching to the desired one. This method computes appropriate amplitude and phase excitation that recovers the radiation pattern of the spherical array set up on a conformal structure up to a radius of 20cm.

It is shown that when the planar array undergo

spherical deformation, the radiation pattern has been distorted severely, i.e., significant reduction up to 80% is noticed in the mainlobe gain, no sidelobes are formed and the nulls are completely lost; however, the QCLSO compensation algorithm accurately recovers the radiation pattern to the desired one. So, the HSDRA algorithm combines the linearly constraint and quadratically constraint Least Squares optimization to calculate the corrected complex weights to synthesize the preferred mainlobe, sidelobes and nulls direction to attain the desired radiation pattern in the planar array which compensate the effects of deformity and mutual coupling occurred due to surface deformation. After compensation algorithm, the distorted pattern recovers successfully which is similar to the planar (desired) array pattern with sidelobe levels and nulls locations nearly in the same position as that of the planar array as shown in the Figs. 5 and 6.

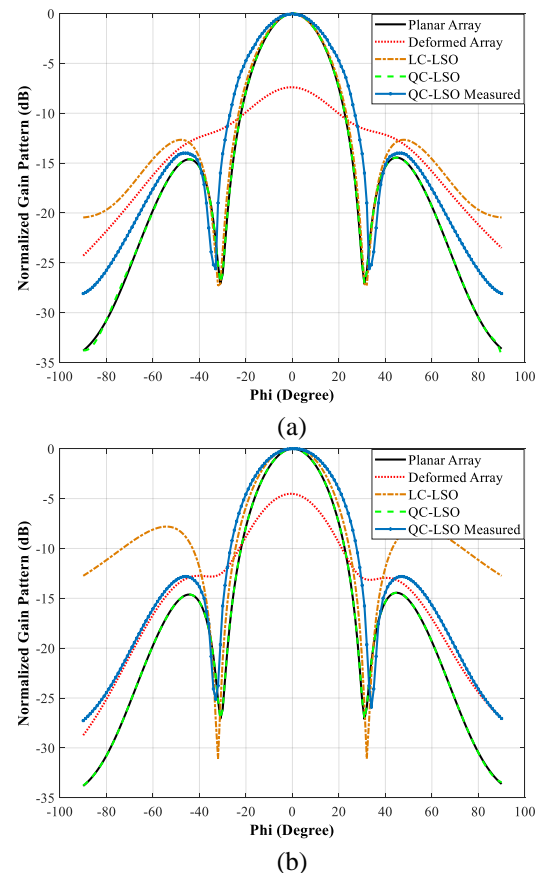


Fig. 5. Results for 4x4 spherical array with equal element spacing ($dx = dy = 0.5\lambda$) with a radius of (a) 30cm and (b) 20cm.

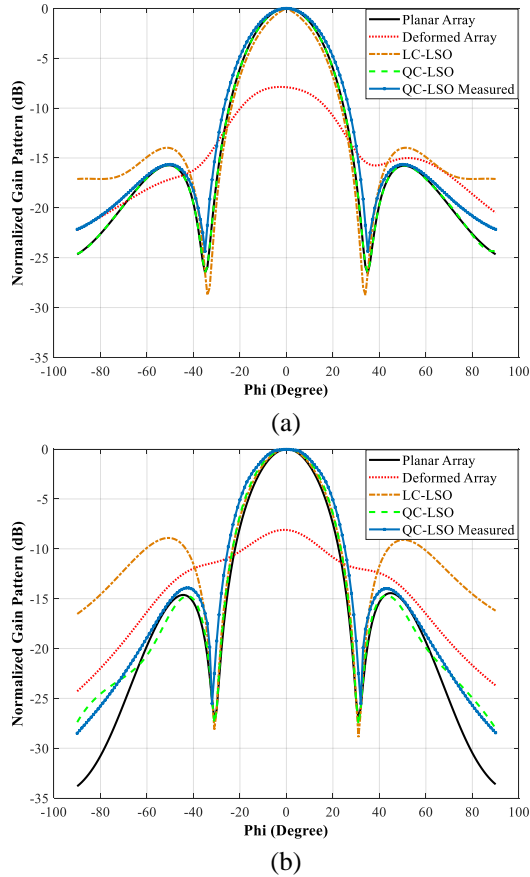


Fig. 6. Results for 4x4 spherical array with unequal element spacing ($dx = 0.4\lambda$, $dy = 0.6\lambda$) with a radius of (a) 30cm and (b) 20cm.

The results of gain analysis is shown in Figs. 7 and 8. It reveals that the 4x4 planar array with equally spaced array has a simulated gain of 16dB and for unequally spaced it is 17.5dB. After deformation the gain loss is more than 26dB for each case. It is observed that after the transformation of the planar array onto the spherical surface the radiation pattern changes significantly, hence phase correction is required to correct the gain and recover the pattern. The unconstrained least squares optimization yields unfeasible excitations for antenna elements, which causes a significant decrease of gain (up to 3dB) in each case whereas, the location of nulls are slightly compromised for both equally and unequally spaced arrays. The distorted pattern obtained with Phase Compensation technique in which the radiation pattern is targeted on a reference tangent plane, the nulls are well recovered however the gain is decreased by 2dB for 30cm radius and 3.5dBs for 20cm radius respectively. Furthermore, Gain Maximization Algorithm is employed to maximize the gain of array. It shows a good increase (up to 2 – 4dBs) in gain as compared to phase

compensation and LSO technique however, the nulls are not recovered properly. In general, the results reveal that gain is recovered very efficiently for unequally spaced spherical patch antenna array, whereas it shows less recovery for equally spaced spherical antenna array.

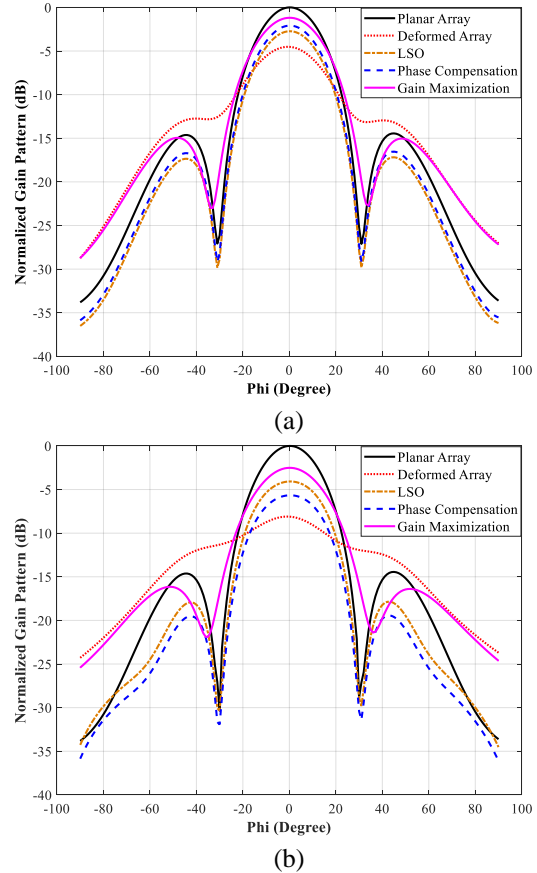
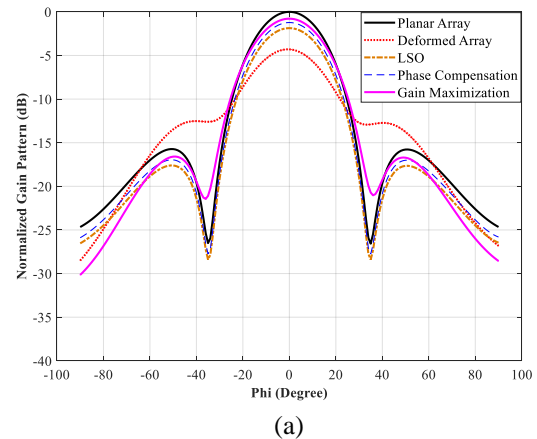


Fig. 7. Comparison of least squares optimization, gain maximization and phase compensation technique for 4x4 spherical array with equal element spacing ($dx = dy = 0.5\lambda$) with a radius of (a) 30cm (b) 20cm.



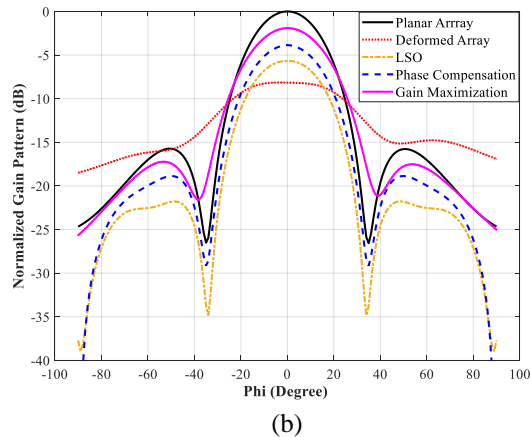


Fig. 8. Comparison of least squares optimization, gain maximization and phase compensation technique for 4x4 spherical array with unequal element spacing ($dx = 0.4\lambda$, $dy = 0.6\lambda$) with a radius of (a) 30cm and (b) 20cm.

V. CONCLUSION

In this Paper, a radiation pattern correction technique based on Hybrid Spatial Distance Reduction Algorithm (HSDRA) is used to reduce the effects of antenna surface deformity and mutual coupling for 4x4 conformal array antenna. The algorithm put together LCLSO and QCLSO techniques to calculate the corrected complex weights to synthesize the radiation pattern. The algorithm is formulated to minimize/reduce the absolute distance between the simulated radiation pattern and the desired radiation pattern while keeping the direction of mainbeam, sidelobe levels, and the nulls position under control to overcome these changes. The results for LCLSO are shown separately. However, with this technique, higher sidelobes levels are observed. The inadequate results obtained with LCLSO are therefore further modified by QCLSO technique. This method gives adequate results at the nulls, at the peak and edges of the mainlobe and has low side lobe level almost approaching to the desired one. This method computes appropriate amplitude and phase excitation that restores the radiation pattern of spherical conformal microstrip array up to a radius of 20cm spherical deformation.

The simulated results for gain analysis between the unconstrained least squares optimization, Phase compensation and Gain Maximization Algorithm is also presented. All the three techniques follow the same approach to optimize the pattern with slight changes in gain. The distorted pattern obtained with Phase Compensation technique and unconstrained least squares optimization yields unfeasible excitations for antenna elements, which causes a significant decrease of gain in each case. The Gain Maximization Algorithm shows a good increase in gain as compared to unconstrained least squares optimization and phase compensation technique however the nulls are not recovered properly in this

method. Furthermore, this algorithm recovers the gain very efficiently for unequally inter-element spacing, whereas it shows less recovery for equally spaced spherical array.

REFERENCES

- [1] L. Josefsson and P. Persson, Conformal array antenna theory and design, John Wiley & sons, 2006.
- [2] G. B.Rhoads and H. L. Brunk, "Body-worn phased-array antenna". United States Patent 9,564,682, 7 February 2017.
- [3] C. Wang, Y. Wang, P. Lian, S. Xue, Q. Xu, Y. Shi, Y. Jia, B. Du, J. Liu and B. Tang, "Space Phased Array Antenna Developments: A Perspective on Structural Design," *IEEE Aerospace and Electronic Systems Magazine*, vol. 35, no. 7, pp. 44-63, 1 July 2020.
- [4] D. L. Goff, G. Riondet, L. Barbier, Y. Song and K. Mouthaan, "Conformal Adaptive Phased Array," in *WSA 2020; 24th International ITG Workshop on Smart Antennas*, Hamburg, Germany, 2020
- [5] T. Haagenson, S. Noghianian, P. d. Leon and Y.-h. Chang, "Textile Antennas for Spacesuit Applications: Design, simulation, manufacturing, and testing of textile patch antennas for spacesuit applications," *IEEE Antennas and Propagation Magazine*, vol. 57, no. 4, pp. 64-73, August 2015.
- [6] H. Singh, H. L. Sneha and R. M. Jha, "Mutual Coupling in Phased Arrays: A Review," *International Journal of Antennas and Propagation*, 2013.
- [7] P. Alinezhad and S. R. Seydnejad, "Broadband Adaptive Beamforming of Conformal Arrays for Wireless Communications Based on Generalized Sidelobe Canceller," *Wireless Personal Communications*, vol. 96, no. 1, pp. 1131-1143, 2017.
- [8] J. T. Bernhard, E. Kiely and G. Washington, "A smart mechanically actuated two-layer electromagnetically coupled microstrip antenna with variable frequency, bandwidth, and antenna gain," *IEEE Transactions on Antennas and Propagation*, vol. 49, no. 4, pp. 597 - 601, 2001.
- [9] I. d. Costa, H. Filgueiras, J. Kelly, S. A. Cerqueira and P. Xiao, "Mechanical beam steering circular patch antenna," in *12th European Conference on Antennas and Propagation (EuCAP 2018)*, London, 2018.
- [10] S. J. Mazlouman, A. Mahanfar, C. Menon and R. G. Vaughan, "Square Ring Antenna With Reconfigurable Patch Using Shape Memory Alloy Actuation," *IEEE Transactions on Antennas and Propagation*, vol. 60, no. 12, pp. 5627-5634, 2012.
- [11] J.-C. Langer, J. Zou, C. Liu and J. T. Bernhard, "Micromachined reconfigurable out-of-plane

- microstrip patch antenna using plastic deformation magnetic actuation," *IEEE Microwave and Wireless Components Letters*, vol. 13, no. 3, pp. 120-122, 2003.
- [12] A. Mahanfar, C. Menon and R. Vaughan, "Smart antennas using electro-active polymers for deformable parasitic elements," *Electronics Letters*, vol. 44, no. 19, pp. 1113-1114, 2008.
- [13] S. Banerjee and D. Mandal, "Array pattern optimization for steerable linear isotropic antenna array using novel particle swarm optimization," *Journal of Electromagnetic Waves and Applications*, vol. 31, no. 2, pp. 182-208, 2007.
- [14] T. M. Bruintjes, A. Kokkeler and G. Smit, "Asymmetric shaped-pattern synthesis for planar antenna arrays," *International Journal of Antennas and Propagation*, vol. 2016, pp. 1-13, 2016.
- [15] M. Mouhamadou, P. Vaudon and M. Rammal, "Smart Antenna Array Patterns Synthesis: Null Steering and Multi-User Beamforming by Phase Control," *Progress In Electromagnetics Research*, vol. 60, pp. 95-106, 2006.
- [16] T. Ng, J. Cheah and F. Paoloni, "Optimization with controlled null placement in antenna array pattern synthesis," *IEEE Transactions on Antennas and Propagation*, vol. 33, no. 2, pp. 215-217, 1985.
- [17] I. Ullah, S. Khattak and B. D. Braaten, "Broadside Pattern Correction Techniques for Conformal Antenna Arrays," in *Advances in Array Optimization*, 2020.
- [18] X.-S. Yang, H. Qian, B.-Z. Wang and S. Xiao, "Radiation Pattern Computation of Pyramidal Conformal Antenna Array with Active-Element Pattern Technique," *IEEE Antennas and Propagation Magazine*, vol. 53, no. 1, pp. 28-37, 2011.
- [19] F. Wang, R. Yang and C. Frank, "A new algorithm for array pattern synthesis using the recursive least squares method," *IEEE Signal Processing Letters*, vol. 10, no. 8, pp. 235-238, 2003.
- [20] C.-M. Seong, M.-s. Kang, C.-S. Lee and D.-C. Park, "Conformal array pattern synthesis on a curved surface with quadratic function using adaptive genetic algorithm," in *2013 Asia-Pacific Microwave Conference Proceedings (APMC)*, Seoul, South Korea, 2013.
- [21] X. Zhang, G. Liao, Z. Yang, X. Zou and Y. Chen, "Effective mutual coupling estimation and calibration for conformal arrays based on pattern perturbation," *IET Microwaves, Antennas & Propagation*, vol. 14, no. 15, pp. 1998-2006, 2020.
- [22] Q. Huang, F. Wei, L. Yuan, H. Zhou and X. Shi, "A new wideband mutual coupling compensation method for adaptive arrays based on element pattern reconstruction," *International Journal of Antennas and Propagation*, vol. 2014, 2014.
- [23] B. D. Braaten, S. Roy, I. Irfanullah, S. Nariyal and D. E. Anagnostou, "Phase-compensated conformal antennas for changing spherical surfaces," *IEEE Transactions on Antennas and Propagation*, vol. 62, no. 4, pp. 1880-1887, 2014.
- [24] B. Wang, Y. Li and B. Tian, "Rotating-element electric-field vector (REV) calibration method based on power measurement for phased array antenna," in *2017 International Applied Computational Electromagnetics Society Symposium (ACES)*, Suzhou, China, 2017.
- [25] I. Chiba, K. Hariu, S. Sato and S. Mano, "A projection method providing low sidelobe pattern in conformal array antennas," in *Digest on Antennas and Propagation Society International Symposium*, San Jose, CA, USA, 1989.
- [26] O. Bucci, G. D'Elia and G. Romito, "Power synthesis of conformal arrays by a generalised projection method," *IEE Proceedings - Microwaves, Antennas and Propagation*, vol. 142, no. 6, pp. 467-471, 1995.
- [27] F. Rigobello, G. Mansutti, A. Capobianco and A. Galtarossa, "Phase sensitivity of the projection method for a beam tilting deformed array," in *12th European Conference on Antennas and Propagation (EuCAP 2018)*, London, 2018.
- [28] F. Rigobello, G. Mansutti, S. Asif, M. S. Khan, A. D. Capobianco and A. Galtarossa, "Robustness of the projection method for an asymmetrically deformed planar antenna array," *Microwave and Optical Technology Letters*, vol. 61, no. 1, pp. 167-172, 2019.
- [29] B. Ijaz, A. Sanyal, A. Mendoza-Radal, S. Roy, I. Ullah, M. T. Reich, D. Dawn, B. D. Braaten, N. F. Chamberlain, and D. E. Anagnostou, "Gain limits of phase compensated conformal antenna arrays on non-conducting spherical surfaces using the projection method," in *IEEE International Conference on Wireless for Space and Extreme Environments*, pp. 1-6. IEEE, 2013.
- [30] R. Chopra and R. Lakhmani, "Design and comparative evaluation of antenna array performance using non blind LMS beamforming algorithms," in *2017 Progress in Electromagnetics Research Symposium - Fall (PIERS - FALL)*, Singapore, 2017.
- [31] I. Salonen, A. Toropainen and P. Vainikainen, "Linear pattern correction in a small microstrip antenna array," *IEEE Transactions on Antennas and Propagation*, vol. 52, no. 2, pp. 578-586, 2004.
- [32] J. Nasir, M. H. Jamaluddin, M. R. Kamarudin, I. Ullah, Y.-C. Lo and R. Selvaraju, "A Four-Element Linear Dielectric Resonator Antenna Array for Beamforming Applications With Compensation of Mutual Coupling," *IEEE Access*, vol. 4, pp. 6427-6437, 2016.

- [33] S. Lou, W. W. H. Bao, N. Hu, G. Ge, X. Hu, S. Qian and C. Ge, "A compensation method for deformed array antennas considering mutual coupling effect," *EEE Antennas and Wireless Propagation Letters*, vol. 17, no. 10, pp. 1900-1904, 2018.



Taimur Ahmed Khan received the B.Sc. degree in Electrical Engineering from CECOS University of IT and Emerging Sciences, Peshawar in 2011, and the M.Sc. Electrical Engineering from UET Peshawar, in 2017. Currently he is doing Ph.D. in Electrical Engineering from UET

Peshawar under the supervision of Associate Professor Dr. Muhammad Irfan Khattak. He is currently working as a Lab Engineer in RF and Microwave Lab in the Department of Electrical Engineering at University of Science and Technology Bannu, where he teaches various electrical engineering subjects and perform labs to undergraduate engineering students.



Muhammad Irfan Khattak

received the B.Sc. degree in Electrical Engineering from the UET, Peshawar, in 2004, and the Ph.D. degree from Loughborough University, U.K., in 2010. After doing his Ph.D. degree, he was appointed as the Chairman of the Electrical Engineering Department, UET Peshawar Bannu Campus, for five years and took care of the academic and research activities at the department. Later in 2016, he was appointed as the Campus Coordinator of UET Peshawar Kohat Campus and took the administrative control of the campus. He is currently working as an Associate Professor with the Department of Electrical Engineering, UET, Peshawar. He is also heading the research group Microwave and Antenna Research Group, where he is also supervising the postgraduate students working on latest trends in antenna technology like 5G and graphene nano-antennas for terahertz, optoelectronic, and plasmonic applications etc. His research interests include antenna design, on-body communications, anechoic chamber characterization, speech processing, and speech enhancement.

Reduced Cross-Polarization Patch Antenna with Optimized Impedance Matching Using a Complimentary Split Ring Resonator and Slots as Defected Ground Structure

N. RajeshKumar¹, P. D. Sathya¹, S. K. A. Rahim², and A. A. Eteng³

¹ Department of Electronics and Communication Engineering, Annamalai University, India
mailtorajeshau@gmail.com, pd.sathya@yahoo.in

² Wireless Communication Center (WCC), Universiti Teknologi Malaysia, UTM Skudai Johor Malaysia
sharulkamal@fke.utm.my

³ Department of Electronic and Computer Engineering, University of Port Harcourt, Nigeria
akka.eteng@uniport.edu.ng

Abstract — An innovative method is proposed to improve the cross-polarization performance and impedance matching of a microstrip antenna by integrating a complimentary split ring resonator and slots as a defected ground structure. An equivalent circuit model (ECM) enables the design take into consideration the mutual coupling between the antenna patch and the Defected Ground Structure. The input impedance and surface current density analysis confirms that the integration of a CSRR within a rectangular microstrip patch antenna leads to uniform comparative cross-polarization level below 40 dB in the H-plane, over an angular range of $\pm 50^\circ$. Introducing parallel slots, as well, leads to a reduction of spurious antenna radiation, thereby improving the impedance matching. Measurements conducted on a fabricated prototype are consistent with simulation results. The proposed antenna has a peak gain of 4.16 dB at 2.6 GHz resonating frequency, and hence is good candidate for broadband service applications.

Index Terms — Cross-polarization, CSRR, defected ground structure, impedance matching, microstrip antenna.

I. INTRODUCTION

Microstrip antennas have gained a wide range of attention and have been elaborately studied due to their small footprint, lighter structure and inexpensive price. The impedance matching of microstrip patch antenna plays an import role in designing a good antenna. The antenna's input impedance depends on its size, profile, type of feeding, and the properties of the antenna material. Results obtained from experiments [1] reveal that, in particular cases, such as feeding from the probe of simple coaxial and a microstrip line, the input

impedance is dependent on the feed position. In general, the cosine-square of the normalized distance of feeding point from the patch edge is proportional to the impedance of the input probe that feeds the microstrip patch antenna. However, with the use of a microstrip line, the dependence of impedance develops proportionate to the fourth-power cosine [2]. While the input impedance is zero for the feed probe at middle of the patch, the input impedance of inset-fed rectangular microstrip patch antenna is influenced by the notch dimensions and the aspect ratio of the patch [3]. This implies that the H-plane cross-polarization is influenced by the notch depth and width dimensions. For fixed input impedance, however, the cross-polarization level is largely insensitive to the notch width. Flexible impedance matching and low cross-polarization has been realized using a novel technique of loading the rectangular microstrip patch antenna with a pair of shorting pins [4]. The symmetric arrangement of the shorting pins retains the symmetric-odd pattern of surface current with respect to the H-plane, and therefore the level of cross-polarization is diminished considerably. The input impedance of the microstrip patch antenna also plays a role in achieving a suitable impedance-bandwidth. An improved bandwidth for a microstrip patch antenna in the X-band has been achieved by implementing a z-shaped defected ground structure [5]. However, the integration of a defected ground structure for enhancing input impedance matching has not been studied. The defected ground structure has also been used to boost the bandwidth of an ultra-wide band antenna along with the suppression of cross-polarization [6]. Although, the level of cross-polarization has been improved by between 10 dB to 25 dB in both the principal planes, a decline in matching can be observed after introducing the defected ground

structure. Among various effects, a simple rectangular microstrip patch antenna is impinged by cross-polarized radiation in the far field, particularly the H-plane. Irregularities in the positioning of probes leads to this proportioned antenna near-fields, resulting in higher cross-polarized radiation in the H-plane. The reduction of cross-polarization using defected ground structure approaches have been studied, such as an arc-shaped symmetrical defected ground Structure [7]; a novel defected ground structure strategy [8]; a defected ground structure with dumbbell shape [9]; defected ground structure with asymmetry, non-affected pattern of co-polarized radiation [10]. From these studies, it can be observed that the reduction of cross-polarization along with proper impedance tuning is a challenging assignment for designers of microstrip patch antennas. Since, an asymmetric feed position is often required for accurate matching of impedance; this unfortunately plays a role in increasing cross-polarization in the H-plane. Although the reduction of the cross-polarization in bore sight is a comparatively easier task, it is difficult to maintain a regular and low cross-polarization over a wide angle range from -50° to $+50^\circ$. In this work, a rectangular microstrip patch antenna, using a complimentary split ring resonator (CSRR) and slots as defected ground structure, is proposed and studied for improved impedance matching and lower cross-polarization level. The location of the defected ground structure is adjusted to obtain the anticipated x-axis directed odd-symmetric distribution of surface current, hence, negating the resultant far field radiation in the H-plane. Taking into the consideration the mutual coupling between the defected ground structure and patch, an equivalent circuit model (ECM) is first developed and analyzed using Advance Design System (ADS-2017). Enhanced input impedance between 2.4 GHz – 2.8 GHz, regular and low cross-polarization over a wide angle range from -50° to $+50^\circ$ and a reasonable peak gain of 4.16 dB will make these type of antenna appropriate for broadband services applications.

II. ANTENNA DESIGN

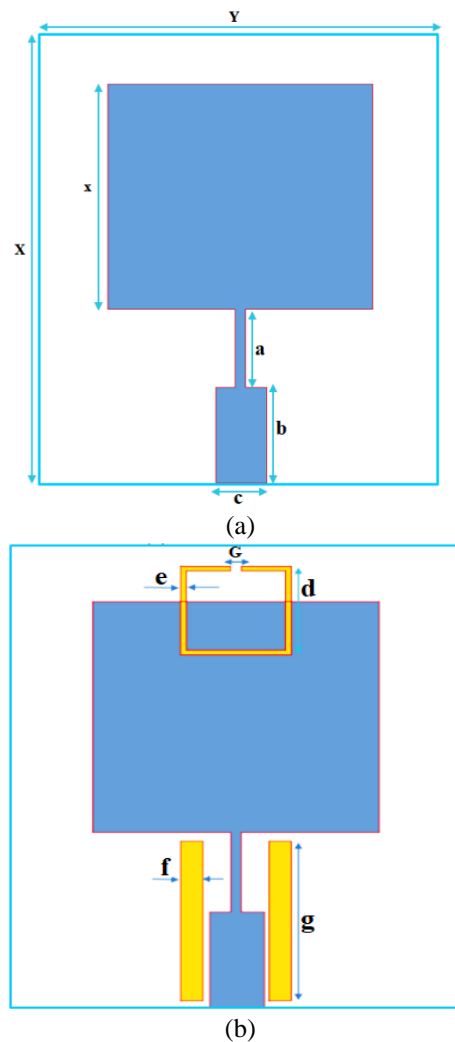
A. Antenna configuration

The proposed configuration for antenna and the model of equivalent circuit are elaborated in this section.

B. Equivalent circuit model

In Fig. 1 and Fig. 2, the descriptive sketch of recommended CSRR+Slots designed defected ground Structure incorporated in microstrip patch antenna and the equivalent circuit of CSRR defected ground structure with microstrip line feed microstrip patch antenna is presented respectively, in which the influence of the

CSRR and slots aperture are accounted for by considering the mutual inductance between the patch and defected ground structure (i.e., the CSRR and slots). The input side, which models the equivalent circuit of the antenna patch, consists of a parallel capacitor (C_p), parallel resistance (R_p), and parallel inductance (L_p). As the defected ground structure involves the ground plane, a parallel circuit LC (L_{DG} and C_{DG}), equivalent to the defected ground structure is conjointly linked with the antenna patch circuit. The proposed antenna equivalent circuit shows the combination of equivalent circuit of radiating patch, the CSRR and the slots. The total value of L_{DG} and C_{DG} are the summation of CSRR and slots individual inductances capacitances. When the CSRR is placed in different positions, the total value of inductance and capacitance will change, and hence the impedance of the patch antenna varies. This leads to poor reflection coefficient.



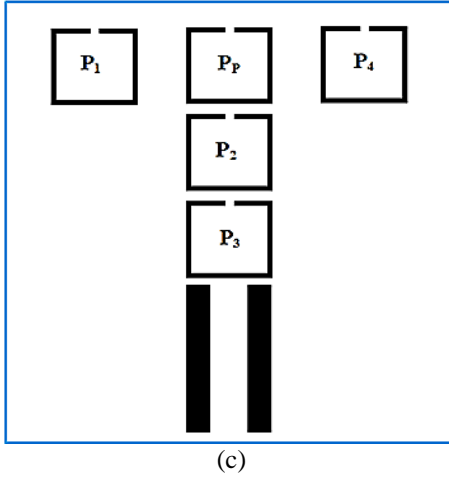


Fig. 1. Descriptive sketch of recommended complementary split ring resonator+slots designed defected ground structure incorporated in microstrip patch antenna: (a) front view, (b) rear view superimposed on front view, and (c) different positions of defected ground structure in rear view.

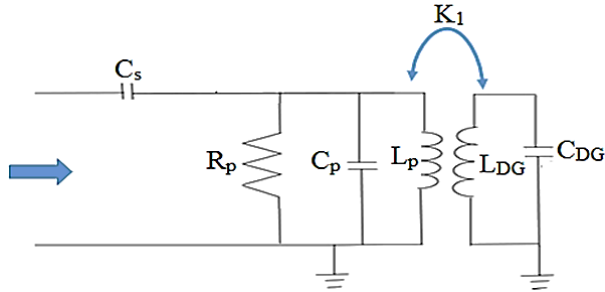


Fig. 2. Equivalent circuit of defected ground structure integrated with antenna.

Table 1: Antenna parameters with enhanced dimensions (in mm)

| Parameters | Dimensions (mm) |
|---|-----------------|
| Length of the Substrate (X) | 52 |
| Width of the Substrate(Y) | 50 |
| Length of the Patch(x) | 26 |
| Length of the Feed Line(a) | 9 |
| Width of a feed line | 1 |
| Length of the transformer (b) | 9.2 |
| Width of the transformer (c) | 5 |
| Length of the Complimentary Split Ring Resonator(d) | 10 |
| Width of the CSRR (e) | 1 |
| Gap of the CSRR (G) | 1 |
| Length of the slot (g) | 16 |
| Width of the slot(f) | 2 |

The resonance frequency is given by the relation,

$$f = \frac{c_0}{0.89(L+W)\sqrt{\epsilon_r}} \quad (1)$$

In which, c_0 is the velocity of light, while W and L indicate the width and length of the patch correspondingly, for a dielectric constant ϵ_r . A length $0.22 \lambda_0$ of CSRR metal from the mid-upper portion of the ground plane has been imprinted to produce a Defected Ground Structure groove on the ground plane, where λ_0 is the free-space wavelength associated with the resonance frequency. The introduction of the defected ground structure adapts the bandpass and bandstop characteristics of the antenna, consequently leading to a display of new resonance behavior. A microstripline feeding technique is applied to feed the antenna structure. The parameters and dimensions details of the antenna are tabulated in Table 1. Equations (2)-(9) are used to extract equivalent circuit model values for the patch segment and defected ground structure [11], [12]:

$$C_s = \frac{\tan(\beta s)}{\omega_0 Z_0} \quad (2)$$

$$C_p = \frac{\epsilon_0 \epsilon_r LW \cos^2\left(\frac{\pi y_0}{L}\right)}{2h} \quad (3)$$

$$R_p = \frac{Q}{\omega C_p} \quad (4)$$

$$Q = \frac{c_0 \sqrt{\epsilon_r}}{4 f_0 h} \quad (5)$$

$$L_p = \frac{1}{4\pi^2 f_0^2 C_p} \quad (6)$$

$$C_{DGS} = \frac{\omega_c}{2Z_0(\omega_0^2 - \omega_c^2)} \quad (7)$$

$$L_{DGS} = \frac{1}{4\pi^2 f_0^2 C_{DGS}} \quad (8)$$

$$f_0 = \frac{1}{2\pi \sqrt{L_{DGS} C_{DGS}}} \quad (9)$$

In these equations, s is the length of stub; Z_0 is the characteristic impedance, β is the wave number; C_s is the capacitance of source; h is the thickness of substrate; while L_{DGS} and C_{DGS} are the values of inductance and capacitance of the Defected Ground Structure equivalent circuit, respectively. Furthermore, ω_0 is the angular resonance frequency; y_0 is the distance from the patch edge to the feed point; and ω_c is the angular lower 3-dB cut-off frequency. The coupling coefficient (K_1) between the inductors is given by:

$$K_1 = \frac{f_e^2 - f_m^2}{f_e^2 + f_m^2} \quad (10)$$

Here, f_m and f_e are the frequencies consistent to the upper and lower 6-dB points around the resonance frequency, and these positions are referred to as the magnetic and electric walls, respectively. Using equation

(10) a value of $K_1 = 0.06$ is obtained [13]. All known parameter values were substituted in equations (4)-(8), and the unknown parameters were found by the calculation - $C_{DGS} = 2.25$ pF, $R_P = 59.8\Omega$, $L_{DGS} = 2.77$ nH, $C_S = 22.5$ pF, and $L_P = 0.62$ nH; since f_m and f_e are 2.25 GHz and 2.8 GHz respectively. Using the Advance Design System (ADS - 2017), the equivalent circuit model shown in Fig. 2 is simulated using the computed parameters. The reflection of measured coefficients (S_{11}) and simulated results are compared with the response of the ECM as depicted in Fig. 7. Meanwhile, the mutual coupling between the defected ground structure and patch leads to a variation of the antenna input impedance, due to a modification of the ground distribution. The fringing field effect is altered by these distribution variations, thereby changing the effective dielectric constant. According to the equation (5), the effective dielectric constant is directly proportional to the square of the quality factor (Q). Furthermore, the quality factor is inversely proportional to the antenna's bandwidth (BW), as can be observed from the relationship:

$$BW = ((VSWR) - 1)/Q\sqrt{VSWR}. \quad (11)$$

Hence, effective dielectric constant changes due to the introduction of a Defected Ground Structure influence the antenna bandwidth and the quality factor.

III. RESULTS AND DISCUSSION

A. Impedance of input

The computer-generated reactance (X_{in}) and input resistance (R_{in}) values with various defected ground structure placements are demonstrated in Fig. 3. The impedance of the antenna is matched to 50Ω through a quarter wave transformer. However, due to the resulting shape discontinuities, the antenna suffers from spurious radiations, which lead to increased cross-polarization. In this design, parallel slots are introduced near the edge feed to reduce cross-polarized radiation. The impact of shifting the CSRR defected ground structure to various positions is shown in Fig. 3 (a). The value of W_{SUB} is set at 50 mm, following which the placement of the CSRR defected ground structure is altered according to the positions illustrated in Fig. 1 (c). The position corresponding to the best impedance match is identified. Fig. 3 (a)-inset shows the antenna rear view with the final proposed position. The recommended placement of the defected Ground structure is position PP, where the best value of $R_{in} = 50\Omega$ and $X_{in} = 0$ are attained at the resonance frequency of 2.6 GHz. The variation in values of the input resistance trail the Gaussian distribution, whereas where the changes in the input reactance approximate a cosine distribution, which further clarifies the choice of the recommended placement. Variations in the current distribution on the ground cause the impedance value to increase or decrease, depending on the position of the CSRR. Here, the impact of surface current distribution on the fringing effect is low at

different positions. However, a maximum distribution occurs at the proposed position because of proper impedance matching and less spurious radiation. The proposed location of the defected ground structure is further investigated with respect to its impact on the antenna reflection coefficient, as displayed in Fig. 4.

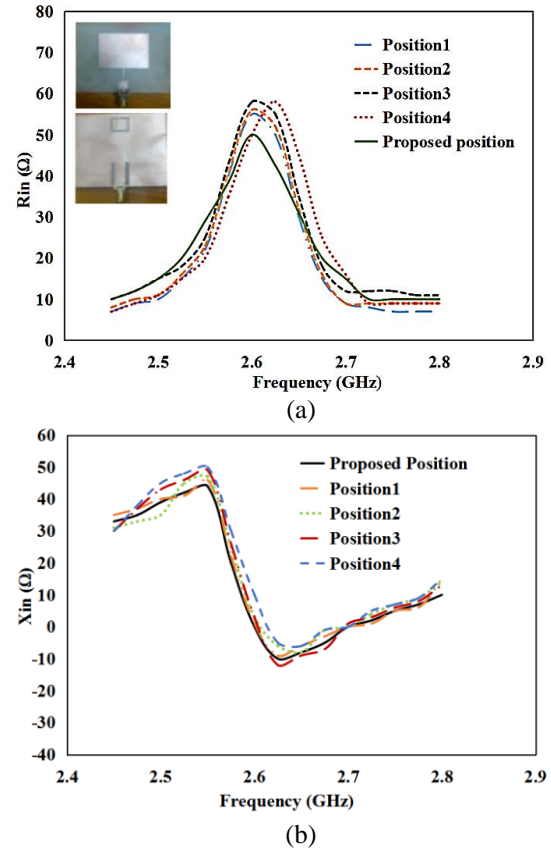


Fig. 3. Impedance of the defected ground structure loaded antenna for various locations of CSRR on the ground plane: (a) input resistance (R_{in}), and (b) input reactance (X_{in}).

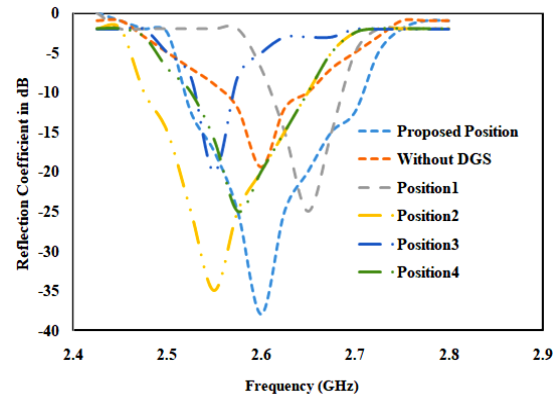


Fig. 4. Differences in simulated reflection coefficients for position deviations of the defected ground structure.

In this study, it can be observed that the resonance frequency increases as the CSRR is shifted vertically downwards. In addition, shifting the CSRR position to the left or right of the center axis changes the anticipated resonance frequency, with lower levels of reflection coefficient attained in both cases than with vertical displacement of CSRR position. Therefore, the location of the defected ground structure plays a crucial role in input impedance matching. The cross-polarization performance is affected by the surface current distribution. The patterns of surface current distribution are likewise dependent on the position of the defected ground structure (i.e., CSRR+slots). An odd-symmetric pattern is needed to reduce the cross-polarization. As a result of proper impedance matching with respect to the CSRR position, the reflection coefficient and surface current distributions are optimum and hence the cross polarization performance changes.

B. Distribution of surface current and performance of cross polarization

In Fig. 5, the surface current vector for the proposed location of the defected ground structure is demonstrated. As a result of the inclusion of a defected ground structure, surface current distribution is altered. The defected ground structure location is adjusted to provide an odd-symmetric pattern in order to reduce the cross-polarization.

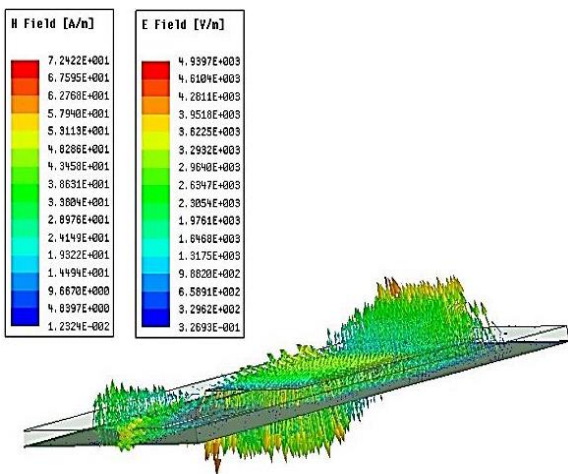


Fig. 5. Distribution of surface current vector and magnetic field paths of CSRR defected ground structure slots of proposed antenna.

No other defected ground structure positions were observed to show the x-axis oriented odd-symmetric surface current paths in the H-plane, as depicted in Fig. 6. Hence, the recommended defected ground structure positioned at middle leads to acceptable surface current vector distributions and lower levels of cross-polarization.

There is no significance alteration in the observed co-polarization patterns as a consequence of the positioning of the defected ground structure. However, the H-plane cross-polarization patterns posted significant changes. The proper termination of radiated fields for the recommended location of defected ground structure containing the CSRR shape leads to a regular cross-polarization pattern in the H-plane, with a comparative decline in cross-polarization of 44 dB over $\pm 50^\circ$, compared to the other defected ground structure locations.

C. Measurement results

Using an appropriate experimental setup in order to authenticate the performance of the proposed prototype antenna, the reflection coefficient and the radiation patterns are measured after the model fabrication. Figure 7 summarizes a comparison of simulated and measured reflection coefficients, with and without the Defected Ground Structure over an operating frequency range.

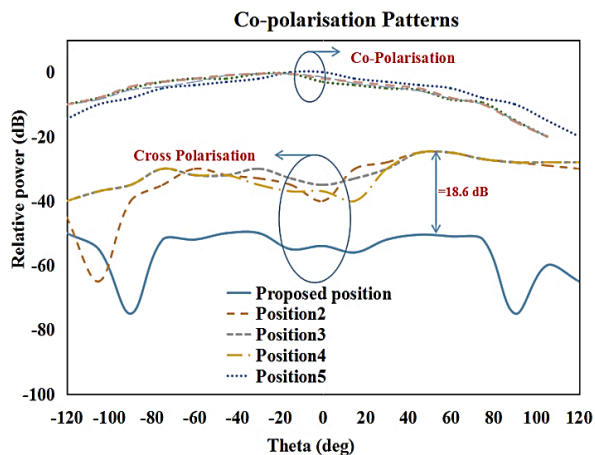


Fig. 6. Patterns of co-polarization for the H- and E-planes and the patterns of cross-polarization for the H-plane.

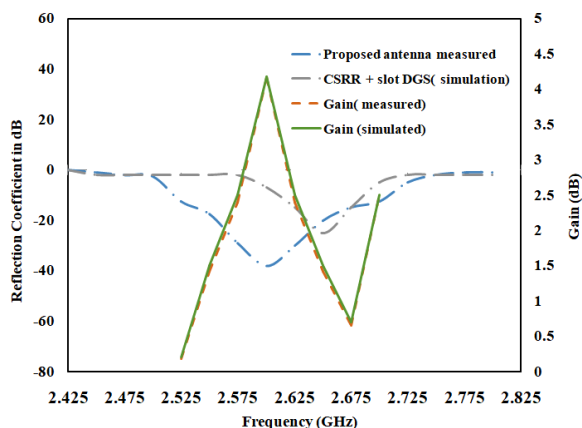


Fig. 7. Characteristics of S_{11} vs frequency, and gain vs frequency.

Table 2: Comparison of the performance of the proposed structure with related works

| S. No | Methodology | Frequency (GHz) | Cross Polarisation Reduction (dB) | Improvements in Impedance Matching (dB) | Year |
|-----------------|--|------------------|---|---|------|
| [4] | Pair of short pins | 2.241,2.478 | 16 | No data | 2009 |
| [6] | DGS+Slotted patch | 2-21 | Reduced by H-Plane by 20 dB | Impedance matching reduced after insert DGS | 2016 |
| [7] | DGS | 5.83-6.03 | 7-12 | 5.2 | 2016 |
| [8] | DGS | 9-10 | 15 | Not mentioned | 2014 |
| [9] | Parallel slots as DGS | 2.9,6 | For both band 15 dB reduction is achieved | No data | 2018 |
| [14] | Horizontal meandered dipoles and vertical parasitic elements | 1.71-2.69 | 10 | No data | 2019 |
| Proposed | CSRR+Slots parallel to feed line | 2.59-2.75 | 18.6 | 24 | |

From this result, it can be determined that, on introducing a Defected Ground Structure will make a change in the operational band of 2.62 GHz –2.70 GHz to 2.59 GHz–2.75 GHz. In addition, the resulting impedance matching upgrades the reflection coefficient from 30 dB (S_{11} without Defected Ground Structure) to 54 dB (S_{11} with Defected Ground Structure). A close agreement is observed between the results of ECM response and measured electromagnetic model as shown in Fig. 8.

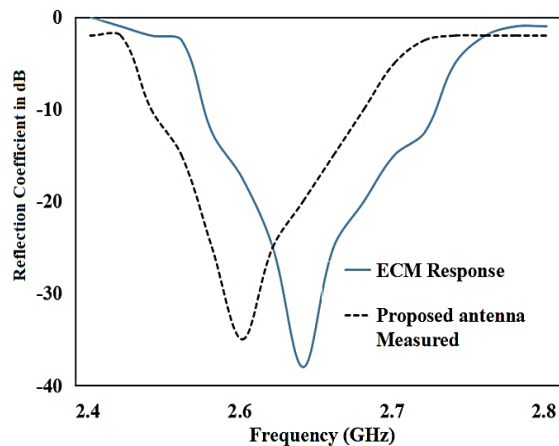


Fig. 8. Proposed antenna measured vs equivalent circuit model response (ECM).

Over the whole functioning band, the advantage is in the range of tolerance and it demonstrates a maximum peak gain of 4.16dB at the resonance frequency. In this investigation, the improvement of bandwidth using defected ground structure, comprising of a CSRR and slots, is around 200 MHz. Although the level of bandwidth improvement is modest, this approach can be useful to

the study of any defected ground structure shape to improve impedance matching, as well as increase microstrip patch antenna bandwidth. To further clarify the benefits of the proposed method over the earlier reported methods, the Table 2 shows that the proposed design is much simpler and can achieve greater levels of cross-polarization reduction, alongside a better matching of impedance.

IV. CONCLUSION

The applicability of a defected ground structure for better impedance matching and a lower level of cross-polarization have been successfully studied. The use of an ECM enabled an understanding of the impact of the inclusion of a CSRR and slots as a defected ground structure on the rectangular microstrip patch antenna. The CSRR positioned at the mid-upper region of the ground plane was shown to offer improved impedance matching results, and a low, uniform cross-polarization over an angle range of $\pm 50^\circ$. The achieved performance is encouraging when compared to the similar reported works. Finally, this study presents a useful insight to optimizing the location of a defected ground structure for a deliberate suppression of cross-polarization and impedance matching improvement.

REFERENCES

- [1] L. I. Basilio, M. A. Khayat, T. Jeffery and J. T. Williams, "The dependence of the input impedance on feed position of probe and microstrip line-fed patch antennas," *IEEE Transactions on Antennas and Propagation*, vol. 49, no. 1, pp. 45-47, 2001, doi: 10.1109/8.910528, 2001.
- [2] T. Samaras, A. Kouloglou, and J. N. Sahalos, "A note on the impedance variation with feed position of a rectangular microstrip-patch antenna," *IEEE*

- Antennas and Propagation Magazine*, vol. 46, no. 2, pp. 90-92, 2004, doi: 10.1109/Map.2004.1305543.
- [3] Y. Hu, D. R. Jackson, and J. T. Williams, "Characterization of the input impedance of the inset-fed rectangular microstrip antenna," *IEEE Transactions on Antennas and Propagation*, vol. 56, no. 10, pp. 3314-3318, 2008, doi: 10.1109/Tap.2008.929532.
- [4] X. Zhang and L. Zhu, "Patch antennas with loading of a pair of shorting pins toward flexible impedance matching and low cross polarization," *IEEE Transactions on Antennas and Propagation*, vol. 64, no. 4, pp. 1226-1233, 2016, doi:10.1109/ Tap.2016.2526079.
- [5] A. Kandwal, R. Sharma, and S. K. Khah, "Bandwidth enhancement using CSRR defected ground structure for a microstrip antenna," *Microwave and Optical Technology Letters*, vol. 55, no. 10, 27836, 2013.
- [6] M. K. Khandelwal, B. K. Kanaujia, and S. Dwari, "Bandwidth enhancement and cross-polarization suppression in ultra wide band microstrip antenna with defected ground plane," *Microwave and Optical Technology Letters*, vol. 56, no. 9, pp. 2141-2146, 2014, doi: 10.1002/Mop.28499.
- [7] D. Guha, C. Kumar, and S. Pal, "Improved cross polarization characteristics of circular microstrip antenna employing arc shaped defected ground structure (Defected Ground Structure)," *IEEE Antennas and Wireless Propagation Letters*, vol. 8, pp. 367-1369, 2009, doi: 10.1109/Lawp.2009.2039462.
- [8] C. Kumar and D. Guha, "Asymmetric geometry of defected ground structure for rectangular microstrip: A new approach to reduce its cross-polarized fields," *IEEE Transactions on Antennas and Propagation*, vol. 64, no. 6, pp. 2503-2506, 2016, doi: 10.1109/Tap.2016.2537360.
- [9] M. I. Pasha, C. Kumar, and D. Guha, "Simultaneous compensation of microstrip feed and patch by defected ground structure for reduced cross-polarized radiation," *IEEE Transactions on Antennas and Propagation*, vol. 66, no. 12, pp. 7348-7352, 2018, doi: 10.1109/Tap.2018.2869252.
- [10] A. Ghosh, S. Chakraborty, and S. Chattopadhyay, "Rectangular microstrip antenna with dumbbell shaped defected ground structure for improved cross polarised radiation in wide elevation angle and its theoretical analysis," *IET Microwaves, Antennas and Propagation*, vol. 10, pp. 68-78, 2016, doi: 10.1049/Iet-Map.2015.0179.
- [11] S. Chattopadhyay, M. Biswas, and J. Siddiqui, "Rectangular microstrips with variable air gap and varying aspect ratio: Improved formulations and experiments," *Microwave and Optical Technology Letters*, vol. 51, no. 1, pp. 169-173, 2009, doi: 10.1002/Mop.24025.
- [12] R. Garg, P. Bhartia, I. Bahl, and A. Ittipiboon, *Microstrip Antenna Design Handbook*. Boston - London: Artech House, 2001, Isbn-13: 978-0890065136.
- [13] H. Hirayama, "Equivalent circuit and calculation of its parameters of magnetic-coupled-resonant wireless power transfer," *Kim, K. I. (Ed.) Wireless Power Transfer Principles and Engineering Explorations. Intech*, pp. 117-132, 2012, Isbn: 978-953-307-874-8.
- [14] O. M. Kadagan, C. Turkmen, and M. Secmen, "Base station antenna with enhanced cross polarization discrimination performance by using horizontal meandered dipoles and vertical parasitic elements," *Advanced Electromagnetics*, vol. 8, no. 2, pp. 28-38, 2019, doi: 10.7716/ aem.v8i2.989.



N RajeshKumar is a Research Scholar pursuing his Ph.D. degree at Department of Electronics and Communication Engineering, Annamalai University, Chidambaram, India. His current research interest includes antenna design and RF circuits.



P. D. Sathya is an Assistant Professor in the Department of Electronics and Communication Engineering at Annamalai University, India. She obtained B.E. (Electronics and Communication), M.E. (Applied Electronics) and Ph.D. degrees from Periyar University, Anna University and Annamalai University in the years 2003, 2005 and 2012, respectively. She has 15 years of experience in teaching and research & development with specialization in signal processing, image and video Processing and antenna design. She has published more than 50 research papers in reputed International Journals including Elsevier and Inderscience, has presented 30 and above papers in various International Conferences.



Sharul Kamal Abdul Rahim received the degree in Electrical Engineering from The University of Tennessee, USA, the M.Sc. degree in Engineering (Communication Engineering) from Universiti Teknologi Malaysia (UTM), and the Ph.D. degree in Wireless Communication System from the University of Birmingham, U.K., in 2007. After his graduation from The University of Tennessee,

he spent three years in industry. After graduating the M.Sc. degree, he joined UTM in 2001, where he is currently a Professor with the Wireless Communication Centre. He has published over 200 learned papers, including the IEEE Antenna and Propagation Magazine, the IEEE Transactions on Antenna and Propagation, IEEE Antenna and Propagation Letters, and taken various patents. His research interests include antenna design, smart antenna system, beamforming network, and microwave devices for fifth generation mobile communication. He is a Senior Member of IEEE Malaysia Section, a member of the Institute of Engineer Malaysia, a Professional Engineer with BEM, a member of the Eta Kappa Nu Chapter, University of Tennessee, and the International Electrical Engineering Honor Society. He is currently an Executive Committee of the IEM Southern Branch.



Akaa Agbaeze Eteng obtained a B. Eng. degree in Electrical/Electronic Engineering from the Federal University of Technology Owerri, Nigeria in 2002, and a M.Eng. degree in Telecommunications and Electronics from the University of Port Harcourt, Nigeria in 2008. In 2016, he obtained a Ph.D. in Electrical Engineering from Universiti Teknologi Malaysia. Currently, he is a Lecturer at the Department of Electronic and Computer Engineering, University of Port Harcourt, Nigeria. His research interests include wireless energy transfer, radio frequency energy harvesting, and wireless powered communications.

Parameter Design of Conformal PML Based on 2D Monostatic RCS Optimization

Y. J. Zhang* and X. F. Deng

Northwestern Polytechnical University, Xi'an, 710072, P.R. China

*zyj19191@nwpu.edu.cn

Abstract – In this study, 2D finite element (FE) solving process with the conformal perfectly matched layer (PML) is elucidated to perform the electromagnetic scattering computation. With the 2D monostatic RCS as the optimization objective, a sensitivity analysis of the basic design parameters of conformal PML (e.g., layer thickness, loss factor, extension order and layer number) is conducted to identify the major parameters of conformal PML that exerts more significant influence on 2D RCS. Lastly, the major design parameters of conformal PML are optimized by the simulated annealing algorithm (SA). As revealed from the numerical examples, the parameter design and optimization method of conformal PML based on SA is capable of enhancing the absorption effect exerted by the conformal PML and decreasing the error of the RCS calculation. It is anticipated that the parameter design method of conformal PML based on RCS optimization can be applied to the cognate absorbing boundary and 3D electromagnetic computation.

Index Terms – 2D conformal PML, monostatic RCS, parameters optimization, sensitivity analysis, simulated annealing algorithm.

I. INTRODUCTION

In FE computation for the electromagnetic scattering, the local boundary condition refers to the most extensively employed open-domain boundary condition. As the scattering target turns larger and more sophisticated, the more rigorous requirement of local boundary condition are raised. How to build a high-performance local boundary condition, save the spatial scattering elements and enhance the solution efficiency of finite element method (FEM) has always been the hotspot in open-domain electromagnetic scattering computation study. Perfectly matched layer (PML) [1-3] refers to the optimal local boundary condition over the past few years. Theoretically, the absorption effect of PML is only determined by the thickness and the number of layers of PML for the electromagnetic wave that exhibits an arbitrary frequency and an incident angle. Moreover, the conformal PML (CPML) does not disturb

the sparsity of the system matrix, i.e., a property to effectively store and solve the FEM solution of electromagnetic scattering. Though the rectangular (2D) or block (3D) PML [4-10] turns into the popular mesh truncation boundary, a more efficient conformal PML [11-13] absorbing boundary is built for the larger size and more complex scattering targets. The conformal method is capable of generating the mesh truncation boundary that is consistent with the shape of scatterers to minimize the scattering space between scatterers and absorbing boundaries; thus, conformal PML can effectively save the spatial scattering elements and enhance the solution efficiency of FEM [14-17]. Accordingly, why conformal PML constantly arouses the attention from researchers is explained. Due to the above advantages and its outstanding role in the finite element scattering computation, the conformal PML is selected as the optimization design object, and the absorption effect and calculation efficiency of conformal PML are expected to be improved through the parametric design and RCS optimization algorithm proposed in this paper. Moreover, it is hoped that this study can provide some research ideas and exploration direction for the optimization design of cognate absorbing boundary conditions.

In this study, to enhance the absorbing efficiency of conformal PML and reduce the error of RCS calculation, a method is proposed in the present study to optimize the basic parameters of 2D conformal PML by the simulated annealing algorithm. By typical numerical cases, the availability and feasibility of the optimization design method are verified. Considering its good availability and applicability, the optimization design method in this paper can be extended from 2D electromagnetic computation to 3D electromagnetic computation.

II. FE SOLUTION OF 2D ELECTROMAGNETIC SCATTERING WITH CONFORMAL PML

Overall, the open domain electromagnetic scattering problem can be addressed in the region surrounded by the conformal PML. The conformal PML can be considered a shell composed of lossy anisotropic media,

exhibiting geometric similarity to the outer surface of scatterers. In the construction of conformal PML (Fig. 1), the surface near the scatterer is termed as the inner surface; besides, the outermost surface away from scatterers is called the outer surface or back surface. On the whole, the conformal PML is designed as the multi-layer shells exhibiting different thicknesses to exhibit a high absorbing efficiency. In the region of conformal PML, the permeability and permittivity are respectively expressed as $\bar{\mu} = \mu_r \bar{\Lambda}$ and $\bar{\varepsilon} = \varepsilon_r \bar{\Lambda}$. In the local coordinate system (ξ_1, ξ_2, ξ_3) , the constitutive parameters of conformal PML are defined in the complex stretching [14, 18]:

$$\bar{\Lambda}_{\xi_1, \xi_2, \xi_3} = \begin{bmatrix} \frac{s_2 s_3}{s_1} & 0 & 0 \\ 0 & \frac{s_1 s_3}{s_2} & 0 \\ 0 & 0 & \frac{s_1 s_2}{s_3} \end{bmatrix}_{\xi_1, \xi_2, \xi_3}, \quad (1)$$

$$\begin{cases} s_1 = (r_{01} + \tilde{\xi}) / r_1 \\ s_2 = (r_{02} + \tilde{\xi}) / r_2 \\ s_3 = s = 1 - j\delta \left(\frac{\xi_3}{t} \right)^m, \\ \tilde{\xi} = \int_0^{\xi_3} s(\zeta) d\zeta \end{cases}, \quad (2)$$

where ξ_1, ξ_2, ξ_3 denote orthogonal local coordinate components; r_{01} and r_{02} represent the principal radiuses of curvature of a given point on the inner surface of conformal PML [14]; $r_1 = r_{01} + \xi_3$ and $r_2 = r_{02} + \xi_3$ refer to the principal radiuses of curvature of point lengthened ξ_3 following the outer normal direction of the given point; s indicates the complex stretching variable [14] in the ξ_3 direction; t is the total thickness of the conformal PML; δ is the loss factor of the conformal PML; m represents the extension order of complex extension variable in the conformal PML.

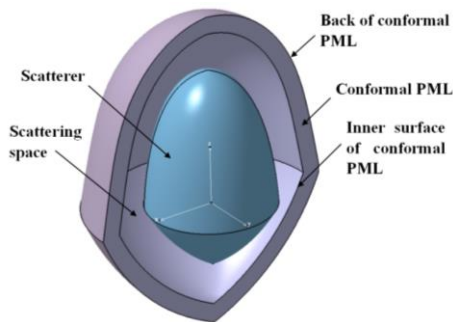


Fig. 1. The construction of a conformal PML.

In the 2D case, assuming that the local coordinate axis direction ξ_3 complies with the z -axis direction of the global coordinate system; the parameters of the conformal PML remains constant along the z -axis direction; the constitutive parameters [15] of conformal PML are defined as:

$$\bar{\Lambda}_{x,y,z} = \begin{bmatrix} \tilde{\Lambda} & 0 \\ 0 & \beta \end{bmatrix}, \quad (3)$$

$$\tilde{\Lambda} = \tilde{J}^t \begin{bmatrix} \alpha & 0 \\ 0 & 1/\alpha \end{bmatrix} \tilde{J}, \quad (4)$$

where $\tilde{\Lambda}$ denotes a 2×2 submatrix; \tilde{J} represents the Jacobi matrix of 2D coordinate transformation. $\alpha = s_2/s_1$ and $\beta = s_1 s_2$.

The following derivation is expressed based on the electric field E_z . By substituting (4) into the wave equation of 2D electromagnetic scattering problem, the wave equation [15] with the conformal PML is expressed:

$$\nabla \cdot \left[\frac{1}{\mu_r} \tilde{\Lambda} \nabla E_z \right] + k_0^2 \beta E_z = 0. \quad (5)$$

The corresponding functional expression is written as:

$$F(E^s) = \frac{1}{2} \iint_{\Omega} \left(\frac{1}{\mu_r} \nabla E_z \cdot \tilde{\Lambda} \cdot \nabla E_z - k_0^2 \beta E_z^2 \right) d\Omega. \quad (6)$$

Thus, in the conformal PML region Ω , the element matrix is expressed as:

$$K_{ik}^e = \iint_{\Omega} \left[\frac{1}{\mu_r} \nabla N_i^e \cdot \tilde{\Lambda} \cdot \nabla N_k^e - k^2 \beta N_i^e \cdot N_k^e \right] d\Omega. \quad (7)$$

If the triangular element is employed for the region discretization, the matrix elements in (7) are expressed as follows:

$$\begin{cases} K_{11}^e = \frac{l_{12}^e l_{12}^e}{\Delta^e} \left[\frac{1}{\mu_r^e} \alpha^e - \frac{k_0^2 \varepsilon_r^e \beta^e}{24} (f_{11}^e + f_{22}^e - f_{12}^e) \right] \\ K_{22}^e = \frac{l_{23}^e l_{23}^e}{\Delta^e} \left[\frac{1}{\mu_r^e} \alpha^e - \frac{k_0^2 \varepsilon_r^e \beta^e}{24} (f_{22}^e + f_{33}^e - f_{23}^e) \right] \\ K_{33}^e = \frac{l_{13}^e l_{13}^e}{\Delta^e} \left[\frac{1}{\mu_r^e} \alpha^e - \frac{k_0^2 \varepsilon_r^e \beta^e}{24} (f_{11}^e + f_{33}^e - f_{13}^e) \right] \\ K_{12}^e = \frac{l_{12}^e l_{23}^e}{\Delta^e} \left[\frac{1}{\mu_r^e} \alpha^e - \frac{k_0^2 \varepsilon_r^e \beta^e}{48} (f_{12}^e + f_{23}^e - 2f_{13}^e - f_{22}^e) \right] \\ K_{13}^e = \frac{l_{12}^e l_{13}^e}{\Delta^e} \left[\frac{1}{\mu_r^e} \alpha^e - \frac{k_0^2 \varepsilon_r^e \beta^e}{48} (f_{12}^e + f_{13}^e - 2f_{23}^e - f_{11}^e) \right] \\ K_{23}^e = \frac{l_{13}^e l_{23}^e}{\Delta^e} \left[\frac{1}{\mu_r^e} \alpha^e - \frac{k_0^2 \varepsilon_r^e \beta^e}{48} (f_{13}^e + f_{23}^e - 2f_{12}^e - f_{33}^e) \right] \end{cases}, \quad (8)$$

where Δ^e denotes the area of element; l_{ij}^e represents the constant coefficient of element; f_{ij}^e is the source function of element. For the specific calculation formula, please refer to [19].

From the theoretical perspective, the electromagnetic wave is completely absorbed at the back surface of the conformal PML, which is expressed as:

$$E_z|_{\Gamma_{CPML}} = 0, \quad (9)$$

where Γ_{CPML} denotes the boundary of back surface of the conformal PML. If the scatterer acts as a conductor, the incident electromagnetic wave is overall reflected. Thus, Dirichlet boundary conditions should be set on the scatterer surface.

After the mentioned element matrixes are assembled to form the global matrix $[k]$ and the corresponding boundary conditions and incident conditions are substituted, the system equations as written in (10) can be solved to yield the electric field distribution:

$$[K]\{E_z\} = \{b\}. \quad (10)$$

The electric field solved is adopted to calculate the single station RCS:

$$\sigma = \lim_{\rho \rightarrow \infty} 2\pi\rho \frac{|E^{sc}|^2}{|E^{inc}|^2} = \lim_{\rho \rightarrow \infty} 2\pi\rho \frac{|H^{sc}|^2}{|H^{inc}|^2}. \quad (11)$$

The normalized RCS can be a popular expression:

$$\sigma/\lambda = 10\lg(\sigma/\lambda). \quad (12)$$

III. NUMERICAL CASE

In the present study, the incident plane electromagnetic waves are defined as:

$$\Phi^{inc} = e^{jk_0(x\cos\varphi^{inc} + y\sin\varphi^{inc})}, \quad (13)$$

where φ^{inc} denotes the incident angle. The wavelength of incident plane electromagnetic waves is expressed as λ .

To subsequently optimize the parameter of 2D conformal PML, three numerical cases are presented in this section based on two typical 2D scatterers.

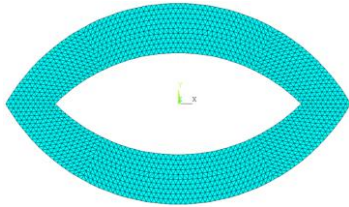


Fig. 2. Meshed ovate.

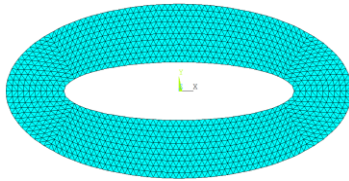


Fig. 3. Meshed ellipse.

Case 1: As shown in Fig. 2, the width and thickness

of conducting ovate are 5λ and 2.07λ , respectively. The scattering area (the distance between the inner surface of conformal PML and the surface of scatterer) exhibits the thickness of 0.5λ . The mesh size reaches 0.05λ .

Case 2: Like the Fig. 2, the width and thickness of conducting ovate are 15λ and 2.14λ respectively. The thickness of scattering area is 0.5λ . The mesh size is 0.05λ .

Case 3: As shown in Fig. 3, the major and minor axes of conducting ellipse are λ and 0.5λ , respectively. The scattering area exhibits the thickness of 0.5λ . The mesh size is 0.05λ .

IV. SENSITIVITY ANALYSIS OF 2D RCS

As indicated from the deduction in the Section II, the basic designed parameters of conformal PML affecting RCS are the loss factor δ , extension order m , layer thickness d and layer number n , i.e.,

$$\sigma \sim f(\delta, m, d, n). \quad (14)$$

To explore the effect of these basic parameters on 2D RCS, a sensitivity analysis for three numerical cases in the Section III is conducted with the central difference method. The basic formula is expressed as:

$$\begin{aligned} F'(x_i) &= \frac{F(x_i+h) - F(x_i-h)}{2h} + O(h^2) \\ &\approx \frac{F(x_i+h) - F(x_i-h)}{2h}, \end{aligned} \quad (15)$$

where the step size h is set to 1% of the corresponding parameter. The sensitivity function $F(x_i)$ can be considered the RCS σ in (14), while the variables x_i can be considered one of the loss factor δ , extension order m , layer thickness d and layer number n in (14).

Supposed that the wavelength of incident electromagnetic wave is set to $\lambda=0.01m$ (only to provide an exact input for program operation), the initial basic parameters of conformal PML are set as $\delta=10$, $m=2$, $d_i=0.05\lambda$, $n=6$, and the disturbance step size is set to $h=1\%$ for the initial basic parameters of conformal PML, the sensitivity function $F(x_i)$ can be calculated as listed

in Tables 1, 2, 3 at the different incident angles φ^{inc} . For example, in the sensitivity analysis process of case 1, the disturbance 1% of loss factor at incident angle 0° is substituted into (15), thus the sensitivity response of RCS at incident angle 0° will be obtained shown as the second row, second column cell of Table 1. In the same way, the sensitivity responses of RCS at the other incident angle will be calculated and listed in the second column of Table 1 for the disturbance 1% of loss factor. Similarly, the sensitivity responses of RCS for the disturbance 1% of extension order, layer thickness and layer number respectively can be obtained shown as the third, fourth and fifth column of Table 1. Repeat the

above sensitivity analysis process and the results are shown in tables 2 and 3.

Obviously, for the 2D RCS with the conformal PML, the most influential parameter is layer thickness, while the effects of other parameters are relatively small. Accordingly, the thickness of each layer will be adopted as the main design variables for the RCS optimization. Since the loss factor and extension order are the vital design parameters of conformal PML, the loss factor and extension order are still selected as design variables

to exhibit the optimal absorbing efficiency in the optimization analysis of next section. Theoretically, the more conformal PML layers (more absorbing media) will bring the better absorbing effect. However, with the increase of the layer number of conformal PML, the interlayer reflection error and the element number of conformal PML also raise. Trading off the absorbing effect, interlayer reflection error and the element number of conformal PML, here the layer number of conformal PML is set to 6.

Table 1: Sensitivity analysis results of case 1

| Incident Angle/(°) | Loss Factor | Extension Order | Layer Thickness | Layer Number |
|--------------------|-------------|-----------------|-----------------|--------------|
| 0 | -0.0216 | 0.1085 | -4.1254 | 0.0391 |
| 5 | 0.0513 | -0.1012 | -1.7991 | -0.0391 |
| 10 | 0.0806 | -0.2090 | 30.6554 | -0.0797 |
| 15 | 0.0065 | -0.0235 | -30.6450 | -0.0083 |
| 20 | -0.0338 | 0.0897 | -70.2444 | 0.0353 |
| 25 | 0.0533 | -0.0205 | 11.7344 | -0.0138 |
| 30 | -0.0167 | 0.0413 | 39.6296 | 0.0162 |
| 35 | -0.0352 | 0.0790 | 0.1706 | 0.0295 |
| 40 | 0.0065 | -0.0193 | -14.6755 | -0.0068 |
| 45 | -0.0076 | 0.0314 | 6.4041 | 0.0115 |
| 50 | 0.0002 | 0.0012 | 36.7430 | 0.0002 |
| 55 | 0.0095 | -0.0301 | 32.3789 | -0.0110 |
| 60 | -0.0025 | 0.0065 | -8.8950 | 0.0027 |
| 65 | -0.0110 | 0.0319 | -27.2776 | 0.0118 |
| 70 | -0.0059 | 0.0204 | 64.2721 | 0.0072 |
| 75 | 0.0003 | -0.0007 | -24.4353 | -0.0005 |
| 80 | 0.0100 | -0.0304 | -22.0506 | -0.0115 |
| 85 | 0.0097 | -0.0307 | -34.9960 | -0.0115 |
| 90 | 0.0133 | -0.0409 | 20.5271 | -0.0152 |

Table 2: Sensitivity analysis results of case 2

| Incident Angle/(°) | Loss Factor | Extension Order | Layer Thickness | Layer Number |
|--------------------|-------------|-----------------|-----------------|--------------|
| 0 | 0.0138 | -0.0023 | -9.2754 | 0.0078 |
| 5 | -0.0007 | 0.0001 | -50.3808 | 0.0029 |
| 10 | -0.0010 | 0.0002 | -89.3209 | -0.0032 |
| 15 | -0.0022 | 0.0004 | 85.3498 | -0.0150 |
| 20 | -0.0008 | 0.0001 | -132.4588 | 0.0681 |
| 25 | 0.0020 | -0.0003 | 41.3835 | -0.0079 |
| 30 | -0.0031 | 0.0005 | 11.0661 | 0.0107 |
| 35 | -0.0019 | 0.0003 | -12.1974 | -0.0131 |
| 40 | -0.0012 | 0.00018 | -39.7161 | 0.0214 |
| 45 | -0.0010 | 0.0002 | 20.7344 | -0.0048 |
| 50 | -0.0007 | 0.0001 | -7.0409 | -0.0044 |
| 55 | 0.0002 | -0.00001 | -13.4454 | -0.0018 |
| 60 | 0.0002 | -0.00001 | 5.4368 | 0.00005 |
| 65 | -0.0003 | 0.00001 | -12.5664 | 0.0004 |
| 70 | 0.0003 | -0.000002 | -10.9907 | 0.0006 |
| 75 | -0.0002 | 0.00001 | 1.6422 | 0.0006 |
| 80 | 0.0001 | 0.0002 | 5.3411 | -0.0015 |
| 85 | -0.00001 | 0.00001 | -9.9341 | 0.0004 |
| 90 | 0.0001 | -0.00001 | 16.2334 | -0.0007 |

Table 3: Sensitivity analysis results of case 3

| Incident Angle/(°) | Loss Factor | Extension Order | Layer Thickness | Layer Number |
|--------------------|-------------|-----------------|-----------------|--------------|
| 0 | 0.0480 | -0.2231 | 4.5503 | -0.0810 |
| 5 | 0.0479 | -0.2239 | -17.1200 | -0.0808 |
| 10 | 0.0467 | -0.2201 | 52.8826 | -0.0784 |
| 15 | 0.0393 | -0.1881 | 27.5349 | -0.0654 |
| 20 | 0.0243 | -0.1191 | 0.7037 | -0.0396 |
| 25 | 0.0064 | -0.0358 | -46.5160 | -0.0097 |
| 30 | -0.0086 | 0.0357 | 20.2953 | 0.0149 |
| 35 | -0.0176 | 0.0816 | -27.5811 | 0.0297 |
| 40 | -0.0176 | 0.0877 | -96.7805 | 0.0303 |
| 45 | -0.0106 | 0.0588 | 52.7488 | 0.0192 |
| 50 | -0.0029 | 0.0189 | 2.0418 | 0.0050 |
| 55 | 0.0053 | -0.0305 | 2.5652 | -0.0116 |
| 60 | 0.0111 | -0.0653 | -32.7123 | -0.0225 |
| 65 | 0.0082 | -0.0476 | -16.9139 | -0.0153 |
| 70 | -0.0001 | 0.0003 | -4.4872 | 0.0013 |
| 75 | -0.0069 | 0.0386 | -11.6805 | 0.0140 |
| 80 | -0.0096 | 0.0535 | -21.9851 | 0.0185 |
| 85 | 0.0098 | 0.0551 | -75.5233 | 0.0186 |
| 90 | -0.0100 | 0.0558 | 19.6414 | 0.0187 |

V. OPTIMIZATION ANALYSIS OF 2D RCS

Given the sensitivity analysis results in the previous section, the thickness of each layer d_i , loss factor δ and extension order m are employed as the optimization design variables. The optimization process aims to minimize the average error of 2D RCS calculated by the conformal PML and ABC absorbing boundary (the solution results with the conventional ABC absorbing boundary are considered the baseline). For the geometric symmetry of the examples, the incident angle is set to $0^\circ \sim 90^\circ$. To enhance the calculation accuracy, the incident angle interval is set to 1° . Accordingly, the optimization function is expressed as:

$$f(d_i, \delta, m) = \frac{\sum_{i=0}^{i=90} |\sigma_{\text{CPML}} - \sigma_{\text{ABC}}|}{91}. \quad (16)$$

The constraints are set as follows:

$$\begin{cases} 0.05\lambda \leq d_i \leq 0.5\lambda \\ 1 \leq \delta \leq 100 \\ 1 \leq m \leq 20 \end{cases}. \quad (17)$$

Given the efficiency and the stability of the optimization iteration, the simulated annealing algorithm (SA) [20] exhibiting the high stability in the global optimization algorithms is employed to search the optimal parameters of conformal PML. The optimization flow chart is illustrated in Fig. 4.

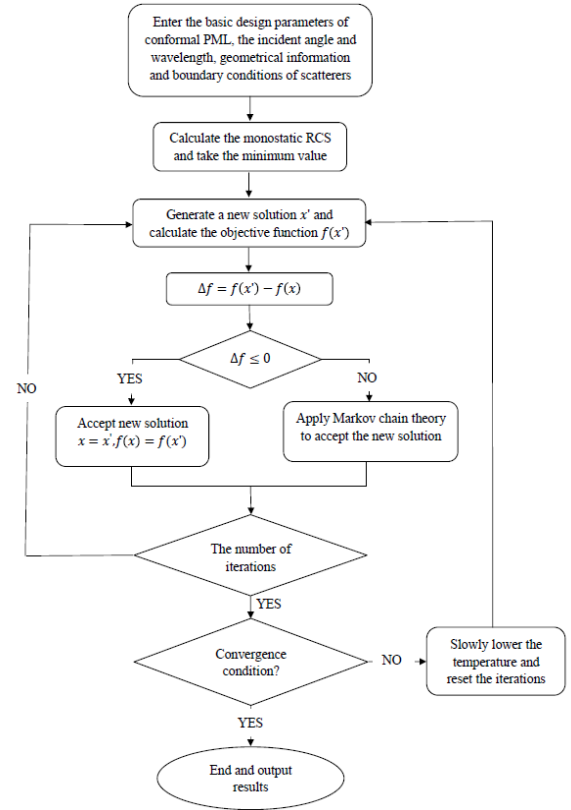


Fig. 4. SA optimization flowchart of 2D RCS with the conformal PML.

As indicated in the flow chart, the optimization program is compiled and run in MATLAB. Considering that the computation time cost for optimization will vary with the computer hardware configuration, here the number of iterations is used to show the optimization process and calculation efficiency. The optimization processes of three numerical cases are illustrated in Figs. 5, 6, 7. It is obvious that for the different shape and size scatterers (case 1, 2, 3), SA optimization algorithm can enter the convergence state in 100 iterations and obtain the convergence solution in 200 iterations. Moreover, the convergence process of SA optimization algorithm is very smooth. Therefore, SA algorithm can be applied into the RCS optimization solution of complex and 3D scatterers.

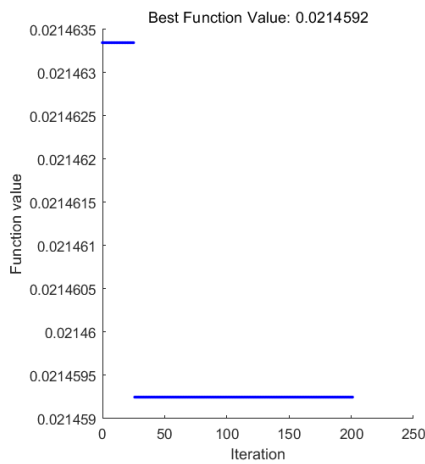


Fig. 5. RCS optimization process of case 1.

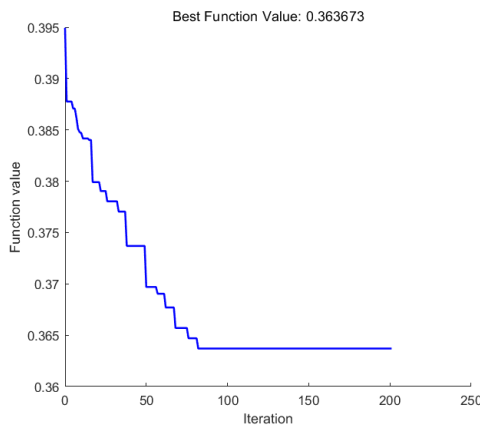


Fig. 6. RCS optimization process of case 2.

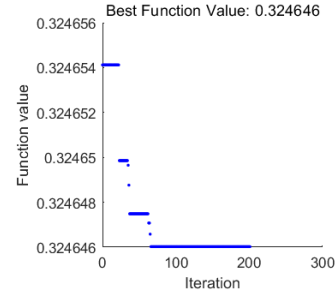


Fig. 7. RCS optimization process of case 3.

In Figs. 8, 9, 10, the 2D Monostatic RCS before and after the optimization for three numerical cases are compared with the conventional ABC absorbing boundary [19]. The parameter optimization results of 2D conformal PML are listed in Table 4. Table 5 lists the average errors of 2D monostatic RCS calculated by the conformal PML and ABC absorbing boundary. As revealed from the results, for the different shape and size scatterers (case 1, 2, 3), 2D monostatic RCS with the conformal PML after optimization is closer to the RCS with the conformal PML before optimization compared with the RCS with the conformal PML before optimization. The main reason is that SA algorithm can search the optimal parameters of conformal PML to minimize the interlayer reflection error and the average error of RCS calculated with the conformal PML and ABC absorbing boundary at the different incident angles. Therefore, the parameters optimization method of conformal PML based on SA is capable of obviously reducing the error, and the RCS calculation results with the optimized conformal PML are more consistent with the calculation results that exhibit the ABC absorbing boundary.

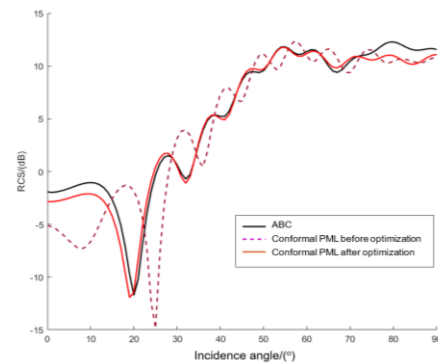


Fig. 8. 2D monostatic RCS before and after the optimization for case 1.

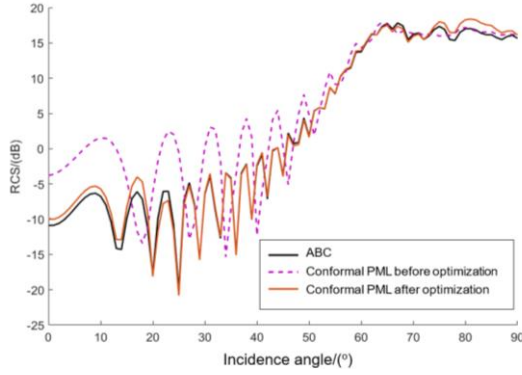


Fig. 9. 2D monostatic RCS before and after the optimization for case 2.

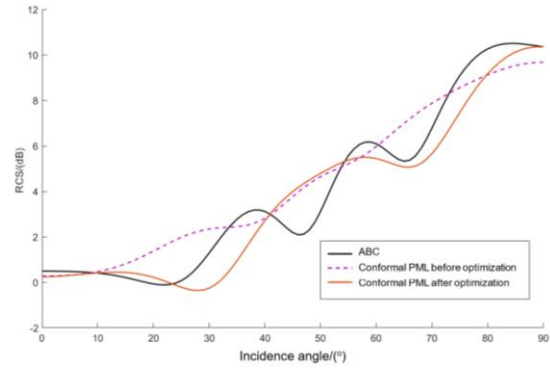


Fig. 10. 2D monostatic RCS before and after the optimization for case 3.

Table 4: Parameter optimization results of 2D conformal PML

| Opti. | Layer Thickness>(*λ) | | | | | | Loss Factor | Extension Order |
|-----------|----------------------|-----------|-----------|-----------|-----------|-----------|-------------|-----------------|
| | 1st Layer | 2nd Layer | 3rd Layer | 4th Layer | 5th Layer | 6th Layer | | |
| Initial | 0.05 | 0.05 | 0.05 | 0.05 | 0.05 | 0.05 | 13 | 2 |
| Example 1 | 0.0727 | 0.4746 | 0.4538 | 0.4769 | 0.4582 | 0.3865 | 5.9995 | 3.8061 |
| Example 2 | 0.1248 | 0.4868 | 0.0711 | 0.0500 | 0.0841 | 0.1219 | 94.2601 | 1.5402 |
| Example 3 | 0.0508 | 0.3656 | 0.3655 | 0.4369 | 0.3536 | 0.1923 | 26.9301 | 15.8849 |

Table 5: Average errors of 2D monostatic RCS calculated by the conformal PML and ABC

| Errors | Example 1 | | Example 2 | | Example 3 | |
|--|--------------|-------------|--------------|-------------|--------------|-------------|
| | Before Opti. | After Opti. | Before Opti. | After Opti. | Before Opti. | After Opti. |
| Average error/(dB) | 2.5399 | 0.0214 | 2.8547 | 0.3637 | 1.2343 | 0.3246 |
| Reduction percentage of average error /(%) | 99.1574 | | 87.2596 | | 73.7017 | |

VI. CONCLUSION

In the present study, the constitutive parameters of 2D conformal PML and FE solving process of electromagnetic scattering with the conformal PML are elucidated. For three numerical cases based on two 2D scatterers whose shapes are originating from the typical scattering targets [19], the sensitivity analysis of the basic design parameters of conformal PML (e.g., layer thickness, loss factor, extension order and layer number) is conducted by applying the 2D monostatic RCS as the objective function. Given the results of sensitivity analysis, the thicknesses of each layer are taken as the major optimization design parameters. Since the loss factor and extension order are also the vital design parameters of conformal PML, the loss factor and extension order are still considered the design variables in the optimization analysis. Lastly, the optimized design parameters of conformal PML with small calculation errors and high absorbing efficiency are conducted with the optimization method based on SA algorithm. Sequentially, the 2D monostatic RCS before and after the optimization for three

numerical cases are compared with the conventional ABC absorbing boundary. The numerical results suggest that the parameter optimization method of conformal PML proposed in the present study possesses the high absorbing performance, also can provide the optimization scheme and technical reference for parameter design of cognate absorbing boundary and 3D electromagnetic computation.

ACKNOWLEDGEMENT

This work was supported by National Science Foundation for Distinguished Young Scholars of China (11201375), Specialized Research Fund for the Doctoral Program of Higher Education of China (20106102120001) and Postdoctoral Science Foundation of China (201003680).

REFERENCES

[1] J. P. Berenger, "A perfectly matched layer for the absorption of electromagnetic waves," *Journal of Computational Physics*, vol. 114, no. 2, pp. 185-200, 1994.

- [2] C. Wu, E. A. Navarro, P. Y. Chung, and J. Litva, "Modeling of waveguide structures using the nonorthogonal FDTD method with a PML absorbing boundary," *Microwave and Optical Technology Letters*, vol. 8, no. 4, pp. 226-228, 1995.
- [3] W. C. Chew and J. M. Jin, "Perfectly matched layer in the discretized space: an analysis and optimization," *Electromagnetics*, vol. 16, no. 4, pp. 325-340, 1996.
- [4] S. D. Gedney, "An anisotropic perfectly matched layer-absorbing medium for the truncation of FDTD lattices," *IEEE Transactions on Antennas and Propagation*, vol. 44, no. 12, pp. 1630-1639, 1996.
- [5] J. P. Berenger, *Perfectly Matched Layer (PML) for Computational Electromagnetics*, Morgan & Claypool, 2014.
- [6] Z. Lou, D. Correia, and J.-M. Jin, "Second-order perfectly matched layers for the time-domain finite-element method," *IEEE Transactions on Antennas and Propagation*, vol. 55, no. 3, pp. 1000-1004, 2007.
- [7] Z. S. Sacks, D. M. Kingsland, R. Lee, and J. F. Lee, "A perfectly matched anisotropic absorber for use as an absorbing boundary condition," *IEEE Transactions on Antennas and Propagation*, vol. 43, no. 12, pp. 1460-1463, 1995.
- [8] O. Ozgun and M. Kuzuoglu, "Iterative leap-field domain decomposition method: A domain decomposition finite element algorithm for 3D electromagnetic boundary value problems," *IET Microwaves Antennas & Propagation*, vol. 4, no. 4, pp. 543-552, 2010.
- [9] Y. Xiao and Y. Lu, "Combination of PML and ABC for scattering problem," *IEEE Transactions on Magnetics*, vol. 37, no. 5, pp. 3510-3513, 2001.
- [10] M. Movahhedi, A. Abdipour, H. Ceric, A. Sheikholeslami, and S. Selberherr, "Optimization of the perfectly matched layer for the finite-element time-domain method," *IEEE Microwave and Wireless Components Letters*, vol. 17, no. 1, pp. 10-12, 2007.
- [11] O. Ozgun and M. Kuzuoglu, "Recent advances in perfectly matched layers in finite element applications," *Turkish Journal of Electrical Engineering and Computer Sciences*, vol. 16, no. 1, pp. 57-66, 2008.
- [12] B. Donderici and F. L. Teixeira, "Conformal perfectly matched layer for the mixed finite element time-domain method," *IEEE Transactions on Antennas and Propagation*, vol. 56, no. 4, pp. 1017-1026, 2008.
- [13] M. Kuzuoglu, B. B. Dundar, and R. Miiitra, "Conformal perfectly matched absorbers in finite element mesh truncation," *IEEE Antennas and Propagation Society International Symposium Digest*, vol. 2, pp. 1176-1179, 2000.
- [14] P. Liu, J. D. Xu, and W. Wan, "A finite-element realization of a 3D conformal PML," *Microwave and Optical Technology Letters*, vol. 30, no. 3, pp. 170-173, 2001.
- [15] P. Liu, "Investigation of PML for the Finite Element Analysis of Electromagnetic Scattering Problem," *Doctoral Thesis, Northwest Polytechnic University*, 2001.
- [16] T. Rylander and J. M. Jin, "Conformal perfectly matched layers for the time domain finite element method," *IEEE Antennas and Propagation Society International Symposium Digest*, vol. 1, pp. 698-701, 2003.
- [17] F. L. Teixeira, K. P. Hwang, W. C. Chew, and J.-M. Jin, "Conformal PML-FDTD schemes for electromagnetic field simulations: A dynamic stability study," *IEEE Transactions on Antennas and Propagation*, vol. 49, no. 6, pp. 902-907, 2001.
- [18] Y. J. Zhang and X. H. Zhang, "Normal directional NURBS arithmetic of conformal PML," *Applied Computational Electromagnetics Society Journal*, vol. 29, no. 11, pp. 904-910, 2014.
- [19] J. M. Jin. *The Finite Element Method in Electromagnetics*, Third Edition. Hoboken, NJ: Wiley, 2014.
- [20] J. Awange, B. Paláncz, R. Lewis, and L. Völgyesi, *Mathematical Geosciences: Hybrid Symbolic-Numeric Methods*, AG: Springer, 2018.

Analysis and Development of an Efficient Cross-Slot Loaded Compact Electromagnetic Band Gap Antenna

El Amjed Hajlaoui^{1,2} and Ziyad M. Almohaimeed²

¹Department of Electrical Engineering EL MANAR University, Tunis, 2092, Tunisia
hajlamjed@yahoo.fr

²Department of Electrical Engineering, College of Engineering, Qassim University, Buraydah, 51452, KSA
z.mohaimeed@qu.edu.sa

Abstract — This paper is devoted to a novel Electromagnetic Band Gap (EBG) single-feed circularly polarized microstrip EBG antenna with compact size proposed for C-Band applications. The antenna structure will include eight slits introduced at the boundary and the corners in the radiating square patch with a cross-slot at the center.

The provided study will effectively approve the various proposed structures and interest occupied by these types of antennas in the enhancement of output parameters (gain, directivity, radiation efficiency, and bandwidth) without much affecting the operating bandwidth at C-band.

At first, the concept and the realization of a directive and circularly polarized antenna using an electromagnetic band gap material whose circular polarization is generated by the structure itself is discussed. The analysis and simulation results are presented for an antenna operating at 6.1 GHz using computer Simulation Technologies (CST). Furthermore, the new compact circular polarized EBG antenna, compared to experimental results, will confirm the pre-studied goal of these kinds of antennas such as radiation efficiency, polarization purity, radiation efficiency, high directivity, and gain.

Index Terms — Circularly polarized cross-slot square patch antenna, dimensional characterization, electromagnetic waves & propagation, Electromagnetic Band Gap (EBG) resonator.

I. INTRODUCTION

Microstrip antennas are devices of choice in high performance applications where size, weight, cost, and ease of installation are prior requirements for specific wireless connexion [1]. Tunability in an antenna system is a quickly evolving feature that aims to control multifunctional antenna designs. Compared to conventional antennas, electromagnetic band gap (EBG) antennas provide an adjustment of diverse antenna parameters, including operational bandwidth, radiation

pattern, gain, and polarization [2]. From the fundamental limit of the classic antennas [3], applying antenna miniaturization techniques for the antennas comes at the expense of the antenna performance. Here, we propose a new approach to achieve the major goal of these designs, with a smaller form factor and better performance in terms of radiation efficiency, polarization purity, radiation pattern, directivity, and gain. Hence, a new single-feed circularly polarized microstrip antenna with compact size is presented where eight slits are introduced at the boundary and the corners in the radiating square patch with a cross-slot at the center. The resonance frequency of the proposed antenna is dependent on the length and width of the cross-slot and corner slit for the entire band of circular polarization. The whole structure is the deposit on the Arlon AD 250 substrate and fed by a single coaxial probe.

In order to perform the gain, the directivity, and the total radiation efficiency, a new concept of directive electromagnetic band gap (EBG) antenna will be analyzed [2]. Hence, the electromagnetic band gap structures are objects that prevent/assist the propagation of electromagnetic waves in a specified band of frequency for all incident angles and all polarization states [3], [4]. They have been used in several applications to improve the antenna's directivity [5] and permit a harmonic control [6].

The proposed antenna is achieved by cutting four equally spaced slits at the corner of the square patch where the dominant mode is TM₁₁ mode. The operating frequency band can be controlled via the cross slits lengths in the center of the square patch and adjusting the length of square patch. An arrangement combining the single feed square cross-slot patch antenna design and feeding sources included is considered necessary. Due to the existing of a single feeding point, the Position of the feeding point will permit Right-hand and Left-hand circular polarization operations due to two orthogonal modes with equal amplitudes, which are in-phase quadrature with the sign determining the sense of left-

hand circular polarization/right-hand circular polarization (LHCP/RHCP) [7]. CP is achieved here using a single feed and does not require an external polarizer [8]. The thickness of the substrate is chosen to reduce the spurious surface wave and width. Coaxial feeding techniques have been used as it is easier to implement. This technique will be used for the EBG circularly polarized cross-slot patch antenna and carry two benefits (such as improvement of bandwidth, beamforming, creating zero radiation beams) and filtering characteristics of the resonator (spatial filtering, increased directivity, misalignment) due to the resonant structure itself. The effect of EBG structures embedded over the patch is studied for enhancing the gain, directivity, and radiation efficiency. Simulation and experimental results at 6.1GHz are presented. Table 1 shows dimensions of the Proposed Structures

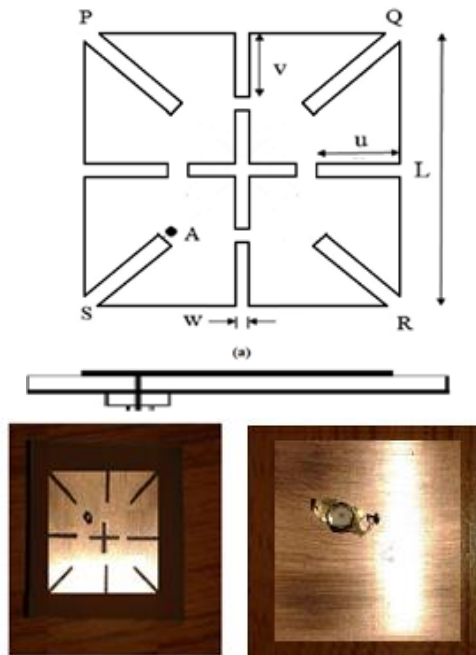


Fig. 1. Proposed cross-slot loaded compact antenna.

Table 1: Geometric parameters of the proposed compact cross-slot antenna

| Antenna Parameters | Value (mm) |
|---|------------|
| Length of square patch, L | 30 |
| Length of slit, u | 10 |
| Length of slit, v | 9.2 |
| Length of slit, w | 1.0 |
| Length of cross slot | 10 |
| Width of cross slot | 1.0 |
| Length of corner slit along diagonal PR | 12.5 |
| Length of corner slit along diagonal QS | 10.5 |
| Width of corner slits | 1.0 |

II. PATCH-SLOT CIRCULAR ANTENNA DESIGN & DEVELOPMENT

The physical and geometric substrate material parameters have an important part in the design and conception of the microstrip patch antenna. Permittivity, conductivity, thermal expansion, and cost are fundamental factors to choose specific material. In this work, the substrate material have a dielectric constant of 2.5 and a dielectric loss tangent of 0.009 [9]. These materials have the ability to open localized electromagnetic modes inside the prohibited frequency band-gap by introducing defects into the periodic structures [10]. EBG structures have been used in several applications, such as Directive antennas [11], harmonic control [12]. Here, an innovative design of single & multilayered patch-slot circular microstrip EBG antenna having a displacement of the coaxial feeding source from the center of the circular patch is proposed and its simulated radiation performance in free space conditions have been presented in comparison with the experimental results.

The proposal considerations for this cross-slot loaded compact circularly microstrip patch antenna as shown in Fig. 1 on Arlon AD 250 substrate material with a relative dielectric constant of 2.5 with a thickness of 1mm and geometric parameters as shown in Table 1. Coaxial feedings are used to ensure the circular polarization in the presence of slots (cross and inserted in boundary). Hence, When the ratio of the total slit length in the slot in the x-direction (L_x) to that in the y-direction (L_y) is properly chosen, the two near-degenerate modes can be excited, using a single feed along the diameter at $\phi=45^\circ$ planes, to be of equal amplitudes and 90° phase difference, which results in a CP radiation. When L_x is greater than L_y , the feed position at point A is for right-hand CP operation, while point B is for left-hand CP operation. The two slits on the x-axis have the same length L_x , and the two slits on the y axis have an equal length L_y , and ensure that $L_x > L_y$. Then, by varying x ($0 < x < y$).

An optimization of the structure thickness to give us best values of Return Loss, VSWR and 2-D Gain for the designed circular patch-slot antenna gave us a thickness 1.6mm

For a specific value of thickness $h=1.6$ and $\epsilon_r=2.5$, and as shown in Fig. 2, the experimental return loss of the antenna S11 is -21.055 at 6.0155 GHz with a measured bandwidth of 247.81MHz. The reflection coefficient value suggests that there is good matching at the frequency point below the -10 dB region. It covers the C-frequency band for military requirements for land, airborne and naval radars applications. The radiation power shows the maximum peak value at the resonant frequency

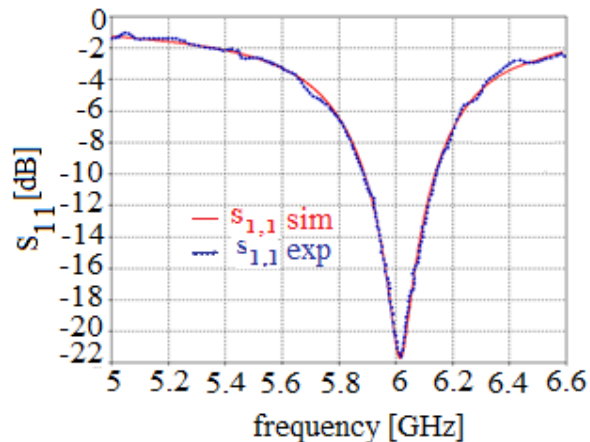


Fig. 2. Simulated versus measured reflection coefficient of the single-feed cross-slot loaded compact circularly polarized microstrip antenna.

In next Table 2, we present additional parameters given by the experimental approach versus the simulation ones. The far-zone electric field lies in the E-plane, and the far-zone magnetic field lies in the H plane. The patterns in these planes are referred to as the E and H plane patterns, respectively. These parameters concern the radiation power, total efficiency, and Return losses (dB).

Table 2: Additional antenna parameters of the circular slot-patch antenna when the thickness is fixed as $h=1.6$ mm

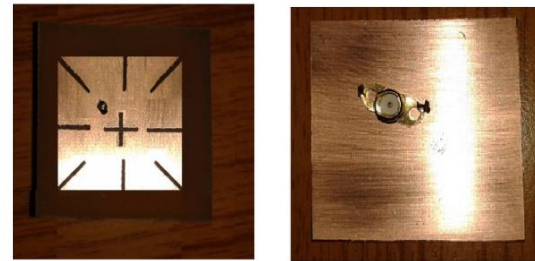
| | | Experimental Results | Simulation Results |
|---|----------------------------|----------------------|--------------------|
| 1 | Directivity(dBi) | 6.08 | 6.014 |
| 2 | Peak realized gain(dB) | 6.28 | 5.979 |
| 3 | Radiation Efficiency | 0.989 | 0.9919 |
| 4 | Total radiation efficiency | 0.564 | 0.5727 |

III. DEVELOPMENT OF THE SINGLE-FEED CROSS-SLOT LOADED COMPACT MICROSTRIP EBG ANTENNA.

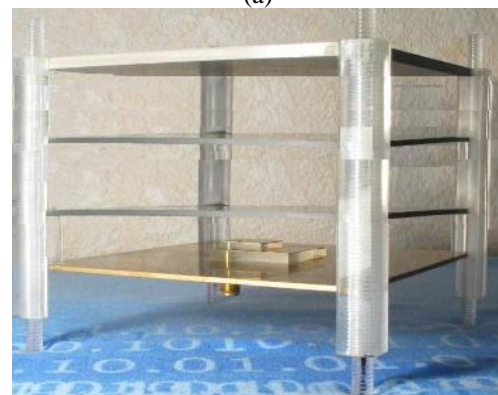
In this section, the antenna prototype was carried out using the LPKF machine, which permits validation of the optimized structure. The measurement of return loss is obtained using Vectorial Network Analyzer (VNA) PNA-X from Agilent Technologies. Figure 3 gives the picture of the fabricated cross loaded antenna.

It shows the kit of calibration of 3.5 mm used to take into consideration the losses in the different transitions; this kit is composed from Open, Short, and Load components. The measured return loss for the achieved

EBG antenna obtained after the calibration, along with the simulation results on CST is taken into account. No massive difference between simulation and experimental data is occurred due to the equipment well adapted to our work.



(a)



(b)

Fig. 3. (a) The proposed single-feed cross-slot loaded compact circularly polarized microstrip antenna, and (b) the antenna when included with the Plexiglass EBG layers.

The new Compact Circularly Polarized microstrip antenna geometry discussed above has been modified by the insertion of new EBG materials and understand the impact of the number of layers on the antenna performances while keeping the same dimensions as before concerning the patch and lateral conditions walls, as shown in figure 4, The distance between the patch and the first dielectric layer is $\lambda_0 / 2 = 24.44$ mm, and the layer thickness is $\lambda_g / 4 = 7.72$ mm.

Here, we add to our original patch, studied previously, new EBG structures and understand the impact of the number of layers on the performance of the antenna while keeping the same dimensions as before the patch and conditions power side (thickness of the substrate $h=1.6$ mm, $\epsilon_r=3.6$, Slot width=1mm, length of the square patch $L=30$ mm). However, the newly inserted dielectric layers will have dielectric permittivity fixed at $\epsilon_r = 2.5$, and the only variation should include the number of layers. For only a one-layered EBG antenna, the return loss is about -46 dB

Figure 4 shows the measured and simulated return loss values at 6.135 GHz. The radiation patterns are well-predicted by the simulations. The beam width gets smaller as the number of EBG structures increases, implying the increasing directivity [12]. The next figure shows the measured 3 dB beam width of 33 degrees. Cross-polarization radiations could not be measured due to the limitation of the antenna measurement setup, but the simulation shows that they are suppressed by at least 25 dB in the broadside direction for both the E- and H-planes of the EBG antenna. Figure 4 will show the importance of EBG Layers in the improvement of the radiation pattern of the antenna

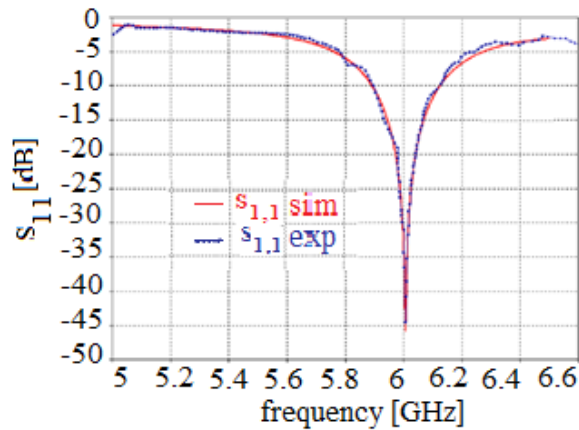


Fig. 4. Simulated versus measured reflection coefficient of the 1-layered single-feed cross-slot loaded compact circularly polarized microstrip EBG antenna.

The most important value for the reflection coefficient S_{11} (dB) = -45.5 dB is shown on a One-Layered Single-Feed Cross-slot compact EBG antenna, so layers of Plexiglas did not destabilize the matching of the antenna. If we search the impact of these layers on the radiation pattern of the antenna, the 3D radiation pattern, as shown in Fig. 5 and Fig. 6, shows that the radiation has a greater directivity equal to 8.150 dB, which is normal, since the parallel EBG materials increase directivity, gain; therefore, we get a longer range of transmission.

The opening angle decreased significantly. In fact, it passes from 80.4 deg to around 22.7 degrees with a preferred direction of propagation along the z-axis which confirms our studies on the effects of these materials defects. So we move from a unidirectional antenna to a directional antenna in the axis perpendicular to the patch. The side lobes pass from -16.5 dB to -0.5 dB, which means an excellent control of the transmission bandwidth.

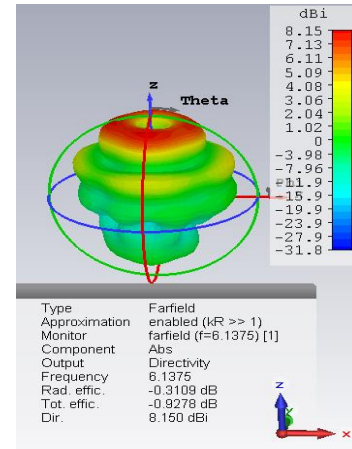


Fig. 5. 3D radiation pattern of a 4-layered circularly polarized slot-patch EBG antenna.

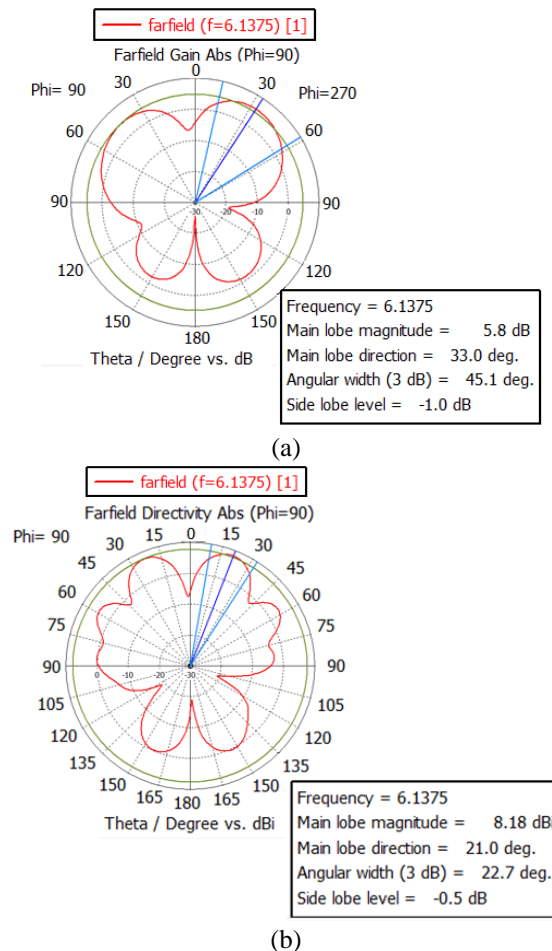


Fig. 6. Polar radiation pattern of the single-feed cross-slot loaded compact circularly polarized patch antenna: (a) without EBG structures and (b) 4-layered EBG structures.

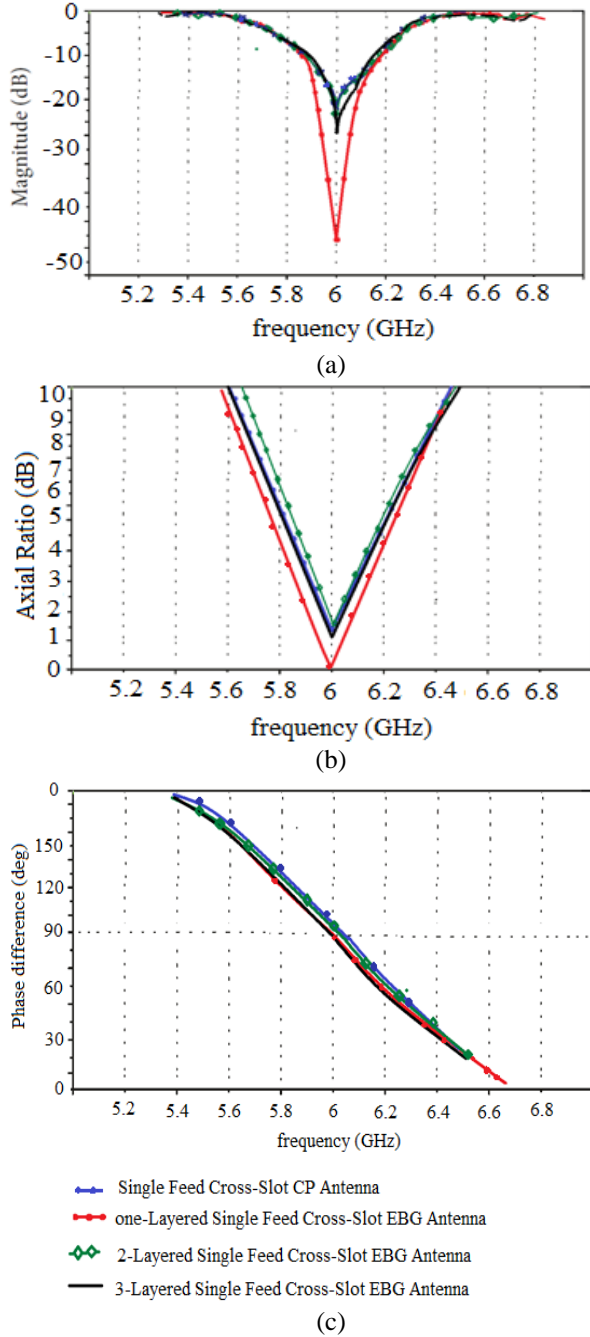


Fig. 7. Simulated results of the proposed cross-slot loaded compact electromagnetic band gap antenna with different Layers: (a) reflection coefficient, (b) AR, and (c) phase difference between two resonant frequencies.

Figure 7 shows the simulated results of the reflection coefficient, axial ratio (AR), and phase difference of the resonant frequency with respect to the number of the EBG structures (L). The remaining parameters are identical to those mentioned above. Here, all geometric parameters of the original antenna are identical. As L

increases, the resonant frequency remains the same except the opening angle that will decrease significantly. In fact, it passes from 80.4 deg to around 22.7 degrees with a preferred direction of propagation along the z -axis, which confirms our studies on the effects of these materials defects.

In our proposed antenna, the number of EBG structures does not substantially reduce the resonant frequency. However, as EBG Structures (L) increase, the frequency of the minimum AR remains unchanged within a small margin of error, and only the minimum value of the AR becomes worse. As shown in Fig. 7, the frequency response of the phase difference changes negligibly with L . Therefore, the frequency at which the phase difference becomes 90° is nearly unchanged. Consequently, the minimum AR frequency is almost intact as well. Because the resonant frequency formed based on the reflection coefficient and the frequency at which the minimum point of AR should coincide, L is selected to get the best compromise between the directivity, gain, and reflection coefficient. From the simulated results, it is observed that L can be fixed at $L=3$ that number corresponding to $S_{11}=-26.5$ and good impact on the total radiation efficiency

As shown in the previous figure and results of simulation and experimental parameters, the design procedure for implementing the EBG structures above the cross-slot loaded compact electromagnetic using the proposed technique can be summarized as follows: Apply identical EBG structures to the proposed patch. At this time, before the procedure begins, we should verify all required outputs (gain, directivity, AR, ...) and stop to add new EBG structures if the AR value reduces to below 3 dB

The Table 3 will summarize the experimental results. The impact of EBG structures is evaluated on the antenna gain, directivity, reflection coefficient, and radiation efficiency. While increasing the number of EBG layers, the radiation efficiency will increase the same to the reflection coefficient. However, a slight variation in the directivity and gain will be shown when the number of layers will pass from one to three. After the third layer, the antenna output will decrease obviously. That is the reason why we have stopped our study to the third EBG layer

Table 3: Impact of the number of layer (L) with $\epsilon_r = 2.5$

| Number of EBG Layers (L) | $L=1$ | $L=2$ | $L=3$ | $L=4$ |
|------------------------------|--------|--------|--------|--------|
| f (GHz) | 6.0065 | 6.0245 | 6.04 | 6.128 |
| S_{11} (dB) | -45.86 | -23.88 | -26.5 | -22.38 |
| Gain (dB) | 7.751 | 8.368 | 8.456 | 7.839 |
| Directivity (dBi) | 7.837 | 8.528 | 8.638 | 8.150 |
| Linear radiation efficiency | 0.5515 | 0.5661 | 0.8660 | 0.8076 |

As the number of layers' increases, the gain increases against the opening angle decreases, so the antenna is more directive. Note that the bandwidth decreases significantly with the number of EBG layers.

IV. CONCLUSION

A Cross-Slot Loaded Compact Circularly Polarized EBG Patch antenna is presented in this paper. The insertion of new EBG structures to the compact antenna as studied in the first section of our paper aims to perform the electromagnetic characteristics (Gain, Bandwidth, radiation efficiency...). Antenna radiation parameters are deeply changing as the number of EBG structures is increasing. In our case, to make a compromise between all different parameters (Gain, bandwidth, directivity...), the best required EBG structures are limited to one layer. Either, the gain is increasing first when thickness increases from 0.8 mm to 1.6 mm and then decreased if the thickness is above 1.6 mm for the Cross-Slot Loaded Compact Circularly Polarized EBG Patch antenna. The same behavior is observed for the case of radiation efficiency, peak gain, and peak directivity.

Globally, we observe that the stability in the performance characteristics for the proposed Cross-Slot Loaded Compact Circularly Polarized EBG Patch antenna is showing better results compared to the same patch antenna without these EBG structures. The gain and directivity at C-band are enhanced from 8.368 dB and 8.528 dBi to 22.6 dB and 22.6 dBi without much affecting the operating bandwidth at C-band. Further enhancement of gain and directivity at the C-band does not affect the nature of broadside radiation characteristics.

REFERENCES

- [1] A. K. Singh, M. P. Abegaonkar, and S. K. Koul, "High-gain and high-aperture-efficiency cavity resonator antenna using metamaterial superstrate," *IEEE Antennas and Wireless Propagation Letters*, vol. 16, pp. 2388-2391, 2017.
- [2] M. J. Al-Hasan, T. A. Denidni, and A. R. Sebak, "Millimeter-wave compact EBG structure for mutual coupling reduction applications," *IEEE Trans. Antennas Propag.*, vol. 63, no. 2, pp. 823-828, 2015.
- [3] E. A. Hajlaoui, "New triple band electromagnetic band gap microstrip patch antenna with two shaped parasitic elements," *J. Comput. Electron.*, vol. 17, no. 1, pp. 452-457, 2018.
- [4] E. Yassini, A. Aguni, L. Ibnyaich, S. Chabaa, and S. Zeroual, "A design of circular patch antenna with a high gain by using a novel artificial planar dual-layer metamaterial superstrate," *Int. J. RF Microw. Comput. Aided Eng.*, vol. 29, no. 11, 2019.
- [5] S. S. Pawar, M. Shandilya, and V. Chaurasia, "Parametric evaluation of microstrip log periodic

dipole array antenna using transmission line equivalent circuit," *Engineering Science and Technology an International Journal*, vol. 20, no. 4, pp. 1260-1274, 2017.

- [6] L. Sun, G.-X. Zhang, and B.-H. Sun, "Slim planar composite antenna with two orthogonal polarizations for WLAN router applications," *Electronics Letters*, vol. 51, no. 18, pp. 1392-1394, 2015.
- [7] T.-N. Chang, J.-M. Lin, and Y. G. Chen, "A circularly polarized ring-antenna fed by a serially coupled square slot-ring," *IEEE Transactions on Antennas and Propagation*, vol. 60, no. 2, pp. 1132-1135, 2012.
- [8] Z. N. Chen and K.-M. Luk, *Antennas for Base Stations in Wireless Communications*, McGraw-Hill, New York, 2009.
- [9] K. F. Lee and W. Chen, *Advances in Microstrip and Printed Antennas*, Wiley, New York, 1997.
- [10] D. M. Pozar and D. H. Schaubert, *Microstrip Antennas: The Analysis and Design of Microstrip Antennas and Arrays*, Wiley, New York, 1995.
- [11] R. Sauleau, "Fabry Perot resonators," *Encyclopedia of RF and Microwave Engineering*, vol. 2, pp. 1381-1401, 2005.
- [12] C. A. Balanis, *Antenna Theory: Analysis and Design*, 4th ed., Wiley, New York, 2016.



El Amjed Hajlaoui received the M.Sc. degrees in Communications Systems from ELManar University-National Engineering School Tunis, Tunisia, the Ph.D degree in Electrical Engineering in 2009. His research interests the analysis and design of microwave circuits for use in communications, radar antenna topics, including design and measurement techniques.



Ziyad M. Almohaimed received the M.Sc. and Ph.D degrees in Electrical and Computer Engineering from University of Victoria, Canada in 2013 and 2017, respectively. His research interests the design and optimization of electronic circuits and frequency dependence of their electrical parameters, including design and measurement techniques.

A Low-Profile Broadband Circularly Polarised Wide-Slot Antenna with an Artificial Magnetic Conductor Reflector

Fangfang Fan, Xiao Fan, Xiaoyu Wang, and Zehong Yan

Science and Technology on Antenna and Microwave Laboratory
Xidian University, Xi'an, Shaanxi, 710071, China

fffan@mail.xidian.edu.cn, fanfanx17@163.com, wxyhongtongtong@163.com, zhyan@mail.xidian.edu.cn

Abstract — In this letter, a novel broadband circularly polarisation (CP) wide-slot antenna with an artificial magnetic conductor (AMC) as the reflector is presented. The wide-slot antenna is composed of a knife-shaped radiator and an improved ground plane. A broadband CP characteristic can be achieved by slotting the ground plane to make it an asymmetric ground shape. However, the average gain of the wide-slot antenna is only about 3 dBic because of bidirectional radiation. An AMC reflector is adopted to enhance the gain of the wide-slot antenna without introducing a high profile similar to the PEC reflector. In addition, the four metal plates are vertically placed around the antenna to broaden the axial ratio (AR) bandwidth of the antenna with the AMC reflector. The measurement results show that the 3dB AR bandwidth of the proposed CP antenna is 32.4% (2.35GHz–3.26GHz), the average gain is 6.5dBic in the AR bandwidth and the value of VSWR in the AR bandwidth is less than 2. The size of the antenna is $0.84\lambda_0 \times 0.84\lambda_0 \times 0.13\lambda_0$ at the centre frequency of 2.805 GHz. The proposed antenna has a low profile, broad AR bandwidth and high gain, thereby being a good candidate for various wireless communication systems.

Index Terms — Artificial Magnetic Conductor (AMC), broadband, Circular Polarisation (CP), low-profile, wide-slot antenna.

I. INTRODUCTION

With the rapid development of the wireless communication technology, researchers have been paying much attention to circularly polarisation (CP) antennas. CP antennas can transmit and receive electromagnetic waves of arbitrary polarisation and have strong anti-interference ability. The traditional microstrip CP antenna has a low profile. However, its CP bandwidth is very narrow due to its inherent high-Q nature. Many types of antenna have been developed to improve the CP bandwidth. Among them, planar monopole and wide-slot antenna are commonly used to achieve ultra-wideband circular polarisation. In the planar monopole design, many attempts have been made by employing

various shapes of the monopole antenna, modifying ground plane or adding a parasitic stub to achieve a wider CP bandwidth [1–7]. In [1], the antenna employs a C-shaped monopole by adding an open-loop on the backside of the monopole and modifying the ground plane, a 65.2% 3dB axial ratio bandwidth (ARBW) is obtained [1]. In [2–4], the similar techniques as in [1] were used, achieving ARBWs of 63.3%, 63.61% and 53.92% for the antennas. In [5], a monopole antenna with a C-shaped patch and two triangular stubs was presented, and an ARBW of 104.7% was obtained. A compact monopole antenna was proposed in [6], the antenna consists of a P-shaped monopole and modified ground plane with a rectangular stub. Results demonstrated that the impedance bandwidth is 118.5% ($S_{11} < -10\text{dB}$) and the 3dB ARBW is 104.4%. Some reported wide-slot CP antennas are shown in [8–10]. In [8], a simple rectangular bracket-shaped parasitic strip was used to excite the CP modes; the 3dB ARBW can reach 49%. Two semicircular slots are etched in the ground plane to be used as the radiators [9], which has a wide 3dB ARBW of 74.3%. However, it was achieved at the expense of a relatively larger size and complex excitation mechanism of the CP modes. A U-shaped slot and two 50 Ω microstrip-fed ports were employed in [10] and can achieve dual circularly polarised radiation while providing an ARBW of 110.5%. The gains of the antennas proposed in the above literature are low, because these antennas have bidirectional radiation. Attempts have been made to increase the gain of these antennas. Placing a metal reflector under a wide-slot antenna enables the antenna to obtain unidirectional radiation, and the gain can be increased by almost 3 dB [11–14], but it results in a higher profile of about $0.25\lambda_0$. At the same time, the metal reflector would deteriorate the inherent wideband CP bandwidth. An artificial magnetic conductor (AMC) reflector is introduced in place of a conventional metal reflector to reduce the profile of the unidirectional antenna. In [15–19], different AMC structures are introduced to increase the antenna gain while reducing its profile. However, these antennas are still large or the 3 dB ARBW is too narrow.

Hence, designing a wideband circularly polarised antenna with high gain and low profile is still a challenge.

In this letter, a novel broadband wide-slot CP antenna with high gain, wide CP bandwidth and low profile is proposed. Firstly, an ultra-wideband wide-slot CP antenna is designed. The wide-slot antenna has bidirectional radiation, which is why an AMC reflector is placed under the antenna to make it unidirectional and improve the gain of the antenna considerably. Then, four metal plates are vertically placed around the AMC reflector as in [20] to further broaden the ARBW of the antenna. The antenna is designed and simulated using the ANSYS HFSS. Finally, a prototype antenna is fabricated and experimented. The measured results verify the feasibility of the simulated antenna well.

II. ANTENNA DESIGN

A. Wide-slot antenna geometry

The geometry of the proposed wide-slot antenna is shown in Fig. 1. The antenna is fabricated on an FR4 substrate with a thickness of $h=1.6\text{ mm}$, a dielectric constant of 4.4 and a loss tangent of 0.02. The size of the substrate is $W \times L=65\text{ mm} \times 70\text{ mm}$. The radiation patch is on the upper layer of the substrate and it adopts a knife-shaped structure, which can improve the impedance matching and CP bandwidth. The lower layer of the substrate is a ground plane. Etching asymmetrical slots on the ground plane enables the antenna to generate two polarised waves perpendicular to each other with a phase difference of 90° , thereby forming circular polarisation.

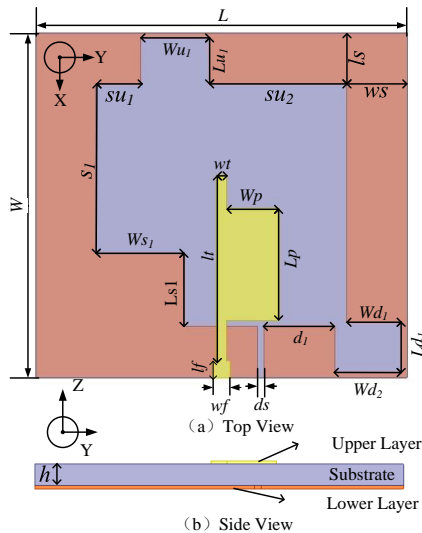


Fig. 1. Geometry of the proposed wide-slot antenna. ($L=70$, $W=65$, $su_1=8.4$, $Wu_1=13$, $Lu_1=8.7$, $su_2=25.9$, $s_1=32$, $Ws_1=16.6$, $Ls_1=13.7$, $lf=3.1$, $wf=3.1$, $ds=1.2$, $d_1=13.35$, $Wd_2=12.5$, $Ld_1=9.4$, $Wd_1=10.2$, $Wp=9.9$, $Lp=21$, $lt=35$, $wt=1.9$, $ls=9.65$, $ws=11.35$). (Unit: mm).

B. Steps in realizing the wide-slot antenna

Six antennas labelled Ant.1—Ant.6 are developed and shown in Fig. 2 to explain the evolution of the broadband CP wide-slot antenna clearly. The VSWR and AR for the six antennas are compared in Fig. 3. Ant.1 is a conventional wide-slot antenna with a strip feedline on the upper layer and a rectangular slot on the lower layer of the substrate, which can radiate wideband linear polarised waves. To further improve the impedance matching of Ant.1, we introduce a rectangular stub with a size of $W_p \times L_p$ on the right side of the feedline, which is shown in Ant.2.

From Fig. 3 (a), we can see that the impedance bandwidth of Ant.1 has been broadened significantly, especially at the upper frequency after adding a rectangular stub. Then, to obtain CP performance, we adopt the method of slotting on the ground plane to obtain two near-degenerate modes. Firstly, an x-direction slit is employed in Ant.3 to change the current path in order to mainly reduce the low frequency AR, but its function in improving the low-frequency AR is not obvious. The slit benefits the impedance matching because of the improved coupling between the feedline and the wide-slot. Moreover, a rectangular slot of size $Ld_1 \times Wd_2$ is introduced on the right side of the slit in Ant.4 to further improve the AR performance at lower frequencies. This step greatly assists CP excitation at a lower-frequency as shown in Fig. 3 (b), because the rectangular slot can adjust the phase difference of the two near-degenerate polarised modes tending to 90° for CP radiation. However, the higher frequency band AR cannot meet the requirement. High-frequency AR should be reduced to extend the ARBW of this wide-slot antenna. In Ant.5, a rectangular slot of $Wu_1 \times Lu_1$ is etched on the top of the ground plane, and the position is approximately diagonal to the lower rectangular slot in Ant.4. These two slots introduce two perpendicular polarisation modes with almost a 90° phase difference at a higher frequency. Figure 3 (b) shows that the AR of Ant.5 is reduced at high frequencies. But the impedance matching in Ant.4 and Ant.5 especially at a lower frequency should be improved. A rectangular perturbation of size $Ls_1 \times Ws_1$ is introduced on the ground plane beside the knife-shaped radiation patch to further reduce the AR and improve the impedance matching. The VSWR was improved significantly compared with the VSWRs in Ant.4 and Ant.5, and the AR around 3 GHz was adjusted below 3 dB, that is to say, the rectangular perturbation acts as an important component in antenna performance in terms of wideband impedance matching and CP excitation. Thus, an ultra-wideband wide-slot CP antenna (Ant.6) with good performance is generated. The impedance bandwidth with VSWR less than 2 is 94.6% (1.42 GHz—3.97 GHz), and the 3dB ARBW is 74.1% (1.41 GHz—3.07 GHz).

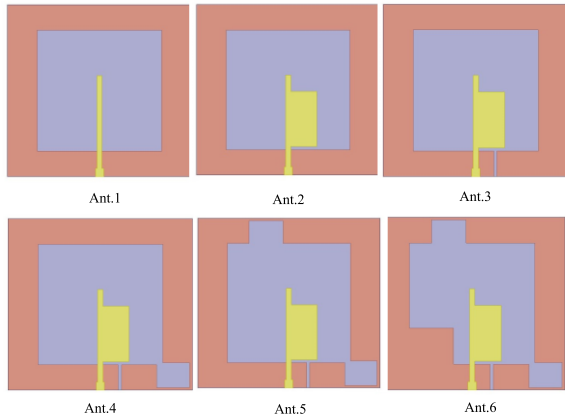


Fig. 2. Design steps of the proposed wide-slot antenna.

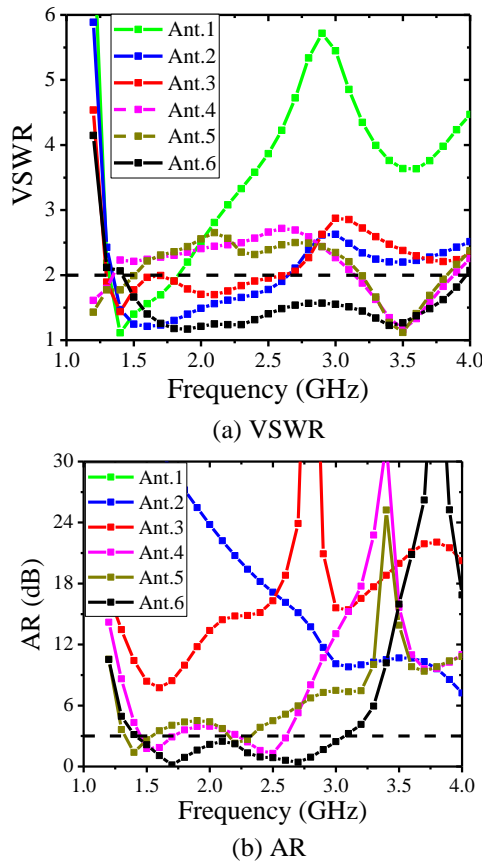


Fig. 3. Simulated results.

C. AMC structure design

Generally, the gain of the wide-slot antenna is not high with the large slot, thereby introducing serious and unwanted backward radiation in wireless communication system applications. A large metal reflector can be added under the wide-slot antenna to enhance the gain of the antenna [12–13]. However, the

profile of the overall antenna will be high, because the distance between the antenna and the metal reflector should be about $1/4\lambda_0$ in order to compensate for the 180° phase difference between the reflected and incident waves. With the reduction in the profile of the overall antenna taken into consideration, we adopt the AMC structure instead of the metal reflector.

AMC is an artificial electromagnetic periodic structure that can imitate the isotropic reflection characteristics of an ideal magnetic conductor. Generally, a subwavelength metal structure is printed on a dielectric substrate with a metal ground plane so that incident waves can achieve isotropic reflection characteristic effectively. In accordance with the principle of isotropic reflection, the reflected and radiated waves on the surface are superimposed in phase, so the distance between the wide-slot antenna and the AMC structure can be reduced to less than $1/4\lambda_0$.

Figure 4 shows the 3D model, reflection phase and coefficient results of the unit cell used in the proposed AMC structure after comparing the performance and size of several types of AMC unit cell. An FR4 substrate with a thickness of $he=1.6\text{ mm}$ and a loss tangent of 0.02 is chosen, hd is the distance between the excitation source and the AMC unit cell. Crossed metal strips are placed in the centre on the upper layer of the substrate, with four quarter circles on the four corners. The lower layer of the substrate is a metal ground plane. The dimensions of the AMC unit cell are given in caption of Fig. 4.

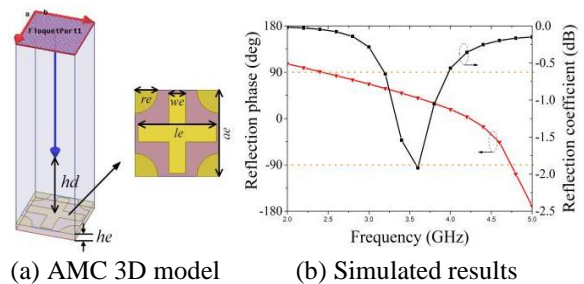


Fig. 4. The 3D model and the simulated reflection phase and coefficient of the AMC unit. And the dimensions of the parameters are $ae=15$, $re=4$, $le=14$, $we=3$. (Unit: mm).

AMC structure after comparing the performance and size of several types of AMC unit cell. An FR4 substrate with a thickness of $he=1.6\text{ mm}$ and a loss tangent of 0.02 is chosen, hd is the distance between the excitation source and the AMC unit cell. Crossed metal strips are placed in the centre on the upper layer of the substrate, with four quarter circles on the four corners. The lower layer of the substrate is a metal ground plane. The dimensions of the AMC unit cell are given in caption of Fig. 4.

Generally, the frequency band of the reflection phase on the AMC surface is defined as the isotropic reflection phase band [16]. From Fig. 4, we can see a frequency bandwidth of 2.35 GHz to 4.65 GHz with the reflection phase varying from 90° to -90° . The AMC unit satisfies the in-phase reflection characteristic in the frequency band of interest.

The parametric study has been done for the AMC unit cell in Fig. 5, we can conclude that the parameter hd influence the reflection phase obviously, which determines the phase difference between the incident and reflected wave, with the increase of hd , the zero reflection phase moves to the higher frequency, but the $\pm 90^\circ$ phase bandwidth decreases. The parameter le influences the reflection phase a little, especially at the lower frequency, the reflection phase does not change.

Then, a 6×6 unit cell composing the AMC structure with a size of $90 \text{ mm} \times 90 \text{ mm}$ is placed under the wide-slot CP antenna, and the distance between them is reduced to about $0.14\lambda_0$ at the centre frequency of 2.805 GHz denoted as $hg=15 \text{ mm}$ as shown in Fig. 6.

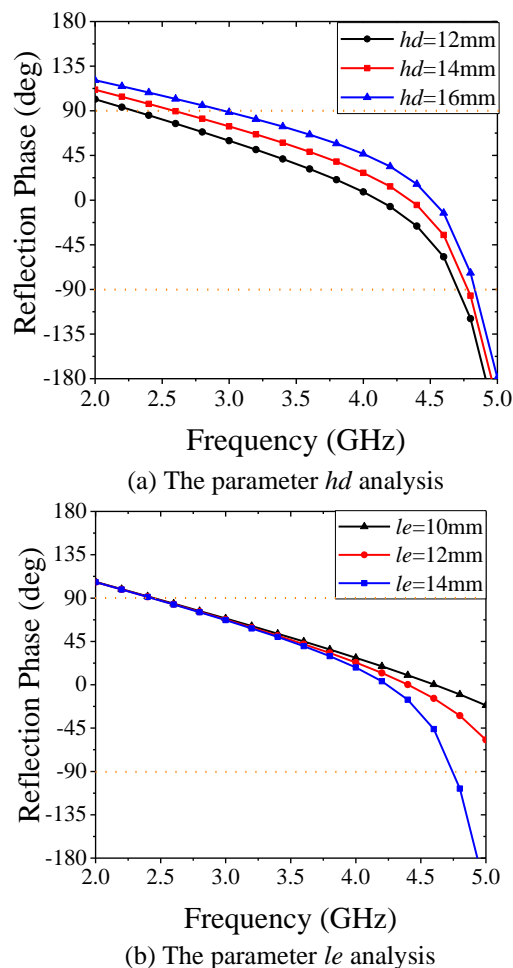


Fig. 5. The parametric analysis of the AMC unit cell.

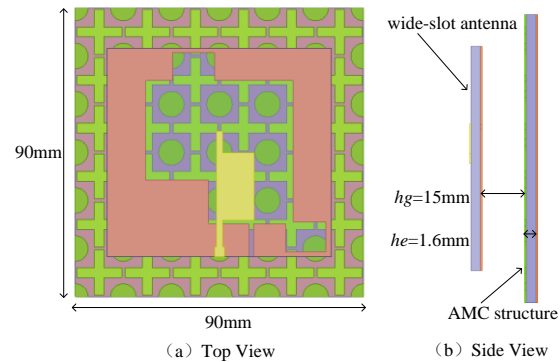
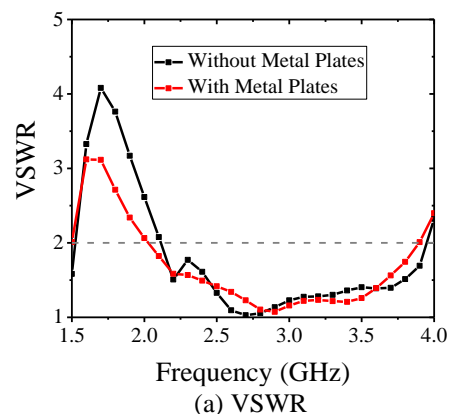


Fig. 6. Top and side views of the AMC antenna.

The simulated VSWR and AR results of the AMC antenna are given in Fig. 7, marked as the plots named without metal plates. The impedance characteristic is good, but the AR bandwidth decreases from 74.1% in Fig. 3(b) to 21.6% (2.6 GHz–3.2 GHz), because the AMC structure has an excellent isotropic reflection phase only near a certain frequency point. Moreover, the distance between the AMC structure and wide-slot antenna is different in wavelength for different frequencies. These conditions have a great impact on the reflected CP waves, thereby reducing the AR bandwidth considerably. Therefore, the AR bandwidth becomes narrower and the CP characteristic becomes worse after the AMC structure is introduced under the bidirectional radiating wide-slot antenna. To further enhance the bandwidth of AR, we introduce four vertical metallic plates around the AMC structure, similar to [20]. The height and length of each vertical plate is 16 mm and 40 mm , respectively. Four nylon mount posts with a diameter of 3 mm are used to fix the antenna which are considered in the simulation.

To get a better insight of the polarization, the E-field of the antenna at 2.8 GHz for various phase (0° , 90° , 180°) observed from $+z$ direction is shown in Fig. 8. The E-field rotates in a clockwise direction, which means a LHCP wave can be obtained.



(a) VSWR

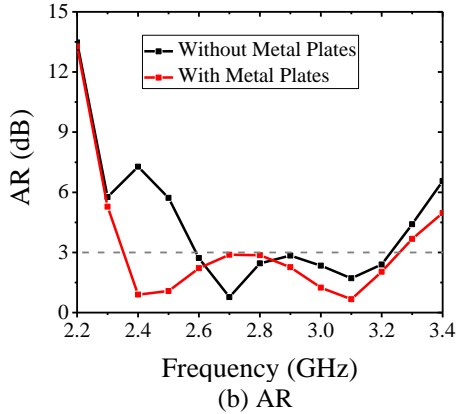


Fig. 7. Simulated results for AMC antenna with and without vertical metal plates.

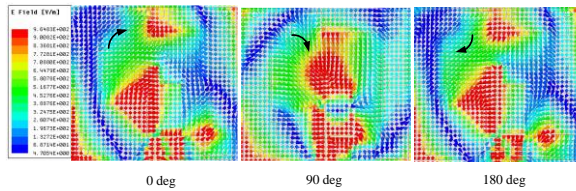


Fig. 8 The rotation of E-field at frequency of 2.8 GHz.

III. EXPERIMENTAL RESULTS

The photo of the fabricated wide-slot antenna with an AMC reflector and four vertical metal plates is shown in Fig. 9 (a). The wide-slot antenna is supported above the AMC structure by four nylon-66 dielectric posts. The performance of the prototype antenna was verified by measuring in a Microwave Anechoic Chamber. The simulated and measured VSWR and AR of the proposed antenna are shown in Fig. 9. The measured AR is generally consistent with the simulated result in the bandwidth of 32.4% (2.35 GHz-3.26 GHz), except that the ARs of two middle frequency points (2.7 GHz and 2.8 GHz) are slightly higher than 3 dB, and the VSWR is less than 2 in the entire ARBW and has an impedance bandwidth of 76% (1.8 GHz-4 GHz). Figure 10 shows the measured gain of the proposed antenna and the simulated gains. From the results, we can see that introducing the AMC reflector can increase the gain effectively. The gain increased by more than 3 dBic over most frequencies compared with the wide-slot antenna without the AMC reflector. The gain of the proposed antenna is greater than 5.5 dBic at the boresight with a peak gain of 7 dBic and an average gain of 6.5 dBic. The measured results prove that the proposed method can enhance the gain of the broadband wideslot CP antenna significantly, along with the decreased profile from $0.25\lambda_0$ to $0.14\lambda_0$. The measured normalised radiation

patterns at three frequencies of 2.4 GHz, 2.8 GHz and 3.2 GHz are shown in Fig. 11. Evidently, the proposed antenna with the AMC reflector has a good and stable unidirectional radiation.

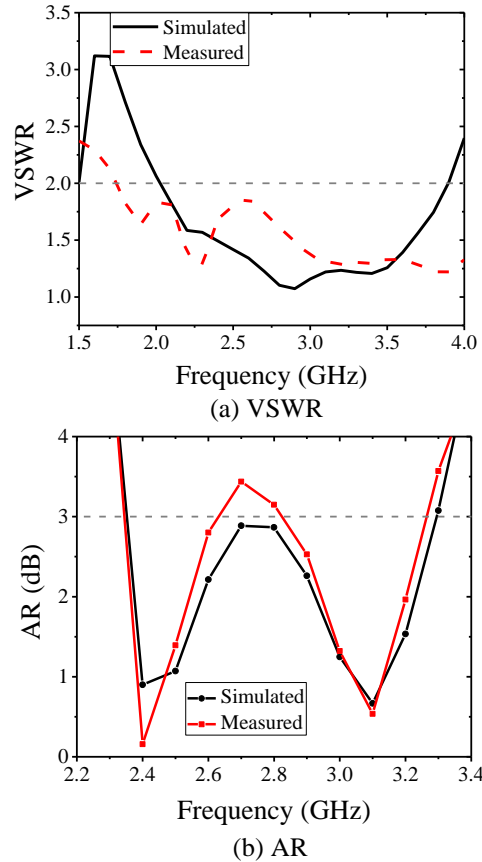


Fig. 9. Simulated and measured results for the proposed antenna.

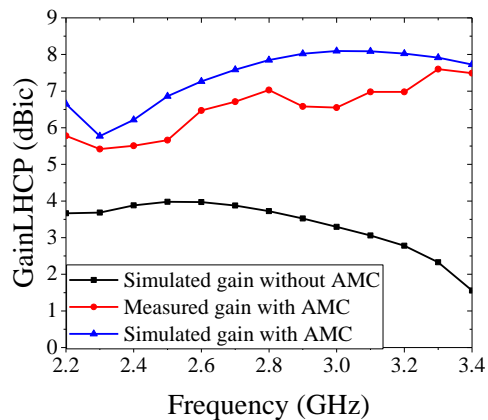


Fig. 10. Gain comparison between the antennas with and without AMC reflector.

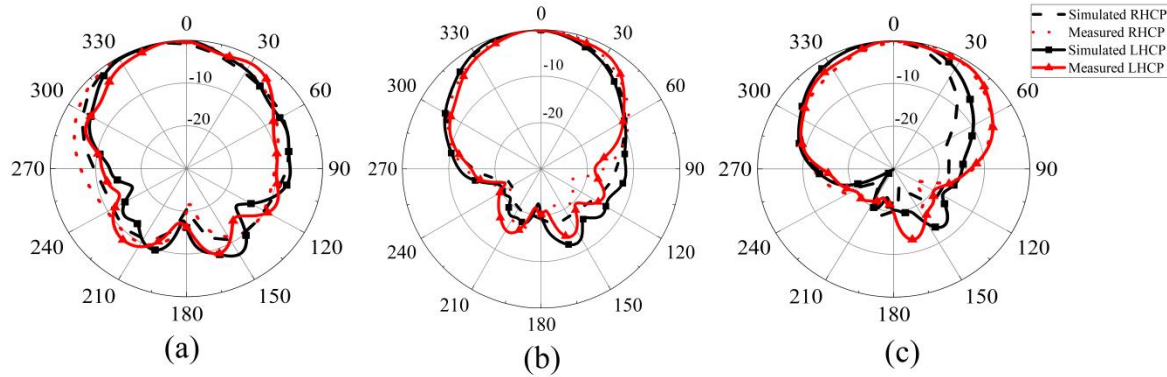


Fig. 11. Simulated and measured radiation patterns of the proposed antenna: (a) 2.4 GHz, (b) 2.8 GHz, and (c) 3.2 GHz.

Table 1 summarises the measured performance of the proposed antenna and other similar previously reported antennas in terms of the overall size, ARBW, impedance bandwidth (IBW) and the gain of the antenna. The antenna size is calculated with respect to the CP center frequency. Although the proposed antenna does not have the smallest size, as in [15], it has a wider ARBW and higher gain. Except [15], the proposed antenna has the the smallest profile among the other antennas. The advantage of this design is that the broadband characteristics were achieved with a simple topology, low profile and high gain.

Table 1: Comparison between the proposed antenna and other similar previously reported antennas

| Ref. | Size ($\lambda_0 \times \lambda_0 \times \lambda_0$) | ARBW (%) | IBW (%) | Gain (dBi) |
|-------|---|-------------|------------|---------------|
| [11] | $1.23 \times 1.23 \times 0.3$ | 60.9 | 110 | 5.1@3GHz |
| [12] | $0.65 \times 0.58 \times 0.32$ | 80 | 82 | 6@4GHz |
| [13] | $0.72 \times 0.6 \times 0.19$ | 33.2 | 36.2 | 7.5@6GHz |
| [14] | $0.54 \times 0.54 \times 0.08$ | 4.1 | 15.9 | 5.5@2.7GHz |
| Prop. | $0.84 \times 0.84 \times 0.13$ | 32.4 | 76 | 7@2.8GHz |

IV. CONCLUSION

A novel broadband wide-slot CP antenna with high gain and low profile is proposed, fabricated and measured. The overall antenna is composed of a wide-slot antenna, an AMC structure and four vertical metal plates. The wide-slot antenna can provide broadband CP characteristics, the AMC structure can enhance the gain while reducing the profile of the antenna, and the vertical metal plates can further broaden the ARBW. The measured results show that the proposed antenna can achieve an ARBW of 32.4% (2.35 GHz–3.26 GHz), and an average gain of 6.5 dBi with the profile of $0.14\lambda_0$ at the centre frequency of 2.805 GHz.

REFERENCES

- [1] K. Ding, C. Gao, T. Yu, and D. Qu, "Broadband C-shaped circularly polarized monopole antenna," *IEEE Trans. Antennas Propag.*, vol. 63, no. 2, pp. 785-790, Feb. 2015.
- [2] K. Ding, Y. Guo, and C. Gao, "CPW-fed wideband circularly polarized printed monopole antenna with open loop and asymmetric ground plane," *IEEE Antennas Wireless Propag. Lett.*, vol. 16, pp. 833-836, 2017.
- [3] M. Samsuzzaman, M. T. Islam, and M. J. Singh, "A compact printed monopole antenna with wideband circular polarization," *IEEE Access*, vol. 6, pp. 54713-54725, 2018.
- [4] M. Midya, S. Bhattacharjee, and M. Mitra, "Broadband circularly polarized planar monopole antenna with G-shaped parasitic strip," *IEEE Antennas Wireless Propag. Lett.*, vol. 18, no. 4, pp. 581-585, Apr. 2019.
- [5] H. Tang, K. Wang, R. Wu, C. Yu, J. Zhang, and X. Wang, "A novel broadband circularly polarized monopole antenna based on C-shaped radiator," *IEEE Antennas Wireless Propag. Lett.*, vol. 16, pp. 964-967, 2017.
- [6] H. Alsariera, Z. Zakaria, and A. Awang Md Isa, "A broadband P-shaped circularly polarized monopole antenna with a single parasitic strip," *IEEE Antennas Wireless Propag. Lett.*, vol. 18, no. 10, pp. 2194-2198, Oct. 2019.
- [7] N. Hussain, H. H. Tran, and T. T. Le, "Single-layer wideband high-gain circularly polarized patch antenna with parasitic elements," *International Journal of Electronics and Communications*, vol. 113, 2020.
- [8] U. Ullah and S. Koziel, "A broadband circularly polarized wide-slot antenna with a miniaturized footprint," *IEEE Antennas Wireless Propag. Lett.*, vol. 17, no. 12, pp. 2454-2458, Dec. 2018.
- [9] T. T. Le, H. H. Tran, and H. C. Park, "Simple-

- structured dual-slot broadband circularly polarized antenna,” *IEEE Antennas Wireless Propag. Lett.*, vol. 17, no. 3, pp. 476-479, Mar. 2018.
- [10] R. Xu, J. Li, J. Yang, K. Wei, and Y. Qi, “A design of U-shaped slot antenna with broadband dual circularly polarized radiation,” *IEEE Trans. Antennas Propag.*, vol. 65, no. 6, pp. 3217-3220, 2017.
- [11] J. G. Baek and K. C. Hwang, “Triple-band unidirectional circularly polarized hexagonal slot antenna with multiple L-shaped slits,” *IEEE Trans. Antennas Propag.*, vol. 61, no. 9, pp. 4831-4835, Sep. 2013.
- [12] G. Li, H. Zhai, L. Li, and C. Liang, “A nesting-L slot antenna with enhanced circularly polarized bandwidth and radiation,” *IEEE Antennas Wireless Propag. Lett.*, vol. 13, pp. 225-228, 2014.
- [13] U. Ullah, S. Koziel, and I. B. Mabrouk, “A Simple-topology compact broadband circularly polarized antenna with unidirectional radiation pattern,” *IEEE Antennas Wireless Propag. Lett.*, vol. 18, no. 12, pp. 2612-2616, Dec. 2019.
- [14] K. Agarwal, Nasimuddin, and A. Alphones, “Wideband circularly polarized AMC reflector backed aperture antenna,” *IEEE Trans. Antennas Propag.*, vol. 61, no. 3, pp. 1456-1461, Mar. 2013.
- [15] J. Li, H. Huo, J. Chen, S. Zhu, H. Shi, and A. Zhang, “Miniaturised artificial magnetic conductor and its application in unidirectional circularly polarised slot antenna design,” *IET Microw. Antenna P.*, vol. 12, no. 12, pp. 1885-1889, 2018.
- [16] A. Feresidis, G. Goussetis, and S. Wang, J. Vardaxoglou, “Artificial magnetic conductor surfaces and their application to low-profile high gain planar antennas,” *IEEE Trans. Antennas Propag.*, vol. 53, no. 1, pp. 209-215, Jan. 2005.
- [17] N. Hussain, M. Jeong, A. Abbas, T. Kim, and N. Kim, “A metasurface-based low-profile wideband circularly polarized patch antenna for 5G millimeter-wave systems,” *IEEE Access*, vol. 8, pp. 22127-22135, 2020.
- [18] N. Hussain, S. I. Naqvi, W. A. Awan, and T. T. Le, “A metasurface-based wideband bidirectional same sense circularly polarized antenna,” *International Journal of RF and Microwave Computer-Aided Engineering*, no. 3, 2020.
- [19] N. Hussain, M. Jeong, A. Abbas, and N. Kim, “Metasurface-based single-layer wideband circularly polarized MIMO antenna for 5G millimeter-wave systems,” *IEEE Access*, vol. 8, pp. 130293-130304, 2020.
- [20] Y. M. Pan, W. J. Yang, S. Y. Zheng, and P. F. Hu, “Design of wideband circularly polarized antenna using coupled rotated vertical metallic plates,” *IEEE Trans. Antennas Propag.*, vol. 66, no. 1, pp. 42-49, Jan. 2018.

Broadband CPW-Fed Circularly Polarized Square Slot Antenna for Universal UHF RFID Handheld Reader

Rui Ma and Quanyuan Feng

Department of Information Science and Technology
Southwest Jiaotong University, Chengdu, 611756, China
marui971213@163.com, fengquanyuan@163.com

Abstract — This paper presents a new coplanar waveguide (CPW)-fed circularly polarized square slot antenna (CPSSA). The proposed antenna uses an inverted Z-shaped feedline protruded from the signal line of the feeding CPW. Circularly polarized (CP) radiation can be achieved by adequately inserting the arc-shaped grounded strip into the upper right corner of the square slot. The widened vertical tuning stub on the L-shaped grounded strip can improve impedance matching and axial ratio (AR) performance. The measured results indicate that the 10 dB impedance bandwidth is 620 MHz (652-1272 MHz), and the 3 dB axial ratio bandwidth is 320 MHz (840-1160 MHz), which has a broadband characteristic. In the range of the universal UHF RFID band, the measured peak gain is about 4.4 dBi. The proposed CPSSA uses low-cost FR4 material as the dielectric substrate. The overall size of the antenna is $119 \times 119 \times 0.5 \text{ mm}^3$. The proposed antenna has a simple structure, easy processing, good performance, wide operating bandwidth, and dual circular polarization characteristic. It can be applied to the universal UHF RFID handheld reader environment.

Index Terms — Circularly polarized, CPW-fed, handheld reader, UHF RFID.

I. INTRODUCTION

Radio-frequency identification (RFID) is a wireless communication technology that uses electromagnetic waves to identify and track objects [1]. RFID technology has the advantages of high accuracy, long reading distance, fast reading speed, strong environmental adaptability, and non-contact. It is widely applied to product tracking, goods flow system, traffic management, medical-care systems, automobile safety, etc. A typical RFID system generally consists of an electronic tag and a reader device. The reader device uses the reader antenna to send radio frequency signals to the tag and receive the tag information [2]. Since the RFID tag is linearly polarized (LP), and the placement orientation of the tag is arbitrary, CP operation can reduce the loss caused by the polarization mismatch and the multipath

effect between the tag antenna and the reader antenna, and improve communication reliability. In the practical RFID applications, the circularly polarized antennas [3-5] are usually required. RFID system can be divided into low frequency (LF), high frequency (HF), ultra-high frequency (UHF), and microwave (MW) frequency bands [6]. UHF RFID has the characteristics of long readable distance, large information storage capacity, and high data transfer rate. Therefore, it is of great significance to study CP reader antennas that cover the universal UHF RFID band. The frequency bands authorized for UHF RFID applications are different in different countries and regions, like 840-845 MHz and 920-925 MHz in China, 908.5-914 MHz in South Korea, 952-955 MHz in Japan, 865-867 MHz in India, 902-928 MHz in America, 866-869 MHz and 920-925 MHz in Singapore, and 920-926 MHz in Australia [7]. The frequency range of the universal UHF RFID is from 840 to 960 MHz.

Numerous circularly polarized reader antennas have been proposed for RFID systems. A novel circularly polarized annular-ring microstrip antenna is presented [8]. The CP operation is realized by an equal-split divided power divider with a phase difference of 90° . In [9], The CP antenna operating within the universal UHF RFID frequency range adopts the technology of loading a corner-truncated square patch to achieve good impedance matching and circular polarization characteristics. In [10-11], the main patch is fed by four adjacent probes sequentially connected to the suspended feeding strip to achieve CP radiation. A circularly polarized stack Yagi antenna for RFID reader applications is proposed [12]. The circular polarization performance is achieved by straight cutting on the two edges of the main patch, the parasitic patch, and the director patch. The above-mentioned CP antennas have wide operating bandwidth and high gain, but they have the disadvantages such as complex structure, complicated processing, large antenna dimension, and poor portability. The printed slot antennas [13-16] have the characteristics of small size, low cost, easy fabrication, and wide coverage bandwidth. Many articles have studied slot antennas. A circularly

polarized annular-ring slot antenna is fed by a microstrip line coupled to the slotline [17]. The measured 10 dB impedance and 3 dB AR bandwidth are about 17.6% and 3.72%, respectively. A CPW fractal circularly polarized antenna was presented in [18], which exhibits a 3 dB axial-ratio bandwidth of 4% and impedance bandwidth of 28.5%. A single coaxial probe microstrip antenna with a symmetrical cross-shaped slot, produces CP radiation [19]. The measured 10 dB impedance matching bandwidth is about 2%, and the measured 3 dB AR bandwidth is only about 0.7%. The AR bandwidth of these antennas is very narrow, which cannot meet the requirements of covering the entire UHF RFID frequency range.

This paper proposes a novel CPW-fed square slot antenna that covers the universal UHF RFID frequency range. The inverted Z-shaped bent feedline increases the electrical length of the antenna and improves the impedance matching characteristic. By inseting the arc-shaped grounded strip into the upper right corner of the square slot of the antenna, two near-orthogonal LP modes with equal amplitude and a phase offset of 90° are excited, thus generating circularly polarized waves. The widened vertical tuning stub of the L-shaped strip embedded in the lower-left corner of the square slot can broaden the impedance bandwidth and the axial ratio bandwidth. Finally, the proposed antenna achieves good impedance matching and broadband characteristics. The experimental results show that the 10 dB impedance bandwidth is about 64.4% (652-1272 MHz), and the 3 dB axial ratio bandwidth is about 32.0% (840-1160 MHz). The overlapping operating bandwidth of the proposed CPSSA covers the universal UHF RFID band (840-960 MHz).

II. ANTENNA DESIGN

Figure 1 illustrates the configuration of the proposed CPW-fed CPSSA. The proposed antenna is printed on a low-cost FR4-epoxy dielectric substrate (relative permittivity $\epsilon_r = 4.4$, loss tangent $\delta = 0.02$, and thickness (H) of 0.5 mm). The antenna adopts a single-sided printing method, and the feedline and the ground plane are on the same side of a square dielectric substrate with the side length of 119 mm. A wide square slot with the dimension of $98 \times 98 \text{ mm}^2$ is etched on the ground plane. The side length of the square slot is approximately equal to $0.5\lambda_g$, where λ_g is the wavelength of the designed center frequency of AR bandwidth at 900 MHz, can be computed as:

$$\lambda_g = \frac{c_0}{f_g \times \sqrt{\epsilon_{\text{eff}}}}, \quad (1)$$

where c_0 is $3 \times 10^8 \text{ m/s}$, and ϵ_{eff} is the effective dielectric constant of the FR4 substrate [20]. The CPW feedline of the antenna has a signal line with a width (W_f) of 3.5 mm and two identical gaps (g_1) of 0.5 mm between the ground plane and the signal line. One end of the signal

line is connected to a 50Ω coaxial SMA connector, and the other end is connected to an inverted Z-shaped feedline. The lengths of the two vertical strips of the feedline parallel to the Y -axis are $L_3 = 46.5 \text{ mm}$ and $L_5 = 22.5 \text{ mm}$, respectively. The length of the horizontal strip of the feedline parallel to the X -axis is $L_4 = 31 \text{ mm}$. By adjusting the length (L_5) of the vertical strip, the impedance matching characteristic can be improved. The arc-shaped grounded strip (point A to point B) with a width of 6.5 mm (R_1 - R_2) is inserted into the square slot. R_1 and R_2 are the outer and inner radius relative to the center (point C), respectively. The arc-shaped grounded strip interferes with the electric field distribution in the square slot and excites two approximately orthogonal linear resonance modes (TE_{01} and TE_{10} modes) with a 90° phase difference, achieving CP radiation. By adjusting the inner and outer radius of the arc-shaped grounded strip, the 3 dB AR bandwidth can meet the required axial ratio bandwidth requirements. The L-shaped grounded strip at the lower-left corner of the square slot is composed of a vertical tuning stub with a width of $W_2 = 12 \text{ mm}$ and a length of $L_1 = 41.5 \text{ mm}$ in the vertical direction and a horizontal strip with a width of 3.5 mm and a length of $L_2 = 20 \text{ mm}$ in the horizontal direction. The length of the L-shaped grounded strip ($L_1 + L_2$) is close to $0.25\lambda_g$. The impedance bandwidth and the axial ratio bandwidth can be further broadened by adjusting the width (W_2) of the vertical tuning stub, so that the antenna can cover the universal UHF RFID frequency range. The CPSSA proposed in this paper is simulated and optimized by the Ansoft high frequency structure simulator software (HFSS, ver.18) based on finite element method (FEM).

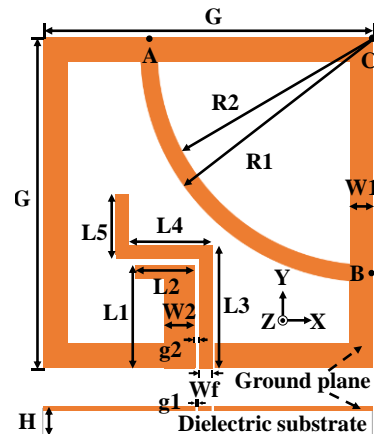


Fig. 1. Geometry of the proposed CPW-fed CPSSA with $G = 119 \text{ mm}$, $L_1 = 41.5 \text{ mm}$, $L_2 = 20 \text{ mm}$, $L_3 = 46.5 \text{ mm}$, $L_4 = 31 \text{ mm}$, $L_5 = 22.5 \text{ mm}$, $W_1 = 10.5 \text{ mm}$, $W_2 = 12 \text{ mm}$, $W_f = 3.5 \text{ mm}$, $R_1 = 83.5 \text{ mm}$, $R_2 = 77 \text{ mm}$, $g_1 = 0.5 \text{ mm}$, $g_2 = 1 \text{ mm}$, $H = 0.5 \text{ mm}$.

As shown in Fig. 2, the design evolution steps of the

proposed antenna are described by five prototypes from Ant. I to Ant. V. Figures 3 (a) and (b) present the simulated results of the frequency response of the reflection coefficient S_{11} and the axial ratio for Ant. I to Ant. V. The wide slot antenna has wide bandwidth characteristic, so the ground plane of Ant. I is designed as a wide square slot structure with an L-shaped feedline. From the simulated results of S_{11} and AR, it is found that the 10 dB impedance bandwidth of Ant. I does not cover the entire UHF RFID band, and linearly polarized waves are radiated. The 10 dB impedance bandwidth is from 0.69 GHz to 0.75 GHz and from 0.93 GHz to 1.09 GHz, and the axial ratio in the frequency band of 0.7-1.3 GHz is much greater than 3 dB, and CP radiation is not realized. In Ant. II, an L-shaped grounded strip is added to the lower-left corner of the square slot to enhance the capacitive coupling between the ground plane and the feed structure, thereby broadening the bandwidth of the antenna. The impedance matching characteristic of Ant. II becomes worse, but the axial ratio is closer to 3 dB, and the CP radiation is still not realized. Ant. III has a vertical strip with a length of L_5 in the vertical direction embedded in the feed structure. As shown by the simulated results of Ant. III, the impedance matching characteristic is improved, and the 10 dB impedance bandwidth is from 0.65 GHz to 0.72 GHz and from 0.87 GHz to 1.08 GHz. The axial ratio in the entire UHF RFID band is about 14 dB. In Ant. IV, an arc-shaped grounded strip is inserted into the upper right corner of the square slot, which interferes with the current distribution in the square slot. In the universal UHF RFID band, the axial ratio is less than 3 dB, which realizes CP radiation and obtains the wide impedance bandwidth and axial ratio bandwidth. The 10 dB impedance bandwidth is from 0.64 GHz to 0.73 GHz and from 0.74 GHz to 1.05 GHz, and the 3 dB axial ratio bandwidth is from 0.83 GHz to 1.16 GHz, realizing broadband and circular polarization characteristics. The S_{11} of Ant. IV achieves a minimum value of -17.68 dB at the resonant frequency of 0.86 GHz. In order to further optimize the performance of the antenna, by widening the vertical tuning stub of the grounded L-shaped strip embedded in the square slot to obtain Ant. V, good impedance matching characteristic can be achieved, and the impedance matching bandwidth and the axial ratio bandwidth are further broadened. The simulated results show that in the entire UHF RFID band, the S_{11} of Ant. V at the resonance frequency of 0.90 GHz achieves the minimum value of -23.68 dB. The 10 dB impedance bandwidth is from 0.64 GHz to 1.27 GHz, and the 3 dB axial ratio bandwidth is from 0.83 GHz to 1.19 GHz. Finally, the proposed CPSSA has a very wide bandwidth coverage, which meets the requirements of covering the universal UHF RFID frequency range.

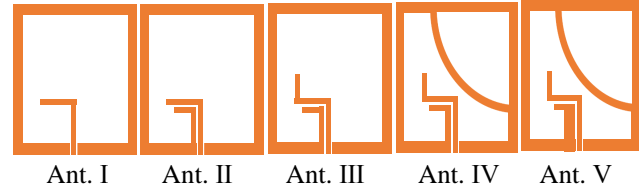


Fig. 2. Five prototypes of the proposed antenna.

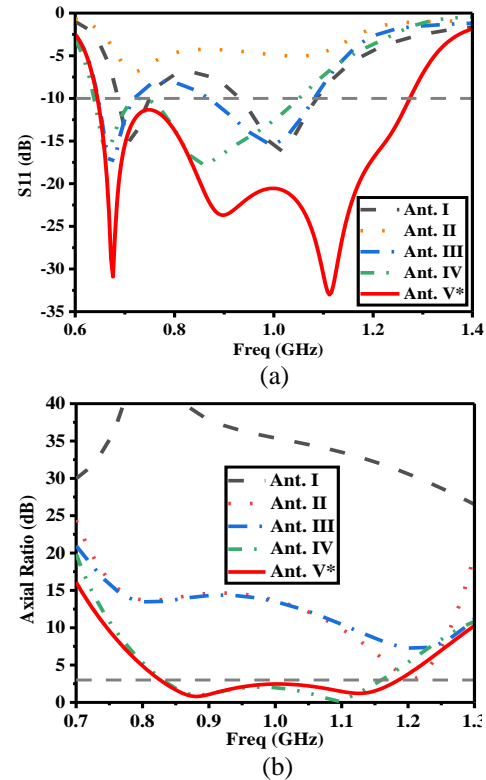


Fig. 3. Simulated results for antennas I-V: (a) reflection coefficient and (b) axial ratio.

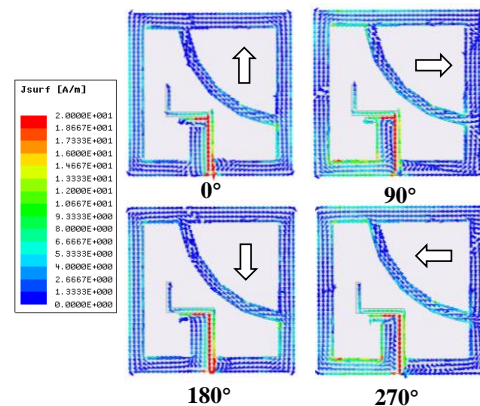


Fig. 4. Surface current distributions of the proposed CPSSA at 900 MHz in 0° , 90° , 180° , and 270° .

In order to explain the mechanism of CP radiation, the surface current distribution of the proposed CPSSA at 900 MHz with four phase angles of 0° , 90° , 180° , and 270° are illustrated in Fig. 4. As shown in the figure, it is observed the surface current distribution with the phase angle of 180° and 270° are opposite to the phase angle of 0° and 90° , respectively. The surface current rotates in a clockwise direction as the phase angle increases by 90° . Therefore, the proposed antenna excites left-handed circular polarization (LHCP) radiation in the $+Z$ direction and right-handed circular polarization (RHCP) radiation in the $-Z$ direction, which has dual circular polarization characteristic. The RHCP radiation can be excited in the $+Z$ direction by simultaneously inverting the directions of the inverted Z-shaped feedline, the arc-shaped grounded strip, and the L-shaped grounded strip with respect to the Y -axis.

III. PARAMETERS STUDIES

Parameter studies are to obtain the optimal impedance matching and CP performance. In this section, the key parameters of the proposed antenna are simulated and optimized using Ansoft HFSS 18.0. The simulated results illustrate the influence of key parameters such as the outer radius of the arc-shaped grounded strip (R_1), the length of the vertical strip of the inverted Z-shaped feedline (L_5), and the width of the vertical tuning stub of the L-shaped grounded strip (W_2) on the reflection coefficient S_{11} and AR bandwidth. When optimizing the parameters, make sure that one parameter is varied, while the other parameters are fixed.

A. Effects of the arc-shaped grounded strip

Good CP performance can be obtained by adequately adjusting the outer radius of the arc-shaped grounded strip (R_1). Figure 5 exhibits the effects of R_1 on the S_{11} and axial ratio. It can be seen from Fig. 5 (a) that different values of R_1 have little effect on the starting frequencies and low-frequency resonance frequencies. As R_1 increases, the high-frequency resonance frequency shifts to lower frequencies, and the stop frequency shifts to higher frequencies. Therefore, the thicker the arc-shaped grounded strip, the wider the 10 dB impedance matching bandwidth. When R_1 is 85.5 mm, the 10 dB impedance bandwidth is the widest, which is from 0.64 GHz to 1.27 GHz. Figure 5 (b) shows the effect of R_1 on the axial ratio. It is observed that as the value of R_1 increases, the low-frequency resonance frequency shifts to higher frequencies, whereas the high-frequency resonance frequency shifts to lower frequencies. Except for $R_1=85.5$ mm, as the thickness of the arc-shaped grounded strip is thicker, the axial ratio bandwidth is wider. When R_1 is 79.5 mm, the 3 dB axial ratio bandwidth is from 0.81 GHz to 0.94 GHz, which can't totally cover the specification of the universal UHF RFID band. When R_1 is 83.5 mm, the 3 dB AR bandwidth is

the widest, ranging from 0.83 GHz to 1.19 GHz, which meets the required bandwidth requirement. The axial ratio at the low-frequency resonance frequency of 0.88 GHz is 0.79 dB. It is worth noting that by adjusting the value of R_1 , that is, adjusting the thickness of the arc-shaped grounded strip, the AR bandwidth can be reconfigured to cover the required UHF RFID frequency range.

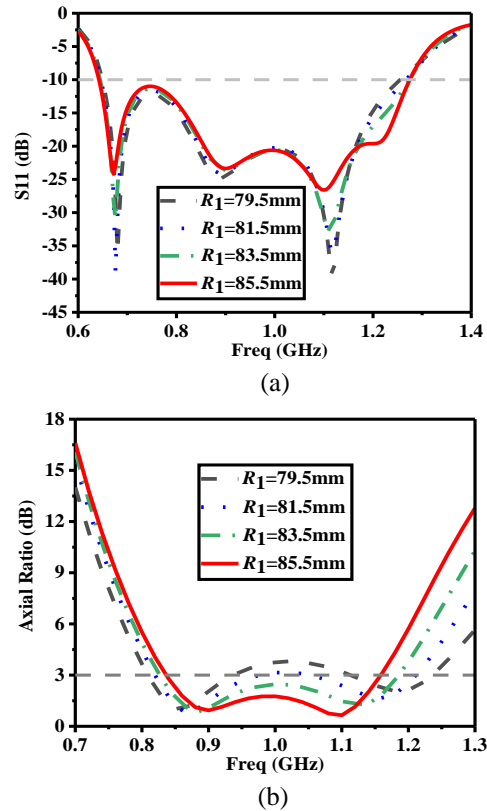


Fig. 5. Simulated results for the proposed broadband CPSSA with different outer radii (R_1) of the arc-shaped grounded strip: (a) S_{11} and (b) axial ratio.

B. Effects of the inverted Z-shaped feedline

Figure 6 shows the influence of the length of the vertical strip of the inverted Z-shaped feedline (L_5) on the antenna performance. Figure 6 (a) illustrates the effect of L_5 on impedance matching characteristic. It is found that when L_5 is increased, both the start frequency and the low-frequency resonance frequency slightly shift to lower frequencies, the high-frequency resonance frequency shifts to higher frequencies. When L_5 is 18.5 mm, the 10 dB impedance bandwidth is the narrowest. When L_5 takes other values, the impedance bandwidth is not much different, but when $L_5=22.5$ mm, the impedance matching characteristic is the best in the universal UHF RFID frequency range. The effect of L_5 on the AR performance is shown in Fig. 6 (b). Different

values of L_5 have a very slight influence on the resonance frequency and the 3 dB axial ratio bandwidth. The parameter L_5 has almost no effect on the axial ratio, which shows that L_5 has strong manufacture tolerance for the proposed broadband CPSSA. When L_5 takes the value of 22.5 mm, the proposed antenna has good impedance matching performance and the 3 dB axial ratio bandwidth is the widest, so the optimal value of L_5 is 22.5 mm.

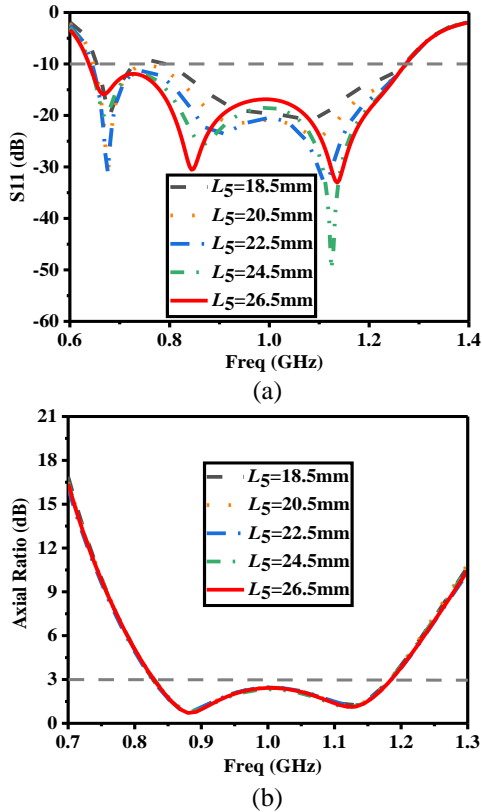


Fig. 6. Simulated results for the proposed broadband CPSSA with different vertical lengths (L_5) of the inverted Z-shaped feedline: (a) S_{11} and (b) axial ratio.

C. Effects of the L-shaped grounded strip

The simulated results of S_{11} and AR versus frequency for the different width of the vertical tuning stub of the L-shaped grounded strip (W_2) is demonstrated in Fig. 7. The simulated S_{11} shows that different values of parameter W_2 have a greater effect on the high-frequency resonance frequency. As the value of W_2 increases, the high-frequency resonance frequency shifts to higher frequencies, and the impedance bandwidth becomes wider. When W_2 is 14 mm, the 10 dB impedance bandwidth is the widest, ranging from 0.64 GHz to 1.29 GHz. Whereas, in the frequency range of 840-960 MHz, the impedance matching characteristic when $W_2 = 12$ mm is better than that when $W_2 = 14$ mm. From the influence of W_2 on the axial ratio characteristic, it is found that the

smaller the value of W_2 , the wider the axial ratio bandwidth, and the different values of W_2 have little influence on the resonance frequency.

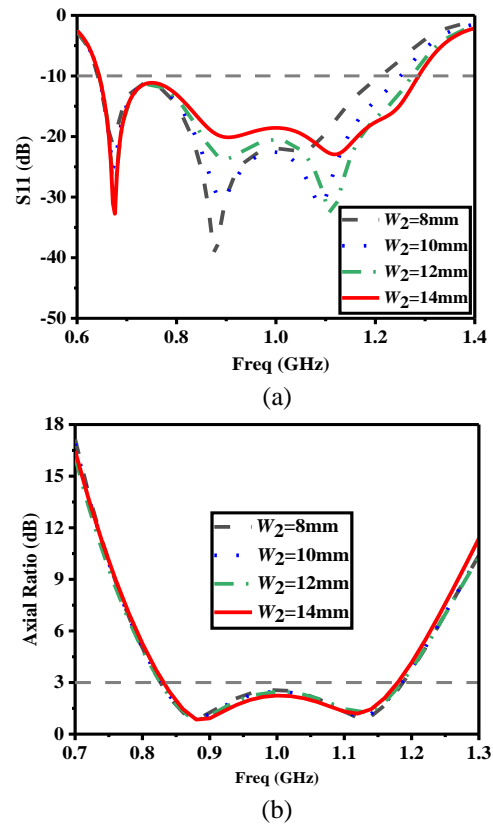


Fig. 7. Simulated results for the proposed broadband CPSSA with different vertical lengths (W_2) of the L-shaped grounded strip: (a) S_{11} and (b) axial ratio.

IV. RESULTS AND DISCUSSION

Figure 8 shows the manufactured prototype and far-field measurement photograph of the proposed CPSSA with the optimum values. The reflection coefficient S_{11} is measured by an Agilent E5071C vector network analyzer. The simulated and experimental reflection coefficient S_{11} of the proposed antenna are exhibited in Fig. 9. The measured 10 dB impedance bandwidth is 64.4% (652-1272 MHz), which agrees well with the simulated 10 dB impedance bandwidth (640-1270 MHz). The minimum values of the simulated and measured results of S_{11} are -33.02 dB and -40.30 dB, respectively. The curve trend of the impedance matching of simulation and measurement is roughly similar. The far-field performances of the proposed antenna, such as axial ratio, gain, radiation efficiency and 2D radiation pattern, are all tested in an anechoic chamber using the SATIMO measurement system. Figure 10 illustrates the comparison of the simulated and measured results of AR. The measured 3 dB AR bandwidth is 32.0% (840-1160 MHz),

which is narrower than the simulated results (830-1190 MHz). The simulated and measured 3 dB AR bandwidths are wide, covering the entire UHF RFID band. The simulated and measured results of peak gain and radiation efficiency are shown in Fig. 11. In the UHF RFID frequency range (840-960 MHz), the measured peak gain fluctuates within 3.4-4.6 dBi. The measured maximum peak gain is 4.6 dBi at 960 MHz and the measured radiation efficiency is about 90%. The slight difference between the simulated and measured results of peak gain and radiation efficiency is mainly attributed to the manufacturing tolerances. Figure 12 shows the simulated and measured LHCP/RHCP radiation patterns for the x-z and y-z planes at the center frequency of 900 MHz in the universal UHF RFID band. The measured results of the radiation patterns in both x-z and y-z planes demonstrate that the proposed antenna has good bidirectional characteristic.

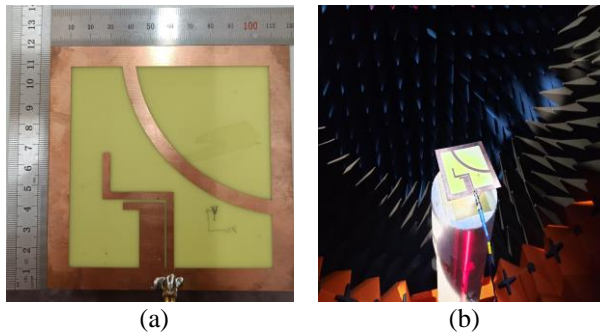


Fig. 8. Photographs of the proposed antenna: (a) manufactured prototype, and (b) far-field measurement.

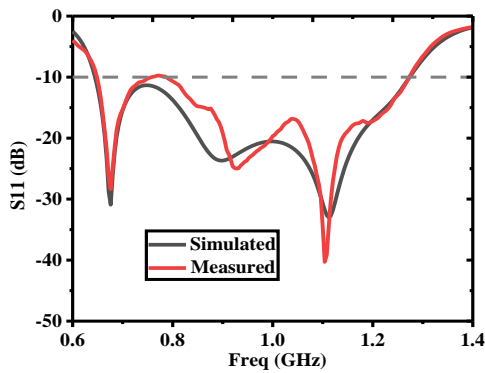


Fig. 9. Simulated and measured reflection coefficient of the proposed broadband CPSSA.

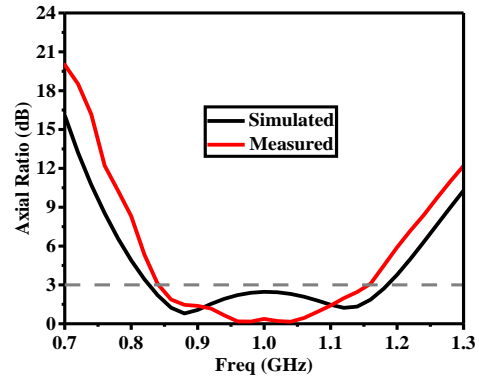


Fig. 10. Simulated and measured axial ratio of the proposed broadband CPSSA.

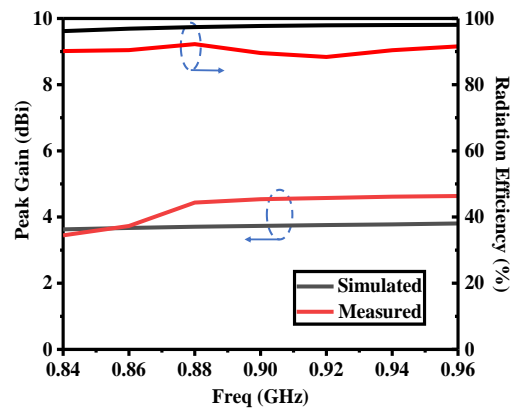


Fig. 11. Simulated and measured peak gain and radiation efficiency of the proposed antenna.

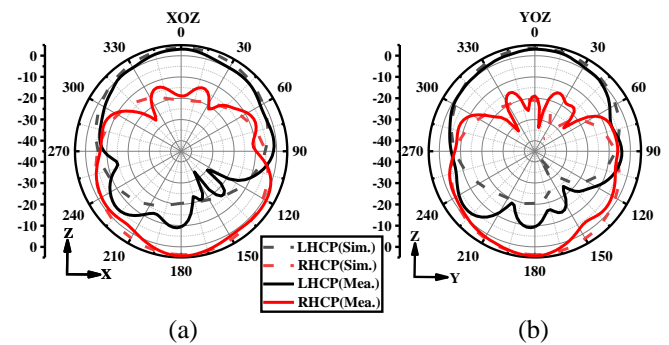


Fig. 12. Simulated and measured LHCP and RHCP radiation patterns of the proposed antenna at 900 MHz: (a) x-z and (b) y-z planes.

Table 1: Comparison of the proposed antenna with other CP antennas in references

| Ref. | Impedance Bandwidth (MHz, %) | 3 dB AR Bandwidth (MHz, %) | Dimensions $L \times W \times H$ (mm ³) |
|----------|------------------------------|----------------------------|---|
| [5] | 835–975, 16.4% | 870-940, 7.7% | 124 × 117 × 33.2 |
| [8] | 870-967, 10.6% | 893-948, 6% | 220 × 220 × 10 |
| [10] | 768-962, 22.4% | 816-957, 15.9% | 250 × 250 × 35 |
| [18] | 800-1056, 28.5% | 900-936, 4% | 90 × 105 × 1.6 |
| [21] | 815–925, 12.6% | 835-870, 4.3% | 83 × 83 × 1.6 |
| Proposed | 652-1272, 64% | 840-1160, 32.0% | 119 × 119 × 0.5 |

Table 1 exhibits the comparison between the proposed broadband CPSSA and the other CP antennas for UHF RFID reader. As shown in Table 1, the proposed antenna covers the universal UHF RFID band and has the merits of wide operating bandwidth and small volume, which is more suitable for universal UHF RFID handheld reader applications than the other CP antennas in the references. Compared with the CP antennas in [18, 21], the antennas in the literature [5, 8, 10] have the wider S_{11} and AR bandwidth, but the corresponding operating bandwidths do not cover the entire UHF RFID band, and the volumes are very large. The antennas proposed in [18, 21] have a compact size, whereas the overlapping operating bandwidth does not meet the requirements.

V. CONCLUSION

A novel broadband CPW-fed CPSSA is proposed. The inverted Z-shaped bent feedline and the arc-shaped grounded strip realize impedance matching and CP characteristics, respectively. By widening the width of the vertical tuning stub of the L-shaped grounded strip embedded in the lower-left corner of the square slot, the impedance matching and CP performance can be improved. Finally, a CP reader antenna with broadband characteristic is obtained. The measured 10 dB impedance bandwidth is 64.4% (652-1272 MHz), and the 3 dB axial ratio bandwidth is 32.0% (840-1160 MHz). The operating bandwidth covers the universal UHF RFID band. The overall size of the proposed antenna is $119 \times 119 \times 0.5$ mm³, which has a wider operating bandwidth compared to other broadband antennas with similar dimensions. The measured peak gain is about 4.4 dBi and radiation efficiency is about 90% in the universal UHF RFID band. The proposed antenna has the advantages of simple structure, low cost, compact size, and good bidirectional radiation characteristic in the x-z and y-z planes, making

it more suitable for universal UHF RFID handheld readers applications.

ACKNOWLEDGMENT

This work is supported by Key Project of the National Natural Science Foundation of China under Grant, 62090012, 62031016, 61831017, the Project under Grant 19-163-21-TS-001-062-01, and the Sichuan Provincial Science and Technology Important Projects under Grant 2019YFG0498, 2020YFG0282, 2020YFG0452 and 2020YFG0028.

REFERENCES

- [1] C. Sim and C. Chi, "A slot loaded circularly polarized patch antenna for UHF RFID reader," *IEEE Trans. Antennas Propag.*, vol. 60, no. 10, pp. 4516-4521, Oct. 2012.
- [2] W. Chen and Y. C. Huang, "A novel CP antenna for UHF RFID handheld reader," *IEEE Antennas and Propagation Magazine*, vol. 55, no. 4, pp. 128-137, Aug. 2013.
- [3] C. S. Lee, Y. Fan, and M. Ezzat, "Single-feed circularly polarized microstrip antenna with Bethe holes on the radiating patch," *IEEE Trans. Antennas Propag.*, vol. 68, no. 6, pp. 4935-4938, June 2020.
- [4] M. Shokri, S. Asiaban, and Z. Amiri, "Study, design and fabrication of a CPW fed compact monopole antenna with circular polarization for ultra wide band systems application," *Applied Computational Electromagnetics Society Journal*, vol. 32, no. 9, pp. 749-753, Sep. 2017.
- [5] T. N. Chang and J. M. Lin, "Circularly polarized ring-patch antenna," *IEEE Antennas Wireless Propag. Lett.*, vol. 11, pp. 26-29, Mar. 2012.
- [6] T. Wu, H. Su, L. Gan, H. Chen, J. Huang, and H. Zhang, "A compact and broadband microstrip stacked patch antenna with circular polarization for 2.45-GHz mobile RFID reader," *IEEE Antennas Wireless Propag. Lett.*, vol. 12, pp. 623-626, May 2013.
- [7] J. Z. Huang, P. H. Yang, W. C. Chew, and T. T. Ye, "A novel broadband patch antenna for universal UHF RFID tags," *Microwave Opt. Technol. Lett.*, vol. 52, no. 12, pp. 2653-2657, Dec. 2010.
- [8] X. Chen, G. Fu, S. Gong, Y. Yan, and W. Zhao, "Circularly polarized stacked annular-ring microstrip antenna with integrated feeding network for UHF RFID readers," *IEEE Antennas Wireless Propag. Lett.*, vol. 9, pp. 542-545, June 2010.
- [9] C. Sim, Y. Hsu, and G. Yang, "Slits loaded circularly polarized universal UHF RFID reader antenna," *IEEE Antennas Wireless Propag. Lett.*, vol. 14, pp. 827-830, Nov. 2015.
- [10] X. Liu, Y. Liu, and M. M. Tentzeris, "A novel circularly polarized antenna with coin-shaped patches and a ring-shaped strip for worldwide

- UHF RFID applications,” *IEEE Antennas Wireless Propag. Lett.*, vol. 14, pp. 707-710, Mar. 2015.
- [11] Z. N. Chen, X. Qing, and H. L. Chung, “A universal UHF RFID reader antenna,” *IEEE Trans. Microw. Theory Tech.*, vol. 57, no. 5, pp. 1275-1282, May 2009.
- [12] Y. Pan and Y. Dong, “Circularly polarized stack Yagi RFID reader antenna,” *IEEE Antennas Wireless Propag. Lett.*, vol. 19, no. 7, pp. 1053-1057, July 2020.
- [13] R. Xu, J. Li, J. Yang, K. Wei, and Y. Qi, “A design of u-shaped slot antenna with broadband dual circularly polarized radiation,” *IEEE Trans. Antennas Propag.*, vol. 65, no. 6, pp. 3217-3220, June 2017.
- [14] T. T. Le, H. H. Tran, and H. C. Park, “Simple-structured dual-slot broadband circularly polarized antenna,” *IEEE Antennas Wireless Propag. Lett.*, vol. 17, no. 3, pp. 476-479, Mar. 2018.
- [15] Y. Xu, Z. Wang, and Y. Dong, “Circularly polarized slot antennas with dual-mode elliptic cavity,” *IEEE Antennas Wireless Propag. Lett.*, vol. 19, no. 4, pp. 715-719, Apr. 2020.
- [16] S. Hao, Q. Chen, J. Li, and J. Xie, “A high-gain circularly polarized slotted patch antenna,” *IEEE Antennas Wireless Propag. Lett.*, vol. 19, no. 6, pp. 1022-1026, June 2020.
- [17] Y. F. Lin, Y. C. Kao, S. C. Pan, and H. M. Chen, “Bidirectional radiated circularly polarized annular-ring slot antenna for portable RFID reader,” *Applied Computational Electromagnetics Society Journal*, vol. 25, no.3, pp. 182-189, Mar. 2010.
- [18] C. Raviteja, C. Varadhan, M. Kanagasabai, A. K. Sarma, and S. Velan, “A fractal-based circularly polarized UHF RFID reader antenna,” *IEEE Antennas Wireless Propag. Lett.*, vol. 13, pp. 499-502, Mar. 2014.
- [19] Nasimuddin, Z. N. Chen, and X. Qing, “A compact circularly polarized cross-shaped slotted microstrip antenna,” *IEEE Trans. Antennas Propag.*, vol. 60, no. 3, pp. 1584-1588, Mar. 2012.
- [20] J. Y. Sze, C. I. G. Hsu, M. H. Ho, Y. H. Ou, and M.T. Wu, “Design of circularly polarized annular-ring slot antennas fed by a double-bent microstripline,” *IEEE Trans. Antennas Propag.*, vol. 55, no. 11, pp. 3134-3139, Nov. 2007.
- [21] J. K. Pakkathillam, M. Kanagasabai, and M. G. N. Alsath, “Compact multiservice UHF RFID reader antenna for near-field and far-field operations,” *IEEE Antennas Wireless Propag. Lett.*, vol. 16, pp. 149-152, Feb. 2017.



Rui Ma was born in Ziyang, Sichuan, China, in 1997. She is currently working toward the Master's degree in Information and Communication Engineering at Southwest Jiaotong University (SWJTU), Chengdu, China.

Her main research interests include antenna design and theory, especially in RFID circularly polarized reader antennas.



Quanyuan Feng (M'06–SM'08) received the M.S. degree in Microelectronics and Solid Electronics from the University of Electronic Science and Technology of China, Chengdu, China, in 1991, and the Ph.D. degree in EM Field and Microwave Technology from Southwest Jiaotong University, Chengdu, China, in 2000.

He is the Head of Institute of Microelectronics, Southwest Jiaotong University, Chengdu, China. He has been honored as the “Excellent Expert” and the “Leader of Science and Technology” of Sichuan Province owing to his outstanding contribution. In recent 5 years, more than 500 papers have been published on *IEEE Transactions on Antennas and Propagation*, *IEEE Transactions on Microwave Theory and Techniques*, *IEEE Antennas and Wireless Propagation Letters* etc, among which more than 300 were registered by SCI and EI.

His current research interests include integrated circuits design, RFID technology, embedded system, wireless communications, antennas and propagation, microwave and millimeter wave technology, smart information processing, electromagnetic compatibility, RF/ microwave devices and materials etc.

Ultra-wideband Flexible Implantable Antenna for Wireless Capsule Endoscopy System with Performance Improvement

Yang Feng, Pan Chen, Shaopeng Pan, and Gaosheng Li*

College of Electrical and Information Engineering, Hunan University, Changsha 410082, China

*gaosheng7070@vip.163.com

Abstract — The implantable antenna is an important part of the wireless capsule endoscopy (WCE) system to achieve wireless communication. This paper designed an ultra-wideband flexible implantable antenna for wireless capsule endoscopy system. With a very wide bandwidth, the antenna can completely cover the industrial, scientific, and medical frequency bands (ISM, 2.4-2.48 GHz) and Wireless Medical Telemetry Service (WMTS, 1.395-1.4 GHz). The expanded size of the proposed antenna is 18mm×10mm×0.1mm. The conformal technology of the antenna has further reduced the space of the system and achieved miniaturization. The capsule antenna in this paper is a compact planar monopole antenna fed by a coplanar waveguide, and it uses a flexible material as a dielectric substrate to achieve the conformal shape of the antenna. U-shaped ground branch (UGB) and a loaded split ring resonator (SRR) structure were used to further improve the antenna performance. Simulation and measurement results were basically the same. On the premise of radiation safety and miniaturization of the antenna, the ultra-wideband operation of the antenna was realized. This antenna design provided reference value for the design and application of the capsule antenna.

Index Terms — Conformal, implantable antenna, ultra-wideband, wireless capsule endoscopy system.

I. INTRODUCTION

Miniature implantable medical devices are commonly used for disease treatment and physiological testing, providing a higher quality of protection for people's health. In the field of electronic medicine, the wireless capsule endoscopy (WCE) system is a non-invasive gastrointestinal detection system that acquires image data of the digestive tract and wirelessly transmits it to determine the physiological condition of the human body [1]. The antenna is a bridge to realize the communication between the wireless capsule endoscopic system and the outside world by performing information transmission and wireless energy transmission and other task. Moreover, more requirements are put forward for the performance of the implanted antenna [2] in that the biological tissue structure of the human body features

high dielectric constant and high loss. In addition, the need to miniaturize the wireless capsule endoscopy system, required us to reduce the overall volume of the antenna to save system space. To fully utilize the space, the antenna formed a conformal structure on the inner wall of the capsule [3-4]. The structure can save more space in the system and further realize the miniaturization of the system. It can also make full use of the surface for radiation and increase the working bandwidth of the antenna [5]. The flexible capsule implantable antenna is of great practical value in the application research of telemetry biomedicine.

In recent years, many scientific research teams have carried out exploration and research on the performance and size of the capsule antennas. Different types of capsule antennas used in different working environments. A capsule microstrip antenna working in ISM frequency band was designed [6] to cater to the requirements of the telemetry capsule in human digestive tract system. In addition, [7] designed a broadband capsule antenna for the Medical Device Radiocommunications Service (MedRadio, 401-406 MHz) frequency band. The antenna loads a metal branch in the center of the zigzag dipole, and adjusts the length of the metal branch to excite another resonance point, which increases the working bandwidth. An implantable capsule conformal antenna was designed to operate in the MediRadio frequency band for WCE [8], in which a zigzag line was adopted to increase the bandwidth, and the peak gain was -31.5 dBi. [9] also proposed an ultra-wideband capsule antenna, which covered the MICS and ISM frequency bands and achieved omnidirectional radiation, but the maximum gain was only -31.5 dBi. [10] proposed a conformal patch antenna design with CSRR loading. However, this was a single narrowband (2.45 GHz) design. A wideband flexible loop antenna loaded with a split ring resonator (SRR) was designed to achieve ultra-wideband operation. The return loss of the antenna was improved by the SRR, and the absorbed power of the human body was reduced [11]. In [12], this paper designed a capsule antenna that works at ISM with a thickness of only 0.1 mm. The size was reduced by geometric fractal, and the antenna gain was -30.6 dBi.

Compared with the general fixed implantable antenna, the antenna of the wireless capsule endoscopy (WCE) system is more flexible and its working environment is more complicated. Since the dielectric properties of human tissues are very complex and changeable, the resonance frequency is prone to shift, so a wide bandwidth is required. The ultra-wideband performance of the capsule antenna helps to resist the frequency shift effect, especially when the capsule is close to different tissues of the intestine and stomach. Further investigation has found that the capsule conformal antenna mainly needs to be improved in two aspects. On the one hand, due to the small size of the capsule itself, miniaturization is the eternal topic of capsule antenna design. While ensuring the performance of the antenna, new methods are still needed to achieve further miniaturization of the antenna size; on the other hand, the antenna design must also consider the ratio absorption rate (SAR), gain and power at the same time. It is still a promising subject to design a compact flexible antenna that can cover multiple operating frequency bands and has good radiation characteristics. In this paper, based on a coplanar waveguide fed planar monopole antenna, the antenna was designed in view of the compact structure of the wireless capsule endoscopy system and the diverse working environment. The antenna was designed using U-shaped ground branch (UGB), radiative patch slotting and loaded split ring resonator (SRR) technology. The antenna realized the ultra-wideband operation of the antenna, covering the two frequency bands of WMTS and ISM for the operation of the implantable antenna, and the frequency range of the antenna was 1.15 - 4.18 GHz. The volume of the antenna was 18 mm³. Considering the miniaturization and performance, this design can save more space in the capsule endoscopic system while realizing the wide bandwidth and miniaturization of the antenna. This paper is organized as follows: The method is introduced in the second part. The third section introduces the design and optimization of the antenna. The fourth section introduces the antenna design results and discussion. Section five summarizes the conclusions.

II. METHODOLOGY

A. Antenna structure design

The planar monopole antenna has the advantages of thin profile, small size, low manufacturing cost, and wide frequency band. Combined with the space structure in the capsule system, a planar monopole antenna is a good choice. To reach the required working frequency band of the antenna, we conducted a preliminary design based on the principle, the formula is as follows:

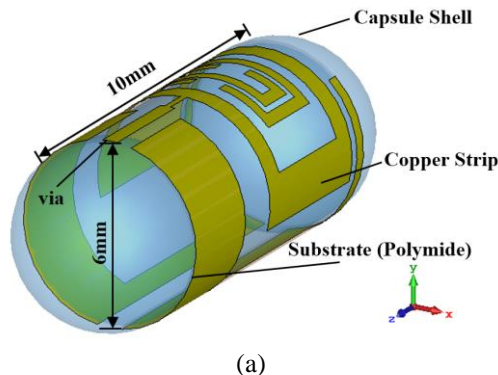
$$f = \frac{c}{4l\sqrt{\epsilon_r}}, \quad (1)$$

where l is the effective length, c is the speed of light in free space, and f is the frequency.

We can know that the effective current path is inversely proportional to the frequency when the dielectric constant is constant. Through (1), a better approximation can be obtained, and the antenna model can be preliminarily designed. In the actual design process, the design can be optimized based on the initial size.

The design adopted the conformal technology of the antenna and the electronic capsule endoscope system, which reduced the space occupation of the system. In this design, the same material as [13] and ($\epsilon_r = 3.5$, $\tan\delta = 0.0027$) was used as the dielectric substrate of the antenna. The thickness of the dielectric substrate of the antenna was 0.1 mm. The unfolded size of the antenna was only 18 mm×10 mm×0.1 mm. The radius of the antenna after conformal in the capsule was 3 mm. The capsule antenna structure is shown in Fig. 1.

The flexible material features strong environmental adaptability, and the dielectric substrate of the antenna can be more suitable for the structure of the system. Conformal processing of the antenna will not affect its performance [2]. It adopts a single-layer metal structure, which is mainly composed of a radiating surface and a dielectric substrate. The antenna feed adopts coplanar waveguide feed. The coplanar waveguide feeding structure has low cost and low parasitic parameters. The radiating unit and the feeding unit in this way are on the same plane, thus reducing the overall volume. This structure is easy to realize the omnidirectional radiation characteristics of the antenna, integrate with active devices, and achieve wide-band and direct, inductive coupling and capacitive coupling multiple feed modes [14]. U-shaped ground branches introduced into the antenna floor can be used to increase the bandwidth of the antenna. The antenna radiation patch is slotted and loaded with split ring resonator design to improve impedance matching, increase bandwidth and improve antenna radiation performance.



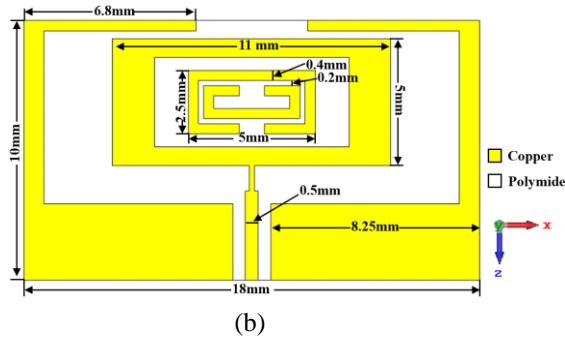


Fig. 1. Schematic diagram of the capsule antenna structure: (a) after conformal and (b) before conformal.

B. Simulation and measurement environment

This paper used the microwave studio in the CST simulation software to design and simulate the antenna. The modeling and simulation of the antenna adopts the time-domain finite integration method. The numerical calculation process uses Finite Integration Technology (FIT). This numerical solution provides a spatial discrete format to solve a variety of electromagnetic problems. FIT technology spatially visually divides the solving domain, and establishes the integral form of discrete Maxwell equations on each unit surface to realize spatial discretization. In the process of meshing, it is necessary to reach 20-35 mesh lines per wavelength, and it is worth noting that the smallest meshing unit contains at most two mediums.

Since the resonant frequencies of the implanted antennas differ little between the single-layer structure and the multi-layer structure models [15-16], we chose the single-layer structure for calculation and analysis in order to simplify the simulation. The simulation environment is shown in Fig. 2 (a). The size of the model is 100 mm×100 mm×50 mm, and the implantation depth is 10 mm. Based on the antenna design and simulation optimization, the actual processing and production were carried out. The actual antenna and the test scene are shown in Fig. 2 (b). In the 300 MHz ~ 3 GHz frequency band, the dielectric properties of pork and chicken breast are very similar to those of the human body. According to literature research, some design teams conduct tests in pork [17-18], and some teams conduct tests in chicken breast [19-20]. In order to verify the correctness of the simulation results, the antenna was tested in pork and chicken breasts. Two kinds of experimental materials were used to verify the performance of the antenna at the same time, which could strengthen the reliability of the experiment and the practicability of the antenna. The test instrument used the E5063A vector network analyzer produced by Keysight. During the test, a flexible 50 Ω coaxial cable was used to connect the feed port of the antenna and the vector network analyzer (VNA) for measurement.

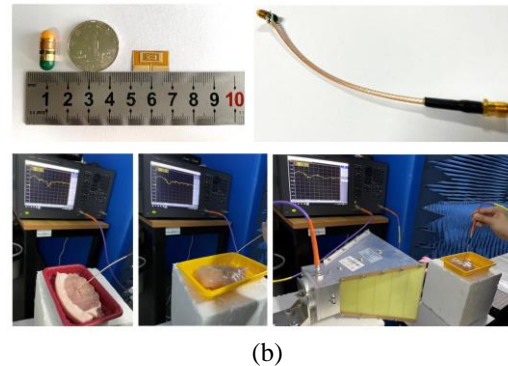
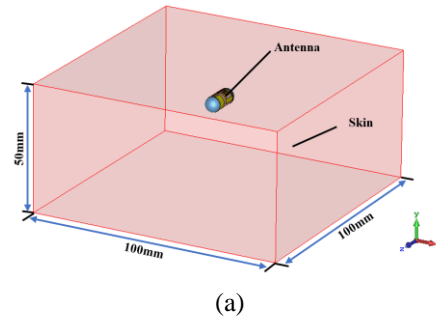


Fig. 2. (a) Schematic diagram of the capsule antenna implanted into the skin model, and (b) implantable conformal antenna structure, and actual test environment setting.

III. ANTENNA DESIGN AND ANALYSIS

A. Antenna design process

The dielectric properties of human tissues are different to some extent, so it is difficult for narrowband antennas to overcome the detuning phenomenon in biological tissue environment. In order to ensure the normal operation of the antenna in the wireless capsule speculum system, the capsule antenna achieved broadband characteristics by adding structure or optimizing its structure. The antenna design process is shown in Fig. 3.

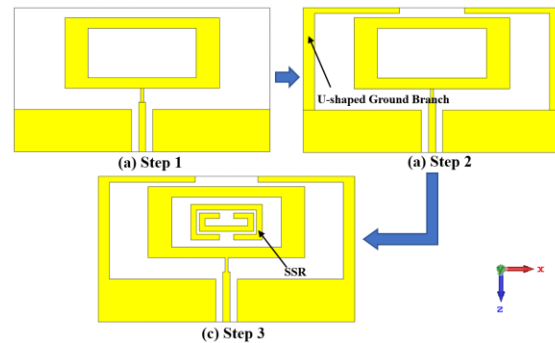


Fig. 3. Implantable antenna design process: (a) unloaded U-shaped ground branch (UGB), (b) unloaded split ring structure (SRR), and (c) final designed antenna structure.

Introduce U-shaped ground branch (UGB): In this design, UGB was introduced on the GND of the antenna to increase the resonance point of the antenna and improve the impedance bandwidth of the antenna. Increasing the U-shaped ground connection in the antenna outer layer is conducive to enlarging the capacitive coupling area between the antenna ground connection and the surrounding frequency band, thereby increasing the electric field strength of the radiating surface [21].

Loaded split ring resonator (SRR): SRR is a metamaterial structural unit with negative permeability properties [22]. When the SRR structure is much smaller than the free wavelength, its structure can be equivalent to an LC resonant circuit. SRR reduces the inductance of the loop, thereby improving the impedance matching characteristics of the antenna [23]. The antenna-loaded SRR structure can not only improve the impedance matching of the antenna and the return loss of the antenna, but also increase the gain of the antenna.

B. Antenna performance comparison

The structure of the antenna is optimized through design steps to achieve the desired performance. S11 represents the return loss characteristics of the antenna. Through the combination of the above design methods, the UWB operation of the antenna is realized. Since the dielectric properties of human tissues are complex and changeable, a wider bandwidth helps to resist the drift of resonance frequency, and thus overcome the detuning effect. As shown in Fig. 4, the working frequency band of the antenna is 1.15 GHz - 4.18 GHz, and the absolute bandwidth is 3.03 GHz, covering WMTS frequency band and ISM frequency band, achieving the effect of ultra-wideband. Comparing steps 1, 2 and 3, we can draw the following conclusion. On the basis of coplanar waveguide feeding technology and radiating patch slotting, the antenna improves impedance matching and realizes ultra-wideband characteristics by introducing a combination of UGB and SRR technologies.

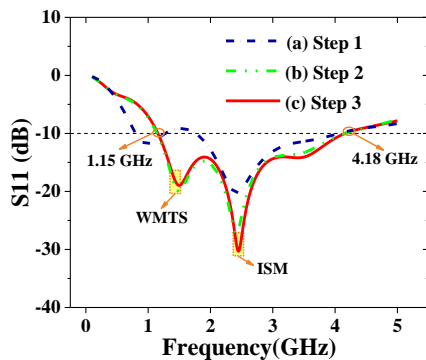


Fig. 5. Comparison of S11 for the steps achieving final design.

As shown in Fig. 5, we expanded the area of the capacitive coupling area of the antenna by loading the SRR and UGB structure, thereby increasing the maximum electric field strength of the original antenna. As the electric field strength of the antenna radiation surface increases, the radiation gain of the antenna will also increase.

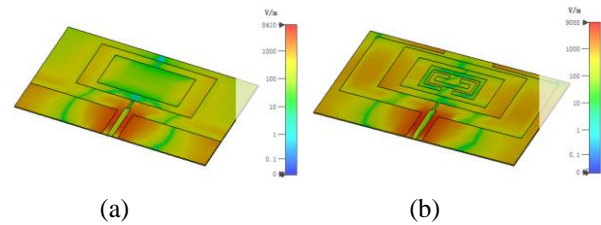


Fig. 5. Electric field of antenna ($f=2.45$ GHz): (a) without UGB and SRR and (b) with UGB and SRR.

The gain of the implanted antenna is mainly affected by its physical size and working environment. While the implanted antenna is miniaturized, the gain is very low. As shown in Figure 6, the gain of the implanted antenna loaded with UGB or SRR has been improved to a certain extent, mainly in the high frequency region of the working frequency band. Adding SRR and UGB structure to optimize antenna gain. We can see that the two structures are loaded at the same time in the working frequency band of the antenna, which further improves the gain of the antenna.

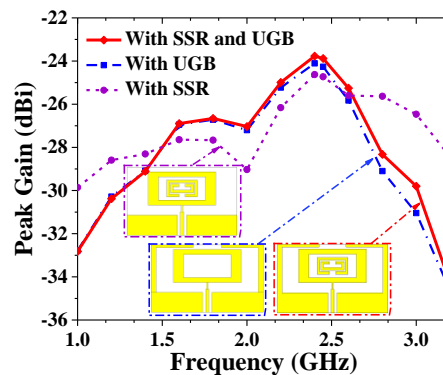


Fig. 6. Antenna gain comparison adding U shaped ground and SRR.

IV. RESULTS AND DISCUSSION

The antenna was processed and tested. As shown in Fig. 7, the simulated and measured S11 results are basically consistent. Although the required operating frequency had been shifted in different biological tissues, the two required operating frequency bands were covered quite well. In addition, we observed that the test frequency band was wider than the analog frequency band. In addition to the experimental error caused by the

processing technology, these differences may be attributed to the two factors. First of all, measurements of environmental effects and differences in the dielectric properties of pork and chicken breasts can cause errors. Secondly, the coaxial cable is welded (See in Fig. 2 (b)), which has a certain influence on impedance matching. Due to the limitations of the manufacturing process, these factors are unavoidable. In general, the measurement results verify the correctness of the simulation results.

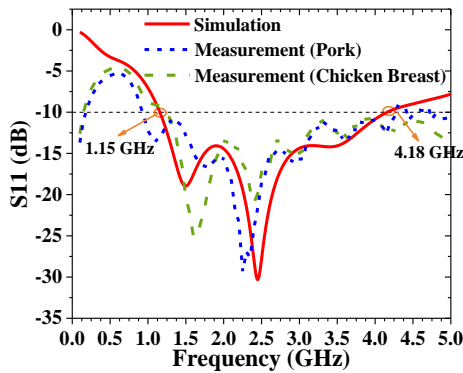


Fig. 7. S11 of the implanted antenna in the simulated and measured environment (pork and chicken breast).

The gain of the antenna represents the ability of the WCE to send and receive signals. For capsule implanted antennas, the gain is generally relatively low. Figure 8 shows the far-field pattern of the antenna at 1.4 GHz and 2.45 GHz. The measurement of the antenna gain was carried out by comparing with the standard gain horn. The designed antenna was tested in pork and chicken breast separately. The maximum gain of the test antenna in the 1 GHz - 3.2 GHz frequency band is shown in Fig. 9. The maximum gain at 1.4 GHz is -29.2 dBi, and the maximum gain at 2.45 GHz is -23.9 dBi. Due to factors such as air loss, feed loss, and test error, the gain of the antenna changes slightly. The actual measured gain is basically consistent with the simulated gain.

Figure 10 shows the antenna radiation efficiency change over frequency band. The antenna works in an implanted environment, and there is a large part of the coupling with the biological environment, and its radiation efficiency is greatly reduced. Generally, the radiation efficiency of implantable antennas is less than 1% [24]. The highest radiation efficiency of the antenna in the target frequency band basically reaches 8×10^{-4} , which is similar to the situation of most implanted antennas. The deviation between simulation and

measurement is mainly caused by environmental interference during the test, but the results are basically consistent.

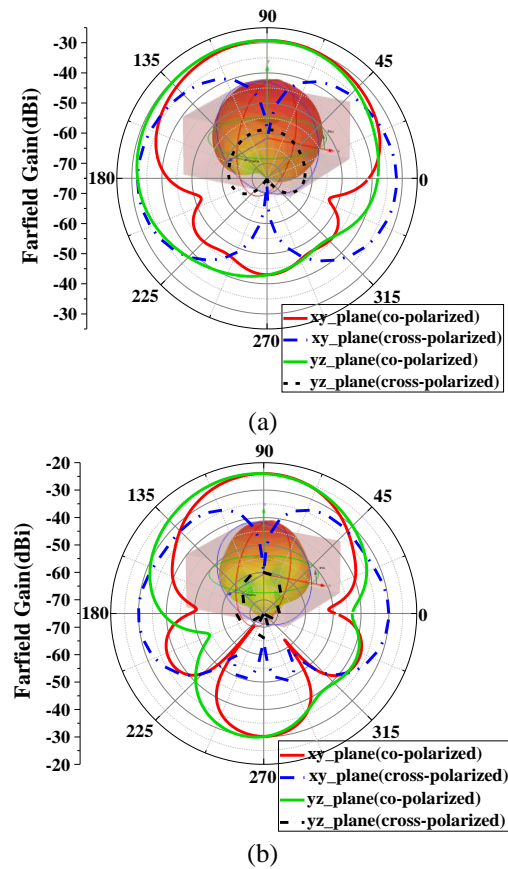


Fig. 8. Gain of the proposed capsule antenna, (a) 1.4 GHz and (b) 2.45 GHz.

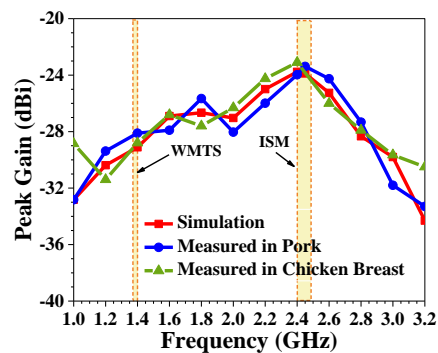


Fig. 9. Gain comparison of the implanted antenna in the simulated and measured environments (pork and chicken breast).

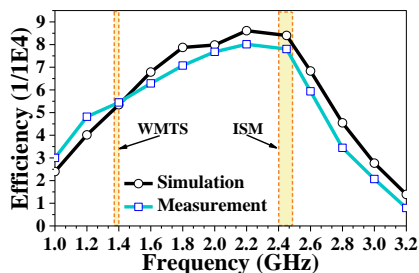


Fig. 10. Simulated and measured radiation efficiency of the proposed antenna.

The working environment of the implanted antenna is special, and we need to ensure the health of the human body. The IEEE C 95.1-1999 standard limits the average specific absorption rate (SAR) of 1g of human tissue to less than 1.6 W/kg, and the average specific absorption rate (SAR) of 10 g human tissues to not exceed 2 W/kg

[25]. When the incident power is set to 1W, the SAR values obtained are 1 g and 10 g, as shown in Table 1, far greater than the specified standard. Therefore, the SAR value is reduced by reducing the incident power to meet the specified criteria. The table also shows the recommended maximum power input as a reference. From the values in the table, we can conclude that the maximum safe input power for 1 g -SAR is 3.3 mW, however, for 10 g -SAR, the maximum allowable input power should be 28 mW. In short, the SAR value calculated in the table complies with IEEE regulations.

As shown in Table 2, the implanted capsule antenna designed in this paper is compared with the antennas in the same type of literatures. Considering multiple parameters of the antenna, we can see that the size of the antenna in this paper is relatively smaller and has a wider bandwidth. This design realized the miniaturization and ultra-wideband of the antenna, while maintaining a better gain.

Table 1: Peak spatial average SAR (input power = 1 W) and maximum allowable input power

| Frequency (GHz) | MAX SAR(W/kg) | | 1g Allowable Input Power (mW) | 10g Allowable Input Power (mW) |
|-----------------|---------------|-----------|-------------------------------|--------------------------------|
| | 1g - Avg | 10g - Avg | | |
| 1.4 | 503 | 82.2 | 3.2 | 25 |
| 2.45 | 517 | 83.1 | 3.3 | 28 |

Table 2: Comparison of the proposed antenna to the same type of capsule antenna literatures

| Ref. | Size (mm×mm×mm) | Coverage Frequency Band | 10 dB Bandwidth (MHz) | Peak Gain (dBi) | Max-Efficiency (1/1E4) | MAX-SAR(W/kg) | |
|------------|-----------------|-------------------------|-----------------------|-----------------|------------------------|---------------|------|
| | | | | | | 1-g | 10-g |
| [7] | 16.5×15.7×1.27 | MedRadio | 162 | -37 | < 2 | 485 | N.M. |
| [8] | 15×15×0.79 | MedRadio | 541 | -31.5 | N.M. | 913 | N.M. |
| [9] | 28×14×0.254 | MICS, ISM | 1850 | -31.5 | N.M. | N.M. | N.M. |
| [11] | 18×18×1.235 | MedRadio, ISM | 3193 | -18.4 | 2.5-41 | 216 | N.M. |
| [12] | 20×12.6×0.1 | ISM | 630 | -30.6 | N.M. | N.M. | N.M. |
| This study | 18×10×0.1 | WMTS, ISM | 3030 | -23.9 | 8 | 517 | 83.1 |

*Ref.= Reference. N.M.= not mentioned.

V. CONCLUSION

In this paper, an ultra-wideband conformal implantable antenna for a wireless capsule endoscope system was designed, which covered WMTS and ISM frequency bands. The structure of the antenna was simulated, analyzed, and optimized, and the ultra-wideband operation was finally realized. The antenna volume was only 18 mm³. The antenna adopted the form of UGB and loaded SRR structure to further improve the performance and achieve better radiation. The maximum gain of the antenna was -23.9 dBi. The SAR value of the antenna also meets IEEE regulations. Compared with the ultra-wideband capsule antenna in the previous literatures, it has higher gain, smaller volume and superior performance. The actual measurement results

are in good agreement with the simulation. This paper verified the performance of the antenna through design, analysis and experiments, and provided reference for further research on the application of the conformal capsule antenna.

REFERENCES

- [1] B. Biswas, A. Karmakar, and V. Chandra, "Miniaturised wideband ingestible antenna for wireless capsule endoscopy," *IET Microwaves, Antennas & Propagation*, vol. 14, no. 4, pp. 293-301, Feb. 2019.
- [2] M. Wang, L. Cai, H. Zheng, and Z. Yang, "Review of flexible antenna technology for electronic capsule," *Electronic Components and Materials*, vol. 36, no. 4, pp. 9-14, Apr. 2017.

- [3] S. Yun, K. Kim, and S. Nam, "Outer-wall loop antenna for ultrawideband capsule endoscope system," *IEEE Antennas and Wireless Propagation Letters*, vol. 9, pp. 1135-1138, Nov. 2010.
- [4] P. M. Izdebski, H. Rajagopalan, and Y. Rahmat-Samii, "Conformal ingestible capsule antenna: A novel chandelier meandered design," *IEEE Transactions on Antennas and Propagation*, vol. 57, no. 4, pp. 900-909, Apr. 2009.
- [5] C. Schmidt, F. Casado, A. Arriola, I. Ortego, P. D. Bradley, and D. Valderas, "Broadband UHF implanted 3-D conformal antenna design and characterization for in-off body wireless links," *IEEE Transactions on Antennas and Propagation*, vol. 62, no. 3, pp. 1433-1444, Mar. 2014.
- [6] B. Huang, G. Yan, P. Zan, and Q. Li, "Design of the microstrip antenna for radiotelemetry capsule," *Journal of Shanghai Jiaotong University*, vol. 41, no. 11, pp. 1830-1833, Nov. 2007.
- [7] L. J. Xu, Y. X. Guo, and W. Wu, "Bandwidth enhancement of an implantable antenna," *IEEE Antennas and Wireless Propagation Letters*, vol. 14, pp. 1510-1513, Nov. 2014.
- [8] J. Wang, M. Leach, E. G. Lim, Z. Wang, R. Pei, and Y. Huang, "An implantable and conformal antenna for wireless capsule endoscopy," *IEEE Antennas and Wireless Propagation Letters*, vol. 17, no. 7, pp. 1153-1157, May 2018.
- [9] S. Kim and H. Shin, "An ultra-wideband conformal meandered loop antenna for wireless capsule endoscopy," *Journal of Electromagnetic Engineering and Science*, vol. 19, no. 2, pp. 101-106, Dec. 2019.
- [10] X. Cheng, D. Senior, C. Kim, and Y. K. Yoon, "A compact omnidirectional self-packaged patch antenna with complementary split-ring resonator loading for wireless endoscope applications," *IEEE Antennas Wireless Propag. Lett.*, vol. 10, pp. 1532-1535, Dec. 2011.
- [11] Z. Jiang, Z. Wang, M. Leach, E. G. Lim, J. Wang, R. Pei, and Y. Huang, "Wideband loop antenna with split-ring resonators for wireless medical telemetry," *IEEE Antennas and Wireless Propagation Letters*, vol. 18, no. 7, pp. 1415-1419, July 2019.
- [12] B. Biswas, A. Karmakar, and V. Chandra, "Fractal inspired miniaturized wideband ingestible antenna for wireless capsule endoscopy," *AEU-International Journal of Electronics and Communications*, vol. 120, pp. 153192, June 2020.
- [13] Z. Duan, Y. X. Guo, M. Je, and D. L. Kwong, "Design and in vitro test of a differentially fed dual-band implantable antenna operating at MICS and ISM bands," *IEEE Trans. Antennas Propag.*, vol. 62, no. 5, pp. 2430-2439, Feb. 2014.
- [14] W. Liu and X. Yang, "Design of electrically small slot antenna fed by CPW," *Chinese Journal of Electron Devices*, vol. 42, no. 2, pp. 300-303, Apr. 2019.
- [15] J. Kim and Y. Rahmat-Samii, "Implanted antennas inside a human body: Simulations, designs, and characterizations," *IEEE Transactions on Microwave Theory and Techniques*, vol. 52, no. 8, pp. 1934-1943, Aug. 2004.
- [16] T. Karacolak, A. Z. Hood, and E. Topsakal, "Design of a dual-band implantable antenna and development of skin mimicking gels for continuous glucose monitoring," *IEEE Transactions on Microwave Theory and Techniques*, vol. 56, no. 4, pp. 1001-1008, Apr. 2008.
- [17] J. Shang and Y. Yu, "An Ultrawideband capsule antenna for biomedical applications," *IEEE Antennas Wireless Propag. Lett.*, vol. 18, no. 12, pp. 2548-2551, Dec. 2019.
- [18] V. Kaim, B. K. Kanaujia, S. Kumar, H. C. Choi, K. W. Kim, and K. Rambabu, "Ultra-miniature circularly polarized CPW-fed implantable antenna design and its validation for biotelemetry applications," *Scientific Reports*, vol. 10, no. 1, pp. 1-16, Apr. 2020.
- [19] S. Das and D. Mitra A, "compact wideband flexible implantable slot antenna design with enhanced gain," *IEEE Transactions on Antennas and Propagation*, vol. 66, no. 8, pp. 4309-4314, May 2018.
- [20] W. Cui, R. Liu, L. Wang, M. Wang, H. Zheng, and E. Li, "Design of wideband implantable antenna for wireless capsule endoscope system," *IEEE Antennas and Wireless Propagation Letters*, vol. 18, no. 12, pp. 2706-2710, Dec. 2019.
- [21] C. Y. Huang, C. L. Tsai, and C. L. Yang, "Compact broadband implantable monopole antenna with gain enhancement," *2014 IEEE Antennas and Propagation Society International Symposium (APSURSI)*. IEEE, pp. 1590-1591, July 2014.
- [22] R. A. Shelby, D. R. Smith, S. C. Nemat-Nasser, and S. Schultz, "Microwave transmission through a two-dimensional, isotropic, left-handed metamaterial," *Appl. Phys. Lett.*, vol. 78, no. 4, pp. 489-491, Jan. 2001.
- [23] R. S. Alrawashdeh, Y. Huang, M. Kod, and A. A. B. Sajak, "A broadband flexible implantable loop antenna with complementary split ring resonators," *IEEE Antennas and Wireless Propagation Letters*, vol. 14, pp. 1506-1509, Feb. 2015.
- [24] M. Zada and H. Yoo, "Miniaturized dual band antennas for intra-oral tongue drive system in the ISM bands 433 MHz and 915 MHz: Design, safety, and link budget considerations," *IEEE Transactions on Antennas and Propagation*, vol. 67, no. 9, pp. 5843-5853, Sept. 2019.
- [25] IEEE Standard for Safety Levels with Respect to Human Exposure to Radio Frequency Electromagnetic Fields, 3 kHz to 300 GHz, *IEEE Standard C95.1-1999*, 1999.

Compact 2x2 and 4x4 MIMO Antenna Systems for 5G Automotive Applications

Mohamed O. Khalifa, Ahmad M. Yacoub, and Daniel N. Aloï

Department of Electrical Engineering
Oakland University, Rochester, Michigan 48309, USA
MKhalifa@Oakland.edu, Ahmadyacoub@Oakland.edu, Aloï@Oakland.edu

Abstract — In this paper, three Vehicular multiple-input multiple-output (MIMO) 5G antenna systems have been constructed from using a newly developed 5G cellular branched Monopole element are presented. The MIMO systems operates in the 5G frequency bands (617MHz-5GHz) with a compact structure that allows for up to four elements to be integrated in the same Sharkfin. The 3 configurations of MIMO systems have been simulated using HFSS, measured on a 1-meter ground plane (GND), then measured on a vehicle roof and the individual antenna parameters in terms of reflection coefficient and efficiency have captured. The MIMO antenna systems performance in terms of passive isolation, combined radiation pattern, envelope correlation coefficient (ECC), and diversity gain (DG) have been reported and discussed.

Index Terms — Automotive antennas, correlation coefficient, 5G, 2x2 and 4x4 MIMO systems.

I. INTRODUCTION

With the expansion of the cellular systems being integrated in cars to support the connected vehicle effort, a need for multiple antennas support wireless service has emerged. The Multiple Input Multiple Output (MIMO) system consists of two antennas or more that receive or transmit multiple layers of orthogonal data streams from cellular base stations which allow for increased channel capacity, data rate and the total throughput of the system without increasing the operating frequency band or the transmit power [1]. To this date, 2X2 MIMO configuration with de-correlated antennas that receive two data streams is being used to realize downlink reception in modern vehicles [2]. The performance of the MIMO system is highly dependable on the efficient design of the MIMO antennas that should low correlation between them and a high total antenna efficiency [3].

An important characteristic of the communication systems is the ECC between received signals of the antennas that construct the MIMO system. Small ECC values are crucial to increase transmission capacity as well as to improve the multipath fading. ECC tells how

independent MIMO antennas radiation patterns are, for example, for a 2X2 MIMO system, if one antenna is vertically polarized and the other one is horizontally polarized then the ECC value will be 0. There are 2 ways to calculate the ECC in a MIMO system [4], the first method used S parameters to find ECC and it assumes lossless/60% or more efficient antennas which is unrealistic. Whereas the second method (which is more accurate) used throughout this paper utilizes radiation patterns of individual antennas to calculate the ECC of MIMO system. Modern vehicles are equipped with multiple wireless services such as Global Navigation Satellite Systems (GNSS), Remote Keyless Entry (RKE), Satellite Digital Audio radio service (SDARS), etc. [5]-[7]. Each of these services requires dedicated antennas and it is unfeasible to distribute them all over the vehicle and consequently they all integrated in a single package (Sharkfin). Since the available space with the Sharkfin for each antenna is much smaller than the wavelengths at the which the antenna expected to operate, issues such as antenna size and bandwidth limitations as well as passive port isolation between different elements within the Sharkfin will take place. Furthermore, the Sharkfin size limitation will also impact the port isolation and correlation of MIMO antennas and impose some challenges to design an antenna system that satisfies the diversity requirements [8],[9].

In [10], [11], 2X2 MIMO systems based on Monopole and PIFA elements respectively have been introduced, however the bandwidth of operation is very small (700-925MHz). The 2X2 MIMO systems bandwidth have been increased to cover from 790MHz to 3GHz with reasonable antenna dimensions and an ECC of less than 0.3 and 0.05 in [12] and [13] respectively but the bandwidth of operation doesn't cover 5G frequencies (617MHz-5GHz). In [14]-[18], the authors have developed 2X2 MIMO structures that are constructed from either Monopoles or PIFA elements with a less than 0.5 ECC however, these MIMO systems are only covering LTE (698MHz-3GHz) frequency bands and not 5G frequencies. A much broader

bandwidth (700MHz-6GHz) with less than 0.16 of ECC (using first method in [4]) is achieved by authors in [19] but it doesn't include the B71 band (617MHz-698MHz) as well as it comes at an increased volume ($70 \times 70 \times 29 \text{mm}^3$) which makes it impossible to fit in production Sharkfins. Finally, a 4X4 MIMO system is presented in [20], However, B71 frequency band is not included (which will introduce a big challenge trying to fit the antenna in a sharkfin), there are no information about system volume, and also the work has not been supported by either ground plane or vehicle measurements data. Several studies outside the automotive industry have targeted decoupling antennas in a MIMO system packaged in a small volume with various techniques like the use of electromagnetic band gap (EBG) structures [21], Ceramic Superstrate-Based Decoupling Method [22], and metamaterials [23]-[27]. The automotive MIMO systems presented in this work do not require a special decoupling mechanism. In fact, decoupling of antennas is obtained by mainly using spatial and pattern diversity at the low and high band respectively which puts more burden on compactness and performance of building block antenna element.

This work introduces three novel MIMO structures; configuration I of a 2x2 MIMO antenna system, configuration II of a 2x2 MIMO antenna system, and a 4x4 MIMO antenna system. The three structures are mainly developed for automotive industry to cover 5G cellular frequencies (617MHz-5GHz), fit in a car roof sharkfin, and have an inherited GNSS frequencies rejection which makes it easy to integrate with other antennas within a sharkfin. In this work, HFSS has been used to simulate the 3 MIMO systems configurations, then the systems have been measured inside and anechoic chamber on ground plane and on a vehicle roof. The antennas important parameters such as of reflection coefficient, isolation, total efficiency, radiation pattern have been captured. Then an Octave code is used to calculate the ECC and DG from the captured data.

The work in this paper is organized in two sections: Section II explains the theory about correlation coefficient and diversity gain calculation equations and it also shows the design goals. Section III presents the proposed 2x2 MIMO configurations, the novel 4x4 MIMO system, and finally a comparison between proposed systems and available work in literature.

II. MIMO ANTENNA SYSTEMS PERFORMANCE METRICS

All the most important metrics in MIMO antenna systems are ECC and DG. The ECC can be related to the electric field radiation pattern through the equation in [4] as below:

$$\rho_{e,ij} = \left| \frac{\int_0^{2\pi} \int_0^\pi (XPR \cdot E_{\theta i} \cdot E_{\theta j}^* \cdot P_\theta + XPR \cdot E_{\phi i} \cdot E_{\phi j}^* \cdot P_\phi) \sin(\theta) d\theta d\phi}{\sqrt{\prod_{k=i,j} \int_0^{2\pi} \int_0^\pi (XPR \cdot E_{\theta k} \cdot E_{\theta k}^* \cdot P_\theta + XPR \cdot E_{\phi k} \cdot E_{\phi k}^* \cdot P_\phi) \sin(\theta) d\theta d\phi}} \right|^2, (1)$$

where $E_{\theta i}$ and $E_{\theta j}$ are the values of electric field in the theta axis while $E_{\phi i}$ and $E_{\phi j}$ are the values of electric field in phi axis. XPR is the cross-polarization discrimination factor tells the difference between incident electromagnetic wave vertical and horizontal polarization. P_θ and P_ϕ are the theta and phi power densities. Equation (1) can be simplified by setting XPR = 1 assuming uniform power densities.

The other MIMO system performance metric is the DG which is defined as the quantified improvement in signal-to-noise ratio (SNR) by the receiving signals from the MIMO antennas and usually calculated in dB. The DG can be calculated as in [28]:

$$DG = DG_0 \cdot DF \cdot K, (2)$$

where DG_0 is the ideal case diversity gain which is 10dB. DF is the degradation factor which shows how much the ECC impacts DG and is calculated as: $\sqrt{(1 - \rho)}$. K represents the ratio of the mean effective gain (MEG) between the MIMO antenna elements ($K = MEG_i / MEG_j$). MEG is the effective gain ratio at the antenna element, in other words MEG is the received to incident power ratio at the element. ($K \sim 1$) condition should be satisfied for received signals by MIMO systems assuming good channel characteristics.

III. COMPARATIVE STUDY OF THE PROPOSED MIMO SYSTEMS

In this section, three different MIMO antennas configurations are being studied. The building block for each configuration is the branched Monopole element in Fig. 1. The MIMO configurations are then simulated and measured on a 1-meter ground plane and on a vehicle's roof inside an anechoic chamber. The obtained data from simulations and chamber measurements are directly reported whereas ECC and DG results are generated using Octave software for each MIMO configuration in this section. Table 1 shows general design guidelines:

Table 1: Design guidelines

| Parameter | Value |
|------------------------|------------------------------------|
| Polarization | Vertical Linear Polarization (VLP) |
| Reflection Coefficient | -5.4dB (3.3VSWR) at 5G bands |
| Avg. Total Efficiency | 60% |
| Isolation | Minimum 10dB across 5G bands |
| ECC | Less than 0.5 |

A. Configuration I of a 2x2 monopole-based MIMO system

Figure 1 shows the Monopole element that will be used construct high order MIMO structures. The antenna functions in the 5G frequency bands (617MHz-5GHz).

Multiple current paths have been realized by adding 2 arms to the antenna covering 5G frequencies of interest. Band (617 MHz – 960 MHz) is mainly covered by Arm 1 currents whereas band (1.71-5 GHz) frequencies are radiated by Arm 2 as in Fig. 1. To obtain omnidirectional radiation pattern, high efficiencies, and good matching performance, Arm1 and Arm2 of the antenna are loaded at $\frac{\lambda_{LB}}{4}$ and $\frac{\lambda_{HB}}{4}$ distances from ground plane respectively where λ_{LB} and λ_{HB} are the mid-low and mid-high bands wavelengths respectively. The geometrical values of the building block antenna are shown in Table 2.

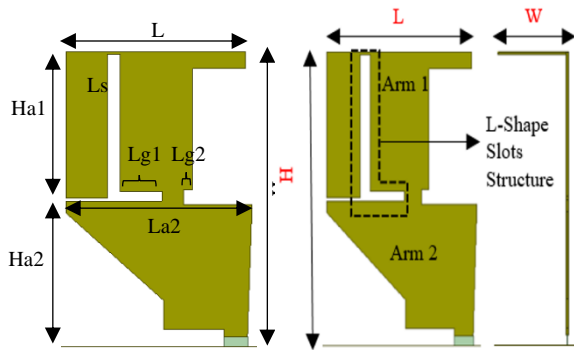


Fig. 1. Building block antenna with side and front views, arms structure, and antenna dimensions.

Table 2: Values of the geometrical parameters of MIMO systems building block antenna

| Parameter | Value (mm) | Parameter | Value (mm) |
|-----------|------------|-----------|------------|
| H | 60 | Lg1 | 9 |
| L | 38.5 | Lg2 | 2 |
| W | 14.9 | Ls | 2.6 |
| Ha1 | 30 | La2 | 39.8 |
| Ha2 | 29.3 | | |

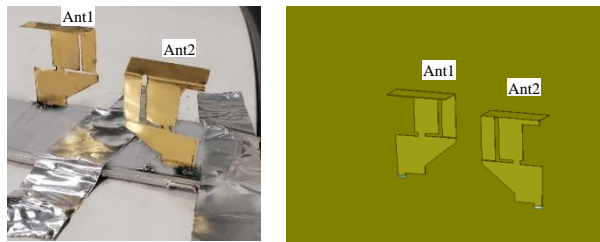


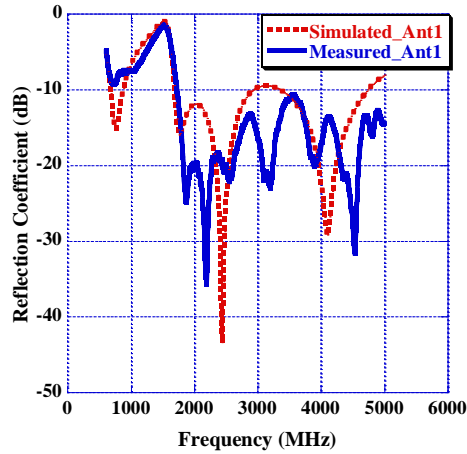
Fig. 2. Configuration I of a 2x2 MIMO system placement on vehicle roof and simulation setup.

The two Monopole elements were cut from a metal sheet and placed in such a way that will result in an omnidirectional combined radiation pattern as well as a minimal ECC value. The system is simulated then measured on 1-meter GND and on a car’s roof with a port-to-port distance of 135mm (which is higher than $\frac{\lambda_{Lowest_freq}}{2*\sqrt{\epsilon_r}} = 114\text{mm}$ on FR4 PCB with $\epsilon_r = 4.4$) between Monopole elements. Figure 2 shows Configuration I of a 2x2 MIMO systems on a car roof.

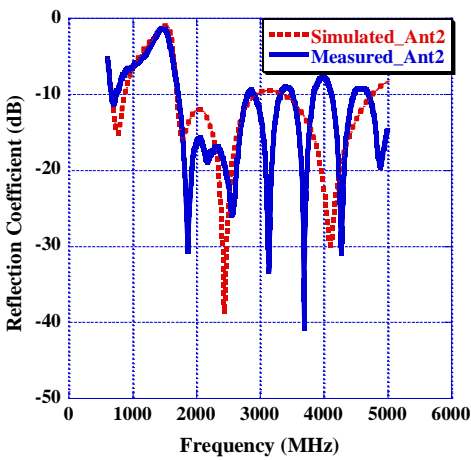
The performance of Antenna1 (Ant1) and Antenna2 (Ant2) of this MIMO system has been reported in terms of reflection coefficient and isolation as in Fig. 3. Both antennas show an agreement between simulation and GND measurement. Good reflection coefficient values have been observed of a worse of -5.6dB and -6.4dB at 617MHz of Ant1 and Ant2 respectively with reasonable GNSS bands (1560MHz-1190MHz) rejection. Figure 3 also shows a good isolation between Ant1 and Ant2 in this configuration of a worse case 12dB (expressed as -12 dB in S21 format).

Next, the total efficiencies of Ant1 and Ant2 have been captured after a successful placement of the MIMO system on 1-meter GND and then on a car roof and the results are shown in Fig. 4. Both antennas exhibit higher efficiencies when placed on GND compared to placement on a car roof. It can be noticed that both antennas measured on GND have an average total efficiency of 79.8% across all 5G frequency bands while the average total efficiencies decrease to 74% and 71% when measured on a car roof for Ant1 and Ant2 respectively.

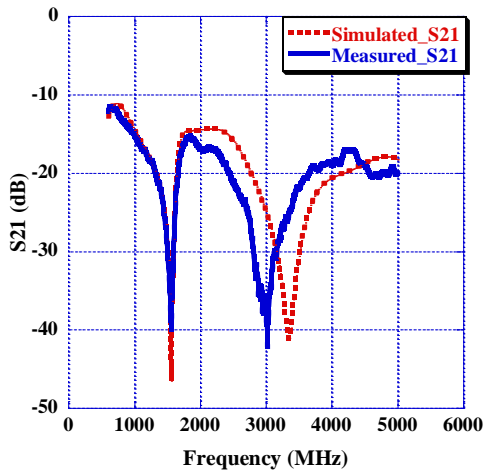
Simulation, GND measurement, and vehicle measurement of a combined MIMO system radiation pattern sample have been presented in Fig. 5. The sample represents a Gain theta horizontal cut at 80 degrees of theta and four frequencies namely 617MHz, 1900MHz, 3900MHz, and 5000MHz to provide a good idea about the system performance. The combined MIMO system pattern is obtained by measuring each antenna when the other antenna is loaded by a 50Ohm terminator and then combine the resultant individual antenna patterns selecting the maximum values of Gain theta between Ant1 and Ant2 measurements for a specific phi-frequency pair at 80 degree of theta. Finally, the average gain of the MIMO system combined radiation patterns measured on car roof is found to be -1.14dBi, 3.15dBi, 1.81dBi, and 2.84dBi at frequencies 617MHz, 1900MHz, 3900MHz, and 5000MHz, respectively.



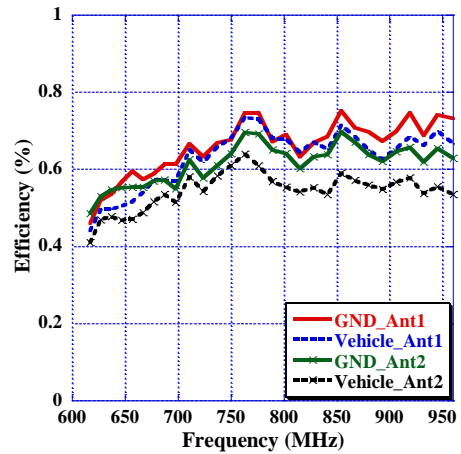
(a)



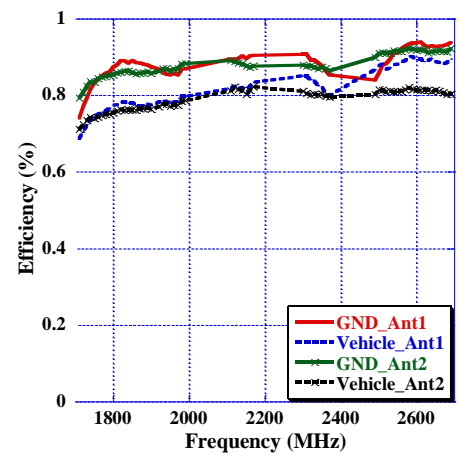
(b)



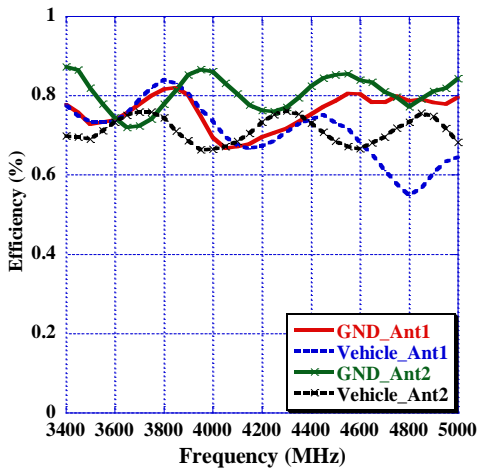
(c)



(a)



(b)



(c)

Fig. 3. Configuration I of a 2x2 MIMO system simulated and measured: (a) Antenna 1 S11 in dB, (b) Antenna 2 S11 in dB, and (c) S21 between Antenna 1 and Antenna 2 in dB.

Fig. 4. Antenna efficiency for Configuration I MIMO systems Monopoles measured on GND and on vehicle roof for frequency ranges: (a) 617-960MHz, (b) 1710-2690MHz, and (c) 3400-5000MHz.

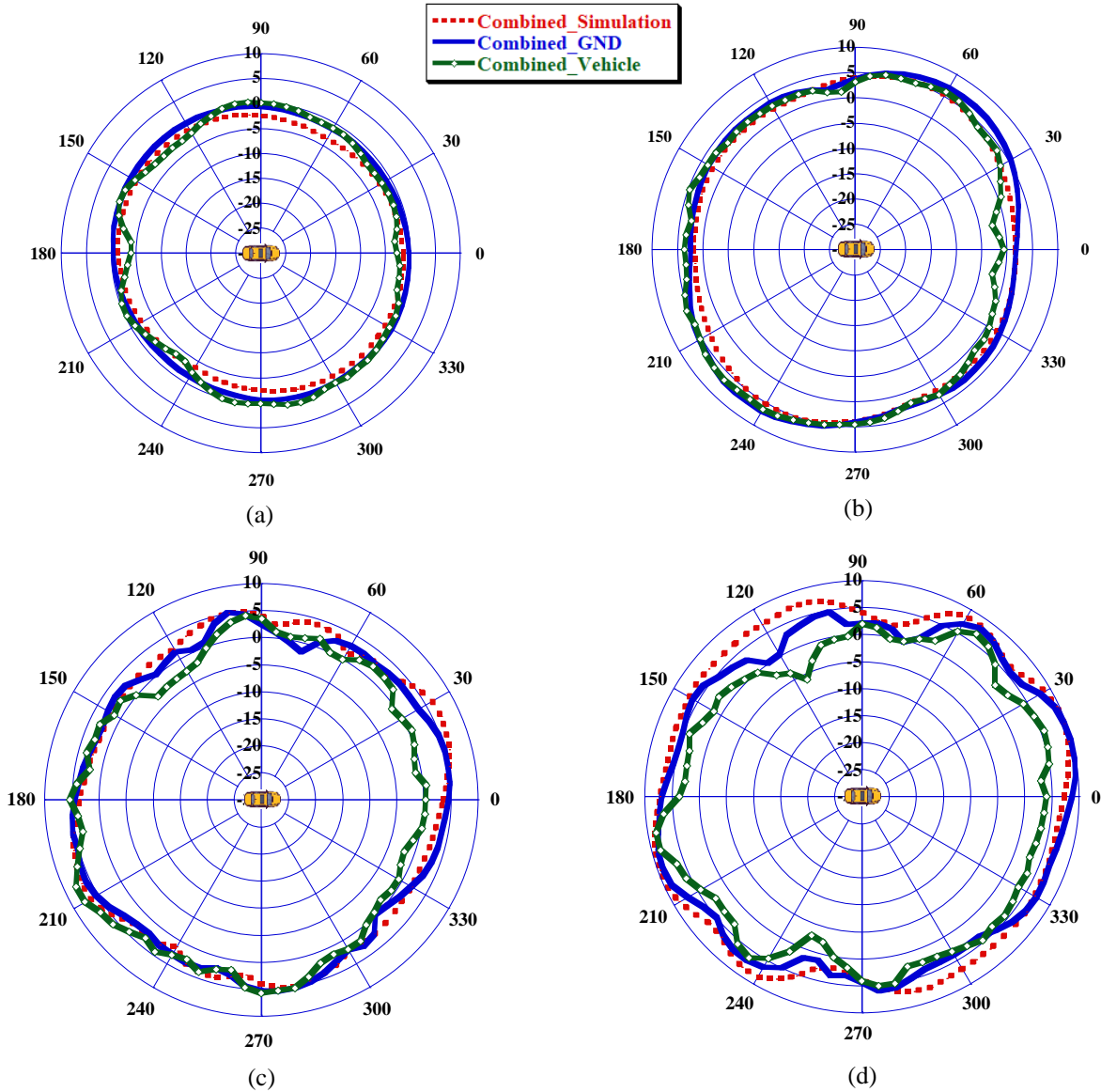
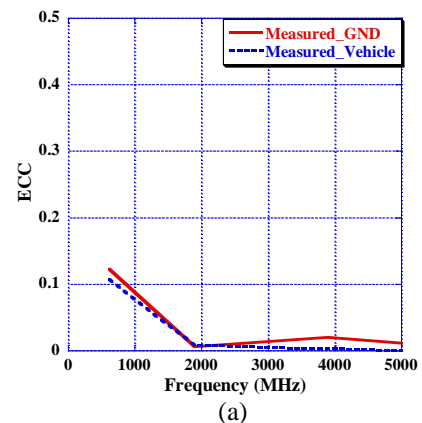


Fig. 5. Combined radiation pattern of simulation, GND measurement, and vehicle measurement in (dBi) at theta = 80 deg. for frequencies: (a) 617 MHz, (b) 1900 MHz, (c) 3900 MHz, and (d) 5000 MHz.

ECC and DG on GND and on car roof for configuration I of a 2x2 MIMO systems are depicted in Fig. 6 (a) and Fig. 6 (b) respectively. The two figures suggests that higher values of ECC and consequently lower values of DG occurs at low frequencies (i.e., 617MHz) because the wavelength is big which leads to more correlation between the antennas. In this MIMO configuration an ECC of better than 0.13 and a DG of better than 9.92dB have been realized.



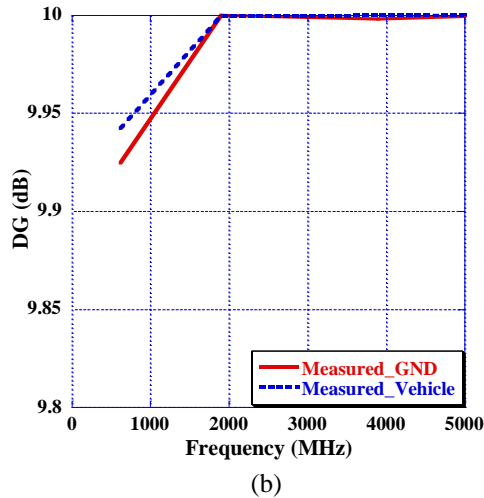


Fig. 6. Configuration I of a 2x2 MIMO system: (a) envelope correlation coefficient, and (b) diversity gain.

B. Configuration II of a 2x2 monopole-based MIMO system

Similar to Configuration I in subsection A, two Monopole elements have been placed on a Printed Circuit Board (PCB) with a distance of 125mm (from port to port) between them. The monopoles are placed on the back of the roof of a car as in Fig. 7 to allow for an omnidirectional combined radiation pattern.

The performance of Ant1 and Ant2 of this MIMO system has been reported in terms of reflection coefficient and isolation as in Fig. 8. Both antennas show an agreement between simulation and GND measurement. Good reflection coefficient values have been observed from GND measurements of a worse of -7.4dB and -6.4dB at 617MHz of Ant1 and Ant2 respectively with reasonable GNSS bands rejection. Figure 8 also shows a good isolation between Ant1 and Ant2 in this configuration of a worse case 15dB (expressed as -15 dB in S21 format).

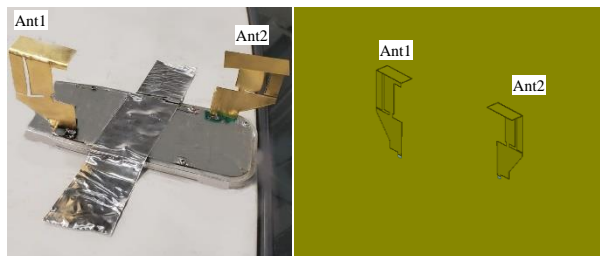


Fig. 7. Configuration II of a 2x2 MIMO system placement on vehicle roof and simulation setup.

A comparison of on GND and on vehicle measurements of Ant1 and Ant2 total antenna efficiencies in this configuration is illustrated in Fig. 9.

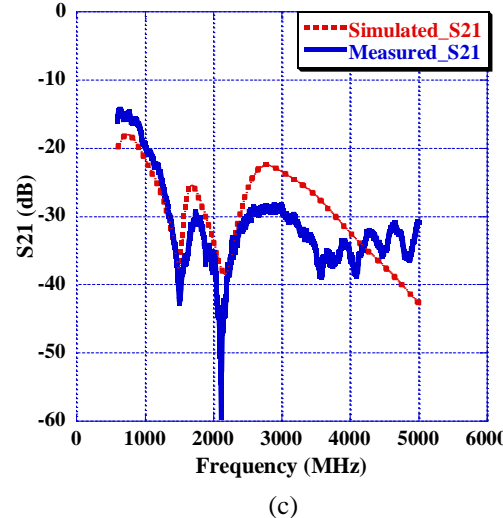
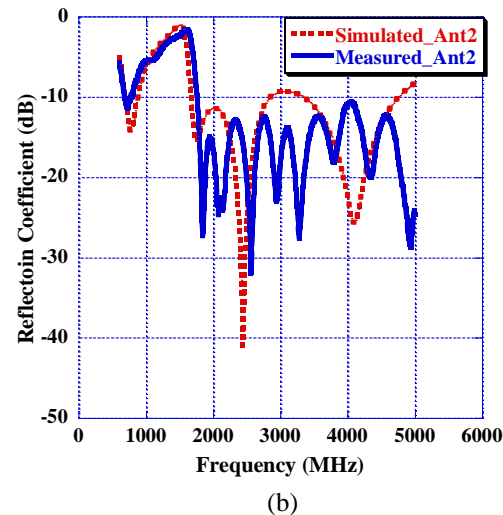
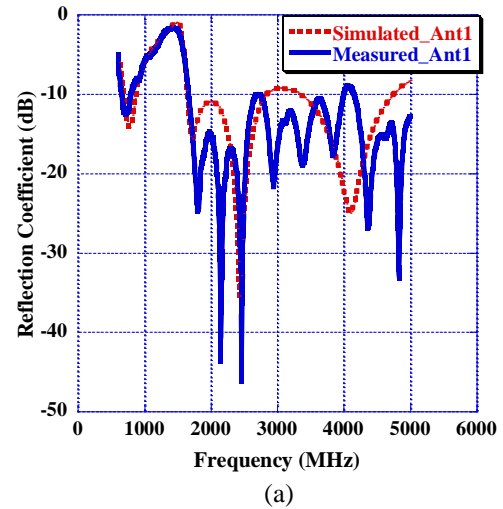


Fig. 8. Configuration II of a 2x2 MIMO system simulated and measured reflection coefficient for: (a) Antenna1, (b) Antenna2 in dB, and (c) S21 between Antenna1 and Antenna2 in dB.

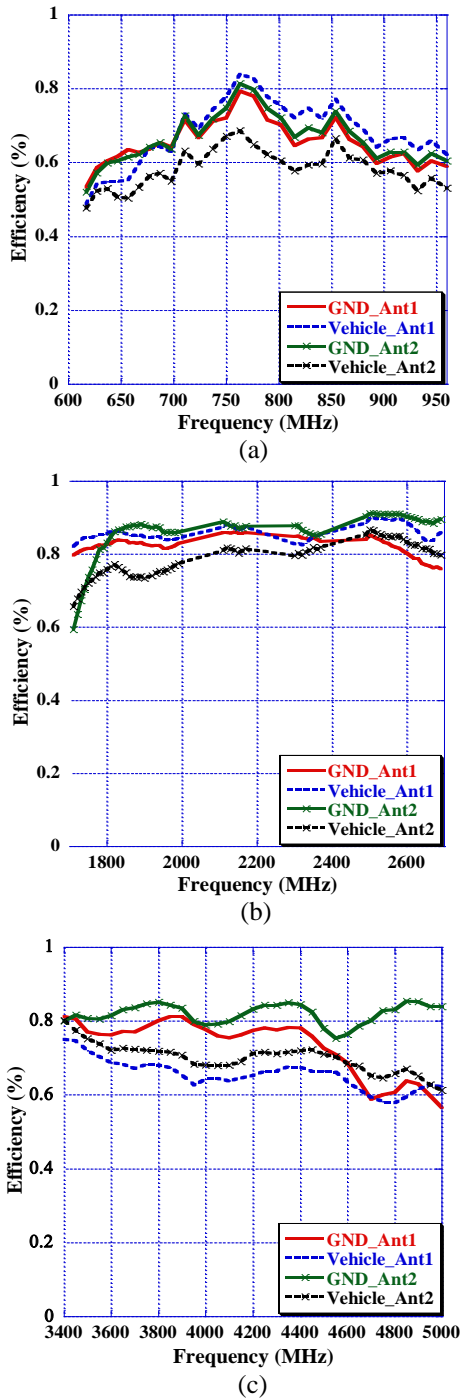


Fig. 9. Total antenna efficiency for Configuration II MIMO systems monopoles measured on GND and on vehicle roof for frequency ranges: (a) 617-960MHz, (b) 1710-2690MHz, and (c) 3400-5000MHz.

The GND measurement has an average efficiency higher than 76% for both elements across all 5G bands

whereas the vehicle measurement is 5% less namely an average total efficiency of 71.7%.

ECC and DG on GND and on car roof for configuration II of a 2x2 MIMO systems is depicted in Fig. 10 where an ECC of better than 0.02 and an approximately 10dB of DG has been achieved using this configuration.

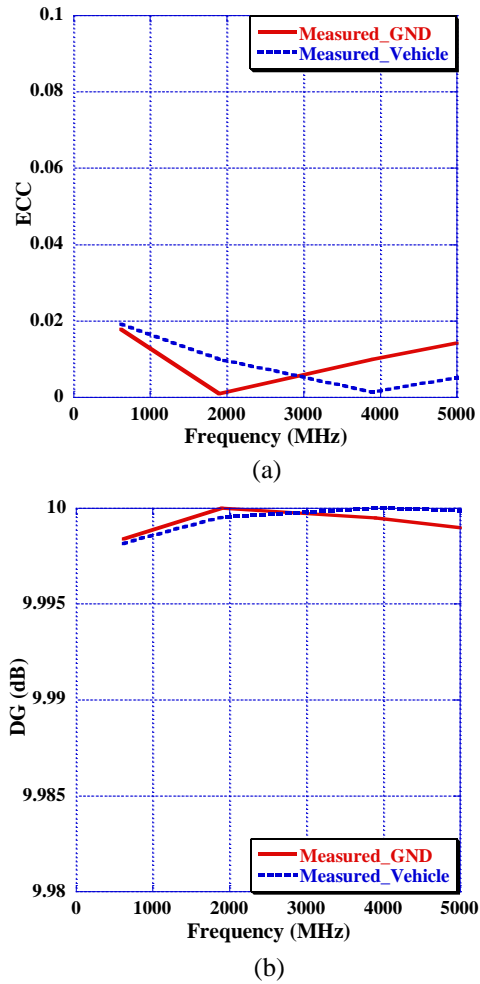


Fig. 10. Configuration II of a 2x2 MIMO system (a) ECC and (b) DG.

Figures 11 (a)-(d) presents combined radiation patterns of horizontal cuts at elevation 80 degrees for frequencies 617MHz, 1900MHz, 3900MHz and 5000MHz utilizing the same method described in subsection A.

The average gain values recorded from the combined vehicle radiation patterns are -0.71dBi, 3.16dBi, 0.57dBi, and 1.51dBi at frequencies 617MHz, 1900MHz, 3900MHz, and 5000MHz, respectively.

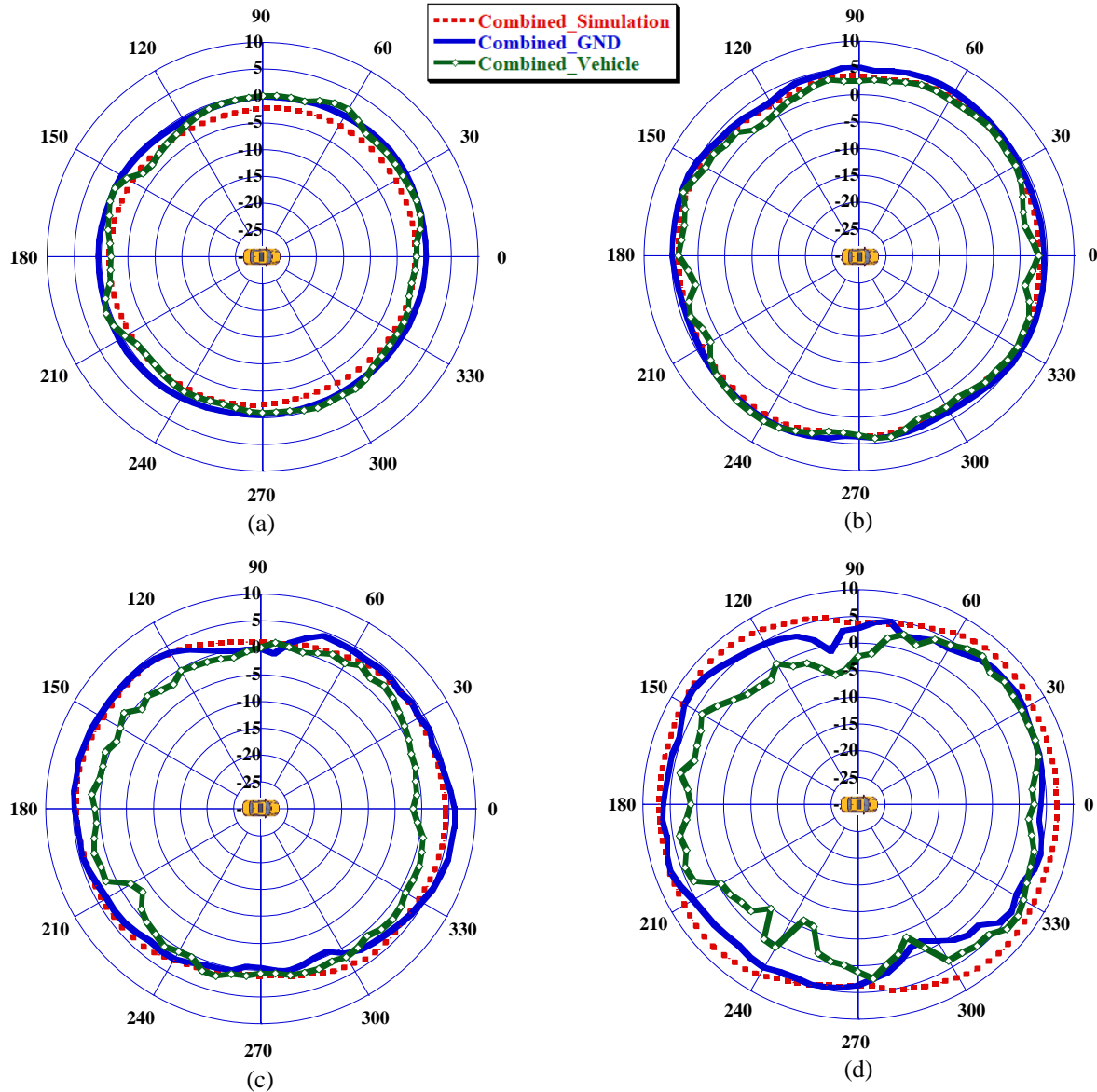


Fig. 11. Combined radiation pattern of simulation, GND measurement, and car measurement in (dBi) at $\theta = 80^\circ$ for frequencies: (a) 617 MHz, (b) 1900 MHz, (c) 3900 MHz, and (d) 5000 MHz.

C. A 4x4 monopole-based MIMO system

In this subsection, four Monopole elements are integrated in the same sharkfin to operate as a 4x4 MIMO system. The building block antenna element for this configuration is the same antenna used in subsections A and B of this section. The four elements are placed in such a way that, the combined radiation pattern is omnidirectional with good isolation and correlation figures between antennas. The system placement on the car roof and simulation setup are shown in Fig. 12. The distances between Monopole pairs in this MIMO systems are listed in Table 3.

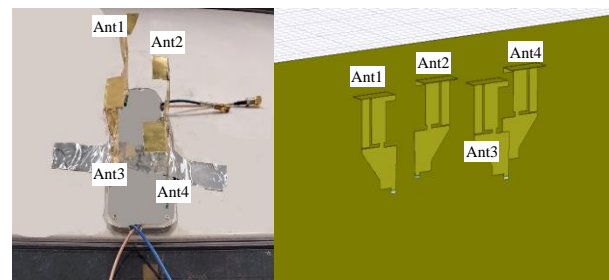


Fig. 12. A 4x4 MIMO system placement on vehicle roof and simulation setup.

Table 3. Values of the geometrical parameters of MIMO systems building block antenna

| Elements Pairs | Distance (mm) |
|----------------|---------------|
| Ant1-Ant2 | 77 |
| Ant1-Ant3 | 141 |
| Ant1-Ant4 | 180 |
| Ant2-Ant3 | 100 |
| Ant2-Ant4 | 118 |
| Ant3-Ant4 | 70 |

The simulated reflection coefficient (in dB) for each element in this configuration is shown in Fig. 13. The four elements from Ant1 to Ant4 shows good matching characteristics across the whole 5G bands with a reflection coefficient of less than -5.2dB and a reasonable GNSS bands rejection.

The isolation in terms of S21 between each pair of antennas within this 4x4 MIMO system is shown in Fig. 14. In general, the shorter the distance between the antennas, the worse the isolation is. However, the antenna placement and orientation also contribute to the overall isolation performance. A worse value of 10dB of isolation between Ant1-Ant2 and Ant2-Ant4 can be observed from the GND measurements on the 617-960MHz band.

Using similar approach for combining individual antennas radiation patterns as in subsection A, the combined radiation patterns at 80 degree of theta for the four elements are shown in Fig. 15. Higher average gain values are observed from the combined vehicle radiation patterns measurements compared to the other 2x2 configurations. The average gain is found to be: -0.88dBi, 4.64dBi, 3.14dBi, and 3.74dBi at frequencies 617MHz, 1900MHz, 3600MHz, and 5000MHz, respectively.

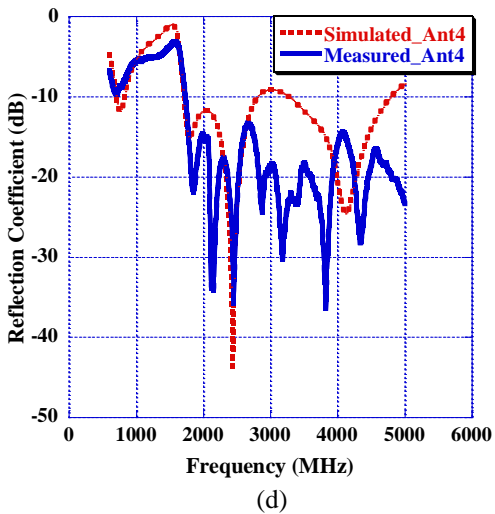
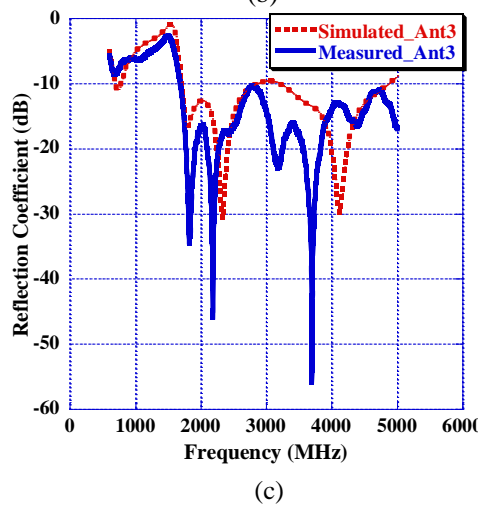
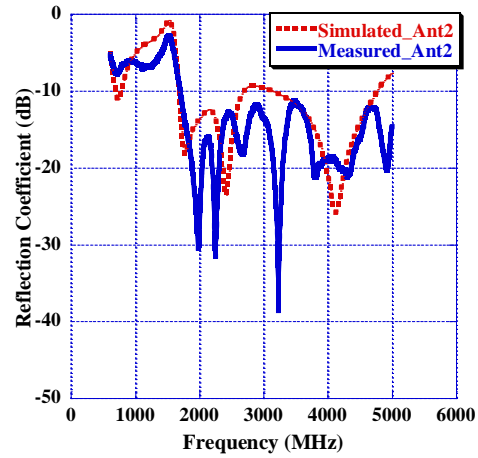
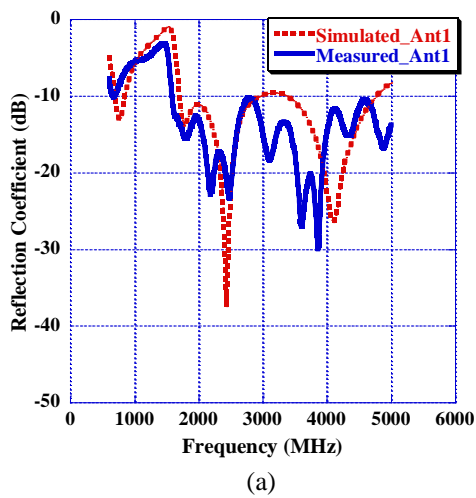


Fig. 13. 4x4 MIMO system simulated and measured reflection coefficient in dB for: (a) Antenna1, (b) Antenna2, (c) Antenna3, and (4) Antenna4.

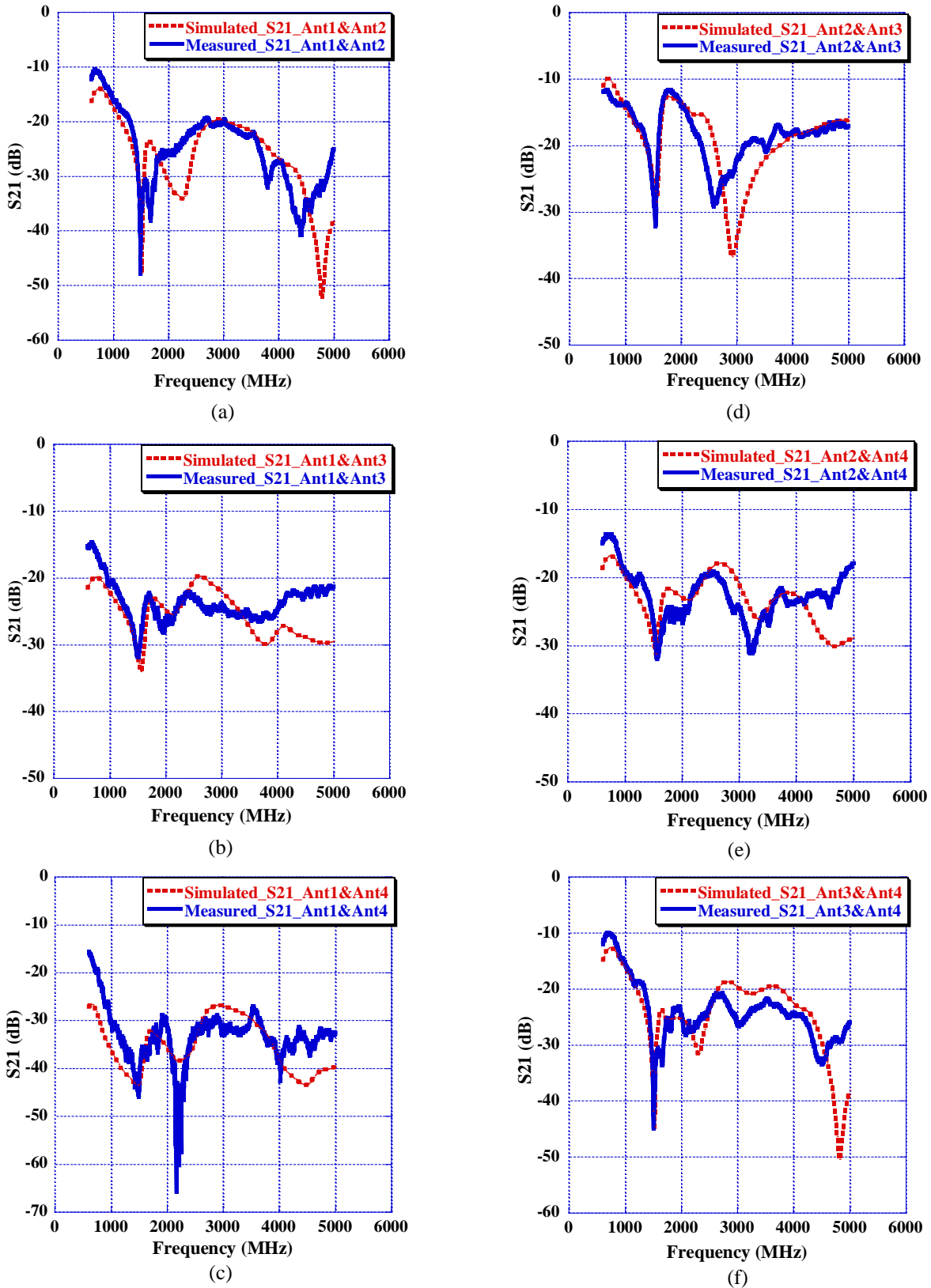


Fig. 14. 4x4 MIMO system simulated and measured Isolation in dB between: (a) Ant1 and Ant2; (b) Ant1 and Ant3; (c) Ant1 and Ant4; (d) Ant2 and Ant3; (e) Ant2 and Ant4; (f) Ant3 and Ant4.

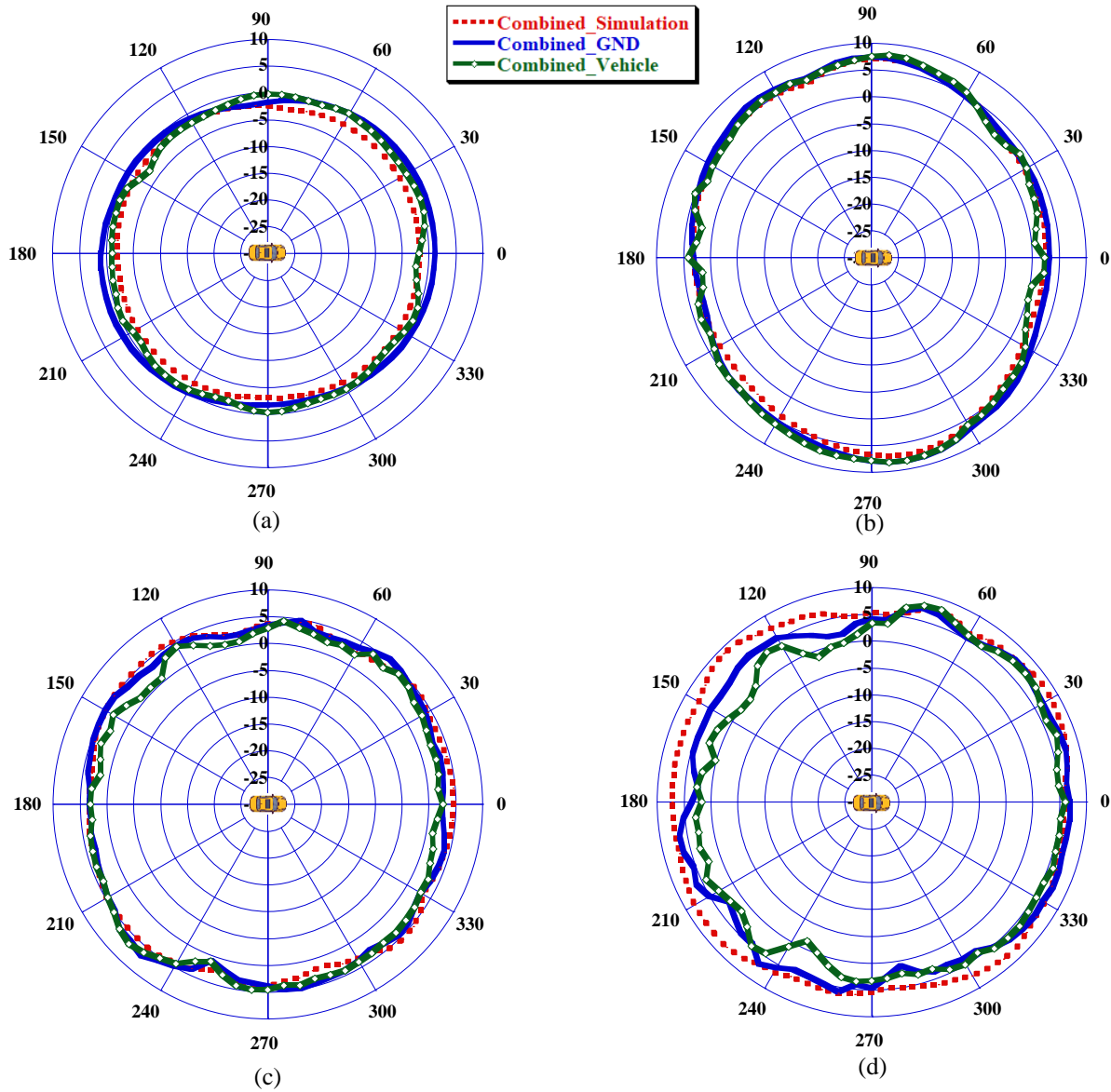
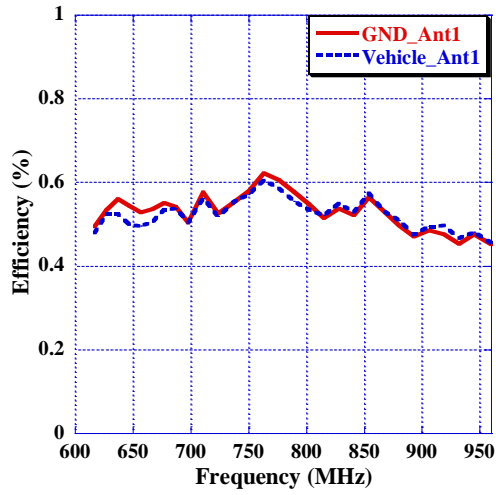


Fig. 15. Combined radiation pattern of simulation, GND measurement, and vehicle measurement (in dBi) at theta = 80 deg. for frequencies: (a) 617 MHz, (b) 1900 MHz, (c) 3900 MHz, and (d) 5000 MHz.

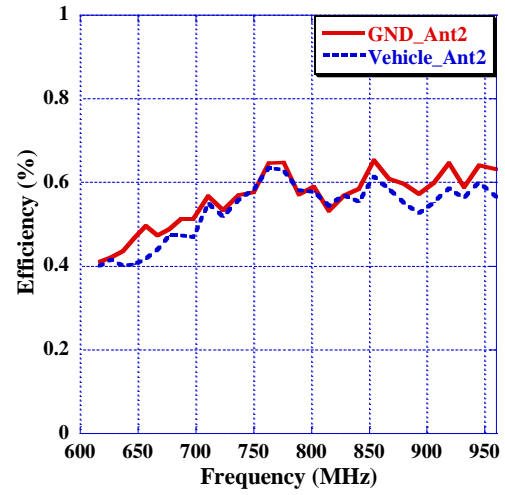
The on GND and on car roof measured efficiencies are reported in Figs. 16 (a), (b), and (c) for the four antenna elements in this MIMO system. It can be noticed that the GND measurement has an average total efficiency higher than 72.5% for all the four elements across the whole 5G frequency bands whereas the vehicle measurement has a reduced average total efficiency of slightly higher than 65% for all elements. The ECC and DG were also calculated in this MIMO configuration with the help of equations (1) and (2) using Octave script. As Fig. 17 suggests, the ECC is well kept

below 0.5 in all the 6 correlation cases with corresponding DG values of higher than 8.9dB. The worst value of ECC (0.45) and DG exists at low frequency bands and it is the same case where worst passive isolation occurs namely between Ant3 and Ant4.

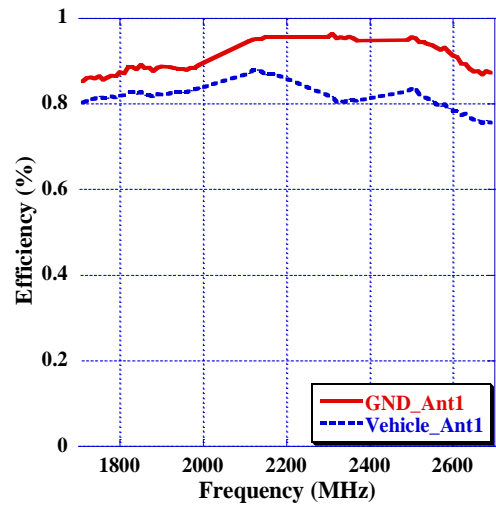
Table 4 lists a literature review summary of MIMO antennas systems used in automotive industry. The table also compares works in terms type of type of antennas, bandwidth of operations, systems volume, and method of ECC calculation in use.



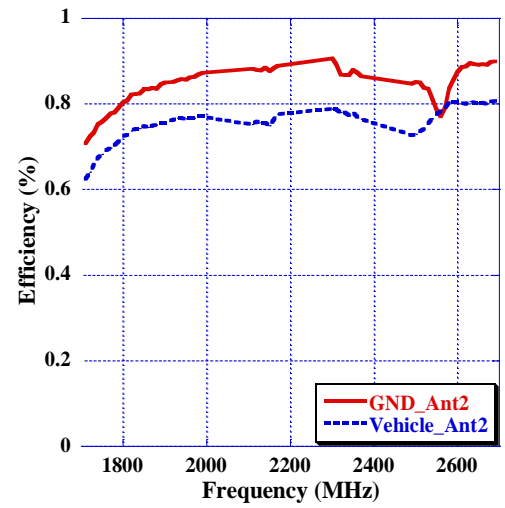
(a) Ant1: 617-960MHz



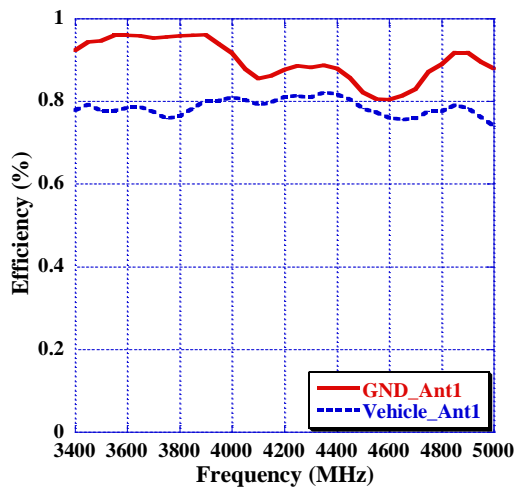
(d) Ant2: 617-960MHz



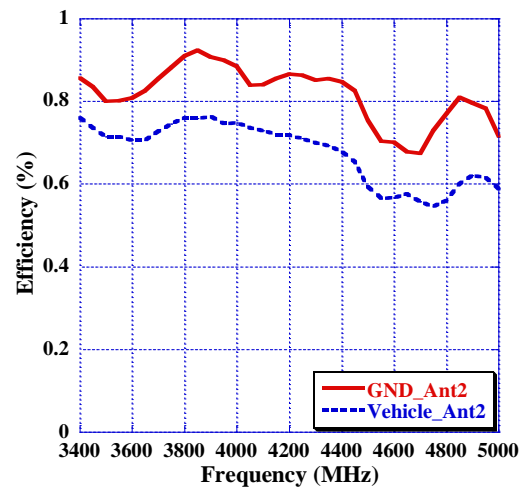
(b) Ant1: 1710-2690MHz



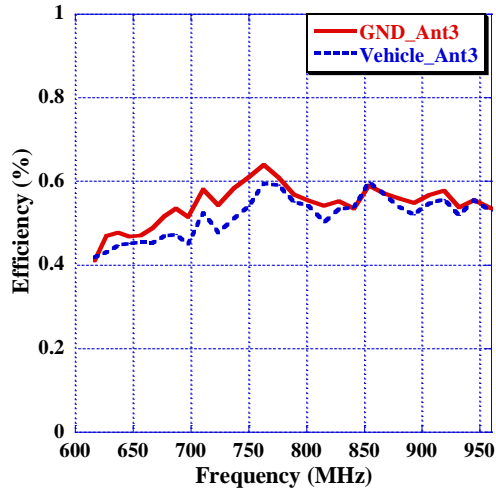
(e) Ant2: 1710-2690MHz



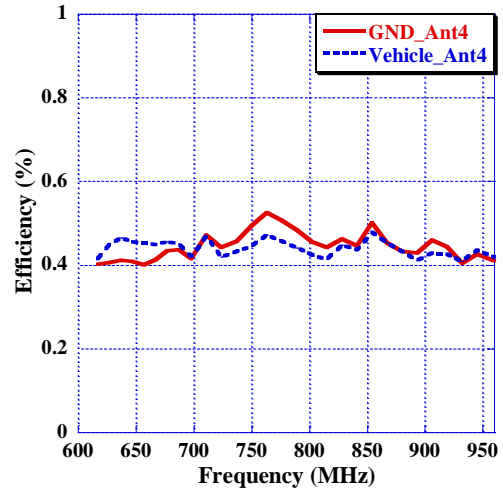
(c) Ant1: 3400-5000MHz



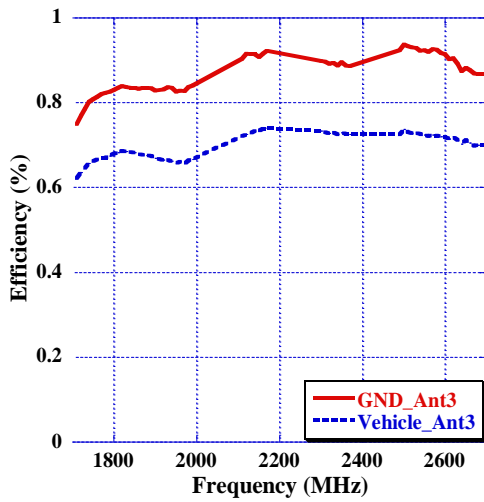
(f) Ant2: 3400-5000MHz



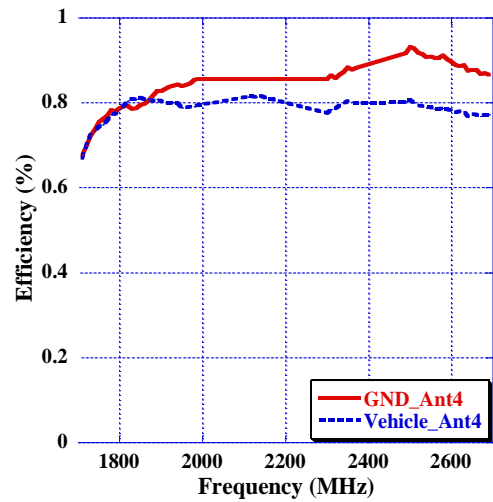
(g) Ant3: 617-960MHz



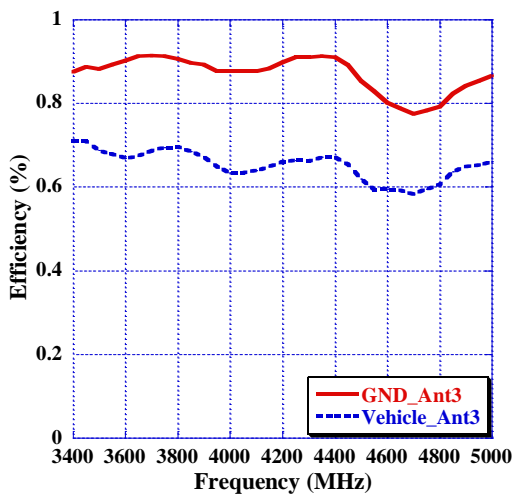
(j) Ant4: 617-960MHz



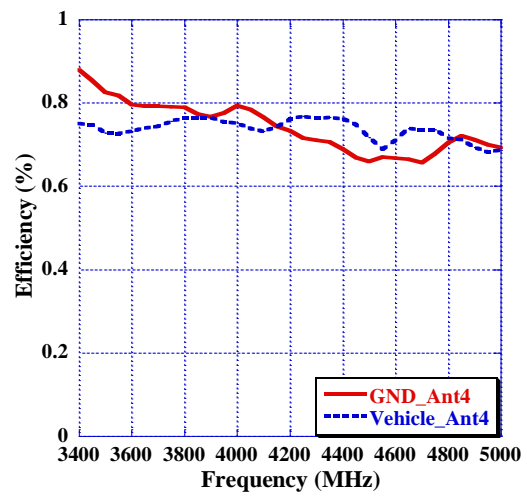
(h) Ant3: 1710-2690MHz



(k) Ant4: 1710-2690MHz



(i) Ant3: 3400-5000MHz



(l) Ant4: 3400-5000MHz

Fig. 16. Antenna efficiency for a 4x4 MIMO system.

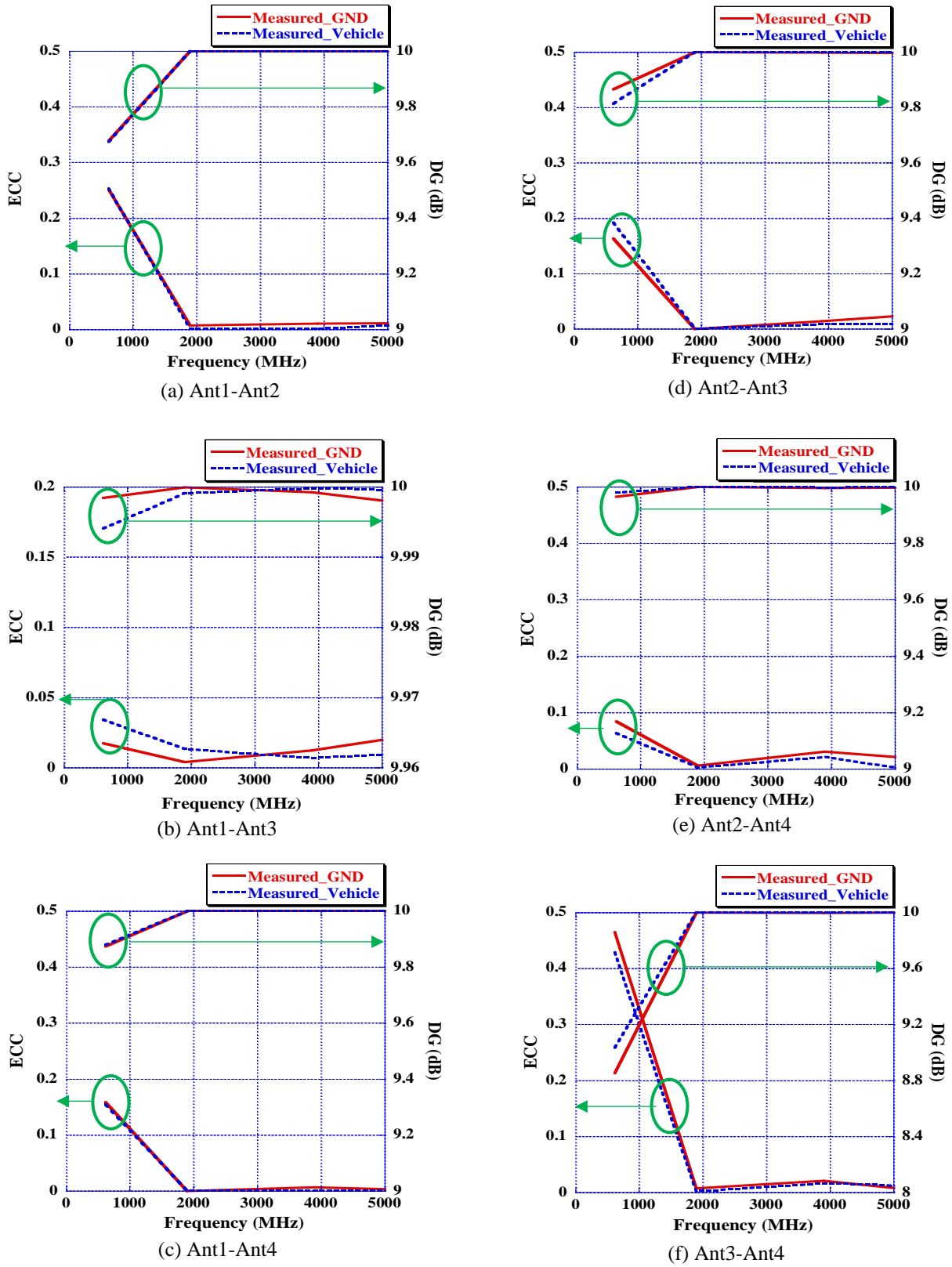


Fig. 17. A 4x4 MIMO system ECC and DG.

Table 4: Literature review summary

| Ref. | Type | BW | Antenna Dimension (LxWxH) (mm ³) | ECC Method / Value |
|------|------------------------------|----------------|--|--------------------------------------|
| 10 | 2x2 monopole | 700MHz-900MHz | Not reported | S-param only / lower than 0.02 |
| 11 | 2x2 PIFA | 775MHz-925MHz | 59.5x12.4x21 | S-param only / lower than 0.5 |
| 12 | 2x2 PIFA | 790MHz-2.69GHz | 50x50x28 | E field components / lower than 0.3 |
| 13 | 2x2 printed monopole | 790MHz-3GHz | 30x0.8x80 | S-param only / lower than 0.05 |
| 14 | 2x2 printed planar monopoles | 698MHz-2700MHz | 52x1.6x65 | S-param only/ lower than 0.5 |
| 15 | 2x2 PIFA | 690MHz-2700MHz | PIFA length is 75.9mm / height 25.5mm | S-param only /lower than 0.5 |
| 16 | 2x2 monopole | 698MHz-2.69GHz | Monopole heights are 55 and 45mm | S-param only / lower than 0.5 |
| 17 | 2x2 printed monopoles | 698MHz-2690MHz | 25x2x55 | Not reported / lower than 0.3 |
| 18 | 2x2 printed monopole PIFA | 698MHz-3GHz | PIFA 65x62x20 / Monopole height is 53 | Not reported |
| 19 | 2x2 Nefer Antenna | 700MHz-6GHz | 70x70x29 | S-param only / lower than 0.16 |
| 20 | 4x4 sleeve monopoles | 790MHz-5GHz | Not reported | Not reported / lower than 0.12 |
| 29 | 2x2 printed Yagi | 2GHz-4.5GHz | 60x1.6x55 | Not reported/ lower than 0.5 |
| 30 | 2x2 loaded monopoles | 2.4GHz-11GHz | 24x2.2x29 | E-field components / lower than 0.02 |

VI. CONCLUSION

Three MIMO systems based on a novel branched Monopole structure that operates in cellular 5G bands (617MHz-5GHz) and can easily be integrated inside a sharkfin package on a car roof have been presented in this paper. The ECC and DG derived from the radiation patterns of each antenna element were calculated for each of the three MIMO configurations. The configuration I MIMO system in Fig. 1 represents a 2x2 MIMO systems with antennas separated by a 135mm distance integrated on a sharkfin module on a car roof and it allows for a passive isolation better than 12dB, total average efficiencies higher than 71% on vehicle across all bands, ECC lower than 0.13, and DG higher than 9.9dB. The configuration II MIMO system in Fig. 7 represents a 2x2 MIMO systems with antennas separated by a 125mm distance integrated on a sharkfin module on a car roof and it provides a passive isolation better than 15dB, total average efficiencies higher than 71.7% on vehicle across all bands, ECC lower than 0.02, and DG of 10dB. Finally, in order to increase the system capacity and data rate by allowing four data streams to be sent and received simultaneously, a novel 4x4 MIMO antenna system constructed of four Monopole elements as in Fig. 12 has been designed. It achieves passive isolation better than 10dB, total average efficiencies higher than 65% on vehicle across all bands, ECC lower than 0.46, and DG higher than 8.9dB. In general, each MIMO configuration has a satisfactory performance and can be used easily in the vehicular application depending on the desired requirement and dimensions.

ACKNOWLEDGMENT

The authors would like to thank Oakland University for supporting this research with measurements tools and simulation software.

REFERENCES

- [1] J. Malik, D. Nagpal, and M. V. Kartikeyan, "MIMO antenna with omnidirectional pattern diversity," *Electronics Letters*, vol. 52, no. 2, pp. 102-104, Jan. 2016.
- [2] L. Lanctot and O. Jonah, "Cellular antenna performance impact on MIMO in vehicle," *2018 IEEE International Symposium on Antennas and Propagation & USNC/URSI National Radio Science Meeting*, Boston, MA, pp. 353-354, July 2018.
- [3] A. M. Elshirkasi, A. Abdullah Al-Hadi, M. F. Mansor, R. Khan, and P. J. Soh, "Envelope correlation coefficient of a two-port MIMO terminal antenna under Uniform and Gaussian angular power spectrum with user's hand effect," *Progress in Electromagnetics Research C*, vol. 92, pp. 123-136, Apr. 2019.
- [4] S. Zhekov, A. Tatomirescu, E. Foroozanfard, and G. F. Pedersen, "Experimental investigation on the effect of user's hand proximity on a compact ultrawideband MIMO antenna array," *IET Microwaves, Antennas Propag.*, vol. 10, no. 13, pp. 1402-1410, Oct. 2016.
- [5] L. L. Nagy, *Automobile Antennas*, McGraw-Hill, New York, 2007.

- [6] K. L. Wong, *Planar Antennas for Wireless Communications*, Wiley Interscience, Hoboken, NJ, Jan. 2003.
- [7] V. Rabinovich, N. Alexandrov, and B. Alkhateeb, *Automotive Antenna Design and Applications*, CRC Press, Taylor & Francis, Boca Raton, FL, Dec. 2017.
- [8] S. Arianos, G. Dassano, F. Vipiana and M. Orefice, "Design of multi-frequency compact antennas for automotive communications," *IEEE Transactions on Antennas and Propagation*, vol. 60, no. 12, pp. 5604-5612, Dec. 2012.
- [9] G. Artner, W. Kotterman, G. Del Galdo, and M. A. Hein, "Automotive antenna roof for cooperative connected driving," *IEEE Access*, vol. 7, pp. 20083-20090, Jan. 2019.
- [10] H. J. Song, A. Bekaryan, J. H. Schaffner, T. Talty, D. Carper, E. Yasan, and A. Duzdar, "Evaluation of vehicle-level MIMO antennas: capacity, total embedded efficiency, and envelope correlation," *2014 IEEE-APS Topical Conference on Antennas and Propagation in Wireless Communications (APWC)*, Palm Beach, FL, pp. 89-92, Aug. 2014.
- [11] O. Kwon, R. Song, and B. Kim, "A fully integrated shark-fin antenna for MIMO-LTE, GPS, WLAN, and WAVE applications," *IEEE Antennas and Wireless Propagation Letters*, vol. 17, no. 4, pp. 600-603, Apr. 2018.
- [12] V. Franchina, A. Michel, P. Nepa, M. Gallo, R. Parolari, A. P. Filisan, and D. Zamberlan, "A compact 3D antenna for automotive LTE MIMO applications," *2017 IEEE-APS Topical Conference on Antennas and Propagation in Wireless Communications (APWC)*, Verona, Italy, pp. 326-329, Oct. 2017.
- [13] A. Heiman, A. Badescu, and A. Saftoiu, "A new multiple input multiple output V2V automotive antenna for long term evolution band applications," *2018 International Symposium on Fundamentals of Electrical Engineering (ISFEE)*, Bucharest, Romania, pp. 1-5, Nov. 2018.
- [14] D. Preradovic and D. N. Aloï, "Cross polarized 2x2 LTE MIMO system for automotive shark fin application," *The Applied Computational Electromagnetics Society (ACES)*, vol. 35, no. 10, pp. 1207-1216, Oct. 2020.
- [15] C. Demien and R. Sarkis, "Design of shark fin integrated antenna systems for automotive applications," *2019 Photonics & Electromagnetics Research Symposium - Spring (PIERS-Spring)*, Rome, Italy, pp. 620-627, June 2019.
- [16] A. Thiel, L. Ekiz, O. Klemp, and M. Schultz, "Automotive grade MIMO antenna setup and performance evaluation for LTE-communications," *2013 International Workshop on Antenna Technology (iWAT)*, Karlsruhe, pp. 171-174, Mar. 2013.
- [17] Y. Liu, Z. Ai, G. Liu, and Y. Jia, "An Integrated shark-fin antenna for MIMO-LTE, FM, and GPS applications," *IEEE Antennas and Wireless Propagation Letters*, vol. 18, no. 8, pp. 1666-1670, Aug. 2019.
- [18] N. Guan, H. Tayama, M. Ueyama, Y. Yoshijima, and H. Chiba, "A roof automobile module for LTE-MIMO antennas," *2015 IEEE-APS Topical Conference on Antennas and Propagation in Wireless Communications (APWC)*, Turin, pp. 387-391, Sep. 2015.
- [19] S. Hastürkoğlu, M. Almarashli, and S. Lindenmeier, "A compact wideband terrestrial MIMO-Antenna set for 4G, 5G, WLAN and V2X and evaluation of its LTE-Performance in an urban region," *2019 13th European Conference on Antennas and Propagation (EuCAP)*, Krakow, Poland, pp. 1-5, Mar. 2019.
- [20] O. Jonah, "5G antenna for automotive applications," *2020 IEEE International Symposium on Antennas and Propagation and North American Radio Science Meeting*, pp. 1493-1494, Web, July 2020.
- [21] T. Jiang, T. Jiao, and Y. Li, "A low mutual coupling MIMO antenna using periodic multi-layered electromagnetic band gap structures," *The Applied Computational Electromagnetics Society (ACES)*, vol. 33, no. 3, Mar. 2018.
- [22] F. Liu, J. Guo, L. Zhao, G. Huang, Y. Li, and Y. Yin "Ceramic superstrate-based decoupling method for two closely packed antennas with cross-polarization suppression," *IEEE Transactions on Antennas and Propagation*, vol. 69, no. 3, pp. 1751-1756, Mar. 2021.
- [23] S. Luo, Y. Li, Y. Xia, G. Yang, L. Sun, and L. Zhao, "Mutual coupling reduction of a dual-band antenna array using dual-frequency metamaterial structure," *The Applied Computational Electromagnetics Society (ACES)*, vol. 34, no. 3, pp. 403-410, Mar. 2019.
- [24] A. Mansoor and R. Amiri, "Mutual coupling reduction of closely spaced MIMO antenna using frequency selective surface based on metamaterials," *The Applied Computational Electromagnetics Society (ACES)*, vol. 32, no. 12, pp. 1064-1068, Dec. 2017.
- [25] K. Yu, Y. Li, and X. Liu, "Mutual coupling reduction of a MIMO antenna array using 3-D novel meta-material structures," *The Applied Computational Electromagnetics Society (ACES)*, vol. 33, no. 7, pp. 758-763, July 2018.
- [26] S. Luo, Y. Li, Y. Xia, and L. Zhang "A low mutual coupling antenna array with gain enhancement using metamaterial loading and neutralization line structure," *The Applied Computational Electromagnetics Society (ACES)*, vol. 34, no. 3, pp. 411-418, Mar. 2019.

- [27] J. Jiang, Y. Xia, and Y. Li “High isolated X-band MIMO array using novel wheel-like metamaterial decoupling structure,” *The Applied Computational Electromagnetics Society (ACES)*, vol. 34, no. 12, pp. 1829-1836, Dec. 2019.
- [28] S. F. Beegum and S. K. Mishra, “Compact WLAN band-notched printed ultrawideband MIMO antenna with polarization diversity,” *Progress in Electromagnetics Research C*, vol. 61, pp. 149-159, Jan. 2016.
- [29] K. Sreelakshmi, P. Bora, M. Mudaliar, Y. Dhanade, and B. T. P. Madhav, “Linear array Yagi-Uda 5G antenna for vehicular application,” *International Journal of Engineering & Technology*, vol. 7, pp. 513-517, Dec. 2017.
- [30] D. Potti, Y. Tusharika, M. G. N. Alsath, S. Kirubaveni, M. Kanagasabai, R. Sankararajan, S. Narendhiran, and P. B. Bhargav, “A novel optically transparent UWB antenna for automotive MIMO communications,” *IEEE Transactions on Antennas and Propagation*, vol. 69, pp. 3821-3828, July 2021.



Mohamed O. Khalifa received the B.S. degree in Electrical and Electronic Engineering from University of Khartoum, Khartoum, Sudan, in 2010 and the M.S. degree in Electrical Engineering from King Fahd University of Petroleum and Minerals, Dhahran, KSA, in 2015.

He is currently pursuing the Ph.D. degree in Electrical and Computer Engineering at Oakland University.

He served as a Research Assistant at King Fahd University of Petroleum and Minerals, Visiting graduate Intern at I-Radio Lab within the School of Engineering at University of Calgary in Alberta, Canada and Research Assistant at Applied EMAG and Wireless Lab at Oakland University from 2012-2018. He has been employed in Ficos North America, Madison Heights, Michigan from 2018-2019 then in Molex LLC, Grand Blanc, Michigan from 2019 until present. His research interests reside in area of Power Amplifier design and linearization techniques and applied electromagnetics with emphasis on antenna measurements, antenna modeling/analysis and antenna design. He has authored/co-authored around 10 technical papers and is an inventor on 3 patents.



Ahmad M. Yacoub received the B.S. degree in Electrical Engineering from Princess Sumaya University for Technology Amman, Jordan, in 2014 and the M.S. degree in Electrical and Computer Engineering from Oakland University, Rochester, Michigan, in 2018. He is currently pursuing the Ph.D. degree in Electrical and Computer Engineering at Oakland University.

He served as a Research Assistant at Applied EMAG and Wireless lab at Oakland University from 2016-2018. He has been employed in Molex LLC, Grand Blanc, Michigan from 2018 until present. Yacoub's research interests reside in area of applied electromagnetics with emphasis on antenna measurements, antenna modeling/analysis and antenna design. He is an inventor/co-inventor of 2 patents.



Daniel N. Aloï received his B.S. (1992), M.S. (1996) and Ph.D. (1999) degrees in Electrical Engineering from Ohio University, located in Athens, Ohio, USA. He served as a Research Assistant from 1995-1999 in the Avionics Engineering Center within the School of Engineering

and Computer Science at Ohio University; Summer Intern at Rockwell International in Cedar Rapids, Iowa, and Senior Project Engineer at OnStar, Incorporated, a subsidiary of General Motors from 2000-2002. He has been employed in the Electrical and Computer Engineering Department at Oakland University in Rochester, Michigan from 2002 until present. He is the Founder and Director of the Applied EMAG and Wireless Lab at Oakland University.

Aloï's research interests reside in area of applied electromagnetics with emphasis on antenna measurements, antenna modeling/analysis and antenna design. He is a member of the Institute of Navigation and is a senior member of the Institute of Electrical and Electronics Engineers (IEEE). He has received in excess of \$4M in research funding from a variety of federal and private entities including the Federal Aviation Administration, Defense Advanced Research Program Agency (DARPA) and the National Science Foundation (NSF). He has authored/co-authored over 100 technical papers and is an inventor on 5 patents.

Complementary SRR-Based Reflector to Enhance Microstrip Antenna Performance

Mustafa H. B. Ucar

Information Systems Engineering Department
Kocaeli University, Umuttepe Campus, 41001 Kocaeli, Turkey
mhbuca@kocaeli.edu.tr

Abstract — In this paper, complementary split ring resonator (SRR) based reflector to enhance the printed slot dipole (PSD) antenna performance is introduced. The numerically calculated return-loss, directivity and radiation pattern results of the PSD antenna, with (w/) and without (w/o) CSRR element etched on reflector plane are presented and investigated. Numerical analysis and modelling of the proposed design are carried out using CST Microwave Studio simulator based on the finite integration technique. According to the simulation results, with the inclusion of the CSRR-based reflector into the PSD antenna, the directivity is increased by values changes from 0.6 dB to 4.25 dB through the operation band, while an improvement in bandwidth (~2.1%) is seen. It is also shown that this improvement in antenna performance is due to the ϵ -negative (ENG) behavior of CSRR structures. Prototype of the proposed antenna is fabricated using Arlon DiClad 880 substrate with electrical permittivity of $\epsilon_r = 2.2$. A quite good agreement between simulation and measurement is obtained. In this study, it is shown that the radiation performance of the antenna can be increased easily by using the CSRR element as a reflector in the antenna structure with a new enhancement approach. Also, the proposed antenna with a compact size of $0.27\lambda \times 0.41\lambda$ is appropriate for operating in IEEE 802.11b/g/n/ax (2.4 GHz) WLAN applications.

Index Terms — Complementary split ring resonator, microstrip antennas, reflector, split ring resonator.

I. INTRODUCTION

Microstrip antennas are widely preferred due to their low-profile, lightweight and easy fabrication, in many applications. On the other hand, it is also well known that, conventional microstrip antennas are featured with their disadvantages such as narrow bandwidth, lower gain and lower power-handling capability [1, 2]. In this context, a series of studies involving changes in either

the antenna element or the ground plane or the feed structure to increase the antenna radiation performance are included in the literature [3–19]. Many enhancement techniques such as including parasitic elements [3–5], modifying antenna [6–7], using metasurfaces [8–12], superstrates [13–15] and utilizing band gap [16, 17] or defected ground structures [18, 19] are also reported in these studies. However, many of these techniques increase the complexity and also the size of the antenna, which makes physical realization difficult. In this context, metamaterials has played an important role in reducing the complexity caused by the addition of extra structures, as well as improving the performance of antenna. As is known to all, SRR structures were originally introduced as metamaterial structures showing μ -negative behavior, which have band stop characteristic in a certain frequency band [20]. Moreover according to Babinet's principle, it is also shown that by utilizing a complementary SRR (CSRR), a band-pass performance can be ensured [21, 22]. Recently, SRRs and CSRRs have been used as an antenna radiation element [5–7], artificial substrate [8–10] and also placed on feeding structure [6] or ground plane [10] to enhance antenna performance. In [5] a dual-band loop-loaded printed dipole antenna with a wideband microstrip balun structure is introduced for 3/5.5 GHz WiMAX applications. In that study, triple-band performance is achieved by improving the return loss performance with the inclusion of the parasitic SRR element in to the antenna structure. In another work [6], a multiband monopole antenna based on CSRR was presented, which covers WLAN and WiMAX frequency bands. Also in that study, CSRRs are used side by side as the main radiator of the antenna to keep the antenna size small. By using the filtering characteristics of the penta-ring SRR element multiband antenna performance was also provided [7]. An artificial substrate composed of SRR elements was proposed for a microstrip patch antenna to provide frequency tuning as well as miniaturization [8].

Table 1: Summary of enhancement techniques for printed antennas using SRR/CSRR structures

| Ref. No. | Operation | Adjustment | | | Enhancement | | |
|------------------|-------------|------------|-----------|---------|-------------|-------------|------------|
| | | On/In | Technique | Element | BW | Directivity | Efficiency |
| [5] | Multi-band | Antenna | Loading | SRR | ✗ | ✗ | ✗ |
| [6] | Dual-band | Antenna | Modifying | CSRRs | ✗ | N/A | N/A |
| [7] | Multi-band | Antenna | Modifying | SRR | N/A | N/A | N/A |
| [8] | Single-band | Substrate | Modifying | SRR | ✗ | ✓ | ✗ |
| [9] | Single-band | Substrate | Loading | 3D-SRR | ✓ | ✗ | N/A |
| [10] | Single-band | Feeding | Loading | SRR | ✓ | N/A | N/A |
| [11] | Multi-band | Ground | Modifying | CSRR | N/A | N/A | N/A |
| [12] | Dual-band | Ground | Modifying | CSRR | ✗ | ✗ | N/A |
| This work | Single-band | Reflector | Etching | CSRR | ✓ | ✓ | ✓ |

N/A denotes that the related performance evaluation "not available" in that paper.

Metamaterials were also used to design electrically large property (ELP) antennas [9]. With the ELP method relatively high gains can be obtained in the same physical dimensions while increasing the bandwidth by using ENG featured metamaterials. However, the proposed array with ELP is of a complexity that can be difficult during the fabrication. In [10], for better impedance bandwidth and to achieve circular polarization, dual SRR elements are placed on the backside of the slot antenna, i.e. the feed plane. In addition, the CSRR structure is etched into the ground plane of the fractal microstrip antenna to achieve multi-band performance [11]. Furthermore, CSRR structures are also incorporated into the multilayer metasurface (MS) design to realize the dual-band operation [12]. On the other hand, in that study fabrication challenges were encountered due to the lamination of the multiple substrates to each other in the production of the proposed layered MS geometry. A detailed summary of enhancement techniques for printed antennas using SRR/CSRR structures are listed in Table 1. Unlike from previous designs reported in literature [5–12], the printed slot dipole antenna (PSD) introduced in this paper utilizes the complementary SRR element as a reflector to enhance the radiation performance. Compared to the aforementioned studies, here the CSRR structure was used in antenna design by etching on the reflector plane at a certain distance from the antenna, with a simplistic approach in terms of modeling and manufacturing. Also, apart from the previously reported literature [6, 11, 12], the use of the CSRR element in the reflector improves the bandwidth performance while providing a slight increase in the directivity and efficiency of the proposed PSD antenna as depicted in Table 1.

In the paper, CST based simulations [23] including the radiation performances, (such as bandwidth, directivity and efficiency) along with the corresponding return loss measurement of the PSD antenna with (w/) and without (w/o) CSRR element etched on reflector are presented and discussed. According to the simulation

and measurement results, when the CSRR element is etched on the reflector of the PSD antenna, while a relatively improvement in bandwidth (~2.1%) was observed, the directivity was also increased by at least 0.6 dB through the operation band. In addition, a slightly increase in antenna efficiency was also seen.

The outline of the paper is organized as follows. Section 2 describes the printed slot dipole (PSD) antenna design with CSRR-based reflector and the intended use of the CSRR in the reflector. In Section 3, the numerical analysis results of the PSD antenna with CSRR-based reflector design are given and discussed. Also in Section 3, the effects of optimized parameters on the radiation performance, such as the dimensions of the PSD, and CSRR elements and the distance of the reflector to the antenna plane are included. In Section 4, the electrical behavior of the CSRR structure through the operating band is examined and its contribution to the improvement of antenna performance is discussed, and finally, the paper is summarized with concluding remarks in Section 5.

II. ANTENNA DESIGN

The proposed microstrip-line coupled printed slot dipole (PSD) antenna with CSRR-based reflector and its detailed views along with physical parameters are shown in Fig. 1 and Fig. 2 respectively. As can be seen, the design consists of stepped microstrip line-fed slot dipole element and CSRR-based reflector to enhance radiation performance of the PSD antenna. The PSD element and microstrip feed line are etched each side of an Arlon DiClad 880 substrate that cover an area of $34 \times 52 \text{ m}^2$ with dielectric constant of $\epsilon_r=2.2$ and thickness of $t=0.76 \text{ mm}$. The PSD antenna is excited by a stepped microstrip line placed on the other side of the dielectric substrate. The feedline is designed to have two sections with 50Ω ($w_f \times l_f$) and $\sim 40\Omega$ ($w_s \times l_s$) characteristic impedances, so as to ensure a better impedance matching. As shown in Fig. 1, the concentrically placed CSRR elements are etched on metallic reflector and located underneath the

PSD antenna element at a distance of $h=11.5$ mm. The slits on outer and inner slots of the CSRR are located perpendicular to the PSD element towards the upper and lower edges of the reflector, respectively.

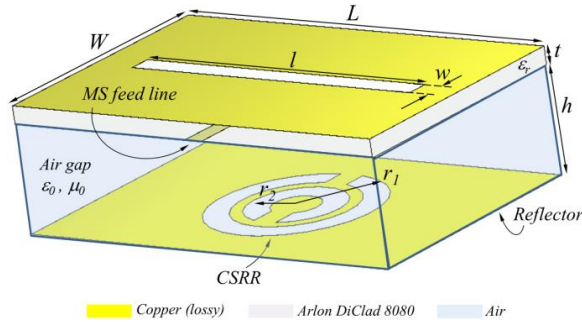


Fig. 1. The proposed MS-line fed PSD antenna with CSRR-based reflector: $L=52$, $W=34$, $l=40.5$, $w=3$, $t=0.76$, $h=11.5$, $r_1=10.9$, $r_2=6.1$, all in mm $\epsilon_r=2.2$.

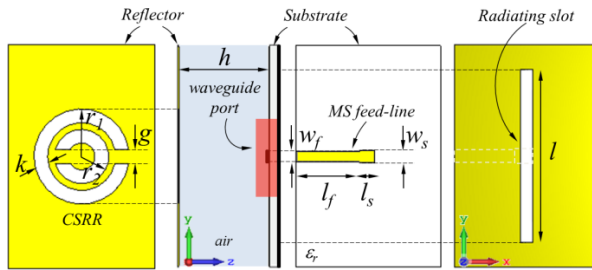


Fig. 2. The detailed views and physical parameters of the proposed PSD antenna with CSRR-based reflector: $k=g=3.15$, $r_1=10.95$, $r_2=6.1$, $h=11.5$, $w_f=2.4$, $l_f=15$, $w_s=3$, $l_s=3.5$ all in mm, $\epsilon_r=2.2$.

The CSRR structure having band-pass filter characteristics over a certain frequency range is a well-known meta-material. Different from the previously reported methods of using SRR/CSRR structures to improve antenna performance in the literature [5–12] in this study, the CSRR is used as a reflector located at a certain distance (h) from the antenna structure to improve the antenna performance in terms of both bandwidth and directivity. Compared to the aforementioned studies, here the CSRR structure was utilized in antenna design by etching on the reflector placed at a certain distance from the antenna, with a simplistic approach in terms of modeling and manufacturing. The interaction of the CSRR structure with the electric field results in occurrence of strong dispersion at the resonance frequency and correspondingly CSRR provides negative dielectric permittivity at the resonance frequency. In this context, to improve the radiation and bandwidth performance of the PSD antenna by creating a new resonance near the resonance frequency of the PSD antenna, firstly the CSRR structure is sized to resonate

around 2.4 GHz. During the design process, while achieving the ultimate CSRR-based reflector backed PSD antenna, the dimensions of the PSD ($w \times l$) and CSRR elements (k , g , r_1 , r_2) and the distance of the reflector to the antenna plane (h) were set as critical design parameters and optimized.

III. RESULTS AND DISCUSSION

The simulated return loss performances of the PSD antenna, utilizing reflector with (w/) and without (w/o) CSRR are displayed in Fig. 3. As seen, while the fully metallic reflector (w/o CSRR) backed PSD has a resonance around 2.4 GHz with a bandwidth of 2.5%, the inclusion of the CSRR into reflector leads to a $\sim 2.1\%$ increase in bandwidth around 2.38 GHz without deteriorating the antenna radiation performance as seen in Fig. 4. The simulated radiation patterns of the PSD antenna backed reflector with and without CSRR at 2.4 GHz are depicted in Fig. 4. It shows that the proposed CSRR-based reflector backed PSD design has an omnidirectional pattern for H-plane and bi-directional pattern for E-plane. Furthermore, the inclusion of CSRR into the reflector does not have any detrimental effect on the antenna radiation performance.

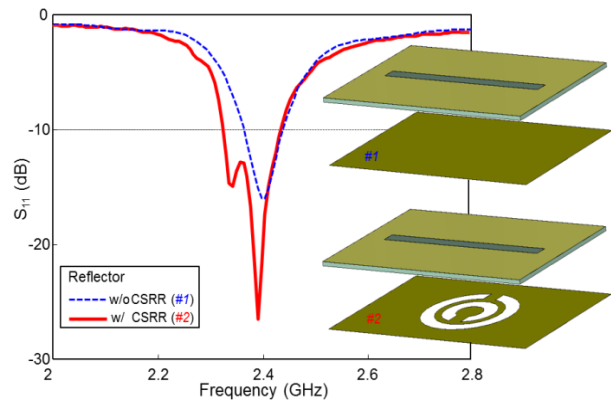


Fig. 3. The simulated return loss performances of the PSD antenna using reflector with (w/) and without (w/o) CSRR.

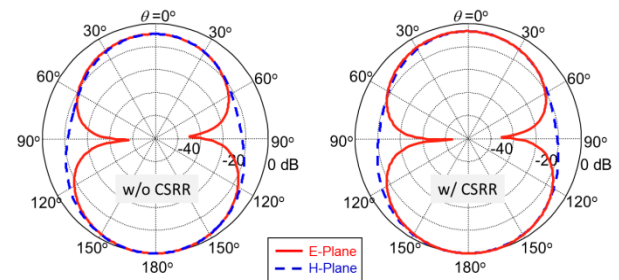


Fig. 4. The normalized radiation patterns of the PSD antenna using reflector with (w/) and without (w/o) CSRR at 2.4 GHz.

In order to validate the simulation results, a prototype of the proposed CSRR-based reflector backed PSD antenna was fabricated on an Arlon DiClad 880 substrate ($\epsilon_r=2.2$, $h=0.79$) according to the optimized design parameters in Fig. 2. A photograph of the fabricated antenna is shown in Fig. 5. The measured and simulated return loss characteristics are presented in Fig. 6. As can be seen in Fig. 6, there is a good agreement between the return loss simulation and measurement results, except for slight differences due to fabrication and material losses. Also measurement reveals that antenna with CSRR etched reflector has impedance bandwidth of 110 MHz ($S_{11}<-10$ dB) 2.32– 2.43 GHz, and is slightly greater than stand-alone reflector backed one. The designed antenna with a compact size of $0.27\lambda \times 0.41\lambda$ is appropriate for operating in IEEE 802.11b/g/n/ax (2.4 GHz) WLAN applications covering 2.32 GHz – 2.43 GHz frequency band. In addition, radiation pattern measurements were performed in an anechoic chamber using the De0530 model horn antenna (0.5-30 GHz developed by Diamond Engineering) with the measurement setup shown in Fig. 7. A Rohde & Schwarz ZVB 20 VNA as well as low loss coaxial cables were used in these measurements. The measured patterns along with the simulations at the operational frequency of 2.4 GHz are shown in Fig. 8, where a good agreement except tolerable discrepancies is observed. The measured gain of the PSD antenna design in which the CSRR-based reflector is included is 3-5.5 dBi in the relevant band. Also note that the inclusion of the CSRR reflector structure provides at least 1dB increase in gain values compared to the design without the CSRR-based reflector.

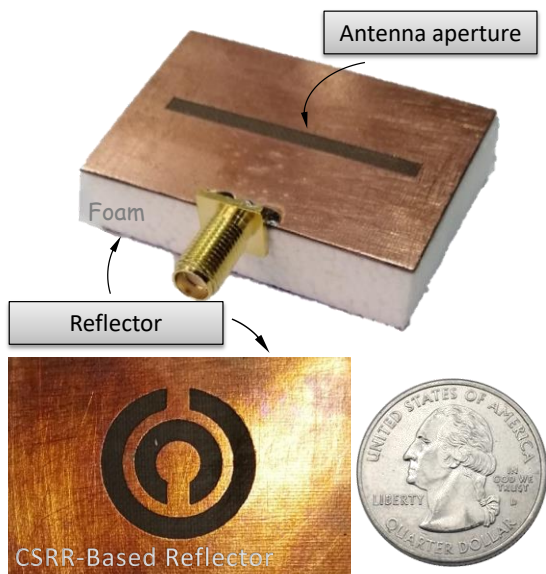


Fig. 5. The perspective and back views of the fabricated PSD antenna with CSRR-based reflector.

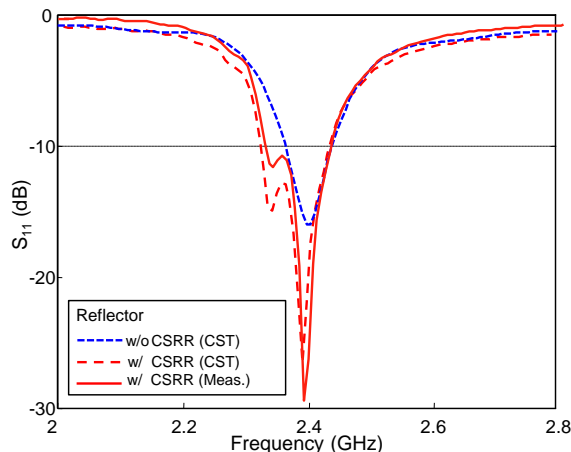


Fig. 6. The simulated and measured return loss performances of the PSD antenna using reflector with (w/) and without (w/o) CSRR.

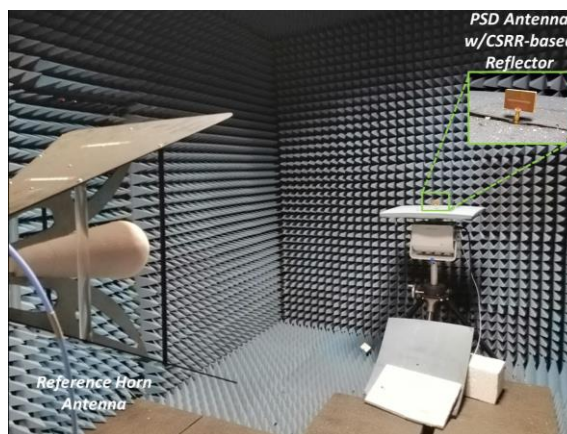


Fig. 7. The measurement setup of the proposed PSD antenna with CSRR-based reflector.

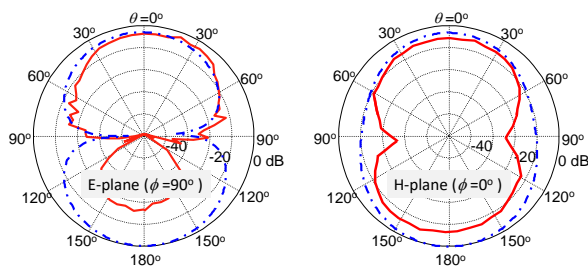


Fig. 8. The measured and simulated radiation patterns of the PSD antenna with CSRR-based reflector at 2.4 GHz.

While etching the CSRR element to the reflector, it was primarily aimed to generate an additional resonance near the operating frequency of the PSD antenna. Thus, these two adjacent bands are joined together by optimizing

the aforementioned critical design parameters and a rather larger bandwidth performance is provided. During the design process, besides the improvement in the bandwidth, some enhancements were also observed in both the directivity and efficiency. To demonstrate the effect of the CSRR based reflector on the antenna directivity, the simulated directivity performance of the PSD antenna utilizing reflector w/ and w/o CSRR through the operation band is depicted in Fig. 9. As can be seen, the inclusion of the CSRR into the reflector results in increases in the directivity which vary from 0.6 dB to 4.5 dB through the operation bands.

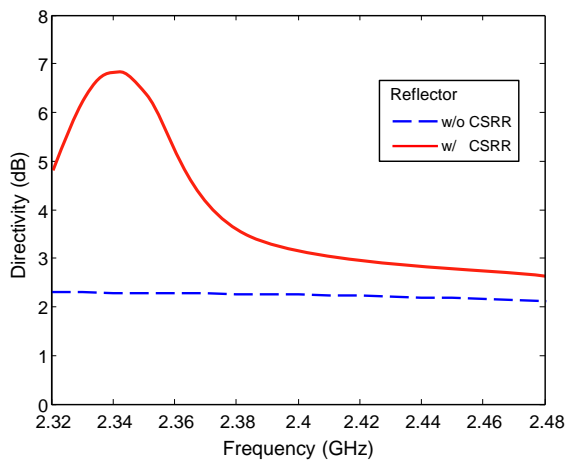


Fig. 9. The simulated directivity performances of the PSD antenna using reflector with (w/) and without (w/o) CSRR through the operation band.

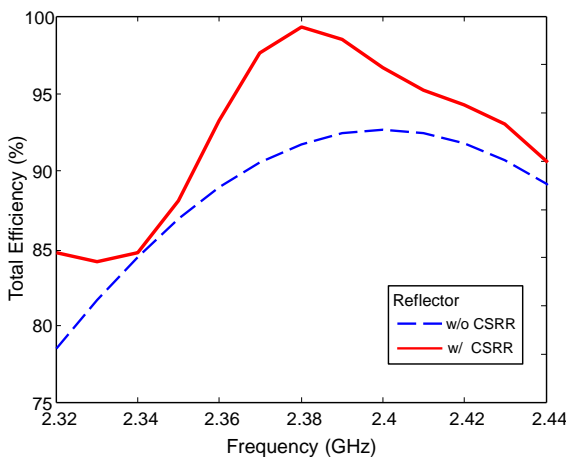


Fig. 10. The calculated total efficiency of the PSD antenna using reflector with (w/) and without (w/o) CSRR through the operation band.

As it is well-known, the total efficiency (e_0) of the antenna is used to account for losses such as reflection (mismatch), conduction and dielectric losses. These

losses directly affect the gain of the antenna, thus the radiation performance. In this context to examine the effect of the CSRR on the antenna efficiency performance, the total efficiency of the PSD is calculated and the results are given in Fig. 10. As seen, the inclusion of CSRR in to the reflector causes an increase, especially at the upper frequencies. It is noted that the calculated efficiency of the PSD antenna with CSRR-based reflector through the operation band is at least 83%. The improvements observed in antenna radiation performance with the incorporation of the CSRR element into the reflector are summarized in Table 2.

Table 2: The summary of enhancements in the radiation performances of the PSD antenna with incorporation of the CSRR in to the reflector

| | | CSRR | | Changes |
|--------------|------------------|--------------|---------------|----------------|
| | | w/o | w/ | |
| Performances | Bandwidth (MHz) | 60 (2.5%) | 110 (4.6%) | 50 (2.1%) ↑ |
| | Directivity (dB) | 2.1~2.3 | 2.8~6.8 | 0.6~4.5 ↑ |
| | Efficiency (%) | 78~92 | 83~98 | 1~8 ↑ |

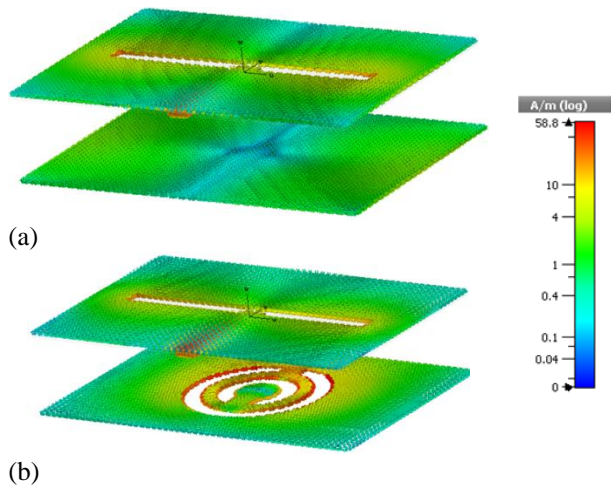


Fig. 11. Surface current distribution of the PSD antenna at 2.38 GHz: (a) stand-alone reflector, and (b) CSRR etched reflector.

The computed surface current distribution of the PSD antenna at the 2.38 GHz is shown in Fig. 11 to endorse the effect of the CSRR-based reflector on the antenna radiation performance. As can be seen, in absence of the CSRR element on the reflector surface (w/o CSRR, i.e., Fig. 11 (a)), the current distribution at 2.38 GHz is mainly concentrated over the PSD element. On the other hand, in presence of the CSRR element

on the reflector surface (w/ CSRR, i.e., Fig. 11 (b)), the distribution at 2.38 GHz is observed predominantly around the PSD as well as the inner and out loops of the CSRR element. Indeed, these results support that the upper and the lower bands of the operation frequency band centered 2.38 GHz occur by means of PSD antenna and CSRR elements, respectively. As a result, by placing the CSRR element on the reflector surface, a secondary resonance is obtained due to the strong resonant behavior of the CSRR structure; thus, the impedance bandwidth is relatively increased ($\sim 2.1\%$).

In antenna design section while achieving the ultimate CSRR-based reflector backed PSD antenna design, it was stated that some of the physical dimensions of the proposed antenna are the crucial design parameters that directly affect the antenna radiation performance. For an efficient design process, it is very important and helpful to reveal these important parameters effect, and especially to associate the geometrical parameters with the operation band. Accordingly, in this section, the effects of the aforementioned critical design parameters such as the length of the slot (l), gaps width (g) and outer ring radius (r_l) of the CSRR and the distance of the reflector to the antenna plane (h) on the antenna return loss performance are also examined. It is noted that, during parametric studies, only one parameter was changed at a time, while the others were preserved constant.

As seen Fig. 12 (a), while the slot length directly contributes the occurrence of the resonance frequency around the 2.4 GHz, it also plays an important role in the creating of an additional resonance in vicinity of the first resonance with the CSRR based reflector. Hence, a considerably large bandwidth is provided by specifying the slot length as 40.5 mm with optimized design parameters. Also, the distance of the CSRR based reflector to the antenna plane is set 11.5 mm to ensure better impedance matching and to achieve the desired broadband performance through the operation band as shown in Fig. 12 (b). In addition, a series of parametric studies were also carried out for the two critical design parameters of CSRR geometry that affect the radiation performance, namely the gap width (g) and the outer ring radius (r_l) and presented in Fig. 12 (c) and Fig. 12 (d) respectively. As shown in Fig. 12 (c), when the gap width of the CSRR is increased from 3 mm to 3.9 mm, the lower resonance due to the CSRR element shifts slightly upward. By setting the gap width as 3.15 mm, better impedance matching is achieved and desired relatively wideband performance realized. In Fig. 12 (d), the effect of the CSRR's outer ring radius (r_l) on the simulated S_{11} performance is shown. It is observed that the outer radius of the CSRR is increased from 10.45 mm to 10.95 mm, the lower resonance due to the CSRR element shifts slightly downward.

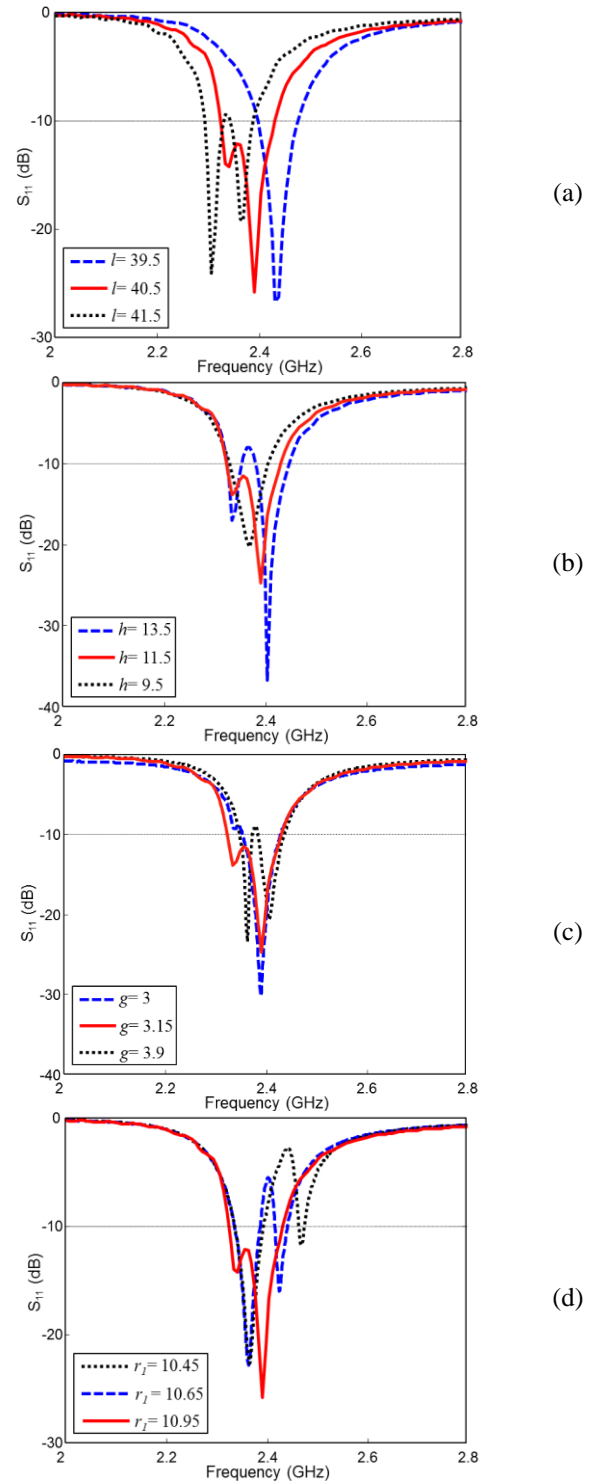


Fig. 12. The effects of critical design parameters on the return loss performance of the proposed CSRR-based reflector backed PSD antenna: (a) slot length; l , (b) distance of the CSRR-based reflector to the antenna plane; h , (c) CSRR's gap width; g , and (d) outer ring radius of the CSRR; r_l , (all in mm).

As a result, according to Fig. 12, it can be stated that while the dipole length mainly controls the fundamental resonance which is centered 2.4 GHz, the CSRR-based reflector plays a key role in occurrence of the additional resonance at the lower frequency. Thus, with the optimization of the relevant physical dimensions, the gap between the lower and upper resonances has been closed and joined to provide a greater bandwidth performance. Also, slot and CSRR dimensions appear to play an important role in improving impedance matching at the operation band for desired rather broadband performance.

IV. ELECTRICAL BEHAVIOUR OF THE CSRR-BASED REFLECTOR

In the previous sections, it is numerically shown that the enhancements in the antenna radiation performances such as bandwidth, directivity and efficiency are mainly due CSRR structure etched on the reflector plane. The interaction of the CSRR structure with the electric field results in occurrence of strong dispersion at the resonance frequency and correspondingly CSRR provides negative dielectric permittivity at the resonance frequency. Actually, those improvements are due to the inherent features of metamaterials, i.e., CSRR structure etched on the reflector plane. To prove that, those improvements in antenna performance is due to the ϵ -negative (ENG) behavior of the CSRR structures, the scattering parameters (transmission- S_{21} and reflection- S_{11}) of the CSRR element in the respective operation band are first examined. The simulated scattering parameters of the CSRR-based reflector along with the simulated waveguide setup are depicted in Fig. 13. In the S-parameter simulations of the CSRR element, the ports (Port-1 and Port-2) are defined along the z-plane at appropriate distances from the CSRR in the waveguide. The boundaries are also specified for the boundary conditions. The CSRR structure is excited by the plane wave to the Port-1, and the simulated transmission and reflection parameters are extracted from the Port-2. As can be seen from Fig. 13, the CSRR structure exhibits band-pass filter performance around 2.4 GHz. Then, using the simulated scattering parameters effective medium parameters (ϵ_{eff} , μ_{eff}) of the CSRR are also numerically extracted using robust method reported in [24]. According to this method, first the effective refractive index n and impedance Z are obtained through the S parameters calculated from a wave incident normally on CSRR-based reflector. n is defined in terms of transmission (S_{21}) and reflection (S_{11}) parameters as follows:

$$n = \frac{1}{kd} \cos^{-1} \left[\frac{1}{2S_{21}} (1 - S_{11}^2 + S_{21}^2) \right], \quad (1)$$

where k and d denote wave number of the incident wave and the thickness of the CSRR-based reflector,

respectively. Also, Z is determined from the scattering parameters as follows:

$$Z = \sqrt{\frac{(1+S_{11})^2 - S_{21}^2}{(1-S_{11})^2 - S_{21}^2}}. \quad (2)$$

Later, the permittivity ϵ_{eff} and permeability μ_{eff} are calculated using relations:

$$\mu_{eff} = nZ, \quad \epsilon_{eff} = n/Z. \quad (3)$$

For metamaterials with resonant characteristics, there is always a frequency region where the branches related with the inverse cosine of equation (1) get too close together and it becomes difficult to get the exact solution. In the study, a more stable and accurate retrieval was achieved with the CST-based result template which utilize the algorithm of the method proposed in [24].

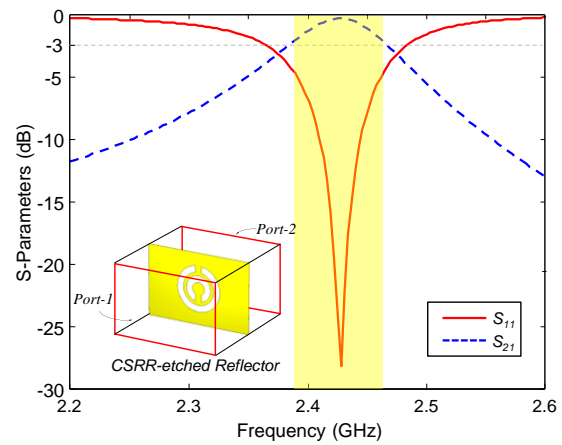


Fig. 13. The simulated scattering parameters of the CSRR-based reflector along with the simulated waveguide setup.

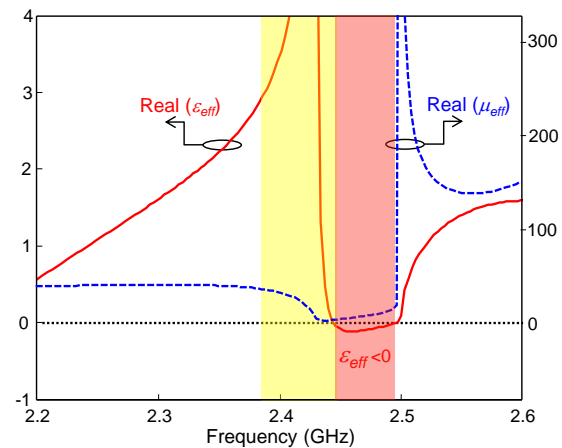


Fig. 14. The extracted material parameters for the CSRR-based reflector considered in Fig. 13.

The extracted material parameters for the CSRR-based reflector using scattering parameters in Fig. 13 are

depicted in Fig. 14. As seen in Fig. 14, while the CSRR exhibits a negative effective permittivity (ENG) above the resonance frequency, the CSRR has a positive effective permittivity below the resonance frequency. These results confirm the effect of the filtering performance of the CSRR-based reflector improving both the bandwidth and directivity of the PSD antenna. Thus, while creating a new resonance with the CSRR based reflector, it can be said that the CSRR structure, with the ε -negative behavior, contributes to the improvement of the antenna performance in terms of the bandwidth, directivity and efficiency.

VI. CONCLUSION

A complementary split ring resonator (CSRR) based reflector to enhance the printed slot dipole (PSD) antenna performance has been presented. In the paper, it is shown that employing the proposed CSRR-based reflector in the geometry of the antenna, the bandwidth and directivity performances of the antenna are enhanced with a simplistic design approach. A prototype of the proposed antenna has been fabricated and a fairly good agreement between simulation and measurement was observed. Measurement reveals that antenna with CSRR etched reflector has impedance bandwidth of 110 MHz ($S_{11} < -10$ dB) 2.32– 2.43 GHz, and is slightly greater than stand-alone reflector backed one. According to the simulation and measurement results, when the CSRR-based reflector was etched on the reflector of the PSD antenna, an improvement in bandwidth ($\sim 2.1\%$) was observed while the directivity and the efficiency were increased by at least 0.6 dB and 1% respectively. In addition, the material properties of the CSRR was extracted and examined. Accordingly, it has been shown that those improvements are due to the metamaterial properties of the CSRR structure, i.e., ε -negative (ENG) feature. It has been also shown with the parametric studies that CSRR dimensions and slot length have critical effects on the achieving greater bandwidth. The proposed antenna with a compact size of $0.27\lambda \times 0.41\lambda$ is appropriate for operating in 2.4 GHz WLAN applications. Besides, this simplistic approach can be easily applied to antenna structures in various wireless communication systems.

ACKNOWLEDGMENT

The author would like to thank all the members of the Microwave and Antenna Laboratory, Kocaeli University, for their assistance during the radiation pattern measurements. The author is also grateful to all the anonymous reviewers for their invaluable comments.

REFERENCES

- [1] R. Garg, P. Bhartia, I. Bahl, and A. Ittipiboon *Microstrip Antenna Design Handbook*, Artech House, Reading, MA, 2001.

- [2] G. Kumar and K. P. Ray, *Broadband Microstrip Antenna*, Norwood, MA, 2003.
- [3] S. Peddakrishna, T. Khan, and B. K. Kanaujia, "Resonant characteristics of aperture type FSS and its application in directivity improvement of microstrip antenna," *AEU- International Journal of Electronics and Communications*, vol. 79, pp. 199-206, Sept. 2017.
- [4] M. H. B. Ucar, A. Sondas, and Y. E. Erdemli, "Dual-band loop-loaded printed dipole antenna with a wideband microstrip balun structure," *Applied Computational Electromagnetics Society (ACES) Journal*, vol. 27, no. 6, pp. 458-465, June 2012.
- [5] M. H. B. Ucar and Y. E. Erdemli, "Triple-band microstripline-fed printed wide-slot antenna for WiMAX/WLAN operations," *Applied Computational Electromagnetics Society (ACES) Journal*, vol. 29, no. 10, pp. 793-800, Oct. 2014.
- [6] S. C. Basaran, U. Olgun, and K. Sertel, "Multiband monopole antenna with complementary split-ring resonators for WLAN and WiMAX applications," *Electron Lett.*, vol. 49, no. 10, pp. 636-638, May 2013.
- [7] N. T. Selvi, P. T. Selvan, S. P. K. Babu, and R. Pandeewari, "Multiband metamaterial-inspired antenna using split ring resonator," *Computers & Electrical Engineering*, vol. 84, 106613, pp. 1-13, 2020.
- [8] A. Sondas, M. H. B. Ucar, and Y. E. Erdemli, "Tunable SRR-based substrate for a microstrip patch antenna," *Turk. J. Elec. & Eng. Comp. Sci.*, vol. 20, no. 1, pp. 159-168, Jan. 2012.
- [9] W. Cao, W. Ma, W. Peng, and Z. N. Chen, "Bandwidth-enhanced electrically large microstrip antenna loaded with SRR structures," *IEEE Antennas Wireless Propagat. Lett.*, vol. 18, no. 4, pp. 576-580, Apr. 2019.
- [10] A. Sharma, D. Gangwar, K. B. Kumar, and S. Dwari, "RCS reduction and gain enhancement of SRR inspired circularly polarized slot antenna using metasurface," *AEU - International Journal of Electronics and Communications*; vol. 91, pp. 132-142, May 2018.
- [11] D. Kaushal and T. Shanmuganatham, "Parametric enhancement of a novel microstrip patch antenna using circular SRR loaded fractal geometry," *Alexandria Engineering Journal*, vol. 57, no. 4, pp. 2551-2557, Dec. 2018.
- [12] T. Yue, Z. H. Jiang, A. H. Panaretos, and D. H. Werner, "A compact dual-band antenna enabled by a complementary split-ring resonator-loaded metasurface," *IEEE Trans. Antennas Propagat.*, vol. 65, no. 12, pp. 6878-6888, Dec. 2017.
- [13] M. Rezvani and Y. Zehforoosh, "A dual-band multiple-input multiple-output microstrip antenna

- with metamaterial structure for LTE and WLAN applications,” *AEU - International Journal of Electronics and Communications*, vol. 93, pp. 277-282, Sept. 2018.
- [14] B. Urul, “Gain enhancement of microstrip antenna with a novel DNG material,” *Micro. Opt. Technol. Lett.*, vol. 62, no. 4, pp. 1824-1829, Jan. 2020.
- [15] P. K. Panda and D. Ghosh, “Isolation and gain enhancement of patch antennas using EMNZ superstrate,” *AEU - International Journal of Electronics and Communications*, vol. 86, pp. 164-170, Mar. 2018.
- [16] J. A. Brown, S. Barth, B. P. Smyth, and A. K. Tyer, “Dual-band microstrip corporate feed network using an embedded metamaterial-based EBG,” *IEEE Trans. Antennas Propagat.*, vol. 67, no. 11, pp. 7031-7039, Nov. 2019.
- [17] B. A. Mouris, A. Fernandez-Prieto, R. Thobaben, J. Martel, F. Mesa, and O. Quevedo-Teruel, “On the increment of the bandwidth of mushroom-type EBG structures with glide symmetry,” *IEEE Trans. Microw. Theory Tech.*, vol. 68, no. 4, pp. 1365-1375, Apr. 2020.
- [18] T. K. Das, B. Dwivedy, and S. K. Behera, “Design of a meandered line microstrip antenna with a slotted ground plane for RFID applications,” *AEU-International Journal of Electronics and Communications*, vol. 118, pp. 153130, pp. 1-7, May 2020.
- [19] N. Pouyanfar, C. Ghobadi, and J. Nourinia, “A compact multi-band MIMO antenna with high isolation for C and X bands using defected ground structure,” *Radioengineering*, vol. 27, no. 3, pp. 686-693, Sept. 2018.
- [20] J. B. Pendry, A. J. Holden, D. J. Robbins, and W. J. Stewart, “Magnetism from conductors and enhance nonlinear phenomena,” *IEEE Trans. Microw. Theory Tech.*, vol. 47, no. 11, pp. 2075-2084, Nov. 1999.
- [21] F. Falcone, T. Lopetegi, M. A. G. Laso, J. D. Baena, J. Bonache, M. R. Beruete, F. Martin, and M. Sorolla, “Babinet principle applied to the design of metasurfaces and metamaterials,” *Phys. Rev. Lett.*, vol. 93, no. 19, pp. 197401, pp. 1-4, Nov. 2004.
- [22] F. Falcone, T. Lopetegi, J. D. Baena, R. Marques, F. Martin, and M. Sorolla, “Effective negative- ϵ stopband microstrip lines based on complimentary split ring resonators,” *IEEE Microwave and Wireless Component Letters*, vol. 14, no. 6, pp. 280-282, June 2004.
- [23] CST Microwave Studio, ver. 2008, Computer Simulation Technology, Framingham, MA, 2008.
- [24] X. Chen, T. M. Grzegorzczuk, B. I. Wu, J. Pacheco Jr, and J. A. Kong, “Robust method to retrieve the constitutive effective parameters of metamaterials,” *Phys. Rev.-E*, vol. 70, no. 1, pp. 016608, pp. 1-7, July 2004.



Mustafa Hikmet Bilgehan Ucar

was born in Istanbul, Turkey, in 1982. He received his B.S., M.S., and Ph.D. degrees from Kocaeli University, Kocaeli, Turkey, all in Electronics and Computer Education Department in 2004, 2007, and 2013, respectively. He currently serves as

an Assistant Professor in the Department of Information Systems Engineering, Kocaeli University, Turkey. His main research interests include numerical analysis and design of reconfigurable antennas/arrays/EM filters and frequency selective surfaces for various communication applications. His research also focuses on embedded systems, user interface design and its usability.

Reconfigurable 2×1 CPW-Fed Rectangular Slot Antenna Array (RSAA) Based on Graphene for Wireless Communications

Dalia M. Elsheakh^{1,2} and Osama M. Dardeer²

¹Electrical Dept., Faculty of Engineering and Technology, Badr University in Cairo, Egypt
dalia-mohamed@buc.edu.eg / daliaelsheakh@eri.sci.eg

²Microstrip Dept., Electronics Research Institute, 11843, El Nozha, Cairo, Egypt

Abstract— This article presents a 2×1 CPW ultra wideband rectangular slot antenna array (UWB-RSAA) with a modified circular slot shape to support a high data rate for wireless communications applications. The proposed antenna array dimensions are $0.7\lambda_0 \times 0.8\lambda_0 \times 0.064\lambda_0$ at the resonant frequency 1.8 GHz. It is fabricated on Rogers RO4003 substrate and fed by using a coplanar waveguide (CPW). A graphene layer is added on one side of the substrate to realize frequency reconfigurability and improve the array gain. The proposed array acquires -10 dB impedance bandwidth of the RSAA that extends from 1.7 GHz to 2.6 GHz, from 3.2 to 3.8 GHz, and from 5.2 GHz to 7 GHz. The proposed array achieved a realized peak gain of 7.5 dBi at 6.5 GHz at 0 Volt bias with an average gain of 4.5 dBi over the operating band. When the graphene bias is increased to 20 Volt, the antenna bandwidth extends from 1 GHz to 4 GHz and from 5 to 7 GHz with a peak gain of 14 dBi at 3.5 GHz and an average gain of 7.5 dBi. The linearly polarized operation of the proposed array over the operating bands makes it suitable for short-range wireless communications.

Index Terms — Antenna array, detection and wireless communication applications, graphene, reconfigurable.

I. INTRODUCTION

Frequency tuning of the microwave systems has gained a great attention in the research field of antennas and wireless communications. Reconfigurable antenna array is one of the most important elements of the RF circuits [1-4]. In addition, the reconfigurable UWB antennas array could be served several selected frequency bands to avoid the unwanted frequencies and frequency fading. However, integrated RF systems needs reconfigurable antennas less space [6-7]. Several techniques have been reported in literature to achieve reconfigurability in the array operation. This includes using varactor diodes [8], PIN diodes [9], MEMS [10], and other techniques [11, 12].

Graphene is one of the most important materials in

21st century with superior electrical properties that can fit different applications. Graphene sheet is honeycomb lattice arrangement of carbon atoms as reported in early investigations at 2004 in 2004 [13]. Many researches have reported graphene applications for radio frequency (RF), microwave (MW), millimeter wave (MM) and terahertz (THz) applications in [14–15]. One of the most effective research areas utilized graphene sheet layer for steering radiation pattern based on its tunable conductivity [16]. Tuning the conductivity of Graphene is based on changing the applied DC bias voltage, which varies the chemical potential [17]. Several reports in the literature present a fabrication of high-quality graphene with controlled properties. So, great efforts have been made in this area for designing frequency reconfigurable antenna arrays [18–21].

In this paper, reconfigurable 2×1 CPW-fed RSAA as shown in Fig. 1 with an acceptable gain is introduced for different wireless communications applications. The antenna array is fed by 3-dB CPW power divider, which makes the structure easy to integrate with other microwave circuits. A graphene pad layer is placed below the feeding network to achieve the frequency reconfigurability action.

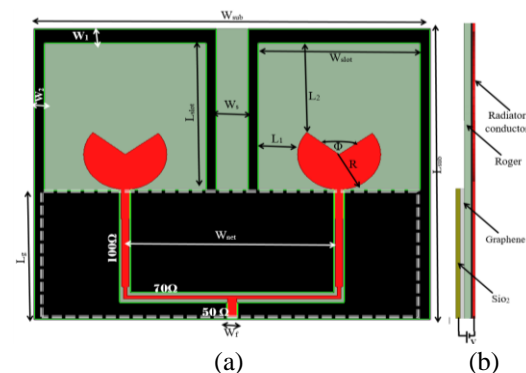


Fig. 1. (a) The structure geometry of the proposed 2×1 RSAA, and (b) side view.

This article is organized as follows; Section I introduces the idea of the paper while section II presents the proposed RSAA design. Section III discusses the graphene layer structure and its properties, then the experimental setup and results are presented in Section IV. After that section V illustrates the group delay results and object detection application and finally Section IV concludes and summarizes the results of the paper.

II. DESIGN OF THE ANTENNA ARRAY

The CPW-fed proposed antenna array is printed on a dielectric substrate Rogers RO4003 with a dielectric constant of 3.5 and a loss tangent of 0.0012. The substrate has dimensions ($L_{\text{sub}} \times W_{\text{sub}}$) of $100 \times 115 \text{ mm}^2$, and a thickness of 0.8 mm. CPW fed slot antennas are very popular and exhibit broad bandwidth and appropriate gain [23]. First design is a conventional 2×1 circular shape of monopole antenna array, which is fed using 3-dB power divider and CPW-fed network as shown in Fig. 2 (a) [24]. The reflection coefficient $|S_{11}|$ of proposed array is shown in Fig. 3 as dash red line. From Fig. 3 (a) the array starts to operate at 3 GHz at reflection impedance bandwidth $\leq -10 \text{ dB}$. Then quarter of the circular shape is etched as shown in Fig. 2 (b) to broaden the bandwidth and the resonant frequency is reduced to 2.5 GHz as shown in Fig. 3 (black line). The rectangular strip is added around the antenna circular shape as shown in Fig. 2 (c) to achieve ultra-wideband impedance bandwidth as shown in Fig. 3 (blue dash dot line), and the array resonant frequency is shifted downwards to operate at 1.7 GHz with improved gain. Figure 3 shows the reflection coefficient variation versus frequency for the prototypes in Fig.3.

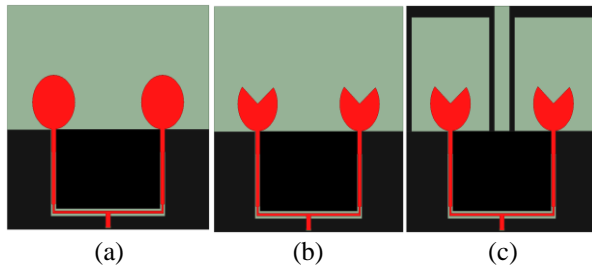


Fig. 2. The design steps of 2×1 array: (a) circular monopole, (b) modified circular, and (c) slot antenna array.

The results illustrate the bandwidth improvement after each step of the design. The complete optimized dimensions of the 2×1 antenna array are shown in Table 1. In addition, the current distribution at different resonant frequencies of the RSAA are shown in Fig. 4. The highest magnitude of the current represent the corresponding elements of the radiation.

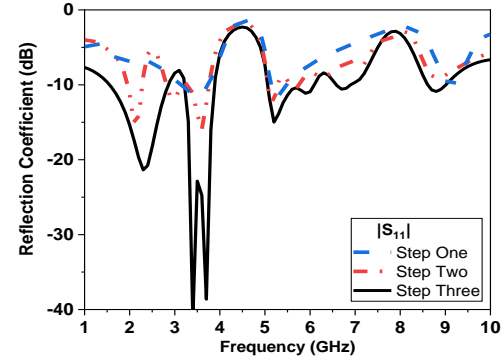


Fig. 3. $|S_{11}|$ versus frequency for the design steps of the proposed antenna array.

III. MODEL OF GRAPHENE ANTENNA

The design of antenna arrays plays a significant role in achieving high gain in a certain specified direction [13]. Moreover, multiband designs offer an excellent opportunity to the system to serve more applications with the same physical components. The previous section described the proposed 2×1 antenna array. However, this section will describe the addition of two graphene layers (on the other side of the substrate) between the Roger substrate and silicon oxide substrate to realize reconfigurable operation in the operating frequency.

A. Graphene conductivity variation

Graphene oxide (GO) has become important material as a result of its low cost, various simple preparation techniques that can be easily transformed to commercial graphene as RGO (reduced graphene oxide) [25-26]. 2D Graphene sheet is a material composed of highly conductive films with high mobility of $0.2 \text{ Mm}^2\text{v}^{-1}\text{sec}^{-1}$ to enhance the antenna performance [27-28], [30]. Graphene sheet has a tunable conductivity of about 10 S/m in the case of 20 voltage bias and about 1000 S/m in the case of zero voltage as shown in Fig. 5. The equivalent circuit model of the graphene layer is an as impedance R_g and inductor L_g in series. The values of graphene impedance vary according to the applied bias voltage as shown in Fig. 6. The change in the graphene properties results in changes in its resistance and inductance as shown in Fig. 6. This could be attributed to design an antenna with tunable operating frequency [31-34]. In this method at such case, the operating frequency is defined where the antenna exhibits the best input matching. Moreover, the maximum gain could be adjusted electronically by modifying the voltage applied to graphene sheet:

$$Z_s = \frac{1}{\sigma} \quad (1)$$

$$\sigma = \frac{\sigma_0}{\sigma(1+j\omega\tau)} \quad (2)$$

$$\sigma_0 = \frac{e^2 K_B T \tau}{\pi \hbar^2} \left[\frac{\mu_c}{K_B} + 2 \ln(1 + e^{-\mu_c/K_B T}) \right] \quad (3)$$

\hbar is reduced Planck’s constant, KB is Boltzmann’s constant, T is the temperature, e is the electron charge, and μ_c is the chemical potential. $T=300K$ and $\tau =0.1Ps$. Z_s is the surface impedance of the graphene, σ is the conductivity of the graphene.

B. Reconfigurable graphene antenna array

The radio technology of ultra-wideband (UWB) uses ultra-low transmitted energy for a high data rate over a large portion of the radio spectrum. The other definitions of UWB is when the antenna realizes bandwidth percentage greater than 25%. There are many wireless applications cover these spectrum as four/five generation of wireless communications. So, a reconfigurable operation is favored in these applications to cover and protect from channel fading and other losses.

Table 1: Dimensions of the 2×1 slot antenna array (all dimensions in mm)

| L_{sub} | W_{sub} | 100Ω | 50Ω | W_f | L_g | W_{net} | R | W_{slot} |
|-----------|-----------|-------------|-------------|-------|-------|-----------|------------|------------|
| 101 | 115 | 2 | 2.8 | 2.8 | 45 | 62 | 12.5 | 47 |
| L_1 | L_2 | 70Ω | Φ | W_s | W_1 | W_2 | L_{slot} | H |
| 5 | 3 | 2.6 | 110° | 9.5 | 5 | 3 | 51 | 0.8 |

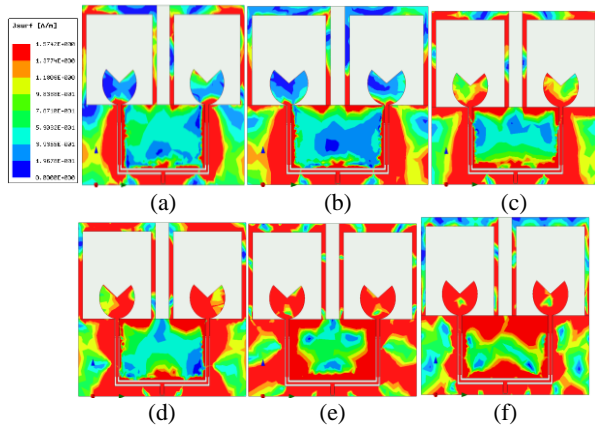


Fig. 4. (a)–(f) Surface current distribution for proposed 2×1 RSAA at 1.8, 2.1, 2.45, 3.5, 5.2 and 7 GHz, respectively.

Since UWB offers higher data rates with lesser multipath interference at lower power levels as compared to the narrow band communication systems as Shannon theorem [35]. So therefore the preferred band for implementation for many 4G and 5G wireless communication services. The operating band of the proposed antenna is extended by applying the DC voltage bias on the graphene layer as shown in Fig. 7.

IV. ANTENNA MEASUREMENT AND RESULTS

The proposed array is designed and all simulations are done by using finite element three dimensional

electromagnetic simulator, HFSS Ansys ver. 15 [29]. To verify the simulation results; the proposed antenna array element is fabricated and measured by using ZVA67 Rohde and Schwarz vector network analyzer from 10 MHz up to 67 GHz with different dc bias at 0 and 20 Volt as shown in Fig. 8 and by using bias Tee connector. Figure 9 and Fig. 10 present the comparison between simulated and measured reflection coefficient and voltage standing wave ratio (VSWR) variation versus frequency for the proposed RSAA at 0 and 20 Volt, respectively.

These figures indicate that good agreement is found between measured and simulated results. Figure 9 shows the performance at 0 Volt in which the $|S_{11}| < -10dB$ array impedance bandwidth extends from 1.7 to 2.5GHz, 3.3 to 3.8 GHz and 5 to 7 GHz. On the other hand, the impedance bandwidth extends from 1.5 GHz with stop bands from 4 to 5 GHz at DC 20 Volt as shown in Fig. 10. These operating bands are suitable for RF energy harvesting at GPS, GSM, UMTS, Wi-Fi, LTE bands, and WMAX. The proposed array exhibits a nearly omnidirectional radiation pattern in the E and H-plane at 0 Volt graphene bias as indicated in Table 2. A comparison of the proposed 2×1 rectangular slot antenna array with other reported arrays is provided in Table 3.

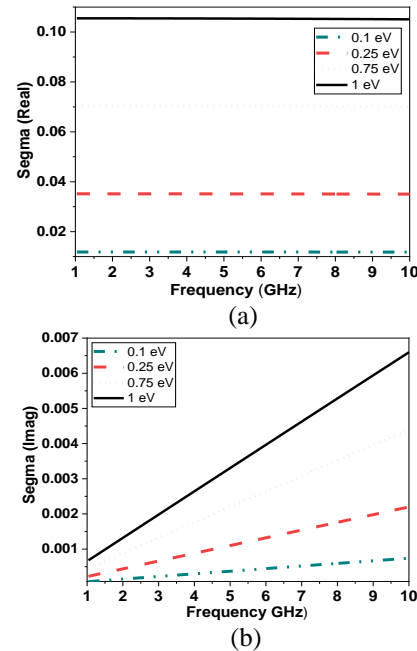


Fig. 5. The conductivity with frequency of the graphene at different bias voltage: (a) real and (b) imaginary part.

It can be deduced that the proposed array exhibits the ability to operate at most of 4G wireless communications and lower band of 5G frequency bands with increased gain and wider operating bandwidth by using single substrate. In addition to the simplicity of the array fabrication process.

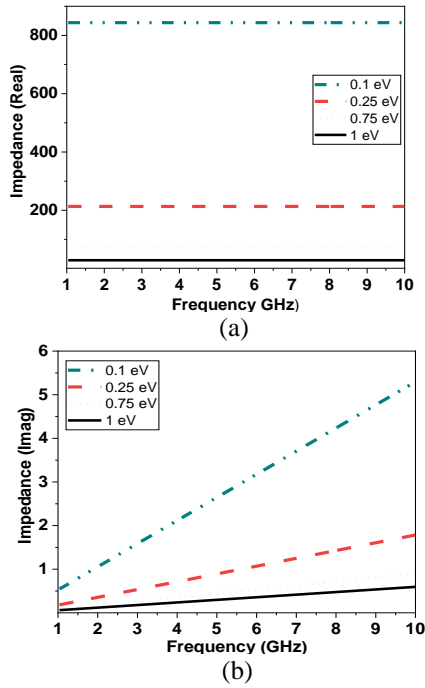


Fig. 6. The impedance with frequency of the graphene at different bias voltage: (a) real and (b) imaginary part.

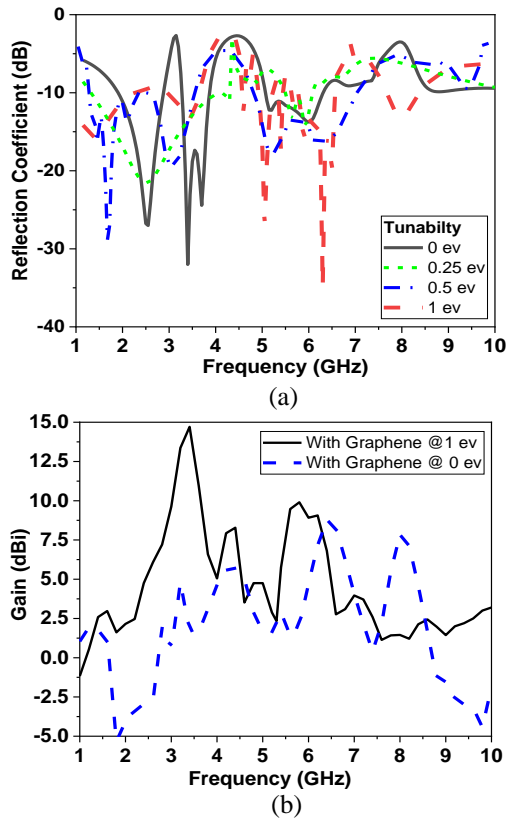


Fig. 7. Design procedures of the proposed array antenna with different graphene DC bias: (a) $|S_{11}|$ and (b) gain.

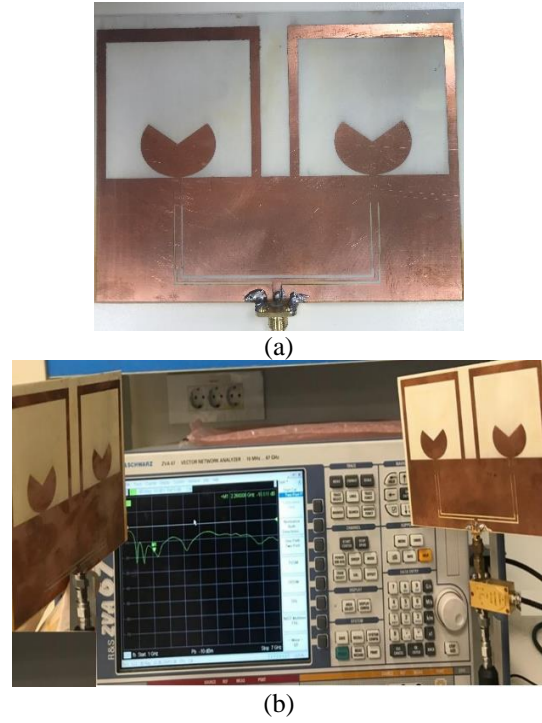


Fig. 8. Fabricated of RSAA: (a) photo of fabricated array and (b) setup measurement.

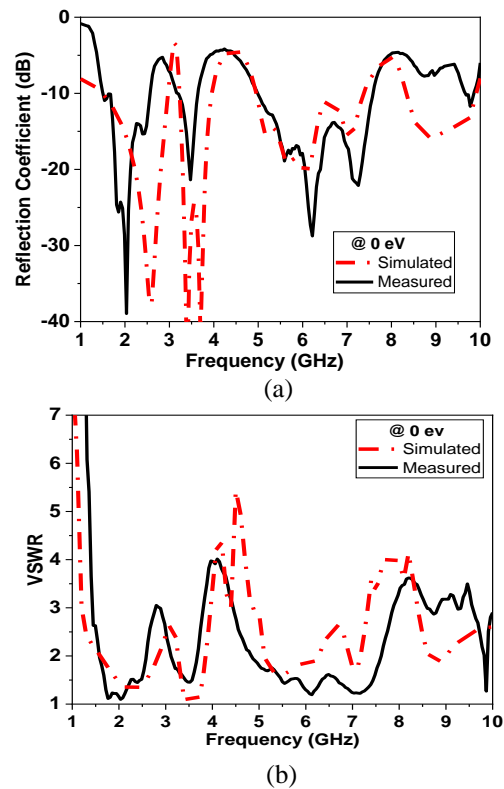


Fig. 9. The comparison between simulated and measured of RSAA at 0 Volt (a) $|S_{11}|$ and (b) VSWR.

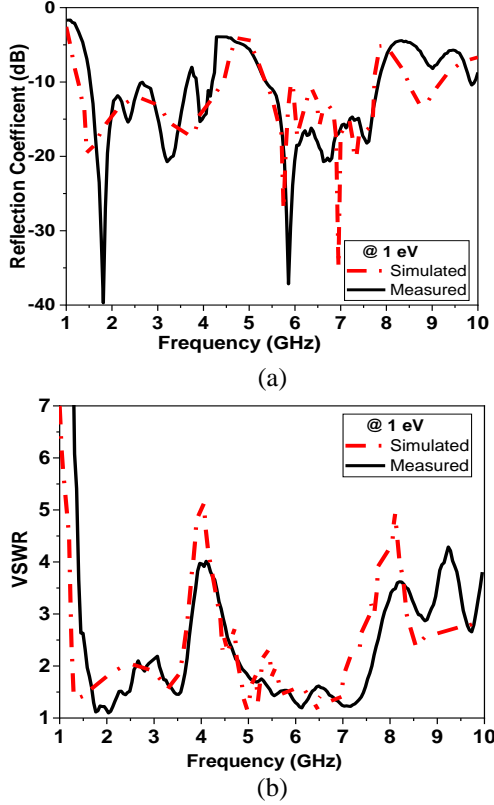
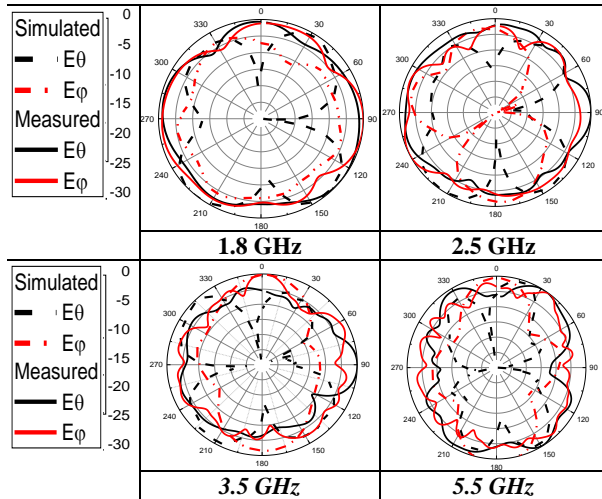


Fig. 10. The comparison between simulated and measured of RSAA at 20 Volt: (a) $|S_{11}|$ and (b) VSWR.

Table 2: Normalized simulated and measured radiation pattern E_θ and E_ϕ for the proposed 2×1 antenna array prototypes



V. RSAA APPLICATIONS

A. Group delay

Group delay is the serious parameter of design

UWB antenna for wireless communications since it could control the distortion of the transmitted pulses. The definition of the group delay is as the derivative with respect to frequency of the phase coupling between two identical UWB antennas $|S_{21}|$ [34-38]:

$$\tau = -\frac{\Delta\phi}{\Delta\omega} = -\frac{1}{360^\circ} \frac{d\phi(f)}{df} \tag{4}$$

The group delay should be close to a constant within the operation bands for perfect pulse transmission to obtain the phase linearity of the transmitted signals in the far field. The two antennas were aligned, and placed face to face orientation with separation distance greater than far field of the lowering operation bands as shown in Fig. 11 (a). The comparison results of $|S_{21}|$ for both measured and simulated HFSS results are shown in Fig. 11. Figure 11 (b) shows that the proposed antenna has perfect performance in this aspect and the group delay over the operating UWB band is less than 1 ns and the group delay and the magnitude transfer function are constant across the whole band except in the notched bands from 4 to 5 GHz. Thus, the proposed array is quite suitable for UWB wireless applications.

B. Object detection

By using face-to-face orientation as shown in Fig. 12 (a) and placement of objects with the same size and different materials as perfect conductor, polyethylene, and water in the far-field region, the magnitude and the convolution angle of the transmission coefficient $|S_{21}|$ between both rectangular slot antenna arrays are changed and they are plotted in Fig. 12 (b) and 12 (c). It is illustrated that the maximum transmission is achieved when the perfect conductor is placed. However, it gives a less commutative angle. On the other side the water produces highest transmission at 4.5 GHz and less transmission at frequency start from 6.5 GHz with largest commutative angle. Figure 13 shows the measured transmission coefficient magnitude and phase with three different objectives (perfect conductor, polyethylene and water) and compared with free space result.

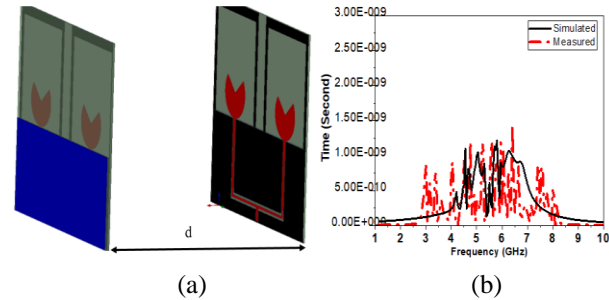


Fig. 11. Comparison between measured and simulated group delay of proposed 2×1 array antenna.

Table 3: Comparison with other reported 2×1 SR antenna arrays

| Ref. Parameters | [36] | [37] | [38] | [39] | This Work |
|---|--------------------|-----------------|-----------------|------------------|----------------------|
| Bandwidth (GHz) | 2—3.2 | 5.75—6.15 | 2.35—2.45 | 2.38—2.41 | 1.5—4 and 5—7 |
| Array gain (dBi) | 6.113 @ 2.65 GHz | 10.77 @ 5.8 GHz | 9.24 @ 2.4 GHz | 9.22 @ 2.4 GHz | 15 @ 3.5 GHz |
| Group delay | NM | NM | NM | NM | Less than 1 ns |
| No. of substrates | One | Two | One | One | One |
| Fabrication complexity | Simple | Complex | Simple | Simple | Simple |
| Feeding network | CPW | Microstrip | Microstrip | Microstrip | CPW |
| Tunability | Yes | No | No | No | Yes |
| Tuning mechanism | Graphene sheet | No | No | No | Graphene sheet layer |
| Object detection capability | No | No | No | No | Yes |
| Circuit size (mm ³) | 101.88×77.64×0.813 | 130×80×1.53 | 180×140×1.6 | 110.5×83×1.56 | 115×101×0.8 |
| Circuit size (λ_0) ³ | 0.9×0.68×0.007 | 2.51×1.54×0.03 | 1.44×1.12×0.013 | 0.88×0.66×0.0125 | 0.7×0.8×0.0064 |

NM: Not mention in the reference paper.

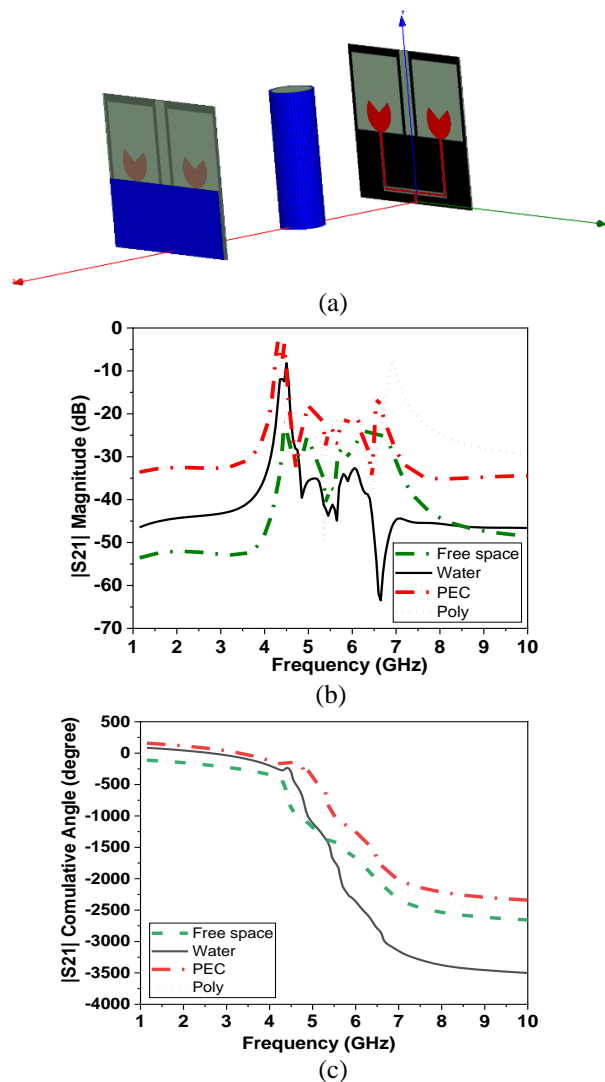


Fig. 12. (a) Simulated proposed array antenna detection system, (b) the $|S_{21}|$ transmission coefficient parameter magnitude, and (c) Phase commutative angle.

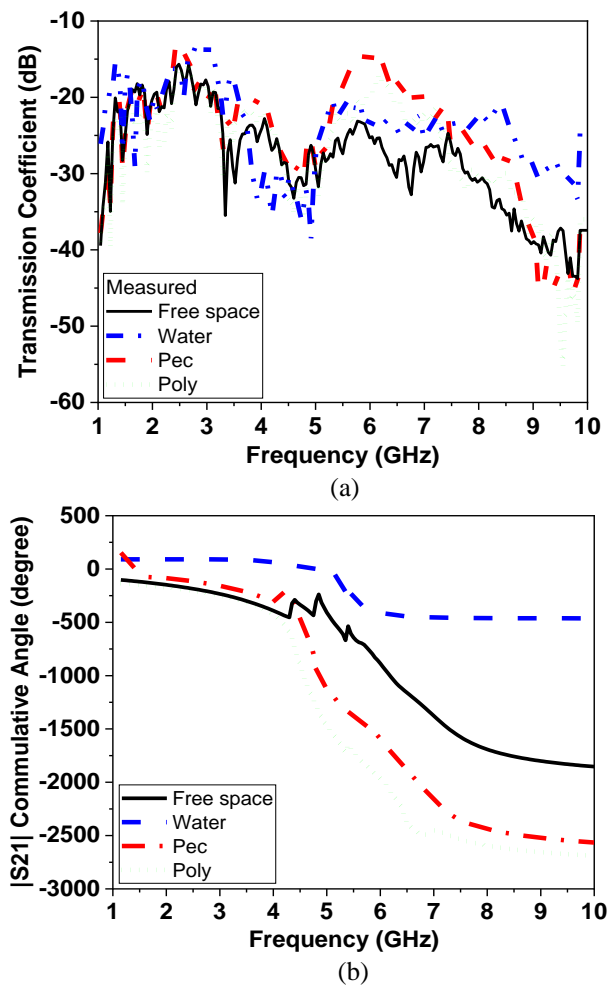


Fig. 13. Measured proposed array: (a) transmission coefficient magnitude, and (b) phase commutative angle.

VI. CONCLUSION

A CPW rectangular slot 2×1 antenna array is presented in this paper with a frequency range extending

from 1.7 to 2.5 GHz, 3.3 to 3.5 GHz, and from 5.5 to 5.8 GHz with an average gain of about 7.5 dBi over the operating bands. Graphene sheet layer was added on the other substrate side under the 2×1 rectangular slot array feeding network to realize reconfigurable frequency operation by changing the DC bias of the graphene layer. The lower band of 5G and other wireless communication bands. The operating frequency range extends from 1.5 to 3.5 GHz at the 4G bands and from 5 to 7 GHz at the lower band of 5G. The proposed antenna array acquires Omni-directional radiation pattern and improved gain values of 15 dBi by applying a 20 V bias voltage on the graphene layer. Experimental results have shown a range of reconfigurable and good agreement with the simulated results. The group delay of the proposed array is also studied with calculated values less than 1ns over the operating band. Moreover, the proposed array could be used to detect objects and to differentiate between different materials.

REFERENCES

- [1] M. Nejatijahromi, M. Rahman, and M. Naghshvarianjahromi, "Continuously tunable WiMAX band-notched UWB antenna with fixed WLAN notched band," *Progress Electromagnet. Res. Lett.*, vol. 75, pp. 97-103, 2018.
- [2] T. Li, H. Zhai, X. Wang, L. Li, and C. Liang, "Frequency reconfigurable bow-tie antenna for bluetooth, WiMAX, WLAN applications," *IEEE Antennas Wirel. Propag. Lett.*, vol. 14, pp. 171-4, 2015.
- [3] B. Zhang, K. Song, B. Xu, Z. Luo, and B. Hu, "Compact reconfigurable bandpass filter with wide frequency tuning range," *Electromagnetics*, vol. 39, no. 2, pp. 89-98, 2019.
- [4] A. A. Ibrahim, H. A. Mohamed, and W. A. E. Ali, "Tunable dual/triple band-pass filter based on stub-loaded resonators for wireless applications," *J. Instrum.*, vol. 12, no. 4, p. 04003, 2017.
- [5] A. Boutejdar, A. A. Ibrahim, and W. A. E. Ali, "Design of compact size and tunable band pass filter for WLAN applications," *Electron. Lett.*, vol. 52, no. 24, pp. 1996-7, 2016.
- [6] M. Peter and D. DiFilippo, "Multifunction RF systems for naval platforms," *Sensors*, vol. 18, 2018.
- [7] X. Huang, T. Leng, J. C. Chen, K. H. Chang, and Z. Hu, "Shielding effectiveness of screen printed graphene laminate at C band," *EuCAP'2016*, Davos, Switzerland, 2016.
- [8] H. A. Atallah, A. B. Abdel-Rahman, K. Yoshitomi and R. K. Pokharel, "Design of miniaturized reconfigurable slot antenna using varactor diodes for cognitive radio systems," in *Proceedings of the Fourth International Japan-Egypt Conference on Electronics, Communications and Computers (JEC-ECC)*, Cairo, pp. 63-66, 2016.
- [9] Y. Abdulraheem, G. Oguntala, A. Abdullah, H. Mohammed, R. Ali, R. Abd-Alhameed, and J. Noras, "Design of frequency reconfigurable multiband compact antenna using two PIN diodes for WLAN/WiMAX applications," *IET Microwaves, Antennas & Propagation*, vol. 11, no. 8, pp. 1098-1105, 2017.
- [10] V. Kumar, D. R. Jahagirdar, A. Basu, and S. K. Koul, "Intra-band frequency reconfigurable antenna using RF MEMS technology," in *Proceedings of the IEEE MTTT International Microwave and RF Conference*, New Delhi, pp. 1-4, 2013.
- [11] J. M. Floc'h and I. Ben Trad, "Printed planar double inverted-F antenna with large frequency reconfigurability range," in *Proceedings of the European Radar Conference (EURAD)*, Nuremberg, pp. 441-444, 2017.
- [12] X. I. Yang, J. C. Lin, G. Chen, and F. L. Kong, "Frequency reconfigurable antenna for wireless communications using GaAs FET switch," *IEEE Antennas and Wireless Propagation Letters*, vol. 14, pp. 807-810, 2015.
- [13] T. Leng, X. Huang, K. Chang, J. Chen, M. A. Abdalla, and Z. Hu, "Graphene nanoflakes printed flexible meanderedline dipole antenna on paper substrate for low-cost RFID and sensing applications," *IEEE Antennas Wireless Propag. Lett.*, vol. 15, pp. 1565-8, 2016.
- [14] X. Huang, Z. Hu, and P. Liu, "Graphene based tunable fractal Hilbert curve array broadband radar absorbing screen for radar cross section reduction," *AIP. Adv.*, vol. 4, no. 11, p. 117103, 2014.
- [15] G. W. Hanson, "Dyadic Green's functions for an anisotropic, non-local model of biased graphene," *IEEE Trans. Antennas Propag.*, vol. 56, no. 3, pp. 747-57, 2008.
- [16] D. Elsheakh "Reconfigurable frequency and steerable beam of monopole antenna based on graphene pads," *International Journal of RF and Microwave Computer-Aided Engineering*, vol. 30, Feb. 2020.
- [17] J. Jin, Z. Cheng, J. Chen, T. Zhou, C. Wu, and C. Xu, "Reconfigurable terahertz Vivaldi antenna based on a hybrid graphene-metal structure," *International Journal of RF and Microwave Computer-Aided Engineering*, vol. 30, Dec. 2020.
- [18] S. K. Yadav, A. Kaur, and R. Khanna, "An ultra-wideband "OM" shaped DRA with a defected ground structure and dual polarization properties for 4G/5G wireless communications," *International Journal of RF and Microwave Computer-Aided Engineering*, vol. 30, 2020.
- [19] J. Zhang, Z. Liu, W. Lu, H. Chen, B. Wu, and Q. Liu, "A low profile tunable microwave absorber based on graphene sandwich structure and high impedance surface," vol. 30, 2020.

- [20] X. Zhou, J. Le Kernec, and D. Gray, "Vivaldi antenna for railway cutting monitoring," *2016 CIE International Conference on Radar (RADAR)*, Guangzhou, pp. 1-5, 2016.
- [21] G. W. Hanson, "Dyadic Green's functions for an anisotropic, non-local model of biased graphene," *IEEE Trans. on Antennas Propag.*, vol. 56, no. 3, pp. 747-757, 2008.
- [22] D. Elsheakh, and E. Abdallah, "Ultra-wide-bandwidth (UWB) microstrip monopole antenna using split ring resonator (SRR) structure," *International Journal of Microwave and Wireless Technologies*, vol. 10, no. 1, pp. 123-132.
- [23] A. A. A. Aziz, M. A. Abdalla, and A. A. Ibrahim, "Enhanced gain tunable two elements antenna array based on graphene," *2018 IEEE International Symposium on Antennas and Propagation & USNC/URSI National Radio Science Meeting*, Boston, MA, pp. 471-472, 2018.
- [24] E. S. Angelopoulos, A. Z. Anastopoulos, D. I. Kaklamani, A. A. Alexandridis, F. Lazarakis, and K. Dangakis, "Circular and elliptical CPW-fed slot and Microstrip-Fed antennas for ultrawideband applications," in *IEEE Antennas and Wireless Propagation Letters*, vol. 5, pp. 294-297, 2006.
- [25] Q. Ayn, P. A. Nageswar Rao, and P. Mallikarjuna Rao, "Design and analysis of high gain 2x1, 4x1, 8x1 and 8x8 circular patch antenna arrays for 2.4 GHz applications," *International Journal of Innovative Research in Science, Engineering and Technology*, vol. 6, no. 8, Aug. 2017.
- [26] M. Niamien, S. Collardey, A. Sharaiha, and K. Mahdjoubi, "An electrically small frequency reconfigurable antenna for DVB-H," *IEEE Int. Workshop Antenna Technol.*, p. 245248, 2012.
- [27] S. Wu, D. Zha, Y. He, L. Miao, and J. Jiang, "Design of a tunable absorber based on graphene in the THz range," *2019 IEEE International Conference on Computational Electromagnetics (ICCEM)*, Shanghai, China, pp. 1-3, 2019.
- [28] C. Fan, B. Wu, Y. Hu, Y. Zhao, and T. Su, "Millimeter-wave pattern reconfigurable Vivaldi antenna using tunable resistor based on graphene," in *IEEE Transactions on Antennas and Propagation*, vol. 68, no. 6, pp. 4939-4943, June 2020.
- [29] www.ansys.com
- [30] A. Q. Zhang, Z. G. Liu, L. Wei-Bing, and H. Chen, "Graphene-based dynamically tunable attenuator on a coplanar waveguide or a slotline," *IEEE Trans. Microw. Theory Techn.*, vol. 67, no. 1, pp. 70-77, Jan. 2019.
- [31] A. K. Geim and K. S. Novoselov, "The rise of graphene," *Nat. Mater.*, vol. 6, pp. 183-91, 2007.
- [32] L. H. Jui, L. Yinying, D. Huilian, S. Poman, and B. Jens, "Time-domain modelling of group-delay and amplitude characteristics in ultra-wideband printed-circuit antennas," 10.1007/978-3-540-68768-9_19, 2008.
- [33] D. Zhao, C. Yang, M. Zhu, and Z. Chen, "Design of WLAN/LTE/UWB antenna with improved pattern uniformity using ground-cooperative radiating structure," in *IEEE Transactions on Antennas and Propagation*, vol. 64, no. 1, pp. 271-276, Jan. 2016.
- [34] J. Wu, Z. Zhao, Z. Nie, and Q. Liu, "A printed UWB Vivaldi antenna using stepped connection structure between slot line and tapered patches," in *IEEE Antennas and Wireless Propagation Letters*, vol. 13, pp. 698-701, 2014.
- [35] <https://www.sciencedirect.com/topics/computer-science/shannon-sampling-theorem>
- [36] A. A. A. Aziz, M. A. Abdalla, and A. A. Ibrahim, "Enhanced gain tunable two elements antenna array based on graphene," *2018 IEEE International Symposium on Antennas and Propagation & USNC/URSI National Radio Science Meeting*, Boston, MA, USA, pp. 471-472, 2018.
- [37] N. Husna, M. A. Jamlos, W. A. Mustafa, and S. Z. S. Idrus, "High gain of 2x1 simulated circularly polarized rectangular microstrip patch array antenna," *International Conference on Technology, Engineering and Sciences (ICTES)*, pp. 1-6, 2020.
- [38] A. B. Obot, G. A. Igwe, and K. M. Udofia, "Design and simulation of rectangular microstrip antenna arrays for improved gain performance," *International Journal of Networks and Communications*, vol. 9, no. 2, pp. 73-81, 2019.
- [39] A. El Alami, Y. Ghzaoui, S. Das, S. D. Bennani, and M. El Ghzaoui, "Design and simulation of RFID array antenna 2x1 for detection system of objects or living things in motion," *International Workshop on Microwave Engineering, Communications Systems and Technologies (MECST)*, Leuven, Belgium, pp. 1010-1015, 2019.

Improved Thevenin Equivalent Model of MMC Considering Pre-charge Conditions and DC Side Fault Conditions

Enshu Jin¹, Zhenyu Song¹, Xiaofan Yang², and Xin Yu²

¹ School of Electrical Engineering
Northeast Electric Power University, 169 Changchun Road, Jilin, 132000, China
413115183@qq.com

² State Grid Jiangsu Electric Power Co., Ltd.
Yancheng Dafeng District Power Supply Branch, Yancheng, 224000, China
715103343@qq.com

Abstract — The traditional Thevenin equivalent Modular Multilevel Converter (MMC) model has poor versatility for the two working conditions of pre-charging and DC-side faults. In this paper, an improved Thevenin equivalent MMC model considering pre-charge conditions and DC side fault conditions is proposed. The model divides the pre-charging condition into a Controllable charging stage and an Uncontrollable charging stage. The DC-side fault condition is divided into the pre-blocking and post-blocking conditions of the converter. The circuit characteristics are analyzed, and the equivalent model topology is comprehensively improved to make it suitable for full-condition simulation, and a control strategy suitable for the equivalent model is proposed. The detailed model and the proposed improved equivalent model were built in PSCAD/EMTDC for comparison and analysis. The simulation results show that the improved equivalent model can be applied to various working conditions, and the versatility of the traditional Thevenin equivalent model is improved.

Index Terms — Converter, electromagnetic transient simulation, improved Thevenin equivalent model, Modular Multilevel Converter (MMC).

I. INTRODUCTION

With the development of modular multilevel converter-based high-voltage direct-current systems (MMC-HVDCs) towards being multi-terminal, high-voltage, and high-power, the number of sub-modules required for MMC bridge arms has increased rapidly. Taking the Dalian Flexible HVDC Transmission Demonstration Project that was put into operation in 2013 as an example, a single bridge arm contains 420 sub-modules (a two-terminal system has 5040 sub-modules). When conducting electromagnetic transient simulations of such a large-scale MMC system, it is necessary to repeatedly invert an ultra-high-order

matrix, which makes these simulations extremely slow. Therefore, the traditional detailed MMC electromagnetic transient model is not suitable for the simulation of large-scale MMC-HVDC systems [1–2]. Directly adopting the method of reducing the order of the complex circuit [3] to reduce the order of the detailed model will shorten the simulation time to a certain extent, but the speed-up effect is not good.

In response to the above problems, the establishment of equivalent electromagnetic transient models has gradually become a popular research topic [4]. Among these models, the average-value model [5–13] and the Thevenin equivalent model [1,14–19] are the most widely used. However, the average-value model omits the capacitor voltage balance control module and the circulating current suppression module, so it cannot be used to study the capacitor voltage balance control algorithm or the circulating current suppression strategy [19]. The Thevenin equivalent model has the advantage of being able to inversely resolve the capacitor current and voltage values of the sub-modules while ensuring the accuracy of the simulation. It is therefore used by many electromagnetic transient simulation software packages.

There have been many studies on Thevenin's equivalence. Reference [1] established the equivalent mathematical model of the MMC sub-module based on the Thevenin equivalence theorem. Reference [14] proposed a fast simulation model based on the Dommel equivalent values of capacitance and inductance components, which is only suitable for the normal working conditions of an MMC and not for pre-charging conditions or DC-side fault conditions. In Ref. [15], the insulated-gate bipolar transistor (IGBT) is equivalent, and the sub-module mathematical model under Thevenin's equivalent theorem is constructed; this model has the same shortcomings as the model proposed in Ref. [14], and it has poor versatility. Reference [16] proposed a model based on numerical calculations and a controlled

voltage source; this model involves detailed numerical calculations, but it requires the establishment of a complex mathematical model to solve the internal parameters of the sub-modules under each fault state, meaning its solution is extremely complicated and unfeasible. Reference [17] proposed a general Thevenin parameter for a single-port sub-module MMC. The calculation method in this report unifies the Thevenin parameter solution process and verifies this based on an MMC with a double half-bridge topology; it has a certain versatility, but it does not give a detailed description of the process of the bridge arm when considering lock-up. Reference [18] extended this general equivalent method to a dual-port sub-module MMC on the basis of Ref. [17], and Ref. [19] further proposed a multi-port method based on Refs. [17] and [18] to produce a general realization method for equivalent models of MMC topology.

The existing Thevenin model still has the shortcoming of poor versatility, and this article will focus on this problem. The specific contributions of this paper include:

1. An analysis of the circuit characteristics of the converter under pre-charge conditions and DC-side fault conditions. Establishing the reason for the poor versatility of the existing Thevenin equivalent model based on the circuit characteristics under these two working conditions. In response to the above problems, improving the equivalent models under these two working conditions.
2. Combining the improved equivalent model under the two working conditions with the traditional Thevenin equivalent model and proposing an equivalent model suitable for full-condition simulations, along with a suitable control strategy.

The remainder of this paper is arranged as follows.

Section 2 introduces the traditional Thevenin equivalent model. In Section 3, the circuit characteristics under pre-charge and DC-side fault conditions are analyzed, and the equivalent models under these two conditions are improved. Section 4 integrates the improved equivalent model into the traditional Thevenin equivalent model, and Section 5 presents a verification of the accuracy and speed of the improved simulation model. Finally, conclusions are summarized in Section 6.

II. TRADITIONAL THEVENIN EQUIVALENT MODEL

Figure 1 shows the half-bridge MMC topology. Each phase is divided into upper and lower bridge arms. These bridge arms are composed of the bridge-arm reactors L_0 and N half-bridge sub-modules (HBSMs) in series. To reduce the number of nodes contained in the bridge-arm unit, an adjoint circuit of MMC is established which is shown in Fig. 2. The values of the equivalent

resistances R_1 and R_2 of the switching tube branch can be determined according to the IGBT trigger signals TS_1 and TS_2 at time t . The corresponding relationship between the trigger signal state and the value of the equivalent resistance of the switching tube branch is shown in Table 1. As shown, R_{ON}/R_{OFF} represents the ON/OFF resistance of the IGBT and the diode. In PSCAD/EMTDC, the R_{ON} resistance value is generally set to 0.01Ω , and the R_{OFF} resistance value is $10^6\Omega$.

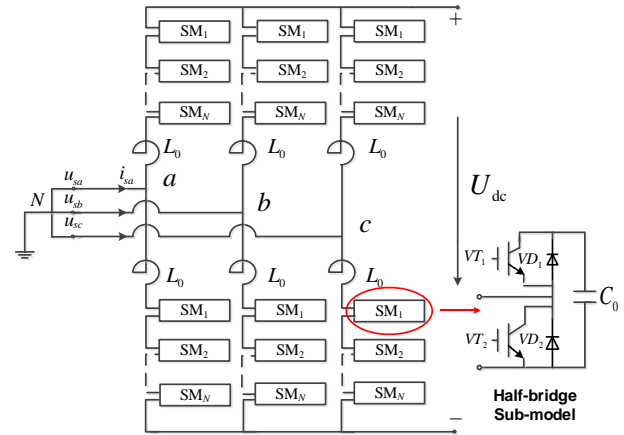


Fig. 1. A MMC and its half-bridge sub-module topology.

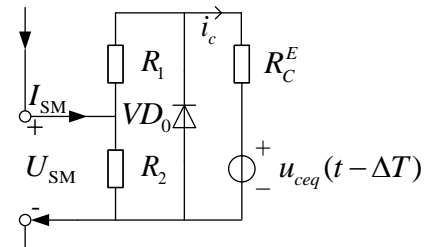


Fig. 2. The adjoint circuit of MMC.

Table 1: Relationship between equivalent resistance of switch tube branch and trigger signal

| | Trigger Signal | Switch Tube Branch Equivalent Resistance |
|----------|----------------|--|
| Put into | $TS_1=1$ | $R_1=R_{ON}$ |
| | $TS_2=0$ | $R_2=R_{OFF}$ |
| Cut off | $TS_1=0$ | $R_1=R_{OFF}$ |
| | $TS_2=1$ | $R_2=R_{ON}$ |

Then a Thevenin equivalent model of a single sub-module based on the backward Euler method is established, as shown in Fig. 3 (a), where $R_{smeq}(t)$ is the Thevenin equivalent resistance of the sub-module at time t , as shown in Eq. (1), $U_{smeq}(t)$ is the Thevenin equivalent voltage source at time t , as shown in Eq. (2), and $i_c(t)$ is the current flowing through the sub-module at time t :

$$R_{smeq}(t) = \begin{cases} \frac{(R_{ON} + R_C^E) \cdot R_{OFF}}{R_{ON} + R_{OFF} + R_C^E} & \text{put into} \\ \frac{(R_{OFF} + R_C^E) \cdot R_{ON}}{R_{ON} + R_{OFF} + R_C^E} & \text{cut off} \end{cases}, \quad (1)$$

$$U_{smeq}(t) = \begin{cases} \frac{u_{ceq}(t - \Delta T) \cdot R_{OFF}}{R_{ON} + R_{OFF} + R_C^E} & \text{put into} \\ \frac{u_{ceq}(t - \Delta T) \cdot R_{ON}}{R_{ON} + R_{OFF} + R_C^E} & \text{cut off} \end{cases}, \quad (2)$$

where R_C^E is the transient equivalent resistance based on the backward Euler method, and ΔT is the simulation step length, $u_{ceq_i}(t - \Delta T)$ is the equivalent historical voltage source of the capacitor of the sub-module.

Since the turn-off resistance R_{off} of the switch tube group is several orders of magnitude larger than the turn-on resistance R_{on} , to reduce the time for each step updating and calculating the inverse solution during simulation, it is assumed that the turn-off resistance is infinite. Calculate the limit of Eq. (1) and Eq. (2) when R_{off} tends to infinity, which can be simplified as Eq. (3) and Eq. (4):

$$R_{smeq}(t) = \begin{cases} R_{ON} + R_C^E & \text{put into} \\ R_{ON} & \text{cut off} \end{cases}, \quad (3)$$

$$U_{smeq}(t) = \begin{cases} u_{ceq}(t - \Delta T) & \text{put into} \\ 0 & \text{cut off} \end{cases}. \quad (4)$$

All the sub-modules on the bridge arm are then superimposed in series to obtain the equivalent model of the traditional MMC bridge arm, as shown in Fig. 3 (b).

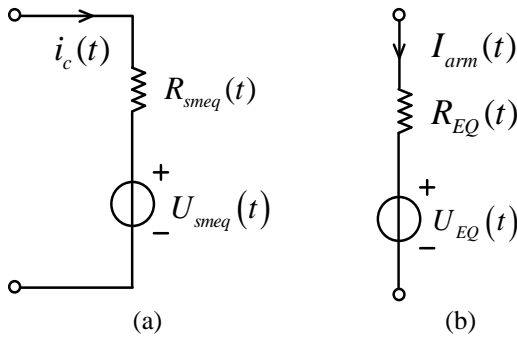


Fig. 3. Thevenin equivalent model of traditional MMC bridge arm, showing (a) sub-module model and (b) bridge-arm model.

In Fig. 3 (b), according to Eq. (3), the equivalent resistance can be obtained using:

$$R_{EQ}(t) = N \cdot R_{on} + n(t) \cdot R_C^E, \quad (5)$$

where $n(t)$ is the number of sub-modules put into at time t , and N is the total number of sub-modules.

And according to Eq. (4), the equivalent voltage

source can be calculated from:

$$U_{EQ}(t) = \sum_{i=1}^n u_{ceq_i}(t - \Delta T). \quad (6)$$

III. IMPROVED THEVENIN EQUIVALENT MODEL

In the traditional Thevenin equivalent model, IGBTs and diodes are not distinguished, and they are treated as switch groups and replaced by variable resistors. Therefore, the traditional Thevenin equivalent model cannot accurately simulate the converter block conditions [20]. The converter will enter a blocked state under pre-charging conditions or DC-side fault conditions. This section will start with these two conditions to improve the traditional Thevenin equivalent model.

A. Pre-charging conditions

Pre-charging of an MMC can be divided into two stages: uncontrollable charging and controllable charging. In the MMC controllable charging stage, the IGBT trigger signal is no longer blocked, and the capacitor can be charged and discharged strategically. At such a time, its equivalent model is consistent with the traditional Thevenin equivalent model, and this will not be repeated here. Here, only the Thevenin equivalent model of the uncontrollable charging stage is improved.

After the converter is blocked during the uncontrollable charging stage, the IGBT is no longer triggered. Figure 4 shows the current-flow path of the MMC bridge arm in the uncontrollable charging stage. It can be seen from the figure that the current only flows through the diodes in the sub-module; the N sub-modules in the same bridge arm that are put into or cut off at the same time are determined by the direction of the bridge-arm current (natural commutation law). At this time, the MMC enters the uncontrollable rectification mode. If the switching time and state variables of this uncontrollable natural turn-off device are not interpolated, then the numerical calculation will produce errors [21]. The accuracy of the traditional Thevenin equivalent model is therefore reduced.

Based on the above analysis, considering the converter structure under the blocking condition, the equivalent model of an HBSM in the uncontrollable charging stage is shown in Fig. 5. First, the Dommel equivalent of the capacitor C_0 is established from an equivalent voltage source and a resistor in series.

The bridge arms are then equalized. Since multiple sub-modules are connected in series on one bridge arm, the bridge arms are equivalent to connecting the equivalent models of their sub-modules in series. Therefore, the improved Thevenin equivalent model of the uncontrollable charging stage can be further established as shown in Fig. 6.

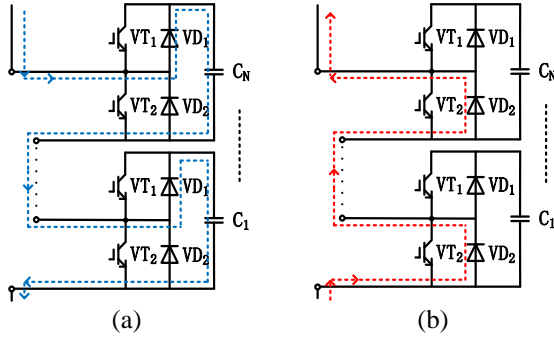


Fig. 4. Current path of MMC bridge arm in the uncontrollable charging stage when (a) $I_{arm}(t) > 0$, and (b) $I_{arm}(t) < 0$.

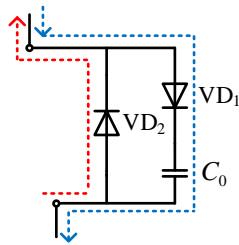


Fig. 5. HBSM Current path of MMC bridge arm in the uncontrollable charging stage.

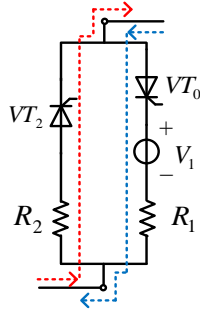


Fig. 6. MMC improved Thevenin equivalent model of the uncontrollable charging stage.

During the uncontrollable charging stage, the controllers VT_0 and VT_2 in the improved Thevenin equivalent model are triggered at the same time. The VT_0 branch provides the bridge-arm charging current path, while the VT_2 branch provides a bypass current path. The current is changed due to the uncontrollable charging stage. The phase law is different and flows through the VT_0 or VT_2 branch.

The value of voltage source V_1 in the equivalent model is:

$$V_1(t) = \sum_{i=1}^N u_{ceq_i}(t - \Delta T), \quad (7)$$

the value of the series resistance element R_1 of the VT_0 branch is:

$$R_1 = N \cdot (R_{on} + R_C^E), \quad (8)$$

and the value of the series resistance element R_2 of the VT_2 branch is:

$$R_2 = N \cdot R_{on}. \quad (9)$$

B. DC-side fault conditions

In the event of DC-side faults such as single-pole grounding faults and inter-pole short-circuit faults, the MMC can divide the DC-side faults into two stages according to the time scale before and after the converter is blocked due to the time delay of the fault block. The electrical characteristics of the two stages before and after the converter is blocked are different, and the MMC bridge-arm models of the two are also different. Therefore, this section will establish the improved Thevenin equivalent models of the two respective stages.

a. Before the converter is blocked

Each bridge arm of the MMC contains N HBSMs. Before the converter is blocked, each bridge arm still normally switches the sub-modules according to the modulation mode. Suppose n HBSMs are in the on state and $(N - n)$ HBSMs are in the off state; the capacitors of the n on-state sub-modules will bear the DC-side voltage before the converter is blocked. When the capacitors of the n on-state sub-modules are discharged, the discharge current is provided to the short-circuit point through the IGBT devices VT_1 of the n on-state sub-modules and the diodes VD_2 of the $(N - n)$ off-state sub-modules. While the capacitor discharge current is formed, the AC system feeds current through the bridge arm. However, this part of the current is usually negligible before blocking, so this stage is mainly dominated by the capacitor discharge process, and before the converter is blocked, the sub-modules of the bridge arm are switched normally according to the modulation strategy. The MMC bridge-arm model is shown in Fig. 7 (a), and the improved Thevenin equivalent model of the bridge arm before the converter is blocked, as shown in Fig. 7 (b), can be obtained. Here, VT_1 provides a capacitor discharge path. The assignments of the resistance element R_1 and the voltage source V_1 are shown in Eqs. (5) and (6).

b. After the converter is blocked

After the converter is blocked, the capacitor discharge current disappears, and only the AC feed current flows in the bridge arm. The AC feed current path in the bridge arm is shown in Fig. 8 (a), and this flows through all the HBSM diode VD_2 branches in the bridge arm. The improved Thevenin equivalent model after the converter is blocked is shown in Fig. 8 (b). Here, VT_2 triggers to provide an AC feed current path, and the series resistance R_2 of the VT_2 branch is shown in Eq. (9).

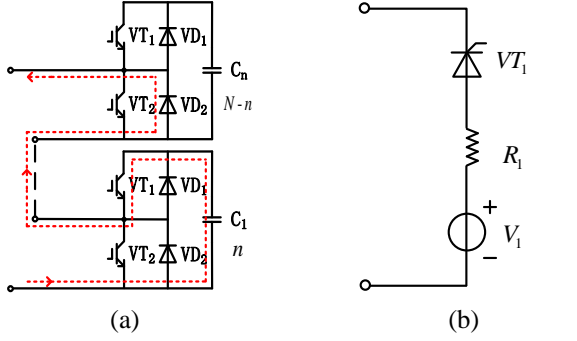


Fig. 7. Equivalent values of MMC bridge arm before converter is blocked, showing (a) capacitor discharge current path, and (b) improved bridge-arm model.

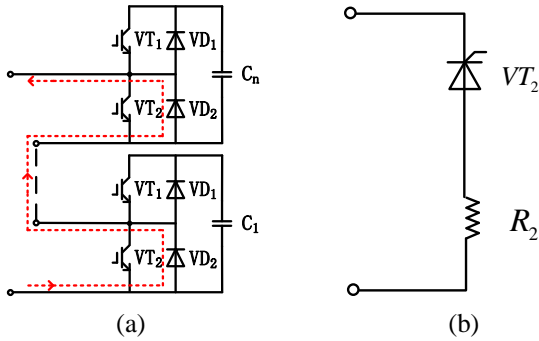


Fig. 8. Equivalent MMC bridge arm after converter is blocked, showing (a) AC feed current path, and (b) improved Thevenin equivalent model.

IV. IMPROVED THEVENIN EQUIVALENT MODEL OF MMC CONSIDERING PRE-CHARGE CONDITIONS AND DC SIDE FAULT CONDITIONS

A. Improved Thevenin equivalent model and its control strategy

The aforementioned traditional Thevenin equivalent model and the improved Thevenin equivalent model under pre-charge conditions and DC-side fault conditions are combined together, and an improved Thevenin equivalent MMC model considering pre-charge conditions and DC side fault conditions is proposed, as shown in Fig. 9. As shown, the switches k_1 , k_2 and k_3 are assigned different switching states under different working conditions of the converter. When the converter is under different working conditions, the calculation formulas for the variable resistors R_1 and R_2 and the controlled voltage source V_1 will change accordingly. The diodes VD_1 and VD_2 ensure unidirectional current flow, and compared with the use of an IGBT, they have the characteristics of simple control. The assignment method for each part is shown in Table 2 (the switch is on when $k(t) = 1$ and the switch is off when $k(t) = 0$).

In view of the improved Thevenin equivalent MMC model proposed in this section, which has considered pre-charge conditions and DC side fault conditions, a suitable control strategy is proposed as shown in Fig. 10. This control strategy can be applied to various operating conditions of the MMC and has the advantages of strong versatility and simple implementation.

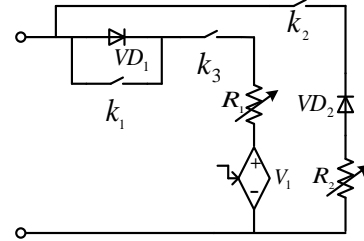


Fig. 9. Improved Thevenin equivalent model of MMC considering pre-charge conditions and DC side fault conditions

Table 2: Assignment method for each part

| | ① | ② | | ⑤ | |
|----------|---------|---------|---------|---------|---------|
| | | ③ | ④ | ⑥ | ⑦ |
| $k_1(t)$ | 1 | 1 | 0 | 1 | 0 |
| $k_2(t)$ | 0 | 0 | 1 | 0 | 1 |
| $k_3(t)$ | 1 | 1 | 1 | 1 | 0 |
| $R_1(t)$ | Eq. (5) | Eq. (5) | Eq. (8) | Eq. (5) | * |
| $R_2(t)$ | * | * | Eq. (9) | * | Eq. (7) |
| $V_1(t)$ | Eq. (6) | Eq. (6) | Eq. (7) | Eq. (6) | * |

Key: ① normal working condition; ② pre-charging condition; ③ controllable charging; ④ uncontrollable charging; ⑤ DC-fault condition; ⑥ before blocking; ⑦ after blocking.

The modulation strategy uses nearest-level approach modulation, and the control flow is as follows:

- 1) At the beginning of the simulation (time $t = 0$), the system simulation step ΔT , the initial running values ($i_c(0) = 0$, $u_c(0) = 0$, and $t = \Delta T$), and the sub-module capacitance C_0 will be given. These values are used to calculate the historical voltage source $u_{ceq}(0) = 0$ and the transient equivalent resistance R_C^E of the capacitor. The switch assignment module assigns values to the switches k_1 , k_2 , and k_3 according to the converter operating conditions.
- 2) The values calculated in the previous step and the conduction state of each sub-module obtained from the sub-module sorting and selection module are input into the bridge-arm assignment calculation module, and then calculate the variable resistance values $R_1(t)$, $R_2(t)$ and the controlled voltage source value $V_1(t)$.

- 3) The bridge-arm current $I_{armj}(t)$ is measured after the variable resistance and the controlled voltage source are assigned, and the bridge-arm current can update the current $i_c(t)$ of each sub-module capacitor using:

$$i_c(t) = \begin{cases} I_{arm}(t) & \text{on} \\ 0 & \text{off} \end{cases}, \quad (10)$$

and the voltage $u_c(t)$ of each sub-module capacitor is then updated.

- 4) The updated current $i_c(t)$ and voltage $u_c(t)$ are used for the next step of calculation, and so on until the end of the simulation.

It should be noted that the sub-module sequence selection module is not put into the control strategy in the Uncontrollable charging stage under the converter pre-charging condition and the post-blocking stage

because at this time all the sub-modules in the bridge arm are blocked.

B. Error-calculation formula

We define the average relative error F_1 as:

$$F_1 = \frac{\sum_{i=M}^N \left| \frac{S_{det}(i) - S_{equ}(i)}{S_{det}(i)} \right|}{N-M+1} \times 100\%, \quad (11)$$

where $S_{det}(i)$ and $S_{equ}(i)$ indicate data from the i -th sampling point of the detailed model and the equivalent model, respectively, and $i = M, \dots, N$. We can then define the maximum relative error F_2 as:

$$F_2 = \max_i \left| \frac{S_{det}(i) - S_{equ}(i)}{S_{det}(i)} \right| \times 100\% \quad i = M, \dots, N. \quad (12)$$

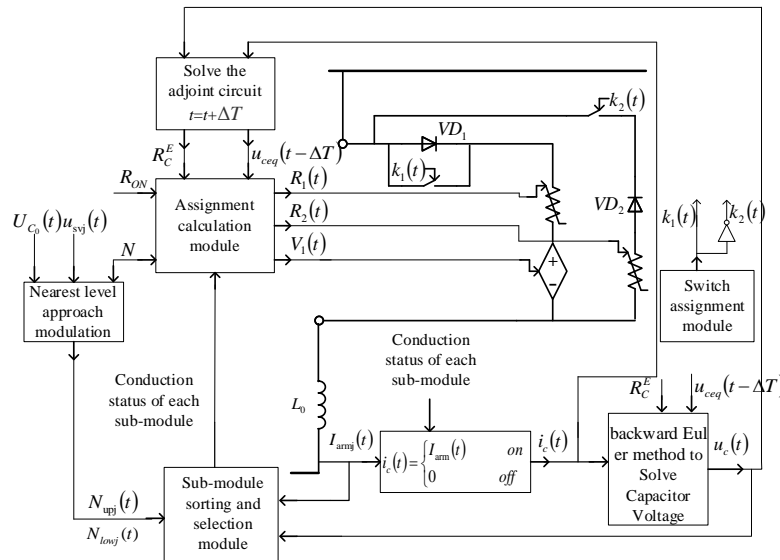


Fig. 10. Control strategy of improved Thevenin equivalent MMC model considering pre-charge conditions and DC side fault conditions.

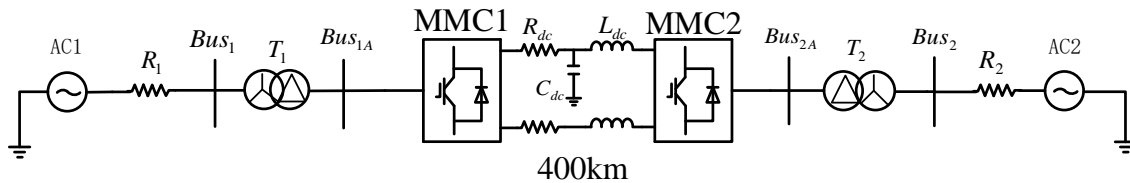


Fig. 11. Diagram of the structure of the simulation system.

V. SIMULATION RESULTS AND ANALYSIS

A double-ended flexible DC-transmission system was built using PSCAD/EMTDC as shown in Fig. 11, where MMC1 and MMC2 are 71-level converters, using detailed models, traditional Thevenin equivalent models, and the improved Thevenin equivalent models proposed in this article. The system parameters are shown in Tables 3–5, and the accuracy and speed of this model are

verified in the subsequent sections.

Table 3: Parameters of transformers

| Transformer1 | Transformer2 |
|-----------------|-----------------|
| S=600MVA | S=600MVA |
| Ratio=230/245kV | Ratio=230/245kV |
| $X_{T1}=15\%$ | $X_{T2}=15\%$ |

Table 4: Parameters of DC system

| | |
|----------|------------------------------|
| DC Cable | $R_{dc}=0.009735 \Omega /km$ |
| | $L_{dc}=0.8489mH/km$ |
| | $C_{dc}=0.01367\mu F/km$ |
| Length | 400km |

Table 5: Parameters of AC system

| | |
|-----------------------|-----------------------|
| AC System1 | AC System2 |
| $V_{BUS1(L-L)}=230kV$ | $V_{BUS2(L-L)}=230kV$ |
| $R_1=1.67 \Omega$ | $R_2=1.67 \Omega$ |
| SCR=2.5 | SCR=2.5 |

A. Normal working conditions

Figure 12 shows the comparison results of the simulation waveforms of the DC-side voltage, converter power, and the current of the phase-A upper bridge based on the detailed MMC model (Red wide dotted line), the traditional Thevenin equivalent model (blue narrow dotted line), and the improved Thevenin equivalent model proposed in this article (green full line) under normal working conditions of MMC1. Since the improved Thevenin equivalent model is the same as the traditional Thevenin equivalent model under normal working conditions, as shown in Fig. 12, the waveforms of the improved Thevenin equivalent model and the traditional Thevenin equivalent model are consistent with the detailed model waveforms. According to Eq. (11), the average relative errors in the DC voltage, converter power, and phase-A upper-arm current based on the improved Thevenin equivalent model are 0.7912%, 0.5631%, and 0.6347%, respectively. This equivalent model therefore has high simulation accuracy.

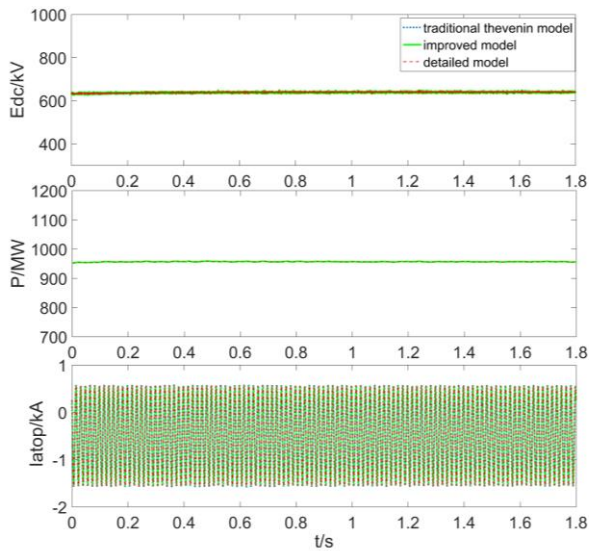


Fig. 12. Simulation comparison results under normal working conditions.

B. Pre-charging conditions

Figure 13 shows the comparison results of the simulation waveforms of the DC-side voltage, converter power, and the current of the phase-A upper bridge on the basis of the detailed model (Red wide dotted line), the traditional Thevenin equivalent model (blue narrow dotted line), and the improved Thevenin equivalent model proposed in this article (green full line) of MMC1 under pre-charging conditions.

It can be seen from Fig. 13 that the traditional Thevenin equivalent model only contains diodes and does not interpolate the switching moments and state variables of this uncontrollable natural turn-off device, resulting in obvious glitches in its waveform compared with the detailed model. According to Eq. (11), the average relative errors of the DC voltage, converter power and phase-A upper-arm current of the traditional Thevenin equivalent model are 0.9872%, 0.9965%, and 1.1254%, respectively, and according to Eq. (12), the maximum relative errors of these three are 4.5123%, 3.9763%, 4.0097%, respectively. The average relative errors in the DC voltage, converter power, and phase-A upper-arm current of the improved Thevenin equivalent model proposed in this article are 0.2214%, 0.2915%, and 0.3123%, respectively, and the maximum relative errors of the three are 0.7234%, 1.2763%, and 1.4547%, respectively. These results are therefore notably closer to the detailed model than the traditional Thevenin equivalent model.

From the above analysis, it can be seen that the improved Thevenin equivalent model has higher simulation accuracy than the traditional Thevenin equivalent model under pre-charging conditions.

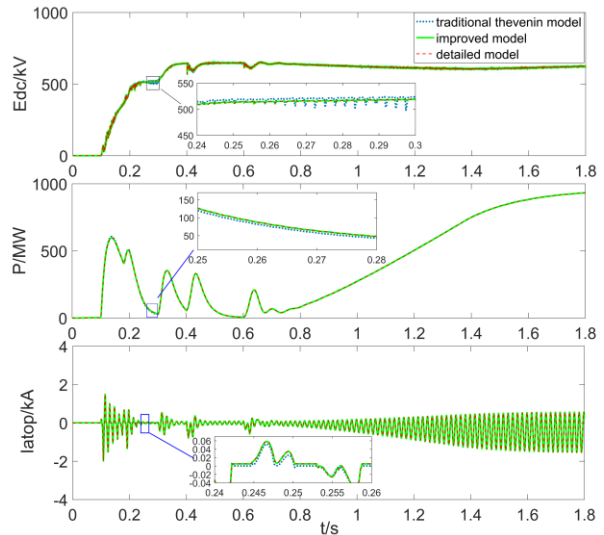


Fig. 13. Simulation comparison results under MMC1 pre-charging conditions.

C. DC-side fault conditions

Figure 14 shows the comparison results of simulation waveforms of the DC-side voltage, converter power, and the current of the phase-A upper bridge based on the detailed model (Red wide dotted line), the traditional Thevenin equivalent model (blue narrow dotted line), and the improved Thevenin equivalent model (green full line) proposed in this article of MMC1 under the condition of a short-circuit fault between the DC-side poles of MMC1.

The occurrence time of the short-circuit fault on the DC side is 0.9 s after the steady state, the fault distance is 0 km to MMC1, the fault is set as a permanent fault, and the system has entered a stable state before the fault occurs. From Eq. (11), the average relative errors of the DC voltage, converter power, and the upper-arm current of phase A of the traditional Thevenin equivalent model are 0.8223%, 0.7146%, and 0.9342%, respectively, and according to Eq. (12), we can get the maximum relative errors of the three as 3.6544%, 1.5643%, and 1.7243%, respectively. The average relative errors of the DC voltage, converter power, and the upper arm current of phase A of the improved Thevenin equivalent model proposed in this article are 0.3231%, 0.6316%, and 0.7667%, respectively, and the maximum relative errors of these three are 0.959%, 0.9261%, and 1.3223%, respectively.

It can be seen from the above data that, compared with the traditional Thevenin equivalent model, the improved Thevenin equivalent model is more consistent with the detailed model and has better simulation accuracy.

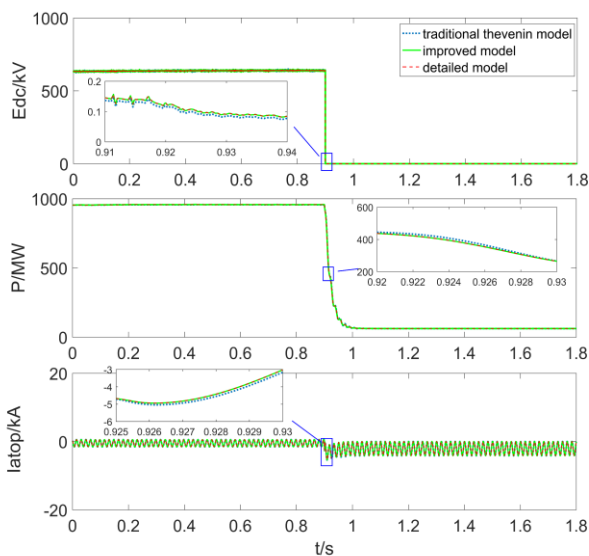


Fig. 14. Comparison of simulation results under a DC-side short-circuit fault.

D. Speed-up effect test

The detailed model, the traditional Thevenin equivalent model, and the improved Thevenin equivalent model proposed in this article of 85-level single-ended MMC were built in PSCAD/EMTDC to verify the speed-up effect. The simulation time is 3s and the step length is 20 μ s. Table 6 shows the comparison results of the running time of the detailed model, traditional Thevenin equivalent model and the improved Thevenin equivalent model; the speedup ratio is defined as the ratio of the running time of the detailed model and the improved Thevenin equivalent model or the traditional Thevenin equivalent model, which is shown in Table 7. From Table 6 and Table 7, it can be seen that the improved Thevenin equivalent model proposed in this paper has the same advantages as the traditional Thevenin equivalent model. When the level number is low, there is no significant difference in the simulation speed of the two equivalent models. When the average number is increased to 85, the speedup ratio of the improved Thevenin model reaches 210.6, and the speedup ratio of the traditional Thevenin equivalent model is 225.64. Although the speed of the improved Thevenin model is slightly slower than the traditional Thevenin equivalent model under the condition of higher level number. However, considering the accuracy advantage of the Thevenin equivalent model mentioned in this article, the slight speed disadvantage is acceptable.

Table 6: Comparison of running times

| Number of Levels | Run Time (s) | | |
|------------------|----------------|----------------------------|---------------------------|
| | Detailed Model | Traditional Thevenin Model | Improved Equivalent Model |
| 5 | 13 | 7 | 7 |
| 11 | 31 | 9 | 9 |
| 21 | 94 | 11 | 11 |
| 35 | 423 | 12 | 12 |
| 85 | 3159 | 14 | 15 |

Table 7: Speed-up ratio changes with the number of levels

| Number of Levels | Speed-up Ratio | |
|------------------|----------------------------|---------------------------|
| | Traditional Thevenin Model | Improved Equivalent Model |
| 5 | 1.86 | 1.86 |
| 11 | 3.4 | 3.4 |
| 21 | 8.55 | 8.55 |
| 35 | 35.25 | 35.25 |
| 85 | 225.64 | 210.6 |

VI. CONCLUSION

This study examined the inapplicability of the

traditional Thevenin equivalent model under pre-charge and DC-side fault conditions, and an improved Thevenin equivalent model under the above two conditions was proposed. This was then combined with the traditional Thevenin model under normal operating conditions to create an improved Thevenin equivalent MMC model considering pre-charge conditions and DC side fault conditions. A suitable control strategy for the model was also proposed.

The results of comparisons of simulations using the detailed MMC model, the traditional Thevenin equivalent model, and the improved Thevenin equivalent model proposed in this article showed that the improved Thevenin equivalent model is suitable for pre-charge conditions and DC side fault conditions, has good versatility, high simulation accuracy, and obvious speed-up effects.

VII. COPYRIGHT AND RELEASE INFORMATION

I, the author of the manuscript, declare that there is no conflict of interest exists in the submission of this manuscript, and the manuscript is approved by all authors for publication. I would like to declare on behalf of my co-authors that the work described was original research that has not been published previously, and not under consideration for publication elsewhere, in whole or in part. All the authors listed have approved the manuscript that is enclosed. Your consideration of this article is highly treasured.

ACKNOWLEDGMENT

This work was supported by the National Key Research and Development Program of China (2016YFB0900600); Technology Projects of State Grid Corporation of China (52094017000W).

AUTHOR CONTRIBUTIONS

Enshu Jin: Conceptualization, methodology, analysis, original draft preparation.

Zhenyu Song: Visualization, analysis, software, validation, writing - review & editing, supervision.

Xiaofan Yang: Methodology, software, writing - review & editing.

Xin Yu: Writing - Review & editing, supervision.

REFERENCES

- [1] U. N. Gnanarathna, A. M. Gole, and R. P. Jayasinghe, "Efficient modeling of modular multilevel HVDC converters (MMC) on electromagnetic transient simulation programs," in *IEEE Transactions on Power Delivery*, vol. 26, no. 1, pp. 316-324, Jan. 2011.
- [2] J. Z. Xu, C. Y. Zhao, and W. J. Liu, "Accelerated model of ultra-large scale MMC in electromagnetic transient simulations," *Proceedings of CSEE*, 2013, vol. 33, no. 10, pp. 114-120, Apr. 2013. (In Chinese).
- [3] S. Barmada and A. Musolino, "A new approach for model order reduction of complex circuits," *28th Annual Review of Progress in Applied Computational Electromagnetics*, 2012, pp. 1099-1104, Apr. 2012.
- [4] W. H. Chen, M. Z. Wu, J. Zhang, H. Yu, and D. K. Liang, "Review of electromagnetic transient modeling of modular multilevel converters," *Power Syst. Technol.*, 2020, vol. 44, no. 12, pp. 4755-4765, Dec. 2020. (In Chinese).
- [5] S. S. Khan and E. Tedeschi, "Modeling of MMC for fast and accurate simulation of electromagnetic transients: A review," *Energies*, 2017, vol. 10, no. 8, p. 1161, Aug. 2017.
- [6] H. Saad, S. Denneriere, J. Mahseredjian, P. Delarue, X. Guilaud, J. Peralta, and S. Nguefeu, "Modular multilevel converter models for electromagnetic transients," *IEEE Trans. Power Del.*, 2014, vol. 29, no. 3, pp. 1481-1489, Oct. 2014.
- [7] H. Zhang, D. Jovicic, W. Lin, and A. J. Far, "Average value MMC model with accurate blocked state and cell charging/discharging dynamics," *4th International Symposium on Environmental Friendly Energies and Applications (EFEA)*, 2016, pp. 1-6, Nov. 2016.
- [8] J. Z. Xu, A. M. Gole, and C. Y. Zhao, "The use of averaged-value model of modular multilevel converter in DC grid," *IEEE Trans. Power Del.*, 2015, vol. 30, no. 2, pp. 519-528, Oct. 2015.
- [9] X. Yi, L. Ningcan, X. Zheng, X. Yaowei, and Z. Xinlong, "Simplified transient calculation model in DC-side of VSC-HVDC systems based on MMC average value model," *2014 International Conference on Power System Technology*, pp. 2128-2133, Dec. 2014.
- [10] A. Beddard, C. E. Sheridan, and M. Barnes, "Improved accuracy average value models of modular multilevel converters," *IEEE Trans. Power Del.*, 2016, vol. 31, no. 5, pp. 2260-2269, May 2016.
- [11] X. Y. Pei, G. F. Tang, H. Pang, M. Kong, J. Yang, and Y. N. Wu, "A general modeling approach for the MMC averaged-value model in large-scale DC grid," *2017 IEEE Conference on Energy Internet and Energy System Integration (EI2)*, Beijing, pp. 1-6, Jan. 2018.
- [12] S. Nanou and S. Papathanassiou, "Generic average-value modeling of MMC-HVDC links considering sub-module capacitor dynamics," *52nd International Universities Power Engineering Conference (UPEC)*, *IEEE*, 2017, 1-5, Dec. 2017.
- [13] H. Y. Yang, Y. F. Dong, and W. H. Li, "Average-value model of modular multilevel converters considering capacitor voltage ripple," *IEEE Trans. Power Del.*, 2017, vol. 32, no. 2, pp. 723-732, Apr.

- 2016.
- [14] Y. Zhou and F. Chang, "Quick model of MMC in electromagnetic transient simulations," *Power Syst. Prot. Control*, 2016, vol. 44, no. 1, pp. 1-8, Jan. 2016. (In Chinese).
- [15] X. M. Liu, M. H. Li, and J. Zhu, "Research of equivalent mathematical model of MMC sub-modules based on Thevenin's theorem," *Power Syst. Prot. Control*, 2016, vol. 44, no. 1, pp. 1-8, Sep. 2014. (In Chinese).
- [16] Yu. F., X. T. Wang, W. X. Lin, and D. Xie, "Fast electromagnetic transient simulation models of modular multilevel converter," *Power Syst. Technol.*, 2015, vol. 39, no. 1, pp. 257-263, Jan. 2015. (In Chinese).
- [17] Y. C. Zhao, Y. L. Xu, C. Y. Zhao, and J. Z. Xu, "Generalized electromagnetic transient (EMT) equivalent modeling of MMCs with arbitrary single-port sub-module structures," *Proceedings of CSEE*, 2018, vol. 38, no. 16, pp. 4658-4667, Aug. 2018. (In Chinese).
- [18] Y. L. Xu, C. Y. Zhao, Y. C. Zhao, L. Shi, and J. Z. Xu, "Generalized electromagnetic transient (EMT) equivalent modeling of MMCs with arbitrary two-port sub-module structures," *Proceedings of CSEE*, 2018, vol. 38, no. 20, pp. 6079-6090, Oct. 2018. (In Chinese).
- [19] J. Z. Xu, Y. L. Xu, Y. C. Zhao, and C. Y. Zhao, "Generalized electromagnetic transient equivalent modeling and implementation of MMC with arbitrary multi-type sub-module structures," *Power Syst. Technol.*, 2019, vol. 43, no. 6, pp. 2039-2048, June 2019. (In Chinese).
- [20] J. Z. Xu, C. Y. Li, Y. Xiong, Y. K. Ji, C. Y. Zhao, and T. An, "A review of efficient modeling methods for modular multilevel converters," *Proceedings of CSEE*, 2015, vol. 35, no. 13, pp. 3381-3392, July 2015. (In Chinese).
- [21] C. S. Wang, P. Li, B. B. Huang, L. W. Wang, and F. Gao, "An interpolation algorithm for time-domain simulation of power electronics circuit considering multiple switching events," *J. Electrotech. Technol.*, 2010, vol. 25, no. 6, pp. 83-88, June 2010. (In Chinese).



Enshu Jin Professor engaged in research on power system relay protection and electromagnetic transient simulation modeling.



Zhenyu Song Postgraduate engaged in modular multilevel converter modeling and equivalent research work.

Characteristic Analysis and Control of a Rotary Electromagnetic Eddy Current Brake

Qiao Ren, Jimin Zhang*, and Jinnan Luo

Institute of Railway Transit
Tongji University, Shanghai, 201800, China
R138150187Q@163.com, *zjm2011@tongji.edu.cn, tjln@tongji.edu.cn

Abstract — This article designs an electromagnetic rotating eddy current brake (ECB), which has the advantages of no wear and low noise compared with traditional friction brake. First, using the magnetic circuit analysis model, a theoretical calculation formula of the ECB's braking characteristics is given. The results show that the braking torque is negatively correlated with the thickness of the air gap as well as the electrical conductivity and the relative magnetic permeability of the brake disc material, and positively correlated with the number of ampere turns and the number of electromagnet poles. Secondly, a three-dimensional finite element (FE) model of the brake is established. The results of braking torque-speed characteristics between finite element calculation and theoretical analysis are compared, and the reasons for the differences between the two are explained. Using the FE model, the influence of the design parameters on torque characteristics is studied. Combined with the theoretical analysis model, the results are explained accordingly, providing a reference for the optimal design of the brake. Finally, a controller for the electromagnetic rotating eddy current brake is designed to control the amplitude of the desired braking torque.

Index Terms — Braking characteristics, braking torque control, Eddy current brake, finite element analysis.

I. INTRODUCTION

With the development of high-speed railways, the running speed of trains has increased significantly [1-4]. Braking systems are the guarantee of operation safety, especially for trains running at high speeds. Because the kinetic energy of high-speed trains is much larger than that of ordinary trains, both the adhesion coefficient between wheels and rails and the friction coefficient between brake shoes and moving wheels are greatly reduced at high speeds, therefore traditional mechanical braking methods cannot meet the emergency braking requirements of high-speed trains [5-7]. And friction brake has obvious defects such as fast wear and loud noise under high-speed braking conditions. The ECB is

one of the most popular braking systems because of significantly lower maintenance, no wear, and excellent braking performance at high speeds [10-11] as compared to other braking devices. The main advantage of an ECB, making it superior to the other brakes [12], is its fast dynamic response.

In this paper, an electromagnetic rotating ECB was designed, as shown in Fig. 1, mainly consisting of two parts: stator and rotor. The rotor, which is termed as the brake disc and is rotating with the axle. The stator, which is the stationary part and fixed to the train, includes several electromagnets and magnetic yokes. Each electromagnet is made up of an iron core and its surrounding coils, corresponding to the red and yellow parts in Fig. 1. When passing a certain amount of direct current (DC) into the coil, the electromagnet will generate an excitation magnetic field, meanwhile the brake disc rotating with the axle cuts magnetic induction lines in the electromagnetic field. According to the principle of electromagnetic induction, the kinetic energy of the train is converted into the eddy current in the brake disc, dissipating into the surroundings in the form of heat to achieve the purpose of braking [8-9].

Braking characteristics are defined as the variation law of braking torque with rotational speed of brake disc. While the study of braking characteristics provides the basis for making full use of ECB, current research work mostly performed their analyses of the braking characteristics of electromagnetic ECB at the theoretical and simulation level. Based on the basic macro-electromagnetic field theory, the variable separation method (VSM) was used to solve the analytical formula of braking torque [1]. In [13], a calculation method using the Laplace and Helmholtz equations was presented to analyze the eddy current generated by the transverse alternating magnetic field in two parallel conductors. In [14], Lee used the mirror image method to calculate the electric field intensity of a conductor plate with a finite radius, then introduced the magnetic flux Reynolds number to consider the armature reaction, and finally obtained a formula for calculating the braking torque through using the Lorentz formula. In [15], Liu used

the Maxwell's equations and appropriate boundary conditions to solve magnetic vector potential and magnetic flux density, and obtained their braking torque formula based on Maxwell stress tensor approach. Most recently, Reza [16] used subdomain analysis to compute the braking force for a magnetic pole moving above the induction plate.

Studies mentioned above have shown that using theoretical analysis methods to find solutions often requires a large number of premise assumptions and problem simplifications, rendering the accuracy of their results limited. For this reason, substantial efforts have been put into finite element analysis (FEA) to improve braking characteristics analysis results. For example, a 2D FE model for linear eddy current brakes was established by [17]. Compared with the simulation results, their calculation results have a higher degree of agreement in the low-speed area but greater deviation in the high-speed area. Using three-dimensional FEA, Mehmet [18] verified the effectiveness of braking torque theoretical modeling, and simulated the resistivity and permeability of the best brake disc material with finite element to obtain the maximum braking torque. Sohel [19] established a parameter model based on the FE model calculation results of braking torque characteristics, fitting the relationship between braking torque and current and speed into a polynomial function. In [20],

eddy current losses of the transformer were calculated by a 2D FE model. Their use of the Galerkin method to apply surface impedance boundary conditions to finite element calculation effectively shortened the calculation time.

As for the research on braking torque control methods, literature [21] designed a constant torque control algorithm based on the principle of controlling a constant ratio between the reference current and the speed, and verified the effectiveness of this algorithm through proportional experiments. In order to keep the braking torque constant, a dynamical compensation scheme for speed control was proposed by [22].

In this paper, an electromagnetic rotating ECB of high-speed trains is designed. We first use the magnetic equivalent circuit (MEC) to study the dynamic characteristics of the ECB system, and offer a brief mathematical model of the braking characteristics to clarify the main parametric factors that affect the braking torque. Secondly, a three-dimensional FE model of the brake is established to specifically quantify the influence of each parameter factor on the braking characteristics. Then the differences between the braking torque-speed-current characteristics curve calculated by the theoretical model and the FE model are compared and analyzed to offer sensible explanations. Finally, a fuzzy controller for the electromagnetic rotating ECB is designed to accurately track the desired braking torque.

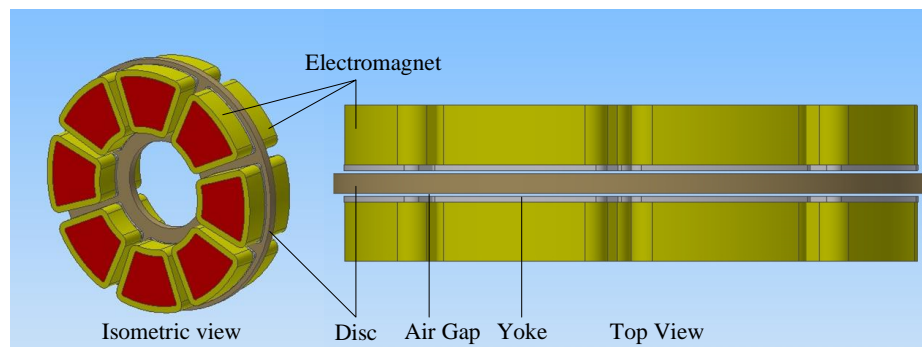


Fig. 1. Configuration of the eddy current brake.

II. ANALYTICAL MODEL

This article derives the brake disc eddy current, air gap magnetic field and eddy current power according to the differential principle. Starting from the law of energy conservation, the eddy current power is regarded equal to braking power, and the braking torque is obtained according to the relationship between power and torque.

A. Model assumptions

To facilitate the derivation of braking torque, the following assumptions are made for the model:

(1) The influence of temperature on the electromagnetic properties are neglected.

(2) The magnetic flux lines are ideally distributed only within the projection areas on the disc of yokes.

(3) The magnetic saturation and nonlinearity of magnetic properties are neglected.

B. Eddy current analysis

The projection area of a single yoke on the brake disc is a sector, as shown in Fig. 2, whose inner and outer radii are r_1 and r_2 , respectively, with a 40° angle. From the perspective of differentiation principle, this sector is regarded as composed of countless similar sector-shaped rings (shadowed) with a width of dr , and the position of these sector-shaped rings can be represented by the

distance r from the inner and outer arcs to the middle radius of the large sector, where $r \in [0, \Delta r]$, $\Delta r = r_c - r_1 = (r_2 - r_1)/2$, $r_c = (r_1 + r_2)/2$.

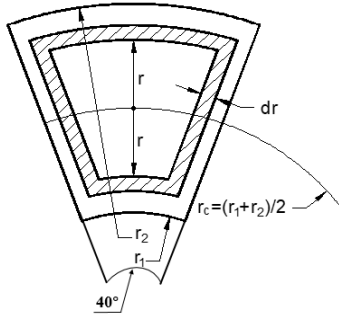


Fig. 2. Projection area of a single yoke on the brake disc.

The magnetic flux passing through the sector area can be expressed as:

$$\phi_r = BS_r \cos \omega_n t = \frac{4\pi r_c r B \cos \omega_n t}{9}, \quad (1)$$

where, S_r is the area of the inner sector surrounded by the sector ring, which can be calculated according to Eq. (2) below. B is the magnetic induction density value on the surface of the brake disc, and ω_n is the electrical angular velocity of the brake disc:

$$S_r = \frac{40^\circ}{360^\circ} \times \pi[(r_c + r)^2 - (r_c - r)^2] = \frac{4\pi r_c r}{9}, \quad (2)$$

$$\omega_n = N_p \cdot \omega = N_p \cdot \frac{2\pi n}{60} = \frac{\pi N_p n}{30}, \quad (3)$$

where N_p is the number of pole pairs on one side of the disc, ω is the angular velocity of the disc, and n is the rotation speed of the disc.

The induced electromotive force is:

$$\varepsilon_r = -\frac{d\phi_r}{dt} = \frac{4\pi r_c r B \omega_n \sin \omega_n t}{9}. \quad (4)$$

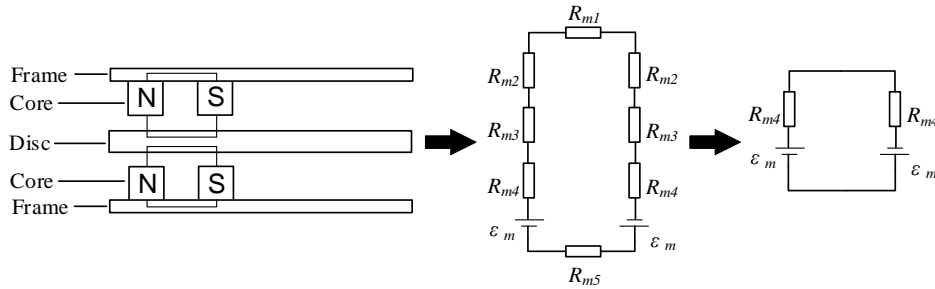


Fig. 3. Magnetic circuits.

According to Fig. 3, the magnetic circuit can be written as:

$$\varepsilon_m = R_{m4} \cdot \phi, \quad (9)$$

The resistance of the sector ring is:

$$R_r = \rho \frac{L_r}{d' \cdot dr}, \quad (5)$$

where, d' and L_r are the skin depth of the vortex and the length of the sector ring, respectively. And d' satisfies the following formula:

$$d' = \sqrt{\frac{2\rho}{\mu_0 \mu_r \omega_n}}, \quad (6)$$

where, ρ is the resistivity of the brake disc, μ_0 is the vacuum permeability, μ_r is the relative permeability of the brake disc.

Thus, according to the Ohm's law, the current value on the sector ring, that is, the eddy current value can be expressed as:

$$i_r = \frac{\varepsilon_r}{R_r} = \frac{\sqrt{2} r_c r B \omega_n \sin \omega_n t dr}{(r + \pi r_c) \sqrt{\rho \mu_0 \mu_r \omega_n}}. \quad (7)$$

C. Magnetic field analysis

The Ohm's law for a magnetic circuit can be derived from Maxwell equations:

$$\varepsilon_m = \sum R_{mi} \cdot \phi_i, \quad (8)$$

where ε_m is the magnetomotive force, ϕ is the magnetic flux, $\phi = BS_p$, S_p is the area of the total sector shown in Fig. 2, R_{mi} represents every magnetic resistance in the magnetic circuit.

The simplified magnetic circuit and the definition of each part reluctances are shown in Fig. 3. R_{m1} , R_{m2} , R_{m3} , R_{m4} , R_{m5} are the magnetic resistances of the frame, core, yoke, air gap, and disc, respectively. Since the relative permeability of the frame, core and disc is much higher than that of air which approximately equals 1, only R_{m4} is taken into consideration in this paper.

where the magnetoresistance of the air gap is:

$$R_{m4} = \frac{\delta}{\mu_0 \mu_{r4} S_p} \approx \frac{\delta}{\mu_0 S_p}, \quad (10)$$

where, δ and μ_{r4} are the length of air gap and air relative permeability, respectively.

The total magnetic motive force ε_m is given as:

$$\varepsilon_m = \varepsilon_0 - \varepsilon_e, \quad (11)$$

where ε_0 and ε_e are the magnetic motive forces generated by electromagnets and eddy current, respectively, and they are given as:

$$\varepsilon_0 = NI, \quad (12)$$

$$\varepsilon_e = k_e \cdot I_e, \quad (13)$$

where N is the number of turns per coil, I is the excitation current, k_e is the computation coefficient, I_e is the RMS eddy current which can be obtained by integration of the eddy current i_r :

$$I_e = \frac{1}{\sqrt{2}} \int_0^{\Delta r} i_r = \frac{r_c B \omega_n}{\sqrt{\rho \mu_0 \mu_r \omega_n}} \cdot (\Delta r - \pi r_c \ln \frac{\Delta r + \pi r_c}{\pi r_c}). \quad (14)$$

From Eqs. (9)-(14), we can derive that the magnetic flux density is:

$$B = \frac{\mu_0 NI \sqrt{\rho \mu_0 \mu_r}}{\delta \sqrt{\rho \mu_0 \mu_r} + k_e r_c \mu_0 \sqrt{\omega_n} (\Delta r - \pi r_c \ln \frac{\Delta r + \pi r_c}{\pi r_c})}. \quad (15)$$

D. Power analysis

The RMS power of eddy current of the whole disc P_e can be obtained by integration of the product of eddy current i_r and the induced electromotive force ε_r :

$$\begin{aligned} P_e &= 2 \times \frac{360^\circ}{40^\circ} \times \frac{1}{\sqrt{2}} \int_0^{\Delta r} i_r \cdot \varepsilon_r \\ &= \frac{4\sqrt{2}\pi r_c^2 B^2 \omega_n^2}{\sqrt{\rho \mu_0 \mu_r \omega_n}} \cdot \left[\frac{1}{2} \Delta r^2 - \pi r_c \Delta r \right. \\ &\quad \left. + (\pi r_c)^2 \cdot \ln \frac{\Delta r + \pi r_c}{\pi r_c} \right]. \end{aligned} \quad (16)$$

E. Torque analysis

The brake power P_b equals the RMS power of eddy current P_e in accordance with the law of conservation of energy, therefore the following expression can be obtained:

$$P_b = P_e = T_b \cdot \omega, \quad (17)$$

where T_b is the torque generated by the eddy current brake. From (16)-(17) and the relation between the angular velocity ω and the train speed v , we can derive that the brake torque is:

$$T = \frac{4\sqrt{10}\pi k_1 r_c^2 \mu_0^{\frac{5}{2}} (\mu_r \rho)^{\frac{1}{2}} (NI)^2 N_p^{\frac{3}{2}} D_w^{-\frac{1}{2}} v^{\frac{1}{2}}}{3(\delta \sqrt{\rho \mu_0 \mu_r} + k_2 k_e r_c \mu_0 \sqrt{\frac{5N_p v}{9D_w}})^2}, \quad (18)$$

where k_1, k_2 are both coefficients that are determined by the geometric parameters of the brake device, D_w is the diameter of the wheel.

III. VALIDATION OF THE FE MODEL

Brake torque is influenced by the geometric and electromagnetic parameters according to the above theoretical model. More specifically, there is a negative correlation between brake torque and the length of air gap, the inner radius of yoke, the product of the resistivity and permeability of disc material, and a positive correlation between brake torque and the number of poles, the outer radius of yoke. In addition, brake torque is proportional to the square of ampere turns of electromagnets. In order to analyze the quantitative effects of each factor on the braking performance and verify the accuracy of the analytical model, a 3D FE model was established for further numerical calculations, as shown in Fig. 4. Only the brake disc, yokes, and electromagnets were considered in the FE model because of the assumption that the other components only act as fixed support and no magnetic lines pass through them. So their effects on the magnetic field can be ignored. In the FE model, the material of electromagnet core and brake disc is mild steel steel_1008. The material of magnetic yoke is mild steel steel_1010, and the material of electromagnet coil is copper. A 1/4Np simplified model is adopted to reduce simulation time. For this reason, a symmetry boundary condition is added in the middle section of the brake disc. Master and slave boundary conditions are implemented in the two sides considering the electromagnets' periodic distribution. Main parameters of the FE model are given in Table 1.

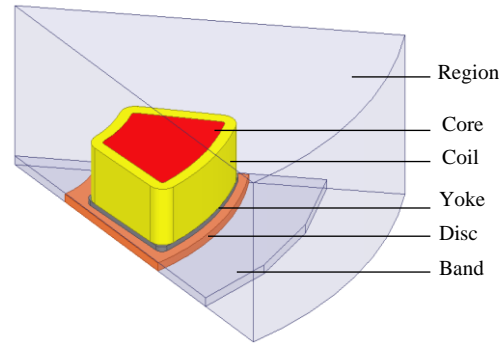


Fig. 4. FE model.

The magnetic flux density map, eddy current losses and the distribution of induced eddy currents are shown in Figs. 5 (a), (b) and (c) respectively. It can be seen that 2.2T magnetic flux density is obtained by the FE model. And at the same parameters, the air gap magnetic flux density of 2.34T is calculated based on the analytical

model. The value of relative error is about 6.3%. Hence, the results of the analytical model are in good agreement with the FE model results. In addition, eddy current losses are calculated by the FE model and Eq. (16), as shown in Fig. 6. It can be seen that both the analytical model and FE model have the same linear growth trend. The eddy current losses increase with the speed increases.

Table 1: ECB parameters

| Parameter | Value |
|---|-------|
| Inner radius of the disc | 210mm |
| Outer radius of the disc | 600mm |
| Disc thickness | 20mm |
| Air gap width | 3mm |
| Inner radius of the yoke | 280mm |
| Outer radius of the yoke | 580mm |
| Yoke thickness | 6mm |
| Core thickness | 60mm |
| Angle covered by a single electromagnet | 40deg |
| Angle between two adjacent electromagnets | 45deg |
| Number of pole pairs on one single side of the disc | 4 |
| Number of turns per coil | 400 |
| Excitation current | 40A |

At the initial simulation time, a large amplitude fluctuation of the braking torque appeared and then converged to a steady value. This phenomenon is inevitable due to the initial value of calculation changes to the target value suddenly. It was only regarded steady-state values as the effective data and calculated the final torque-speed characteristic curve. Figure 7 shows a comparison between the FE model and analytical model of braking torque-speed characteristics. It is observed that the braking characteristics tendency of the analytical model is consistent with that of the FE model. Still, the results from analytical method in Eq. (18) are slightly larger than those from FE at the whole speed range. When the vehicle speed is higher than the critical speed, the decrease of braking torque calculated by FE is more evident than that calculated by Eq. (18). This is due to the assumptions made to simplify the theoretical analysis, especially assumption (3), in which we assumed that the magnetic saturation and nonlinearity of magnetic properties are neglected. Additionally, in the analytical model, the effects of flux leakage and uneven distribution of magnetic field lines are ignored, which also cause the theoretical value to be too large.

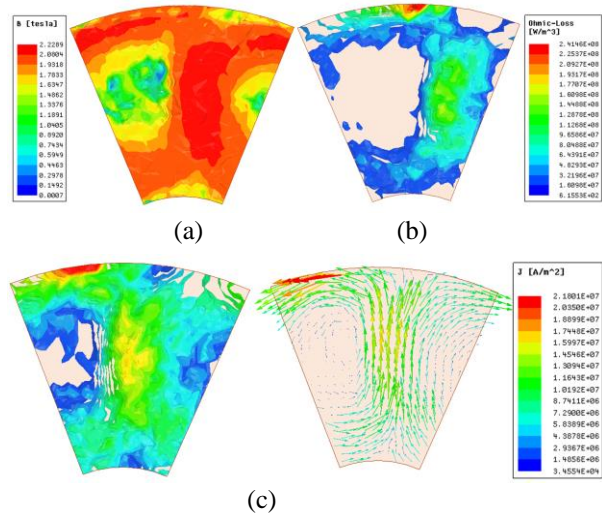


Fig. 5. (a) The magnetic flux density map, (b) eddy current loss, and (c) distribution of induced eddy currents.

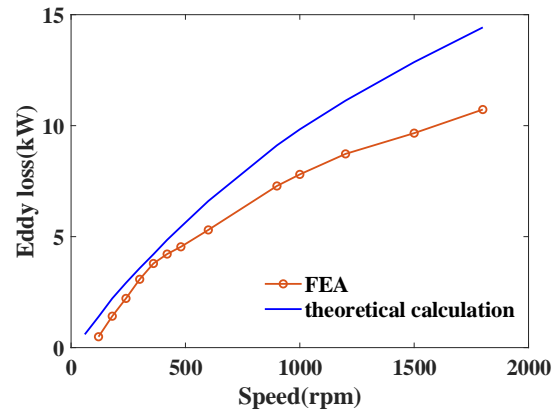


Fig. 6. Eddy current losses.

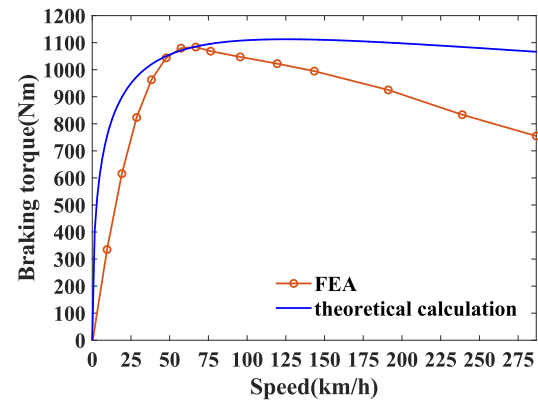


Fig. 7. Braking torque-speed characteristic.

IV. PARAMETER ANALYSIS

It is found by FEA that the excitation current, air gap thickness, brake disc thickness and electromagnet core shape have more significant influence on the braking characteristic, so the influence of these four factors on braking characteristics is specifically analyzed in this paper.

A. Influence of the excitation current

Figure 8 shows the variation of braking torque characteristics for $I=40,60,80,100\text{A}$ while keeping other parameters unchanged. It is obvious that the braking torque increases gradually as the excitation current increases. And the peak torque increases in a trend of linear function. However, from Eq. (18), the braking torque should be proportional to the square of the excitation current. The main reason for this difference is that electromagnets have nonlinear magnetization characteristics. The magnetic permeability decreases as the excitation current increases so that the magnetic induction intensity shows a nonlinear growth trend with a declining growth rate. Furthermore, the critical speed increases with the increase of excitation current. According to Eq. (6), the skin depth increases as the magnetic permeability decreases, which weakens the eddy current skin effect. Therefore, if the eddy current magnetic field is to reach its original strength, it needs to increase the speed [17].

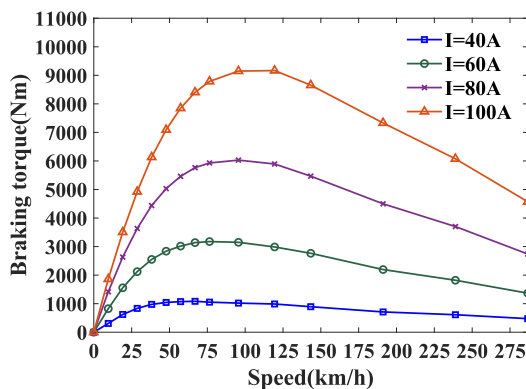


Fig. 8. Braking torque-speed characteristics for different excitation currents.

B. Influence of the air gap length

Figure 9 shows the variation of braking torque characteristics for air gap=3,4,5,6mm, while other parameters are kept to values introduced earlier. It is observed that a shorter air gap length leads to higher braking torque values. This is due to a large air gap length will result in a larger magnetoresistance, which will cause a lower magnetic density. In addition, for a large air gap, the torque-speed characteristic curves of the high-speed region are flatter than that of a small air

gap. This is due to the former's eddy current being far away from the yoke compared to the latter, which causes a lesser demagnetization effect on the original magnetic field.

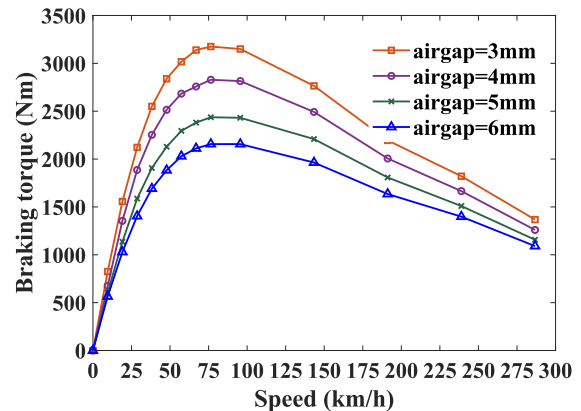


Fig. 9. Braking torque-speed characteristics for different air gap lengths.

C. Influence of the conductor plate thickness

The effect of the conductor plate thickness on the braking torque-speed characteristic has been studied by changing the thickness from 15 to 30 mm in a step of 5mm. From Fig. 10, the thinner the conductor plate is, the higher the peak torque and the critical speed would be for the ECB. The reason is that eddy currents in the conductor plate increase as the thickness of the conductor plate increases, which intensifies the influence of the eddy current magnetic field on the excitation magnetic field. Therefore, the braking torque reaches the peak value at a low speed, and the peak torque becomes small due to the eddy current demagnetization effect.

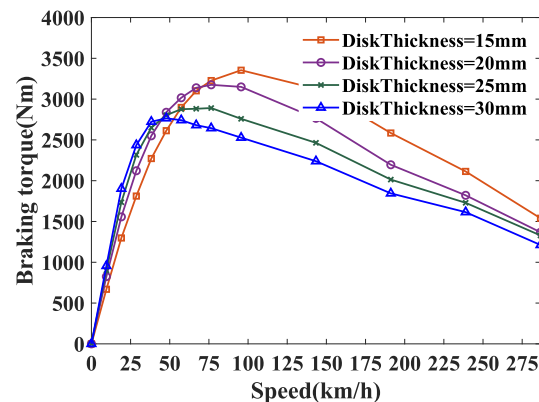


Fig. 10. Braking torque-speed characteristics for different disc thicknesses.

D. Influence of the pole shape

The electromagnet core is designed to be round,

square, and sector in turn while keeping the cross-sectional area of the electromagnet core unchanged. The torque-speed characteristics for three kinds of electromagnet core shapes are shown in Fig. 11. We can observe that an optimum torque generation capacity exists for the sector-shaped section electromagnet. Because of the fact that only the tangential electromagnetic force generated by the radial eddy current can contribute to the braking torque. In contrast, the tangential eddy current is ineffective for braking torque generation. Electromagnets with circular and square cross-sections have a lesser radial coverage of the projection area on the brake disc than sector-shaped section electromagnets, resulting in a small effective braking torque. In order to enlarge the path of the radial eddy current, a sector-shaped section electromagnet is designed. The adequate electromagnetic torque can be enhanced by increasing the eddy current flowing along

the radius of the disc with the sector pole [18].

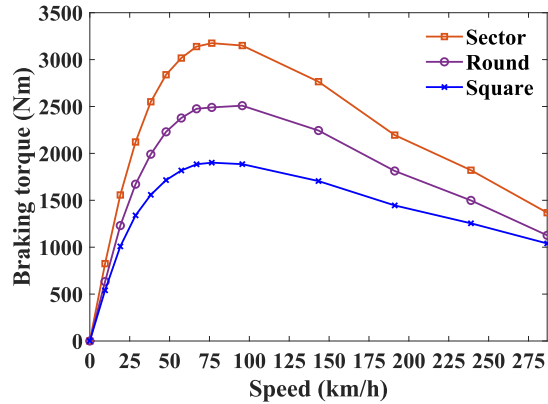


Fig. 11. Braking torque-speed characteristics for different pole shapes.

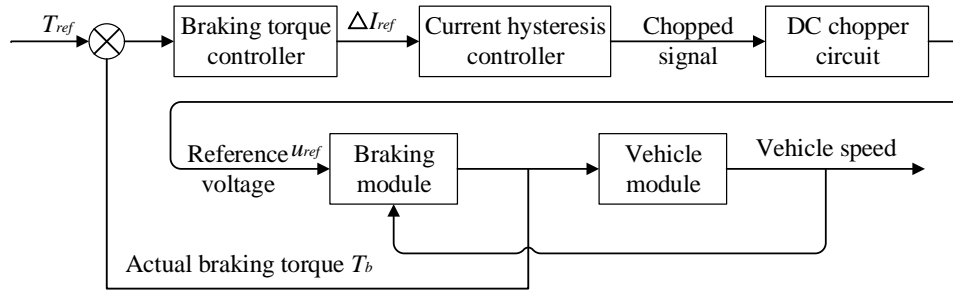


Fig. 12. The overall scheme of the torque control system.

V. EDDY CURRENT BRAKE CONTROL SYSTEM

A. Braking torque controller design

Based on the above theoretical calculation of braking torque and the FEA of braking characteristics, the braking torque decreases with the increase of speed in the high-speed region. In order to track the desired braking torque accurately, this paper presents a controller based on the fuzzy method to control the amplitude of the braking torque. Figure 12 shows the control scheme of the ECB. It consists of a braking torque controller and a current controller. The braking torque controller outputs the reference of the excitation current change ΔI_{ref} according to the error between the desired braking torque T_{ref} and the actual braking torque T_b . The current controller is composed of a current hysteresis controller and a DC chopper circuit, which outputs a reference voltage u_{ref} according to the reference

value of the excitation current change. One can adjust the excitation current to regulate the value of the braking torque by controlling the reference voltage.

B. Control algorithm description

In the fuzzy controller, the system input variables are the braking torque error e and its rate of change ec . The output variable is the change of reference current ΔI_{ref} . Design variables use the same set of fuzzy state words {NB, NS, PS, PB}, in which each fuzzy state corresponds to {‘negative big’, ‘negative small’, ‘positive small’, ‘positive big’}, denoting the variables sign and absolute value size. The membership function for the fuzzy sets is set as a triangular function, as shown in Fig. 13. According to the qualitative relationship between the braking torque error and the change of reference current, the fuzzy rule table is formulated as shown in Table 2. The center of gravity method, the most commonly used defuzzification method, is used in this paper.

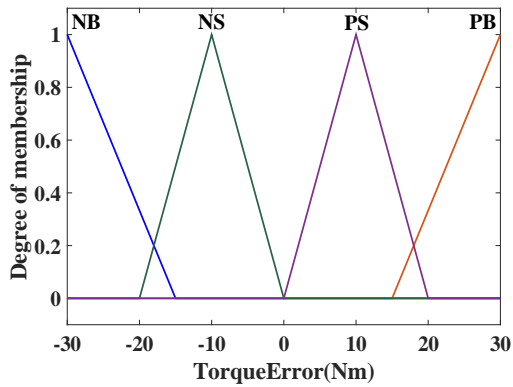


Fig. 13 Membership function for fuzzy sets.

Table 2: Fuzzy rules

| Error e | Change of ec | | | |
|-----------|----------------|----|----|----|
| | NB | NS | PS | PB |
| NB | NB | NB | NB | NB |
| NS | NB | NS | NS | NS |
| PS | NS | PS | PS | PB |
| PB | PB | PB | PB | PB |

VI. ANALYSIS OF THE SIMULATION RESULTS

In Fig. 14, the variation of the braking torque is plotted with respect to varying speeds of the rotating disk under open-loop control and closed-loop control algorithms. In this paper, PID control and fuzzy control are carried out. It is evident that the braking torque increases firstly and then decreases as the speed increases under open-loop control, which causes the fluctuation of the train braking deceleration. Note that the braking torque keeps constant as the speed varies under closed-loop control. This is because the control system adjusts the excitation current in real-time according to the braking torque feedback. In the speed range of 20-160 km/h , the actual braking torque is controlled near the desired braking torque. As the speed continues to decrease, the maximum braking torque output is limited by the coil current in the low-speed region, the braking torque starts to drop. It can be concluded that the two control algorithms mentioned can effectively control the braking torque to remain constant in an extensive speed range.

In Fig. 15, the time response curve of the braking torque is shown. In order to quantitatively illustrate the control effect of the two algorithms, the transient and steady-state performance indicators of the system are calculated in Table 3. It can be seen that from transient performance indicators, the maximum overshoot of the system under PID control is 111.7N·m, which is far greater than the overshoot of 26.2N·m under fuzzy

control. In addition, the adjustment time of the system under PID control is 3.210s, which is longer than 0.318s under fuzzy control. In terms of steady-state performance indicators, the steady-state value of the system under the fuzzy control is closest to the desired braking torque of 3500N·m. However, the result under the PID control deviates from the expected value significantly. It can be concluded that fuzzy control is better than PID control in both transient and steady-state indicators.

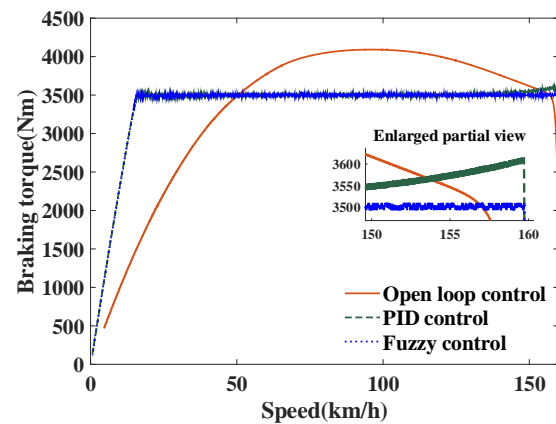


Fig. 14. Brake torque versus train speed under different control algorithms.

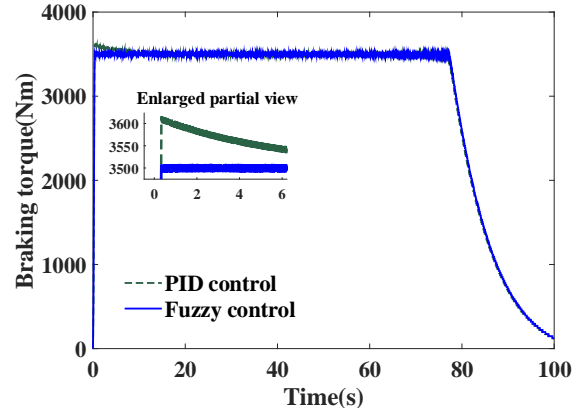


Fig. 15. Brake torque under different control algorithms.

Table 3: System performance indicators

| | Performance | PID | Fuzzy Control |
|------------------------|----------------------------------|--------|---------------|
| Transient indicator | Adjustment time t_s /(s) | 3.210 | 0.318 |
| | Peak time t_p /(s) | 0.333 | 0.323 |
| | Maximum overshoot σ /(Nm) | 111.7 | 26.2 |
| Steady-state indicator | Steady state average/(Nm) | 3502.3 | 3499.3 |
| | Steady state maximum/(Nm) | 3524.4 | 3504.6 |
| | Steady state minimum/(Nm) | 3489.1 | 3497.3 |

VII. CONCLUSIONS

In this paper, an electromagnetic rotating eddy current brake is regarded as the research object. Studying the braking characteristic from two aspects of theoretical analysis and FEA, and designing a braking torque controller. The main conclusions can be drawn as follows:

(1) The theoretical model shows that the braking torque is negatively correlated to the air gap length, the electrical conductivity and relative permeability of the brake disc material, and positively correlated to the number of ampere turns and the number of pole pairs.

(2) There are differences between the results of FEA and theoretical analysis. The main reason for the difference is that the theoretical model neglects nonlinear characteristics of the brake disc material, the magnetic saturation phenomenon of electromagnets, and the non-ideal distribution of the magnetic flux.

(3) The relationship between the braking torque and the design parameters such as excitation current, air gap length, brake disc thickness, and electromagnet shape on the braking characteristics is analyzed using the FEA, which provides a reference for the optimal design of the ECB.

(4) An ECB controller based on fuzzy control theory is designed. Compared with open-loop control and PID control, the proposed controller can keep the braking force stable during the train braking process.

REFERENCES

- [1] X. Zhu and X. Zhang, "Analysis and calculation of braking force on rail Eddy current braking of high speed trains," [J]. *Journal of Tongji University (Natural Science)*, vol. 17, no. 4, pp. 1-8, Dec. 1996.
- [2] C. Yin and K. Zhang, "Electromagnetic force calculation of conductor plate double Halbach permanent magnet electrodynamic suspension," *Applied Computational Electromagnetics Society Journal*, vol. 29, no. 11, pp. 916-922, Nov. 2014.
- [3] M. Fujita, T. Tokumasu, T. Yamada, T. Hirose, Y. Tanaka, N. Kumagai, and S. Uchida, "3-dimensional electromagnetic analysis and design of an eddy-current rail brake system," *IEEE Transactions on Magnetics*, vol. 34, no. 5, pp. 3548-3551, Sept. 1998.
- [4] S. Surenkhorloo and J. K. Byun, "Analysis and case study of permanent magnet arrays for eddy current brake systems with a new performance index," *Journal of Magnetics*, vol. 18, no. 3, pp. 276-282, Sept. 2013.
- [5] C. Aldo and B. Vusini, "Design of axial Eddy-current couplers," *IEEE Transactions on Industry Applications*, vol. 39, no. 3, pp. 725-733, May 2003.
- [6] L. Thierry and A. Rezzoug, "3-D analytical model for axial-flux eddy-current couplings and brakes under steady-state conditions," *IEEE Transactions on Magnetics*, vol. 51, no. 10, pp. 1-12, July 2015.
- [7] Z. Ali and A. Mirabadi, "Railway wheel detector in the presence of eddy current brakes," *Applied Computational Electromagnetics Society Journal*, vol. 28, no. 1, pp. 77-84, Jan. 2013.
- [8] B. Kou, Y. Jin, H. Zhang, L. Zhang, and H. Zhang, "Analysis and design of hybrid excitation linear eddy current brake," *IEEE Transactions on Energy Conversion*, vol. 29, no. 2, pp. 496-506, Mar. 2014.
- [9] K. Kerem, A. Suleman, and E. J. Park, "Analytical modeling of eddy current brakes with the application of time varying magnetic fields," *Applied Mathematical Modelling*, vol. 40, no. 2, pp. 1168-1179, Jan. 2016.
- [10] J. R. Tibola, R. L. Sari, T. D. M. Lanzanova, M. E. S. Martins, and H. Pinheiro, "Modeling and control of a low-cost driver for an eddy current dynamometer," *Journal of Control, Automation and Electrical Systems*, vol. 27, no. 4, pp. 368-378, Apr. 2016.
- [11] B. Kou, Y. Jin, L. Zhang, and H. Zhang, "Characteristic analysis and control of a hybrid excitation linear eddy current brake," *Energies*, vol. 8, no. 7, pp. 7441-7464, July 2015.
- [12] C. Tian, M. Wu, L. Zhu, and J. Qian, "An intelligent method for controlling the ECP braking system of a heavy-haul train," *Transportation Safety and Environment*, vol. 2, no. 2, pp. 133-147, June 2020.
- [13] T. Szczegielniak, P. Jabłoński, D. Kusiak, and Z. Piątek, "Eddy currents induced in two parallel round conductors," *Applied Computational Electromagnetics Society Journal*, vol. 34, no. 12, pp. 1922-1930, Dec. 2019.
- [14] L. Kapjin and K. Park, "Modeling eddy currents with boundary conditions by using Coulomb's law and the method of images," *IEEE Transactions on Magnetics*, vol. 38, no. 2, pp. 1333-1340, Aug. 2002.
- [15] Y. Reza and M. Mirsalim, "Axial-flux wound-excitation Eddy-current brakes: Analytical study and parametric modeling," *IEEE Transactions on Magnetics*, vol. 50, no. 6, pp. 1-10, Jan. 2014.
- [16] Z. J. Liu, A. Vourdas, and K. J. Binns, "Magnetic field and eddy current losses in linear and rotating permanent magnet machines with a large number of poles," *IEE Proceedings A-Science, Measurement and Technology*, vol. 138, no. 6, pp. 289-294, Dec. 1991.
- [17] M. Hecquet, P. Brochet, L. Jin, and P. Delsalle, "A linear Eddy current braking system defined by finite element method," *IEEE Transactions on Magnetics*, vol. 35, no. 3, pp. 1841-1844, May 1999.

- [18] G. Mehmet, E. Yolacan, and M. Aydin, "Design, analysis and real time dynamic torque control of single-rotor-single-stator axial flux Eddy current brake," *IET Electric Power Applications*, vol. 10, no. 9, pp. 869-876, Nov. 2016.
- [19] A. Sohel, "A parametric model of an eddy current electric machine for automotive braking applications," *IEEE Transactions on Control Systems Technology*, vol. 12, no. 3, pp. 422-427, May 2004.
- [20] J. M. Díaz-Chacón, C. Hernandez, and M. A. Arjona, "A comprehensive 2D FE-SIBC model for calculating the Eddy current losses in a transformer tank-wall," *Applied Computational Electromagnetics Society Journal*, vol. 27, no. 8, pp. 646-653, Aug. 2012.
- [21] H. J. Ryoo, J. S. Kim, D. H. Kang, G. H. Rim, Y. J. Kim, and C. Y. Won, "Design and analysis of an eddy current brake for a high-speed railway train with constant torque control," *Conference Record of the 2000 IEEE Industry Applications Conference*, Rome, Italy, vol. 1, pp. 277-281, Oct. 2000.
- [22] S. Emmanuel and D. Georges, "Modeling and control of Eddy current brake," *IFAC Proceedings Volumes*, vol. 28, no. 8, pp. 109-114, July 1995.



Jimin Zhang received his M.Sc. and Ph.D. degrees from Southwest Jiaotong University, Chengdu, China, in 1999, and 2004, respectively. Since 2004, he has been with Tongji University, where he is currently a Professor. His research interests include magnetic levitation control, electromechanical coupling and active vehicle safety control, etc.



Jinnan Luo received his B.S. degree in 2018 and M.Sc. degree in 2021 from Tongji University, Shanghai, China. His interest is high-speed magnetic field analysis and eddy current brake.



levitation control.

Qiao Ren graduated from Changan University in 2018 with a bachelor's degree. She is currently working toward the Ph.D. degree with the Institute of Railway Transit, Tongji University, China. Her current research interests include eddy current brake, high-speed magnetic

Modeling the Microwave Transmissivity of Row Crops

Jeil Park¹, Praveen Gurralla¹, Brian K. Hornbuckle², and Jiming Song¹

¹Department of Electrical and Computer Engineering
Iowa State University, Ames, Iowa 50011-1046, USA
cptpark@iastate.edu, praveeng@iastate.edu, jisong@iastate.edu

²Department of Agronomy
Iowa State University, Ames, Iowa 50011-1051, USA
bkh@iastate.edu

Abstract — We develop a method to model the microwave transmissivity of row crops that explicitly accounts for their periodic nature as well as multiple scattering. We hypothesize that this method could eventually be used to improve satellite retrieval of soil moisture and vegetation optical depth in agricultural regions. The method is characterized by unit cells terminated by periodic boundary conditions and Floquet port excitations solved using commercial software. Individual plants are represented by vertically oriented dielectric cylinders. We calculate canopy transmissivity, reflectivity, and loss in terms of S-parameters. We validate the model with analytical solutions and illustrate the effect of canopy scattering. Our simulation results are consistent with both simulated and measured data published in the literature.

Index Terms — HFSS, scattering, SMOS, SMAP, soil moisture, S-parameters, transmissivity, vegetation optical depth.

I. INTRODUCTION

Both NASA's Soil Moisture Active Passive (SMAP) satellite mission [1] and the European Space Agency's Soil Moisture Ocean Salinity (SMOS) satellite mission [2] use L-band radiometry to estimate soil moisture. Their retrieval algorithms are based on a zeroth-order solution of radiative transfer commonly called the τ - ω model because it uses two parameters, τ and ω , to characterize attenuation and scattering by vegetation [3, 4]. Assessment of SMAP and SMOS performance in croplands reveal that soil moisture retrievals do not satisfy either mission's accuracy goal. It is likely that unrealistic values of τ and ω are part of the problem [5, 6]. The τ - ω model assumes that the vegetation scattering is almost zero at L-band ($f = 1.4$ GHz, $\lambda = 21$ cm). However, when the electrical size of plants becomes comparable with the wavelength, the scattered radiation and its coherent wave interactions generated from all of

the plants are no longer negligible [7, 8].

The τ and ω parameters currently in use are empirical: they have largely been determined by fitting the τ - ω model to observations. There is a need to find more realistic values of τ and ω in order to increase the accuracy of soil moisture estimates in agricultural regions. One approach is to represent the vegetation canopy with models that include vegetation scattering effects. The τ parameter, also called the vegetation optical depth (VOD), is a measure of the transmissivity of vegetation canopy. Experimental observations [9] and theoretical models [10, 11] show that vegetation transmissivity depends on the operation frequency, incidence angle, polarization, and type of vegetation.

We model the vegetation canopy using the FEM solver in HFSS [12], incorporating several key features of croplands in the remote sensing point of view [13, 14]. First, crops are generally planted in regularly-spaced rows, and there are a large number of plants (scatterers) within an L-band satellite footprint (30-40 km). Second, the scattered fields and all the coherent wave interactions need to be considered. Third, the radiation is treated as a plane wave, and the polarization and incident angle should be dealt with. Floquet ports and periodic boundary conditions are used in our proposed approach to realize the features described above. We utilize S-parameters from HFSS directly to calculate the transmissivity of the vegetation canopy. The CPU time and memory requirement for running the simulations are tractable because of restricting the computational domain to a unit cell.

In the following sections, we explain how we model the vegetation canopy in HFSS, and then validate our simulations against analytical results. Finally, we compare our results with published data [9, 10] for a corn and a grass canopy.

II. METHODOLOGY

To model the layer of vegetation, we propose to use

the unit cell comprising the PBC (periodic boundary condition) and two Floquet ports, as shown in Fig. 1. The PBC enforces field periodicity in the x - and y -direction through master/slave boundary pairs, and hence, an infinite array of the 3D structure is created. The Floquet port excites plane waves consisting of an infinite series of TE_z (transverse electric to z , h-pol) and TM_z (transverse magnetic to z , v-pol) Floquet modes [15].

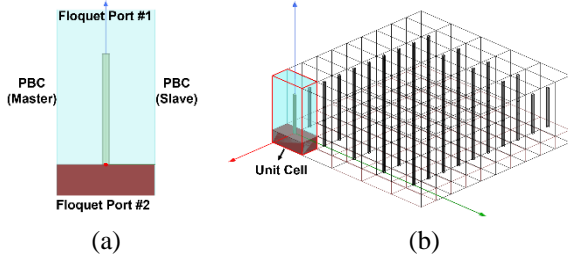


Fig. 1. HFSS modeling of a layer of vegetation: (a) unit cell and (b) infinite array of 3D structure.

A. Plane wave with oblique incidence

The S-parameters as a function of the observation angle can be obtained by defining the phase shift through the slave boundary, as shown in Fig. 2. Formulations in this section follow [16].

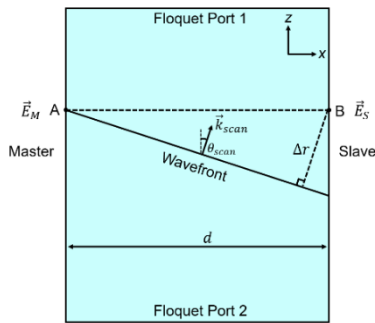


Fig. 2. A pair of master and slave boundaries.

The propagation vector of the radiated wave is given by:

$$\vec{k}_{\text{scan}} = k_0 [\cos \phi_{\text{scan}} \sin \theta_{\text{scan}}, \sin \phi_{\text{scan}} \sin \theta_{\text{scan}}, \cos \theta_{\text{scan}}], \quad (1)$$

where θ_{scan} and ϕ_{scan} are our intended direction in spherical coordinates, $k_0 = \omega \sqrt{\mu_0 \epsilon_0}$ is the free-space wave number, and ϵ_0 and μ_0 are the permittivity and permeability of free space, respectively. The radiated fields at Point A on the master boundary and at Point B on the slave boundary are represented relatively as:

$$\vec{E}_M = \vec{E}_0 \exp[j(\omega t - k_0 r_0)], \quad (2)$$

$$\vec{E}_S = \vec{E}_M \exp(-jk_0 \Delta r), \quad (3)$$

where, ω is the angular frequency. Assuming that the radiated wave is traveling in the xz -plane ($\phi_{\text{scan}} = 0$), as

shown in Fig. 2, the phase shift between Point A and B is obtained by (4), and Eq. (3) can be rewritten as (5):

$$\Delta r = d \sin \theta_{\text{scan}}, \quad (4)$$

$$\vec{E}_S = \vec{E}_M \exp(-jk_0 d \sin \theta_{\text{scan}}). \quad (5)$$

The relationship between the scan angle and the phase shift ($\Delta\Phi$) in degrees through a pair of master/slave boundaries can be expressed as:

$$\Delta\Phi = 360^\circ d \sin \theta_{\text{scan}} / \lambda. \quad (6)$$

Thus, we can excite a plane wave in our intended direction so that transmissivity is computed as a function of the observation angle.

B. TE_z and TM_z Floquet modal fields

The benefit of using the Floquet theory is to be able to derive the electromagnetic fields in terms of Floquet series when solving Maxwell's equations [17]. Also, an arbitrary uniform plane wave can be decomposed into the sum of orthogonal Floquet modal fields (TE_z and TM_z) such that the scattering problem is solved for each polarization. The mathematical expressions for the normalized Floquet modal fields are introduced, and formulations in this subsection follow [17]. The TE_z modal fields, which are referred to as the transverse electric field to z -axis, are generated from the electric vector potential \vec{F} with only z -component. In terms of Floquet harmonics, \vec{F} can be expressed as:

$$\vec{F} = \hat{z} A \exp[-j(k_{xmn} x + k_{ymn} y + k_{zmn} z)], \quad (7)$$

where A is a constant and k_{xmn} , k_{ymn} are the mode wave numbers for the TE_{zmn} Floquet mode. For a rectangular grid, the mode wave numbers for the (m, n) Floquet mode are given by:

$$k_{xmn} = k_{x0} + 2m\pi/a, \quad k_{ymn} = k_{y0} + 2n\pi/b, \quad (8)$$

where a and b are intervals on the xy -plane respectively and analogous to the unit cell size in x - and y -directions in our modeling; m and n are integers varying from $-\infty$ to $+\infty$; k_{x0} and k_{y0} are two constants that determine the progressive phase shift between the nearby cells and are related to the intended direction of radiation (θ_0, ϕ_0). This yields,

$$k_{x0} = k_0 \sin \theta_0 \cos \phi_0, \quad k_{y0} = k_0 \sin \theta_0 \sin \phi_0. \quad (9)$$

Then, the wave number along z -direction is expressed as:

$$k_{zmn}^2 = k^2 - k_{xmn}^2 - k_{ymn}^2, \quad (10)$$

where k is the wave number in the medium. It is noted that the propagation direction of the Floquet modal fields is parallel to the vector \vec{k}_{mn} as follows:

$$\vec{k}_{mn} = \hat{x} k_{xmn} + \hat{y} k_{ymn} + \hat{z} k_{zmn}. \quad (11)$$

The electric fields are derived by solving the relation $\vec{E} = -\nabla \times \vec{F}$. This yields,

$$\vec{E} = jA (\hat{x} k_{ymn} - \hat{y} k_{xmn}) \exp(-j\vec{k} \cdot \vec{r}), \quad (12)$$

where $\vec{r} = x\hat{x} + y\hat{y} + z\hat{z}$. The magnetic fields are also

determined by the Maxwell equation:

$$\nabla \times \vec{E} = -j\omega\mu\vec{H}, \quad (13)$$

as

$$\vec{H} = jAY_{mn}^{\text{TE}} \left(\hat{x}k_{xmn} + \hat{y}k_{ymn} - \hat{z} \frac{k^2 - k_{zmn}^2}{k_{zmn}} \right) \exp(-j\vec{k} \cdot \vec{r}), \quad (14)$$

where Y_{mn}^{TE} is the modal admittance for the TE_{zmn} Floquet mode, and given by:

$$Y_{mn}^{\text{TE}} = k_{zmn} / (\omega\mu). \quad (15)$$

The modal fields are normalized by choosing the constant term A such that the complex power through the Floquet port becomes equal to the complex conjugate of the modal admittance of the TE_{zmn} mode. This yields,

$$\iint_{\text{port}} (\vec{E} \times \vec{H}^*) \cdot \hat{z} \, dx \, dy = Y_{mn}^{\text{TE}*}. \quad (16)$$

Substituting (12) and (14) into (16) yields,

$$A = \frac{1}{j\sqrt{ab}(k^2 - k_{zmn}^2)}. \quad (17)$$

Finally, using (17) in (12), the TE_z modal fields are re-expressed as:

$$\vec{E} = \frac{\hat{x}k_{ymn} - \hat{y}k_{xmn}}{\sqrt{ab}(k^2 - k_{zmn}^2)} \exp(-j\vec{k} \cdot \vec{r}). \quad (18)$$

The TM_z Floquet modal fields can be also solved from the magnetic vector potential \vec{A} , which is expressed as:

$$\vec{A} = \hat{z}B \exp(-j\vec{k} \cdot \vec{r}), \quad (19)$$

where B is a constant. Applying the relation $\vec{H} = \nabla \times \vec{A}$ and the Maxwell equation $\nabla \times \vec{H} = j\omega\epsilon\vec{E}$, the modal admittance is obtained by:

$$Y_{mn}^{\text{TM}} = \omega\epsilon / k_{zmn}. \quad (20)$$

Using a similar procedure as above, the TM_z Floquet modal fields are expressed as:

$$\vec{H} = \frac{(-\hat{x}k_{ymn} + \hat{y}k_{xmn})}{\sqrt{ab}(k^2 - k_{zmn}^2)} \exp(-j\vec{k} \cdot \vec{r}). \quad (21)$$

In the context of our modeling, two factors are considered. First, the unit-cell size ($a \times b$) is determined based on the density of plants, the row spacing, and the average plant spacing. Also, since k_{zmn} is real or imaginary depending on the wavelength and the unit-cell size, it is essential to include all the propagation modes and exclude the evanescent modes [12]. This improves simulation efficiency and interpretation of the S-parameters of interests. Second, we utilize the S-parameter of the zeroth order Floquet mode ($m = n = 0$), which propagates along our intended angle (θ_0, ϕ_0) , as shown in Fig. 3.

C. Generalized scattering matrix

The HFSS solution provides us with S-parameters which are cast in the form of a generalized scattering matrix (GSM), as shown in Fig. 4, where a_{mn} and b_{mn}

are the incident voltage vectors at the two Floquet ports and c_{mn} and d_{mn} are the reflected voltage vectors corresponding to a_{mn} and b_{mn} . The S-matrix interrelates the TE_z (h-pol) and TM_z (v-pol) Floquet modes, where S_{11} and S_{22} are the reflection coefficients, and S_{12} and S_{21} are the transmission coefficients. Also, the coupling effect with two different polarizations is given in the GSM.

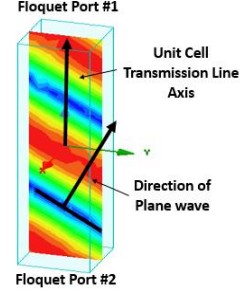


Fig. 3. Field overlays of the zeroth order Floquet mode with scan angle $(\theta_0, \phi_0) = (40^\circ, 90^\circ)$.

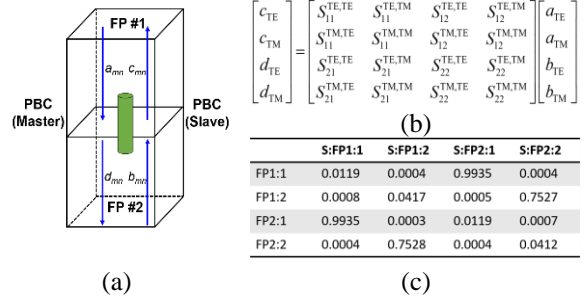


Fig. 4. (a) Configuration of the unit cell. (b) Generalized scattering matrix. (c) HFSS solution.

Therefore, we obtain the S-parameters for the vegetation canopy case consisting of an infinite number of 3D structures which represent the plants that make up the canopy of a row crop. The transmissivity, γ , of the vegetation canopy is computed as:

$$\gamma_u = \left[|S_{12}^{\text{hh}}|^2 + |S_{12}^{\text{hv}}|^2 + |S_{12}^{\text{vh}}|^2 + |S_{12}^{\text{vv}}|^2 \right] / 2, \quad (22)$$

$$\gamma_v = |S_{12}^{\text{vv}}|^2, \quad \gamma_h = |S_{12}^{\text{hh}}|^2, \quad (23)$$

where the superscripts and subscripts u, v , and h denote the unpolarized, vertically-polarized (v-pol), and horizontally-polarized (h-pol) transmissivities, respectively, and the denominator 2 is the total excitation power of two polarizations from Port 2. In detail, we assign the same power of 1 W to each TE_{00} and TM_{00} Floquet mode.

III. VALIDATION AND SIMULATIONS

Our method is validated with analytical solutions and then compared with results from [9-10, 18].

A. 2-layer and 3-layer case

A 2-layer case (air and soil) is simulated to compute the Fresnel reflectivity and transmissivity as shown in Fig. 5. The analytical solutions for $|S_{11}|^2$ and $|S_{21}|^2$ when the wave propagates from Port 1 to Port 2 are computed as:

$$|S_{11}|^2 = |R_{12}|^2 \quad \text{for v-pol and h-pol,} \quad (24)$$

$$|S_{21}|^2 = \begin{cases} e^{-2\alpha_{2z}d} \frac{\text{Im}[\gamma_{2z}]}{\text{Im}[\gamma_{1z}]} |T_{21}^h|^2 & \text{for h-pol,} \\ e^{-2\alpha_{2z}d} \frac{\text{Im}[\gamma_{2z}/\epsilon_2]}{\text{Im}[\gamma_{1z}/\epsilon_1]} |T_{21}^v|^2 & \text{for v-pol,} \end{cases} \quad (25)$$

where R is the Fresnel reflection coefficient, T is the transmission coefficient, subscripts 1 and 2 denote air and soil respectively, γ ($=\alpha + j\beta$) is the complex propagation constant consisting of the attenuation constant (α , Np/m) and the phase constant (β , rad/m), d is the soil depth, and the soil attenuation constant α_{2z} along the z -direction is calculated by:

$$\gamma_i = \alpha_i + j\beta_i = \sqrt{-\omega^2 \tilde{\epsilon}_i \mu_0}, \quad i=1,2$$

$$\gamma_{iz} = \alpha_{iz} + j\beta_{iz} = \sqrt{\gamma_i^2 - \gamma_{ix}^2}, \quad (26)$$

$$\gamma_{2x} = \gamma_{1x} = jk_1 \sin \theta_1,$$

where $\tilde{\epsilon}_i$ is the complex permittivity.

The analytical solutions for $|S_{22}|^2$ and $|S_{12}|^2$ when the waves propagate from Port 2 to 1 are computed as:

$$|S_{22}|^2 = e^{-4\alpha_{2z}d} |R_{21}|^2 \quad \text{for v-pol and h-pol,} \quad (27)$$

$$|S_{12}|^2 = \begin{cases} e^{-2\alpha_{2z}d} e^{-2\alpha_{1z}h} \frac{\text{Im}[\gamma_{1z}]}{\text{Im}[\gamma_{2z}]} |T_{12}^h|^2 & \text{for h-pol,} \\ e^{-2\alpha_{2z}d} e^{-2\alpha_{1z}h} \frac{\text{Im}[\gamma_{1z}/\tilde{\epsilon}_1]}{\text{Im}[\gamma_{2z}/\tilde{\epsilon}_2]} |T_{12}^v|^2 & \text{for v-pol,} \end{cases} \quad (28)$$

where h is the height of air layer, and the attenuation constants for each layer are calculated using (26) with $\gamma_{2x}^2 = \gamma_{1x}^2 = -\omega^2 \text{Re}[\tilde{\epsilon}_2] \mu_0 \sin^2 \theta_1$. Figures 6 and 7 show that the reflected or transmitted power can be computed accurately using our method.

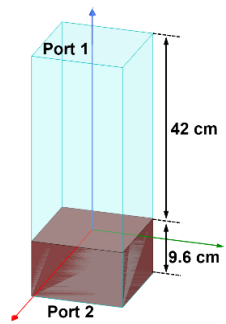
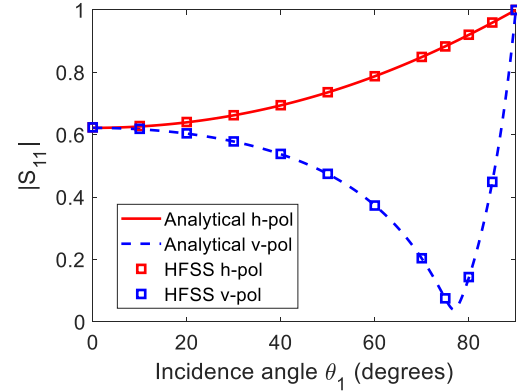
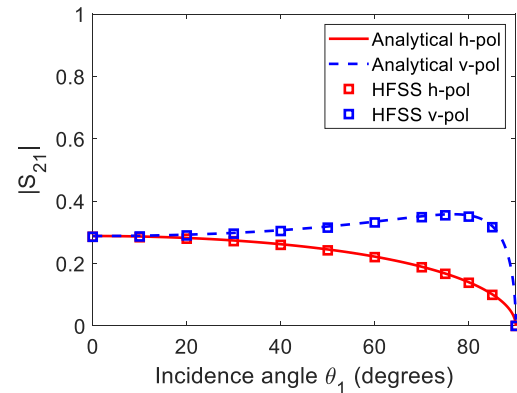


Fig. 5. HFSS model for the 2-layer case (soil and air) where the soil relative complex permittivity $\tilde{\epsilon}_{r,\text{soil}} = 18 - j3$ at the operation frequency of 1.41 GHz.



(a) Reflection coefficient



(b) Transmission coefficient

Fig. 6. Reflection coefficient $|S_{11}|$ and transmission coefficient $|S_{21}|$ of the 0th-order Floquet mode when the wave propagates downward in Fig. 5.

A 3-layer case where the vegetation canopy is added between the soil layer and the air layer in the unit cell as shown in Fig. 8 is also simulated to illustrate the effect of scattering.

In the homogeneous layer case, the vegetation canopy is treated as a homogeneous medium with an effective permittivity. The effective permittivity $\tilde{\epsilon}_{\text{eff}}$ ($= 1.98 - j0.35$) is obtained by:

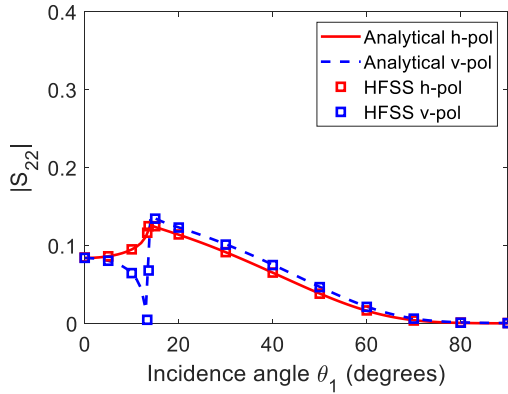
$$\tilde{\epsilon}_{\text{eff}} = \frac{V_{\text{air}}}{V_{\text{total}}} \epsilon_{\text{air}} + \frac{V_{\text{stem}}}{V_{\text{total}}} \tilde{\epsilon}_{\text{stem}}, \quad (29)$$

where the dimension of cylinder is 1.5 cm in radius and 30 cm in height, the volume fraction of cylinder (stem) is 7.1% ($V_{\text{total}} = 3 \times 10^{-3} \text{ m}^3$, $V_{\text{air}} = 2.788 \times 10^{-3} \text{ m}^3$ and $V_{\text{stem}} = 2.12 \times 10^{-4} \text{ m}^3$), and the cylinder's relative permittivity is $\tilde{\epsilon}_{\text{stem}} = 15 - j15$ [10]. The analytical solution for $|S_{11}|$ in the homogeneous layer case is computed as [19]:

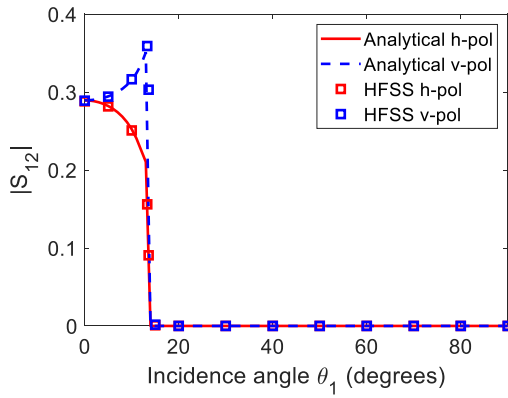
$$R^{\text{total}} = \frac{R_{12} + R_{23} e^{-2\gamma_{2z}h}}{1 + R_{12}R_{23} e^{-2\gamma_{2z}h}}, \quad (30)$$

where R^{total} is the total reflection coefficient of the wave propagating upward in medium 1 (air), R_{12} and R_{23} are

the half-space reflection coefficients at each interface, and h is the vegetation canopy’s height.



(a) Reflection coefficient



(b) Transmission coefficient

Fig. 7. Reflection coefficient $|S_{22}|$ and transmission coefficient $|S_{12}|$ of the 0th-order Floquet mode when the wave propagates upward in Fig. 5.

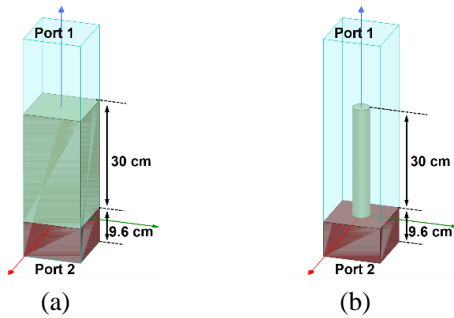
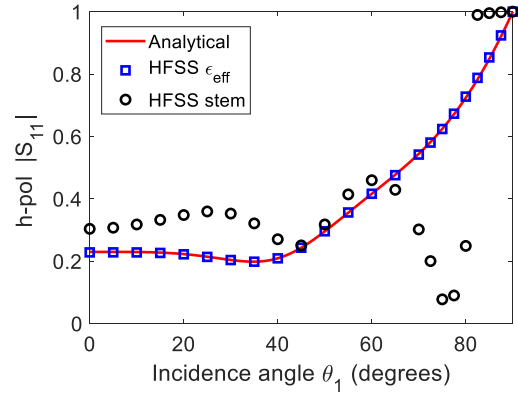


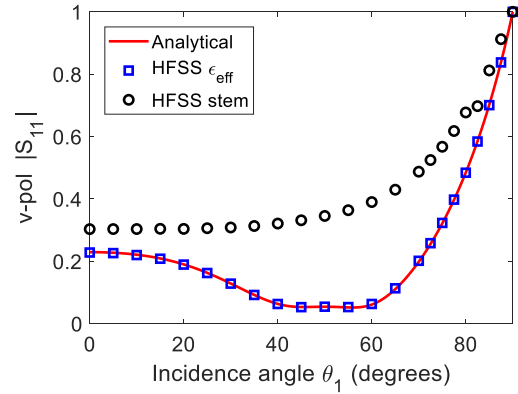
Fig. 8. HFSS model for the 3-layer case when the wave propagates downward from Port 1 to Port 2: (left) the homogeneous layer case (right) and the stem case.

In the stem case, where the vegetation canopy consists of an infinite number of finite-length cylinders, the incident wave from Port 1 induces currents on the

cylinders, which generate the scattered radiation. Therefore, $|S_{11}|$ in this case accounts for vegetation scattering and coherency induced by scattering between the stem and the soil surface. Fig. 9 shows that first, the results of the two approaches (analytical solution and homogeneous layer case) are in good agreement. Second, the reflectivity simulated using the homogenous layer and effective permittivity based on the volume fraction of air to stem is not the same as the reflectivity of the more realistic vegetation canopy (stem).



(a) H-pol



(b) V-pol

Fig. 9. Reflection coefficient $|S_{11}|$ of the 0th-order Floquet mode for each polarization when the wave propagates downward in Fig. 8.

B. Grass canopy

Two cases, as shown in Fig. 10 are compared with each other: the randomly distributed case was studied using the NMM3D (numerical Maxwell model in 3D simulations) [10], and the periodically distributed case is simulated in this work using the HFSS model.

Parameters used in these two cases are as follows: the cylinder has a radius of 1 mm, length of 30 cm, and relative complex permittivity of $30.7 - j5.5$, the operation frequency is 5.4 GHz (C-band), the density is 2122 cylinders per m^2 , and the incidence angle is 40° .

These parameters represent the water column density of a $1\text{ kg} \cdot \text{m}^{-2}$ grass canopy. The transmissivity of the grass canopy is computed by using the HFSS model, as shown in Fig. 11.

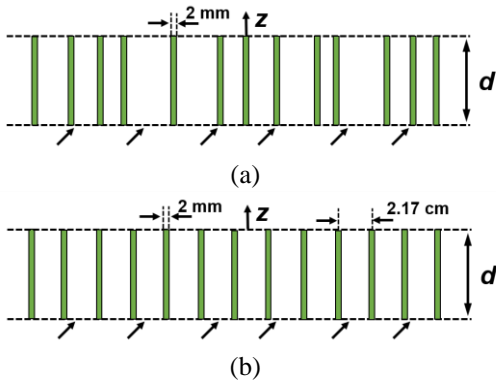


Fig. 10. One layer consisting of long and thin cylinders (a) randomly distributed [10] and (b) periodically distributed with a spacing of 2.17 cm between cylinders in both directions.

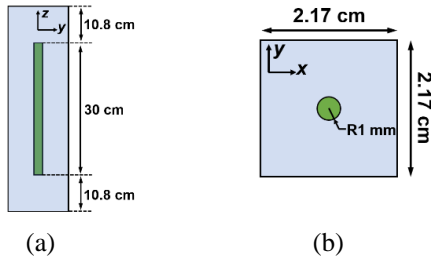


Fig. 11. Schematic of HFSS model for the grass canopy: (a) front view and (b) top view.

Table 1 shows the comparison between our method and the NMM3D for the cases of Fig. 10. The transmissivity found using our method for the periodically distributed case (0.78) is similar to, but not the same as, the transmissivity found using the NMM3D for the randomly distributed case (0.70). However, the standard deviation of multiple realizations of the randomly-distributed case is 0.2. We hypothesize that more coherent wave interactions take place among the vegetation scatters in the periodically distributed case than in the randomly distributed case.

For the model in Fig. 10 (b), we also compute the transmissivity for each polarization as a function of frequency. Figure 12 shows that the transmissivity decreases as the frequency increases. In other words, the grass vegetation canopy is increasingly opaque as the wavelength becomes shorter. Also, the loss for the

vertical polarization is greater than the horizontal polarization since the vegetation canopy consists of vertically-oriented stems.

Table 1: Transmissivity at an incident angle 40° for the grass canopy. $\tau = -\cos\theta \ln\gamma$

| Methodology / Distribution | HFSS / Periodically | NMM3D / Sparsely [10] |
|-----------------------------|---------------------|-----------------------|
| Transmissivity (γ) | 0.78 | 0.70 |
| VOD (τ) | 0.64 | 0.89 |

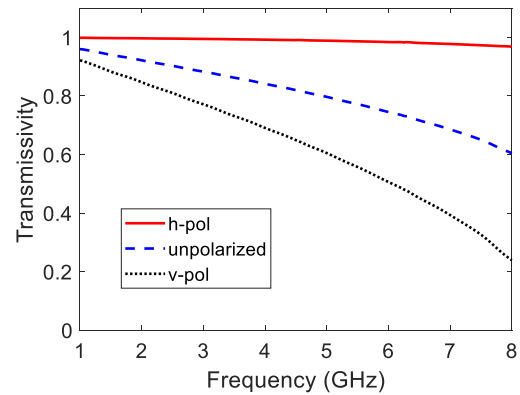


Fig. 12. Transmissivity at an incident angle 40° for the grass canopy as a function of frequency (f : 1 – 8 GHz, λ : 30 cm – 3.75 cm).

C. Corn canopy

Experimental observations for the vegetation canopy consisting of vertically oriented stalks were conducted in [9]. Parameters are as follows: row spacing is 76 cm, average plant spacing is 19.8 cm, average plant height is 2.7 m with average diameter 1.7 cm, relative complex permittivity is $16.9 - j5.6$, and the operation frequency is 1.62 GHz. Based on these parameters, the HFSS model is created, as shown in Fig. 13.

The radiation excited from the Floquet port is set up to propagate at $\theta = 20^\circ, 40^\circ, 60^\circ$, and $\phi = 90^\circ$ in accordance with the measurement set-up in the literature. The loss L in dB for the corn canopy can be computed as:

$$L_v = -20 \log(|S_{21}^{vv}|), \quad L_h = -20 \log(|S_{21}^{hh}|). \quad (31)$$

Table 2 shows the comparison between our method and the experimental observation. First, our simulation results are in the range of the measured data. Second, h-pol loss is less than v-pol loss. Also, it is observed that the loss increases as the incidence angle increases for the v-pol, whereas h-pol does not exhibit the same pattern. We hypothesize this is because the stem diameter of 1.7 cm is small compared to the wavelength of 18.5 cm.

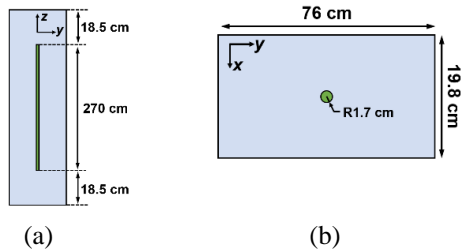


Fig. 13. Schematic of HFSS model for the corn canopy: (a) front view and (b) top view.

Table 2: Loss for the corn canopy where the experiment result presents the mean value of the measured loss and the $\pm 25\%$ confidence interval

| Incident angle | V-pol loss | |
|----------------|----------------------|--------|
| | Experiment [9] | HFSS |
| 20° | 1.4 dB (1.0–1.7 dB) | 1.0 dB |
| 40° | 5.3 dB (3.3–9.2 dB) | 6.3 dB |
| 60° | 8.5 dB (6.5–11.9 dB) | 9.0 dB |

| Incident angle | H-pol loss | |
|----------------|---------------------|--------|
| | Experiment [9] | HFSS |
| 20° | 0.7 dB (0.2–1.3 dB) | 0.4 dB |
| 40° | 0.7 dB (0–1.7 dB) | 0.2 dB |
| 60° | 1.2 dB (0.3–2.0 dB) | 0.3 dB |

IV. CONCLUSION

We used a method consisting of Floquet ports and periodic boundary conditions to model a layer of vegetation where an infinite number of vegetation elements (plants) are arrayed in the x - and y -direction like in a row crop. The scattered fields and its coherent interactions are considered by solving Maxwell's equations directly using HFSS, and the transmissivity is computed by utilizing the S -parameters. The simulation results from our proposed model and the NMM3D model for a grass canopy, as well as experimental measurements of a corn canopy, are similar. Some of the differences are likely due to the periodicity enforced in our method, which limits the distribution of vegetation elements within rows, when in reality the in-row spacing between elements is somewhat random. Our method could be used to find the transmissivity of different crops. In the future, we plan to enhance our plant models by adding leaf-like structures to the cylinders (stalks). We hope our method can eventually be used to find more realistic values of the parameters of the $\tau - \omega$ model used by SMOS and SMAP and consequently improved retrievals of soil moisture and VOD in croplands.

REFERENCES

- [1] D. Entekhabi, E. G. Njoku, P. E. O'Neill, K. H. Kellogg, W. T. Crow, W. N. Edelstein, J. K. Entin, S. D. Goodman, T. J. Jackson, J. Johnson, J. Kimball, J. R. Piepmeier, R. D. Koster, N. Martin, K. C. McDonald, M. Moghaddam, S. Moran, R. Reichle, J. C. Shi, M. W. Spencer, S. W. Thurman, L. Tsang, and J. Van Zyl, "The soil moisture active passive (SMAP) mission," *Proceedings of the IEEE*, vol. 98, no. 5, pp. 704-716, May 2010.
- [2] Y. H. Kerr, P. Waldteufel, J.-P. Wigneron, S. Delwart, F. Cabot, J. Boutin, M.-J. Escorihuela, J. Font, N. Reul, C. Gruhier, S. N. Juglea, M. R. Drinkwater, A. Hahne, M. Martín-Neira, and S. Mecklenburg, "The SMOS mission: New tool for monitoring key elements of the global water cycle," *Proceedings of the IEEE*, vol. 98, no. 5, pp. 666-687, May 2010.
- [3] J.-P. Wigneron, Y. Kerr, P. Waldteufel, K. Saleh, M.-J. Escorihuela, P. Richaume, P. Ferrazzoli, P. de Rosnay, R. Gurney, J.-C. Calvet, J.P. Grant, M. Guglielmetti, B. Hornbuckle, C. Mätzler, T. Pellarin, and M. Schwank, "L-band microwave emission of the biosphere (L-MEB) model: Description and calibration against experimental data sets over crop fields," *Remote Sensing of Environment*, vol. 107, no. 4, pp. 639-655, 2007.
- [4] P. O'Neill, S. Chan, E. Njoku, T. Jackson, and R. Bindlish, "Algorithm theoretical basis document level 2 & 3 soil moisture (passive) data products; revision B," *Jet Propulsion Lab., California Inst. Technol.: Pasadena, CA, USA*, 2017.
- [5] V. A. Walker, B. K. Hornbuckle and M. H. Cosh, "A five-year evaluation of SMOS level 2 soil moisture in the corn belt of the United States," *IEEE Journal of Selected Topics in Applied Earth Observations and Remote Sensing*, vol. 11, no. 12, pp. 4664-4675, Dec. 2018.
- [6] V. A. Walker, B. K. Hornbuckle, M. H. Cosh, and J. H. Prueger, "Seasonal evaluation of SMAP soil moisture in the U.S. corn belt," *Remote Sensing*, vol. 11, no. 21, pp. 5-7, 2019.
- [7] M. Kurum, "Quantifying scattering albedo in microwave emission of vegetated terrain," *Remote Sensing of Environment*, vol. 129, pp. 66-74, 2013.
- [8] B. K. Hornbuckle and T. L. Rowlandson, "Evaluating the first-order tau-omega model of terrestrial microwave emission," *IEEE International Geoscience and Remote Sensing Symposium (IGARSS)*, pp. 193-196, July 2008.
- [9] F. T. Ulaby, A. Tavakoli, and B. A. Thomas, "Microwave propagation constant for a vegetation canopy with vertical stalks," *IEEE Transactions on*

Geoscience and Remote Sensing, vol. 25, no. 6, pp. 714-725, Nov. 1987.

- [10] H. Huang, L. Tsang, E. G. Njoku, and A. Colliander, "A new vegetation model based on numerical 3D solutions of Maxwell equations," *IEEE International Geoscience and Remote Sensing Symposium (IGARSS)*, pp. 2903-2906, July 2017.
- [11] A. Colliander, E. G. Njoku, H. Huang, and L. Tsang, "Soil moisture retrieval using full wave simulations of 3-D Maxwell equations for compensating vegetation effects," *IEEE International Geoscience and Remote Sensing Symposium (IGARSS)*, pp. 1418-1421, July 2018.
- [12] HFSS documentation: Floquet Ports, Ansoft Corporation, Canonsburg, PA, USA, 2016.
- [13] M. Malajner and D. Gleich, "Soil moisture estimation using UWB," *Applied Computational Electromagnetics Society Conference*, pp. 298-299, Honolulu, HI, USA, Mar. 2016.
- [14] K. P. Prokopidis and T. D. Tsiboukis, "Modeling of ground-penetrating radar for detecting buried objects in dispersive soils," *Applied Computational Electromagnetics Society Journal*, vol. 22, no. 2, pp. 287-294, July 2007.
- [15] HFSS Workshop 9-1: Unit cell analysis (infinite array), Ansoft Corporation, Canonsburg, PA, USA, 2015.
- [16] S. N. Makarov and A. Puzella, "Scan impedance for an infinite dipole array: Hansen's formulas compared with Ansoft HFSS simulations [EM programmer's notebook]," *IEEE Antennas and Propagation Magazine*, vol. 49, no. 4, pp. 143-156, Aug. 2007.
- [17] A. K. Bhattacharyya, *Phased Array Antennas: Floquet Analysis, Synthesis, BFNs and Active Array Systems*, 1st ed. Wiley-Interscience, 2006.
- [18] C. A. Balanis, *Advanced Engineering Electromagnetics*, 2nd ed., pp. 188-208, John Wiley & Sons, 2012.
- [19] W. C. Chew, *Waves and Fields in Inhomogeneous Media*, 1st ed., pp. 49-53, Wiley-IEEE Press, 1995.



Jeil Park was born in Seoul, Korea. He received the B.E. degree from Korea Military Academy, Korea, in 2011 and the M.S. degree in Electrical Engineering from Iowa State University, USA, in 2020. He is servicing active duty in the ROK army. His research interests focus on modeling and simulations of vegetation canopy and scattering parameter analysis.



Praveen Gurralla received the B.Tech degree from Indian Institute of Technology Madras in 2014, and the Ph.D. degree from Iowa State University in 2020, both in electrical engineering. He is currently an EMI characterization engineer at Micron Technology, Inc. His research interests include computational modeling of ultrasonic and eddy current NDE inspections, fast-multipole boundary element methods, and capacitance tomography.



Brian K. Hornbuckle received the Ph.D. degree in Electrical Engineering and Atmospheric Science from the University of Michigan in 2003. He is presently a Professor in the Department of Agronomy at Iowa State University. Hornbuckle's research goal is to use satellite microwave remote sensing to monitor the movement of water among the soil, vegetation, and atmosphere in agricultural regions. He is a member of the IEEE Geoscience and Remote Sensing Society, the American Geophysical Union, the Soil Science Society of America, and the American Society of Agronomy.



Jiming Song received Ph.D. degree in Electrical Engineering from Michigan State University in 1993. From 1993 to 2000, he worked as a Postdoctoral Research Associate, a Research Scientist and Visiting Assistant Professor at the University of Illinois at Urbana-Champaign. From 1996 to 2000, he worked part-time as a Research Scientist at SAIC-DEMACO. Song was the principal author of the Fast Illinois Solver Code (FISC). He was a Principal Staff Engineer/Scientist at Semiconductor Products Sector of Motorola in Tempe, Arizona before he joined Department of Electrical and Computer Engineering at Iowa State University as an Assistant Professor in 2002.

Song currently is a Professor at Iowa State University's Department of Electrical and Computer Engineering. His research has dealt with modeling and simulations of electromagnetic, acoustic and elastic wave propagation, scattering, and non-destructive evaluation, electromagnetic wave propagation in metamaterials and periodic structures and applications, interconnects on lossy silicon and radio frequency components, antenna radiation and electromagnetic wave scattering using fast algorithms, and transient electromagnetic fields. He received the NSF Career Award in 2006 and is an IEEE Fellow and ACES Fellow.